

Fire Performance of Complex Light Gauge Steel Framed Wall Systems

By

Harikrishnan Magarabooshanam



*A thesis submitted to the
School of Civil and Environmental Engineering,
Queensland University of Technology
in fulfilment of the requirements for the degree of*

Doctor of Philosophy

School of Civil and Environmental Engineering
Science and Engineering Faculty
Queensland University of Technology
Australia
2020

[This page is intentionally left blank]

Keywords

Complex Light gauge steel-framed (LSF) walls, Cold-formed steel, Double stud, Staggered stud, Shaftliner, Time-temperature curve, Buckling, Load bearing, Non-load bearing Fire Dynamics Simulator (FDS), Effective cavity depth, Stud depth, Convection, Load ratio, Fire Resistance Level (FRL).

[This page is intentionally left blank]

Abstract

Cold-formed steel in the Australian construction industry is experiencing a phenomenal growth. In the residential sector light gauge steel framed (LSF) walls with single stud arrangement are commonly used as load bearing and non-load bearing walls. But in situations where higher acoustic insulation levels and load bearing capacities are required such as theatres, hospitals and town houses, complex LSF walls including double stud, shaftliner and staggered stud LSF walls are used. However, fire performance of these complex LSF walls has not been investigated adequately unlike in the case of single stud LSF walls. Fire resistance of LSF wall systems is important in the emerging mid-rise cold-formed steel construction. Many studies have been conducted in recent times to improve the acoustic, thermal (energy) and fire performance of non-load bearing LSF walls. Increasing the wall cavity depth provides superior acoustic and thermal performance characteristics of LSF walls. There is insufficient research data on the fire performance of these wall systems. The problems in determining the fire performance of these LSF walls have been identified and the investigations conducted in addressing the same are summarised below.

Firstly, this research investigated the fire performance of complex LSF walls under standard fire conditions using full scale test panels ($3\text{ m} \times 3\text{ m}$) made of lipped channel studs. Ten full-scale fire tests were conducted to investigate the fire performance of load bearing and non load bearing double stud, shaftliner and staggered stud walls. Ambient capacity tests on the double and staggered stud walls were also conducted to determine the ambient temperature axial load carrying capacities of these walls. Direct Strength Method based design capacity equations were also used to determine the ambient temperature axial compression capacities of these complex LSF wall systems and their suitability was also investigated. The fire test results of double stud, shaftliner and staggered stud LSF walls were then compared with those of single stud LSF walls with varying stud depth. The fire test results revealed the presence of a unique heat

transfer mechanism, resulting in an enhanced fire performance for these complex LSF walls. The discontinuous stud arrangement within the cavity of double stud LSF walls was identified as the main contributor for the delayed heat transfer mechanism. Fire test results show that the temperatures across the wall depth decrease with increasing cavity depth. LSF walls with two layers of plasterboard lining and wider cavity resulted in increased fire resistance. This research also highlights the detrimental effects of staggered stud LSF wall arrangement causing structural failure of thin-walled steel studs.

Cavity insulation is an integral part of the LSF wall system. However, the fire performance of the cavity insulated LSF walls are often misunderstood. Past research studies have investigated the fire performance of cavity insulated LSF walls. But, the research studies were again limited to LSF walls with single row of studs. Often, cavity insulated double and staggered stud LSF walls are used as partition walls in apartments under load bearing conditions and understanding their structural behaviour when exposed to fire becomes utmost necessity. This research study has also focused on investigating the fire performance of cavity insulated double stud LSF walls exposed to fire under load bearing conditions through full-scale fire tests. Attempts were also made to alter the position of the insulation within the cavity and investigate the effects through full-scale fire tests. This included positioning the insulation on the ambient side of the test wall and also by arranging it in a staggered pattern.

Since conducting full-scale fire tests are expensive and time consuming there arises a need to develop a robust numerical model to determine the thermal and structural performance of these complex LSF walls. Therefore attempts were made to develop numerical models in SAFIR, ABAQUS and FDS to determine the thermal performance of these complex LSF walls. The conventional thermal models developed through finite element (FE) method in ABAQUS was suitable for predicting the thermal behaviour of conventional single stud LSF walls. However, these models had many limitations such as neglecting the effects of convection within the cavity and longer computational time. Likewise the SAFIR thermal model over predicted the time-temperature curves. Also, the effects of radiation were assumed to be predominant mode of heat transfer within the cavity. Despite these limitations these models were used to validate single stud LSF wall fire tests as the effect of convection was less in these walls. However,

the presence of discontinuous stud arrangements within the cavity complicates the situation making the current FE thermal models to become ineffective in predicting the thermal performance of the complex LSF walls. It was found that the complex heat transfer mechanism in these LSF walls could be better simulated with FDS. Validations of the thermal models were made against the conducted full-scale fire tests and were found to exhibit good agreement. These models were then used to conduct a detailed parametric study on the LSF wall configurations which could not be tested through full-scale fire tests.

The FE structural models were created in ABAQUS to predict the ambient temperature axial compression capacities and the failure times of the complex LSF walls under fire. The developed FE structural model in ABAQUS was also able to predict the axial compression capacities and failure times of the conducted full-scale ambient temperature and fire tests. The developed numerical models resulted in reasonable agreement with the experimental results and was used to predict the thermal and structural response of the complex LSF walls with and without cavity insulation under different load ratios, thereby reducing the necessity of full-scale fire tests. The details, results and limitations of the thermal and structural models are also presented and discussed in detail.

Overall, this research has investigated in detail the fire performance of complex LSF walls which includes double stud, shaftliner and staggered stud LSF walls. The conducted experimental investigations alongside the developed numerical models have facilitated the enhancement of knowledge on the thermal and structural performance of the complex LSF walls systems, thereby providing helpful insights to the cold-formed steel industry.

[This page is intentionally left blank]

Publications

International Journal Papers

1. H. Magarabooshanam, A. Ariyanayagam, and M. Mahendran, “Behaviour of load bearing double stud LSF walls in fire,” *Fire Safety Journal*, vol. 107, pp. 15–28, Jul. 2019.
2. H. Magarabooshanam, A. Ariyanayagam, and M. Mahendran, “Fire resistance of non-load bearing LSF walls with varying cavity depth,” *Thin-Walled Structures*, vol. 105, May 2020, 106675.
3. H. Magarabooshanam, A. Ariyanayagam, and M. Mahendran, “Effect of Cavity Insulation on the Fire Performance of Double Stud LSF Walls,” (To be submitted)

Peer Reviewed International Conference Papers

1. H. Magarabooshanam, A. Ariyanayagam, and M. Mahendran, “Fire tests of load bearing double stud LSF walls,” in *Proceedings of the 10th International Conference on Structures in Fire 2018.*, 2018, pp. 641–648.
2. H. Magarabooshanam, A. Ariyanayagam, and M. Mahendran, “Behaviour of Load Bearing Staggered Stud LSF Walls in Fire,” (Accepted) in the *11th International Conference on Structures in Fire 2020*.

[This page is intentionally left blank]

Contents

Keywords	iii
Abstract	v
Publications	ix
List of Tables	xv
List of Figures	xvii
Acknowledgement	xxix
Abbreviations	xxxi
Statement of Original Authorship	xxxiii
1 Introduction	1-1
1.1 General	1-1
1.2 LSF Wall System	1-2
1.2.1 LSF Wall Components	1-2
1.2.2 Cold-formed Steel Sections	1-5
1.2.3 Buckling Behaviour of Cold-Formed Steel Members	1-6
1.2.4 Design Guidelines	1-7
1.2.5 Fire and Structural Performance of LSF walls	1-7
1.3 Complex LSF Wall Systems	1-9
1.4 Research Problem	1-11
1.5 Research Aim	1-12
1.6 Outline of Thesis	1-13
2 Literature Review	2-1
2.1 Background	2-1
2.2 Experimental and Numerical Investigations of LSF Walls	2-2
2.3 Thermal and Mechanical Properties of Cold-Formed Steels	2-23
2.4 Thermal Properties of Plasterboard	2-26
2.5 Numerical Simulation	2-28
2.6 Computational Fluid Dynamics (CFD)	2-40
2.7 Literature Review Findings	2-45

3 Experimental Investigations of LSF Walls under Ambient Conditions	3-1
3.1 General	3-1
3.2 Test Wall Panels	3-1
3.3 Test Set-up	3-3
3.4 Test-AT1	3-7
3.5 Test-AT2	3-8
3.6 Test-AT3	3-12
3.7 Test-AT4	3-15
3.8 Test-AT5	3-17
3.9 Summary of Ambient Temperature Capacity Test Results	3-22
3.10 Comparison of Ambient Temperature Capacity Test Results	3-23
3.11 Tensile Coupon Tests	3-28
3.12 Design Capacity Predictions Based on Direct Strength Method (DSM)	3-31
3.13 Summary of Findings	3-37
4 Experimental Investigations of Complex LSF Walls under Fire Conditions	4-1
4.1 General	4-1
4.2 Heat Transfer in LSF Walls	4-1
4.3 Small-Scale Fire Test of Double Stud LSF Walls	4-4
4.3.1 Small-Scale Fire Test Details	4-4
4.3.2 Small-Scale Fire Test - Results and Discussion	4-6
4.4 Full-scale Fire Tests of Double, Staggered and Shaftliner LSF Walls . .	4-8
4.4.1 Fire Test Panel Details	4-8
4.4.2 Temperature Sensors and Displacement Transducers	4-11
4.4.3 Fire Test Set-up and Procedure	4-13
4.5 Fire Test-T1	4-14
4.5.1 Test-T1 Failure Time and Mode, and Observations	4-14
4.5.2 Test-T1 Results and Discussion	4-17
4.6 Fire Test-T2	4-22
4.6.1 Test-T2 Failure Time and Mode, and Observations	4-22
4.6.2 Test-T2 Results and Discussion	4-22
4.7 Fire Test-T3	4-27
4.7.1 Test-T3 Failure Time and Mode, and Observations	4-27
4.7.2 Test-T3 Results and Discussion	4-27
4.8 Fire Test-T4	4-32
4.8.1 Test-T4 Failure Time and Mode, and Observations	4-32
4.8.2 Test-T4 Results and Discussion	4-33
4.9 Fire Test-T5	4-38
4.9.1 Test-T5 Failure Time and Mode, and Observations	4-38
4.9.2 Test-T5 Results and Discussion	4-41
4.10 Fire Test-T6	4-43
4.10.1 Test-T6 Failure Time and Mode, and Observations	4-43
4.10.2 Test-T6 Results and Discussion	4-46
4.11 Fire Test-T7	4-49
4.11.1 Test-T7 Failure Time and Mode, and Observations	4-49
4.11.2 Test-T7 Results and Discussion	4-50
4.12 Fire Test-T8	4-53
4.12.1 Test-T8 Failure Time and Mode, and Observations	4-53

4.12.2	Test-T8 Results and Discussion	4-55
4.13	Fire Test-T9	4-59
4.13.1	Test-T9 Failure Time and Mode, and Observations	4-59
4.13.2	Test-T9 Results and Discussion	4-63
4.14	Fire Test-T10	4-67
4.14.1	Test-T10 Failure Time and Mode, and Observations	4-67
4.14.2	Test-T10 Results and Discussion	4-71
4.15	Summary of Full-Scale Fire Tests	4-74
4.16	Comparison with Single Stud Wall Test Results	4-82
4.16.1	Comparison of Non-Cavity Insulated Fire Test Results - Tests-T1, T2, T4, SS-T1 and SS-T2	4-82
4.16.2	Comparison of Cavity Insulated Fire Test Results - Tests-T5, T7, T10 and SS-T3	4-88
4.16.3	Comparison of Non-Cavity Insulated Shaftliner and Staggered Stud Fire Test Results - Tests T8, T9 and SS-T4	4-91
4.16.4	Comparison of Axial Displacement and Lateral Deflection Versus Time Curves	4-93
4.17	Conclusions	4-96
5	Thermal FE Modelling of Complex LSF Walls	5-1
5.1	Introduction	5-1
5.2	Thermal modelling in SAFIR	5-3
5.3	Thermal modelling in ABAQUS	5-13
5.4	Thermal modelling in FDS	5-19
5.4.1	Thermal model description in FDS	5-19
5.4.2	Thermal model validation - Non-cavity insulated Tests-T1, T2, T3, T4, T8 and T9	5-21
5.4.3	Thermal model validation - Cavity insulated Tests-T5, T6, T7 and T10	5-34
5.4.4	Thermal model validation - Non-cavity insulated Tests-T1, T2, T3, T4, T8 and T9 with plasterboard open-up	5-43
5.4.5	Influence of Plasterboard Open-Up	5-50
5.5	Conclusions	5-59
6	Structural FE Modelling of Complex LSF Walls	6-1
6.1	Numerical Analysis of Complex LSF Walls-Ambient Conditions	6-1
6.2	ABAQUS Modelling Set-up	6-2
6.3	Structural FE Model Prediction - Ambient Temperature Capacity Tests	6-6
6.4	Summary of Ambient Temperature Capacity Predictions	6-14
6.5	Coupled Temperature Displacement Structural Analysis	6-16
6.6	Summary and Conclusions	6-45
7	Thermal and Structural FE Modelling Parametric Study	7-1
7.1	Introduction	7-1
7.2	Parameters considered	7-2
7.3	Thermal Parametric Models	7-5
7.3.1	Double stud wall with 70 mm studs	7-5
7.3.2	Double stud walls with 90 mm studs	7-13
7.3.3	Shaftliner stud walls with 70 mm studs	7-15

7.3.4	Shaftliner stud walls with 90 mm studs	7-23
7.3.5	Staggered stud walls with 70 mm studs	7-25
7.3.6	Staggered stud walls with 90 mm studs	7-30
7.4	Ambient Temperature Structural Models	7-36
7.5	Elevated Temperature Structural Models	7-39
7.5.1	FRL Predictions for Wall Configurations from Experimental Study	7-40
7.5.2	FRL Predictions for Wall Configurations from Parametric Study	7-43
7.5.2.1	FRL Predictions of Double Stud LSF Wall Configurations	7-43
7.5.2.2	FRL Predictions of Shaftliner LSF Wall Configurations	7-45
7.5.2.3	FRL Predictions of Staggered Stud LSF Wall Configurations	7-49
7.6	Summary and Conclusions	7-52
8	Conclusions	8-1
8.1	Summary	8-1
8.2	Research Outcomes	8-2
8.2.1	Selection of Complex LSF wall Systems	8-2
8.2.2	Ambient Temperature Structural Performance of Complex LSF Walls	8-2
8.2.3	Fire Performance of Complex LSF Walls	8-3
8.2.4	Thermal modelling of Complex LSF Walls	8-7
8.2.5	Structural modelling of Complex LSF Walls	8-8
8.3	Future Research and Recommendations	8-8
A	FDS code	A-1
B	Axial Compression Capacity Prediction based on DSM	B-1
C	Full-scale fire test results	C-1
Bibliography		xxxv

List of Tables

2.1	Test wall configurations used by Gunalan et al. (2013)	2-17
2.2	Reduction Factors for Cold-Formed Steels at Elevated Temperatures	2-24
3.1	Test wall panel details	3-2
3.2	Ambient temperature test capacity results	3-22
3.3	Comparison of ambient temperature test capacities	3-24
3.4	Tensile coupon test results of 0.75 mm thick studs	3-29
3.5	Tensile coupon test results of 0.95 mm thick studs	3-29
3.6	Elastic buckling loads of studs from CUFSM	3-32
3.7	Ultimate axial compression capacities from DSM predictions and experiment	3-35
4.1	Fire test panel details	4-9
4.2	Fire test results	4-75
4.3	Details of single and double stud wall tests considered for comparison	4-83
6.1	Ambient temperature capacity predictions by FEA and comparison with experimental capacities	6-16
7.1	FDS Thermal models considered in the parametric study	7-4
7.2	Ambient temperature axial compression capacities from structural FE models	7-38
7.3	FRL predictions of 70 mm and 90 mm deep studs configuration based on experiments	7-41
7.3	Continued...	7-42
7.4	FRL of double stud walls with 70 mm deep studs	7-44
7.5	FRLs of double stud walls with 90 mm deep studs	7-46
7.6	FRL of shaftliner walls with 70 mm deep studs	7-47
7.7	FRLs of shaftliner walls with 90 mm deep studs	7-48
7.8	FRLs of staggered stud walls with 70 mm deep studs	7-50
7.9	FRLs of staggered stud walls with 90 mm deep studs	7-51

[This page is intentionally left blank]

List of Figures

1.1	Mid-rise buildings with LSF walls	1-3
1.2	Components of LSF wall system	1-3
1.3	Plan view of LSF wall with Lipped C-Studs and double layers of plasterboard	1-4
1.4	Typical Cold-Formed Steel Sections (CFS)	1-5
1.5	Different buckling modes of a channel section column	1-6
1.6	Buckling plot from BS EN 1993-1-3 (2005a)	1-6
1.7	Different types of sections (a) Mono-symmetric (b) Double-symmetric (c) Point symmetric (d) Unsymmetric	1-8
1.8	Neutral axis shift due to thermal bowing (Gunalan and Mahendran, 2014)	1-9
1.9	Lateral deflection due to thermal bowing (Gunalan and Mahendran, 2014)	1-9
1.10	Typical complex LSF wall configurations (a) Double stud (b) Shaft-liner (c) Staggered stud	1-10
2.1	Major fire accidents in recent times	2-1
2.2	Compartment dimensions used by Manzello et al. (2005)	2-11
2.3	Proposed effective width table from Knobloch and Fontana (2006)	2-13
2.4	Lipped Channel Stud (LCS) failure in the fire test of Chen et al. (2013)	2-18
2.5	Hollow Flange Channel (HFC) studs used by Kesawan and Mahendran (2015)	2-19
2.6	Test configurations used by Dias et al. (2019a) (a) Internal and (b) External steel sheathing	2-22
2.7	Web-stiffened studs used by Dias et al. (2019a)	2-22
2.8	Thermal conductivity used by Kontogeorgos et al. (2011)	2-27
2.9	Thermal properties of plasterboard from Keerthan and Mahendran (2012b)	2-31
2.10	Proposed thermal properties of plasterboard from Keerthan and Mahendran (2012b)	2-32
2.11	Buckling analysis results from Gunalan and Mahendran (2013b)	2-33
2.12	Model and domain used by Horvat et al. (2009)	2-41
3.1	Cross-section of (a) 70 mm stud (b) 90 mm stud	3-3
3.2	Construction and testing of LSF wall panels (a) Construction (b) Finished test wall	3-4
3.3	Screw details	3-4
3.4	Typical loading set-up (a) Test rig (b) Test wall set-up (c) Staggered stud loading ram details (d) Staggered stud wall loading arrangement	3-5
3.4	Typical loading set-up (a) Test rig (b) Test wall set-up (c) Staggered stud loading ram details (d) Staggered stud wall loading arrangement	3-6

3.5	Test-AT1 wall configuration	3-7
3.6	Local compressive failure in Test-AT1 wall (a) Test wall (b) Stud3	3-8
3.7	Test-AT1 results - (a) Applied load versus axial displacement and (b) Applied load versus lateral deflection	3-9
3.8	Test-AT2 configuration	3-10
3.9	Local compressive failure in Test-AT2 wall (a) Test wall (b) Stud2	3-10
3.10	Test-AT2 results - (a) Applied load versus axial displacement and (b) Applied load versus lateral deflection	3-11
3.11	Test-AT3 configuration	3-12
3.12	Local bearing failure in Test-AT3	3-13
3.13	Test-AT3 results - (a) Applied load versus axial displacement and (b) Applied load versus lateral deflection	3-14
3.14	Test-AT4 configuration	3-15
3.15	Test-AT4 results - (a) Plasterboard crack and (b) Buckling of stud	3-15
3.16	Test-AT4 results - (a) Applied load versus axial displacement and (b) Applied load versus lateral deflection	3-16
3.17	Test-AT5 configuration	3-17
3.18	Test-AT5 wall components - (a) Omega nogging clip (b) Omega nog- ging rail (c) End cleat	3-18
3.19	Test-AT5 wall construction- (a) Omega nogging and clip connection (b) Staggered stud wall construction with end cleats	3-19
3.20	Test-AT5 - failure (a) Plasterboard open up (b) Buckling of studs in test wall (c) Buckling of studs - close up	3-20
3.21	Test-AT5 results - (a) Applied load versus axial displacement and (b) Applied load versus lateral deflection	3-21
3.22	Comparison of applied load versus axial displacement curves - 90 mm studs	3-25
3.23	Comparison of applied load versus axial displacement curves - 150 mm studs	3-25
3.24	Comparison of applied load versus axial displacement curves from Test-AT1 and AT5	3-26
3.25	Tensile coupon details	3-28
3.26	Tensile coupon test set-up	3-28
3.27	Stress-strain curves from tensile coupon tests of 0.75 mm G550 steel (a) Stud Web (b) Stud Flange	3-30
3.28	Stress-strain curves from tensile coupon tests of 0.95 mm G550 steel (a) Stud Web (b) Stud Flange	3-30
3.28	Stress-strain curves from tensile coupon tests of 0.95 mm G550 steel (a) Stud Web (b) Stud Flange	3-31
3.29	Signature curves from CUFSM finite strip analysis for Tests (a) AT1 (b) AT2 (c) AT4 (d) AT5	3-33
3.29	Signature curves from CUFSM finite strip analysis for Tests (a) AT1 (b) AT2 (c) AT4 (d) AT5	3-34
3.30	Buckling modes from CUFSM finite strip analysis for Test-AT1 at dif- ferent lengths (a) 70 mm (b) 300 mm (c) 500 mm (d) 1000 mm (e) 3000 mm	3-34
3.31	Buckling modes from CUFSM finite strip analysis for Test-AT2 at dif- ferent lengths (a) 70 mm (b) 300 mm (c) 1000 mm (d) 3000 mm	3-34

3.32	Buckling modes from CUFSM finite strip analysis for Test-AT4 at different lengths (a) 50 mm (b) 300 mm (c) 1000 mm (d) 3000 mm	3-35
3.33	Buckling modes from CUFSM finite strip analysis for Test-AT5 at different lengths (a) 40 mm (b) 200 mm (c) 300 mm (d) 1000 mm (e) 3000 mm	3-35
4.1	Typical section of (a) Double stud (b) Shaftliner and (c) Staggered stud LSF wall	4-2
4.2	Plan view of double stud LSF wall panels used in Test-ST1	4-5
4.3	Small-scale fire Test-ST1 (a) Test panel (b) Test set-up	4-5
4.4	Post-fire observations of Test-ST1 (a) Plasterboard fall-off (b) Studs after fire test	4-5
4.5	Plasterboard and stud time-temperature curves of Test-ST1 (a) Average plasterboard temperatures (b) Stud temperatures	4-7
4.6	Elevation of LSF Wall Panel showing LVDT and thermocouple locations	4-9
4.7	Typical stud and plasterboard thermocouple locations for (a) Double stud (b) Shaftliner and (c) Staggered stud LSF wall	4-10
4.8	Locations of plasterboard screws	4-10
4.9	Full scale fire test set-up (a) Furnace with pilot flame (b) Test panel	4-12
4.10	Instrumentation set-up (a) Furnace controller (b) UDAQ	4-13
4.11	Plan view of double stud LSF wall panels used in Tests-T1-T3	4-14
4.12	Test-T1-T4 wall construction sequence (a) Stud frame assembly (b) Plasterboard joint (c) Constructed test wall	4-15
4.13	Failure of Test-T1 wall (a) Fire exposed side (b) Crack on ambient side plasterboard (c) Local compressive failure of Stud3	4-16
4.14	Plasterboard and stud time-temperature curves of Test-T1 (a) Average plasterboard temperatures (b) Stud3 and 4 temperatures	4-18
4.15	Axial displacement and lateral deflection versus time curves from Test-T1 (a) Axial displacement versus time (b) Lateral deflection versus time curves	4-21
4.16	Failure of Test-T2 wall (a) Fire exposed side (b) Smoke patches and discolouration of ambient side plasterboard (c) Local compressive failure of Studs4 and 5	4-23
4.17	Plasterboard and stud time-temperature curves of Test-T2 (a) Average plasterboard temperatures (b) Studs3 and 4 temperatures	4-25
4.18	Axial displacement and lateral deflection versus time curves from Test-T2 (a) Axial displacement versus time (b) Lateral deflection versus time curves	4-26
4.19	Failure of Test-T3 wall (a) Fire exposed side (b) Ambient side plasterboard (c) Local compressive failure of Stud3	4-28
4.20	Plasterboard and stud time-temperature curves of Test-T3 (a) Average plasterboard temperatures (b) Studs3 and 4 temperatures	4-29
4.21	Axial displacement and lateral deflection versus time curves from Test-T3 (a) Axial displacement versus time (b) Lateral deflection versus time curves	4-31
4.22	Plan view of double stud LSF wall panel used in Test-T4	4-33
4.23	Failure of Test-T4 wall (a) Fire exposed side (b) Ambient side plasterboard (c) Local compressive failure of Studs2, 3 and 4	4-34

4.24 Plasterboard and stud time-temperature curves of Test-T4 (a) Average plasterboard temperatures (b) Stud3 and 4 temperatures	4-35
4.25 Axial displacement and lateral deflection versus time curves from Test-T4 (a) Axial displacement versus time (b) Lateral deflection versus time curves	4-37
4.26 Plan view of double stud LSF wall panels with cavity insulation on both stud rows used in Tests-T5 and T6	4-38
4.27 Test-T5 and T6 wall construction sequence (a) Cavity insulation installation (b) Constructed test wall	4-39
4.28 Failure of Test-T5 wall (a) Fire exposed side (b) Crack on ambient side plasterboard (c) Local compressive failure of Studs3 and 4	4-40
4.29 Plasterboard and stud time-temperature curves of Test-T5 (a) Average plasterboard temperatures (b) Stud3 and 4 temperatures	4-42
4.30 Axial displacement and lateral deflection versus time curves from Test-T5 (a) Axial displacement versus time (b) Lateral deflection versus time curves	4-44
4.31 Failure of Test-T6 wall (a) Fire exposed side (b) Crack on ambient side plasterboard (c) Discolouration of insulation (d) Local compressive failure of stud	4-45
4.32 Plasterboard and stud time-temperature curves of Test-T6 (a) Average plasterboard temperatures (b) Stud3 and 4 temperatures	4-47
4.33 Axial displacement and lateral deflection versus time curves from Test-T6 (a) Axial displacement versus time (b) Lateral deflection versus time curves	4-48
4.34 Plan view of double stud LSF wall panel with cavity insulation on ambient stud row used in Test-T7	4-49
4.35 Test-T7 wall construction	4-50
4.36 Failure of Test-T7 wall (a) Fire exposed side (b) Excessive bowing on ambient side plasterboard (c) Local compressive failure of stud	4-51
4.37 Plasterboard and stud time-temperature curves of Test-T7 (a) Average plasterboard temperatures (b) Stud3 and 4 temperatures	4-52
4.38 Axial displacement and lateral deflection curves from Test-T7 (a) Axial displacement versus time (b) Lateral deflection versus time curves	4-54
4.39 Plan view of shaftliner LSF wall panel used in Test-T8	4-55
4.40 Test-T8 wall construction sequence (a) Test frame assembly (b) Plasterboard installation (c) Constructed test wall	4-56
4.41 Failure of Test-T8 wall (a) Fire exposed side (b) Discolouration of ambient side plasterboard (c) Local compressive failure of studs	4-57
4.42 Plasterboard and stud time-temperature curves of Test-T8 (a) Average plasterboard temperatures (b) Studs3 and 4 temperatures (c) Ambient side plasterboard temperatures (Pb5)	4-58
4.42 Plasterboard and stud time-temperature curves of Test-T8 (a) Average plasterboard temperatures (b) Studs3 and 4 temperatures (c) Ambient side plasterboard temperatures (Pb5)	4-59
4.43 Axial displacement and lateral deflection versus time curves from Test-T8 (a) Axial displacement versus time (b) Lateral deflection versus time curves	4-60
4.44 Plan view of staggered stud LSF wall panel used in Test-T9	4-61

4.45	Test-T9 wall construction sequence (a) Test wall frame construction (b) Test frame end connection (c) Constructed test wall	4-61
4.46	Failure of Test-T9 wall (a) Fire exposed side (b) Discolouration of ambient side plasterboard and excessive thermal bowing (c) Local compressive failure of studs	4-62
4.47	Plasterboard and stud time-temperature curves of Test-T9 (a) Average plasterboard temperatures (b) Studs3 and 4 temperatures (c) Ambient side plasterboard temperatures (Pb5)	4-65
4.48	Axial displacement and lateral deflection versus time curves from Test-T9 (a) Axial displacement versus time (b) Lateral deflection versus time curves	4-66
4.49	Plan view of staggered stud LSF wall panel with cavity insulation used in Test-T10	4-67
4.50	Test-T10 wall construction sequence (a) Test frame construction (b) Cavity insulation installation (c) Constructed test wall	4-68
4.51	Failure of Test-T9 wall (a) Fire exposed side (b) Crack on ambient side plasterboard and joint (c) Discolouration of glass fibre insulation (d) Buckling of fire side studs	4-69
4.51	Failure of Test-T9 wall (a) Fire exposed side (b) Crack on ambient side plasterboard and joint (c) Discolouration of glass fibre insulation (d) Buckling of fire side studs	4-70
4.52	Plasterboard and stud time-temperature curves of Test-T10 (a) Average plasterboard temperatures (b) Stud3 temperatures	4-72
4.53	Axial displacement and lateral deflection versus time curves from Test-T10 (a) Axial displacement versus time (b) Lateral deflection versus time curves	4-73
4.54	Comparison of average plasterboard time-temperature curves from Tests (a) T1, T2 and T3 (b) T1 and T4	4-76
4.55	Comparison of critical stud time-temperature curves from (a) T1, T2 and T3 (b) T1 and T4	4-77
4.56	Comparison of average plasterboard time-temperature curves from Tests-T1, T8 and T9	4-79
4.57	Critical stud time-temperature curve comparison between Tests-T1, T8 and T9	4-80
4.58	Comparison of average plasterboard time-temperature curves from Tests-T5, T6, T7 and T10	4-81
4.59	Comparison of critical stud time-temperature curves from Tests-T5, T6, T7 and T10	4-81
4.60	Comparison of average plasterboard time-temperature curves from Tests-T1, T2, SS-T1 and SS-T2	4-84
4.61	Comparison of average plasterboard time-temperature curves from Tests-T1, T4, SS-T1 and SS-T2	4-85
4.62	Comparison of critical stud time-temperature curves from Tests-T1, T2, SS-T1 and SS-T2	4-86
4.63	Comparison of critical stud time-temperature curves from Tests-T1, T4, SS-T1 and SS-T2	4-87
4.64	Comparison of average plasterboard time-temperature curves from Tests-T5, T7, T10 and SS-T3	4-89

4.65 Comparison of critical stud time-temperature curves from Tests-T5, T7, T10 and SS-T3	4-90
4.66 Comparison of average plasterboard time-temperature curves from Tests-T8, T9 and SS-T4	4-91
4.67 Comparison of critical stud time-temperature curves from Tests-T8, T9 and SS-T4	4-92
4.68 Comparison of axial displacement and lateral deflection versus time curves from Tests-T1, T2, T4, SS-T1 and SS-T2 results - (a) Axial displacement versus time and (b) Lateral deflection versus time	4-94
4.69 Comparison of axial displacement and lateral deflection versus time curves from Tests-T5, T6, T7 and SS-T3 results - (a) Axial displacement versus time and (b) Lateral deflection versus time	4-95
5.1 Heat transfer mechanism in (a) Single stud (b) Double stud LSF walls	5-2
5.2 Elevated temperature thermal properties of plasterboard from Dodangoda (2018) (a) Conductivity versus temperature (b) Specific heat versus temperature (c) Density versus temperature	5-4
5.2 Elevated temperature thermal properties of plasterboard from Dodangoda (2018) (a) Conductivity versus temperature (b) Specific heat versus temperature (c) Density versus temperature	5-5
5.3 Elevated temperature thermal properties of steel from Dodangoda (2018) (a) Conductivity versus temperature (b) Specific heat versus temperature	5-5
5.4 Elevated temperature thermal properties of glass fibre insulation from Dodangoda (2018) (a) Conductivity versus temperature (b) Specific heat versus temperature	5-6
5.4 Elevated temperature thermal properties of glass fibre insulation from Dodangoda (2018) (a) Conductivity versus temperature (b) Specific heat versus temperature	5-6
5.5 2D model of Test-T1 in SAFIR using GiD interface	5-7
5.6 2D model mesh of Test-T1 in SAFIR using GiD interface	5-8
5.7 Thermal analysis output from SAFIR 2D model	5-9
5.8 Thermal analysis output of studs from SAFIR 2D model (a) Fire side stud (b) Ambient side stud	5-9
5.9 Comparison of the time temperature curves from SAFIR thermal analysis and experiments (a) Average plasterboard temperatures (b) Stud4-Mid temperatures	5-11
5.10 3D model of double stud wall in ABAQUS	5-14
5.11 Mesh arrangement in the thermal model from ABAQUS	5-15
5.12 Thermal analysis output from ABAQUS for wall	5-15
5.13 Thermal analysis output from ABAQUS for studs	5-16
5.14 Comparison of time-temperature curves from ABAQUS thermal analysis and experiments (a) Average plasterboard temperatures (b) Stud4-Mid temperatures	5-18
5.15 Model of Double Stud LSF Wall Panel	5-20
5.16 Thermal model of Test-T1 wall	5-22
5.17 Output from FDS thermal analysis (a) Temperature profile (b) Velocity slice for convection	5-22

5.18	Comparison of time-temperature curves from experiment and FDS model for Test-T1 (a) Average Plasterboard (b) Stud4-Mid	5-24
5.19	Comparison of time-temperature curves from experiment, SAFIR, FDS and ABAQUS models for Test-T1 (a) Average Plasterboard (b) Stud4-Mid	5-25
5.20	Comparison of time-temperature curves from experiment and FDS model for Test-T2 (a) Average Plasterboard (b) Stud3-Mid	5-26
5.21	Comparison of time-temperature curves from experiment and FDS model for Test-T3 (a) Average Plasterboard (b) Stud4-Mid	5-28
5.22	Comparison of time-temperature curves from experiment and FDS model for Test-T4 (a) Average Plasterboard (b) Stud3-Mid	5-29
5.23	Thermal model of Test-T8 wall	5-30
5.24	Thermal model output for Test-T8 wall	5-30
5.25	Comparison of time-temperature curves from experiment and FDS model for Test-T8 (a) Average Plasterboard (b) Stud4-Mid	5-31
5.26	Thermal model of Test-T9 wall	5-32
5.27	Thermal output for Test-T9 wall	5-32
5.28	Comparison of time-temperature curves from experiment and FDS model for Test-T9 (a) Average Plasterboard (b) Stud4-Mid	5-33
5.29	Thermal model of Test-T5 wall	5-35
5.30	Comparison of time-temperature curves from experiment and FDS model for Test-T5 (a) Average Plasterboard (b) Stud3-Mid	5-36
5.31	Temperature output for Test-T5 from FDS thermal analysis (a) Before plasterboard open-up at 78 min (b) After plasterboard open-up at 79 min (c) At 240 min (End of Simulation)	5-37
5.32	Comparison of time-temperature curves from experiment and FDS model for Test-T6 (a) Average Plasterboard (b) Stud4-Mid	5-38
5.33	Thermal model of Test-T7 wall	5-39
5.34	Comparison of time-temperature curves from experiment and FDS model for Test-T7 (a) Average Plasterboard (b) Stud3-Mid	5-40
5.35	Temperature output for Test-T7 from FDS thermal analysis (a) Before plasterboard open-up at 79 min (b) After plasterboard open-up at 80 min (c) At 240 min (End of Simulation)	5-41
5.36	Thermal model of Test-T10 wall	5-41
5.37	Comparison of time-temperature curves from experiment and FDS model for Test-T10 (a) Average Plasterboard (b) Stud3-Mid	5-42
5.38	Temperature output for Test-T10 from FDS thermal analysis (a) Before plasterboard open-up at 79 min (b) After plasterboard open-up at 80 min (c) At 240 min (End of Simulation)	5-43
5.39	Comparison of time-temperature curves from experiment and FDS model with plasterboard open-up for Test-T1 (a) Average Plasterboard (b) Stud4-Mid	5-44
5.40	Comparison of time-temperature curves from experiment and FDS model with plasterboard open-up for Test-T2 (a) Average Plasterboard (b) Stud4-Mid	5-45
5.41	Comparison of time-temperature curves from experiment and FDS model with plasterboard open-up for Test-T3 (a) Average Plasterboard (b) Stud4-Mid	5-47

5.42 Comparison of time-temperature curves from experiment and FDS model with plasterboard open-up for Test-T4 (a) Average Plasterboard (b) Stud3-Mid	5-48
5.43 Comparison of time-temperature curves from experiment and FDS model with plasterboard open-up for Test-T8 (a) Average Plasterboard (b) Stud4-Mid	5-49
5.44 Comparison of time-temperature curves from experiment and FDS model with plasterboard open-up for Test-T9 (a) Average Plasterboard (b) Stud4-Mid	5-51
5.45 Comparison of time-temperature curves from FDS model with and without plasterboard open-up for Test-T1 (a) Plasterboard (b) Studs	5-53
5.46 Comparison of time-temperature curves from FDS model with and without plasterboard open-up for Test-T2 (a) Plasterboard (b) Studs	5-54
5.47 Comparison of time-temperature curves from FDS model with and without plasterboard open-up for Test-T3 (a) Plasterboard (b) Studs	5-55
5.48 Comparison of time-temperature curves from FDS model with and without plasterboard open-up for Test-T4 (a) Plasterboard (b) Studs	5-56
5.49 Comparison of time-temperature curves from FDS model with and without plasterboard open-up for Test-T8 (a) Plasterboard (b) Studs	5-57
5.50 Comparison of time-temperature curves from FDS model with and without plasterboard open-up for Test-T9 (a) Plasterboard (b) Studs	5-58
6.1 Input screen for sketching showing typical LCS stud - ABAQUS	6-3
6.2 Typical double stud model in ABAQUS (a) Support condition (b) Mesh density	6-5
6.3 Support and restraint conditions of double stud wall model in ABAQUS	6-5
6.4 Test-AT1 wall configuration	6-7
6.5 Comparison of load versus displacement curves of Test-AT1 wall from FEA and experiment	6-7
6.6 Buckling failure of studs in Test-AT1 wall (a) FEA (b) Experiment	6-8
6.7 Test-AT2 wall configuration	6-9
6.8 Comparison of load versus displacement curves of Test-AT2 wall from FEA and experiment	6-9
6.9 Buckling failure of studs in Test-AT2 wall (a) FEA (b) Experiment	6-10
6.10 Test-AT3 wall configuration	6-11
6.11 Comparison of load versus displacement curves of Test-AT3 wall from FEA and experiment	6-11
6.12 Test-AT4 wall configuration	6-12
6.13 Comparison of load versus displacement curves of Test-AT4 wall from FEA and experiment	6-12
6.14 Buckling failure of studs in Test-AT4 wall (a) FEA (b) Experiment	6-13
6.15 Test-AT5 wall configuration	6-14
6.16 Test-AT5 - Staggered stud model (a) MPC beam constraints to simulate end restraints (b) MPC beam constraints at service holes to simulate nogging restraints (c) Sweep meshes around service holes	6-15
6.17 Comparison of load versus displacement curves of Test-AT5 wall from FEA and experiment	6-15
6.18 Buckling failure of studs in Test-AT5 wall (a) FEA (b) Experiment	6-16

6.19	Temperature variation of studs in double stud LSF walls	6-17
6.20	Elevated temperature mechanical properties of G550 steel from Kankanamge and Mahendran (2011)	6-18
6.21	Test-T1 wall configuration	6-20
6.22	Comparison of displacement versus time curves of Test-T1 from FEA based on stud flange temperatures from experiment and experimental results (a) Axial displacement versus time (b) Lateral deflection versus time curves	6-22
6.23	Buckling failure of studs in Test-T1 wall (a) FEA based on stud temperatures from experiment (b) Experiment	6-23
6.24	Comparison of displacement versus time curves of Test-T1 from FEA based on stud flange temperatures from FDS and experiment (a) Axial displacement versus time (b) Lateral deflection versus time curves . .	6-24
6.25	Buckling failure of studs in Test-T1 wall (a) FEA based on stud flange temperatures from FDS (b) Experiment	6-25
6.26	Comparison of displacement versus time curves of Test-T2 from FEA and experiment (a) Axial displacement versus time (b) Lateral deflection versus time curves	6-27
6.27	Buckling failure of studs in Test-T2 wall (a) FEA (b) Experiment . .	6-28
6.28	Comparison of displacement versus time curves of Test-T3 from FEA and experiment (a) Axial displacement versus time (b) Lateral deflection versus time curves	6-30
6.29	Buckling failure of studs in Test-T3 wall (a) FEA (b) Experiment . .	6-31
6.30	Test-T4 wall configuration	6-32
6.31	Comparison of displacement versus time curves of Test-T4 from FEA and experiment (a) Axial displacement versus time (b) Lateral deflection versus time curves	6-34
6.32	Buckling of studs in Test-T4 wall (a) FEA (b) Experiment	6-35
6.33	Test-T5 wall configuration	6-36
6.34	Comparison of displacement versus time curves of Test-T5 from FEA and experiment (a) Axial displacement versus time (b) Lateral deflection versus time curves	6-37
6.35	Buckling failure of studs in Test-T5 wall (a) FEA (b) Experiment . .	6-38
6.36	Comparison of displacement versus time curves of Test-T6 from FEA and experiment (a) Axial displacement versus time (b) Lateral deflection versus time curves	6-39
6.37	Buckling failure of studs in Test-T6 wall (a) FEA (b) Experiment . .	6-40
6.38	Test-T7 wall configuration	6-42
6.39	Buckling of studs in Test-T7 wall (a) FEA (b) Experiment	6-43
6.40	Comparison of displacement versus time curves of Test-T7 from FEA and experiment (a) Axial displacement versus time (b) Lateral deflection versus time curves	6-44
6.41	Test-T10 plan view	6-45
6.42	Comparison of displacement versus time curves of Test-T10 from FEA and experiment (a) Axial displacement versus time (b) Lateral deflection versus time curves	6-46
6.43	Buckling failure of studs in Test-T10 wall (a) FEA (b) Experiment . .	6-47

7.1	Double Stud Wall with 70 mm studs (a) No insulation (b) Ambient side cavity insulation (c) Both sides cavity insulation	7-3
7.2	Shaftliner Wall with 70 and 90 mm studs (a) 70 mm wall no cavity insulation (b) 70 mm wall full cavity insulation (c) 90 mm wall full cavity insulation	7-3
7.3	Staggered Stud Wall with 70 mm studs (a) No insulation (b) Full cavity insulation	7-3
7.4	Staggered Stud Wall with 90 mm studs (a) No insulation (b) Full cavity insulation	7-4
7.5	General notation for thermal parametric models	7-4
7.6	Model DS-70-0.75 - Plasterboard and stud time-temperature curves of non-cavity insulated double stud wall with 70×0.75 mm studs - (a) Plasterboard temperatures (b) Stud temperatures	7-7
7.7	Model DS-70-0.75-AI - Plasterboard and stud time-temperature curves of ambient cavity insulated double stud wall with 70×0.75 mm studs - (a) Plasterboard temperatures (b) Stud temperatures	7-8
7.8	Model DS-70-0.75-BI - Plasterboard and stud time-temperature curves of both sides cavity insulated double stud wall with 70×0.75 mm studs - (a) Plasterboard temperatures (b) Stud temperatures	7-10
7.9	Model DS-70-0.95-AI - Plasterboard and stud time-temperature curves of both sides cavity insulated double stud wall with 70×0.95 mm studs - (a) Plasterboard temperatures (b) Stud temperatures	7-11
7.10	Model DS-70-0.95-BI - Plasterboard and stud time-temperature curves of both cavity insulated double stud wall with 70×0.95 mm studs - (a) Plasterboard temperatures (b) Stud temperatures	7-12
7.11	Model DS-90-0.75-AI - Plasterboard and stud time-temperature curves of ambient side cavity insulated double stud wall with 90×0.75 mm studs - (a) Plasterboard temperatures (b) Stud temperatures	7-14
7.12	Model DS-90-0.75-BI - Plasterboard and stud time-temperature curves of both cavity insulated double stud wall with 90×0.75 mm studs - (a) Plasterboard temperatures (b) Stud temperatures	7-16
7.13	Model SL-70-0.75 - Plasterboard and stud time-temperature curves of non-cavity insulated shaftliner wall with 70×0.75 mm studs - (a) Plasterboard temperatures (b) Stud temperatures	7-17
7.14	Model SL-70-0.75-FI - Plasterboard and stud time-temperature curves of cavity insulated shaftliner wall with 70×0.75 mm studs - (a) Plasterboard temperatures (b) Stud temperatures	7-19
7.15	Model SL-70-0.95 - Plasterboard and stud time-temperature curves of non-cavity insulated shaftliner wall with 70×0.95 mm studs - (a) Plasterboard temperatures (b) Stud temperatures	7-20
7.16	Model SL-70-0.95-FI - Plasterboard and stud time-temperature curves of cavity insulated shaftliner wall with 70×0.95 mm studs - (a) Plasterboard temperatures (b) Stud temperatures	7-22
7.17	Model SL-90-0.75-FI - Plasterboard and stud time-temperature curves of cavity insulated shaftliner wall with 90×0.75 mm studs - (a) Plasterboard temperatures (b) Stud temperatures	7-24

7.18	Model SL-90-0.95 - Plasterboard and stud time-temperature curves of non-cavity insulated shaftliner wall with 90×0.95 mm studs - (a) Plasterboard temperatures (b) Stud temperatures	7-26
7.19	Model SL-90-0.95-FI - Plasterboard and stud time-temperature curves of cavity insulated shaftliner wall with 90×0.95 mm studs - (a) Plasterboard temperatures (b) Stud temperatures	7-27
7.20	Model ST-70-0.75 - Plasterboard and stud time-temperature curves of non-cavity insulated staggered stud wall with 70×0.75 mm studs - (a) Plasterboard temperatures (b) Stud temperatures	7-28
7.21	Model ST-70-0.75-FI - Plasterboard and stud time-temperature curves of cavity insulated staggered stud wall with 70×0.75 mm studs - (a) Plasterboard temperatures (b) Stud temperatures	7-29
7.22	Model ST-70-0.95 - Plasterboard and stud time-temperature curves of non-cavity insulated staggered stud wall with 70×0.95 mm studs - (a) Plasterboard temperatures (b) Stud temperatures	7-31
7.23	Model ST-70-0.95-FI - Plasterboard and stud time-temperature curves of cavity insulated staggered stud wall with 70×0.95 mm studs - (a) Plasterboard temperatures (b) Stud temperatures	7-32
7.24	Model ST-90-0.75-FI - Plasterboard and stud time-temperature curves of cavity insulated staggered stud wall with 70×0.75 mm studs - (a) Plasterboard temperatures (b) Stud temperatures	7-34
7.25	Model ST-90-0.95 - Plasterboard and stud time-temperature curves of non-cavity insulated staggered stud wall with 90×0.95 mm studs - (a) Plasterboard temperatures (b) Stud temperatures	7-35
7.26	Ambient temperature axial compression capacity of complex LSF walls considered in the parametric study (a) DS-70-0.75, (b) SL-70-0.75, (c) SL-70-0.95, (d) SL-90-0.75, (e) SL-90-0.95, (f) ST-70-0.75, (g) ST-70-0.95, (h) ST-90-0.75	7-37
7.27	Comparison of axial compression load-displacement curves from experiment and parametric FE model	7-38
7.28	FRL of LSF wall configurations from experimental study	7-40
7.29	FRLs of double stud wall configurations from parametric study	7-43
7.30	FRLs of shaftliner wall configurations from parametric study	7-47
7.31	FRL of staggered stud wall configurations from parametric study	7-50
B.1	Nominal external dimensions of stud	B-1

[This page is intentionally left blank]

Acknowledgement

I would like to express my sincere thanks and gratitude to my principal supervisor Professor Mahen Mahendran, for his guidance, support and encouragement throughout my research. I am also grateful to my associate supervisor Dr Anthony Ariyanayagam for not only guiding me throughout this research, but also for the help and support both in professional and personal levels. The support from both my supervisors were invaluable without which completing this thesis would have been a nightmare.

I am grateful to the Queensland University of Technology (QUT) for supporting me with the QUTPRA award for my research. I also wish to express my sincere thanks to the Australian Research Council (ARC), National Association of Steel Framed Housing (NASH) and Stoddart group for providing the required materialistic support to conduct this research.

Many thanks to Barry Hume and Glenn Atlee and all the other supporting staffs at QUT Banyo Pilot Plant Precinct for providing their assistance in conducting the experimental study for this research. My heartiest thanks to my fellow researchers Edward, Jashnav, Nilakshi, Janarthanan, Myuran, Thananjayan, Sayilacksha, Yomal, Imran, Rusthi for their help and support during this research at professional and personal levels. My Sincere thanks to all the undergraduate students who assisted me with the experimental study.

Finally, I would like to express my gratitude to my parents for their support, encouragement and blessings and my family members for their extended support. I am grateful to my wife Niveditha, the woman behind my success for her unconditional love, care and support.

[This page is intentionally left blank]

Abbreviations

AS/NZS - Australian Standard/New Zealand Standard

AISI - American Iron and Steel Institute

BS - British Standard

CFS - Cold-formed steel

CFD - Computational Fluid Dynamics

DSC - Differential Scanning Calorimetry

EDTA - Ethylenediaminetetraacetic acid

FEA - Finite Element Analysis

FRL - Fire Resistance Level

FSM - Finite Strip Method

NCC - National Construction Code

LCS - Lipped Channel Section

LSF - Light Gauge Steel Frame

LR - Load Ratio

LVDT - Linear Variable Displacement Transducers

UB - Universal Beam

UCS - Unlipped Channel Sections

UC - Universal Column

[This page is intentionally left blank]

Statement of Original Authorship

The work contained in this thesis has not been previously submitted to meet requirements for an award at this or any other higher education institution. To the best of my knowledge and belief, the thesis contains no material previously published or written by another person except where due reference is made.

Signature.....

Date.....

[This page is intentionally left blank]

Chapter 1

Introduction

1.1 General

Walls in the building construction industry are defined as structural elements that generally form an enclosed area. The walls form an integral entity of a construction unit in any sector in the construction industry (residential, commercial, industrial). Different types of walls are used and the type of wall varies with respect to the utility in the building. For instance, in the residential sector, the walls used are made of wood, solid masonry and cavity masonry etc. Apart from these conventional methods of wall construction the usage of light gauge steel frames (LSF) in walls has been found to be a better alternative in drywall systems due to the many advantages including speedy construction .

The use of LSF walls is rapidly increasing in the residential and commercial sectors of the construction industry. In the LSF walls, cold-formed steel channel sections are generally used as a skeleton for the wall panels which are usually sandwiched between plasterboards. The plasterboards are generally a combination of gypsum inner core lined with heavy duty paper. The LSF walls can also include cavity or external insulation and can be load bearing or non-load bearing. Many factors influence the structural and thermal performance of these LSF walls exposed to fire conditions. Apart from the structural loads such as dead/live loads, seismic and wind loads acting on the building, thermal loads due to the outbreak of fire in a building can also be a vital cause for the failure of the walls. The structural performance of LSF walls is generally governed by the behaviour of cold-formed steel studs under the applied loads at

elevated temperatures. Thermal performance of LSF walls is mainly governed by the plasterboards and steel studs as both these entities transfer heat. The geometric configuration of the studs within LSF walls significantly governs the thermal performance of LSF walls and thus also the structural performance of load bearing LSF walls. But to date majority of research has been carried out only for walls with single row of studs. Few researchers have attempted to investigate the fire behaviour of double stud walls but had many shortcomings in their research. For instance, Kodur and Sultan (2006) experimentally investigated the thermal performance of LSF walls with double rows of typical stud section. Numerical validation for the same was not carried out. Likewise, it is inferred that the use of typical LSF wall system with lipped channel sections for heights exceeding 3 m is not preferred. However, this situation can occur in places such as cinema theatres, hospitals, schools, partitions between houses in an apartment and between town houses.

In the above-mentioned places, acoustic insulation is also a major concern, and the performance of single stud walls even with cavity insulation is not sufficient. The weighted sound residual index R_w of LSF wall varies with respect to its configuration. R_w value of 60 is considered to be an excellent insulation against sound from external sources. Therefore, to achieve the required R_w index, complex LSF wall systems are widely used. The use of LSF walls with multi-stud wall systems will be beneficial in mid-rise buildings built with cold-formed steel sections as shown in Figures 1.1 (a) and (b). Mid-rise buildings are generally residential apartments and small commercial complexes, where the effective height is not more than 25 m as per National Construction Code (NCC). To satisfy the sound insulation requirement between the partitions, walls with two rows of stud are used. Various components and properties of LSF wall systems are briefly described next. However, this research is focused on the double and staggered stud wall systems.

1.2 LSF Wall System

1.2.1 LSF Wall Components

Light gauge steel frame / Lightweight steel frame wall systems are the latest advancements in modern wall construction. The main components of LSF wall systems in-



(a)

(b)

Images extracted from (a)

<https://starcash.co/steel-frame-building/astonishing-modular-products-prefabmarket/> (b)<https://ssfengineers.com/wp-content/uploads/2015/07/><ballard-onthepark-b-copyright-bumgardner-architects-1920x1080.jpg>

Figure 1.1: Mid-rise buildings with LSF walls

clude gypsum plasterboards, cold-formed steel sections (skeleton for the wall system), screws and other types of fasteners. The auxiliary components such as studs, tracks and noggings together form the skeleton of LSF wall system. The outer layer of the LSF wall system comprises of gypsum plasterboards. Figure 1.2 shows the components of a conventional LSF wall system based on a single row of studs in detail. The commonly used C-section studs with double layers of plasterboard are shown in Figure 1.3

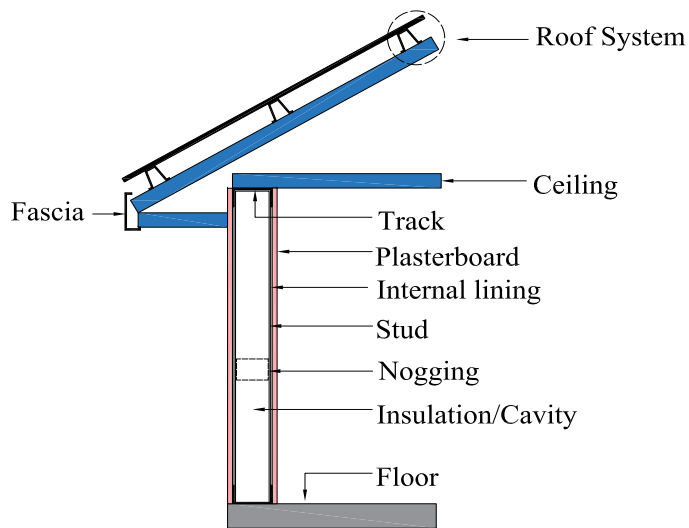


Figure 1.2: Components of LSF wall system

In recent times, LSF wall, known as drywall, is an important constituent of modular building construction. Drywall also known as plasterboard are panel boards resembling plywoods and cardboards which are made of gypsum possessing the chemical name

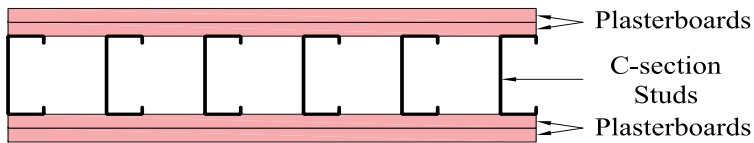


Figure 1.3: Plan view of LSF wall with Lipped C-Studs and double layers of plasterboard

of Calcium sulphate dihydrate ($\text{CaSO}_4 \cdot 2\text{H}_2\text{O}$). Plasterboards are manufactured by a process where the raw gypsum is dehydrated and then rehydrated to form calcium sulphate hemi hydrate. This is followed by mixing plaster with plasticizers and a foaming agent to achieve the necessary consistency. Ethylenediaminetetraacetic acid (EDTA) is used as a retardant in the manufacturing process to reduce the dew point, finally resulting in a pulp. This pulp is then sandwiched between two hard papers or fibre glass mats to form plasterboards. Some of the advantages of the plasterboard include ease of installation, thermal insulation, acoustic insulation and cost effectiveness.

Listed below are some of the advantages of LSF wall systems over conventional wall systems.

- Relatively low cost involved in the mass production of cold-formed steel sections.
- Self-weight of the structure is less resulting in easier handling on site, minimizing the equipment handling cost.
- Less time involved in constructing these walls in comparison with other wall systems.
- Non-combustible in nature providing better fire resistance when compared to other wall systems as steel is the major component.
- Better acoustic insulation as insulation layers can be customized within the wall panels as per end user requirement.
- Eco-friendly construction as steel is the major component.
- Resistance to termite attacks and weathering.

Even though the LSF wall systems possess many advantages, there are few areas in which the structural stability and strength of these wall systems can be compromised.

One such area is the exposure of the LSF walls to elevated temperatures during fire exposure within or outside the building. Since steel is a good conductor of heat and the fact its mechanical properties deteriorate rapidly with increasing temperature, the cold-formed steel sections used within the LSF walls are vulnerable to both thermal and structural effects. Structural behaviour of LSF walls varies significantly at elevated temperatures when compared to ambient temperature conditions.

1.2.2 Cold-formed Steel Sections

Cold-formed steel sections are generally formed by cold pressing of thin steel sheets to the desired shape and size at ambient temperatures. Stamping and rolling methods are also employed for manufacturing some of the cold-formed steel sections. Cold-formed steel sections are generally designated as Channel/C-sections, Lipped channels, Nested Channels, I-sections, RHS (Rectangular Hollow Sections), CHS (Circular Hollow Sections), SHS (Square Hollow Sections), RHFCB (Riveted Hollow Flange Channel Beam) sections and Built-Up sections. Typical cold-formed steel sections are shown in Figure 1.4. Unlike the manufacturing process of hot-rolled steel sections, where the rolling of steel takes place at a very high temperature of 1700 °F (greater than the recrystallization temperature of steel), cold-formed steel sections are manufactured at room temperature.

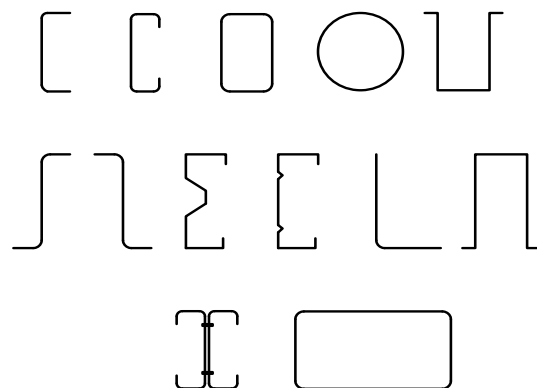


Figure 1.4: Typical Cold-Formed Steel Sections (CFS)

Cold-formed steel can be termed as a derivative of hot-rolled steel as it is hot-rolled steel with further processing with a better surface finish than hot-rolled steel. The manufacturing process generally involves cold drawing, turning, grinding, polishing to get a smoother finish when compared to hot-rolled steel.

1.2.3 Buckling Behaviour of Cold-Formed Steel Members

As the name suggests, cold-formed steel sections are thin and their thickness varies from 0.55 mm to 8 mm. The thickness of cold-formed steel section is small in comparison with its width and thus local buckling of flanges/web will occur before section yielding. However, local buckling of the section does not imply that the section has reached its ultimate capacity. This phenomenon is referred to as post-buckling strength. Local buckling takes place at low compressive stresses as the width to thickness ratio is high in cold-formed steel sections.

The structural behaviour of cold-formed steel sections varies when compared to hot-rolled steel sections. This behaviour change is noticeable not only at ambient temperatures, but also at elevated temperatures. For instance, the plate and column slenderness ratios of cold-formed steel columns are higher than those of hot-rolled steel columns. This results in increased local and global buckling effects when compared to hot-rolled steel section columns. These effects can worsen at elevated temperatures. Figure 1.5 shows the different types of buckling modes of a cold-formed steel column while Figure 1.6 shows the corresponding buckling curve/plot.

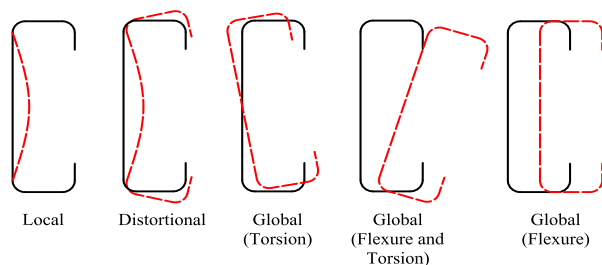


Figure 1.5: Different buckling modes of a channel section column

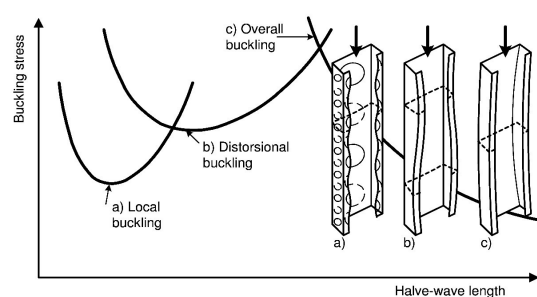


Figure 1.6: Buckling plot from BS EN 1993-1-3 (2005a)

1.2.4 Design Guidelines

The design standard pertaining to the structural design of cold-formed steel sections in Australia is AS/NZS 4600 (2014). Other design standards generally used in the cold-formed steel member design are AISI S100-12 (2007), AISI S202-15 and BS/EN 1993-1-3:2006, which provide the ambient temperature capacity equations for cold-formed steel members subjected to various actions such as compression, bending and their combinations. In the capacity calculations, the yield stress is taken as 0.2% proof stress. When cold-formed steel members are exposed to fire conditions, specific design capacity equations are needed to predict the capacity deterioration due to fire. EN 1993-1-2 provides appropriate fire design rules, but they were mostly developed to suit hot-rolled steel members. Recent research by Ranawaka and Mahendran (2009b), Kankanamge and Mahendran (2011) and Rokilan and Mahendran (2019) have therefore focused on the behaviour and capacity determination of cold-formed steel members at elevated temperatures.

1.2.5 Fire and Structural Performance of LSF walls

Fire resistance level is used in the construction industry to determine the resistance to failure offered by structural components of a building in fire. This grading is designated in minutes under the following three criteria by NCC (2016).

- Structural adequacy - the ability to maintain adequate stability in fire.
- Integrity - the ability to resist the passage of wall flames and fumes from the fire-exposed face of the wall to the unexposed face.
- Insulation - the ability to maintain a temperature on the surface of the unexposed face of the system to the limits specified as in AS/NZS 1530.4:2014 (SA, 2014).

The limiting values for the structural adequacy, integrity and insulation are specified in NCC for various structural systems. The fire resistance level of an LSF wall is generally given in minutes (or hours) for each of the three criteria above.

Fire resistance of LSF walls is dependant on the thermal properties of the materials used in the wall system such as thermal conductivity, specific heat and relative density.

Keerthan and Mahendran (2012a) investigated the thermal properties of gypsum plasterboards under standard fire conditions and provided a set of the thermal properties for use in the numerical models for validation purposes. The proposed thermal properties were also compared with the experimental fire test results of plasterboards and were observed to have good correlation. Cold-formed steel sections are often point symmetric, mono-symmetric or unsymmetric, i.e. not doubly symmetric as shown in Figure 1.7. Hence, they are subjected to more complex buckling modes. When the

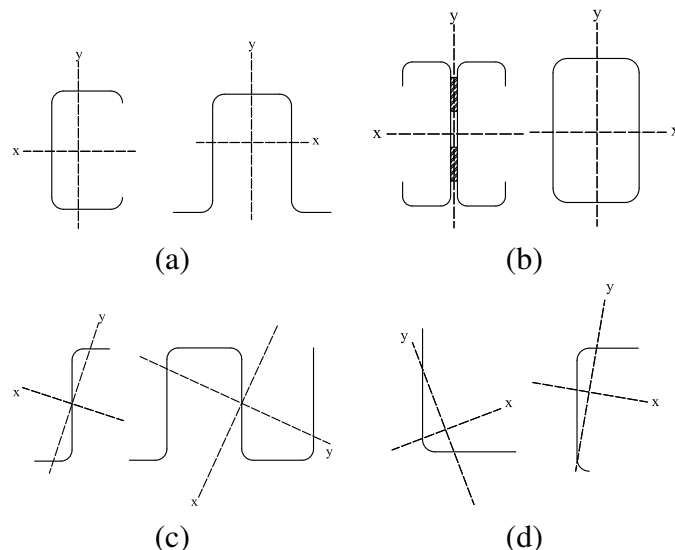


Figure 1.7: Different types of sections (a) Mono-symmetric (b) Double-symmetric (c) Point symmetric (d) Unsymmetric

mono-symmetric lipped channel studs are exposed to fire on one side, they are subjected to the following

- Temperature gradient across the depth resulting in thermal bowing.
- Non-uniform mechanical properties across the cross-section as the hot flange mechanical properties are much less than those of cold flange.

The presence of non-uniform mechanical properties leads to neutral axis shift of the stud section (Figures 1.8 and 1.9). These actions caused by fire exposure on one side induce the thin-walled stud to be subjected to a bending moment in addition to the applied axial compression load.

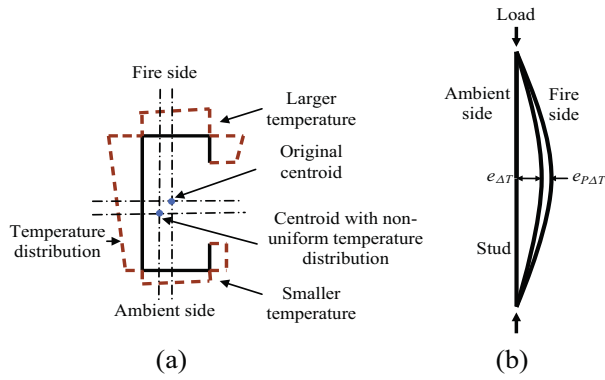


Figure 1.8: Neutral axis shift due to thermal bowing (Gunalan and Mahendran, 2014)

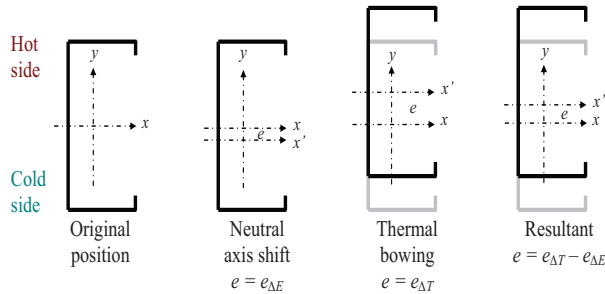


Figure 1.9: Lateral deflection due to thermal bowing (Gunalan and Mahendran, 2014)

1.3 Complex LSF Wall Systems

Complex LSF wall systems are needed and are being used in various applications in the building sector. Some of these wall systems are based on double and staggered stud configurations as shown in Figures 1.10 (a) to (c). To withstand heavy structural loads in the case of mid-rise construction, such systems are preferred. Also, to achieve higher acoustic insulation in places where sound insulation is important, these wall systems are used. Double stud walls are those with two parallel rows of studs with studs located directly opposite to each other whereas studs in parallel rows are staggered in the case of staggered stud walls. Lipped channel steel sections are widely used as the studs in LSF walls. The major components of the double and staggered stud walls include two rows of cold-formed steel studs, tracks, noggings, bracings, and plasterboards. These components are fixed together using self-piercing screws of different types. The physical and thermal properties of the double and staggered stud wall components are similar to single stud LSF walls. But due to the increased cavity depth, the behaviour of the components such as studs under fire exposure is different. The acoustic, thermal and structural performance of double and staggered stud walls is likely to be superior

compared to single stud walls. Plasterboard manufacturers such as USG Boral, CSR and Knauf Plasterboard include double and staggered stud wall systems in their product manuals although their main focus is on double stud wall systems. To date no detailed research has been undertaken on the thermal and structural behaviour of these complex wall systems with different configurations.

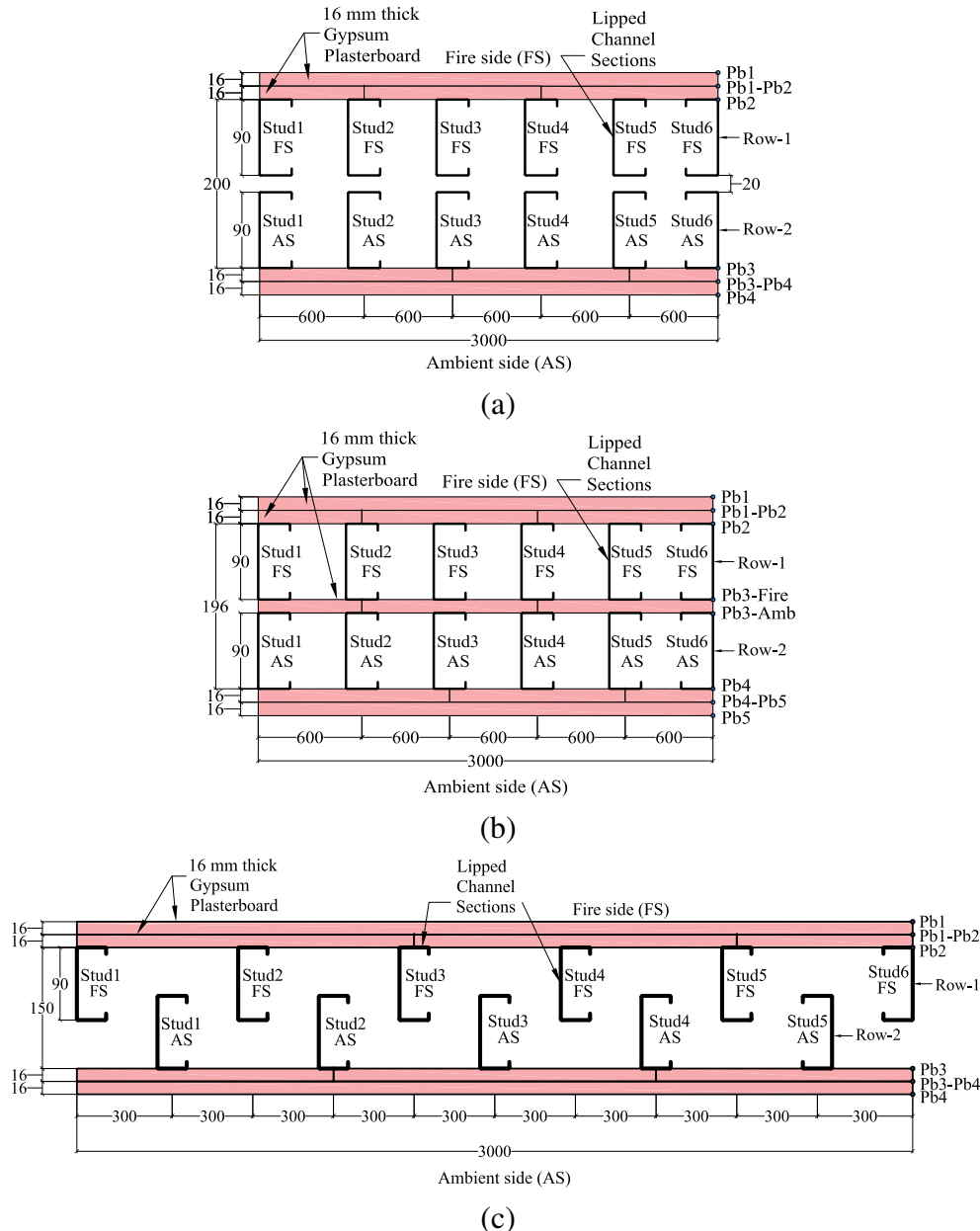


Figure 1.10: Typical complex LSF wall configurations (a) Double stud (b) Shaftliner (c) Staggered stud

The construction of double stud LSF walls is also different from that of single stud walls. The double stud walls generally consist of a small air gap as shown in Figure 1.10 (a) or may contain a shaftliner or a plasterboard layer between two rows of

stud as shown in Figure 1.10 (b). These arrangements are present to split the cavity into two or more to yield a better fire and acoustic performance. The presence of two rows of studs in different arrangements within the LSF wall will increase the load carrying capacity of the wall system and its fire performance. This will be beneficial in mid-rise buildings as the loads on the walls will be higher when compared to low rise buildings.

1.4 Research Problem

Increasing the Fire Resistance Level (FRL) of LSF wall is the need of the day. Researchers implement their ideas to ultimately increase the FRL of wall systems and make it structurally stable so that in the event of fire outbreak loss of life due to structural failure can be nullified. Past research studies focused only on varying the plasterboards by changing the type of boards, increasing the number of plasterboard layers in the wall, changing the type of stud section, improving the thermal performance of plasterboard using an external insulation layer etc. to achieve higher FRL. Effects of the arrangement of studs inside the wall via more complex wall systems was not the primary focus in many research studies. Earlier investigations focused on walls with less than 3 m height, which are primarily used in residential buildings. In residential buildings, the acoustic insulation is not a major concern as the intensity of sound for transmission through the wall is minimum. But in movie theatres, studios and in wall partitions between houses in an apartment, acoustic insulation is very important and the wall height can exceed 3 m. Especially in situations where the wall height exceeds 3 m, single stud arrangement cannot be used as the cold-formed steel sections are slender in nature. In these situations, complex wall systems with double rows of studs with or without a middle layer of plasterboard can be used (Figures 1.10 (a) and (b)). They can also be used as staggered stud wall systems (Figure 1.10 (c)). Similarly, with the focus on developing mid-rise building systems using cold-formed steel members, LSF wall systems with complex wall systems are needed in the lower storeys for higher load bearing purposes. In mid-rise buildings, the axial compression load acting on the bottom stories will be higher when compared with the top levels. Fire resistance and structural adequacy of building components in mid-rise buildings are utmost importance to prevent a structural collapse during fire outbreak. However, past research has

addressed only the thermal and structural behaviour of LSF wall systems with single row of studs. This research will therefore focus on the complex LSF wall systems with double and staggered stud LSF wall systems.

Another important research problem is the lack of a robust numerical model and analysis technique for LSF walls exposed to fire conditions. Many parameters such as free water evaporation from the plasterboard, effects of cavity radiation due to heat transfer from one face of the wall to another, pressure build-up within the cavity due to heat transfer and air movement within the cavity through natural convection were not considered in the past numerical modelling studies to reduce the complexity of numerical analysis.

Fire tests of load bearing and non-load bearing walls are an effective means to investigate the thermal and structural performance of complex LSF wall systems. But when the cost and time consumed in these tests are taken into consideration, it becomes uneconomical and practically impossible to study many iterations of wall systems within a short span of time. With the advancement of high-performance computing in recent times, it becomes beneficial for the researchers to study the thermal and structural behaviour of LSF walls with ease. Finite element analysis (FEA) is considered as the key to many multi-physics problems. Research on the thermal and structural performance of LSF wall systems is carried out using FEA software such as ABAQUS, ANSYS etc. Most common heat transfer problems such as combustion inside an engine are modelled and analysed by Computational Fluid Dynamics (CFD) technique as heat transfer happens in 3-dimensionsional space. Past research has focused on modelling the design or real fire as 1-dimensional entity only. Therefore, attempts should be made to use CFD models to investigate the thermal behaviour of complex LSF wall systems by considering the fire loads in 3-dimensional space.

1.5 Research Aim

The aim of this research is to investigate the thermal and structural performance of selected complex double and staggered stud LSF wall systems using full scale standard fire tests and advanced numerical modelling. The key tasks of this research to achieve this aim are as follows.

- Undertake a detailed review of complex LSF wall systems and their fire performance, and thermal and mechanical properties of wall components and, establish their appropriateness.
- Conduct a series of full scale standard fire tests and ambient temperature load bearing capacity tests of double and staggered stud wall systems to investigate their thermal and structural performance in fire.
- Compare the full-scale fire test results with the available fire test results of conventional single stud wall systems to evaluate the effects of complex stud wall arrangements on structural and thermal performance.
- Develop advanced finite element models to simulate the thermal and structural performance of double and staggered stud wall systems exposed to fire conditions and validate them using full scale fire test results.
- Improve the fundamental understanding of the thermal and structural performance of double and staggered stud wall systems through the use of validated finite element models in investigating the LSF wall behaviour in fire and associated failure modes of studs in detail.
- Undertake a detailed parametric study of double and staggered stud wall systems with different structural and thermal parameters of LSF wall components.

1.6 Outline of Thesis

Based on the research aim and the specific tasks as listed above, this research was conducted in a sequential manner and a brief outline of the contents included within each of the chapters are presented next.

Chapter 2 details the extensive literature review conducted on LSF walls. Topics include the ambient and fire performance of simple and complex LSF wall assemblies. This covers the experimental and numerical investigations on LSF walls. Initial investigations were carried out by sampling the real-time problems faced by the LSF wall industry with respect to complex wall systems (double and staggered stud walls). Literatures were collected and reviewed to identify the problems to be taken up for the

current research. Ground surveys by contacting industry experts to know about the current practice in the complex LSF wall arrangements such as double and staggered stud walls were carried out to determine the best possible complex LSF wall configurations to be investigated in the current study. Finally, a summary of the reviewed literature is presented and the possible techniques to address the research aim are proposed.

Chapter 3 presents the ambient temperature capacity test results conducted on selected complex LSF walls based on the detailed literature review. Test results include the axial compression capacity, axial displacement and lateral deflection curves. The buckling behaviour of studs in double and staggered LSF wall configurations under axial compression is also discussed in detail. Finite strip and finite element analyses conducted on double and staggered LSF wall configurations to predict the ambient temperature axial compression capacity are also discussed.

Chapter 4 reports the findings of one small scale fire test and 10 full-scale fire tests conducted on double and staggered stud LSF wall systems. Illustrations are made for the tested complex LSF wall configurations and fire test results in the form of time-temperature curves are presented in detail. Increase in the FRL of the double and staggered stud LSF walls in comparison with similar single stud LSF wall assemblies and the detrimental effect of cavity insulation in double and staggered stud LSF walls are discussed in detail. Detailed comparison of the fire test results are made against full-scale fire test results of single stud LSF walls and the unique heat transfer mechanism observed in complex LSF walls is summarised.

Chapter 5 presents the developed thermal FE models to predict the thermal performance of complex LSF wall systems. Firstly, three different software packages were used to develop thermal models and a detailed comparison was made amongst them to find the most appropriate software package to use for developing the thermal models in this research. A detailed comparison was made considering the advantages and shortcoming in the thermal model results and the numerical model results were validated against the small-scale and full-scale experimental results to establish the suitability of the model. Based on the developed model, a detailed parametric study was conducted on complex LSF wall configurations to predict the fire performance and this chapter provides the details of the development of thermal FE models and the results in detail.

Chapter 6 details the FRL predictions from structural FE model which was devel-

oped alongside the thermal models to predict the structural behaviour of the studs in fire. The structural model inputs were extracted from the fire test results from Chapters 4 and 5 and the FRL predictions were made. The FRL predictions were made for different load ratios based on the axial compression capacity determined in Chapter 3.

Chapter 7 presents the parametric analysis results obtained using validated thermal and structural FE models. The parameters for the stud includes different wall configurations and stud thicknesses. FRLs of the selected wall configurations are presented in a table format and the closest FRLs in min corresponding to the NCC requirements are also provided.

Chapter 8 provides a summary of the findings from this research study. Conclusions are drawn from the experimental and numerical investigations and suitable recommendations are also proposed for future work in relation to the fire performance of complex LSF walls.

[This page is intentionally left blank]

Chapter 2

Literature Review

2.1 Background

The importance of fire protection in buildings has become an important concern in recent times. Fire outbreak in buildings has led to significant loss of life and property in many instances. Some major fire accidents in recent times leading to considerable loss of life and severe damage to the property are shown in Figure 2.1.

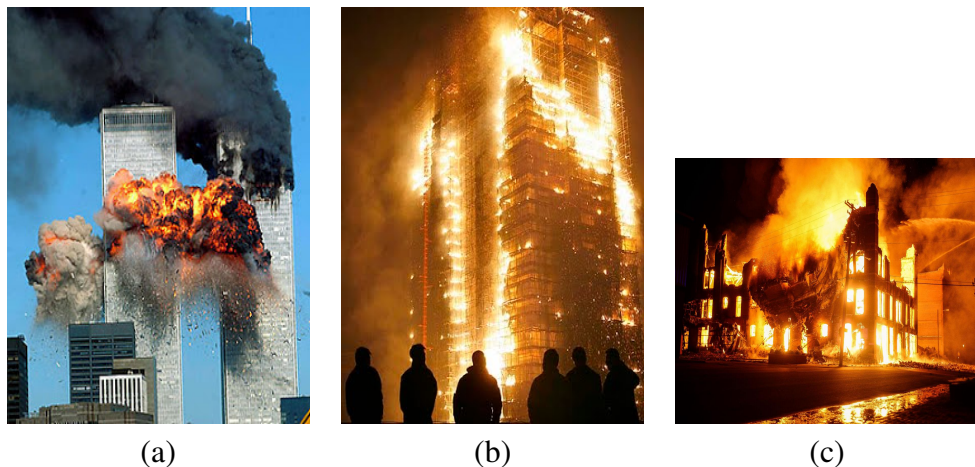


Figure 2.1: Major fire accidents in recent times

This has led the researchers to concentrate on the fire safety of buildings. Most common forms of building construction include materials which are more susceptible to fire exposure. For instance, the major components of a residential building include concrete, hot-rolled steel and wood. The fire performance of a building is greatly dependent upon the fire performance of these individual materials. Therefore, researchers focus on these materials and are keen to improve their performance of these materials

under fire exposure. During a fire incident, the structural elements of a building are subjected to additional fire loads apart from the existing permanent and imposed loads. This results in premature failure of the structural members if they are not properly designed to take the fire loads apart from the structural loads. As this research is focused on the complex LSF walls used in buildings, past literatures with respect to this are reviewed.

2.2 Experimental and Numerical Investigations of LSF Walls

The LSF walls used in buildings are load bearing and non-load bearing. The non-load bearing walls are generally used in partition separations in RC framed buildings whereas the load bearing walls are generally found in day to day low rise to mid-rise residential buildings. This section gives a detailed insight of the experimental and numerical investigations carried out on both load bearing and non-load bearing LSF walls in the past.

B.C. Son; H. Shoub (1973) experimentally investigated the fire performance of partition walls under load bearing conditions as per ASTM E119-71 standards using two fire tests. The test wall dimensions were 8 foot high and 16 foot long. Lipped channel section of size $3'' \times 1\frac{3}{4}'' \times \frac{1}{2}''$ inch was used as studs in the former while the latter used tubular sections of $3'' \times 2''$ inches as studs in the wall assembly. 18 ga (1.02 mm) thick steel studs were used. Both test walls consisted of two plasterboard sheathed frames separated by $\frac{1}{2}''$ inch air gap between them. The plasterboards were $\frac{5}{8}''$ inch inches thick for both fire tests, but the thermomechanical properties of the same are unavailable. Single layer of Type X gypsum plasterboard was used on both test specimens. $3\frac{1}{2}''$ inch thick glass wool compressed to 3" inch was used as the insulation. However, the sound insulation values and the material properties were not provided in detail. During the fire tests, the phenomenon of thermal bowing was noticed and reported. Inward thermal bowing was significant, where the test specimen bowed towards the furnace. The first test wall with lipped channel section survived 75 min after which flames were visible on the unexposed side. The second test wall with tubular studs survived 97 min after which visible smoke was seen through cracks

on the unexposed side of the test wall. Time-temperature curves were plotted for the plasterboards, but the individual stud time-temperature curves are not available. It was suggested that the usage of two layers of Type X gypsum plasterboard will increase the fire resistance level (FRL).

The history of fire tests dates back over a century. Babrauskas and Williamson (1978) summarised the fire tests conducted from 1880 to 1918 and listed the key features in conducting fire tests of walls. Their report was summarised in two parts. The first part reported about the history in forming the fire testing standards, while the second part described the various fire tests carried on different building elements across the globe. It was mentioned that ASTM E119 was the first standard issued on the fire testing of building elements. This report included the major fire tests from the year 1880 and tried to summarise all the fire test reports available in English during that time. However, test reports in other languages were ignored due to the difficulties in interpretation. The need for fire proofing on steel, concrete and timber elements back then was debatable and the necessity for the same was explained. The first report explained in detail about the very first fire test on walls and the difficulties in measuring the temperatures during the fire test. Fire testing of columns was also reported in detail. Details about the fire tests of walls were summarised in the second part of the report.

It was reported that the first controlled fire test was conducted in Germany in 1891 on a small hut. This emphasised the importance of fire tests over a century ago. The test room was constructed using timber studs and had the dimensions of $2.01\text{ m} \times 2.63\text{ m} \times 2.63\text{ m}$. From this report it is evident that until early 1900's the fire tests were conducted on the whole compartment rather than individual building elements. All the fire tests were conducted in a gas-fired chamber, but the dimensions of the test specimens were not consistent. The usage of different organic building elements at different time period were also reported. From the year 1915 it was reported that the furnace dimensions were increased to $3.6\text{ m} \times 4.5\text{ m} \times 0.4\text{ m}$. This was the new standard for testing the wall specimens in Underwriters Laboratory (UL) and thermocouples were used for temperature measurements instead of thermometers. Apart from the tests on walls, the report also elaborated the fire tests of other building components such as doors and openings. However, temperature distribution across the wall was not reported in detail. The establishment of the standard fire curve in the year 1917 and the inclusion of the

same into the ASTM E119 standards was also described in detail. This also included various failure criteria for different building elements and their level of fire protection. Also, the validation checks conducted to verify the suitability of the standard fire curve was also discussed in detail.

Klippstein (1978) used the fire test results conducted on LSF walls based on ASTM E119 to propose analytical methods to predict the structural failure time of gypsum plasterboard sheathed LSF walls. Initially, he conducted tests to determine the mechanical properties of the steel sections used in the LSF walls. The test walls used for this study were $3.05\text{ m} \times 3.05\text{ m}$. Only the axial loads were considered in the fire design while the wind loads were neglected in the calculations. The phenomenon of plasterboards not providing effective lateral restraints to the studs at elevated temperatures was discussed in detail. The concept of unequal load sharing in LSF walls was also discussed, i.e., higher load carried by the stronger studs (less temperatures) during full-scale fire test. Failure of the stud was assumed to happen by weaker axis buckling in formulating the design equations. The concept of load ratio (LR), P_T/P , was used, where P_T is the calculated failure load at elevated temperature T while P is the failure load at ambient temperature. The failure load was determined theoretically using the following equation.

$$P = \frac{23}{12} F_{al} A \quad (2.1)$$

Elastic buckling was the governing failure mode in studs more than 4.5 m height assuming pinned end conditions. As the studs in LSF walls are generally 3 m tall, inelastic buckling was the critical failure mode. The equation to predict the inelastic buckling load was proposed as shown next.

$$F_{al} = \frac{12}{23} Q F_y - \frac{3}{23} \frac{(Q F_y)^2}{\pi^2 E} \left(\frac{K L}{r} \right)^2 \quad (2.2)$$

Where

Q = strength reduction factor at room temperature

F_y = actual yield strength at room temperature

E = modulus of elasticity at room temperature

K = effective length factor of the stud

L = length of the stud

r = radius of gyration about the major axis.

Based on the above Equation (2.2) the failure load at room temperature was determined using the next equation.

$$P = \left[QF_y - \frac{1}{E} \left(\frac{QF_y L}{2\pi r} \right)^2 \right] A \quad (2.3)$$

During the fire test, the studs deflect laterally causing bending stresses and these effects have to be included in calculating P_T . Therefore, the interaction equation for combined axial and bending action available in the AISI manual was used and is shown next.

$$\frac{f_a}{F_{alT}} + \frac{C_{mx}}{\left(1 - \frac{f_a}{F'_e} \frac{f_b}{F_{blT}} \right)} < 1.0 \quad (2.4)$$

Where

f_a = compressive stress due to axial load

F_{alT} = allowable stress for axial load at failure temperature

$\frac{C_{mx}}{\left(1 - \frac{f_a}{F'_e} \frac{f_b}{F_{blT}} \right)}$ = modification factor for bending stresses

f_b = bending stress at mid-height

F_{blT} = allowable bending stress at failure temperature

F_{yT} = allowable strength at failure temperature

Q_T = column-strength reduction factor at failure temperature

E_T = modulus of elasticity at failure temperature

Based on the above mentioned equations the load ratio (LR) was computed by the following equation.

$$LR = \frac{1}{\left(\frac{1}{F_{alT}} + \frac{23A\delta_T}{128x F_{yT}} \right) F_{al}} \quad (2.5)$$

To determine the capacity reduction in the members, elevated temperature material properties were determined and used in the above mentioned equations. It was found that at elevated temperatures, the elastic modulus of sheet steel decreased rapidly in comparison with that of plate steel. Stub column tests were also conducted to determine the column strength reduction factors at elevated temperatures. The proposed equations resulted in conservative results in comparison with the experiments.

Gerlich et al. (1996) investigated the design of LSF walls under standard ISO 834 fire curve and some real fire curves. They proposed suitable methods for calculating the reduction in strength of LSF wall at elevated temperatures, and the stud deflections caused by elevated temperature gradients and P- Δ effects. Three design standards, AS 1538, BS 5950 and AISI specifications were compared for the limit state design of cold-formed steel sections at room temperature. It was found that the AISI design manual gave accurate capacity predictions. The experimental structural test was initially conducted for 3m length columns under axial loads and bending to verify the AISI design method at ambient conditions. An equation for specific heat (k) until 900°C of fire exposure was also developed.

$$k = -0.022T + 48, \text{ for } 0 < T < 900^\circ\text{C} \quad (2.6)$$

It was concluded that with the help of experimental and analytical studies, the P- Δ effect at elevated temperatures can be predicted with good accuracy. Buckling of the compression flange of cold-formed steel stud on the ambient side was the main cause of structural failure at elevated temperatures.

Alfawakhiri et al. (1999) reviewed the fire resistance of load bearing steel stud walls protected with gypsum board. They suggested that there were robust experimental methods to test the thermal performance of LSF walls, but there was a gap in the numerical analyses and the design procedures for LSF walls. The importance of using insulation such as mineral wool, glass fibre, cavity insulation etc, within the wall was highlighted. The thermal conductivity of various gypsum boards was discussed and a relationship was established between thermal conductivity and temperature. Likewise, the relationship between specific heat and temperature was also developed. The variation in the modulation of elasticity of the cold-formed steel sections with respect to temperature was also reviewed. It was concluded that factors such as specific heat, thermal conductivity and modulus of elasticity of studs with variation in temperature will have a significant effect on the fire performance of steel studs.

Sultan and Kodur (2000) summarised the performance based parameters to be considered in designing LSF walls in fire. Seventeen full-scale fire tests conducted previously were considered as reference for this study. All the considered wall specimens were 3 m high and 3.7 m wide. Both steel and wood stud assemblies were considered

in this study. However, the wall specimens were lined using gypsum plasterboard only. All the steel stud assemblies considered were non-load bearing. The reference fire tests were conducted in accordance with CAN/ULC-S101-M89 (1989). It was found that the presence of cavity insulation resulted in rapid increase of the plasterboard temperatures in comparison with uninsulated wall assemblies. The average temperature on the unexposed side of the test wall was lower in specimens with rock fibre insulation in comparison with non-insulated assemblies. The use of cavity insulation in non-load bearing LSF wall assemblies resulted in increased FRL. However, the effects of insulation in loadbearing LSF walls were not discussed in detail. It was also reported that, the type of insulation did not significantly affect the FRL, provided the insulation had a perfect fit between the studs resulting in no gaps.

Another important finding was that the presence of resilient channels and proper positioning of the same, significantly increased the FRL in non-load bearing LSF wall assemblies. However, the effective restraints provided by the resilient channels along with the plasterboards were not reported in detail, as all the LSF wall tests were conducted under non-load bearing conditions. The presence of second layer of plasterboard with staggered joint arrangement significantly increased the FRL in comparison with single plasterboard layer. It was reported that under non-load bearing conditions, the type of stud such as wood or steel did not affect the FRL.

Collier (2002) reviewed the BRANZ method of height extrapolation to study the resistance of non-load bearing steel framed walls under fire. The wall specimen chosen was set at 4 m × 4 m panel in comparison to the conventional 3 m × 3 m panel. The horizontal joints appeared to fail prematurely in comparison with vertical joints when exposed to fire. This premature failure can expose the stud flanges directly to fire. This research also compared the test results of wall panels with and without vertical lining joints.

Feng et al. (2003c) studied the thermal performance of cold-formed thin-walled steel panel systems in fire using small-scale fire tests of 1.5 × 1.5 × 1.5 m wall panels made of lipped channel studs with and without service holes. The performance of gypsum board in fire was the principal focus of this research. Focus was given in developing a finite element model to predict the thermal performance of gypsum boards and steel studs. Time-temperature curves were plotted for panels tested with different

layers of gypsum board and insulation under fire. ABAQUS finite element analyses (FEA) were conducted using the material properties of gypsum board, steel studs and insulation in BS EN 1993-1-3 (2006) Part 1.2. Tests and FEA results and several conclusions were made as follows. The free water content present in the gypsum boards was not considered in the numerical analysis. Hence the results from FEA were reasonable, but were not accurate in accordance with the experimental results. Different layers of gypsum boards along with insulation on the fire side were used both in experiments and analyses and it was found that the steel stud temperature had a high influence on the usage of insulation and not the number of layers of gypsum board on the exposed side. It was concluded that increasing the number of gypsum boards increased the FRL. The failure of gypsum boards on the exposed face, did not promote fire spread to the unexposed face due to the presence of insulation. Isowool and Rockwool insulations were used and the results were compared with a non-insulated wall panel. It was found that, the presence of insulation on the fire exposed side of the wall resulted in higher stud temperature. The thermal performance of the wall might get affected if the insulation is provided on the unexposed face of the wall to reduce cold bridging in warm construction. The shape of the thin-walled cold-formed steel cross section had the least effect on the thermal performance, whereas in the case of a cassette section the thermal performance was affected by its layout.

Based on the fire test results Feng et al. (2003b) then investigated the structural behaviour of LSF wall panels. Numerical analysis and design calculation were carried out based on 52 channel sections with FE package ABAQUS. Modified design equations for channel sections were proposed to include the effects of distortional buckling failure and change in strength and stiffness of steel at elevated temperatures based on BS5950 Part 5 and Eurocode 3 Part 1.3. They also included the service holes present in the steel studs, and their effect on the ultimate strength based on AISI (1996). The geometric non-linearities, imperfections and stress-strain relationships at elevated temperatures based on Eurocode 3 Part 1.2 or Outinen et al. (1997) were also considered. The equation for calculating the effective width of a flange for distortional buckling was modified as follows.

$$\frac{b_{eff,de}}{b} = 1 \text{ for } \lambda \leq 0.673 \quad (2.7)$$

$$\frac{b_{eff,de}}{b} = \sqrt{\frac{\sigma_{de}}{f_y}} \left(1 - 0.22 \sqrt{\frac{\sigma_{de}}{f_y}} \right) \text{ for } \lambda \geq 0.673 \quad (2.8)$$

Based on the design modifications and numerical analysis, it was concluded that the design formulations used for ambient capacity calculation can be extended and used for elevated temperatures as well. This is achieved, when the reduced yield strength derived from 0.2% proof stress and the reduced elastic modulus are used. The effect of distortional buckling can be included in the design calculations based on Young and Gregory (1992). Service holes can be considered in the design, based on AISI specifications. ABAQUS FE models can be used to stimulate the behaviour of cold-formed steel sections at elevated temperatures, provided proper material properties and boundary conditions are used. Feng et al. (2003a) extended the study to investigate the axial strength of CFS channels under non-uniform elevated temperatures due to fire. Two methods were adopted for the design process. First the EN1993-1-3 ambient temperature design equation was modified and the second using the limiting temperature method. The design equations for the cold-formed steel columns under combined axial load and bending moments were based on the following equations from Eurocode 3 Part 1.2.

$$\frac{N_{sd}}{\chi_{min} f_{yb} A_{eff}} + \frac{k_y(M_{y,sd} + \Delta M_{y,sd})}{f_{yb} W_{eff,y,com}} + \frac{k_y(M_{z,sd} + \Delta M_{z,sd})}{f_{yb} W_{eff,z,com}} \leq 1 \quad (2.9)$$

$$\frac{N_{sd}}{\chi_{lat} f_{yb} A_{eff}} + \frac{k_y(M_{y,sd} + \Delta M_{y,sd})}{f_{yb} W_{eff,y,com}} + \frac{k_y(M_{z,sd} + \Delta M_{z,sd})}{f_{yb} W_{eff,z,com}} \leq 1 \quad (2.10)$$

Later the results from the modified design equations from the EN1993-1-3 were compared with ABAQUS simulation results based on S4R shell FE models. 100 x 54 x 15 x 1.2 mm lipped channel sections were used in the study. Appropriate restraints were applied to the studs to simulate the full-scale fire test conditions. Sequential uncoupled FE analysis was conducted and the results showed that failure temperatures of the stud sections were similar in the experimental and numerical studies irrespective of the number of plasterboard layers. The use of more than one layer of plasterboard delayed the temperature of the studs.

Sakumoto et al. (2003) conducted ISO 834 standard fire tests of walls and floors using various light gauge steel stud shapes. Partition walls and exterior walls were the

main aim of the study. The wall specimens of 1820×2700 mm consisted of 0.5 to 1.6 mm studs and 12.5 mm thick plasterboards. Unlike other fire tests, the partition walls consisted of two rows of studs separated by 9 mm plywood. The studs were lipped channel sections with different depths ranging from 89 mm to 235 mm and were spaced at 500 mm centres. Two layers of non-fire rated plasterboards were present on either side of the wall and an axial load of 34 kN was applied to some specimens. Glass wool insulation was present in both cavities of the partition wall, which resulted in the highest FRL. The fire tests for the partition walls were carried out by varying the studs and the configuration with plywood between the rows of stud resulted in the highest with 67 min of FRL. Likewise different floor-ceiling configurations of 2950 mm \times 4260 mm were also tested. It was concluded that the gypsum board fall-off was an important criterion in determining the FRL. The plasterboard fall-off can be reduced by increasing the number of plasterboard layers. The collapse temperature, time and sequence of failure of the structural members in the LSF wall were also detailed. Most of the tests conducted on wall panels had single layer plasterboards and the FRL was about 45 min. In the case of wall panels with plywood the FRL was just above 60 min.

Feng and Wang (2005) investigated the cold-formed, thin-walled steel panels with service holes in fire. The holes were provided in the channel sections, one near the top and one near the bottom. Full-scale tests were carried out at different load ratios of 0.2, 0.4 and 0.7. The main observation in the failure of the steel studs was that the studs failed by local buckling near the service holes at ambient temperature. Flexural-torsional buckling along the major axis with lateral deflection caused by thermal bowing due to the temperature gradients was also observed. Increase in the stud temperature was noticed during some tests due to the complete burning of the insulation layer. Detachments of the fasteners along the unexposed side of the panels were also noticed during the test.

Manzello et al. (2005) studied the performance of partition assemblies under real fire conditions. This research was different from others as their fire test was performed in real-scale compartment instead of a conventional furnace setup. This test was carried out for non-load bearing conditions. A compartment shown in Figure 2.2 was constructed, the fire curve based on ASTM E119 was simulated within the compartment and the thermal performance of the partition walls was investigated. Thermo-

couples, infra-red cameras, normal cameras and heat flux sensors were used for the test. It was observed that the rate of temperature rise on the plasterboard surfaces was higher compared to those tested in the furnace. It was also reported that the total heat flux measured was dependent on the wall height. But the rate of increase of the heat flux was smaller when compared to the furnace fire test. Numerical simulations of the experiments were then performed by Manzello et al. (2007). The model was entirely mathematical instead of widely used FE models. It was able to predict the fire behaviour only upto certain level of precision due to the effects of smoke movement, plasterboard fall-off etc.

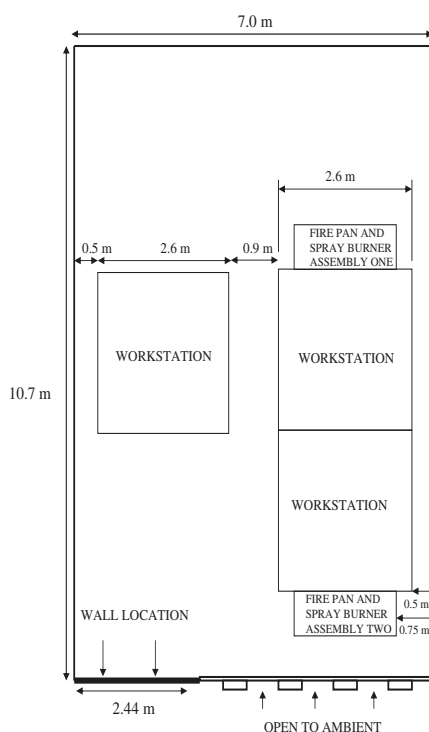


Figure 2.2: Compartment dimensions used by Manzello et al. (2005)

Kodur and Sultan (2006) investigated the important factors that influenced the fire resistance of load bearing steel stud walls. Spacing of the studs and their thickness of the steel used, the magnitude of load acting on the panel, shear membrane and type of installation were the parameters analysed by them. It was found that the insulation type and the number of layers of gypsum board in the panel were highly influential. The use of cavity insulation was shown to reduce the fire rating of the wall assemblies. Increasing the layers of plasterboard resulted in higher fire resistance. Provision of the OSB shear membrane in place of gypsum boards in load bearing wall panels resulted

in the deterioration of fire resistance. Studs arranged in a staggered manner in two rows resulted in higher fire resistance when compared to a single layered stud arrangement. It was discussed that this higher fire resistance of the double layered staggered stud arrangement was due to the larger heat sink caused by the larger cavity within the wall. Another finding was that MSG 20 light steel section performed better than ordinary MSG 20 section in providing fire resistance.

Knobloch and Fontana (2006) proposed a strain based approach to local buckling of steel sections exposed to fire. Generally, stress based design approach based on ambient temperatures is used to design them. Unaltered effective width and a reduced 0.2% proof stress based yield strength were only used for elevated temperature design. This has resulted in unsatisfactory design results. Hence, a strain based method was developed for unstiffened and stiffened elements of CFS members. Strength curve based on yield line theory considering the initial imperfection was also formulated. Calculations are done based on the proposed design methods and compared with the results from the numerical analysis. The procedure involved in this proposed design is as follows.

- For different support conditions the non-dimensional slenderness at elevated temperature is determined.
- Then the reduction factor for plate buckling at elevated temperature $\rho\theta$ is calculated based on Desmond et al. (1981), also known as Winter's equation as shown next.

$$\rho\theta = \frac{1}{\bar{\lambda}_{\rho\theta}} \left(\frac{1 - 0.22}{\bar{\lambda}_{\rho\theta}} \right) \quad (2.11)$$

- Later the effective width is calculated using the proposed stress-strain relationships at elevated temperatures and the stress distribution of the element is obtained.
- Finally, the axial and bending moment resistances are calculated by integration.

The proposed effective width formulae for unstiffened and stiffened elements are as shown in Figure 2.3. The proposed effective width formula for unstiffened and stiffened elements are as shown in Figure 2.3. It was concluded that, the local buckling of the studs and the additional capacity due to the plastic behaviour of cross section

Strain and stress distribution	Effective widths
<p>The diagram shows two cases of effective width distribution. In the first case, the effective width $f_{\epsilon,\theta}$ is constant across the width b, with segments $b_{e1,\theta}$ and $b_{e2,\theta}$ indicated. In the second case, the effective width $f_{\epsilon,\theta}$ is distributed such that $b_{e1,\theta} < b_{e2,\theta}$. Both cases show strain ϵ at the top and bottom edges.</p>	$\frac{b_{\text{eff},\theta}}{b} = \rho_\theta \quad (30a)$ $\frac{b_{e2,\theta}}{b} = \frac{\rho_\theta}{2} \quad (30b)$
<p>The diagram shows two cases of effective width distribution. In the first case, the effective width $f_{\epsilon,\theta}$ is constant across the width b, with segments $b_{e1,\theta}$ and $b_{e2,\theta}$ indicated. In the second case, the effective width $f_{\epsilon,\theta}$ is distributed such that $b_{e1,\theta} < b_{e2,\theta}$. Both cases show strain ϵ at the top and bottom edges.</p>	$\frac{b_{\text{eff},\theta}}{b} = \rho_\theta \quad (31a)$ $\frac{b_{e2,\theta}}{b} = \frac{0.12}{\lambda_{p,\theta}^2 + \bar{\lambda}_{p,\theta}} \quad (31b)$

Figure 2.3: Proposed effective width table from Knobloch and Fontana (2006)

had a strong influence on the resistance the steel in fire. Also, the local buckling was dependent largely on strain.

Experimental investigation of different cold-formed steel materials at elevated temperatures were conducted by Chen and Young (2007). Primary focus of this research was to report the material properties of cold-formed steels at elevated temperatures. Elevated temperatures tensile coupon tests at elevated temperatures of G550 and G450 grade steels with varying thicknesses were conducted to determine the elastic modulus and yield strength at different strain levels, ultimate strength, ultimate strain and thermal elongation for comparison with Australian, British and Eurocode Standards. A unified equation to predict the above mentioned material properties was also proposed. Comparisons between the test results and proposed equations were also carried out. Both transient and steady state methods were used in the tensile coupon tests. But the transient method is more practical in real time fire exposure. Yield strengths at 0.5%, 1.5% and 2% strain levels were obtained and comparisons among them were undertaken. Serration was observed on the stress-strain curve at high temperatures. Static drop was obtained in the stress-strain curve at room temperature of 22°C. This was achieved by pausing the strain applied for 1 minute thereby allowing the stress relax-

ation associated with plastic strain. This reduces the effect of loading rate. A series of tests was also conducted to study the effects of static drop at different temperatures. Based on the experimental investigations, an equation for determining yield strength, ultimate strength and ultimate strain of cold-formed steels was proposed as follows.

$$\text{Yield Strength} \rightarrow \frac{f_{0.2,T}}{f_{0.2,normal}} = a - \frac{(T - b)^n}{c} \quad (2.12)$$

$$\text{Ultimate Strength} \rightarrow \frac{f_{u,T}}{f_{u,normal}} = a - \frac{(T - b)^n}{c} \quad (2.13)$$

$$\text{Ultimate Strain} \rightarrow \frac{\varepsilon_{u,T}}{\varepsilon_{u,normal}} = a - \frac{(T - b)^n}{c} \quad (2.14)$$

A modified stress-strain curve model based on the Ramberg-Osgood model was proposed as follows.

$$\varepsilon_T = \frac{f_T}{E_T} + 0.002 \left(\frac{f_T}{f_{y,T}} \right)^{nT} \text{ for } f_T \leq f_{y,T} \quad (2.15)$$

$$\varepsilon_T = \frac{f_T - f_{y,T}}{E_{y,T}} + \varepsilon_{u,T} \left(\frac{f_T - f_{y,T}}{f_{u,T} - f_{y,T}} \right)^{mT} + \varepsilon_{y,T} \text{ for } f_T > f_{y,T} \quad (2.16)$$

Where

$$E_{y,T} = \frac{E_T}{1 + 0.002 n_T E_{y,T} / f_{y,T}} \quad (2.17)$$

$$n_T = 20 - 0.6\sqrt{T} \quad (2.18)$$

$$m_T = 1 + \frac{T}{350} \quad (2.19)$$

From this study, it was concluded that the Australian, British and European standards were conservative in predicting the yield strength, elastic modulus and thermal expansion except for G550 1 mm steel between 450°C to 970°C and for G450 1.9 mm steel at 600°C.

Kolarkar and Mahendran (2008) studied the thermal performance of LSF walls with double layer plasterboards, where the insulation was sandwiched between the

plasterboards externally. The investigation was conducted by using small-scale fire tests of non-load bearing LSF walls exposed to the standard fire curve. It was found that sandwiching of insulation externally between the plasterboards resulted in better thermal performance when compared to traditional stud walls with cavity insulation.

Ranawaka and Mahendran (2009a) investigated the distortional buckling behaviour of cold-formed steel compression members at elevated temperatures. Lipped and Un-lipped channel compression members were tested at temperatures ranging from 20 to 800°C. Their ultimate compression capacities from the tests were compared with design code predictions. The distortional ambient temperature buckling capacities from the tests were compared with those predicted by direct strength and buckling strength equations in AS/NZS 4600 and were found to agree well. At elevated temperatures, the reduced mechanical properties were used to predict the compression capacities, in which case the comparison with the test results showed that the AS/NZS 4600 design equations were over-conservative.

Rahmanian (2011) conducted 12 medium-scale (1 m × 1 m) standard fire tests of LSF walls under load bearing conditions. The number of plasterboard layers was varied to study the thermal behaviour of gypsum plasterboard assemblies using different types of plasterboards. The concept of cyclic condensation-evaporation of the moisture content in the plasterboard during fire tests was also investigated. Material property tests were also conducted on various gypsum plasterboards to study the effect of moisture transfer in gypsum plasterboard assemblies and the data was used to develop thermal finite element models in ABAQUS.

Chen et al. (2012) conducted five full scale fire tests of conventional single stud load bearing LSF wall systems lined with different types of fire protective boards including gypsum plasterboard. Bolivian magnesium boards and calcium silicate boards were used in this study. Load ratios of 20%, 40% and 70% were used in the fire tests. Fire tests showed that the load bearing LSF walls without cavity insulation provided better FRL when compared to those with cavity insulation. Also, the thickness of the stud section influenced the FRL. Thicker the stud higher was the FRL. This effect was reported by previous researchers also. It was concluded that the calcium silicate boards when used as the base layer provided better fire performance than gypsum plasterboards. However, due to the spalling behaviour of calcium silicate boards at higher

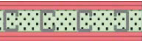
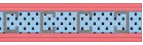
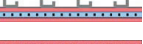
temperatures, it does not possess a noticeable advantage than compared to gypsum plasterboards. Bolivian magnesium oxide plasterboards performed better in fire when compared to gypsum plasterboards. Staggered arrangement of boards were followed in the fire tests, but there were no significant changes in the steel temperatures when compared with conventional plasterboard arrangement.

Kolarkar and Mahendran (2012) investigated the fire performance of LSF walls using small-scale fire tests. Nine small-scale tests were conducted under to ISO 834 standard time-temperature exposure. A novel LSF wall configuration of external insulation was introduced and its fire performance was investigated using small-scale fire tests. The test wall dimensions were 1280 mm × 1015 mm. Insulation materials such as glass fibre, rock wool and cellulose were considered. The following findings were drawn from this research.

- Presence of plasterboard joints did not significantly affect the thermal performance, in comparison with the tests without plasterboard joints in small-scale fire test. However, the plasterboard joints can have a significant effect during full-scale fire tests and under load bearing conditions.
- LSF test walls with single plasterboard configurations tend to exhibit steep rise in temperatures as the plasterboard calcinates after 20 min of fire test. This leads to premature structural failures in load bearing LSF walls when exposed to fire.
- Heat transfer in non-cavity insulated LSF walls was more uniform in comparison with cavity insulated LSF walls resulting in reduced thermal bowing of the LSF wall.
- The studs of LSF walls with rock fibre insulation resulted in higher temperatures on the hot flanges while the stud temperatures of LSF walls with cellulose insulation were the lowest. This indicates that the non-uniformity in temperature distribution is the highest in LSF walls with rock fibre insulation and can result in premature structural failures under load-bearing conditions.

Gunalan et al. (2013) investigated experimentally the behaviour of 11 full-scale (2.4 m × 2.4 m) load bearing LSF wall systems exposed to ISO fire curve (Table 2.1). This research focused on the LSF walls used in Australia. Conventional LSF wall

Table 2.1: Test wall configurations used by Gunalan et al. (2013)

Test Specimen	Configuration	Condition	Insulation	Load ratio	Vertical plasterboard joints
1		Ambient	None	0.2	Studs 2 and 4
2		Fire	None	0.2	Studs 2 and 4
3		Fire	None	0.2	Studs 2 and 4
4		Fire	Glass fibre (cavity insulation)	0.2	Studs 2 and 4
5		Fire	Rock fibre (cavity insulation)	0.2	Studs 2 and 4
6		Fire	Cellulose fibre (cavity insulation)	0.2	Studs 1 and 3
7		Fire	Glass fibre (external insulation)	0.2	Studs 1 and 3
8		Fire	Rock fibre (external insulation)	0.2	Studs 2 and 4
9		Fire	Cellulose fibre (external insulation)	0.2	Studs 2 and 4
10		Fire	Glass fibre (external insulation)	0.4	Studs 1 and 3
11		Fire	Rock fibre (external insulation)	0.4	Studs 2 and 4

assemblies with single row of studs were used in this research. The LSF wall panel arrangement was made of four studs connected by tracks on top and bottom. Noggings were not used in any of the wall panels. The wall panels had different kinds of insulation such as glass fibre, rock fibre and cellulose fibre. New LSF panels by sandwiching insulation between the plasterboards (external insulation) were also developed as part of this research. The studs used were $92 \times 40 \times 15 \times 1.15$ (G500) lipped channel sections with varying number of plasterboard layers (one or two). Load ratios of 0.2 and 0.4 were used (9 and 2 tests). It was found that providing external insulation in the load bearing LSF walls significantly improved the FRL of the wall system even at higher loads.

Chen et al. (2013) investigated different types of plasterboard and insulation materials to improve the fire performance of load-bearing LSF wall systems. Plasterboard types such as gypsum plasterboard, oriented standard boards (OSB), Bolivian magnesium board, rockwool boards and autoclaved lightweight concrete (ALC) boards were used in this research. Aluminium silicate insulation was also used in the full-scale fire tests. Total of six full-scale fire tests were conducted for this research. The experimental setup included lipped channel stud sections with depth varying from 89 to 140

mm. Back to back lipped channel stud sections were used in the fire tests with higher load ratios. Figure 2.4 shows the typical failure of studs in the test wall after the fire test. Fire test results showed that the FRL will decreased with increasing in load ratio.

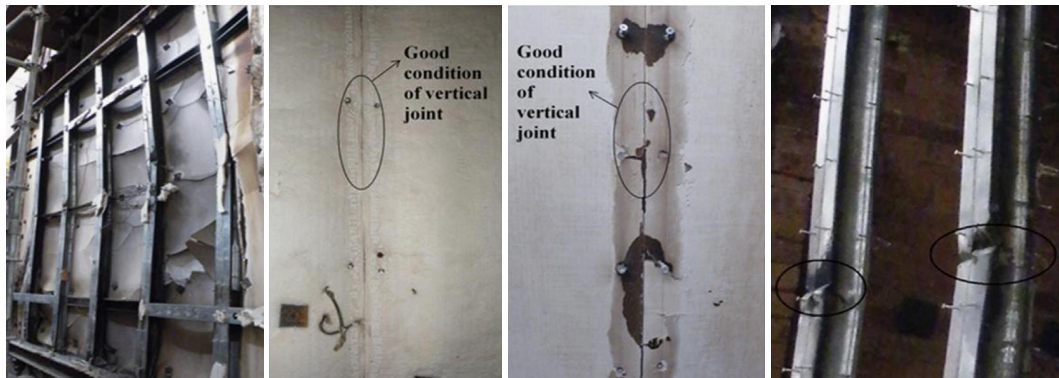


Figure 2.4: Lipped Channel Stud (LCS) failure in the fire test of Chen et al. (2013)

The failure modes of the studs in the test walls with Bolivian magnesium board were different in comparison with other type of lining boards. Gypsum boards and bolivian boards were found to be less suitable for use in external walls due to durability reasons, whereas ALC boards are preferred to be used in external walls. Increased screw-to-panel edge distance reduced the collapse of boards thereby preventing board open up on the fire side and cracks on the ambient side.

Kolarkar and Mahendran (2014) investigated the fire performance of gypsum plasterboards and composite panels. Fifteen small scale tests with 13 and 16 mm plasterboards were considered in their experimental investigation. Glass fibre, rock fibre and cellulose fibre insulations with different thickness and density were used as external insulation in the small scale LSF wall panels and their fire performance was investigated. It was found that, the composite wall panels in which the insulations were provided externally, performed better under fire exposure when compared to wall panels with cavity insulations. Another important observation is that the glass fibre insulation disintegrates at about 700°C, which is achieved at about 50 minutes of fire exposure resulting in premature failure of the walls with cavity insulation when compared with walls without cavity insulation. The cellulose fibre insulation resulted in better fire performance, provided low density cellulose is used when spraying the insulation within the cavity. Also, the process of spraying cellulose insulation within the cavity was not uniform always and could lead to varying results. Out of all the combinations used in this research, the rockwool external insulation was found to withstand

disintegration better when compared with its counterparts. This is because the rockwool insulation did not disintegrate till end of the fire test, whereas other insulation materials disintegrated easily which ultimately reduced the FRL.

Ariyanayagam and Mahendran (2014) studied the thermal performance of LSF walls under realistic design fires. Their test results were compared with those from LSF walls tested with standard ISO fire curve. Finite element models were developed for transient and steady state analyses and the results were compared with the test results. The FEA results for the realistic design fire curve were in good correlation with the experimental results. This research illustrated the difference between the effects caused by a standard fire and a realistic design fire in buildings. It also emphasized the use of realistic fire curves for the design of LSF walls. The effects of plasterboard joints and their arrangements were also investigated experimentally. It was observed that back blocking plasterboard joint arrangement used over the studs increased the FRL of LSF walls significantly by 25% when compared with the traditional plasterboard joints. Numerical studies were also carried out to validate these results and were found to be in good correlation with experimental results.

Kesawan and Mahendran (2015) proposed the use of welded hollow flange channel (HFC) sections as studs in LSF walls. HFC sections have two flanges connected to the web through welding as shown in Figure 2.5. Investigations were carried out

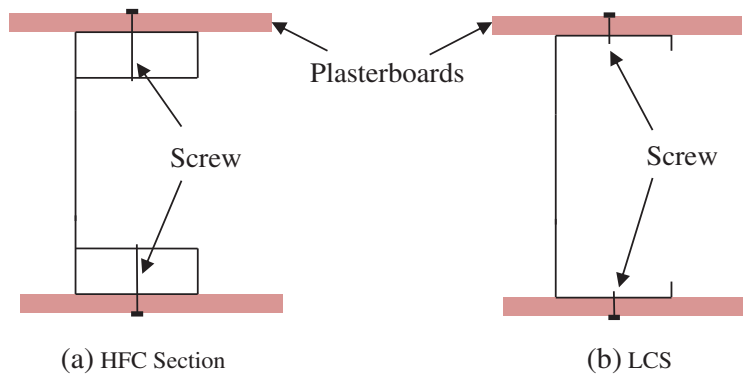


Figure 2.5: Hollow Flange Channel (HFC) studs used by Kesawan and Mahendran (2015)

on LSF walls with HFC stud sections to determine the thermal performance of LSF walls in fire. Initially the mechanical properties of the flange and web elements of the HFC sections were determined by tensile coupon tests at elevated temperatures. Secondly, full-scale fire tests of load bearing LSF walls with hollow flange channel

studs were conducted. New parameters such as specific heat, density, emissivity and enthalpy were proposed for the thermal FE modelling of this new LSF wall configuration. The experimental investigation was carried out for various profiles of the HFC sections with and without insulations. Numerical models were created with measured mechanical properties and validated by comparing the results with experimental results. A numerical parametric study was conducted by varying the section geometry and stud thickness. Their results showed that the FRL was not improved by the stud section geometry, provided the section depth and thickness remain the same.

Rusthi et al. (2017a) conducted full-scale fire tests of LSF walls using Australian Magnesium Oxide (MgO) boards instead of the conventional gypsum plasterboards with lipped channel sections. This research investigated the thermal properties of the MgO boards in detail followed by full-scale fire tests. All the fire tests were conducted under non-load bearing conditions. Three full-scale fire tests were conducted, which included, LSF walls with and without cavity insulation. Significant cracking sound were observed with cracks on the ambient side after 25 min of fire test. Heavy delamination and cracking of MgO boards was noticeable on the fire exposed side after the fire test. Integrity based failure was the mode of failure in all fire tests. Despite the usage of mortar in board joints that can withstand high temperature, the cracking of the joints during fire test could not be nullified. It was also found that the usage of noggings in LSF walls with MgO boards, resulted in more cracking in comparison with wall assemblies without noggings. Therefore, it was recommended to exclude noggings in LSF walls subjected to large deformations.

Rusthi et al. (2017b) developed heat transfer models in ABAQUS to predict the thermal behaviour of LSF walls under fire. 3D solid heat transfer brick elements were used for steel studs and plasterboards to create the heat transfer model. Tie constraints were used in the model to fix the steel studs and plasterboards for the heat transfer analysis. Five different LSF wall configurations were considered for the purpose of validation. Limiting hot flange temperatures proposed by Gunalan et al. (2013) and Ariyanayagam and Mahendran (2014) were considered in the parametric study to determine the failure times of the considered LSF wall configurations. The limiting hot flange temperatures were found to be decreasing with the increase in load ratio. The boundary conditions for the heat transfer model included the following.

- ISO 834 standard time-temperature curve on the fire exposed side of the model.
- The model was enclosed on all the sides and cavity radiation was specified within the cavity with an emissivity co-efficient of 0.9.
- Convective film transfer coefficient of $10 \text{ W/m}^2/\text{°C}$ was specified on the ambient surface while $25 \text{ W/m}^2/\text{°C}$ was specified on the fire exposed surface.
- Radiation was assumed to be the dominant mode of heat transfer within the cavity, neglecting the effects of convection within the cavity.

Time-temperature curves were extracted from the thermal analysis and compared against the corresponding experimental results. The model predictions were found to exhibit reasonable match with the time-temperature curves from the experiments.

Ariyanayagam and Mahendran (2018a) conducted five full-scale tests to investigate the fire performance of non-load bearing LSF walls. Gypsum plasterboard thicknesses of 13 and 16 mm were used along with 92 mm deep lipped channel studs. Test wall configurations included different plasterboard layers, cavity insulation and noggings to investigate the influence of these components on the fire performance of non-load bearing LSF walls. The test results showed that the typical failure mode in the non-load bearing LSF wall fire tests was insulation criterion, where the ambient surface plasterboard temperatures exceeded the limiting temperature. Finding from the research showed that the increase in plasterboard thickness resulted in increased FRL. The presence of noggings in non-load bearing LSF walls did not significantly influence the thermal behaviour. However, this can have considerable contribution to the structural behaviour under load bearing conditions. It was also found that the melting point of the insulation material used should be higher to achieve higher FRL for non-load bearing walls.

Ariyanayagam and Mahendran (2018b) then investigated the effects of low strength steel studs subjected to fire under load bearing conditions. Full-scale fire tests were conducted under 0.4-0.6 load ratios. Material properties at elevated temperatures were obtained through experimental investigation for the low strength steel studs and a parametric study was conducted using ABAQUS. Structural FE analysis results showed that the use of low strength steel resulted in reduction of FRLs by 25% in comparison with a similar LSF wall made of high strength steel. The critical hot flange temperatures

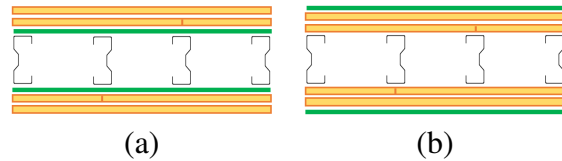


Figure 2.6: Test configurations used by Dias et al. (2019a) (a) Internal and (b) External steel sheathing

were also lower due to the reduction in the mechanical properties of steel at elevated temperatures. It was found that the usage of appropriate elevated temperature mechanical property reduction factors in FE analysis is critical in predicting the FRL through numerical methods.

Dias et al. (2018a) conducted an experimental investigation on the fire performance of LSF walls with steel sheathing under non-load bearing conditions. Small-scale fire tests were conducted on $1\text{ m} \times 1\text{ m}$ LSF wall assemblies with 0.5 mm steel sheathing placed at different positions Figure 2.6. Steel sheathing was used in the internal cavity wall facing surface and also on the fire exposed and ambient surfaces. The entrapment of water molecules from gypsum plasterboard on to the steel sheets resulted in increased thermal performance under non-load bearing conditions.

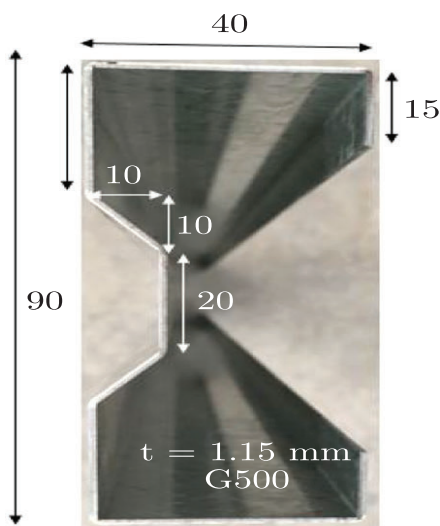


Figure 2.7: Web-stiffened studs used by Dias et al. (2019a)

Later, Dias et al. (2019a) extended the investigation by conducting three full scale fire tests on LSF walls with steel sheathing. Web-stiffened studs were used instead of the conventional lipped channel sections (LCS) as shown in Figure 2.7. The proposed new web-stiffened studs were able to withstand higher axial compression load in comparison with conventional LCS studs under ambient and fire conditions. However,

when the FRL is considered based on the non-dimensional load ratios, these new wall configurations were found to provide only a marginal increase in the FRL in comparison with the conventional LSF wall configuration with LCS studs.

2.3 Thermal and Mechanical Properties of Cold-Formed Steels

To study the behaviour of cold-formed steel structures under fire conditions, it becomes a necessity to account for the yield strength and elastic modulus values at elevated temperatures, as these parameters contribute to the structural strength of cold-formed steel members. The elevated temperature mechanical properties that are used in the research and design of cold-formed steel sections are based on BS EN 1993-1-3: (2006) and are shown in Table 2.2. These mechanical properties with the corresponding reduction factors belong to hot-rolled steels and are also generally used for cold-formed steel sections. But Kankamge and Mahendran (2011) investigated this issue and proposed modified reduction factor equations for cold-formed steel sections. Tensile coupon tests were conducted under steady state conditions to study the behaviour of various grades cold-formed steels at elevated temperatures. The effect of creep was neglected in this study, as the experiments were concluded within an hour.

Specimen thicknesses of 1.50 and 1.95 mm with G250 and G450 steel grades and 0.95 mm thickness with G550 steel grade were used in their investigations. They also used the previous test results for cold-formed steel thicknesses upto 1 mm obtained by Ranawaka and Mahendran (2009b) and developed suitable design equations for the yield strength and elastic modulus reduction factors of cold-formed steels at elevated temperatures ($\frac{f_{y,T}}{f_{y,20}}$ and $\frac{E_T}{E_{20}}$) as follows.

Yield Strength for Low Strength Steels

$$20 \leq T \leq 200^{\circ}C, \frac{f_{y,T}}{f_{y,20}} = -0.0005T + 1.01 \quad (2.20)$$

$$200 \leq T \leq 800^{\circ}C, \frac{f_{y,T}}{f_{y,20}} = 25(1.16 - T^{0.022}) \quad (2.21)$$

Table 2.2: Reduction Factors for Cold-Formed Steels at Elevated Temperatures

Stud	Temperature	Reduction factor (relative to f_y) for effective yield strength	Reduction factor (relative to f_y) for satisfying yield deformation criteria	Modified factor (relative to f_y) for satisfying proportional limit criteria	Reduction factor (relative to f_y) for proportional limit criteria	Reduction factor (relative to E_a) for the slope of linear elastic range	$k_E \theta = E_a \theta / E_a$
	20 °C	$k_y \theta = f_{y,0} \theta / f_y$	$k_x \theta = f_{x,0} \theta / f_y$	$k_p \theta = f_{p,0} \theta / f_y$	$k_f \theta = f_{f,0} \theta / f_y$		
	100 °C	1	1	1	1	1	1
	200 °C	1	1	0.922	0.807	0.9	
	300 °C	1	0.845	0.613	0.42	0.7	
	400 °C	1	0.77	0.354	0.36	0.6	
	500 °C	0.78	0.615	0.167	0.18	0.31	
	600 °C	0.47	0.354	0.087	0.072	0.13	
	700 °C	0.23	0.051	0.051	0.0375	0.0675	
	800 °C	0.11	0.034	0.034	0.025	0.045	
	900 °C	0.06	0.017	0.017	0.0125	0.0225	
	1000 °C	0.04	0	0	0	0	
	1100 °C	0.02	0	0	0	0	
	1200 °C	0	0	0	0	0	

Yield Strength for High Strength Steels

$$20 \leq T \leq 300^{\circ}C, \frac{f_{y,T}}{f_{y,20}} = \left\{ 1 - \frac{(T - 20)^{4.56}}{1 * 10^{10}T} \right\} \quad (2.22)$$

$$300 \leq T \leq 600^{\circ}C, \frac{f_{y,T}}{f_{y,20}} = \left\{ 0.95 - \frac{(T - 300)^{1.45}}{7.76T} \right\} \quad (2.23)$$

$$600 \leq T \leq 800^{\circ}C, \frac{f_{y,T}}{f_{y,20}} = -0.0004T + 0.35 \quad (2.24)$$

Elastic Modulus for Low and High Strength Steels

$$20 \leq T \leq 200^{\circ}C, \frac{E_T}{E_{20}} = -0.0008355T + 1.0167 \quad (2.25)$$

$$200 \leq T \leq 800^{\circ}C, \frac{E_T}{E_{20}} = -0.00135T + 1.1201 \quad (2.26)$$

Kankanamge and Mahendran (2011) improved the elevated temperature stress-strain models developed by Ranawaka and Mahendran (2009a) for cold-formed steels by the following equation.

$$\varepsilon_T = \frac{f_T}{E_T} + \beta \left(\frac{f_{y,T}}{E_T} \right) \left(\frac{f_T}{f_{y,T}} \right)^{\eta_T} \quad (2.27)$$

For high strength steels (G550), $20 \leq T \leq 800^{\circ}C$,

$$\eta_T = -3.05 \times 10^{-7}T^3 + 0.0005T^2 - 0.2615T + 62.653 \quad (2.28)$$

$$\beta = 0.86$$

For low strength steels, $300 \leq T \leq 800^{\circ}C$,

$$\eta_T = 0.000138T^2 - 0.085468T + 19.212 \quad (2.29)$$

$$\beta = 1.5$$

This research concluded that steel grade influences the yield strength at elevated temperatures. However, there was no effect on the yield strength with respect to thickness of steel. The proposed equations predicted the mechanical properties with good accuracy for low and high-grade cold-formed steels. All these equations (Equa-

tions (2.20) to (2.29)) are now included in Section 9 of AS/NZS 4600 SA (2018).

2.4 Thermal Properties of Plasterboard

Gypsum plasterboards are widely used in the construction of walls in Australia and throughout the globe. Like other materials, gypsum plasterboards provide resistance to fire, but through time several industries have come up with improved plasterboards capable of resisting fire. But to predict the thermal performance of LSF wall systems the thermal properties of plasterboards are needed. Thermal properties include conductivity, specific heat, mass loss etc. Many studies were conducted to determine the thermal properties of gypsum plasterboard and are discussed next.

The effect of moisture transfer at high temperatures on the specific heat of gypsum plasterboard was investigated by Ang and Wang (2009). Numerical techniques and experimental methods were used to investigate the effects of moisture transfer on specific heat when gypsum plasterboards were exposed to fire. The equivalent energy required at higher temperatures for the water to evaporate from the plasterboard was not known. Therefore, an approximate temperature of 100°C was assumed for the initial trials. Apart from ablation, shrinkage and collapse of the plasterboards under fire as reported by Jones (2001), the size and the loading conditions were found to affect the specific heat. In this study the effects of ablation, shrinkage and collapse were neglected. Combined heat and mass transfer was the modelling technique adopted in this study. To solve this heat transfer problem, thermal and pressure boundary conditions were considered in the model. Computer program called HEATMASS was developed based on the laws of heat and mass transfer. Additional inputs such as porosity and permeability along with normal heat transfer analysis inputs such as specific heat, density and thermal conductivity of plasterboard were used. It is to be noted that gypsum contains 3% free water and 21% chemically bound water as per Mehaffey et al. (1994). This water content is responsible in preventing fire from spreading to the other side of the board. At higher temperatures, the plasterboard calcinates and the water is lost from the plasterboard resulting in plasterboard fall-off during fire exposure. Experimental investigations were conducted to determine the saturated permeability of gypsum plasterboard. It was assumed that, the permeability of gypsum remains un-

changed at high temperatures due to the micro nature of the particles, thereby resulting in micro-cracks. It was concluded that the appropriate value of permeability of gypsum plasterboard was 5×10^{-9} m/s. This was derived by validating the experimental results with the numerical model in HEATMASS. It was also found that the specific heat for numerical analysis is a function of gypsum plasterboard's permeability. It was also proposed that a modification factor of 1.45 along with the permeability in standard fire condition is to be included to achieve good agreement in the numerical analysis.

Kontogeorgos et al. (2011) investigated the thermal performance of gypsum plasterboard at various dehydration temperatures. Past research studies showed that the first dehydration of gypsum plasterboard occurs at around 150°C. In this study the thermal conductivity, specific heat and density were measured as a function of the dehydration temperature i.e. until 300°C. Relationship between the dehydration energy as a function of mass loss during dehydration process was also investigated. Different heating rates were used in determining the thermal properties of gypsum plasterboard. Specimen sizes of 200 × 150 × 20 mm and 160 × 40 × 40 mm were used. Thermocouples were fixed on eight different locations in the specimen and the temperature was recorded at 2 s intervals.

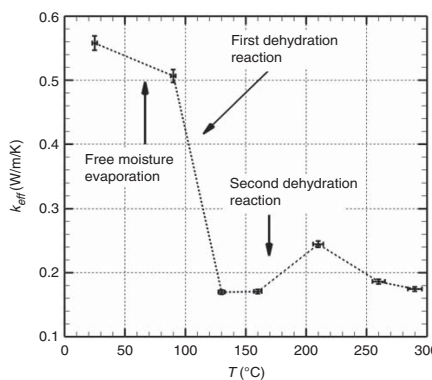


Figure 2.8: Thermal conductivity used by Kontogeorgos et al. (2011)

Hot wire method was used to measure the thermal conductivity of the specimen. This method is based on the transient method of heat transfer as per ISO 8894-1 (2010) (latest amendment). OHAUS scale was used to measure the weight of the samples exposed to elevated temperatures and to calculate the mass loss. The energy required for dehydration was calculated using Differential Scanning Calorimetry (DSC) at a heating rate of 20°C/min using airflow from 0 °C to 600°C. The thermal conductivity as a function of temperature obtained from the experiments is shown in Figure 2.8. This

investigation concluded that due to the evaporation of free moisture content at about 100°C, the thermal conductivity decreases after the first dehydration point. Also, it provided an experimental method to predict the energy absorbed by the gypsum plasterboard at dehydration point when exposed to elevated temperatures.

2.5 Numerical Simulation

Sultan (1996) proposed a one-dimensional mathematical model to predict the heat transfer in non-load bearing and non-insulated LSF walls. Single row of steel studs spaced at 600 mm centres and 0.45 m thick were considered. To reduce the complexity of the analysis the radiative heat transfer from the studs to the plasterboards was ignored. Also the moisture movement and cracking of the plasterboards were not considered. Time-Temperature profile from CAN/ULC-S 101-M89 was adopted for the model based on ASTM 119-16 (2016).

$$T_f = T_\infty + 750[1 - \exp(-3.79553)\sqrt{\tau}] + 170.41\sqrt{\tau} \quad (2.30)$$

Where

T_f = Temperature of fire curve (source) (°K);

T_∞ = Temperature of Ambient side;

τ = time, h.

The heat transfer through the wall from the fire side to the ambient side was governed by the basic heat transfer equations of conduction, convection and radiation. The emissivity of the plasterboard was kept constant at 0.8 throughout the model. The convective heat transfer co-efficient was varied for different faces such as the fire exposed face, wall cavity and the unexposed face of the LSF wall as in Equations (2.31) to (2.33).

$$h_{exp} = 0.95(T_f - T_g)^{0.33} \quad (2.31)$$

$$h_{exp} = 0.95(T_f - T_g)^{0.33} \quad (2.32)$$

$$h_{uexp} = 1.42(T_g - T)/L^{0.33} \quad (2.33)$$

Where

h_{exp} = Convective heat transfer co-efficient (fire exposed side)

h_{cav} = Convective heat transfer co-efficient (cavity)

h_{uexp} = Convective heat transfer co-efficient (unexposed side)

T_f = Temperature of fire curve (source) ($^{\circ}\text{K}$)

T_g = Temperature of gypsum board ($^{\circ}\text{K}$)

T = Temperature ($^{\circ}\text{K}$)

L = Wall height (m)

d = Wall cavity depth (m)

Finite difference method was adopted to predict the temperature history across the wall and corresponding equations were proposed for different locations of the wall because of the varying boundary conditions. To validate the mathematical model, small-scale fire tests of specimens $1\text{ m} \times 1\text{ m}$ and $1\text{ m} \times 2\text{ m}$ were conducted with the same configuration adopted in the mathematical model. The failure criteria for the fire test were in accordance with CAN/ULC-S 101-M89. The heat transfer mechanism in the fire test within the cavity was through natural and forced convection at different time of fire exposure and through radiation. This was not considered in the mathematical model. This research work resulted in clear insight of the heat transfer mechanisms across the LSF wall assembly.

Keerthan and Mahendran (2012b) conducted numerical studies of gypsum plasterboard panels. The thermal inputs such as thermal conductivity, specific heat, relative density and mass loss for the numerical analysis were derived through thermal property test conducted on gypsum plasterboards. From the past research conducted on gypsum plasterboards by Mehaffey et al. (1994) and Sultan (1996) and other researchers, it is evident that the plasterboard when exposed to fire above 800°C as per the ISO 834 standard fire curve will not stay intact. So apparent thermal conductivity values were used in the numerical models after 800°C . This is because, the plasterboard cracks after this temperature letting the hot gases to pass through, which cannot be predicted by the numerical model. The thermal conductivity, specific heat and relative density of plas-

terboards obtained from past research are shown in Figures 2.9 (a) to (c). Since there were discrepancies in the specific heat peak values, second dehydration point and relative density of plasterboards measured by past research works, experiments were carried out by Keerthan and Mahendran (2012a) using differential scanning calorimetry (DSC) and thermo gravimetric analysis (TGA). From the DSC heat flow data, specific heat was calculated as per ASTM E1269 (2011). Their experimental results for specific heat, relative density and the proposed idealised thermal conductivity are shown in Figures 2.10 (a) to (c).

These thermal properties were then used in the FE model developed in SAFIR and the results from the thermal analysis were compared with the results from the small-scale fire tests of plasterboards. It was concluded that, when the default thermal properties in SAFIR were used in the thermal analysis, there was not a good agreement between the FE model and the fire test. However, when the measured thermal properties were used in the thermal analysis, a good agreement was found between the small-scale fire test and FE model. The effect of moisture movement was not considered in the numerical analysis as the effect is not significant in temperatures above 120°C.

Gunalan and Mahendran (2013b) developed structural numerical models and validated them using the experimental results. Initially elastic buckling analysis was conducted using a finite strip analysis software called CUFSM. Various restraint conditions were used to study the elastic buckling behaviour. Then the elastic buckling load was expressed as load factor vs half-wave lengths and the different buckling modes were presented as shown in Figure 2.11.

Finite element modelling and analysis were carried out in ABAQUS for the conducted experiments. Mechanical properties such as Young's modulus were determined by conducting tensile coupon tests. Since ABAQUS accepts true stress and logarithmic plastic strain, the engineering stress and strain from tensile coupon tests were converted to true stress and logarithmic plastic strain using the equations given next.

$$\sigma_{true} = \sigma_{eng}(1 + \epsilon_{eng}) \quad (2.34)$$

$$\epsilon_{true}^{pl} = \ln(1 + \epsilon_{eng}) - \frac{\sigma_{true}}{E} \quad (2.35)$$

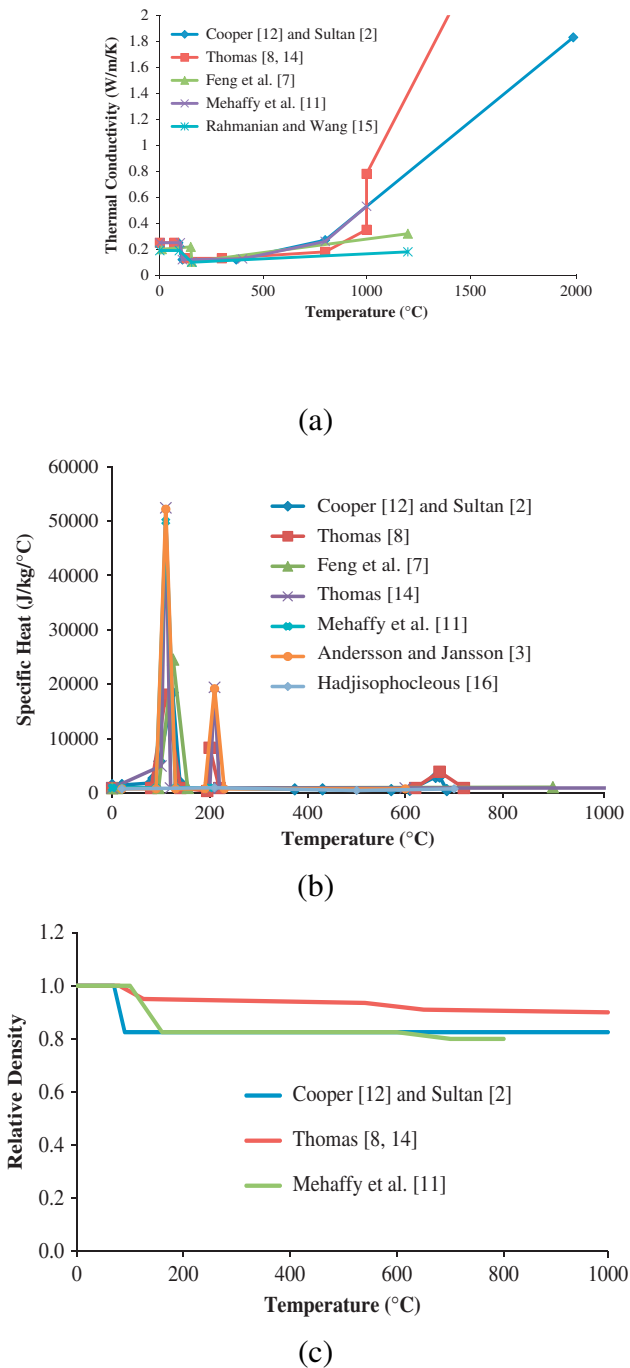


Figure 2.9: Thermal properties of plasterboard from Keerthan and Mahendran (2012b)

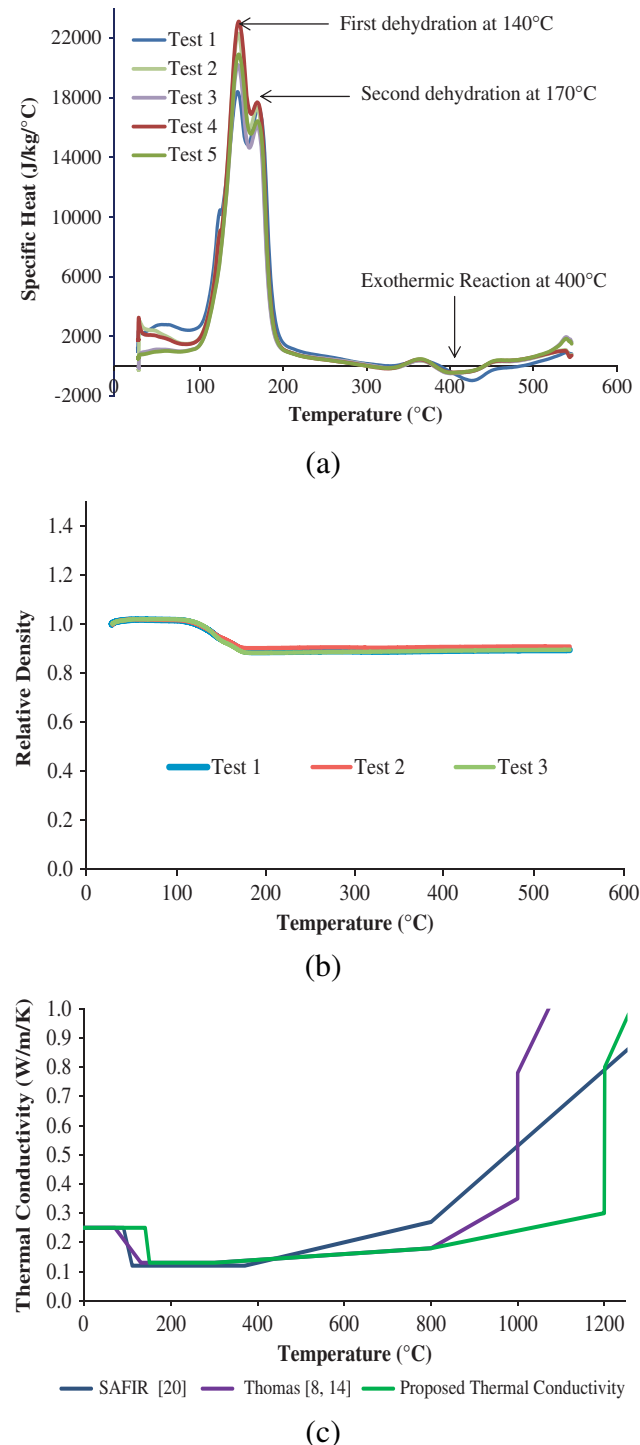


Figure 2.10: Proposed thermal properties of plasterboard from Keerthan and Mahendran (2012b)

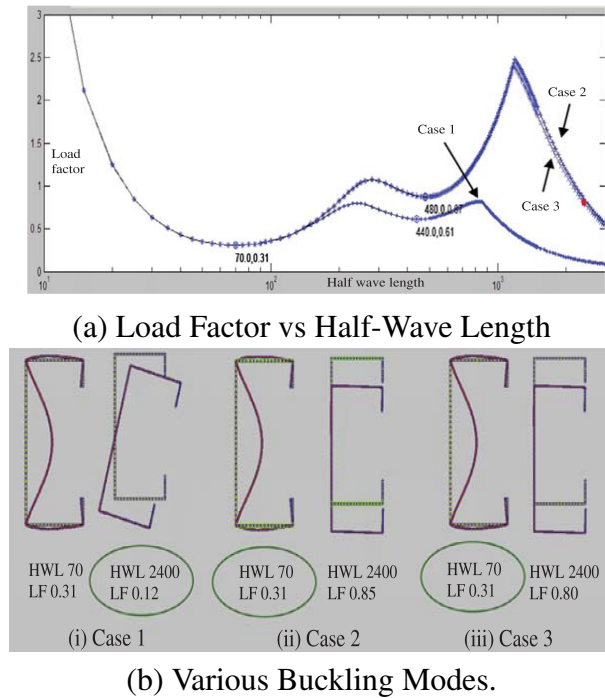


Figure 2.11: Buckling analysis results from Gunalan and Mahendran (2013b)

The true stress and logarithmic plastic strain were then fed as input to the structural analysis. Thermal and structural boundary conditions were assumed in accordance with the experiments conducted and non-linear static structural analysis was conducted in ABAQUS. To simplify the thermal boundary conditions, it was assumed that the temperature distribution is linear on the webs from hot flange to cold flange and constant on the flanges. More complex effects such as thermal bowing and deterioration of the mechanical properties at elevated temperatures were studied from the numerical model and validated with the experimental results. New design rules based on AS/NZS 4600 and Eurocode 3 Part 1.3 were proposed by providing allowances for the thermal bowing effects, neutral axis shifts and magnification effects. These proposed design rules were then validated using the results from numerical parametric studies and were found to have good correlation.

Nassif et al. (2014) proposed a numerical model to predict the transient thermo-mechanical behaviour of LSF walls under fire. Full-scale $3\text{ m} \times 3\text{ m}$ wall panels were constructed with single row of studs and gypsum plasterboards were attached on both sides. Sequentially coupled analysis was carried out in ABAQUS and the results were compared with the experimental results. The thermal and mechanical properties for the numerical model were extracted from past literature and Eurocode. The numerical

model was developed by considering the transient heat transfer behaviour of the LSF wall during fire. Conduction and convection on the fire exposed and unexposed faces of the wall were considered in the analysis. It was observed from the experiments and numerical models that the plasterboards provide considerable restraints to the steel studs against out of plane deflection. The proposed numerical model predicted the temperature of the steel studs and plasterboard to certain accuracy. However, during the plasterboard fall-off, the temperatures increase rapidly during the experiments and the model could not predict this uncertain behaviour.

Chen et al. (2014) developed a numerical model to predict the thermal and mechanical response of cold-formed steel (CFS) studs in fire. With the help of measured material properties, a one dimensional thermal response model was formulated to predict the heat transfer mechanism across the width in LSF walls under fire. Gauss-Seidel method was used to solve the governing equations expressed in the form of finite-difference equations. A thermomechanical response model was also developed to predict the axial and lateral deformations in the CFS wall system. Following assumptions were made to simplify the model.

- Heat transfer was assumed to happen in the horizontal direction across the width of the wall only.
- Variation in heat transfer due to the steel studs was ignored.
- Apparent thermal properties for specific heat were assumed to incorporate the effects of moisture transfer and plasterboard cracking.
- Plasterboard cracking was assumed to happen when the temperature increases beyond the threshold limit.
- Despite the variation in temperatures along the height of the wall due to the air movement, this effect was neglected in the numerical model.
- As the cross-section area of studs is comparatively less than the cavity area, conduction through studs was assumed to be less significant and the corresponding effects were also neglected.
- Different failure mode criteria were assumed to predict the failure time for CFS wall assemblies in the thermomechanical model.

Despite the above mentioned simplifications, the numerical model was able to predict the experimental time-temperature and lateral deflection curves with reasonable accuracy.

Batista Abreu and Schafer (2015) proposed advanced numerical modelling of the LSF wall panels. Conventionally, the studs were modelled individually for thermal and structural analysis. However, the plasterboards were also modelled along with the studs and the opening of the joints were assumed, so that, the numerical model simulated the experimental behaviour to greater precision. Sequentially coupled thermal and structural analyses were used in the numerical model developed in ABAQUS. The stiffness of fasteners sheathing system was also investigate numerically as a part of this study. Design equations for normal and fire rated gypsum boards were also proposed. It was concluded that the Finite Strip Method (FSM) and Finite Element Analysis (FEA) are the most efficient methods of structural analysis for cold-formed steel sections.

Cheng et al. (2015) developed a model to perform buckling analysis of the lipped channel cold-formed steel sections at elevated temperatures. Their investigation was conducted by performing heat transfer analysis initially, followed by pre-buckling and post-buckling analysis. Finite element analysis was used for the heat transfer problem. Bernoulli's beam theory was used for the pre-buckling analysis by considering the strain effects due to variation in mechanical properties at elevated temperature. Finite strip analysis and classical Fourier solutions were used in the buckling analysis. It was observed that the buckling behaviour of cold-formed steel sections varied under non-uniform temperature exposure when compared with uniform temperature exposure. It was concluded that the higher temperature regions (hot-flange) had lower pre-buckling stresses whereas the lower temperature regions (cold-flange) had higher pre-buckling stresses. Also, the fire design formula for beams under uniform temperature exposure will not be suitable for sections with non-uniform temperature distribution.

The local buckling effects of cold-formed steel compression members were investigated in detail by Gunalan et al. (2015). Using 91 local buckling tests, experimental results were compared with the numerical predictions from ABAQUS for validation purposes. The cold-formed sections for the local buckling tests were selected using ABAQUS and CUFSM on condition that local buckling occurred at ambient conditions. For elevated temperatures, reduced mechanical properties were used in

ABAQUS and CUFSM to find the elastic buckling loads. Shell S4 elements were used in the finite element model. Geometric imperfections proposed by Schafer et al. (2010) for lipped channel sections and Camotim et al. (2006) for plain channel sections were used. Steel grades of G250, G450 and G550 were used in this research. The ambient temperature mechanical properties of G250 and G550 steels were used based on Ranawaka and Mahendran (2009b) while for G450 steel, they were obtained from Kankanamge and Mahendran (2011). It was concluded that the ambient temperature design rules can be used to predict the buckling behaviour at uniform elevated temperature by considering reduced mechanical properties. The effective area method at ambient temperatures as per Eurocode 3 Part 1.2 resulted in over-conservative results at elevated temperatures. It was also proposed that at elevated temperatures the current design rules can be improvised by incorporating the effects of non-linear stress-strain relationships.

Kesawan and Mahendran (2016c) developed a 2D numerical heat transfer model using SAFIR. The aim of this research was to develop a numerical model for validating the fire tests conducted using HFC steel studs by Kesawan and Mahendran (2015). A 2D model replicating the fire test was created in SAFIR and the corresponding thermal properties of the materials were keyed in to carry out heat transfer analysis. Heat transfer along the height of the wall was neglected for computational efficiency. GiD, a general purpose pre and post processor software, was used to create models, assign meshes and view the results after analysis. Overall mesh dimension of 8 mm was incorporated into the model based on the research by Keerthan and Mahendran (2012a). Moisture transfer and plasterboard cracking effects were ignored in the thermal analysis considering their insignificant contribution to the FRL. Localised temperature rise in studs due to plasterborard fall-off was also ignored due to the complexity in modelling the same. From the thermal analysis results, it was found that the time-temperature curves of the plasterboards and studs agreed reasonably well with the experimental results in non-cavity insulated HFC walls, while there were minor disagreement with cavity insulated HFC walls.

A detailed parametric study by considering the variation in stud depth and flange width was also carried out in SAFIR as part of this research. The parametric thermal analysis results shows that the variation in stud time-temperature curves with increase

in cavity depth/ stud width did not significantly change. This indicates that, the heat transfer through conduction in stud remains unchanged with increase in cavity depth. However, the time-temperature curves comparison of plasterboards were not presented. It was stated that the same time-temperature profile of studs can be used to determine the FRL irrespective of the cavity depth, which is debatable. The effect of stud thickness was also investigated. Stud thicknesses from 0.6 mm to 3 mm were taken for the parametric study. The thermal analysis results showed that for thicker stud section the hot flange temperatures were lower, while the cold flange temperatures were higher in comparison with the thinner sections. The effect of stud thickness was found to affect the temperature profiles in cavity insulated walls significantly. Increase in stud spacing was also investigated and was found to have no significant effects on the time-temperature curve. The thermal performance of different wall configurations was also investigated. Later, Kesawan and Mahendran (2016a) extended the study to develop fire design rules for hollow flange channel sections subjected to non-uniform temperatures under fire. The improved fire design equations were based on AS/NZS 4600 and Eurocode 3 Part 1.3. Direct strength method (DSM) based equation was also proposed and verified based on the experimental and numerical work conducted earlier. The load ratio versus FRL curves derived earlier by Kesawan and Mahendran (2016c) were now obtained using the AS/NZS 4600 and Eurocode 3 design equations. The modified design equations used in this study were based on Gunalan and Mahendran (2013a) along with those from AS/NZS 4600.

The section moment capacities at stud mid-height and supports were computed by the Equations (2.36) and (2.37) shown next.

$$M_{x,eff} = \frac{\bar{f}_{yt}\bar{I}_{eff},t}{y_{max}} \quad (2.36)$$

$$M_{x,eff} = \frac{f_{yt,hf}\bar{I}_{eff},t}{y_{max}} \quad (2.37)$$

The thermal bowing effects were computed based on the modified equation by Baleshan and Mahendran (2016) as they were found to be less complex and is given in Equation (2.38).

$$e\Delta_T = \frac{(\alpha_{OHF}OHF - \alpha_{OCF}OCF)L^2}{8d} \quad (2.38)$$

The ratio between end moments ψ , was taken as -1 at stud mid-height despite the fact that the value of ψ is greater than -1 and also the actual values. Comparison was made against conventional LCS section with HFC section of similar web depth to understand these effects. The following modifications were made to the design equations. At the stud supports the P- Δ effects were neglected. Thermal bowing equations from Baleshan and Mahendran (2016) were used and the actual value of ψ for the bending capacity calculations were computed. Improvements were made to the Eurocode 3 Part 1.3 based equations apart from the AS/NZS 4600 based design equations. Design capacities were also predicted based on the Direct Strength Method (DSM) as well. It was found that the proposed design modifications to the existing equations were able to predict the structural capacities of HFC stud sections in fire to a reasonable accuracy. Comparisons were also made against the FE model predictions from ABAQUS by Kesawan and Mahendran (2016b) to investigate the suitability of these modified design equations.

Later, Kesawan and Mahendran (2018) reviewed the parameters influencing the fire performance of LSF walls. Important parameters such as plasterboard fall-off, wall configuration, geometric profile of the studs, thermal and mechanical properties of various components at elevated temperatures were discussed in detail based on previously conducted experimental and numerical studies. The effect of plasterboard joints was also discussed in detail. As the fire performance of cavity insulated walls is significantly less in comparison with non-cavity insulated walls, four new LSF wall configurations by externally insulating the walls were proposed in this research. The option of providing plasterboard strips as back blocking to the studs was also proposed to improve the fire performance. However, only limited experimental studies were conducted for the proposed configurations and detailed FE analysis has to be conducted to support the above claims. It was also proposed that the usage of longer fasteners would increase the contact area of screws on plasterboards thereby reducing the plasterboard fall-off during fire. But it is difficult to quantify these effects as substantial experimental and numerical investigations havw not been carried out on these effects. The temperature gradient within the studs was found to have significant influence on the FRL, as the difference in stud hot and cold flanges can result in premature structural failure. Different geometric shaped studs was also proposed and the influence of tem-

perature distribution amongst them was also compared with the help of FE analysis. However, these also need to be validated with the help of experimental studies.

Ariyanayagam et al. (2016b) investigated the detrimental effects of plasterboard joints on the fire performance of LSF walls. 150 mm wide plasterboard back blocking was used in the LSF wall panels and standard fire tests were conducted to investigate the detrimental effects of plasterboard joints in fire. Two full scale fire tests at 0.2 load ratio were conducted. The first LSF wall had plasterboard joints between the studs and the second LSF wall had plasterboard joints between the studs with the help of back blocking. The test wall panel was 2.1 m × 2.4 m with four studs spaced at 600 mm centres. No noggings were used in the LSF wall panel. Fire test results showed that the middle studs (2 & 3) recorded higher hot flange temperatures in the wall panel, where plasterboard joints were present on the studs when compared to the wall panel with plasterboard joints on back blocking. The failure time of the wall with back blocking plasterboard joint was 74 minutes whereas the conventional specimen lasted only 58 minutes. Numerical investigations were carried out in two steps. Initially, steady state analysis with temperature inputs from the experiments at different time periods were carried out. S4R elements were used for the studs with a mesh size of 4 mm and rigid body with R3D4 elements were used to apply the load to the studs. The studs used in this investigation were made of 1.15 mm G550 steel and were maintained at different temperatures in correspondence with the experiments. The axial compression load was applied and Riks analysis was carried out to achieve the failure of the stud. It was concluded that by providing back blocking to the plasterboard joint in load bearing LSF walls, the FRL of the wall was increased by up to 25%. However, the plasterboard joints did not have any effect on the non-load bearing LSF walls, which is generally governed by insulation failure.

Dias et al. (2018b) developed a thermal FE model in ABAQUS to investigate the thermal behaviour of web-stiffened stud LSF walls in fire. Thermal and structural modelling were conducted for the tested LSF wall configurations using small-scale fire tests. The modelling techniques were adopted from Rusthi et al. (2017b). Web stiffened studs were found to yield better compression capacity under ambient condition in comparison with the conventional lipped channel studs. However, the capacity of the same was not found to provide better results under fire when non-dimensional

parameter FRL was considered. The susceptibility of non-load bearing LSF walls failing under structural inadequacy criterion was also discussed based on the conducted FE analysis. However, experimental results were not available to validate this claim.

2.6 Computational Fluid Dynamics (CFD)

Computational fluid dynamics is a branch of fluid mechanics, in which the numerical problems with respect to fluid flows are solved by numerical analysis and algorithms. Problems related to wind flow and heat transfer are also solved by CFD. The discretization of the problem is undertaken using various methods in CFD such as Finite Element Method, Finite Volume Method, Finite Difference Method, Spectral element method and Boundary element method. Any ideal CFD model will be dependent on the Navier-Stokes equation.

To solve a heat transfer problem using a model based on Finite Element Method (FEM), coupled temperature displacement method is used. In this, the conduction, convection and radiation coefficients are used as input to the analysis and the heat transfer problem is solved, whereas in a CFD model these parameters can be input as a 3-D entity to arrive at precise results. ABAQUS CFD / ANSYS Fluent / FDS package is proposed for the numerical analysis of the advanced heat transfer problems to be taken up in this research as part of the numerical validation process.

Horvat et al. (2009) proposed a semi-analytical treatment of wall heat transfer coupled to numerical simulation model of fire. Their objective was to develop a computational technique to predict the heat flow through walls by simulating mass and momentum across the wall when exposed to fire. A numerical heat transfer model was developed in ANSYS CFX. Figure 2.12 shows the 1.2 m long \times 0.8 m wide \times 0.8 m high room considered, which is one third of the ISO room. A 25 mm thick insulation was considered in the walls and ceiling of the model.

The fuel boundary was from the back-left corner of the room with sizes of 0.25 m \times 0.25 m with 8 cm elevation. Methanol was used as the fuel source for the inlet boundary condition. This combustion modelling in ANSYS CFX was based on an eddy-dissipation model proposed by Magnussen and Hjertager (1977). The emissivity of the walls was assumed to be opaque with an emissivity value of 0.9.

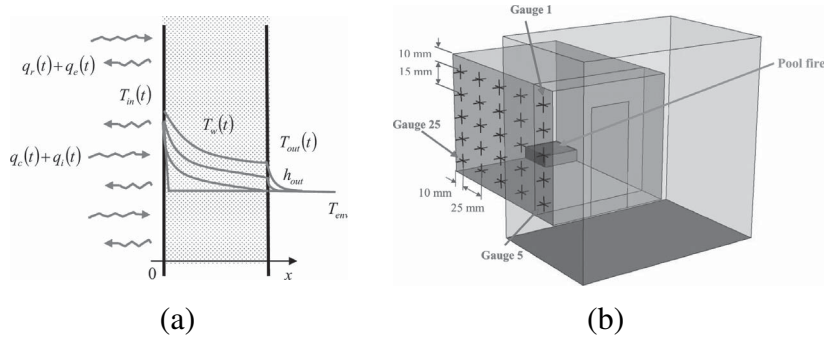


Figure 2.12: Model and domain used by Horvat et al. (2009)

The radiation within the cavity is modelled as per discrete transport model. The thermal model of the wall considered in the numerical analysis is shown in Figure 2.12. The values of thermal heat transfer co-efficient to determine the effect of convection within the cavity were also considered. The convective heat transfer co-efficient h_w varies with time. It was also reported that the heat transfer through the wall takes place by two mechanisms, one through the thermal radiation and the other through the convection of gases. Transient state heat transfer analysis was considered in this study. This developed heat transfer model was validated by comparing its results with experimental results from Tofilo et al. (2005). The comparison showed good agreement and the benefits of this semi-analytical computational technique.

The fire resistance of plasterboard entirely depends on the first dehydration point, which takes place at 80°C to 250°C during fire exposure. Therefore, Kolaitis and Founti (2013) developed a solid reaction kinematics dehydration model for gypsum plasterboards exposed to fire in CFD simulations. They addressed the important shortcoming from previous research by Horvat et al. (2009). The model developed by them included the thermos-physical properties of gypsum plasterboard (density, thermal conductivity and specific heat) and water vapour released from the plasterboard through mass diffusion and convection when exposed to fire. These effects were considered in the model to accurately predict the behaviour of gypsum plasterboards under fire exposure. In this model, the dehydration reactions were not predicted by effective specific heat formulation, whereas a two step solid reaction kinematic scheme was used for the predictions. Arrhenius equation was used to estimate the respective reaction rate. Fire Dynamic Simulator (FDS) code was developed based on the above-mentioned criteria and validated with constant thermo-physical property model and an

effective specific heat model. The constant thermo-physical model is used as an effective benchmarking model in CFD problems and was used in this research. It was concluded that the proposed CFD model predicted the gypsum plasterboard behaviour with a good agreement level when compared to small-scale fire test results. It was also reported that if the constant thermo-physical properties of the gypsum plasterboard are used, the results showed discrepancies with the experimental results. The quantifying of the water vapour content in the model improves the prediction.

The influence of wall emissivity and convective heat transfer coefficient within the wall cavity at elevated temperatures was investigated by Andreozzi et al. (2013). Adiabatic Surface Temperature (AST) model proposed by Wickstrom was investigated with CFD. Conjugate heat transfer analysis is a method that involves the interaction of thermal and structural analysis within the same software. Since this method is computationally very expensive, the AST method is preferred. The AST method used in this study consists of two steps. In the initial step, the thermal analysis was conducted with CFD and later the net heat flux obtained as a result from CFD was transferred to FEM for structural analysis. In this research, conjugate heat transfer analysis and standalone beam analysis were carried out under similar fire exposure and the results were compared. Good agreement was observed between the experimental results and the model when the AST was used as the parameter to transfer CFD results to structural model. The geometry of the model considered was $3\text{ m} \times 3\text{ m}$ with four openings of 200 mm on all sides of the wall.

Arendt and Krzaczek (2014) developed a fully transient model of heat transfer in buildings. Transient envelope model and transient CFD model were used to develop this heat transfer model. Reynolds-averaged-Navier-Stokes (RANS) equation was utilized in this research. Higher Reynolds number was used to make the meshes coarser to reduce the computational time during the heat transfer analysis. It was assumed from the CFS solution that there existed a surface-averaged and time-dependent heat transfer coefficient for a given surface. This study was conducted by considering a room with walls possessing thermal capacitance and single ventilation. Developing a transient coarse meshed CFD (RANS) model and transient heat transfer in the building was the principal focus of this research. From the outcomes of this research, it was concluded that the proposed CFD method can be used in reducing the analysis time.

Lázaro et al. (2016) studied the variations in the thermal models used for gypsum plasterboard assemblies in a standard fire test. Numerical analysis results were compared with the experimental results and discrepancies in the current thermal models were reported. Experiments were conducted to determine the thermal and mechanical properties of fire rated gypsum plasterboards. Four full scale fire tests $3\text{ m} \times 3\text{ m}$ were conducted with different configurations. Three fire tests consisted of single row of studs, whereas one test consisted of double rows of studs, separated by air gap. All the fire tests were conducted under non-load bearing conditions in accordance with Eurocode EN 1363 and EN 1364. Two layers of fire rated plasterboards were used for three tests and four layers of fire rated plasterboards were used for one test. Sudden increase in temperature was observed on the ambient face of the LSF wall panel after the first plasterboard layer fall-off in the tests with two layers of plasterboards. This was found to be the combined effect of ablation causing convection of hot air within the cavity. Fire Dynamics Simulator (FDS) was used in the numerical study. The model size was $50\text{ mm} \times 50\text{ mm}$ with 5 mm mesh size. Ablation was considered at the third peak reaction corresponding temperature of gypsum in the numerical model. Apparent thermal properties were used in the model to match the numerical results with the experimental results. A new hypothesis was proposed by assuming that the ablation in the plasterboard occurs at about 360°C , which was considered as the third endothermic reaction point. It was concluded that the approximation of the thermal properties was held valid for numerical models with two layers of plasterboards. In the case of wall specimen with four layers of plasterboards, the numerical results did not match well with the experimental results. This is because the thermal conductivity between the interface of the plasterboards is difficult to determine causing the discrepancy. Although this research modelled the fire behaviour of LSF walls with CFD only the non-load bearing LSF walls were considered for both experimental and numerical investigations. Also, the temperature gradient along the width of the wall panel was not investigated. The numerical model was validated by comparing the ambient side plasterboard temperatures only.

Thanasoulas et al. (2016) investigated the heat transfer through CFS wall systems using ANSYS CFX software. Structural analysis was conducted using ADINA to determine the structural failure of the CFS walls. Transient heat transfer analysis tech-

nique was used for the ANSYS CFX model. Sequentially coupled analysis approach was followed in this study, where the thermal analysis is conducted first and the output is transferred to the structural analysis in the later stages. The models were validated against the experimental results of Gunalan et al. (2013) and also the FE models developed by Gunalan and Mahendran (2013b). 2D conduction elements were used in the heat transfer model and the thermo-mechanical properties for the thermal and structural analyses were extracted from Ghazi Wakili et al. (2007) and Kolaitis and Founti (2013). A plateau region was observed on the time-temperature curves during the gypsum dehydration process when exposed to the standard ISO fire curve. It was reported that the plateau region happens at 80°C, which is debatable. Shell elements were used for structural modelling, wherein the temperature outputs from the thermal analysis were used as input to perform linear and non-linear analyses. Geometric and material non-linearities were included in the structural model. Four full-scale fire tests were considered for the purpose of model validation. It was concluded that, based on the numerical simulations, cavity insulation with mineral wool did not significantly alter the FRL in comparison with non-cavity insulated wall specimen under load bearing conditions, which does not agree with other researchers' findings. The limiting temperature of 350°C was found to be conservative for the design of steel studs as the stud load-bearing capacities were satisfactory at the limiting temperature.

Malendowski and Glema (2017) developed a coupling method for CFD-FEM analysis of steel structures exposed to natural fire. Scripts were developed to translate the CFD results into transient boundary condition in FE analysis. The CFD code JAS-MINE was coupled with an FE code SAFIR. Convective and radiative heat flux are given as input to the FE model. A compartment with dimensions 8 m × 20 m and 3.2 m high was considered for the computational model as per a full scale fire test conducted by Pyl et al. (2012). FDS and ABAQUS input files were generated with scripts from Scilab software. UTEMP subroutine was used for defining the boundary conditions in ABAQUS. This UTEMP subroutine was used to create the non-uniform temperature boundary condition in ABAQUS because of heat transfer analysis results from FDS. Real fire curves were used in this study as per Pyl et al. (2012) rather than the standard fire curves used in the furnace fire tests. This is because of the non-uniform radiative heat transfer on the structural elements in the case of a real fire exposure. Pool fire sce-

nario and equally distributed fires were used in the numerical analysis and the results agreed well with experimental results. It was found that the distributed fire scenario is more intense when compared to the local fire by over four times. The deformation plots from structural analysis for both fire scenarios agreed well with the experimental results.

Thanasoulas et al. (2018) extended the modelling techniques to develop a fully coupled model and to investigate the thermal and structural response of CFS drywall systems. 3-D solid elements were used for modelling the plasterboard, steel studs and insulation to simulate heat transfer through the thickness and also to simulate the structural response in a coupled way. ADINA was used as the software package for the analyses. All the structural elements including the fasteners were modelled in the thermo-mechanical analysis. Appropriate thermal and structural boundary conditions including contact interaction properties were specified along with the elevated temperature material properties. Thermal properties of air were also taken into consideration in the thermo-mechanical analysis. The analysis results showed that the FRL of LSF walls with cavity insulation was higher in comparison with non-cavity insulated LSF walls. This is highly debatable as many other past research studies have shown that the presence of cavity insulation significantly reduces the FRL of LSF walls.

2.7 Literature Review Findings

The following findings are derived from the conducted literature review.

- Fire resistance is considered as an important parameter for walls in LSF constructions. The quantum of research data on the fire resistance of LSF walls is extensive supporting this claim. However, there prevails substantial gaps in this research area, where the fire performance for different fire curves and complex wall configurations has not been investigated in detail.
- Experimental investigations were conducted extensively on simple LSF wall configurations. The tested walls included single row of studs sandwiched between boards of different materials and thickness. This also included the variation in steel stud thickness and grade of steel. But only single row of studs was

used in all the experimental investigations. LSF wall configurations with complex stud arrangements were investigated by very few researchers and their fire test data is also not readily available.

- Attempts were made to improve the FRL of LSF wall systems by changing various parameters. This includes increasing the number of plasterboard layers on both the fire exposed and unexposed sides, changing the type of insulation used within the cavity and using different geometry of studs. But, attempts were not made to achieve it by the complexity of LSF wall systems through altering their stud arrangements. A research gap is present in relation to the heat transfer mechanism in LSF walls with complex stud arrangements. The presence of more than one row of studs will result in increased cavity depth and change the heat transfer mechanism in comparison with conventional single stud LSF walls.
- Many research studies have been conducted on the effect of plasterboard restraints provided to the studs under ambient and fire conditions. However, this effect was investigated only for single stud LSF walls. In the case of complex LSF walls such as double or staggered stud walls, the level of effective plasterboard restraint varies significantly. This phenomenon has to be investigated in detail using experimental investigations on the fire performance of complex LSF walls. Also, during a fire test, the LSF wall is subjected to thermal bowing. This effect results in neutral axis shift providing additional bending moments to the LSF walls under axial compression loading. The thermal bowing effect has been investigated in detail for LSF walls with single row of studs only. However, it has not been investigated in detail for complex LSF walls.
- Based on the past experimental and numerical research studies, the stud hot flange limiting temperatures have been predicted for different single stud LSF wall configurations such as cavity insulated and non-cavity insulated LSF walls. Through the limiting hot flange temperatures, the FRL of a given wall configuration can be easily derived with reasonable accuracy. But, no such data is available for complex LSF wall configurations. Therefore, it becomes a necessity to investigate the stud hot flange temperatures in complex LSF wall configurations and therefore can be used to determine the failure times with the existing design

equations in future research.

- The numerical models developed to predict the heat transfer in LSF walls were based on software packages such as SAFIR, ABAQUS, ANSYS, ADINA and FDS. The models were created using 2D and 3D elements and their predictions were compared against experimental results for validation purposes. However, there does not exist a robust numerical model that can predict the heat transfer mechanism in complex LSF wall configurations. Some of the existing heat transfer models included only the radiation mode of heat transfer within the cavity and could still validate the time-temperature curve predictions from the experiments. However, in LSF walls all three modes of heat transfer, conduction, convection and radiation, occur within the cavity. Only numerical models created with CFD software packages could account for these effects. The FE packages such as ANSYS-FLUENT, ADINA and FDS were used by other researchers for developing heat transfer model using CFD techniques, but ANSYS and ADINA are commercial versions and involve a licencing cost while FDS is an open source package. Therefore, FDS is found to be the best option to develop heat transfer models in this research study.
- Structural models were also developed by past research studies to predict the structural failure capacities at ambient and elevated temperatures. These models were either sequentially coupled and executed after the thermal analysis or fully coupled and executed alongside the thermal analysis to predict the FRL of LSF walls. However, the fully coupled models were found to be computationally expensive and time consuming. Therefore, sequentially coupled analysis is considered as the preferred method, where the temperature data is extracted from thermal analysis and used in structural analysis.
- Numerical models were found to be the most feasible option to predict the FRL of LSF walls. However, the quantum of computational resources and technical skills to conduct these analyses is challenging. Therefore design equations were made available in various standards such as AS/NZS 4600 and Eurocode 3 Part 1.2. Design equations based on the existing standards pertaining to LSF walls were also developed by past research studies. Alternate methods such as DSM

and EWM are available to predict the FRL of LSF walls with reasonable accuracy. However, the suitability of these equations for complex LSF walls needs further investigation.

- The design equations rely on the hot and cold flange temperatures from either experimental or numerical studies. For single stud LSF walls, past research studies assumed a constant temperature on the hot and cold flanges while the web temperatures were assumed to be linearly varying. This assumption holds true for LSF wall with single row of studs and the FRL predictions from design equations match reasonably well with the experimental results. However, in complex LSF wall configurations, with more than single row of studs, the applicability of this assumption is questionable. Therefore, extensive experimental and numerical studies are necessary to determine the level of variation in the temperature gradient along the studs. This data can then be used in the design equations to predict the FRL of complex LSF wall configurations.

Chapter 3

Experimental Investigations of LSF Walls under Ambient Conditions

3.1 General

This chapter details the experimental investigations conducted on complex LSF wall systems under ambient conditions. Despite the advancements in numerical models, experiments are necessary to determine the ambient load carrying capacity of the complex LSF wall systems and to validate the developed finite element models to predict their axial load carrying capacity. Also, the ambient temperature wall capacities are required to conduct full-scale fire tests under load bearing conditions in which a percentage of ambient temperature wall capacity is applied during fire tests. Therefore, the ambient temperature load capacities of the five complex double and staggered stud LSF wall panels of 3 m height were determined first using a series of full-scale wall tests. Tensile coupon tests were also conducted on the steel studs to determine their mechanical properties for use in numerical analyses and parametric studies.

3.2 Test Wall Panels

Table 3.1 presents a summary of the five ambient temperature capacity tests conducted as part of this research study. The test wall panels had Lipped Channel Sections (LCS) 90×36×7×0.75 mm, 90×36×7×0.95 mm and 70×29.5×8×0.95 mm as studs made of G550 steel manufactured by Bluescope steel with a minimum guaranteed yield

strength of 550 MPa as shown in Figures 3.1 (a) and (b). All the studs were measured and were found to have marginal difference from the manufacturer specified dimensions. Therefore the above mentioned manufacturer specified dimensions were followed throughout this research. The steel studs had pre-punched holes drilled on them at the required positions for easier construction. Buildex M6.0 × 15 GX Ca smooth top GA point steel frame screws were used to connect the steel studs to the tracks and noggings. Unlipped Channel Sections (UCS) were used for the top and bottom tracks and pre-punched holes were made in the flanges of the tracks and corresponding locations to fix the studs. UCS were used as noggings at 1 m intervals in all the tests except for Test-AT5. However, the UCS noggings were replaced by omega noggings and details about the same are provided in the corresponding section.

Table 3.1: Test wall panel details

Test Name	Description	Stud Depth (mm)	Cavity Depth (mm)	Stud Thickness (mm)	No of Studs
AT1	Double Stud	90	200	0.95	4
AT2	Double Stud	90	200	0.75	4
AT3	Double Stud	90	200	0.75	6
AT4	Double Stud	70	160	0.95	4
AT5	Staggered Stud	90	200	0.95	6

All the test wall panels were lined with two layers of 16 mm fire rated gypsum plasterboard (Figure 3.2). The plasterboards were connected to the stud flanges using D type 10 GA self-piercing screws (Figure 3.3). The first layer of plasterboard was fixed to the studs using 32 mm long screws while the second layer was fixed using 45 mm long screws. The plasterboard joints were not sealed with joint compound as the corresponding effect on the ambient temperature load carrying capacity is negligible. The plasterboards were fixed to studs with a screw spacing of 200 mm along the joints in a staggered manner while a linear arrangement with 300 mm spacing was adopted at the edges and plasterboard centres. A 60 mm gap for first layer and a 80 mm gap for the second layer of plasterboard from the top and bottom edges of the test wall were provided to prevent plasterboards being screwed to the top and bottom tracks to allow for expansion during the tests. Details of the variations in the individual ambient temperature capacity tests and their corresponding results are discussed in Section 3.4.

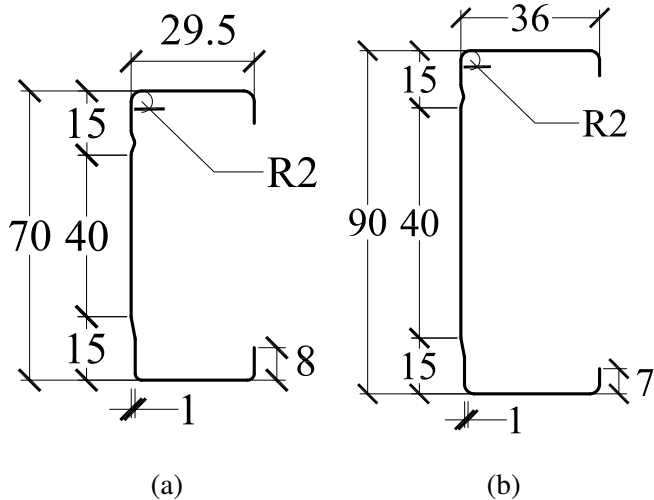


Figure 3.1: Cross-section of (a) 70 mm stud (b) 90 mm stud

3.3 Test Set-up

Ambient temperature capacity tests are used to determine the axial compression capacity of the studs to be used in the fire tests in accordance with AS 1530.4. However, the testing procedures to determine the ambient temperature capacity are not given in this standard. Therefore tests were conducted similar to full-scale fire tests, but without the fire exposure. The ambient temperature capacity tests were conducted on a specially built test frame, which can accommodate test wall panels up to 3 m × 3 m in external dimensions. The test frame consists of two Universal Columns (UCs) fixed to the strong floor. At the top the columns are connected through a Welded Beam (WB) and at the bottom through a Universal Beam (UB) resting on the floor. Individual hydraulic ramps placed on the bottom Universal Beam (UB) were used to load the test wall at the stud locations. Test wall panels were loaded from the bottom rather than from the top to simplify the test set-up. LSF wall panels were constructed on a table in a horizontal position and then they were positioned into the test frame using a forklift and an Electric Overhead Travelling (EOT) crane. Linear Variable Displacement Transducers (LVDTs) were used to measure the axial displacements and lateral deflections at various locations during the test. The axial displacements were measured at the bottom loading plate near the rams. Lateral deflections were measured at three locations on the critical studs, mid-height and 750 mm from the top and bottom of the wall panel. Details of a typical test wall panel of 3 m height and the loading frame are shown in Figures 3.4 (a) and (b).

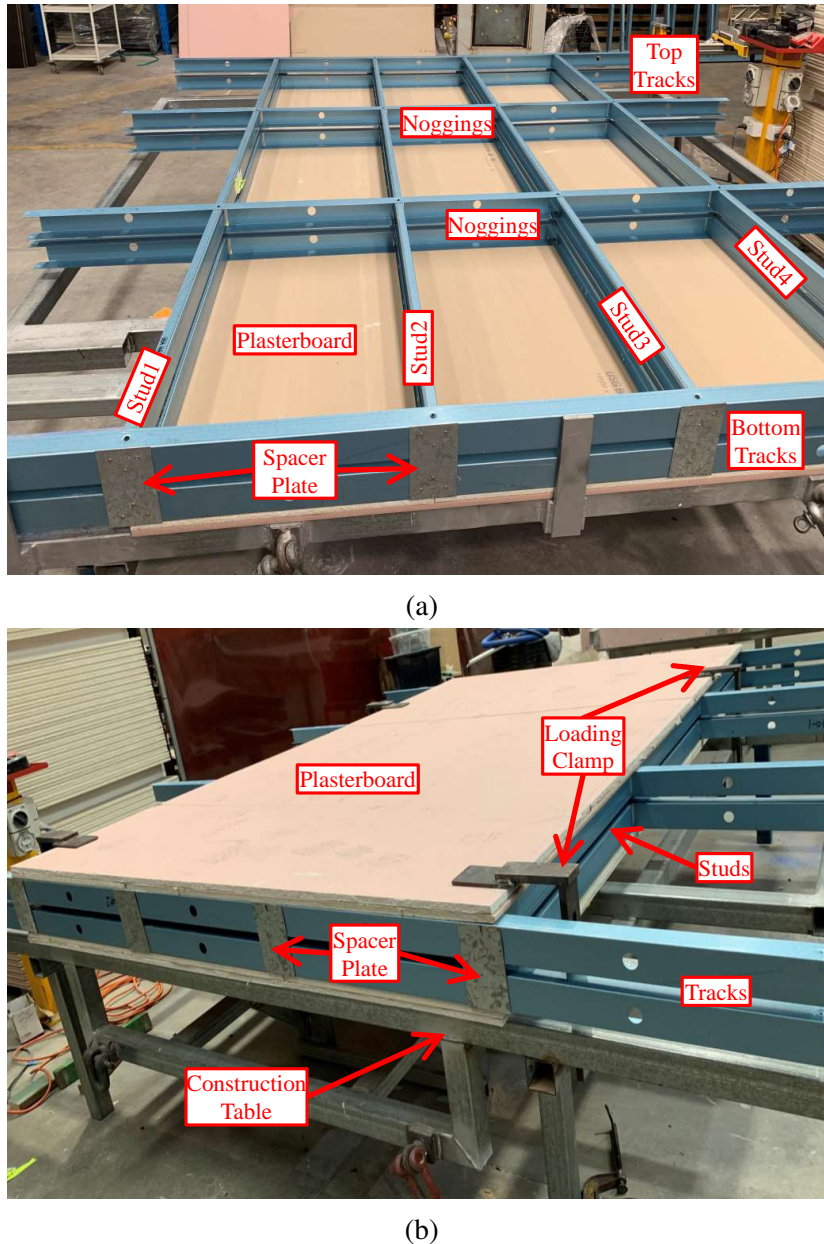


Figure 3.2: Construction and testing of LSF wall panels (a) Construction (b) Finished test wall

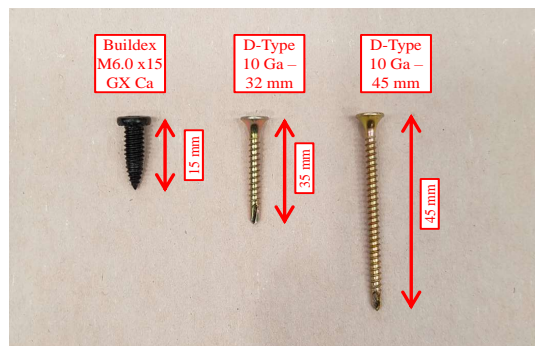


Figure 3.3: Screw details

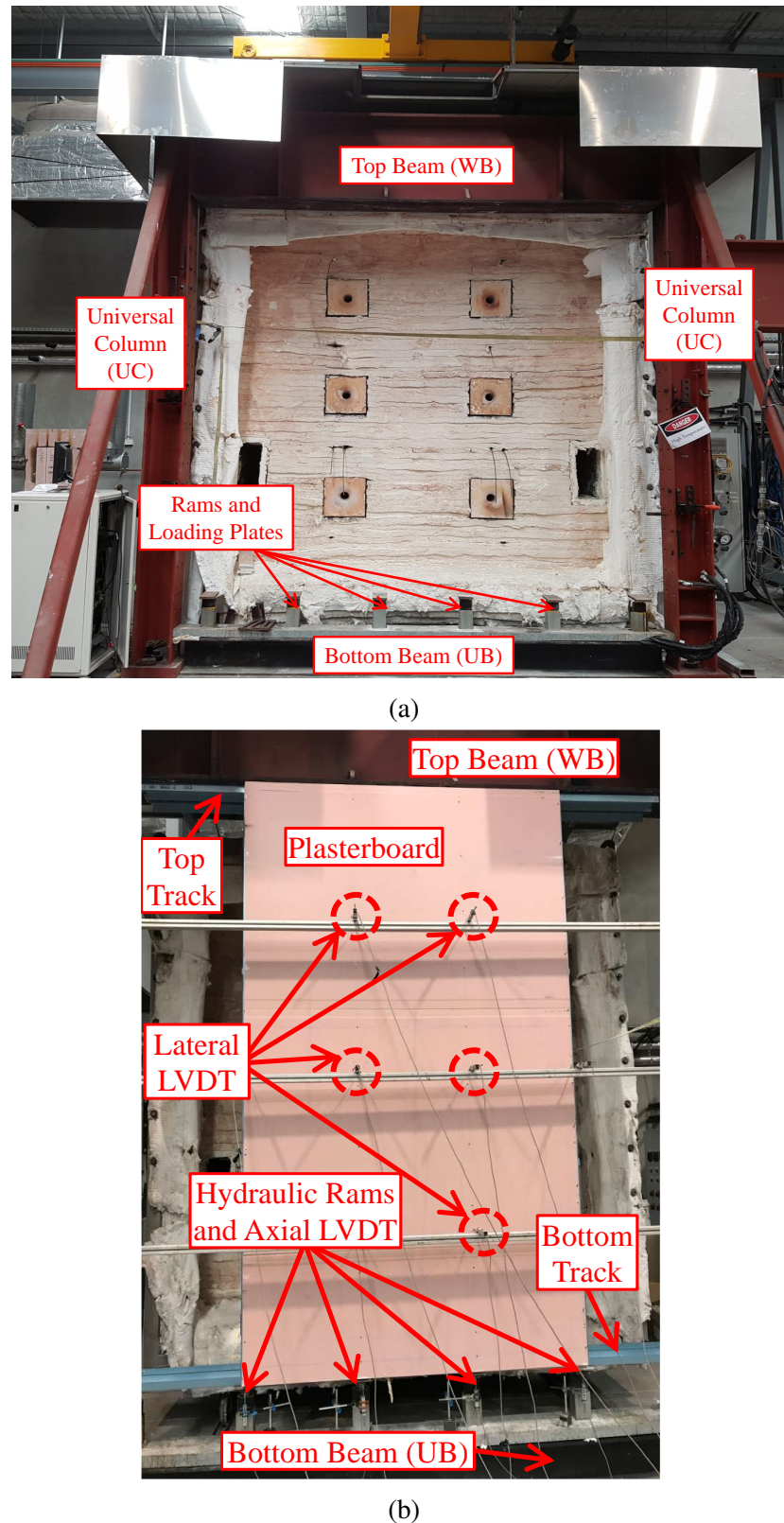
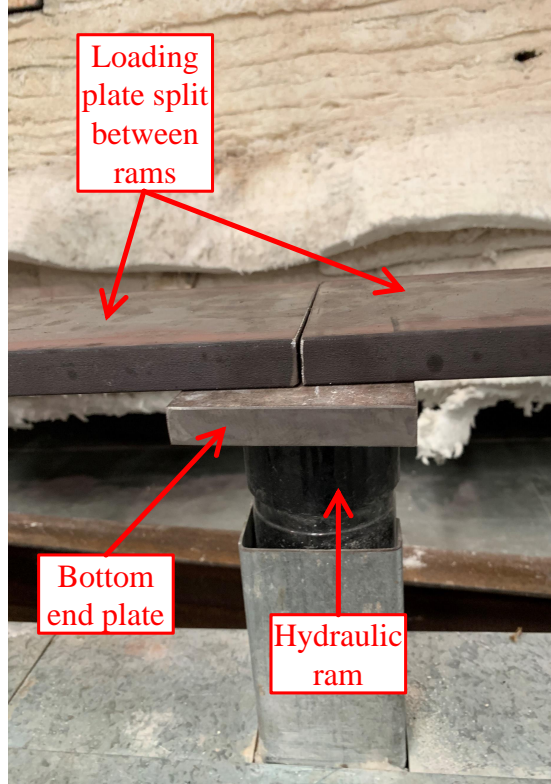
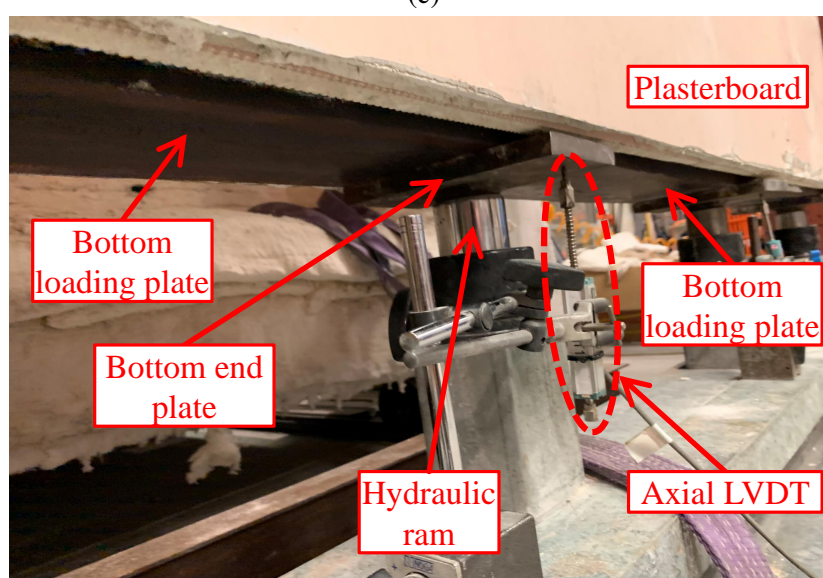


Figure 3.4: Typical loading set-up (a) Test rig (b) Test wall set-up (c) Staggered stud loading ram details (d) Staggered stud wall loading arrangement



(c)



(d)

Figure 3.4: Typical loading set-up (a) Test rig (b) Test wall set-up (c) Staggered stud loading ram details (d) Staggered stud wall loading arrangement

For staggered stud wall Test-AT5 the test set-up was altered by providing a 20 mm thick loading plate between the rams. Five loading plates were arranged on six rams as shown in Figures 3.4 (c) and (d). This is to facilitate loading to the staggered studs due to the limitation in the test set-up. The bottom loading plate was used to support and load the floating stud between the rams.

3.4 Test-AT1

The first ambient temperature capacity test was conducted on a double stud LSF wall constructed with four G550 $90 \times 36 \times 7 \times 0.95$ mm studs. $90 \times 40 \times 0.95$ mm unclipped channel sections (UCS) were used as noggings at 1 m intervals. The noggings were connected to the studs through slots made on the webs of the UCS. Top and bottom of the test wall panel were connected through 90 mm unclipped channel sections. In this test, the test wall had two rows of studs, separated by a 20 mm gap as shown in Figure 3.5. The edge studs were strengthened since the plasterboard provided fully effective in-plane restraints only to the middle studs. The height of the test wall panel was 3 m while its width was 1.8 m.

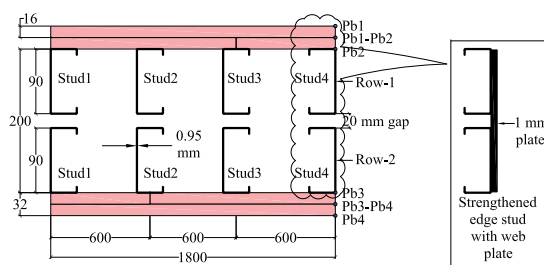


Figure 3.5: Test-AT1 wall configuration

Firstly, the test wall panel was loaded to 10% of the predicted ambient temperature capacity twice before loading it to failure. The load was applied on the geometric centre of the studs through individual rams as shown in Figure 3.4 (a). Test-AT1 gave an ultimate axial compression capacity of 73 kN when Stud3 of Row-1 failed by local buckling of flanges as shown in Figures 3.6 (a) and (b). It is to be noted that this capacity was based on the ram load applied to two studs (one from each row). No pull-out failures of the plasterboard screws were observed during the test. Generally, in ambient temperature capacity tests the application of load is continued till the ultimate failure load is reached when the monitored load in the data logger displays a sudden

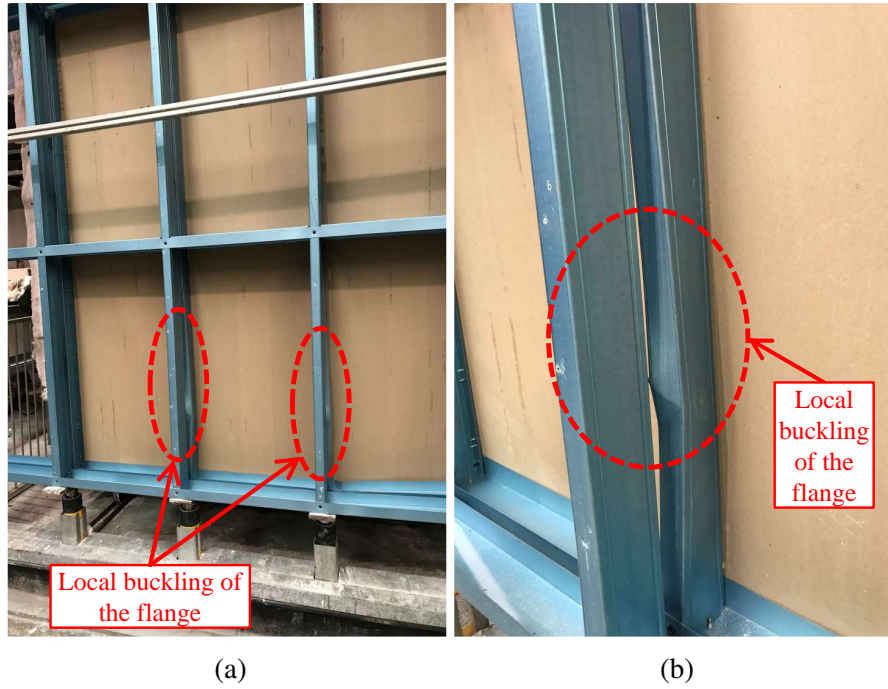


Figure 3.6: Local compressive failure in Test-AT1 wall (a) Test wall (b) Stud3

drop. The failure was also inferred through visual changes to the test panel which includes cracks on the plasterboard surface due to buckling of studs. The application of load through hydraulic rams is stopped after this stage. Figures 3.7 (a) and (b) show the applied axial compression load versus axial displacement and lateral deflection results from the test wall. A maximum axial displacement of 15.83 mm was observed in Stud4 (Figure 3.7 (a)) while the maximum lateral deflection recorded was 9.75 mm at Stud3-Mid (Figure 3.7 (b)). Buckling of studs was not evident in both rows of stud as the stud flanges had a small difference in their widths. This facilitates the nesting of studs in real world applications, but causes a small eccentricity during axial compression loading resulting in buckling of studs in one row.

3.5 Test-AT2

The second ambient temperature capacity test was conducted on a four-stud wall constructed of thinner stud sections (0.75 mm G550) with stud dimensions of $90 \times 36 \times 7 \times 0.75$ mm. It was conducted to determine the effect of stud thickness on the axial compression capacity of double stud walls. The test specimen was constructed and tested with four studs. The stud dimensions were identical to those of Test-AT1

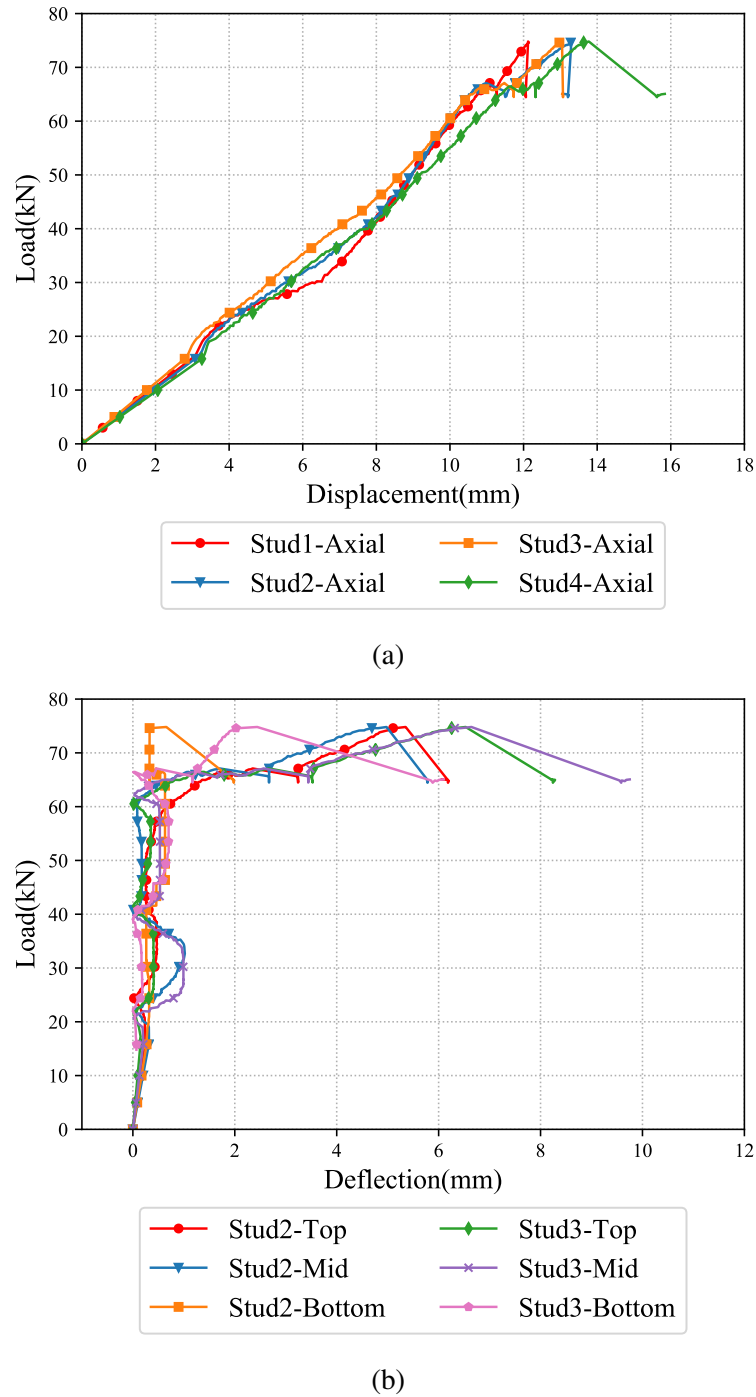


Figure 3.7: Test-AT1 results - (a) Applied load versus axial displacement and (b) Applied load versus lateral deflection

wall studs except the stud thickness (0.95 mm versus 0.75 mm) as shown in Figure 3.8. Testing procedure was similar to that adopted in Test-AT1. Test-AT2 gave an ultimate maximum axial compression capacity of 47.08 kN (capacity of two studs), when local compressive failure of the flanges in Stud2 of Row-2 occurred as shown in Figures 3.9 (a) and (b). No crack in plasterboards or pull-out failure of screws at the plasterboard connections were observed after the test.

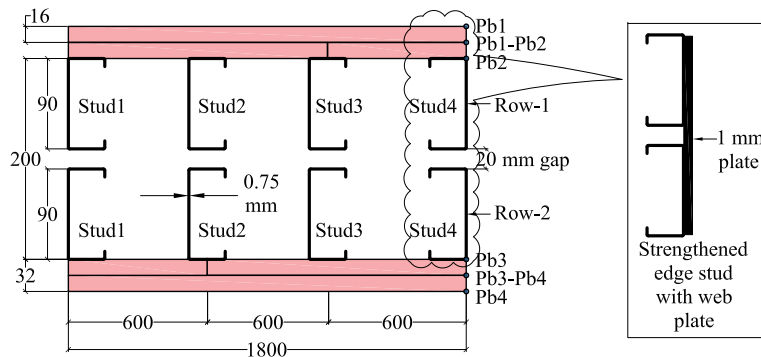


Figure 3.8: Test-AT2 configuration

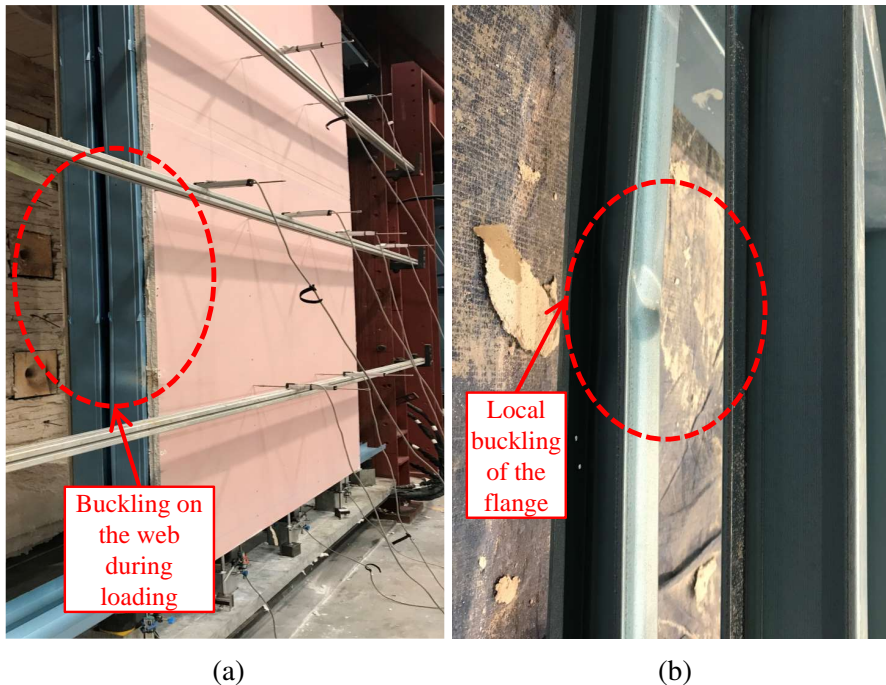


Figure 3.9: Local compressive failure in Test-AT2 wall (a) Test wall (b) Stud2

Figures 3.10 (a) and (b) show the applied axial compression load versus the axial displacement and lateral deflection curves from the test. The maximum axial displacement recorded was 11.08 mm as shown in Figure 3.10 (a). A lateral deflection of 12.98 mm at Stud3-Mid was recorded as shown in Figure 3.10 (b). The axial displacement

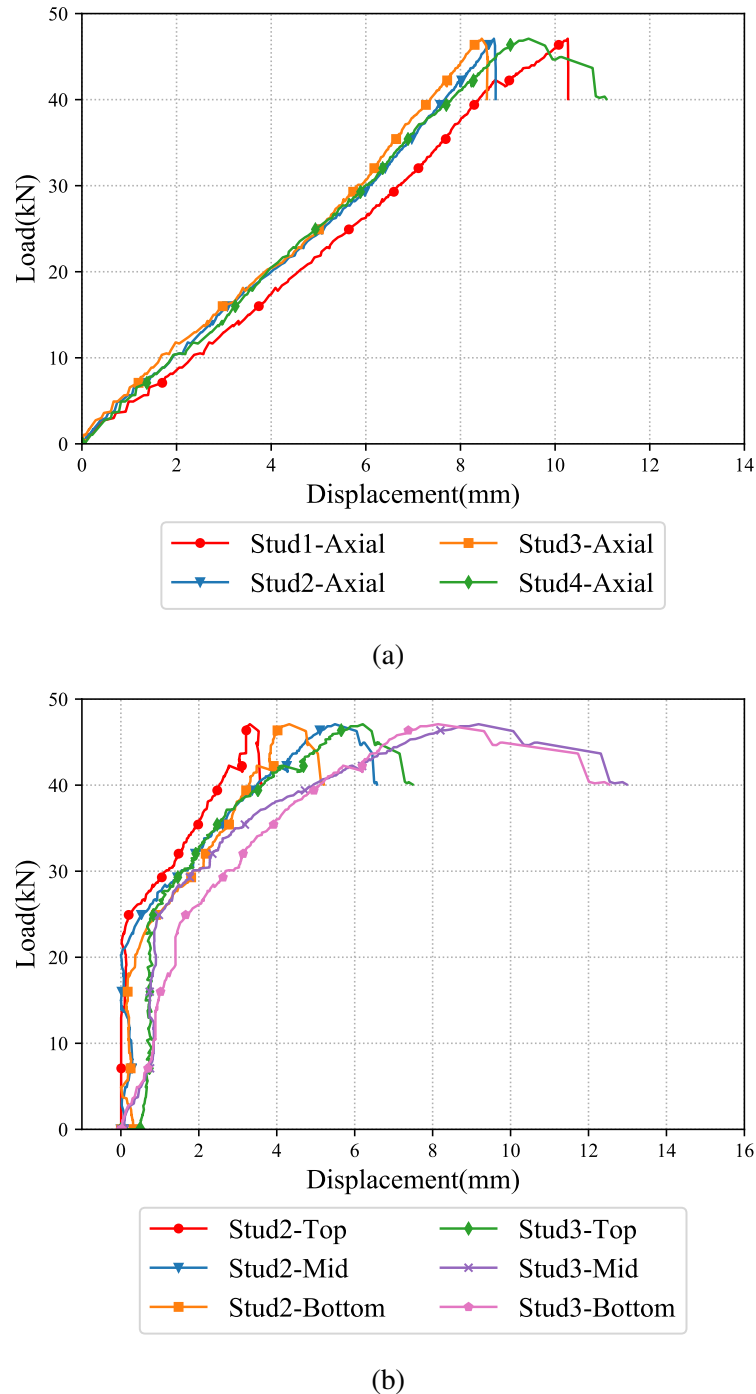


Figure 3.10: Test-AT2 results - (a) Applied load versus axial displacement and (b) Applied load versus lateral deflection

was lesser in comparison to Test-AT1 by 4.75 mm. However, the lateral deflections were more by 3.23 mm in comparison with Test-AT1. This is because of the use of thinner stud sections in this test.

3.6 Test-AT3

The third ambient temperature capacity test was similar to Test-AT2 but had six studs in the test wall. This test was conducted with six studs to verify the axial compression capacity of double stud wall of Test-AT2. Figure 3.11 shows the test configuration of double stud wall tested with six studs. Despite having six studs in the test wall, fully effective in-plane restraints were available only to the four studs in the middle. Similar to the previous ambient temperature capacity tests, after the initial pre-loading cycle, the ambient temperature capacity of the test wall was determined by applying the axial compressive load to the individual studs until one or more studs failed. The test wall gave an ultimate axial compression capacity of 39.42 kN (capacity of two studs). No significant buckling was observed in other studs as shown in Figure 3.12 (a). However, local bearing failure was observed in the edge stud as shown in Figure 3.12 (b). Bearing failure might have occurred in the edge studs due to insufficient plasterboard restraints to the edge studs. The plasterboard restraints provided to the edge studs are not symmetrical in comparison to the middle studs, thereby leaving the edge studs more susceptible to failure. This issue can be addressed by strengthening the edge studs by providing nested or back to back stud sections in ambient temperature capacity tests.

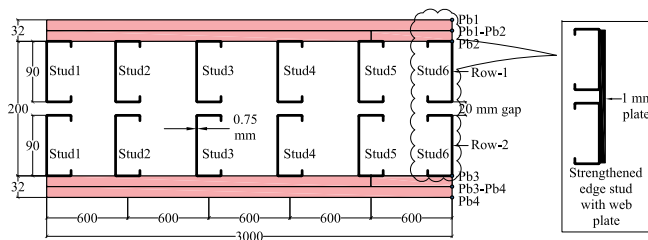
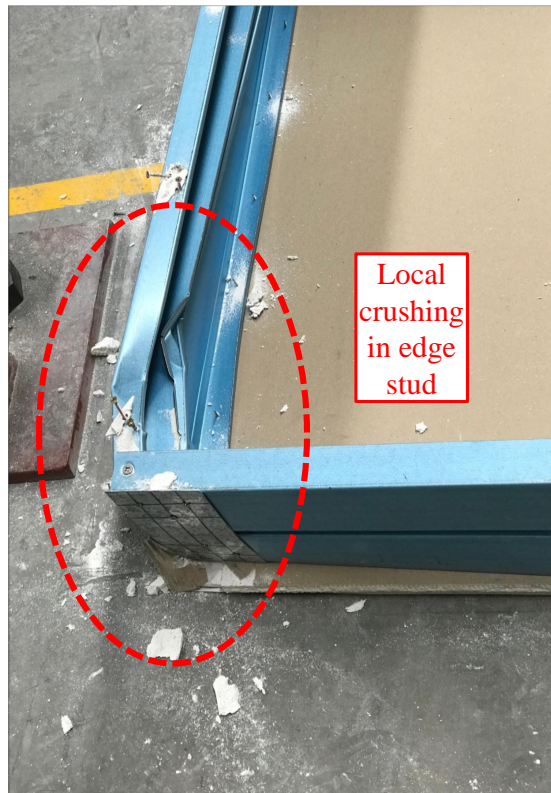


Figure 3.11: Test-AT3 configuration

Figures 3.13 (a) and (b) show the applied axial compression load versus axial displacement and lateral deflection curves. A maximum axial displacement of 9 mm was recorded in Stud2 and a maximum lateral deflection of 6.41 mm was observed at Stud4-Bottom. In comparison with Test-AT2 the axial compression capacity was re-



(a)



(b)

Figure 3.12: Local bearing failure in Test-AT3

duced by 7.66 kN. This was due to the bearing failure of the edge stud in comparison to the local buckling failure of studs in Test-AT2. However, the axial displacement and lateral deflection results were similar in both Tests-AT2 and AT3 (Stud1 and 6) shown in Figure 3.13 (a). This is because, the plasterboards do not provide effective lateral restraints to the edge studs.

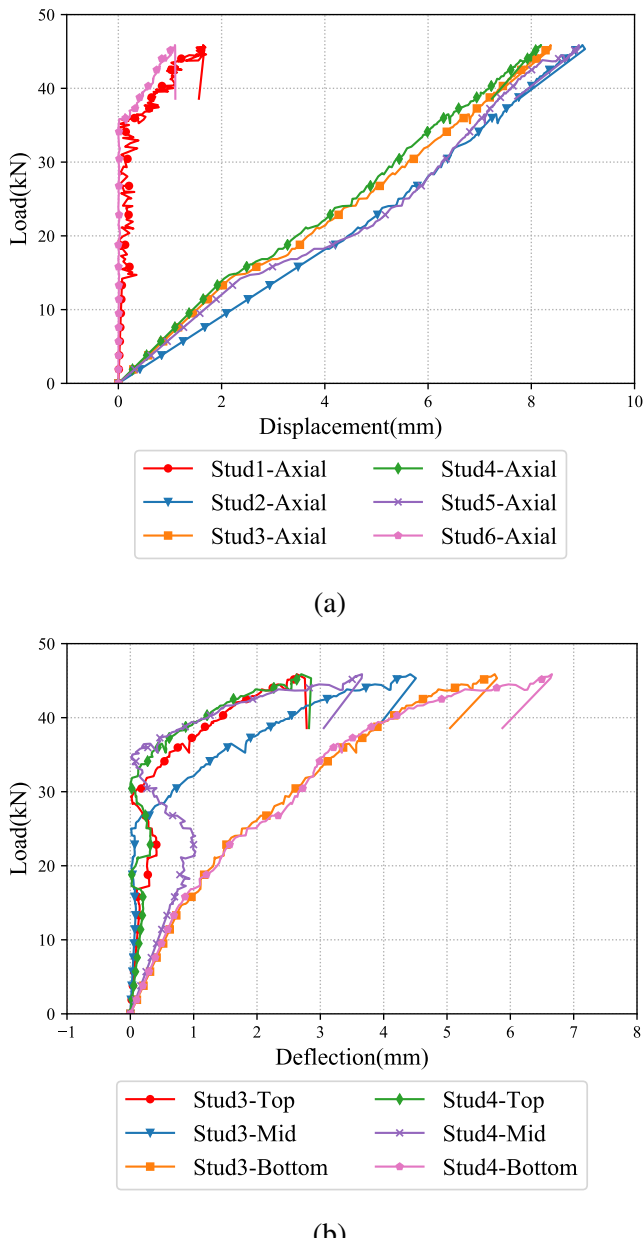


Figure 3.13: Test-AT3 results - (a) Applied load versus axial displacement and (b) Applied load versus lateral deflection

3.7 Test-AT4

The fourth ambient temperature capacity Test-T4 was conducted on double stud LSF wall with 70 mm stud depth. The stud dimensions were $70 \times 29.5 \times 8 \times 0.95$ mm (G550 steel). This test was conducted to investigate the ambient temperature capacity of double stud LSF walls with commonly used 70 mm studs. Four studs were used in the test wall and the test configuration is shown in Figure 3.14. As a result of bearing failure of edge studs in Test-AT3 the edge studs in Test-AT4 were nested. The test wall gave an axial compression capacity of 86.21 kN (capacity of two studs). Significant local web and flange buckling of Stud3 of Row-2 was observed as shown in Figure 3.15 (b). The buckling failure was only observed on Stud3 of Row-1. A large crack was observed on the plasterboard at the stud failure location as shown in Figure 3.15 (a).

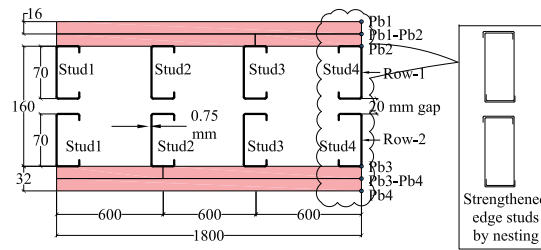


Figure 3.14: Test-AT4 configuration

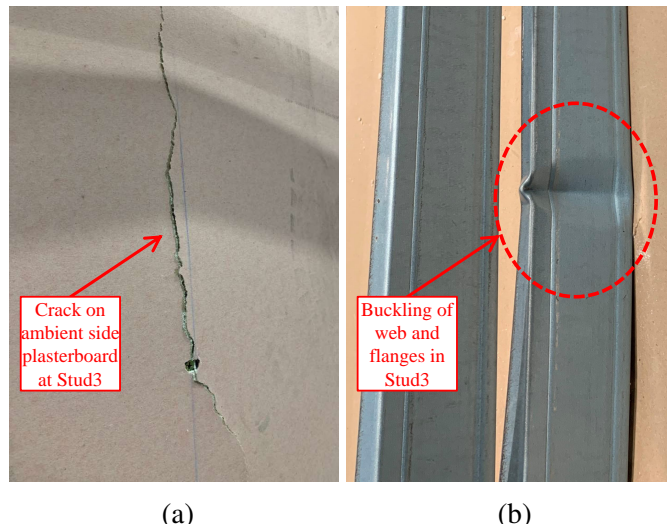


Figure 3.15: Test-AT4 results - (a) Plasterboard crack and (b) Buckling of stud

The applied axial compression load versus the axial displacement and lateral deflection curves of Test-AT4 are shown in Figures 3.16 (a) and (b). Maximum axial displacement of 15.46 mm was recorded for Stud3. This indicates the structural failure

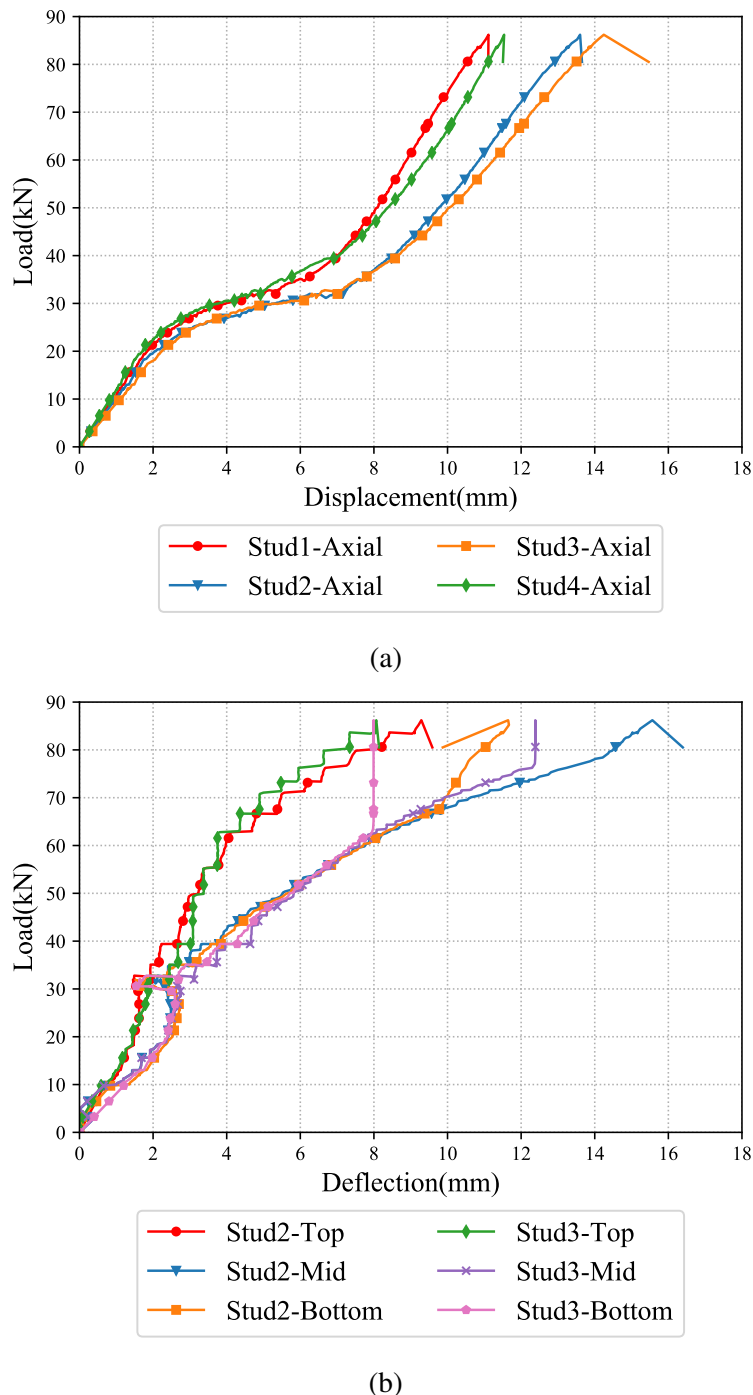


Figure 3.16: Test-AT4 results - (a) Applied load versus axial displacement and (b) Applied load versus lateral deflection

of Stud3 of Row-2 as shown in Figure 3.15 (b). The maximum lateral deflection was 16.39 mm at Stud2-Mid (1500 mm) indicating the out-of plane deflection in the test wall. Comparison with the ambient temperature capacity of Test-T1 revealed that the axial compression capacity increased by 13.21 kN (86.21-73 kN) in comparison with Test-AT1 with the same thickness of 0.95 mm. This increase in axial compression capacity would have been attributed to several factors such as the geometric dimensions and slenderness ratios of the studs. It is to be noted that the lips are 1 mm longer in the 70 mm deep studs in comparison with the 90 mm deep studs as shown in Figures 3.1 (a) and (b). Also, the maximum slenderness ratio (b/t) of the studs used in Test-T1 is 94.73 (90/0.95) while it is 73.68 (70/0.95) for Test-T4 if the local buckling of the web is considered. Hence Test-T4 gave an increased axial compression capacity.

3.8 Test-AT5

The last ambient temperature capacity test in this test series was conducted on a staggered stud LSF wall. The test wall consisted of two rows of studs positioned in a staggered manner. The studs were $90 \times 36 \times 7 \times 0.95$ mm (G550 steel). Eleven studs were used in the staggered configuration as shown in Figure 3.17.

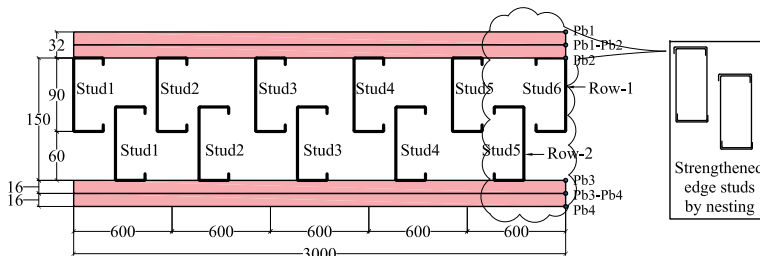


Figure 3.17: Test-AT5 configuration

Edge studs were nested to avoid bearing failure of studs in the test wall. Previous ambient temperature capacity tests (AT1-AT4) had UCS noggings connecting the flanges and provided lateral restraints at 1 m intervals against minor axis buckling. However, in a staggered stud wall, the discontinuity between the stud rows is necessary to achieve the required acoustic rating. Therefore, omega noggings were used at 1 m intervals to provide the required lateral restraints to the studs. As the name suggests, the omega noggings are shaped as the greek symbol omega (Ω). The omega noggings were connected to every alternate studs on the stud webs at service

holes through a connecting clip. Details of the omega nogging and the connecting clip are shown in Figures 3.18 (a) and (b). The clips are held on to web at one end and snapped on to the grooves of the omega nogging at two locations. The nogging to stud connection details are shown in Figure 3.19 (a). Unlike other tests, the stud to track connection needed additional components. As the arrangement of the studs are staggered, the tracks are connected to only one flange of the stud. Hence an end cleat shown in Figure 3.18 (c) was used between the unsupported flange and the track. The end cleats were manufactured in-house at QUT Wind and Fire Engineering Laboratory and were made with one lip longer than the other. The longer lip of the cleat was attached to the unrestrained stud flanges while the shorter lip was attached to the tracks' lip using two D-Type 16 mm screws. End cleats were used in the stud to track connections to improve their fixity conditions in the ambient capacity test as shown in Figure 3.19 (b).

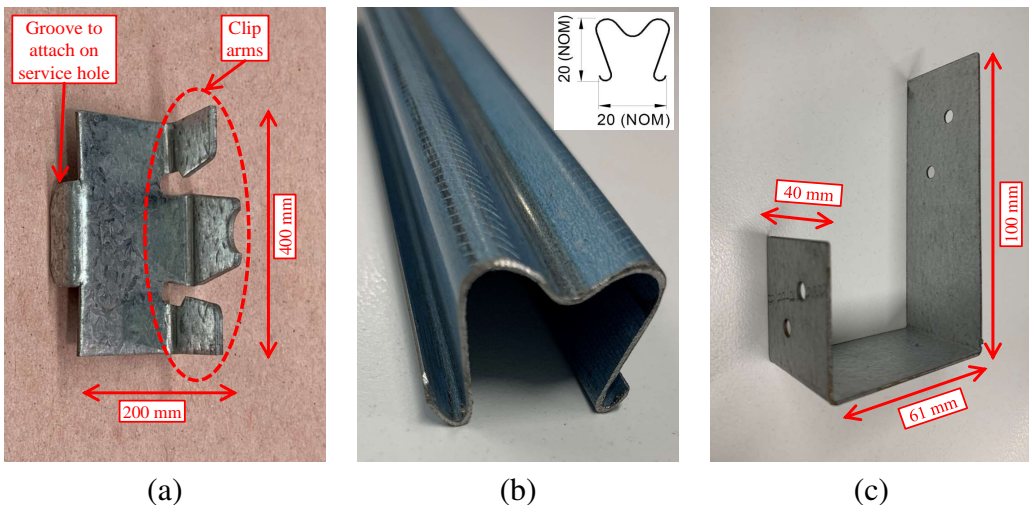
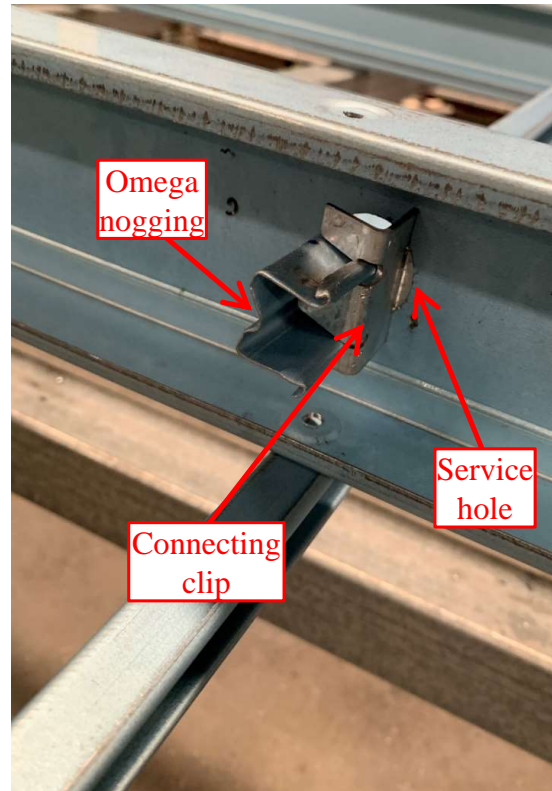
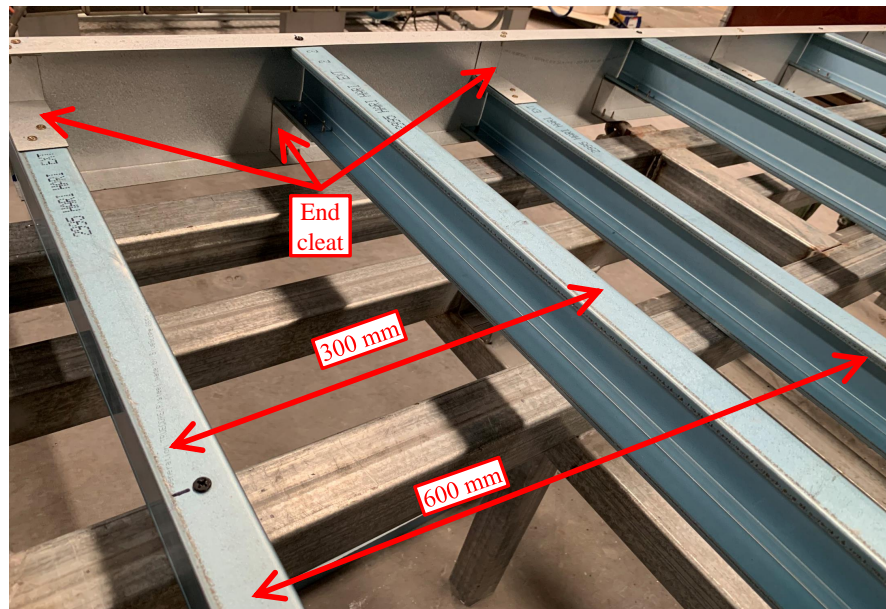


Figure 3.18: Test-AT5 wall components - (a) Omega nogging clip (b) Omega nogging rail (c) End cleat

The test wall was loaded through a 20 mm thick base plate connecting the rams and the axial compression load was applied individually to the staggered studs as shown in Figure 3.4 (d). The edge studs of the test wall were strengthened as the plasterboards do not provide effective lateral restraints to the edge studs as discussed in Section 3.6 (Figure 3.17). After the application of an initial preload the ambient capacity test was conducted by gradually increasing in the applied axial compression load till failure. The test wall gave an axial compression capacity of 68.49 kN, effectively the capacity of two adjacent studs (one on each row). A maximum axial displacement of 21.62 mm



(a)



(b)

Figure 3.19: Test-AT5 wall construction- (a) Omega nogging and clip connection (b) Staggered stud wall construction with end cleats

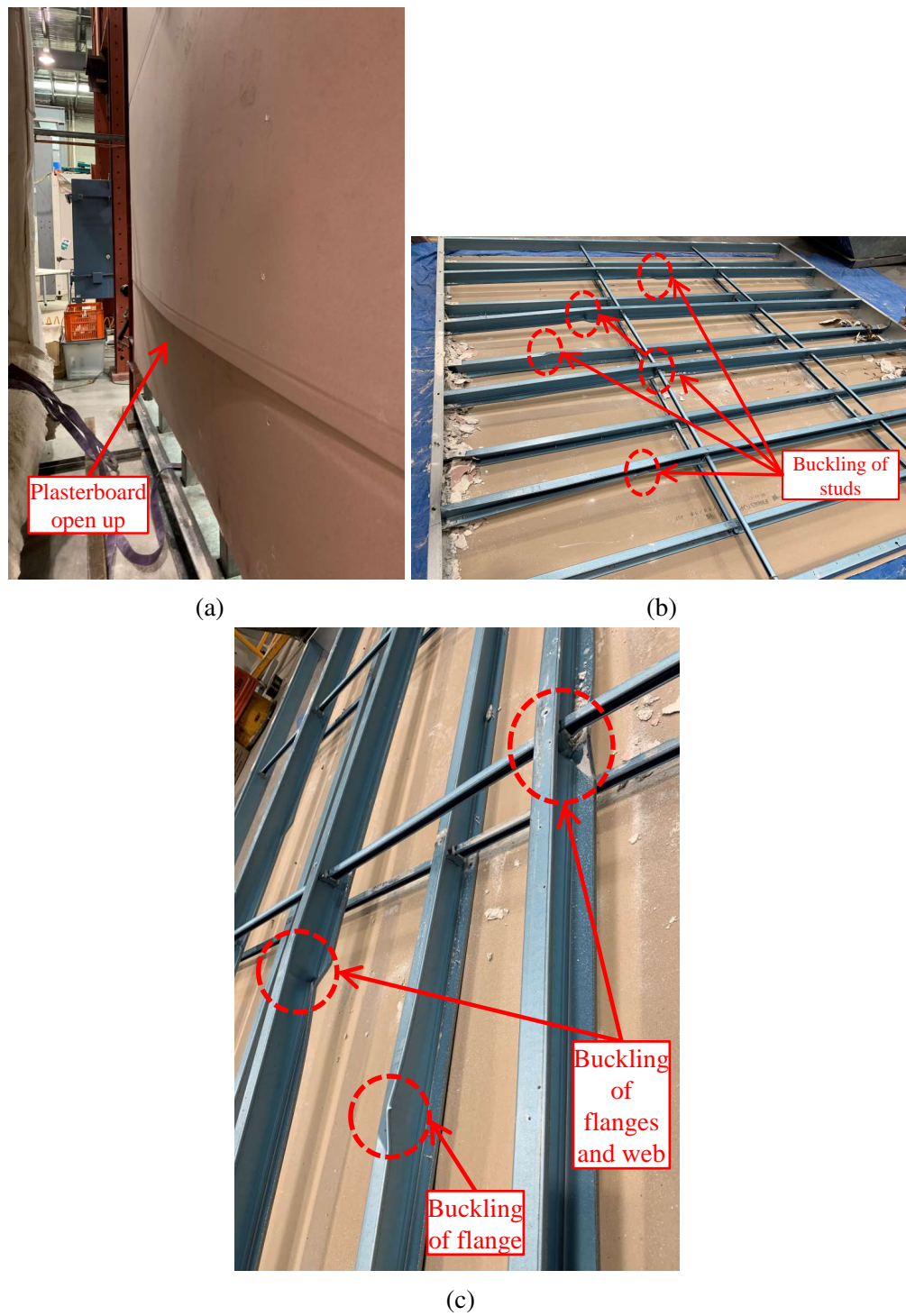


Figure 3.20: Test-AT5 - failure (a) Plasterboard open up (b) Buckling of studs in test wall (c) Buckling of studs - close up

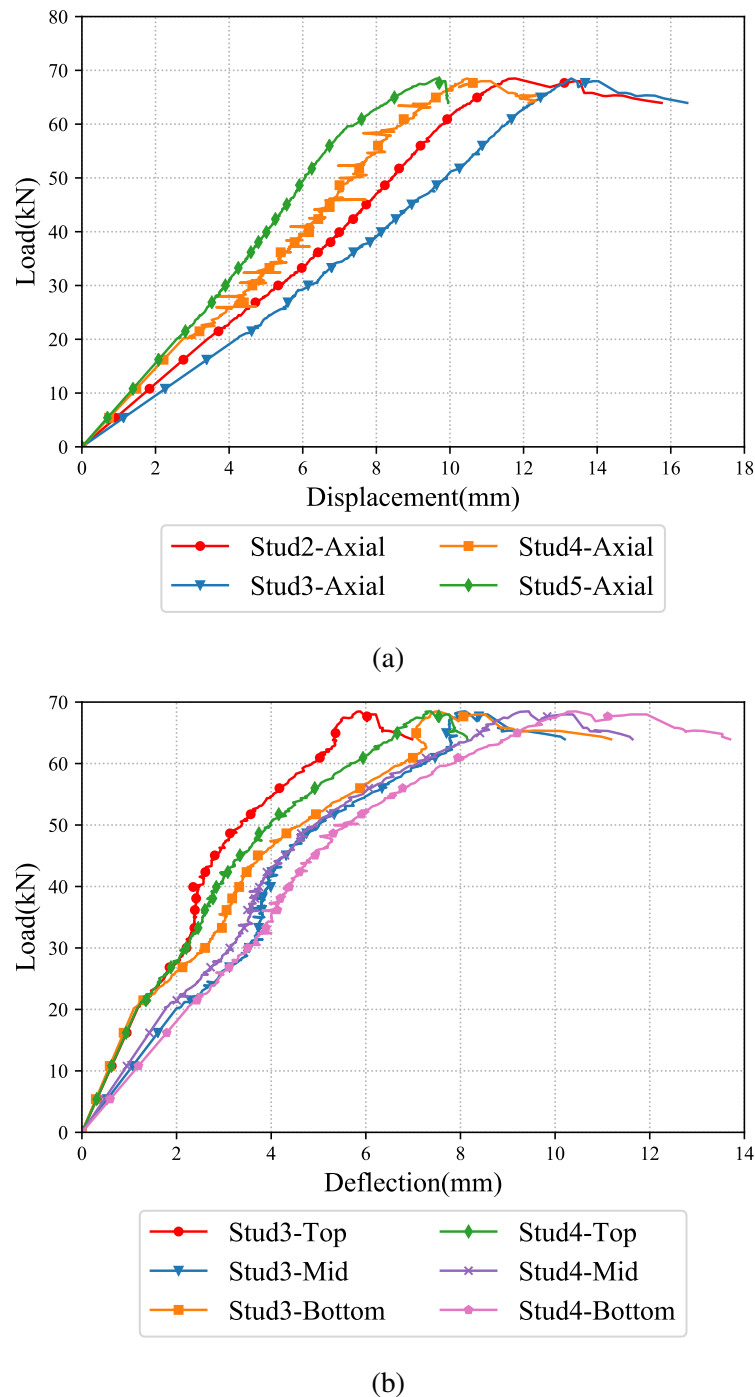


Figure 3.21: Test-AT5 results - (a) Applied load versus axial displacement and (b) Applied load versus lateral deflection

was recorded in Stud3 at the end of the test. The maximum lateral deflection of 13 mm was recorded at 750 mm from the bottom of the specimen near Stud4. Plasterboard open up was noticeable near the stud failure locations as shown in Figure 3.20 (a). Local buckling of the web and flange elements were observed during the post-test investigation as shown in Figures 3.20 (b) and (c).

3.9 Summary of Ambient Temperature Capacity Test Results

A summary of all the ambient temperature capacity tests conducted on double and staggered stud LSF walls is presented and discussed in this section. Five ambient temperature capacity tests were conducted and the results are summarised in Table 3.2. The axial compression capacity of 90 mm and 70 mm deep studs with various thicknesses and stud configurations were considered in this investigation. Ambient temperature capacity tests AT1 to AT4 were conducted on double stud walls made of 90 mm and 70 mm deep studs. The cavity depth of the test wall was 200 mm for Tests-AT1 to AT3 while it was 160 mm for Test-AT4. Thicknesses of the studs were 0.95 mm for Tests-AT1 and AT4 while the thickness was 0.75 mm for Test-AT2 and AT3. Test-AT5 was conducted on staggered stud LSF wall comprising of 90 mm studs with a cavity depth of 150 mm and a stud thickness of 0.95 mm.

Table 3.2: Ambient temperature test capacity results

Test Name	Description	Stud Depth (mm)	Cavity Depth (mm)	Stud Thickness (mm)	No of Studs	Failure Load (kN)	Failure Load Per Stud (kN)
AT1	Double Stud	90	200	0.95	4	73.00	36.50
AT2	Double Stud	90	200	0.75	4	47.08	23.54
AT3	Double Stud	90	200	0.75	6	39.42	19.71
AT4	Double Stud	70	160	0.95	4	86.21	43.10
AT5	Staggered Stud	90	200	0.95	6	68.49	34.24

The double stud wall Test-AT1 with 0.95 mm thick 90 mm wide studs resulted in an axial compression capacity of 73.0 kN while Test-AT4 which had the same stud

thickness with 70 mm wide studs resulted in an axial compression capacity of 86.21 kN. This is 13 kN higher in comparison with Test-AT1. The difference in axial compression capacity is attributed to the higher slenderness ratio of the studs in Test-AT1. The Tests-AT2 and AT3 gave axial compression capacities of 47.08 and 39.42 kN. Despite the same testing configuration and stud thickness the number of studs in Test-AT2 was four while Test-AT3 were six. The difference in their axial compression capacities was due to the absence of effective plasterboard restraints to the edge studs resulting in bearing failure at the supports. However, the difference in the axial compression capacity between Tests-AT2 and AT3 is small and can be ignored. But, it demonstrated the need to strengthen the edge studs in ambient temperature capacity tests to avoid premature bearing failure of studs. The staggered stud wall Test-AT5 resulted in an axial compression capacity of 68.49 kN which is comparatively closer to that of Test-AT1 with the same stud depth and thickness. However, the arrangement of studs was different in these tests (AT1 and AT5). In Test-AT1 the test wall had the stud rows in a linear pattern while in Test-AT5 the studs were staggered. The effective centre-to-centre distance between the studs was 600 mm in the double stud wall Test-AT1 while it was 300 mm in the staggered stud wall Test-AT5. But it is to be noted that the cavity depth of Test-AT1 was 200 mm while it was 150 mm for Test-AT5 which is beneficial in reducing the effective floor space in LSF wall construction.

3.10 Comparison of Ambient Temperature Capacity

Test Results

As the ambient temperature capacity tests were conducted for two different wall configurations, it becomes a necessity to compare the test results to determine a better understanding about the axial compression behaviour of these complex LSF walls under ambient conditions. Also, Tests-T1 to T4 were conducted using LCS noggings while Test-T5 was conducted with omega noggings. The stud flanges in single stud walls are effectively restrained by plasterboard on both sides while in complex LSF walls the effective restraints provided by the plasterboard is limited to one flange only. Therefore, comparisons are made against the ambient temperature capacity test results from single stud walls made of 92 mm studs and 150 mm studs to understand the dif-

ference in axial compression behaviour of complex LSF walls. Test results used for the comparison are given in Table 3.3. Comparisons with a 90 mm single stud wall are made for two thicknesses of 0.75 and 1.15 mm, while for 150 mm single studs the comparisons are made for 1.15 mm thickness only. This is due to the limited availability of the ambient temperature capacity test results. Single stud wall tests were conducted previously at the QUT Wind and Fire Engineering Laboratory. Further details of Test-S-AT2 can be found in Gunalan et al. (2013), while those of Tests-S-AT1 and S-AT2 details are available as internal reports (Ariyanayagam et al., 2016a).

Table 3.3: Comparison of ambient temperature test capacities

Test Name	Description	Stud Depth (mm)	Cavity Depth (mm)	Stud Thickness (mm)	No of Studs	Failure Load (kN)
AT1	Double Stud	90	200	0.95	4	73.00
AT2	Double Stud	90	200	0.75	4	47.08
AT4	Double Stud	70	160	0.95	4	86.21
AT5	Staggered Stud	90	150	0.95	11	68.49
S-AT1	Single Stud	90	90	0.75	2	33.10
S-AT2	Single Stud	90	90	1.15	4	79.24
S-AT3	Single Stud	150	150	1.15	6	45.43

Firstly comparisons were made against 90 mm studs on single and double stud LSF walls. This includes stud thicknesses of 0.75, 0.95 and 1.15 mm. Secondly, comparisons were made against staggered stud wall and single stud wall with 150 mm cavity depth. The stud thickness used in staggered stud wall was 0.95 mm with 90 mm stud depth while for single stud wall 150 mm deep studs with 1.15 mm thickness were used. Also, the 70 mm stud double stud wall Test-AT4 was also compared to understand the axial compression capacity of the single and double stud walls under different plasterboard restraint conditions. Comparisons are made using the ultimate axial compression capacities (applied ram load at failure). Variations in effective lateral restraints provided by plasterboards for different configurations are also discussed and their effects on the ultimate axial compression capacities were also investigated. Figures 3.22 and 3.23 show the applied load versus axial displacement curves for single and double stud walls with 90 and 150 mm cavity depth.

The ultimate axial compression capacity of 79.24 kN was recorded in single stud wall with stud thickness of 1.15 mm (S-AT2). The least axial compression capacity

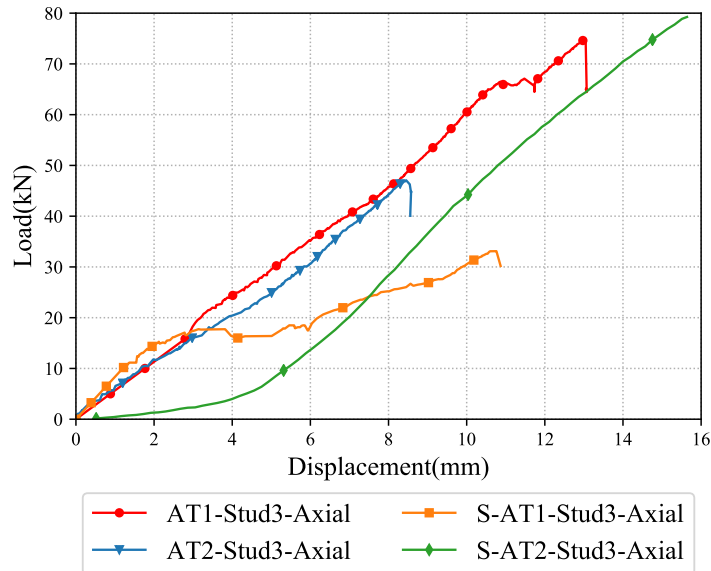


Figure 3.22: Comparison of applied load versus axial displacement curves - 90 mm studs

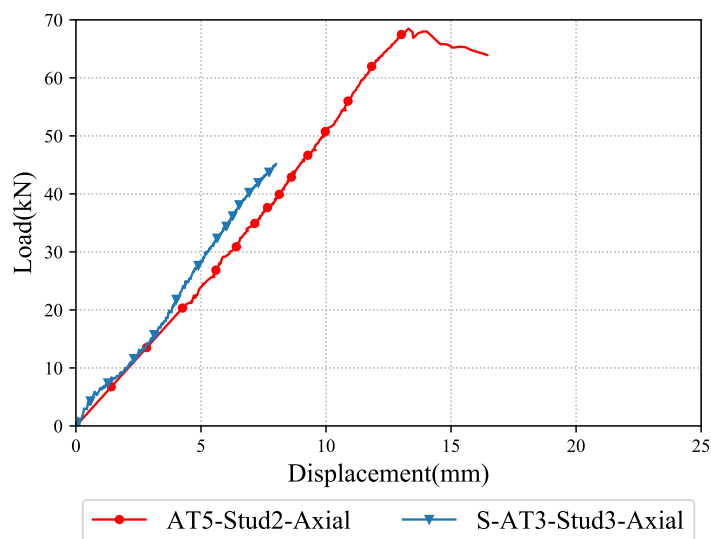


Figure 3.23: Comparison of applied load versus axial displacement curves - 150 mm studs

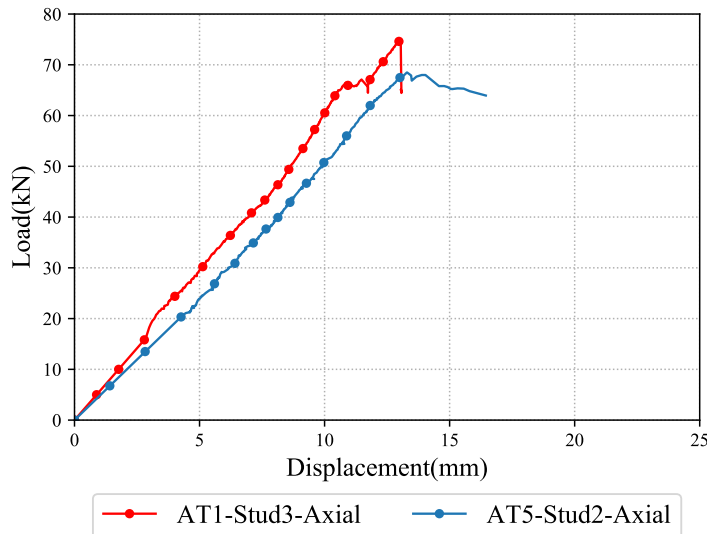


Figure 3.24: Comparison of applied load versus axial displacement curves from Test-AT1 and AT5

of 33.1 kN was recorded for the single stud wall with 0.75 mm stud (S-AT1). In single stud LSF walls, the plasterboards provide effective lateral restraints preventing the in plane (minor axis) buckling of studs. As the webs of studs locally buckle, the out of plane plasterboard restraint is not generally critical under ambient conditions. However, in the case of single stud wall with 150 mm studs the axial compression capacity was 45.43 kN, which is 33.81 kN less than the corresponding single stud wall with 90 mm studs. This is attributed to the wider web depth in 150 mm studs, resulting in lower axial compression capacity.

In the case of double stud LSF walls the effective plasterboard restraints are provided to one flange only on each stud row. The inner stud flanges in the LSF wall are restrained at 1 m intervals through noggings. This results in inadequate in-plane plasterboard restraints to the studs resulting in reduced axial compression capacity. If the single stud wall Test-S-AT1 is compared with the double stud wall Test-AT2, the stud thicknesses were 0.75 mm in both cases, the axial compression capacity was 23.54 kN per stud ($47.08/2$) in double stud wall Test-AT2, whereas it was 33.10 kN in single stud wall Test-S-AT1. The reduction in axial compression capacity was 9.56 kN. This emphasises the importance of effective plasterboard restraint to both stud flanges in LSF walls under axial compression loading.

Another finding was the double stud wall Test-AT4 with 70 mm studs resulted in a higher axial compression capacity of 86.21 kN ($86.21/2 = 43.10$ kN per stud) in

comparison with double stud wall with 90 mm studs (Test-AT1) resulting in an axial compression capacity of 73.0 kN ($73.0/2 = 36.50$ kN per stud). Despite having the same stud thickness and wall configuration, the 70 mm double stud wall resulted in a higher axial compression capacity. This can be attributed to higher slenderness of 90 mm studs in comparison with the 70 mm studs. However, the axial compression capacity of 90 mm single stud LSF wall lined with plasterboard on both sides resulted in a higher compression capacity in comparison with double and staggered stud walls.

Comparing the LSF walls with 150 mm cavity depth, the axial compression capacity was 68.49 kN in staggered stud wall Test-AT5 and 45.43 kN in 150 mm single stud wall Test-S-AT3. This is a significant reduction in the axial compression capacity. It is to be noted that the stud spacing was staggered with an effective spacing of 300 mm in staggered stud wall Test-AT5 while the stud spacing was 600 mm in 150 mm wide single stud wall Test-S-AT3. Also, the omega noggings were connected through the stud webs in Test-AT5 while no nogging restraints were provided for Test-S-AT3. Despite having a higher stud thickness of 1.15 mm the 150 mm wall Test-S-AT3 resulted in a reduced axial compression capacity.

Figure 3.24 shows the applied load versus displacement curves comparison from Tests-AT1 and AT5. The axial compression capacity from Test-AT1 was 73 kN ($73.0/2 = 36.50$ kN per stud) while the Test-AT5 gave 68.49 kN ($68.49/2 = 34.25$ kN per stud). Despite the difference in wall configuration and restraint conditions the staggered stud wall performed equal to that of double stud wall. This is attributed to the omega noggings supporting the stud webs, thereby providing equal restraints in comparison with conventional noggings connecting the stud flanges. Through the staggered stud arrangement the overall wall thickness was maintained at 214 mm (150 mm cavity depth + $(32 \times 4 = 64$ mm plasterboard thickness)) while it was 264 mm (200 mm cavity depth + $(32 \times 4 = 64$ mm plasterboard thickness)) in the case of a similar double stud LSF wall configuration. This can result in significant savings in the effective floor space in the construction industry and also achieving similar axial compression capacity.

3.11 Tensile Coupon Tests

Tensile coupon tests were conducted to determine the Young's Modulus and yield strength of the steel studs. Details of the tensile coupons are given in Figure 3.25. Tensile coupons were cut from the web and flanges of the studs at three locations along the 3 m long studs. Tensile coupon tests were conducted using Instron testing machine which operates on Bluehill software. Extensometers were used to measure the strain. Figure 3.25 shows the details of tensile coupons.

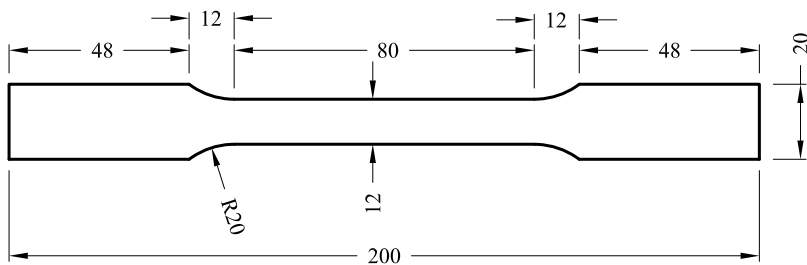


Figure 3.25: Tensile coupon details

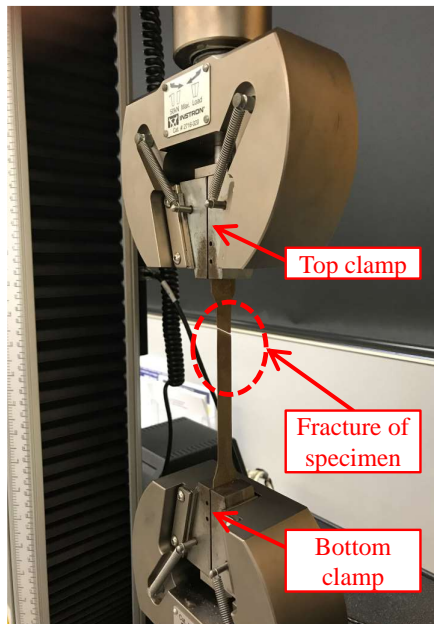


Figure 3.26: Tensile coupon test set-up

Figure 3.26 shows the tensile coupon test set-up. Details of the tensile coupon tests are shown in Tables 3.4 and 3.5. Fifteen tensile coupon tests were conducted to determine the Young's Modulus and yield strength of the steel used in the ambient temperature capacity wall tests. Figures 3.27 and 3.28 show the stress-strain curves obtained for 0.75 mm and 0.95 mm studs while Tables 3.4 and 3.5 give the measured

Table 3.4: Tensile coupon test results of 0.75 mm thick studs

Test No	Coupon Location	Young's Modulus (GPa)	Yield Strength (MPa)
1	Web	202.5	634.4
2	Web	232.3	658.4
3	Web	220.5	633.0
4	Web	214.3	642.9
5	Web	218.2	643.6
6	Web	212.9	642.9
7	Flange	212.4	648.7
8	Flange	216.4	658.3
9	Flange	217.5	660.5
Average		216.3	646.9

Table 3.5: Tensile coupon test results of 0.95 mm thick studs

Test No	Coupon Location	Young's Modulus (GPa)	Yield Strength (MPa)
10	Web	216.5	612.9
11	Web	219.1	623.7
12	Web	202.8	622.9
13	Flange	217.9	620.7
14	Flange	218.6	620.6
15	Flange	218.3	604.4
Average		215.5	617.5

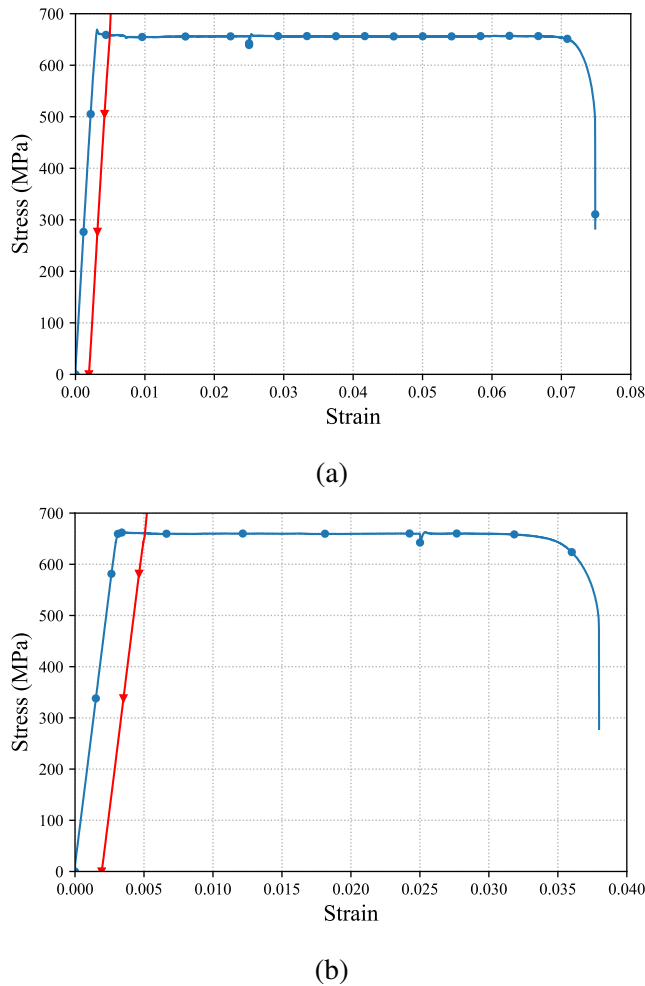


Figure 3.27: Stress-strain curves from tensile coupon tests of 0.75 mm G550 steel (a) Stud Web (b) Stud Flange

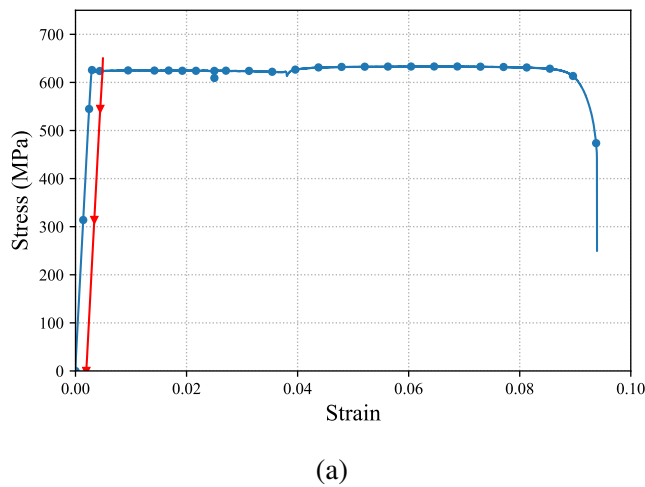


Figure 3.28: Stress-strain curves from tensile coupon tests of 0.95 mm G550 steel (a) Stud Web (b) Stud Flange

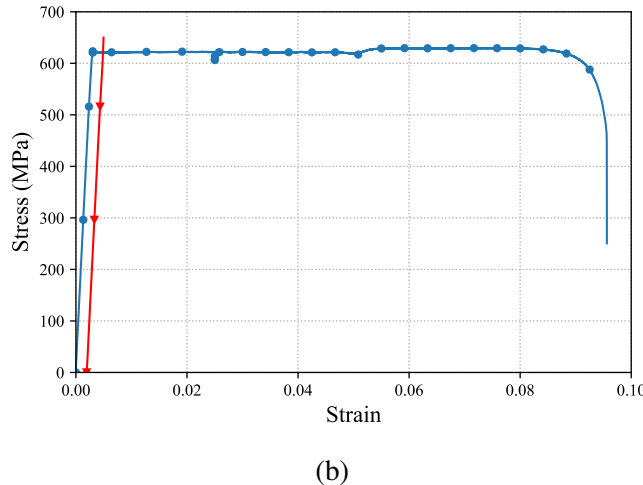


Figure 3.28: Stress-strain curves from tensile coupon tests of 0.95 mm G550 steel (a) Stud Web (b) Stud Flange

Young's modulus and yield strength values. The average Young's Modulus and yield strength of 0.75 mm thick studs were 216.4 GPa and 647.0 MPa, respectively. Likewise, for 0.95 mm thick steel, the average Young's Modulus and yield strength were 215.6 GPa and 617.5 MPa, respectively. The yield strength of 0.75 mm thick steel was higher in comparison with 0.95 mm steel.

3.12 Design Capacity Predictions Based on Direct Strength Method (DSM)

Conducting full-scale tests to determine the ambient temperature capacity of the LSF wall configurations is precise but expensive and time consuming. Therefore researchers have developed equations based on experimental and numerical studies to determine the ambient temperature axial compression capacities of these thin-walled LSF walls. Cold-formed steel members are generally designed based on the Effective Width Method (EWM) or the Direct Strength Method (DSM). The DSM is widely used in recent times over EWM due to less cumbersome calculations involved as stated by Yu and Schafer (2007), Schafer (2008), Shahbazian and Wang (2011), and Shahbazian and Wang (2012). Suitable DSM equations were successfully developed and used by Kessawan and Mahendran (2016a) to predict the reduced load bearing capacities of Hollow Flange Channel (HFC) studs when exposed to non-uniform temperature distributions during standard fire tests. Their applicability to other cold-formed steel sections such

as Lipped Channel and Web Stiffened channel sections were then verified by Rusthi et al. (2018). The DSM equations have been recently included in AS/NZS 4600 (SA, 2018). These two research studies of Kesawan and Mahendran (2016a) and Rusthi et al. (2018) have enabled the use of DSM based design equations to determine the load bearing capacity of cold-formed steel studs. This research has also investigated the applicability of these design equations to predict the ambient temperature capacities of the double and staggered stud LSF wall configuration considered for experimental investigation in this chapter.

To determine the ambient temperature capacities through DSM equations, parameters such as stud dimensions, mechanical properties and load factors from elastic buckling analysis are required. The stud dimensions were obtained from the manufacturer's data specification sheet and the mechanical properties were determined from the tensile coupon tests discussed previously in Section 3.11. The load factors were determined from the elastic buckling analyses conducted using Constrained and Unconstrained Finite Strip Method (CUFSM) software developed by Li and Schafer (2010). The stud sections were modelled using centre line dimensions and appropriate boundary conditions were assigned to the stud flanges and the finite strip analysis was performed using CUFSM. It is to be noted that CUFSM possesses capabilities to perform elastic buckling analysis corresponding to cross-section only. Therefore, the lateral restraints provided at the flanges to simulate intermittent plasterboard and nogging restraints were considered along the full length of the stud instead of only at intermittent locations. This shortcoming might result in conservative results when the load factors are substituted in the AS/NZS 4600 (SA, 2018) based design capacity equations. Figure 3.29 shows the signature curve outputs from the CUFSM highlighting the important load factors corresponding to different buckling modes.

Table 3.6: Elastic buckling loads of studs from CUFSM

Description	A_g (mm ²)	Critical Load Factor	Buckling Load (kN)
AT1	160.35	0.22	21.85
AT2	128.37	0.14	9.69
AT4	128.07	0.30	20.30
AT5	160.35	0.63	44.34

CUFSM analysis was conducted for three studs of dimensions 90 × 0.95 mm, 90

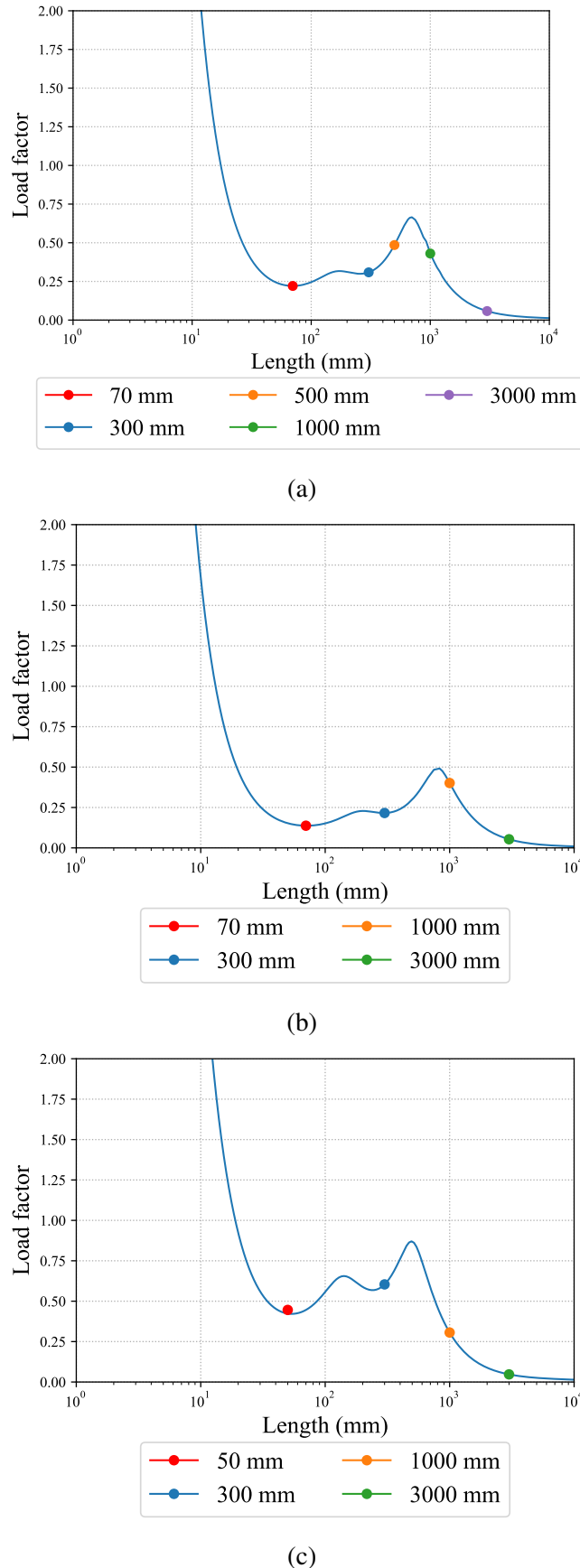
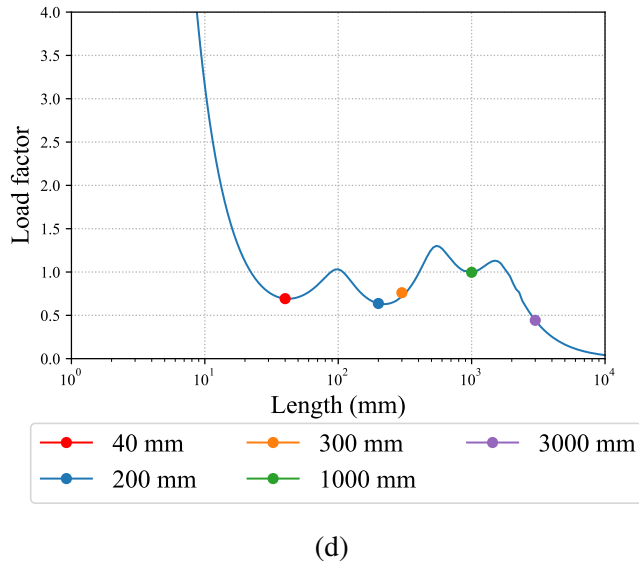


Figure 3.29: Signature curves from CUFSM finite strip analysis for Tests (a) AT1 (b) AT2 (c) AT4 (d) AT5



(d)

Figure 3.29: Signature curves from CUFSM finite strip analysis for Tests (a) AT1 (b) AT2 (c) AT4 (d) AT5

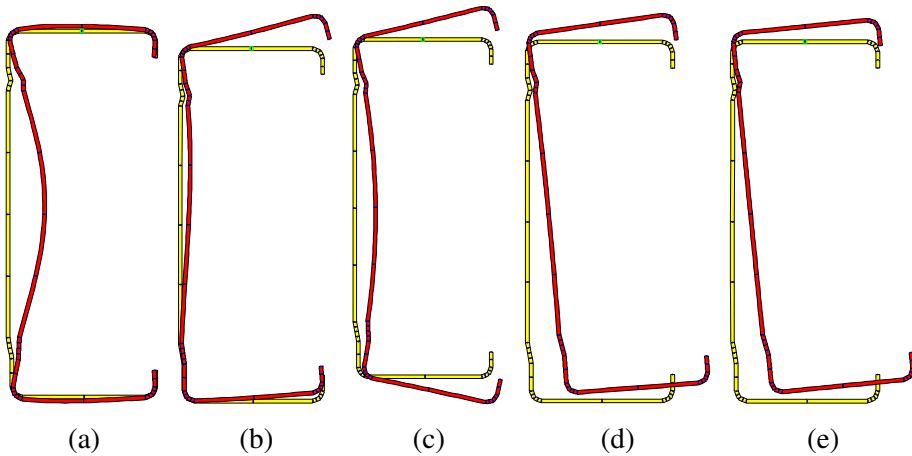


Figure 3.30: Buckling modes from CUFSM finite strip analysis for Test-AT1 at different lengths (a) 70 mm (b) 300 mm (c) 500 mm (d) 1000 mm (e) 3000 mm

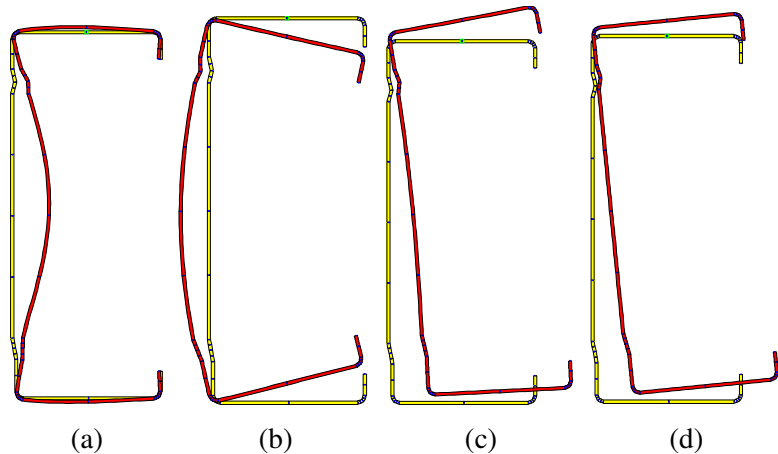


Figure 3.31: Buckling modes from CUFSM finite strip analysis for Test-AT2 at different lengths (a) 70 mm (b) 300 mm (c) 1000 mm (d) 3000 mm

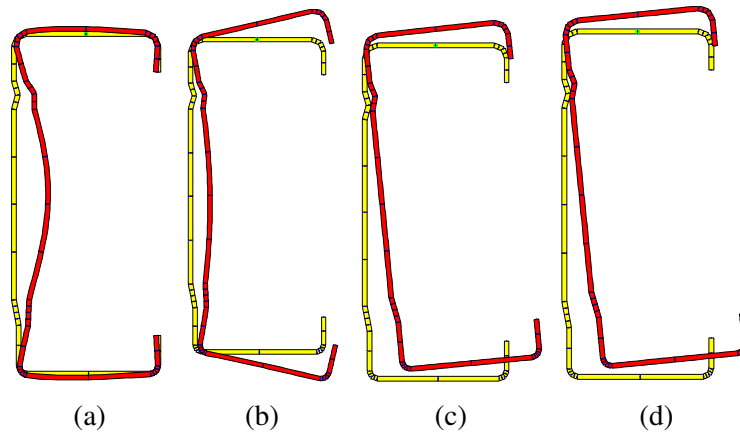


Figure 3.32: Buckling modes from CUFSM finite strip analysis for Test-AT4 at different lengths (a) 50 mm (b) 300 mm (c) 1000 mm (d) 3000 mm

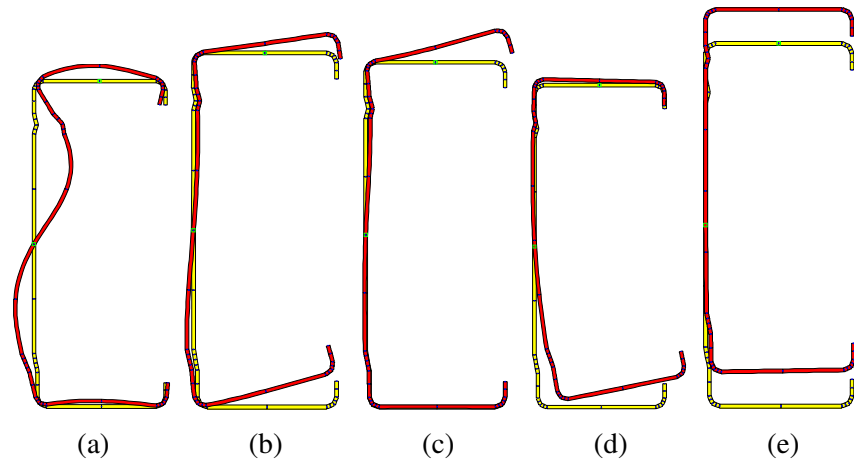


Figure 3.33: Buckling modes from CUFSM finite strip analysis for Test-AT5 at different lengths (a) 40 mm (b) 200 mm (c) 300 mm (d) 1000 mm (e) 3000 mm

Table 3.7: Ultimate axial compression capacities from DSM predictions and experiment

Test	Ultimate Axial Compression Capacities (kN)			Difference
	DSM (per stud)	DSM combined	Experiment	
AT1	28.43	56.86	73	16.14
AT2	18.88	37.76	47.08	9.32
AT4	17.8	35.6	86.21	50.61
AT5	38.89	77.78	68.49	-9.29

$\times 0.75$ mm and 70×0.95 mm corresponding to the ambient temperature capacity Tests-AT1, AT2, AT4 and AT5. Test-AT3 was not considered for the CUFSM analysis as the stud dimensions were similar to that of Test-AT2. Also, for Test-AT5 90×0.95 mm stud was used wherein the restraints were provided on the web in addition to the one flange provided in other models as shown in Figures 3.30 to 3.33 which includes the buckling modes of the studs from CUFSM analysis. For the DSM based design calculations, the lowest load factor from the signature curves are extracted to determine the ambient temperature compression capacities of the conducted full-scale tests. Local buckling was the lowest failure mode in all the studs as inferred from the signature curves shown in Figure 3.29. The local buckling factor from the signature curve corresponding to Tests-AT1 and AT2 occurred at half wave lengths of 70 mm while it was 50 mm and 40 mm for Tests-T4 and T5. The corresponding load factors were incorporated in the DSM equations and the ultimate compression capacities of the stud sections were determined and is shown in Table 3.7.

Single studs were modelled in CUFSM to determine the load factor for substitution in the DSM equations. Therefore, the arrived capacities are doubled to determine the ultimate axial compression capacity of a stud set. The critical buckling load factor along with the elastic buckling loads of studs are presented in Table 3.6. The axial compression capacity predictions from the AS 4600 based DSM equation resulted in lower capacities in comparison with the experiments except Test-AT5. The DSM predictions resulted a maximum ambient temperature axial compression capacity for Test-AT5 (staggered stud wall with 90×0.95 mm studs). However, the experiment gave a maximum axial compression capacity for Test-AT1. This was attributed to the continuous restraints considered on the stud web and flanges resulting in higher local buckling load factors in comparison with the double stud wall Test-AT1. Since the continuous restrain is considered only on one flange, in Test-AT1, the local buckling load factor was lower and resulted in a reduced ultimate axial compression capacity. Likewise the DSM based ultimate compression capacity for Test-AT5 was lower than the experiment. The difference in predicted capacity and experiment for Test-AT4 may be attributed by various reasons which includes the load sharing to the stiffened nested edge studs and may also be due to the higher yield strength of steel studs used in the test wall. This was possible as the studs for Test-AT4 were procured from a different

batch of studs. This shows the need to develop a finite element (FE) structural model to better predict the axial compression capacities of the double and staggered stud LSF wall systems and will be discussed in Chapter 6. There also prevails a limitation in assigning intermittent lateral restraints to the stud flanges and near the service holes in the web in determining the load factors through CUFSM.

3.13 Summary of Findings

The following findings can be drawn from the ambient temperature capacity tests on double and staggered stud LSF walls and tensile coupon tests.

- Axial compression capacity of LSF wall is dependent on the thickness and depth of the studs.
- The effect of plasterboards on the stud flanges providing in-plane lateral restraints significantly influences the axial compression capacity of single stud LSF walls. The absence of effective plasterboard restraints on the inner stud flanges in double stud walls affects the axial compression capacity of double stud LSF walls despite the use of noggings at 1 m intervals.
- In the case of staggered stud LSF walls, despite the absence of plasterboard restraint on one flange, the omega noggings connecting the stud webs at 1 m intervals provide significant in-plane lateral restraints to the studs and together with additional end cleats at the supports gave a similar axial compression capacity in comparison with double stud LSF walls.
- The axial compression capacity of plasterboard lined double stud walls is significantly higher for walls with 70 mm studs in comparison with 90 mm studs of the same thickness. This is attributed to the increased plate slenderness of 90 mm studs.
- Tensile tests of coupons taken from G550 steel studs show that the minimum guaranteed yield strength of 550 MPa is achieved in all the tests. 0.75 mm steel has a higher yield strength in comparison with 0.95 mm steel despite the same grade of steel. This is because of the higher cold work in steel with lower

thicknesses. However, the Young's Modulus is almost similar irrespective of the thickness. The Young's Modulus and yield strength results from the coupon tests reported in this chapter can be used in the numerical analysis of LSF walls.

- Ultimate compression capacities predicted by the DSM equations in AS/NZS 4600 resulted in reasonable agreement for double stud wall Tests-AT1, AT2 and staggered stud wall Test-AT5. However, the design capacity predictions for AT4 was lower in comparison with the experiment. This may be attributed to the load sharing in the studs due to nesting of the edge studs and may also be due to the difference in mechanical properties of the steel used for Test-AT4. The limitation of providing intermittent lateral restraints to determine the load factors for DSM calculation needs to be addressed to better determine the axial compression capacities of the studs.

Chapter 4

Experimental Investigations of Complex LSF Walls under Fire Conditions

4.1 General

This chapter details the experimental investigations conducted on complex LSF wall systems. To determine the fire performance of LSF wall systems, fire tests are still the preferred method and are generally accurate. Therefore, extensive experimental investigations were carried out on a series of complex LSF walls under load bearing and non-load bearing conditions. Three complex LSF wall systems known as double stud walls, shaftliner walls and staggered stud walls were considered in these full-scale experimental investigations (Figures 4.1 (a) to (c)). The ambient temperature capacity test results from Chapter 3 were used to apply the appropriate loads in the fire test as discussed in this chapter.

4.2 Heat Transfer in LSF Walls

In single stud LSF walls exposed to fire on one side the heat transfer happens by conduction through plasterboards from fire side to ambient side. This is followed by convection and radiation within the cavity. Conduction and radiation through the studs also contribute significantly to the heat transfer across the wall. In single stud walls the

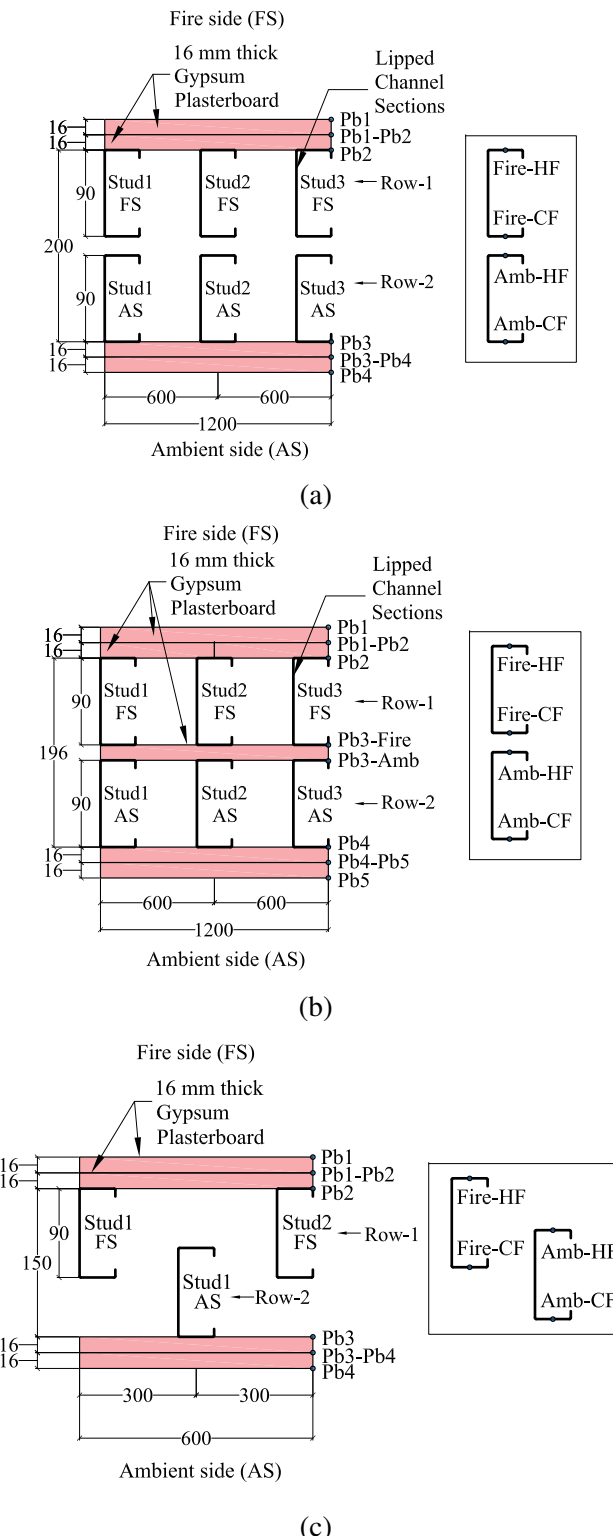


Figure 4.1: Typical section of (a) Double stud (b) Shaftliner and (c) Staggered stud LSF wall

plasterboards provide intermittent lateral restraints to both flanges of the stud depending on the screw locations and protect the steel studs during fire. The fire resistance level is greatly influenced by the number of plasterboard layers used as shown by Kodur and Sultan (2006) and Ariyanayagam et al. (2016b).

Generally, in a single stud wall with two layers of plasterboard lining the fire exposed plasterboard transfers the heat to the subsequent plasterboard layer and reaches the stud hot flange through conduction. But within the cavity, the heat transfer from fire side cavity surface to the ambient side cavity surface occurs through both convection and radiation. Air within the cavity offers certain resistance to the heat transfer depending upon the depth and volume of the air cavity. There is also a certain amount of heat transfer through the conduction of air within the cavity. But the conductivity of air is low when compared to plasterboard at higher temperatures. There is also a significant amount of radiation into the cavity and conduction through the studs in single stud walls.

In double and staggered stud walls, the heat transfer mechanism from fire side to ambient side is not well understood. The air gap between the two rows of stud reduces the heat transfer through conduction from fire side to ambient side cavity. This results in lower temperatures on the ambient side plasterboard. This can reduce the temperatures across the wall resulting in uniform temperature distribution in the studs. Such reduced temperature gradient can result in reduced thermal bowing and neutral axis shift in comparison with single stud LSF walls. During the fire exposure on one side, the plasterboard on the fire side calcinates at 140°C, which is the first dehydration point (Keerthan and Mahendran, 2012b). The temperature distribution on the stud will be non-uniform causing thermal bowing. This also leads to non-uniform mechanical properties of steel, resulting in neutral axis shift for studs. These actions caused by fire exposure on one side induce the thin-walled studs to be subjected to a bending moment in addition to the applied axial compression load (Gunalan et al., 2013). But there is lack of research data to fully understand these effects in double and staggered stud walls. Therefore, this research investigated the structural fire performance of load bearing double and staggered LSF walls using full scale standard fire tests. It also included the double stud wall with a middle plasterboard layer (shaftliner) and a staggered stud wall under non-load bearing conditions.

4.3 Small-Scale Fire Test of Double Stud LSF Walls

To investigate the fire performance of complex LSF walls and determine the thermal behaviour, a small-scale fire test was conducted on double stud LSF wall. Small-scale fire tests were considered as a pilot study to determine the thermal performance of LSF walls by past researchers. The results from small-scale fire tests are valuable to predict the thermal behaviour of LSF walls through full-scale fire tests beforehand. However, only the insulation and integrity failure criteria based FRL can be determined using small-scale fire tests. Structural failure criterion based FRL of an LSF wall configuration could be determined only through full-scale fire tests.

4.3.1 Small-Scale Fire Test Details

One small-scale fire test of non-cavity insulated double stud LSF wall was conducted in this research study (referred to as Test-ST1). The test wall dimensions were 1.2 m × 1.2 m with an exposed area of 1 m × 1 m as shown in Figure 4.2. A propane gas furnace with a single burner was used in the fire test. Two rows of two 90 mm studs with 0.95 mm thickness with a 20 mm gap were used in the fire tests. Two layers of 16 mm thick gypsum plasterboard were used on both sides of the test wall panel. Test wall panel details are shown in Figure 4.3 (a). K-type thermocouples were used to measure the temperatures across the test wall at various locations during the fire test. The test was conducted under non-load bearing conditions. Therefore the axial and lateral displacements were not measured during the fire test. Apart from the temperature measurements through thermocouples the ambient side temperatures were closely monitored with an infrared gun to detect insulation failure, which is one of the critical failure criteria in non-load bearing LSF wall fire tests.

Test wall was clamped to the small furnace and ceramic insulation was wrapped around the specimen to prevent heat loss around the sides during the fire test as shown in Figure 4.3 (b). The test wall was then exposed to AS 1530.4 standard fire time-temperature curve. Mild smoke was observed from 30 min till 80 min of the fire test representing the calcination of fire side plasterboard. Also, water droplets were visible on the clamps used for attaching the test wall to the furnace at certain intervals. The fire test was conducted for 176 min after which the test was stopped due to in-

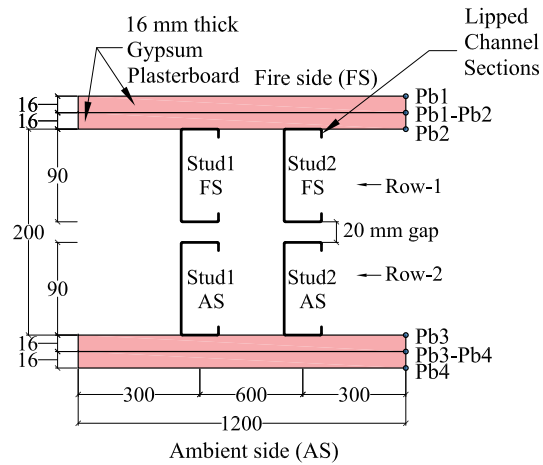


Figure 4.2: Plan view of double stud LSF wall panels used in Test-ST1

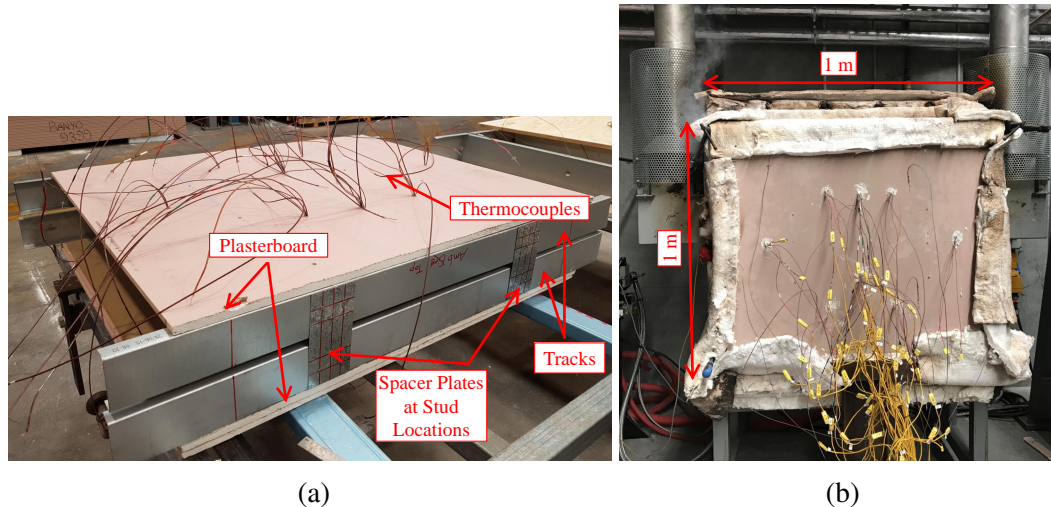


Figure 4.3: Small-scale fire Test-ST1 (a) Test panel (b) Test set-up

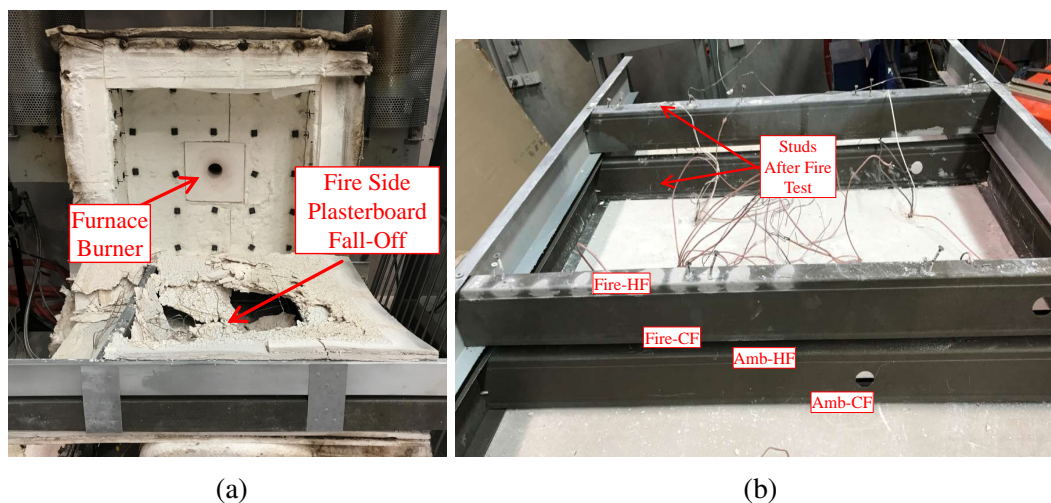


Figure 4.4: Post-fire observations of Test-ST1 (a) Plasterboard fall-off (b) Studs after fire test

sulation failure criterion, when the temperatures on the ambient side at the top left corner exceeded the limiting temperature of 200°C (180°C + initial room temperature of 20°C). Post-fire test observations revealed severe plasterboard fall-off on the fire side (Figure 4.4 (a)) resulting in sudden increase in temperature on the ambient side at a particular point. However, the thermocouple measured ambient side plasterboard surface (Pb4) temperatures were well below 100°C till the end of the fire test. No deformation was observed in the studs as shown in Figure 4.4 (b) as this was a non-load bearing test with shorter stud sections. The plasterboard fall-off was due to the hot air from the furnace concentrated on a small area of the small-scale test frame for a longer time period.

4.3.2 Small-Scale Fire Test - Results and Discussion

The small-scale fire test results showing the time-temperature evolution of the plasterboards and studs are shown in Figure 4.5. Fire side plasterboard interface temperatures (Pb1-Pb2) was flat for the initial 20 min after which a steep rise in the curve was noticed Figure 4.5 (a). This was followed by a unique plateau region from 70 min to 120 min after which the curve increased gradually till the end of the fire test. This unique behaviour with a plateau region in the Pb1-Pb2 time-temperature curve is also reflected on the fire side cavity (Pb2) and the ambient side cavity (Pb3) surfaces. A sudden increase in the time-temperature curves were observed in all the plasterboard surfaces near the end of the test, indicating plasterboard fall-off. The possibility of joint opening cannot happen as the specimen did not have any plasterboard joints. However, the ambient side plasterboard interface surface (Pb3-Pb4) recorded temperatures less than 100°C till 150 min and reached a maximum of 280° at the end of fire test. The stud time-temperature curves are plotted in Figure 4.5 (b).

The hot and cold flange temperatures of Stud1 and Stud2 recorded temperatures less than 200°C till 65 min of the fire test. A sudden increase in the time-temperature curve of the fire side hot and cold flanges (ST1-Stud1 and Stud2-Top-Fire-HF and CF) was noticed after 65 min, after which the curve exhibits a gradual increase correlating with the corresponding plasterboard temperature curves. However, the plateau region was not as significant as in the plasterboard time-temperature curves. The sudden increase in the hot flange temperatures near the end proves the presence of plasterboard

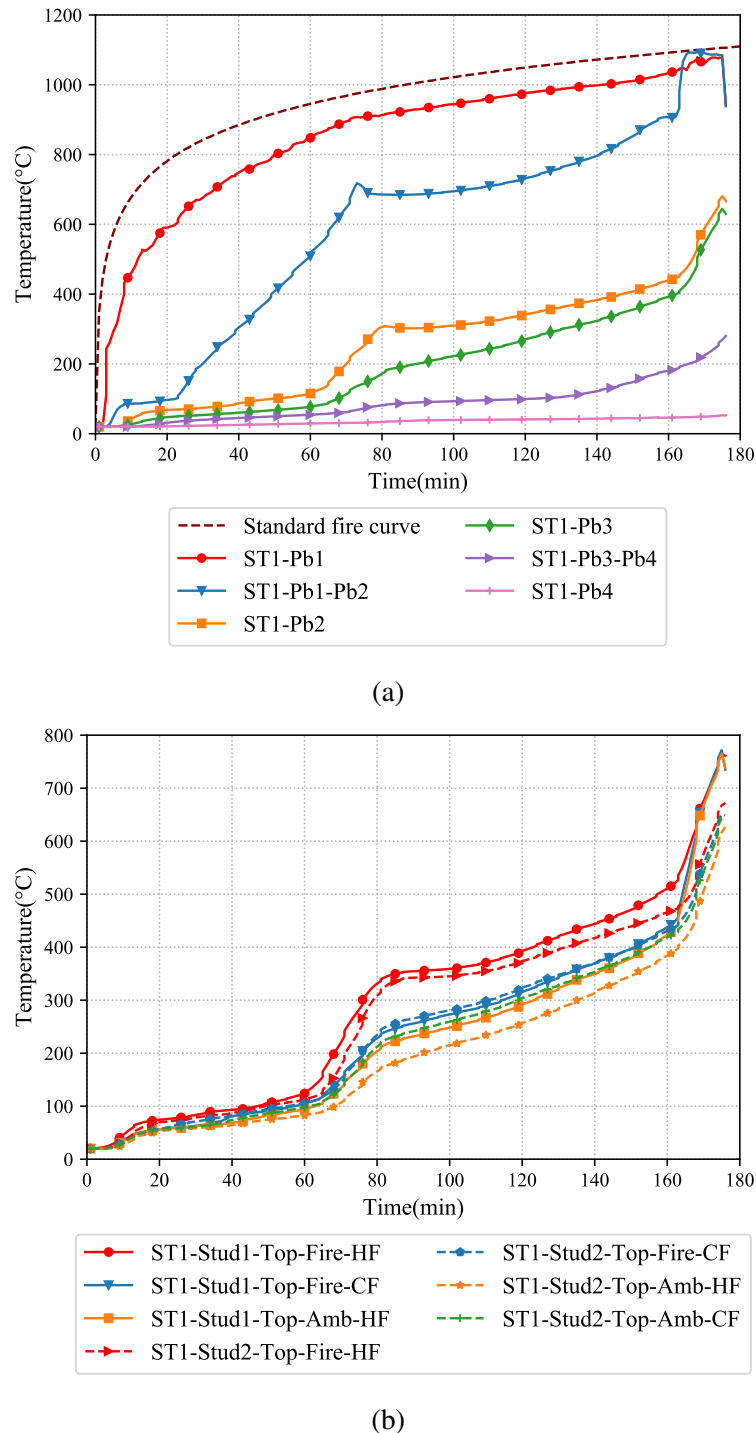


Figure 4.5: Plasterboard and stud time-temperature curves of Test-ST1 (a) Average plasterboard temperatures (b) Stud temperatures

fall-off in the fire test. The cold flange temperatures were in close relation with the corresponding hot flange temperatures as shown in Figure 4.5 (b). It is to be noted that the difference in temperature gradients between the fire side cold flange (ST1-Stud1 and Stud2-Top-Fire-CF) and the ambient side hot and cold flanges (ST1-Stud1 and Stud2-Top-Amb-HF and CF) were small in comparison with the fire side hot and cold flanges. This indicates the delayed heat transfer mechanism in the wider cavity of this double stud LSF wall. This is further investigated and discussed in the full-scale fire test section of this chapter.

4.4 Full-scale Fire Tests of Double, Staggered and Shaftliner LSF Walls

4.4.1 Fire Test Panel Details

To investigate the heat transfer mechanism in detail, 10 full-scale fire tests were conducted on the complex LSF wall systems made of two rows of studs (Figures 4.1 (a) to (c)). The test wall panels were constructed with frame dimensions of 3 m × 3 m. Lipped Channel Sections (LCS) were used as studs and Unlipped Channel Sections (UCS) were used as tracks. The nominal dimensions of LCS used in this study were 90×36×7×0.75 mm, 90×36×7×0.95 mm and 70×29.5×8×0.95 mm. Intermittent lateral restraints using 0.55 mm thick noggings located at 1000 mm intervals were provided in all the fire tests except Tests-T9 and T10. However, Test-10 had omega noggings and the details are discussed in the corresponding section. Stud thickness, cavity depth, load ratio and cavity insulation were the variable parameters and are detailed in Table 4.1. G550 steel (minimum yield strength of 550 MPa) was used in all the fire tests. For each frame (Figure 4.6) six studs, two tracks and two noggings were connected using Buildex M6.0 × 15 GX Ca smooth top GA point steel frame and truss screws with studs at 600 mm centres. A 20 mm gap was maintained between the two rows of steel frames by using 50 mm × 200 mm spacer plates for double stud walls.

Two layers of 16 mm thick USG Boral Firestop gypsum plasterboards measuring 1200 × 3000 mm were used as lining on both sides of the test wall and were attached to the frames using D type 10 GA self-piercing screws at 300 mm spacing in all the

Table 4.1: Fire test panel details

Test Name	Description	Stud Depth (mm)	Stud Thickness (mm)	Cavity Depth (mm)	Cavity Insulation	Load Ratio
T1	Double Stud	90	0.95	200	No	0.4
T2	Double Stud	90	0.75	200	No	0.4
T3	Double Stud	90	0.75	200	No	0.6
T4	Double Stud	70	0.95	160	No	0.4
T5	Double Stud	90	0.95	200	Both ⁺	0.4
T6*	Double Stud	90	0.95	200	Both ⁺	0.4
T7	Double Stud	90	0.95	200	Ambient ⁺⁺	0.4
T8	Shaftliner	90	0.75	196	No	NLB
T9	Staggered Stud	90	0.75	150	No	NLB
T10	Staggered Stud	90	0.95	150	Full* ⁺	0.4

* Repeat of Test-T5

+ Cavity insulation on both stud rows

++ Cavity insulation on ambient stud row only

*+ Cavity insulation staggered alongside the studs

NLB - Non-Load Bearing

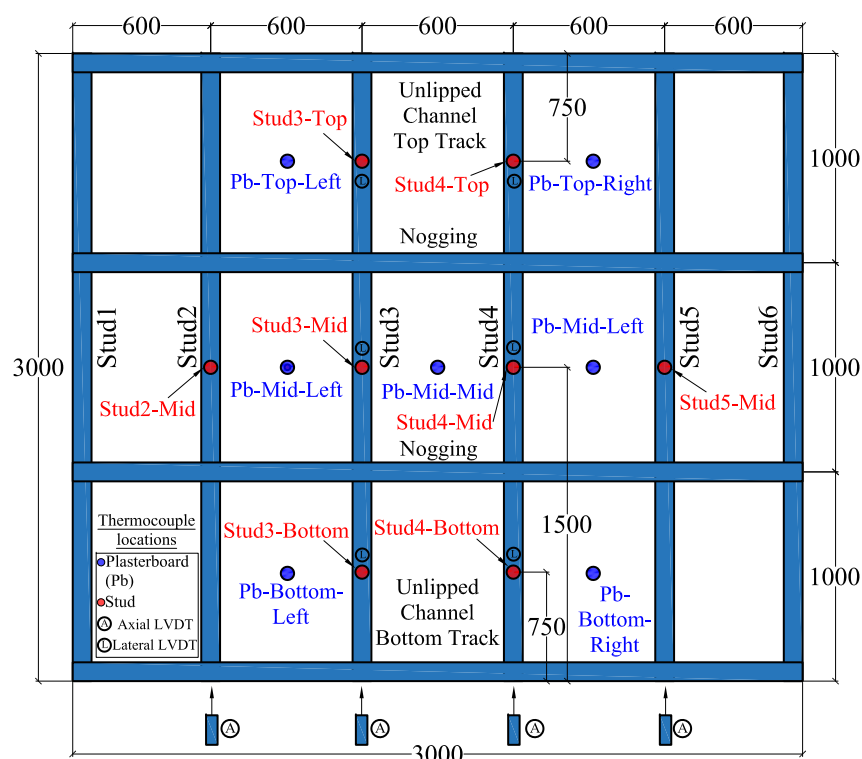


Figure 4.6: Elevation of LSF Wall Panel showing LVDT and thermocouple locations

Note : All dimensions are in mm.

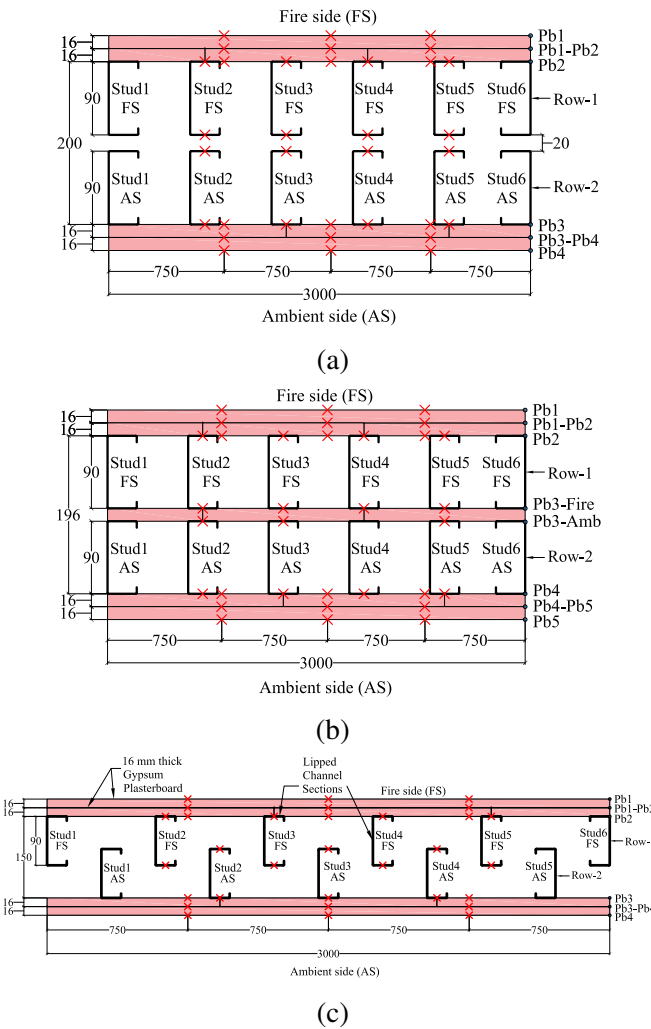


Figure 4.7: Typical stud and plasterboard thermocouple locations for (a) Double stud (b) Shaftliner and (c) Staggered stud LSF wall

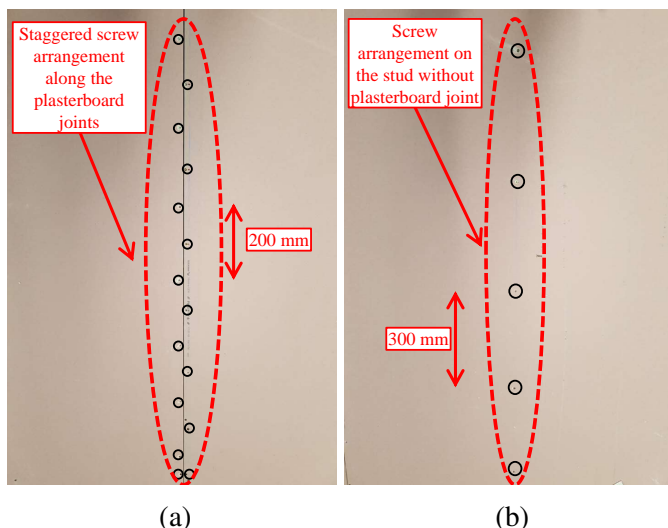


Figure 4.8: Locations of plasterboard screws

Note : All dimensions are in mm.

fire tests. The first layer of plasterboard was attached using 32 mm long screws while the second layer was attached using 45 mm long screws. They were screw fastened only to the studs (not tracks). This is achieved by providing a 60 mm gap from the frame end to the screws when fixing the first plasterboard layer, while a 80 mm gap was provided for the second plasterboard layer. The first layer of plasterboard was placed vertically with two vertical joints and the second layer was placed horizontally with two horizontal joints. The screws were staggered at 200 mm near the plasterboard joints as shown in Figure 4.8 (b). An edge distance of 10 to 15 mm was provided along all the plasterboard edges to prevent shearing of the screws from the plasterboard. USG Boral Basecoat 60 was used as the joint compound with 50 mm wide cellulose based joint tape. For fire designs, LSF walls are considered to be subjected to an axial compression load in the range of 40 to 60% of the ambient temperature load bearing capacity, i.e. load ratio (LR) of 0.4 to 0.6. Therefore, all the load bearing tests were conducted within this load range. In addition, two non-load bearing tests were also conducted for staggered and shaftliner wall systems (Table 4.1).

4.4.2 Temperature Sensors and Displacement Transducers

Sixty four thermocouples were used to measure the temperatures across the width and depth of the test wall at various locations (Figure 4.6). Ten Linear Variable Displacement Transducers (LVDTs) were used to measure the axial shortening and lateral deflection of the wall as shown in Figure 4.9 (b). K-Type thermocouples that can measure the temperature within the range of -200°C to 1100°C were used. They were positioned at quarter heights (750 mm, 1500 mm, 2250 mm) along the stud height and on the fire exposed side (Pb1), fire side cavity (Pb2), ambient side cavity (Pb3) and the ambient side (Pb4) of plasterboards as shown in Figure 4.7. For the plasterboard interfaces on the fire side (Pb1-Pb2) and ambient side (Pb3-Pb4) thermocouples were placed only at mid-height of the panel. For studs, thermocouples were placed on stud flanges at quarter heights (750 mm, 1500 mm, 2250 mm) of Studs 3 and 4 only whereas on Studs 2 and 5 they were placed only at mid-height (1500 mm) as shown in Figure 4.6. LVDTs were placed under Studs 2 to 5 to measure the axial displacements and at quarter heights along Studs 3 and 4 to measure the lateral deflections as shown in Figure 4.9(b).

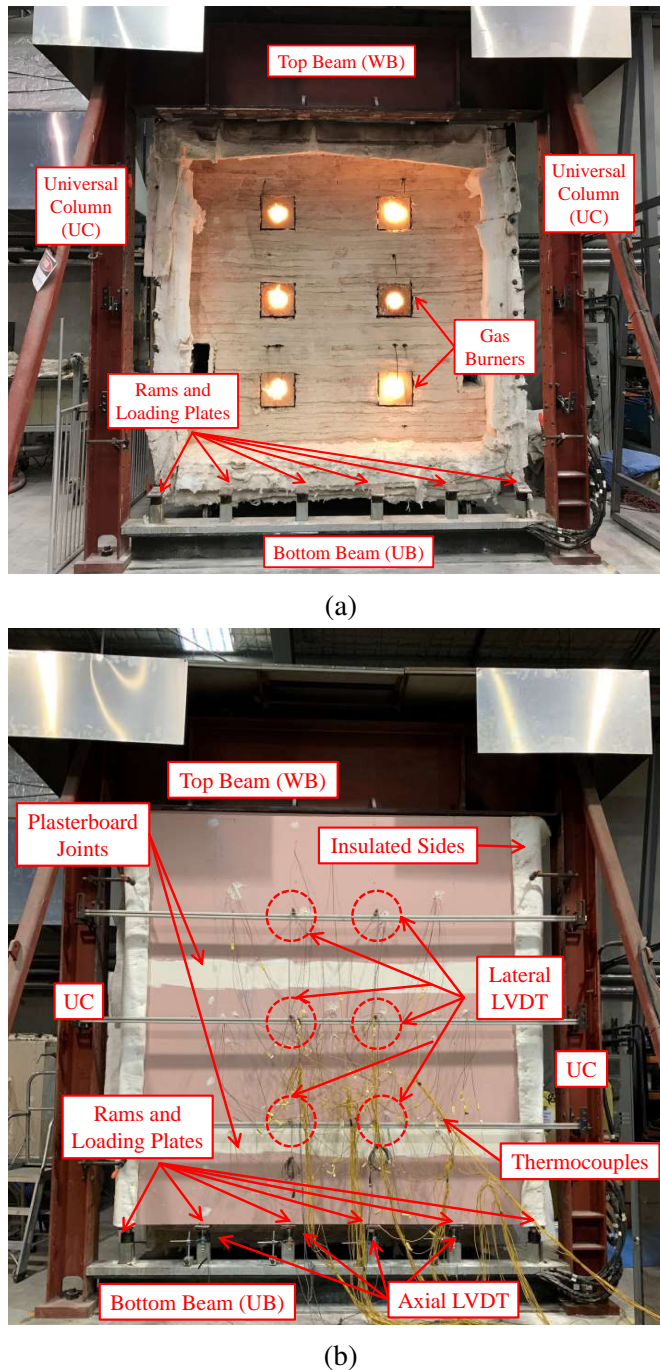


Figure 4.9: Full scale fire test set-up (a) Furnace with pilot flame (b) Test panel

4.4.3 Fire Test Set-up and Procedure

Fire tests were conducted using a $3 \times 3 \times 0.4$ m furnace consisting of six propane gas fuelled burners controlled by a EUROTHERM 3504 hybrid controller (Figure 4.10 (a)) after applying the pre-determined axial compression loads using six hydraulic rams (Figure 4.9 (a)). The test rig was built with two universal columns (UC) bolted to the strong floor at the bottom and to a universal beam (UB) at the top. At the bottom end, a UB was fixed to the strong floor upon which six hydraulic rams were placed and connected to a pressure transducer. Once the wall panel was placed on the test rig an initial preload of 3 kN was applied to each stud to keep the wall panel in position before the fire test. The required load based on the load ratio was then applied to each stud by the hydraulic ram via a thick loading plate at the bottom end and was monitored through the data acquisition system. The test wall panel was then exposed to the standard fire time-temperature curve in AS 1530.4 (SA, 2014). The test panel was insulated with ceramic fibre blankets along the edges to prevent any heat loss through the sides. The thermocouple and LVDT measurements were recorded using a Universal Data Acquisition (UDAQ) system with NI-LabView software until failure occurred as shown in Figure 4.10 (b).

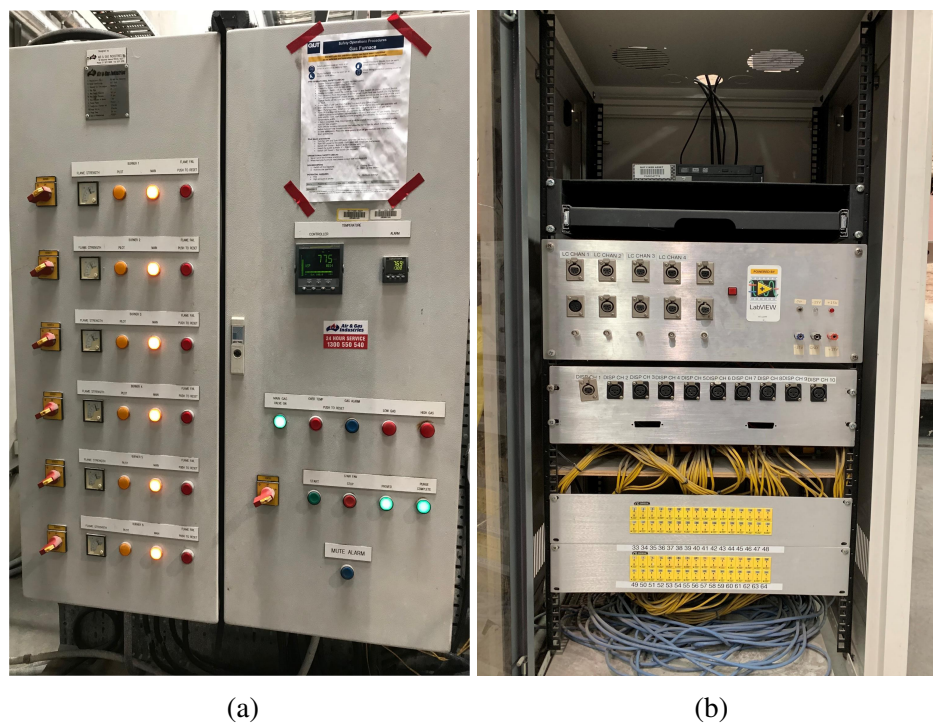


Figure 4.10: Instrumentation set-up (a) Furnace controller (b) UDAQ

To easily identify the thermocouple and LVDT measurement locations, the fire and ambient side plasterboards are referred to as Pb1 and Pb4 while the internal plasterboards are referred to as Pb2 and Pb3 (Figure 4.11). The interface between the two plasterboard layers on the fire side is referred to as Pb1-Pb2 while the interface between the ambient side plasterboards is referred to as Pb3-Pb4. The hot and cold flanges of single stud walls are referred as HF and CF. In double and staggered stud walls with two rows of stud, the hot and cold flanges of studs on the fire exposed side are referred to as Fire-HF and Fire-CF whereas those on the ambient side are referred to as Amb-HF and Amb-CF.

4.5 Fire Test-T1

4.5.1 Test-T1 Failure Time and Mode, and Observations

Figure 4.12 shows the typical construction details of double stud walls (Tests-T1 to T3). Ambient capacity test conducted on the wall initially gave a stud capacity of 73.0 kN. Hence the fire test was conducted with studs loaded to 29.2 kN, i.e., 0.4 LR. The wall panel failed structurally after 176 min. No significant plasterboard fall-off was noticed during the fire test as shown in Figure 4.13 (a). The plasterboard cracked at 750 mm above the bottom track on the ambient side near the LVDT but no flames were visible as shown in Figure 4.13 (b). Local buckling of studs was the predominant mode of failure, which was clearly visible in Stud3 on the fire side (Row-1) as shown in Figure 4.13 (c). It was significant only on the fire exposed row of studs. This is due to the effect of the 20 mm air gap between the two rows of studs.

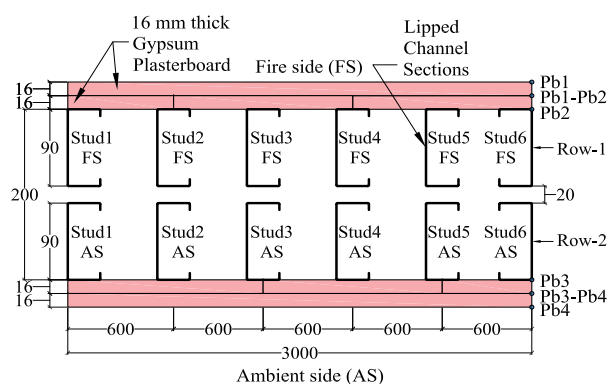


Figure 4.11: Plan view of double stud LSF wall panels used in Tests-T1-T3

Note : All dimensions are in mm.

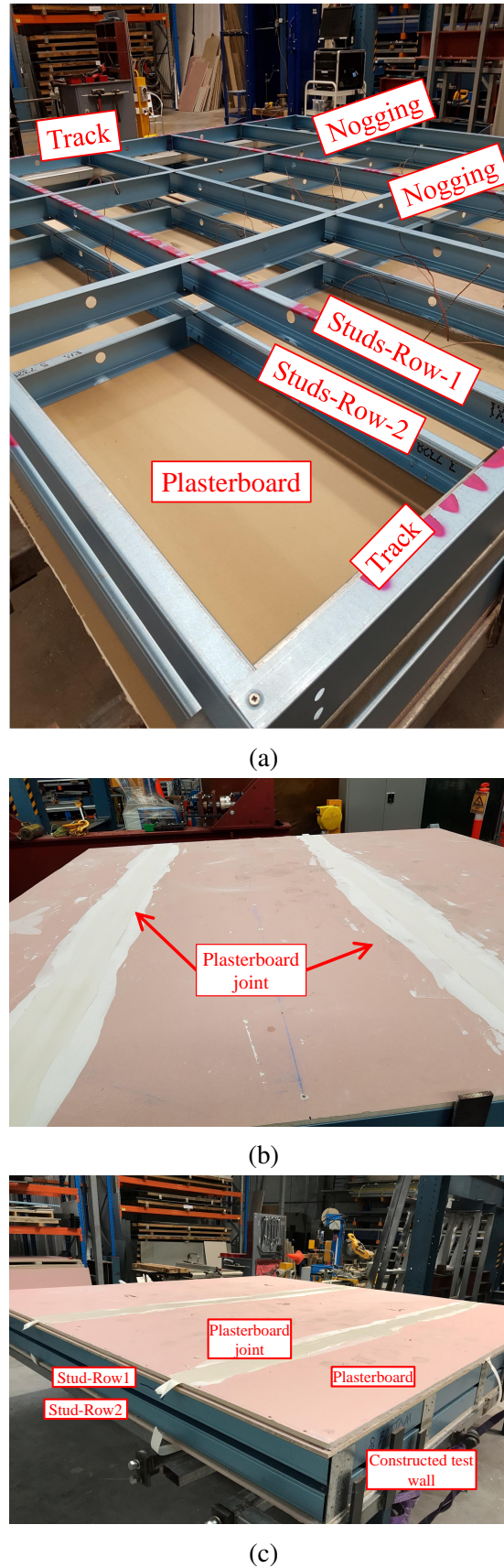


Figure 4.12: Test-T1-T4 wall construction sequence (a) Stud frame assembly (b) Plasterboard joint (c) Constructed test wall

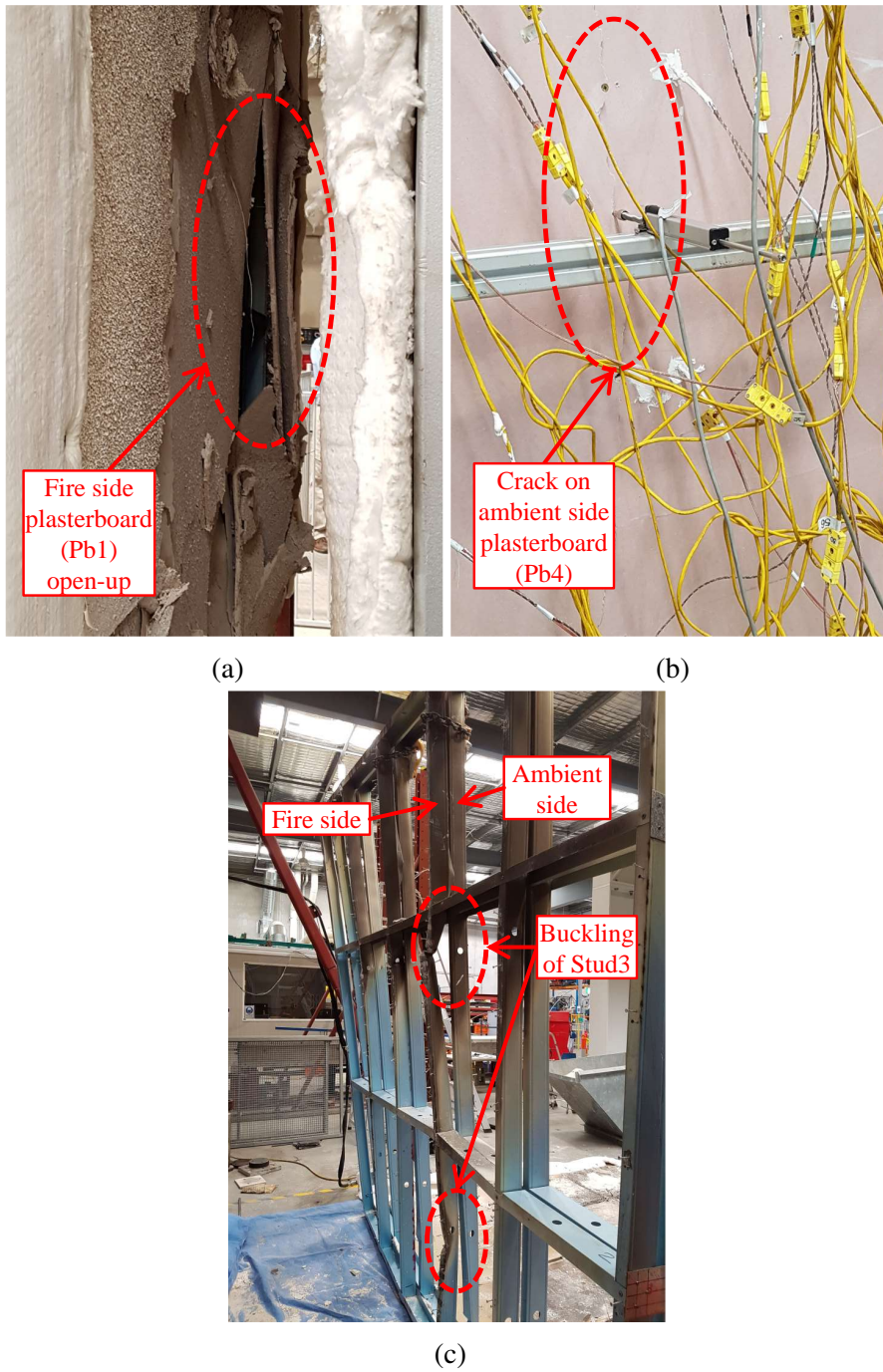


Figure 4.13: Failure of Test-T1 wall (a) Fire exposed side (b) Crack on ambient side plasterboard (c) Local compressive failure of Stud3

4.5.2 Test-T1 Results and Discussion

The time-temperature curves of the plasterboards and studs for Test-T1 are shown in Figure 4.14. The fire exposed plasterboard temperature matched reasonably well with the standard fire curve. After 22 min of fire exposure, plasterboard joint compound started to fall-off indicating that the paper layer has been completely burnt. The Pb1 temperature at this stage was 740°C. No water droplets were visible till 40 min. At 41 min water patches were visible on the top right and left corners of the ambient side plasterboard. This was accompanied by mild smoke from the bottom of the test panel. There was visible smoke again at 75 min indicating the burning of paper layer. At this time the temperature recorded at Pb1-Pb2 was 638°C. The time-temperature curve on the fire side cavity (Pb2) was nearly flat during the early stages of the fire test until 60 min and the temperature recorded was well below 100°C as shown in Figure 4.14 (a). From 60 to 80 min the time-temperature curve suddenly increased with a steep slope to attain a peak value of 256°C and then increased gradually to a maximum value of 423°C at 176 min (at failure). It can also be noted that the steep rise is in correlation with the time-temperature curve recorded on the interface between the two plasterboard layers on the fire side (Pb1-Pb2). At 80 min the temperatures of fire side plasterboard (Pb1), the interface (Pb1-Pb2) and the fire side cavity (Pb2) were 963°C, 656°C and 256°C, respectively. The temperature difference between the fire side (Pb1) and the fire side interface (Pb1-Pb2) was 280°C whereas the difference between the interface (Pb1-Pb2) and fire side cavity (Pb2) was 400°C after 80 min of fire exposure.

Also during 80 to 120 min, the time-temperature curve of the Pb1- Pb2 interface as shown in Figure 4.14 (a) is nearly flat, whereas the time-temperature curve of Pb2 rises slowly. But the difference in temperature between these two surfaces is large. This infers that plasterboard has lost its ability to store heat at the interface (Pb1-Pb2). There is no significant rise in the time-temperature curve of Pb1-Pb2 during 80 to 120 min because the fire curve is also nearly flat during this time interval. The wider cavity in the double stud wall also has a significant contribution to this behaviour as the heat from Pb1-Pb2 surface gets transferred to Pb2, which emits it into the large cavity. The standard fire and Pb1 surface temperatures rise rapidly to 80 min but very slowly after 80 min. Therefore, the fire input to the wall is nearly constant helping the system to attain equilibrium during this time frame. Another important observation was that the

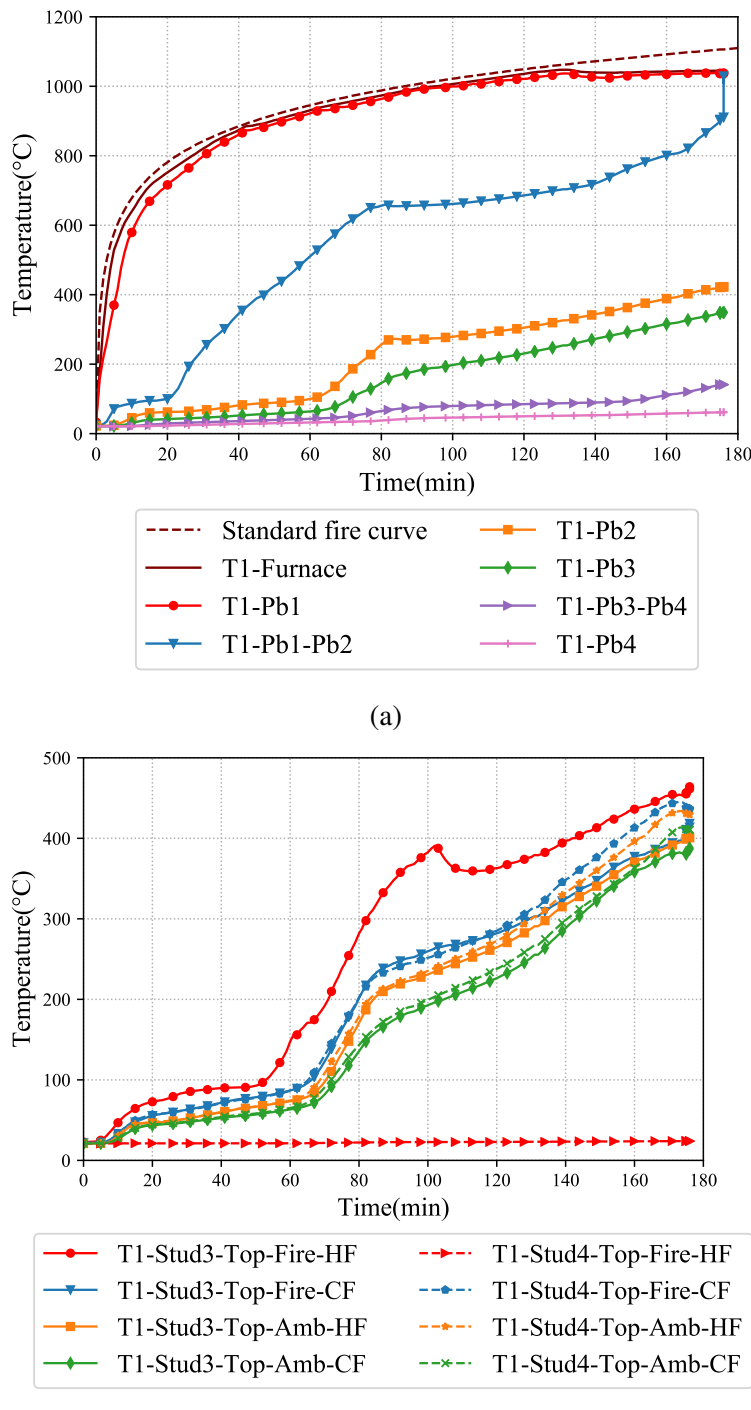


Figure 4.14: Plasterboard and stud time-temperature curves of Test-T1 (a) Average plasterboard temperatures (b) Stud3 and 4 temperatures

Note: Thermocouple T1-Stud4-Top-Fire-HF malfunctioned.

time-temperature curve of Pb1-Pb2 increased suddenly from 20 to 80 min following plasterboard dehydration as shown in Figure 4.14 (a), which is also in correlation with the standard fire curve.

The ambient side cavity (Pb3) time-temperature curve exhibited a similar behaviour to the fire side cavity (Pb2) curve. The first peak at 85 min was recorded as 166°C which is 90°C lower than the fire side cavity (Pb2) temperature of 256°C. The time-temperature curve of the ambient side interface (Pb3-Pb4) recorded a maximum temperature of 150°C at 176 min with the first peak of 67°C at 80 min. The curve then shows only a gradual rise which is in accordance with its source (Pb3). This indicates that cavity depth greatly influences the passage of heat from the fire exposed side to the ambient side because of natural convection within cavity. The ambient side plasterboard (Pb4) recorded a peak temperature of 68°C at 176 min, which is less than the limiting temperature of 180°C + room temperature at any point on the unexposed face or an average temperature of 140°C + room temperature on the unexposed face as specified in AS 1530.4 (SA, 2014). This infers the absence of insulation failure in this fire test.

The time-temperature curves for Stud3 as recorded at the top (2250 mm) are shown in Figure 4.14 (b). They are used for discussion because of the severe local compressive failure observed at the top of Stud3 (Figure 4.13 (c)). The temperature curves showed no steep increase until 50 min of fire exposure. The hot flange temperatures on the fire and ambient sides were well below 100°C (T1-Stud3-Top-Fire-HF and T1-Stud3-Top-Amb-HF). From 50 to 80 min of fire exposure there was a sudden increase in the time-temperature curve on the fire side hot flange (T1-Stud3-Top-Fire-HF) reaching the first peak of 390°C at 102 min as shown in Figure 4.14 (b), followed by a small reduction in the temperature for about 10 min, reaching 358°C at 114 min. This reduction in temperature of 32°C is a result of the flat region in the temperature of plasterboards Pb1-Pb2 and Pb2, which act as a source for the fire side hot flange. From 120 min there was a gradual increase in the time-temperature curves of the fire side hot flanges until the end and recorded a temperature of 592°C at the end. The fire side cold flange (T1-Stud3-Top-Fire-CF) recorded 263°C at 102 min, which is 127°C less than the hot flange temperature. But the ambient side hot and cold flange temperatures at 102 min were 234°C (T1-Stud3- Top-Amb-HF) and 196°C (T1-Stud3-Top-Amb-CF), respec-

tively. The difference in temperatures between the fire side hot and cold flanges was 127°C but the difference in temperature between the ambient side hot and cold flange was only 38°C . The difference in temperatures between the fire side cold flange and ambient side hot flange was only 29°C .

The axial displacement and lateral deflection variations with respect to time are also discussed in this section. The axial displacement was measured under the end plate that connected both rows of studs. The lateral deflection was measured at quarter heights (750 mm, 1500 mm, 2250 mm). In the fire tests the maximum deflection occurred at mid-height (1500 mm), which is considered in this discussion. In the fire tests, LVDTs measured the lateral deflections only on the ambient side studs. Therefore, it becomes difficult to predict the neutral axis shift as a result of thermal bowing in LSF walls. The axial displacement and lateral deflection versus time curves are shown in Figures 4.15 (a) and (b).

The axial displacement curve was almost flat for all the studs in fire till 60 min as shown in Figure 4.15 (a). This implies that no significant axial shortening occurred until 60 min of fire exposure. After this there was a steady increase in the axial displacement representing stud expansion due to fire exposure. This was observed till the end of fire test (176 min) after which the axial displacement curve changed sign and exhibited a sudden increase. The sudden increase in the curve is due to the axial contraction of the studs indicating structural failure of the test wall. The lateral deflection curve with respect to time recorded at mid-height (1500 mm) is shown in Figure 4.15 (b). The curve was nearly flat until 75 min. There was a small inward bowing of studs measuring 2 mm until 75 min after which the lateral deflection curve dropped to -11.16 mm at 82 min and reached a maximum of -14.44 mm in Stud3 (T1-Stud3-Mid) at the end of the test. This indicates that there was an outward thermal bowing on the ambient side studs. It is to be noted that the lateral deflection is for the ambient side studs only.

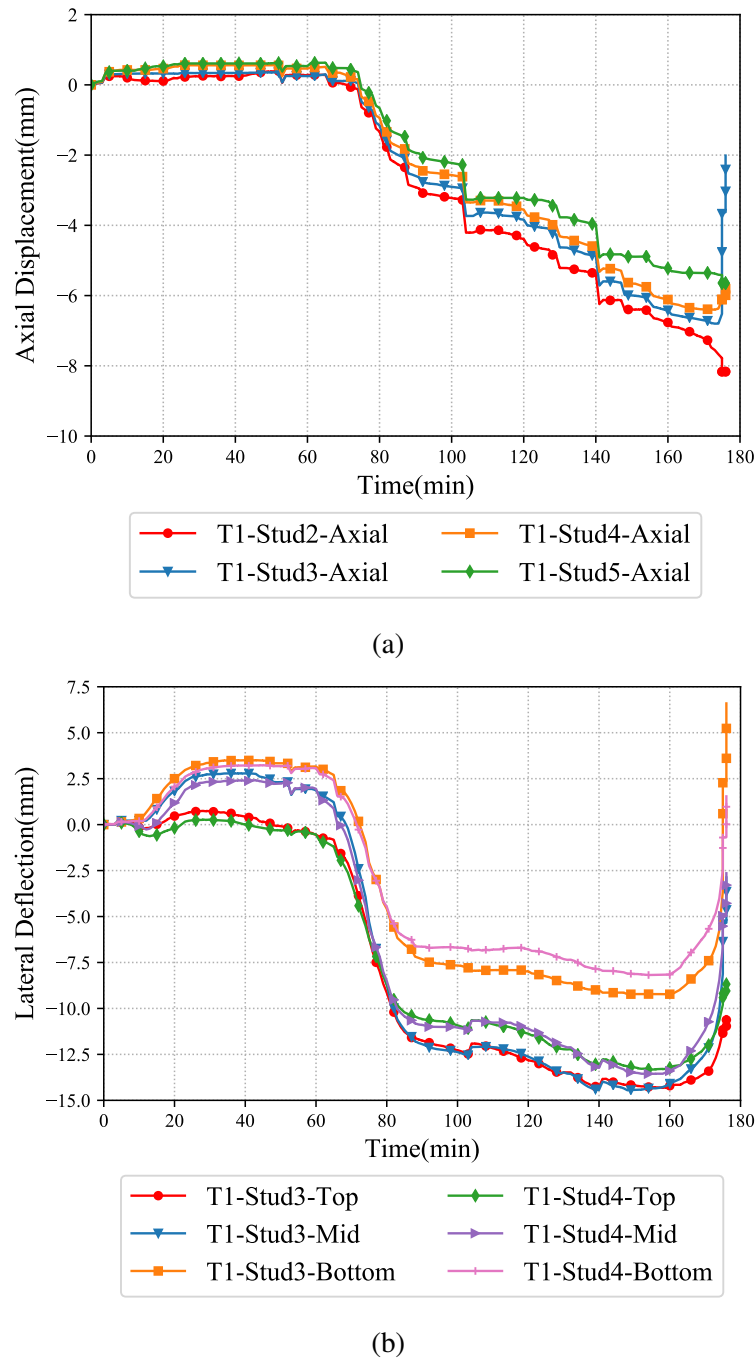


Figure 4.15: Axial displacement and lateral deflection versus time curves from Test-T1
 (a) Axial displacement versus time (b) Lateral deflection versus time curves

4.6 Fire Test-T2

4.6.1 Test-T2 Failure Time and Mode, and Observations

This test was conducted with 0.75 mm thick studs to determine the fire performance of double stud walls with thinner stud sections. Ambient capacity test conducted on the wall initially gave a stud capacity of 47.08 kN. Each stud was subjected to an axial compression load of 18.83 kN to simulate the same load ratio of 0.4 as in Test-T1. The test wall panel failed after 132 min due to structural inadequacy compared to 176 min obtained for 0.95 mm thick stud wall panel. Unlike Test-T1, there was a significant plasterboard fall-off on the fire exposed side (Pb1) as shown in Figure 4.16 (a). However, no cracks were observed on the ambient side of plasterboard. Discolouration of plasterboard was observed on the ambient side top right corners at the end of the fire test (Figure 4.16 (b)). Studs 4 and 5 on Row-1 (fire side) were subjected to severe local compressive failures as shown in Figure 4.16 (c).

4.6.2 Test-T2 Results and Discussion

The standard fire curve was achieved with good agreement. The time-temperature curve of Pb1-Pb2 interface was similar to Test-T1 till 25 min of fire exposure. Water droplets were visible near the bottom after 30 min. Similar to Test-T1 the time-temperature curve of Pb1-Pb2 interface showed a steep rise and reached a maximum of 709°C at 84 min. This was followed by a flat region until 110 min. Unlike Test-T1 this flat region did not last for a longer period of time. This is because of the fire side plasterboard fall-off as shown in Figure 4.16 (a). Such plasterboard fall-off on the fire side makes a significant contribution to the difference in the time-temperature curve between the two tests T1 and T2. The corresponding temperature on the fire side plasterboard (Pb1) was 971°C at 82 min, which acts as a source for Pb1-Pb2 interface.

The time-temperature curve on the fire side cavity (Pb2) also exhibited a similar behaviour as for Test-T1. The temperature was well below 100°C for the initial 60 min. There was a sudden increase in the curve from 60 to 80 min and attained the first peak of 342°C at 82 min. Then the curve was nearly flat and showed only a gradual increase till the end. The maximum temperature recorded at the end of fire test (132 min) was 443°C. The difference in temperature at 82 min between Pb1-Pb2 and Pb2 was 348°C.

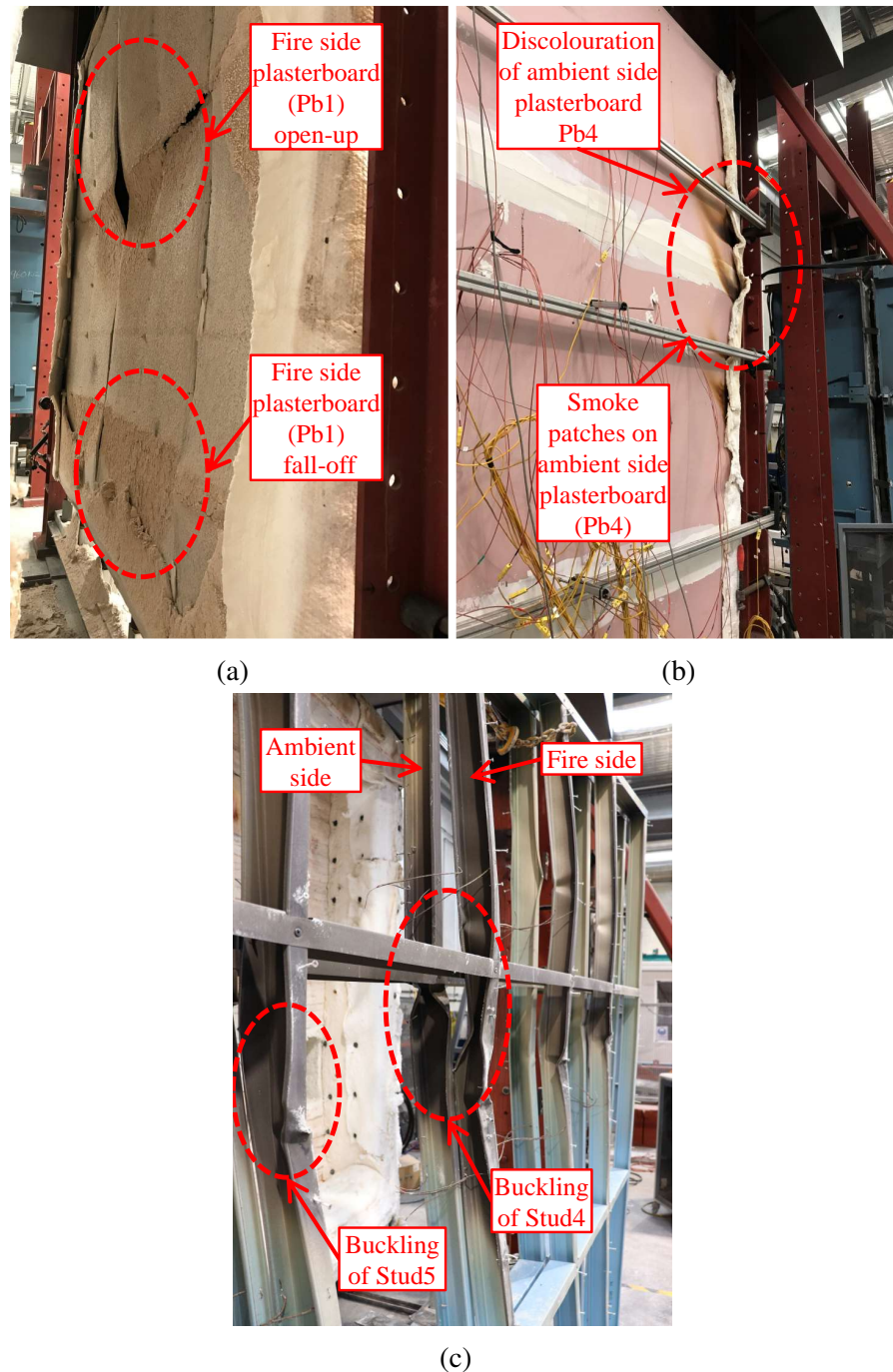


Figure 4.16: Failure of Test-T2 wall (a) Fire exposed side (b) Smoke patches and discolouration of ambient side plasterboard (c) Local compressive failure of Studs 4 and 5

The ambient side cavity Pb3 was nearly flat until 75 min as shown in Figure 4.17 (a). The temperature difference between Pb2 and Pb3 at 82 min was 170°C. After 82 min there was a gradual increase in the time-temperature curve reaching a maximum of 395°C at the end. Time-temperature curves of the ambient side plasterboard interface Pb3-Pb4 and ambient side Pb4 recorded a maximum of 128°C and 58°C at the end (132 min). The ambient side plasterboard temperatures did not exceed the average and the maximum insulation temperature limits given in AS 1530.4 (SA, 2014), indicating no insulation failure in this fire test.

The time-temperature curves of Stud4 recorded at the top of Stud4 (2250 mm) are shown in Figure 4.17 (b) as the local compressive failure was severe at the top of Stud4 as shown in Figure 4.16 (c). Temperatures recorded at the top of the stud were found to be higher at the top of Stud4 in comparison with other studs. The time-temperature curve on the fire side hot flange (T2-Stud4-Top-Fire-HF) was nearly flat till 55 min and the temperatures recorded were well below 100°C. From 55 min the curve exhibited a steep rise reaching the first peak of 470°C at 97 min. There was a reduction in temperature at 106 min measuring 441°C as shown in Figure 4.17 (b). The difference in temperature during this 9 min time period was 29°C. This behaviour was similar to that of the fire side hot flange time-temperature curve observed in Test-T1. The curve started to rise rapidly from 110 min and recorded a temperature of 592°C at the end.

The time-temperature curve of the fire side cold flange (T2-Stud4-Top-Fire-CF) followed a trend similar to the fire side hot flange till 60 min. There was a steep increase in the time-temperature curve from 60 to 80 min after which the rise was gradual until 110 min. The ambient side hot and cold flanges exhibited a behaviour similar to the fire side cold flange. The corresponding temperatures of the fire side hot flange (T2-Stud4-Top-Fire-HF), fire side cold flange (T2-Stud4-Top-Fire-CF), the ambient side hot flange (T2-Stud4-Top-Amb-HF) and the ambient side cold flange (T2-Stud4-Top-Amb-CF) were 451°C, 344°C, 307°C and 253°C, respectively. The difference between the fire side hot and cold flanges was 107°C while the difference between the ambient side hot and cold flange was 54°C. But the difference between the fire side cold flange and ambient side hot flange was only 37 °C . The peak temperatures of the fire side hot flange (T2-Stud4-Top-Fire-HF), fire side cold flange (T2-Stud4-Top-Fire-CF), the ambient side hot flange (T2-Stud4-Top-Amb-HF) and the ambient side cold flange

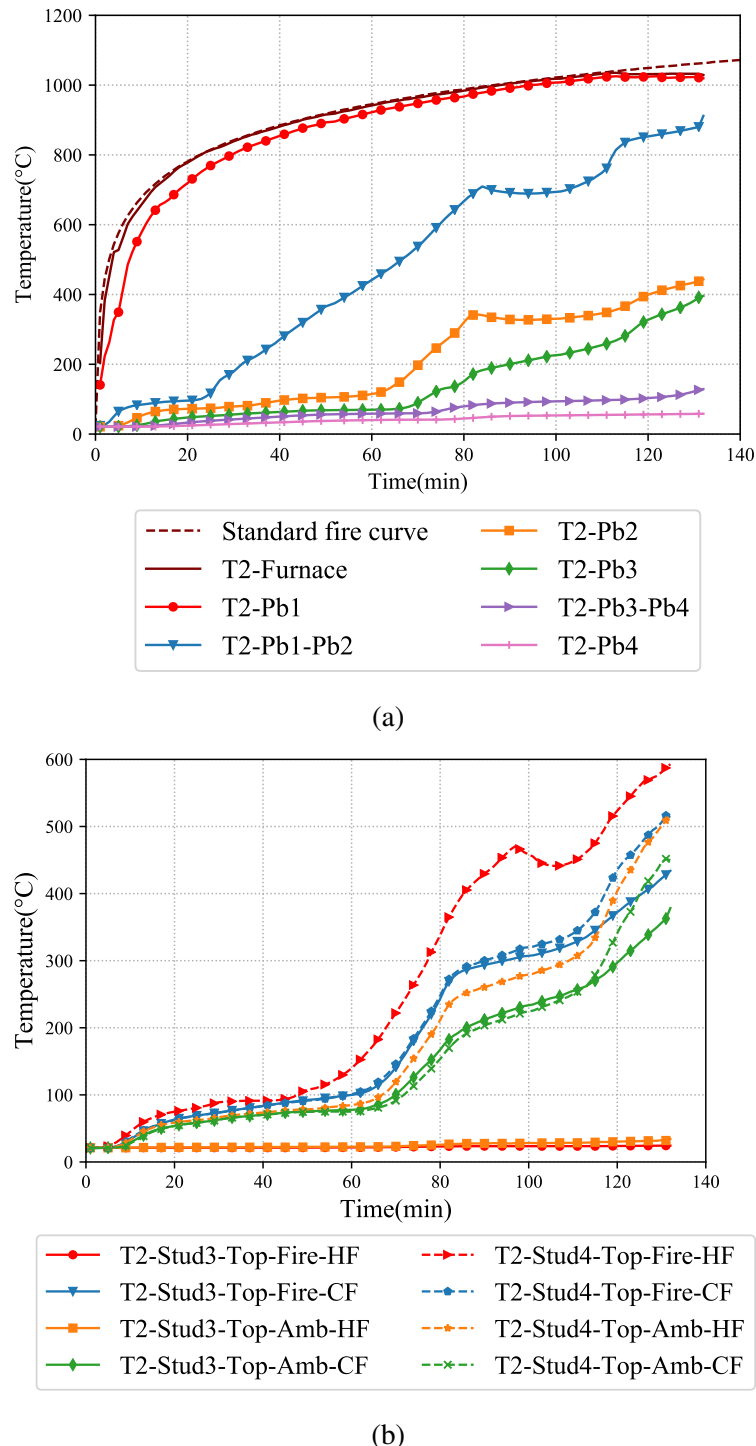


Figure 4.17: Plasterboard and stud time-temperature curves of Test-T2 (a) Average plasterboard temperatures (b) Studs 3 and 4 temperatures

Note: Thermocouple T2-Stud3-Top-Fire-HF and T2-Stud3-Top-Amb-HF malfunctioned.

(T2-Stud4-Top-Amb-CF) were 592°C, 516°C, 508°C and 451°C at the end of the fire test.

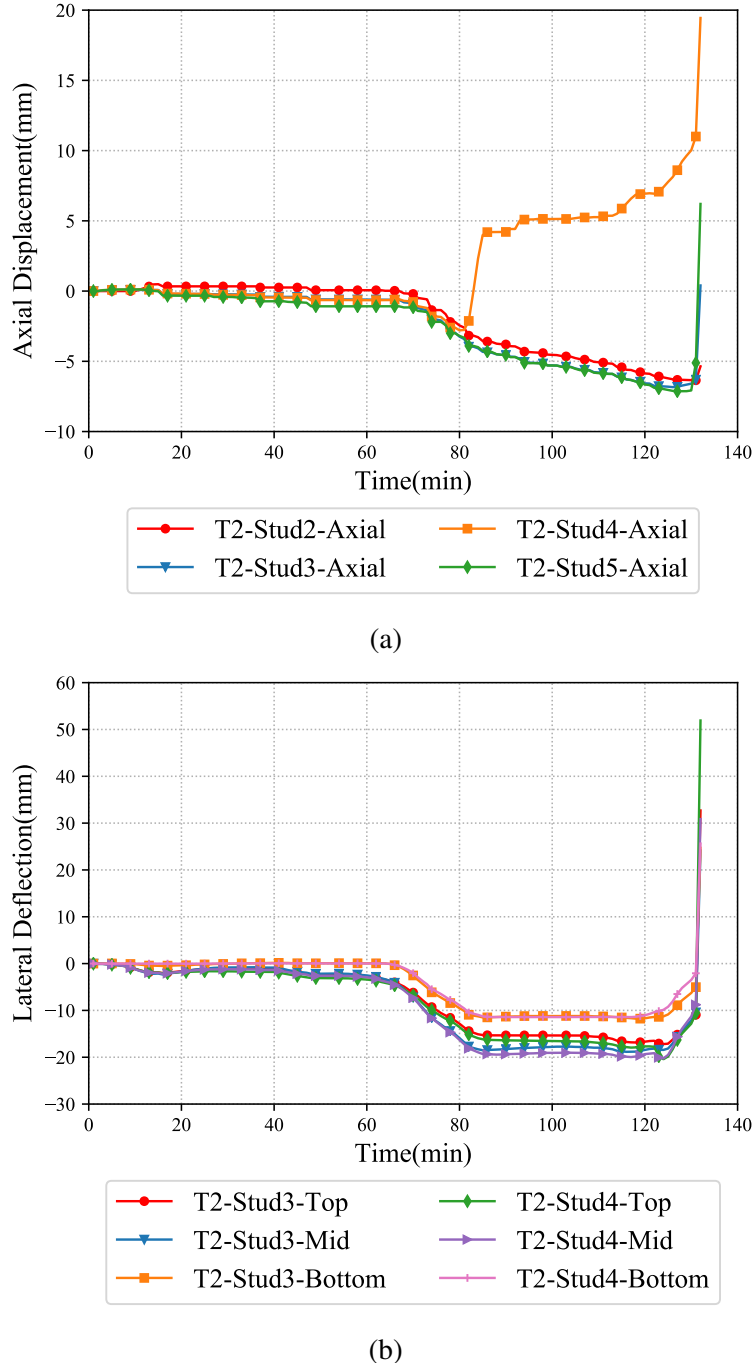


Figure 4.18: Axial displacement and lateral deflection versus time curves from Test-T2
(a) Axial displacement versus time (b) Lateral deflection versus time curves

The axial displacement and lateral deflection variations with respect to time in Test-T2 are presented in Figure 4.18. The axial displacement was measured in a similar way similar to Test-T1. LVDT T2-Stud4-Axial malfunctioned and should be ignored. In Test-T2 there were small axial displacement measuring 1.083 mm in T2-Stud5-Axial

at 60 min. The maximum axial displacement was 7.13 mm in T2-Stud5-Axial at 132 min. The axial displacement in Test-T1 is less than in Tests-T2 and T3 due to the use of thinner studs in the latter. The lateral deflection exhibited outward thermal bowing from the start of the fire test. A maximum lateral deflection of -20.25 mm was recorded in Stud4 (T2-Stud4-Mid).

4.7 Fire Test-T3

4.7.1 Test-T3 Failure Time and Mode, and Observations

Test-T3 was conducted to investigate the fire performance of double stud LSF walls made of 0.75 mm thick LCS studs under a higher LR of 0.6 (28.24 kN per stud). The wall panel failed after 81 min due to structural inadequacy in Stud3 on the fire side as shown in Figure 4.19 (c). As expected this failure time is less than that of Test-T2 with a LR of 0.4 (132 min). Plasterboard fall-off was noticed in a small region on the fire side (Pb1) after the fire test as shown in Figure 4.19 (a) while the ambient side plasterboard had no cracks or smoke patches. Water droplets were visible on the bottom of the wall due to dehydration process after 32 min.

4.7.2 Test-T3 Results and Discussion

The time-temperature curve on the fire side (Pb1) matched reasonably well with the standard fire curve. The Pb1-Pb2 interface curve was flat until 25 min with temperatures less than 100°C. From 25 to 80 min, it rose rapidly, reaching a maximum of 651°C at 81 min as shown in Figure 4.20 (a). This test does not exhibit the unique behaviour of the time-temperature curve remaining flat from 80 min as observed in Tests-T1 and T2. This is because the fire test lasted only 81 min under the higher LR. The Pb1-Pb2 temperature dropped slightly to 633°C at 81 min. This 18°C difference in temperature happened within a short period of 2 min. This is where the phase change happens in the cavity similar to Test-T2. But due to the sudden plasterboard fall-off and the higher load ratio the test wall panel could not survive any further.

The time-temperature curve on the fire side cavity (Pb2) was below 100°C till 52 min with a sudden increase during 65 to 80 min to reach a peak temperature of 295°C at

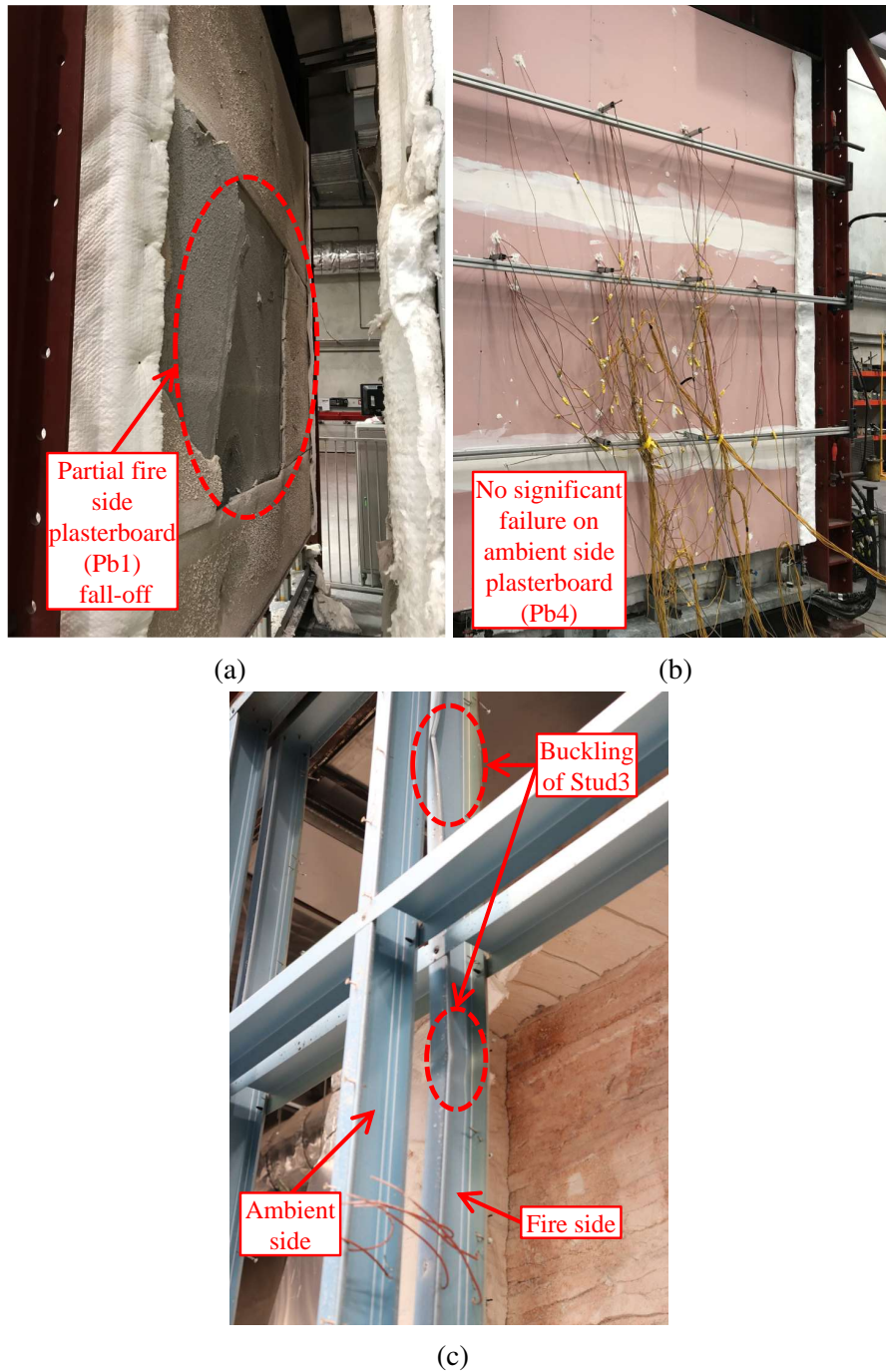


Figure 4.19: Failure of Test-T3 wall (a) Fire exposed side (b) Ambient side plasterboard (c) Local compressive failure of Stud3

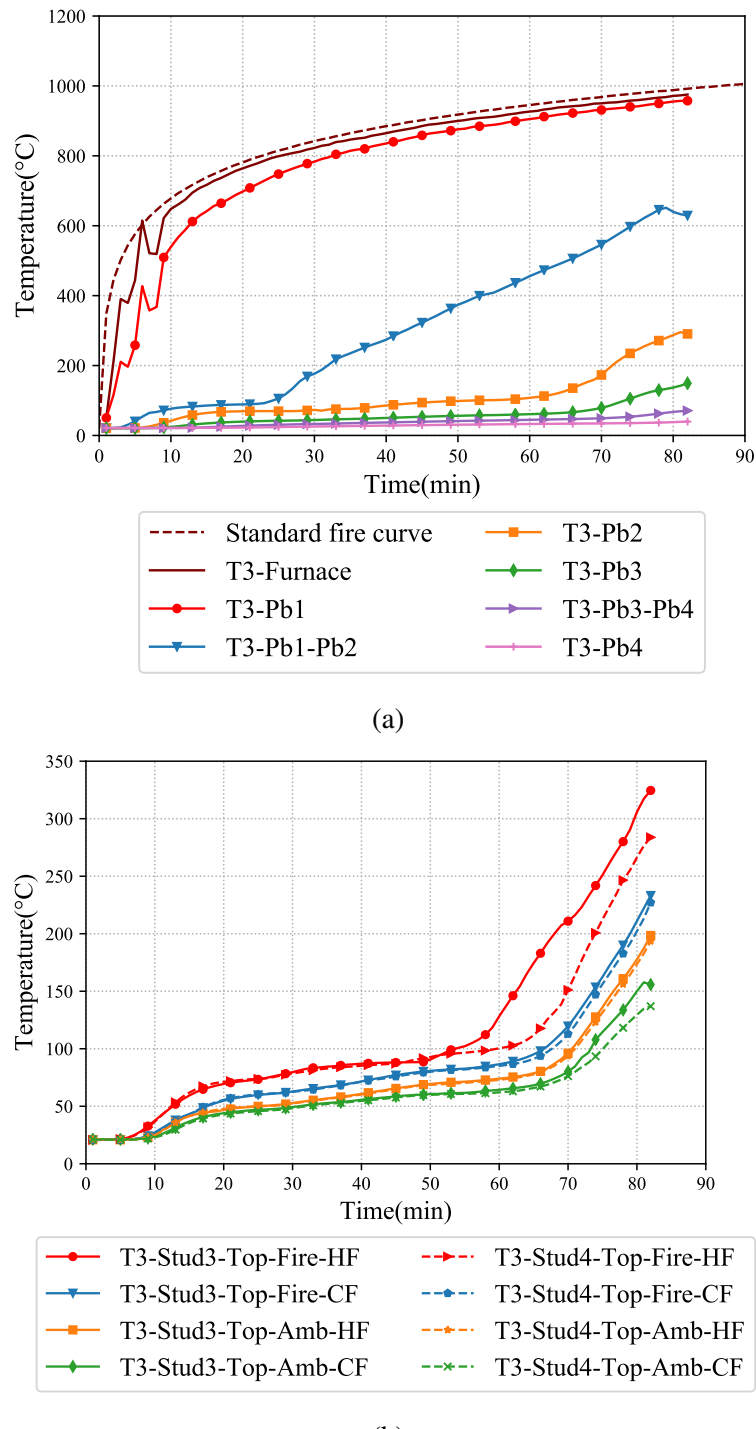


Figure 4.20: Plasterboard and stud time-temperature curves of Test-T3 (a) Average plasterboard temperatures (b) Studs 3 and 4 temperatures

81 min (end of fire test). Plasterboard on the ambient side cavity recorded temperatures less than 100°C until 75 min after which there was a gradual rise reaching a maximum of 149°C at the end. The temperatures on the ambient side plasterboard interface (Pb3-Pb4) and ambient side (Pb4) recorded 71°C and 39°C, respectively, indicating no insulation failure as per AS 1530.4 (SA (2014)).

The time-temperature curves of the studs also did not exhibit the drop in the fire side hot flange temperatures as seen in Tests-T1 and T2. Local compressive failure was observed at the top of Stud3 as shown in Figure 4.19 (c) and hence the time-temperature curves recorded at the top of Stud3 (Figure 4.20 (b)) are used here in discussion. The fire side hot flange temperature (T3-Stud3-Top-Fire-HF) was below 100°C until 55 min with a steep rise to reach a maximum temperature of 332°C at the end of the test. The fire side cold flange (T3-Stud3-Top-Fire-CF) recorded a temperature less than 100°C until 65 min after which there was a steep rise, reaching the maximum temperature of 226°C at the end, which is 106°C less than the corresponding hot flange. The ambient side hot and cold flanges followed a similar trend to that of fire side cold flange. The maximum temperatures recorded at T3-Stud3-Top-Amb-HF and T3-Stud3-Top-Amb-CF were 187°C and 157°C, respectively, with 30°C difference. The difference in temperature between the fire side cold flange and ambient side hot flange temperature was 39°C at the end of the fire test.

The axial displacement and lateral deflection variations with respect to time are discussed in this section. The axial displacement was measured under the end plate that connected both rows of studs. The lateral deflection was measured at quarter heights (750 mm, 1500 mm, 2250 mm). In the fire tests the maximum deflection occurred at mid-height (1500 mm), which is considered in this discussion. The axial displacement and lateral deflection versus time curves of the three fire tests are shown in Figures 4.21 (a) and (b). LVDT T2-Stud4-Axial malfunctioned and should be ignored.

The axial displacement curve was almost flat for all the studs in fire Test-T1 till 60 min as shown in Figure 4.21 (a). But in Tests-T2 and T3 there were small displacements measuring 1.083 mm in T2-Stud5-Axial and 1.47 mm in T3-Stud3-Axial at 60 min. This implies that no significant axial shortening occurred until 60 min of fire exposure in all three fire tests. Test-T1 curve showed a gradual increase in the axial displacement reaching a maximum of 8.17 mm in T1-Stud2- Axial. But in Tests-T2

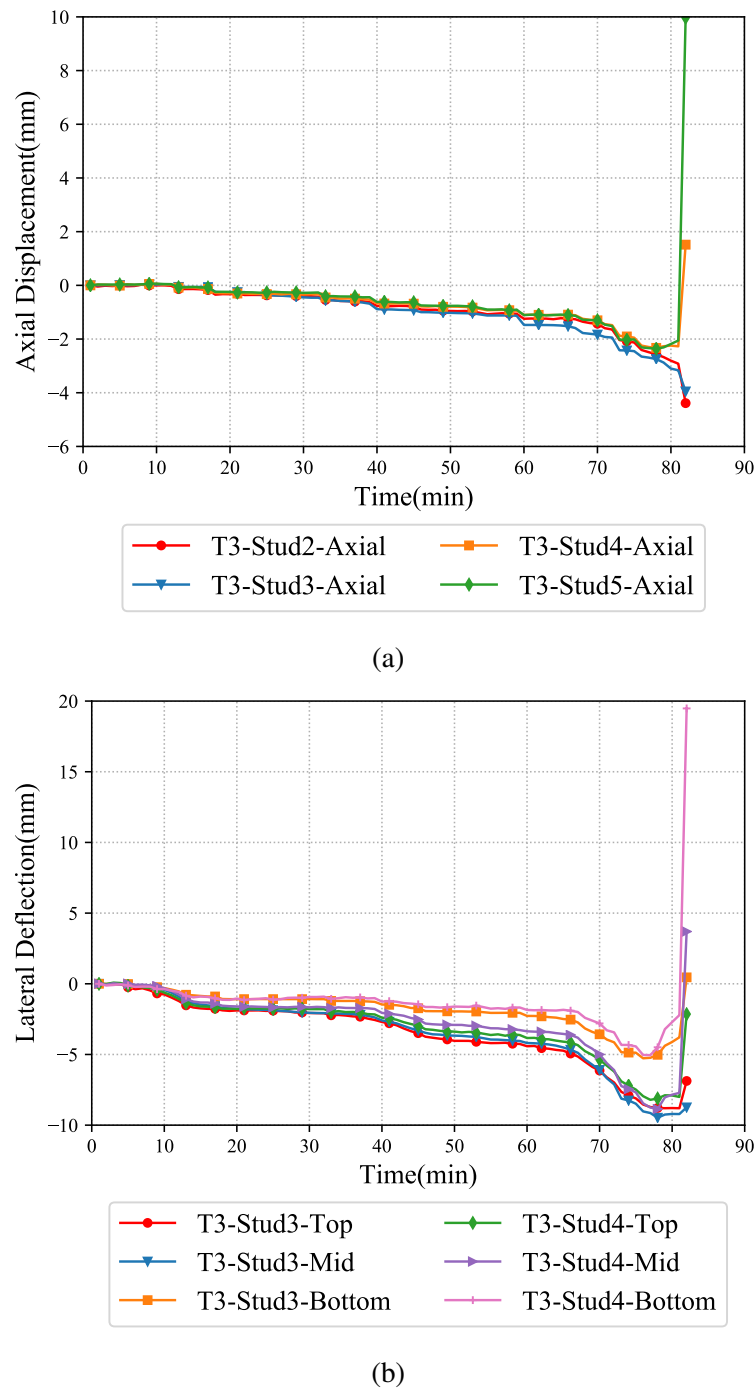


Figure 4.21: Axial displacement and lateral deflection versus time curves from Test-T3
 (a) Axial displacement versus time (b) Lateral deflection versus time curves

and T3 the curve was steep. For Test-T2 the maximum axial displacement was 7.13 mm in T2-Stud5-Axial at 132 min. Likewise for Test-T3 the maximum axial displacement was 10 mm in T3-Stud5-Axial at 81 min. The corresponding deflections at 81 min in Tests-T1 and T2 were 1.68 mm and 3.41 mm. The axial displacement in Test-T1 is less than in Tests-T2 and T3 due to the use of thinner studs in the latter.

The lateral deflection curve with respect to time recorded at mid-height (1500 mm) is shown in Figure 4.21 (b). For Test-T1 the curve was nearly flat until 75 min. There was a small inward bowing of studs measuring 2 mm until 75 min after which the lateral deflection curve dropped to -11.16 mm at 82 min and reached a maximum of -14.44 mm in Stud3 (T1-Stud3-Mid) at the end of the test. This indicates that there was an outward thermal bowing on the ambient side studs. It is to be noted that the lateral deflection is for the ambient side studs only. The lateral deflection in Tests-T2 and T3 exhibited outward thermal bowing from the start of the fire test. Test-T2 exhibited a maximum lateral deflection of -20.25 mm in Stud4 (T2-Stud4-Mid) while Test-T3 recorded a maximum outward deflection of -9.43 mm in Stud3 (T3-Stud3-Mid). The lateral deflections recorded in Tests-T2 and T3 were higher than Test-T1 deflection. This is also because of the use of thinner studs used in Tests-T2 and T3.

4.8 Fire Test-T4

4.8.1 Test-T4 Failure Time and Mode, and Observations

To determine the fire performance of double stud wall with a reduced cavity depth Test-T4 was conducted with 70 mm deep studs. Along with a 20 mm air gap between the two rows of stud, the effective cavity depth in this test wall was 160 mm. Plan view/cross-section of Test-T4 wall is shown in Figure 4.22. Initial ambient capacity test resulted in a maximum axial compression capacity of 86.21 kN and an LR of 0.4 (34.48 kN) was used to conduct the full-scale fire test.

After 17 min from the start of the fire test a cracking sound was heard. This was followed by joint compound fall-off at 30 min. A small patch of smoke was visible from the top left corner of the test wall at 34 min indicating calcination of the fire side plasterboard. At 86 min, smoke was visible from the top right corner of the test wall. This indicates the calcination of the second layer of plasterboard on the fire side.

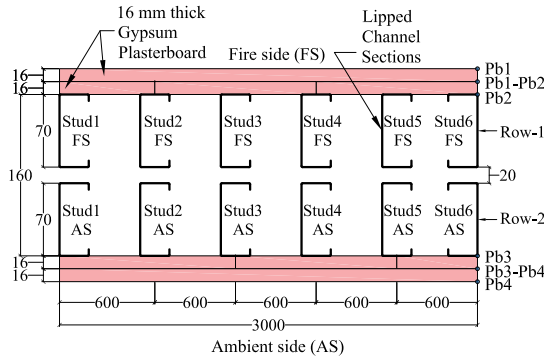


Figure 4.22: Plan view of double stud LSF wall panel used in Test-T4

Note : All dimensions are in mm.

A crack on the fire side plasterboard was noticed through furnace camera at 120 min, which resulted in a small portion of the fire side plasterboard to fall-off at 132 min. The fall-off was witnessed near the plasterboard joints, which are prone to be the weakest part of the test wall in a full-scale fire test. The test wall survived 171 min after which the test wall could not withstand the applied axial compression load experiencing a sudden drop indicating failure due to structural inadequacy. Figure 4.23 shows the details of test wall failure including the buckling failures of Studs 2,3 and 4 on the fire side (Row-1).

4.8.2 Test-T4 Results and Discussion

The time-temperature curves of plasterboard from the fire test is shown in Figure 4.24 (a). The furnace time-temperature curves exhibit reasonable agreement with the input standard time-temperature curve. The fire side interface Pb1-Pb2 curve was less than 100°C till 30 min of fire test after which it exhibited a steep rise to achieve the first peak of 663°C at 84 min. The curve then flattens to form a plateau till 120 min and rises gradually till the end of fire test. This behaviour in time-temperature curve is similar to those witnessed in Tests-T1 and T2. The plateau region is also observed in the fire side cavity time-temperature curve Pb2 where the curve reaches a maximum of 358°C at the end of fire test at 171 min. The ambient side plasterboard time-temperature curve Pb3 was well below 100°C till 75 min of fire test after which it exhibited a gradual rise reaching a maximum of 282°C at 171 min. The ambient side time-temperature curves were well below 200°C till the end of fire test indicating no insulation failure.

The stud time-temperature curves from the fire test are shown in Figure 4.24 (b).

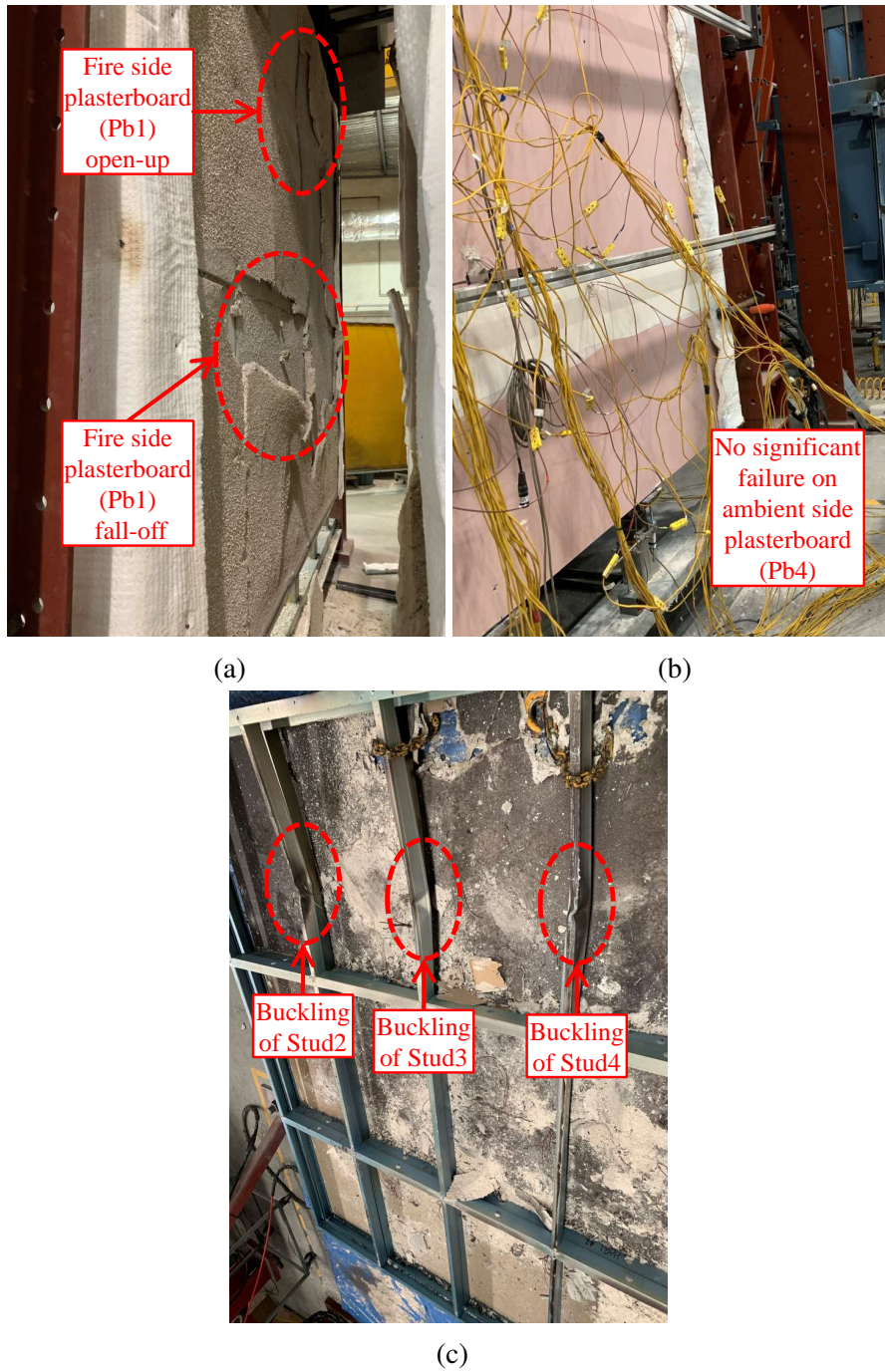


Figure 4.23: Failure of Test-T4 wall (a) Fire exposed side (b) Ambient side plasterboard (c) Local compressive failure of Studs 2, 3 and 4

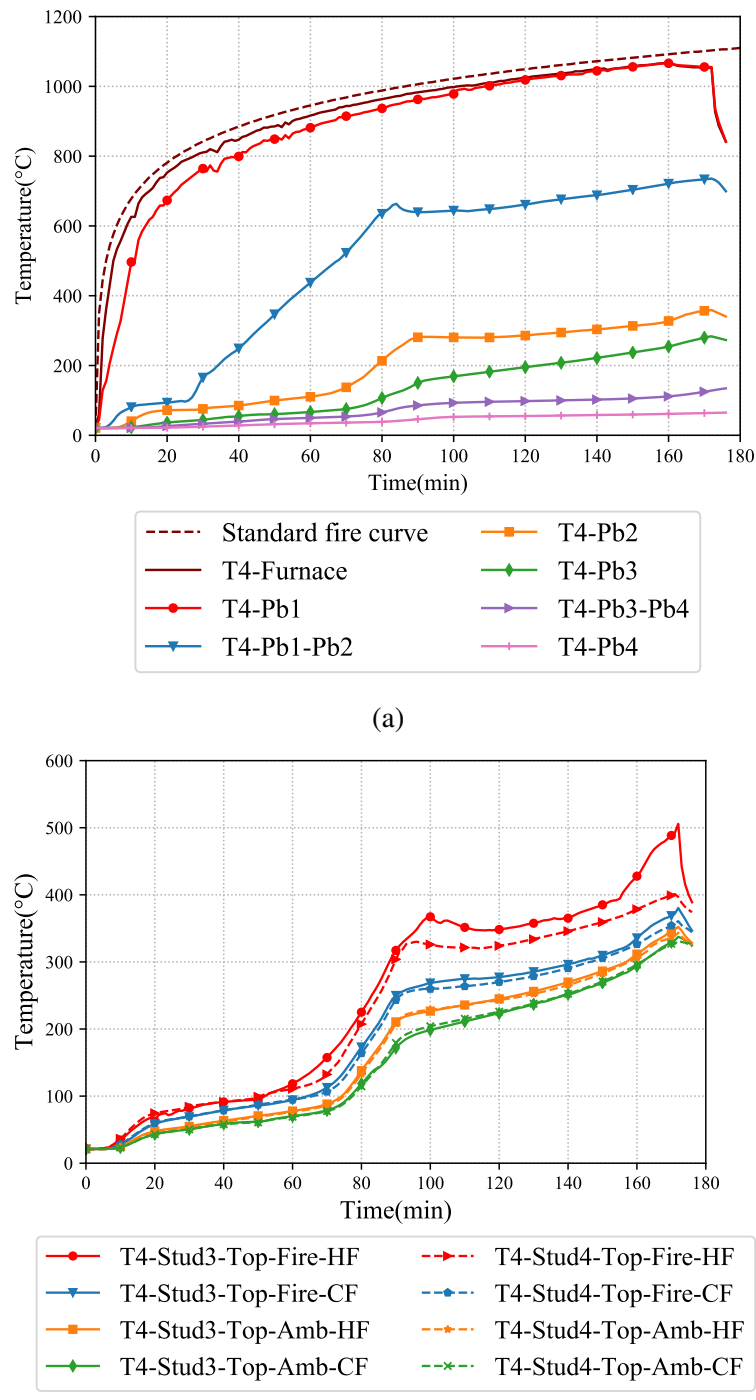


Figure 4.24: Plasterboard and stud time-temperature curves of Test-T4 (a) Average plasterboard temperatures (b) Stud3 and 4 temperatures

All the stud hot and cold flanges time-temperature curves were less than 100°C till 50 min. A steep increase in the T3-Stud4-Top-Fire-HF was observed after 60 min reaching a first peak of 325°C at 100 min of fire test. After this, there was a drop in the time-temperature curve reaching a lower temperature of 320°C at 114 min. This reduction in temperature of 5°C was attributed to the plateau region observed in the Pb2 plaster-board time-temperature curve. This further evolves to a maximum of 491°C at the end of fire test. The corresponding cold flange time-temperature curve T4-Stud3-Top-Fire-CF followed a similar trend in correlation with the hot flange T4-Stud3-Top-Fire-HF. The maximum temperature recorded by T4-Stud3-Top-Fire-CF was 371°C at the end of fire test. The difference between the fire side hot and cold flanges was 120°C. However, the ambient side hot and cold flanges exhibited a similar behaviour throughout the fire test. The temperatures of T4-Stud3-Top-Amb-HF and CF were 348°C and 332°C with a temperature difference of 16°C only. This infers that the temperature difference between the fire side hot and cold flanges is larger in comparison with the ambient side hot and cold flanges in non-insulated cavity walls. This behaviour was also observed in Tests-T1 and T2.

The axial displacement versus time plots are shown in Figure 4.25 (a). Axial displacements of studs were less than -2 mm till 80 min of the fire test after which the curves exhibited a gradual increase reaching a maximum of -5.95 mm at 169 min. This indicates thermal expansion in the studs during the fire test. After this the curve exhibited a sudden reversal reaching -1.59 mm indicating shortening and failure of the studs. Lateral deflection versus time plots are shown in Figure 4.25 (b). In accordance with the axial displacement plots the lateral deflections in the test wall was less than -10 mm in all the studs till 80 min of fire test. The curve exhibited gradual increase in the lateral deflection reaching a maximum of -24.43 mm at 171 min in T4-Stud3-Mid. After this the curve reversed indicating a sudden reversal reaching a peak of 0.35 mm, indicating structural failure of studs. The curve T4-Stud4-Top also recorded a deflection of 30.15 mm at the end of the fire test, which confirms the structural failure of the test wall. The behaviour of axial displacement curves from this fire test was similar to the other non-cavity insulated double stud LSF wall fire Tests-T1 to T3 wherein the maximum axial displacement during the fire test was less than 10 mm. The lateral deflection curves also exhibited a similar behaviour in all non-cavity insulated double

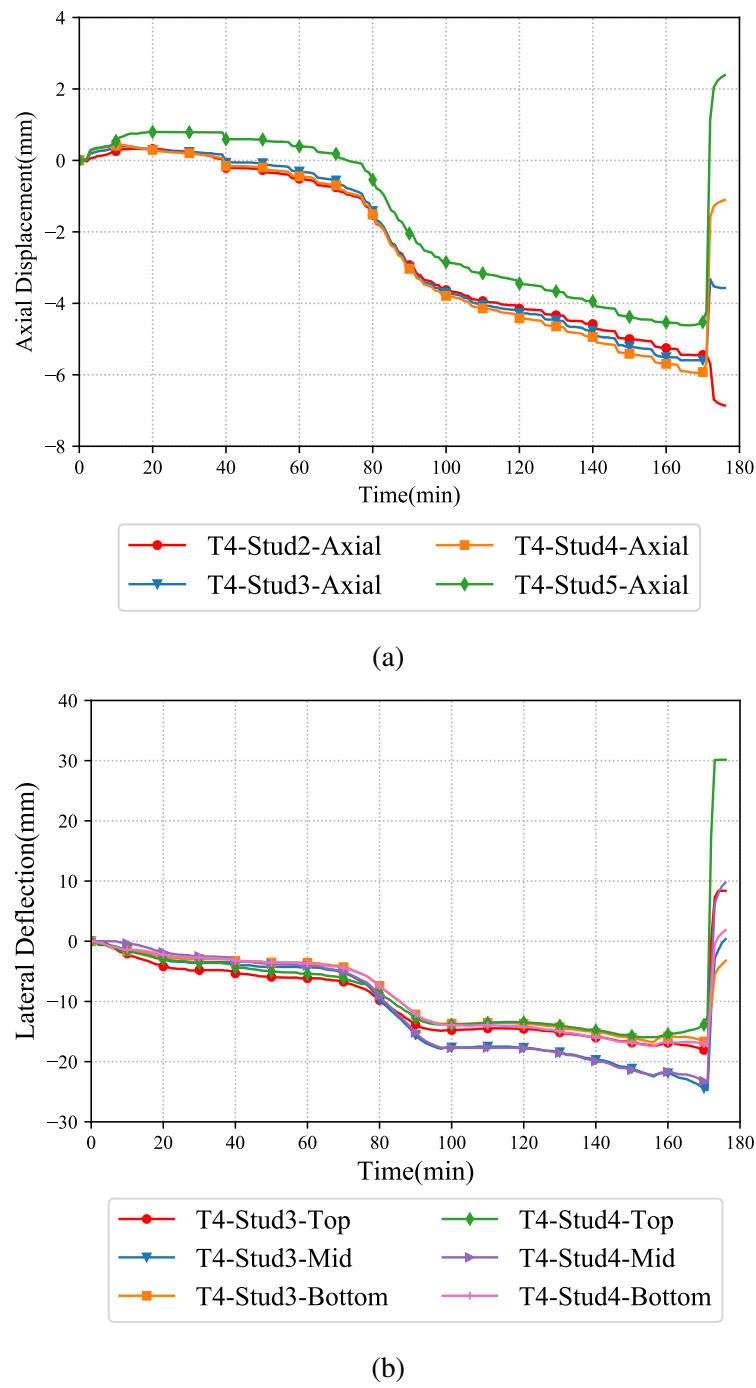


Figure 4.25: Axial displacement and lateral deflection versus time curves from Test-T4
 (a) Axial displacement versus time (b) Lateral deflection versus time curves

stud wall fire tests.

4.9 Fire Test-T5

4.9.1 Test-T5 Failure Time and Mode, and Observations

Test-T5 was conducted on double stud wall with cavity insulation located within both rows of the studs. Figures 4.26 and 4.27 show the details of test wall and construction. 90 mm Lipped Channel Sections (LCS) made of 0.95 mm BMT G550 steel were used as studs. Glass fibre insulation bats of 75 mm were used as cavity insulation with a density of 11 kg/m^3 . A 20 mm air gap was present between the two rows of studs.

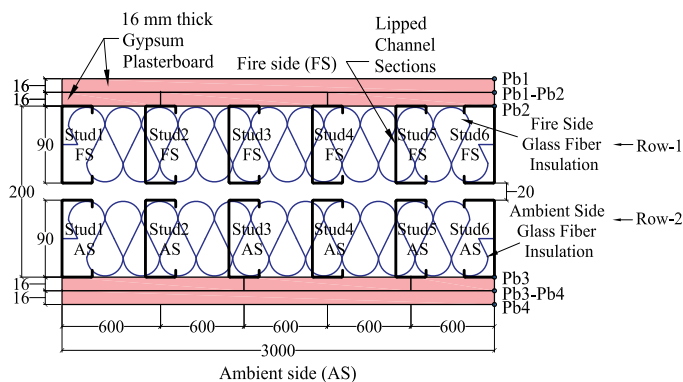


Figure 4.26: Plan view of double stud LSF wall panels with cavity insulation on both stud rows used in Tests-T5 and T6

After 13 min from the start of fire test, plasterboard joint compound fall-off from the fire side plasterboard surface was observed. No significant changes to the ambient side plasterboard was observed till 40 min. Mild smoke was visible at 43 min of fire test signifying the calcination of the fire exposed plasterboard. Evaporation of the chemically bound water molecules from the plasterboard resulting in vapour was not observed due to the presence of cavity insulation. Dark and heavy smoke patches were observed on the top right corner of the test wall indicating the entrapment of heat on the fire side of the test wall at 56 min. The test wall survived 76 min of fire exposure and the test was terminated due to structural inadequacy failure of the studs. Post-fire test examination of the test wall revealed significant local buckling of the fire side studs as shown in Figure 4.28 (c). Also, the cavity insulation on the ambient side of the wall was unaffected. This shows that the heat was trapped only on the fire side of

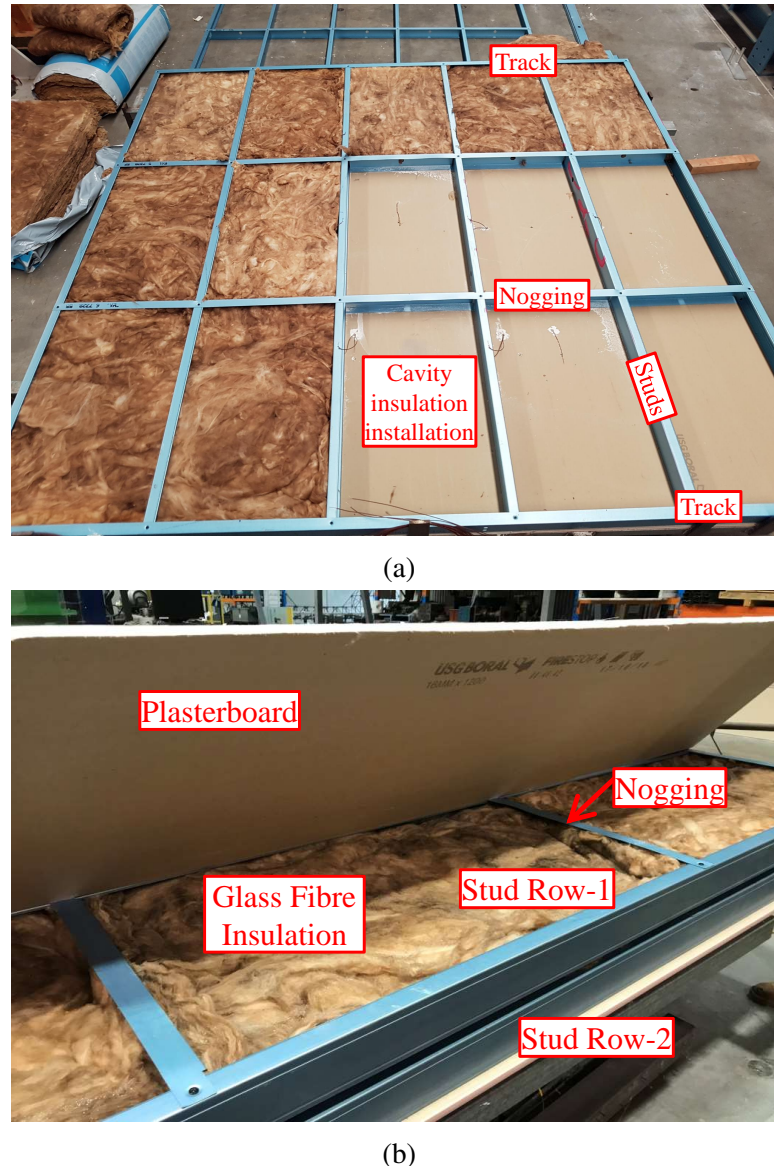


Figure 4.27: Test-T5 and T6 wall construction sequence (a) Cavity insulation installation (b) Constructed test wall

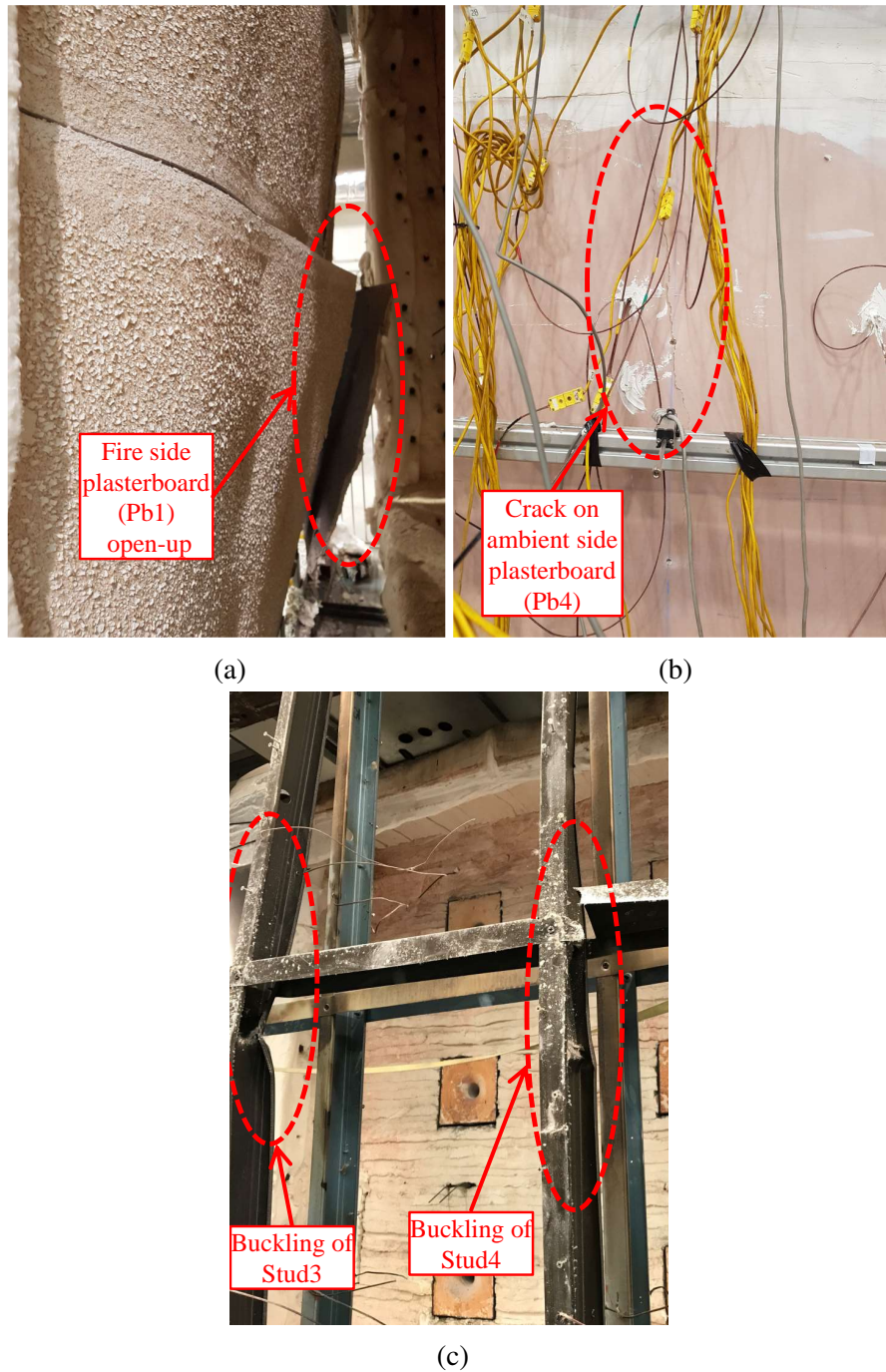


Figure 4.28: Failure of Test-T5 wall (a) Fire exposed side (b) Crack on ambient side plasterboard (c) Local compressive failure of Studs3 and 4

the test wall. However, the ambient side studs were also unaffected and no buckling was observed. This also confirms the entrapment of heat on the fire side of the test wall, which was the main contributor for the fire side stud buckling failures. It is evident from the post-fire test investigation that severe opening of the plasterboard is due to the entrapment of heat on the fire exposed side of the test wall only. The glass fibre cavity insulation prevents the hot gases from entering the 20 mm cavity thereby resulting in reduced temperature on the ambient side studs. The time-temperature, axial displacement versus time and lateral deflection versus time curves from the fire test are presented and discussed next.

4.9.2 Test-T5 Results and Discussion

The average plasterboard time-temperature curves are presented in Figure 4.29 (a). The fire side plasterboard interface time-temperature curve (Pb1-Pb2) exhibits a flat region till 25 min. Then the curve exhibits a steep rise till the end of fire test reaching a maximum of 621°C. This implies the calcination of the fire exposed plasterboard, thereby transferring the heat to the next surface, which is the fire side plasterboard interface (Pb1-Pb2). But this trend is not noticeable on the fire side cavity surface (Pb2). The time-temperature curve is nearly flat till 65 min of the fire test after which the curve takes a steep increase and reaches 425 °C. This implies that the heat from the fire side interface (Pb1-Pb2) is not effectively dissipated into the cavity because of the presence of cavity insulation. This is also evident from the ambient side plasterboard time-temperature curves. The ambient side cavity surface (Pb3), ambient side plasterboard interface (Pb3-Pb4) and the ambient side surface (Pb4) did not exhibit any significant variation in the time-temperature curve and recorded temperatures less than 200°C till the end of fire test. This is less than the limiting temperature for the insulation failure criterion proving the absence of insulation failure in the fire test. This behaviour of the time-temperature curve also supports the earlier statement regarding the heat being entrapped on the fire side only.

Likewise, the stud time-temperature curves presented in Figure 4.29 (b) also exhibit a similar pattern to that of the fire side plasterboard interface (Pb1-Pb2). The fire exposed stud hot flange time-temperature curve (T5-Stud4-Mid-Fire-HF) exhibited only a progressive increase till 55 min of the fire test. The recorded temperature

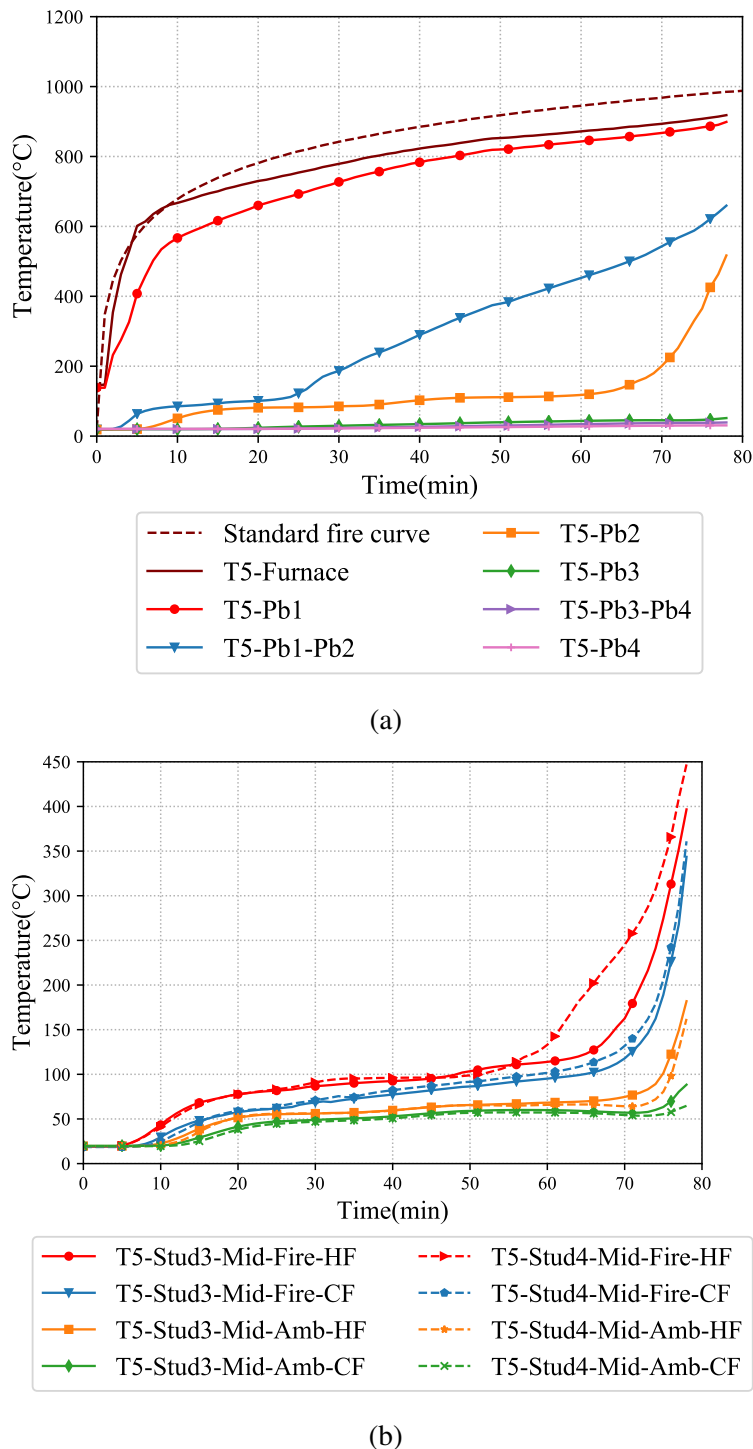


Figure 4.29: Plasterboard and stud time-temperature curves of Test-T5 (a) Average plasterboard temperatures (b) Stud3 and 4 temperatures

was well below 150°C. There was a sudden increase in the time-temperature curve from 60 min and the curve reached a maximum of 447°C at the end of fire test. The corresponding cold flange (T5-Stud4-Mid-Fire-CF) exhibited a similar trend reaching a maximum of 360°C. However, the temperatures on the ambient side hot and cold flanges are comparatively less than those of the fire side studs. The ambient hot and flange time-temperature curves (T5-Stud4-Mid-Fire-HF and CF) were well below 100°C till 70 min of the fire test. The temperatures on the ambient side studs were less than the limiting temperatures for studs proposed by past researchers under load bearing conditions (Feng et al., 2003a; Gunalan and Mahendran, 2013a).

The axial displacement and lateral deflection versus time curves from the fire test are shown in Figures 4.30 (a) and (b). No significant axial displacement was observed till 50 min. Small axial expansion was observed after which the curve propagates to a maximum axial displacement of -2 mm. The curve then indicated a reversal and a maximum displacement of 15.86 mm was observed indicating severe axial compression indicating the end of the fire test. This shows that the effect of temperature entrapment plays a significant role in the structural failure of double stud LSF walls with cavity insulation. This is also evident from the time versus lateral deflection curves. No significant lateral deflection was observed till 65 min. Then the test wall started to bow inwards causing a deflection of -10 mm. After this the test wall bowed outwards resulting in a lateral deflection of 32.72 mm at the end of fire test. This implies that the severity of thermal bowing is less in cavity insulated double stud LSF walls in comparison with non-cavity insulated double stud walls.

4.10 Fire Test-T6

4.10.1 Test-T6 Failure Time and Mode, and Observations

Test-T6 was a repeat test of Test-T5 and was conducted on a double stud LSF wall with cavity insulation within both rows of stud as shown in Figure 4.26. Since Test-T5 resulted in an FRL of 76 min, which is 100 min less than the corresponding non-cavity insulated wall fire test, it was repeated to determine the validity of results for cavity insulated double stud walls. The test wall panel was constructed similar to Test-T5 and the full-scale fire test was conducted under the same load ratio of 0.4. After 28 min,

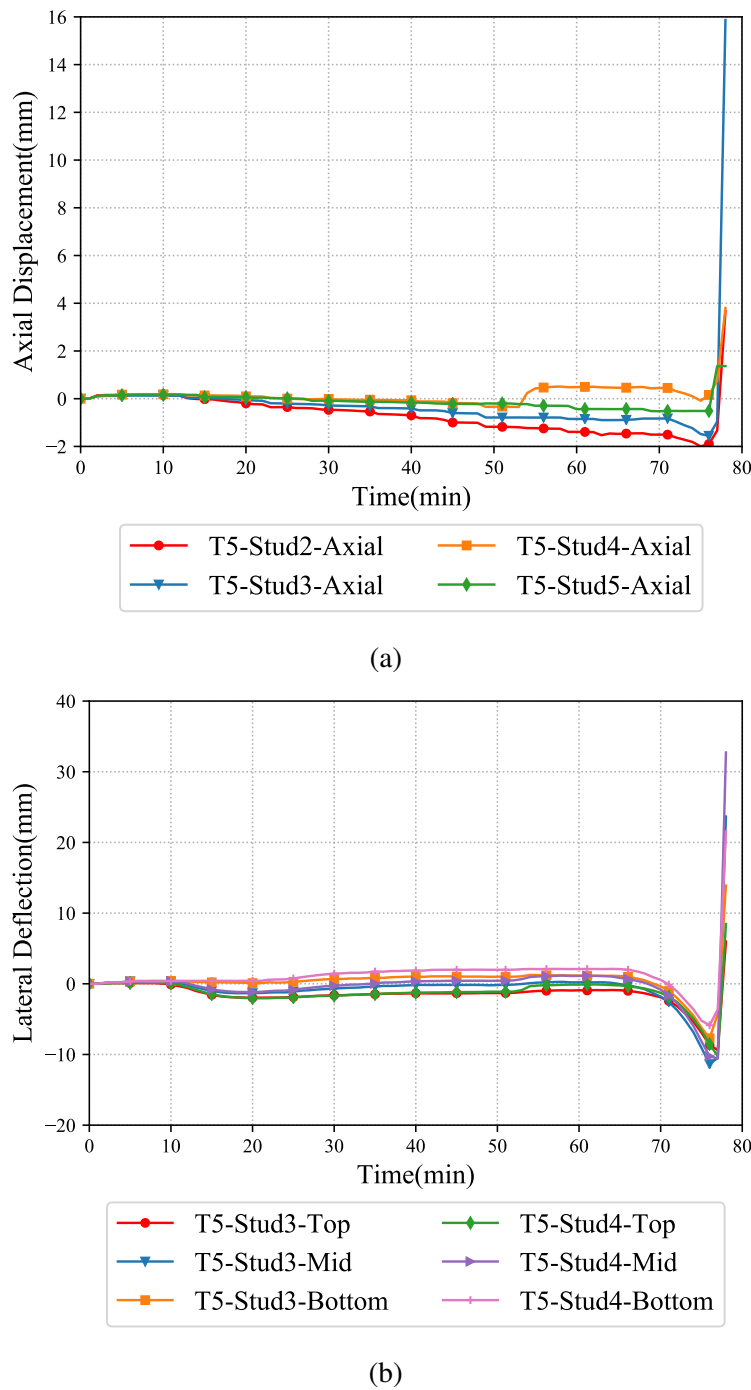


Figure 4.30: Axial displacement and lateral deflection versus time curves from Test-T5
 (a) Axial displacement versus time (b) Lateral deflection versus time curves

joint compound fall-off from the fire side plasterboard surface (Pb1) was observed. Mild smoke was visible from the top right corner of the test wall at 46 min of the fire test.

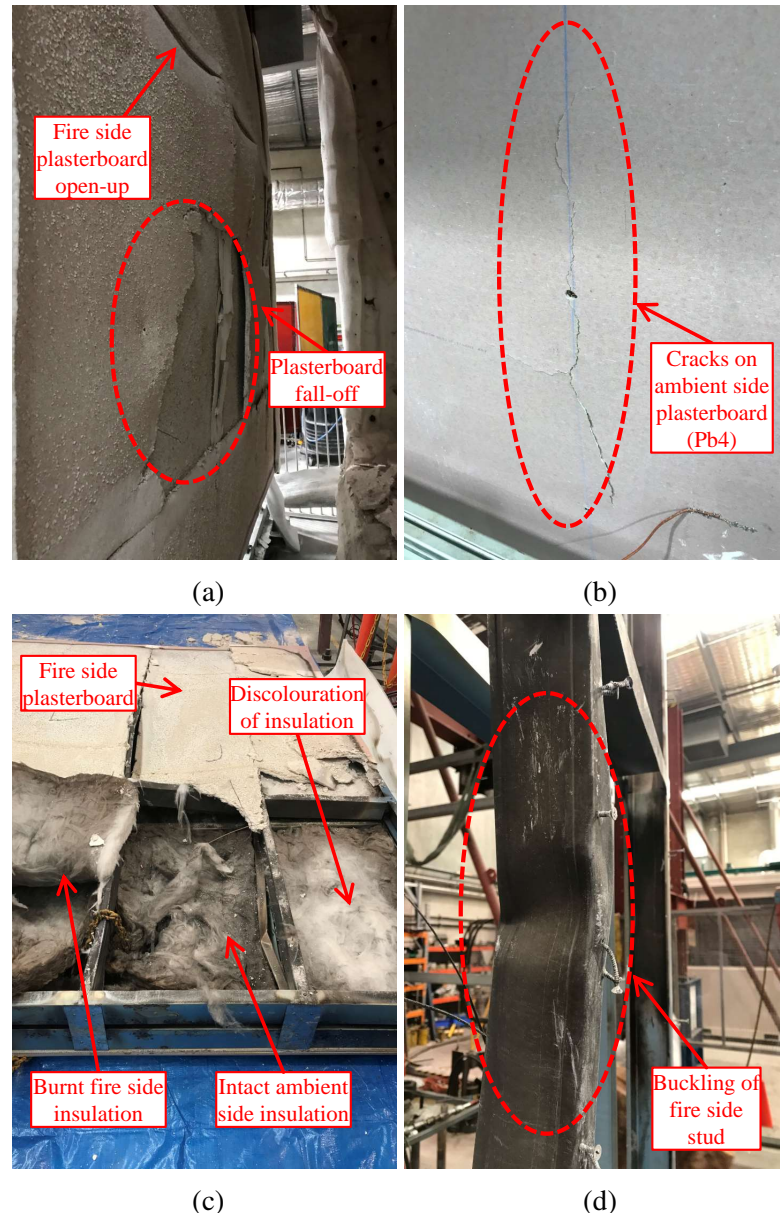


Figure 4.31: Failure of Test-T6 wall (a) Fire exposed side (b) Crack on ambient side plasterboard (c) Discolouration of insulation (d) Local compressive failure of stud

Intensity of the smoke increased at 50 min and stopped at 59 min indicating the calcination process on the fire side plasterboards. At 59 min the Pb1 joint compound was completely burnt and a small opening was noticeable on the fire side plasterboard. Again at 77 min high intensity smoke was observed on the top right corner of the test specimen and continued till 82 min, showing the calcination of second plasterboard layer on the fire side (Pb2). Later, at 91 min the test wall could not withstand the ap-

plied axial compression load and failed due to structural inadequacy criterion. Cracks on the ambient side plasterboard (Pb4) were observed at the time of failure due to excessive lateral deflection in studs as shown in Figure 4.31 (b). Post-fire test investigations showed the discolouration in the fire and ambient side glass fibre insulation (Figure 4.31 (c)). Also, after removing the plasterboards, local buckling of the fire side studs as shown in Figure 4.31 (d) was noticeable and found to be the dominant failure mode.

4.10.2 Test-T6 Results and Discussion

The plasterboard time-temperature curves from Test-T6 are shown in Figure 4.32 (a). The fire side plasterboard interface Pb1-Pb2 recorded temperatures less than 100°C till 25 min. A sudden increase in the Pb1-Pb2 time-temperature curve was noticeable after 25 min from the start of fire test reaching a maximum of 800°C at the end of fire test (91 min). However, similar to the previous Test-T5 the fire side cavity (T6-Pb2) temperatures were well below 200°C till 69 min of the fire test after which the T6-Pb2 time-temperature curve exhibited a sudden increase reaching a peak of 570°C at 82 min indicating the calcination of the second plasterboard layer on the fire exposed side of the test wall. After this, there was a small dip in the time-temperature curve dropping down to 518°C at 91 min indicating a reduction in temperature of 52°C in 9 min. Plasterboard open-up letting the hot gases inside the cavity could be attributed to the drop in time-temperature curve on the fire side cavity plasterboard surface (T6-Pb2). The ambient side plasterboard cavity (T6-Pb3), ambient side plasterboard interface (T6-Pb3-Pb4) and ambient side (Pb4) surface temperatures were well below 100°C till the end of fire test. This indicates the absence of insulation failure in the test wall.

Stud time-temperature curves also exhibited a similar pattern in comparison with the fire test results from Test-T5. All the stud hot and cold flange temperatures were well below 200°C till 69 min, which are in correlation with the T6-Pb2 plasterboard time-temperature curve. After this the hot flange (T6-Stud4-Top-Fire-HF) exhibited a sudden rise reaching a peak of 544°C at the end of fire test. However, the maximum temperature recorded at T6-Stud3-Top-Fire-HF was 547°C at 85 min after which there is a dip in the time-temperature curve. The T6-Stud3-Top-Fire-HF recorded 507°C at 91 min, which is a 40°C drop in 6 min. This behaviour is attributed to the time-

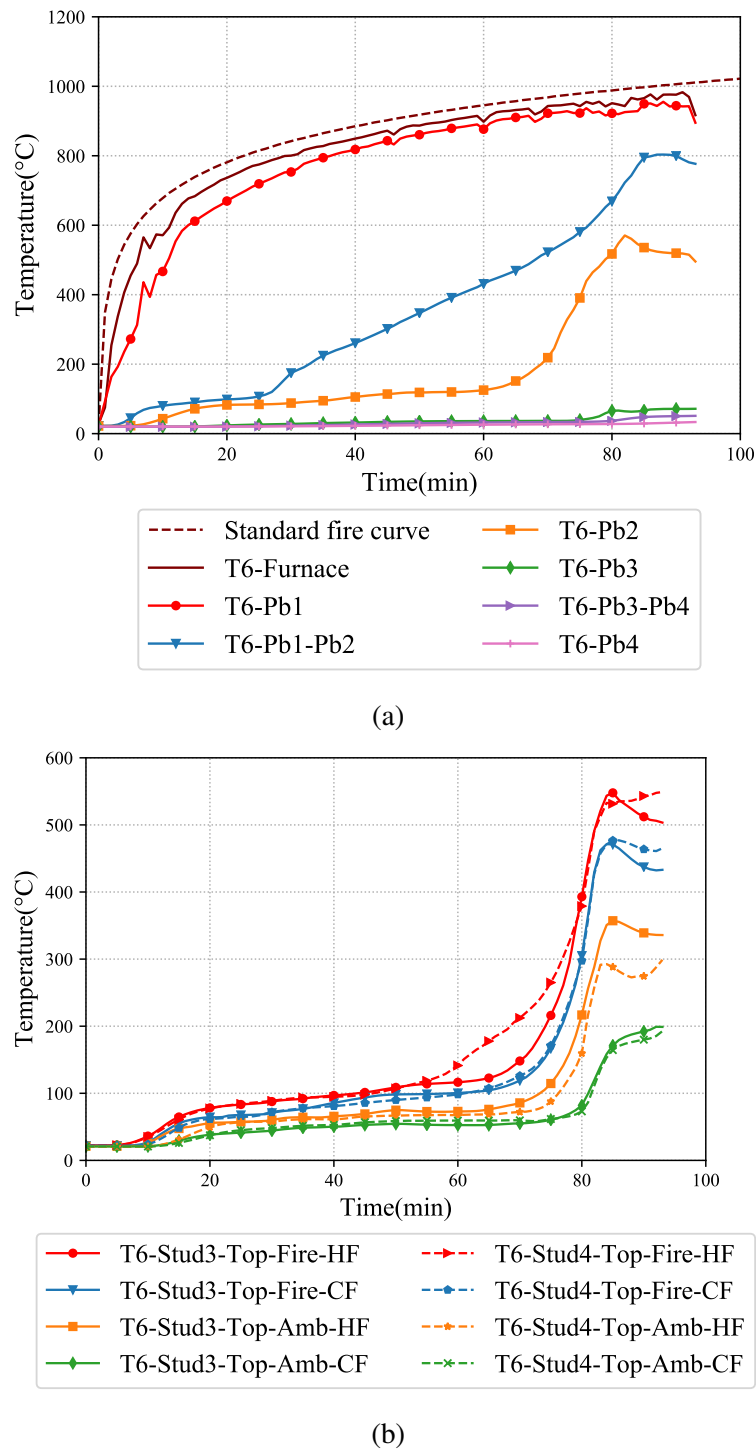


Figure 4.32: Plasterboard and stud time-temperature curves of Test-T6 (a) Average plasterboard temperatures (b) Stud3 and 4 temperatures

Note: Thermocouple T6-Stud4-Top-Fire-HF malfunctioned.

temperature curve dip on the fire side plasterboard as a result of plasterboard open-up as shown in Figure 4.31 (a).

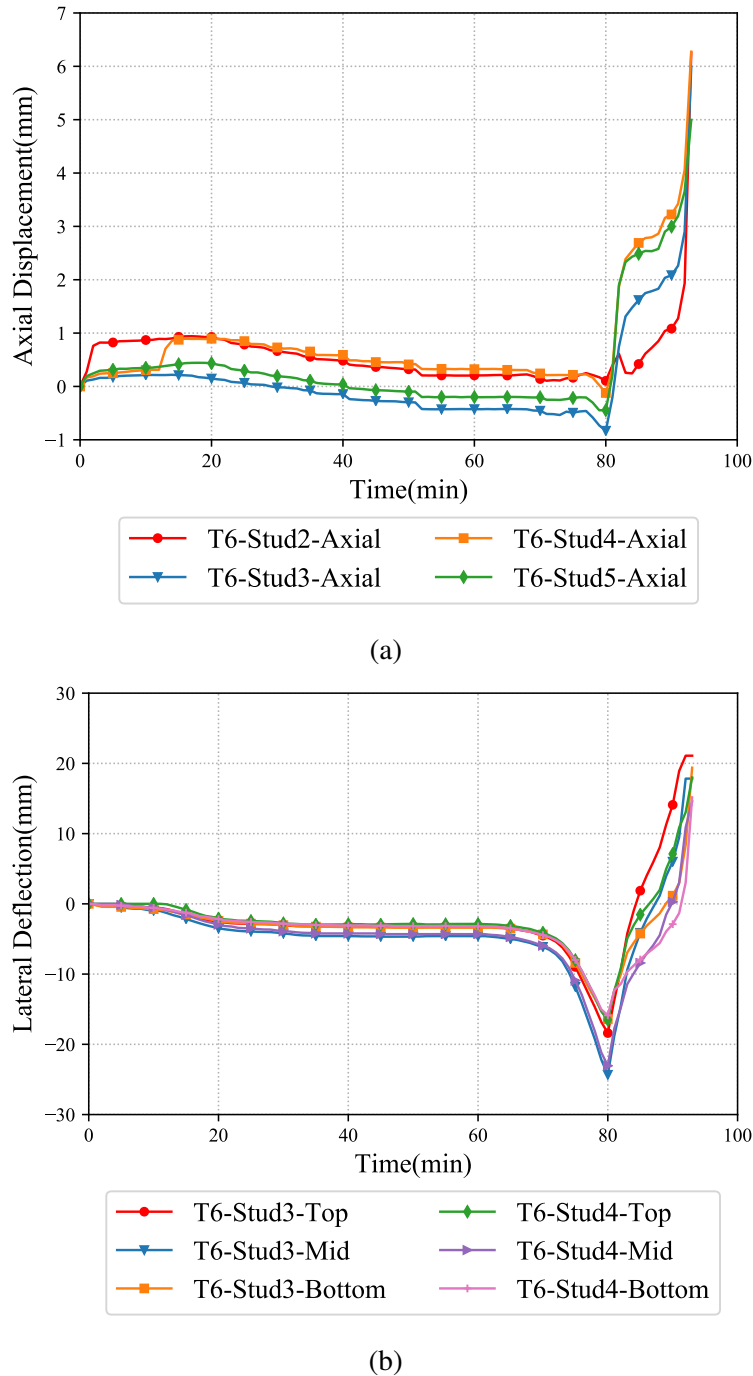


Figure 4.33: Axial displacement and lateral deflection versus time curves from Test-T6
 (a) Axial displacement versus time (b) Lateral deflection versus time

The axial displacement experienced by the test wall was less and also similar to Test-T5. The maximum axial displacement recorded was -0.12 mm at 80 min of fire test in T6-Stud4-Axial. A sudden axial contraction was noticeable at 81 min whereby the axial displacement reached 2.68 mm at 85 min. A sudden failure due to buckling

of fire side studs was the reason behind this failure after which the load was probably transferred to the ambient side studs. This is evident from the undulations in the axial displacement curve at 82 min as shown in Figure 4.33 (a). The test wall could not withstand the applied axial load any further and failed due to structural adequacy at 91 min. Lateral deflection versus time curves also exhibited a similar behaviour to Test-T5 as shown in Figure 4.33 (b). No significant lateral deflection was noticeable till 70 min of the fire test after which the curve reached a maximum of -24.33 mm at T6-Stud3-Mid (1500 mm from the top) at 80 min indicating inward thermal bowing towards the furnace. Outward thermal bowing was observed after 80 min wherein the curve reached a maximum displacement of 17.83 mm at the end of the fire test.

4.11 Fire Test-T7

4.11.1 Test-T7 Failure Time and Mode, and Observations

To determine the effect of cavity insulation position on the fire resistance of double stud LSF walls, Test-T7 was conducted with cavity insulation on the ambient row of studs only as shown in Figure 4.34. The test frame dimensions were maintained similar to that of Tests-T5 and T6 and similar test set-up and boundary conditions were used. However, the effective cavity depth including the 20 mm gap was 110 mm in this fire test. Figure 4.35 shows the construction of the test wall. The cavity insulation was placed away from the fire side to allow the passage of heat into the cavity so that the entrapment of heat on the fire side does not occur as in Test-T5.

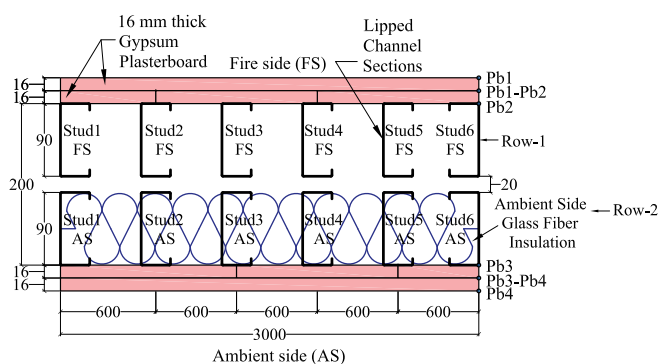


Figure 4.34: Plan view of double stud LSF wall panel with cavity insulation on ambient stud row used in Test-T7

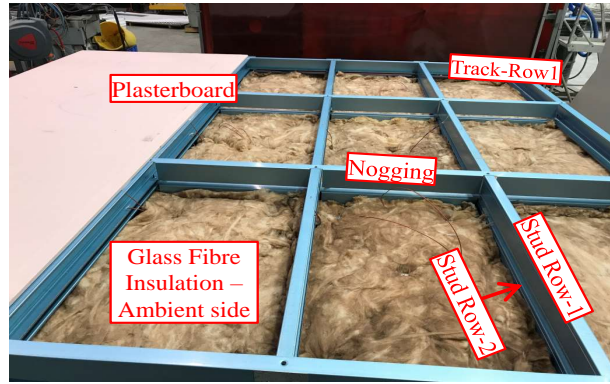


Figure 4.35: Test-T7 wall construction

After 11 min from the start of the fire test mild smoke was seen from the top left corner of the test wall. The smoke continued without any change in intensity until 28 min of the fire test. Water droplets dripping from the bottom of the test wall near Stud1 was also noticed due to the moisture movement in plasterboard. Water patches were also visible on the ambient side plasterboard surface (Pb4) at mid-height of the test wall. Severe plasterboard fall-off was observed on the fire exposed side as shown in Figure 4.36 (a). Post-fire test examination revealed the occurrence of buckling of the fire side studs only as shown in Figure 4.36 (c). Another important observation was that the cavity insulation was completely intact after the fire test.

4.11.2 Test-T7 Results and Discussion

The average plasterboard time-temperature curves from Test-T7 are presented in Figure 4.37 (a). Similar to Test-T5 the Pb1-Pb2 time-temperature curve was flat till 25 min of fire test after which the curve exhibited a steep rise reaching a maximum temperature of 718°C at the end of fire test. But the corresponding fire side plasterboard cavity time-temperature curve (T7-Pb2) was flat till 60 min of the fire test. A gradual increase in the time-temperature curve was noticed after that till the end of fire test reaching a maximum of 400°C at the end. This indicates that similar to Test-T5 the cavity insulation did not allow the heat to pass into the ambient side of the test wall. This is further evident from the time-temperature curves of the ambient side plasterboard. The time-temperature curve on the ambient side cavity (Pb3), ambient side plasterboard interface (Pb3-Pb4) and the ambient side plasterboard surface (Pb4) all resulted in temperatures less than 100 °C till the end of fire test.

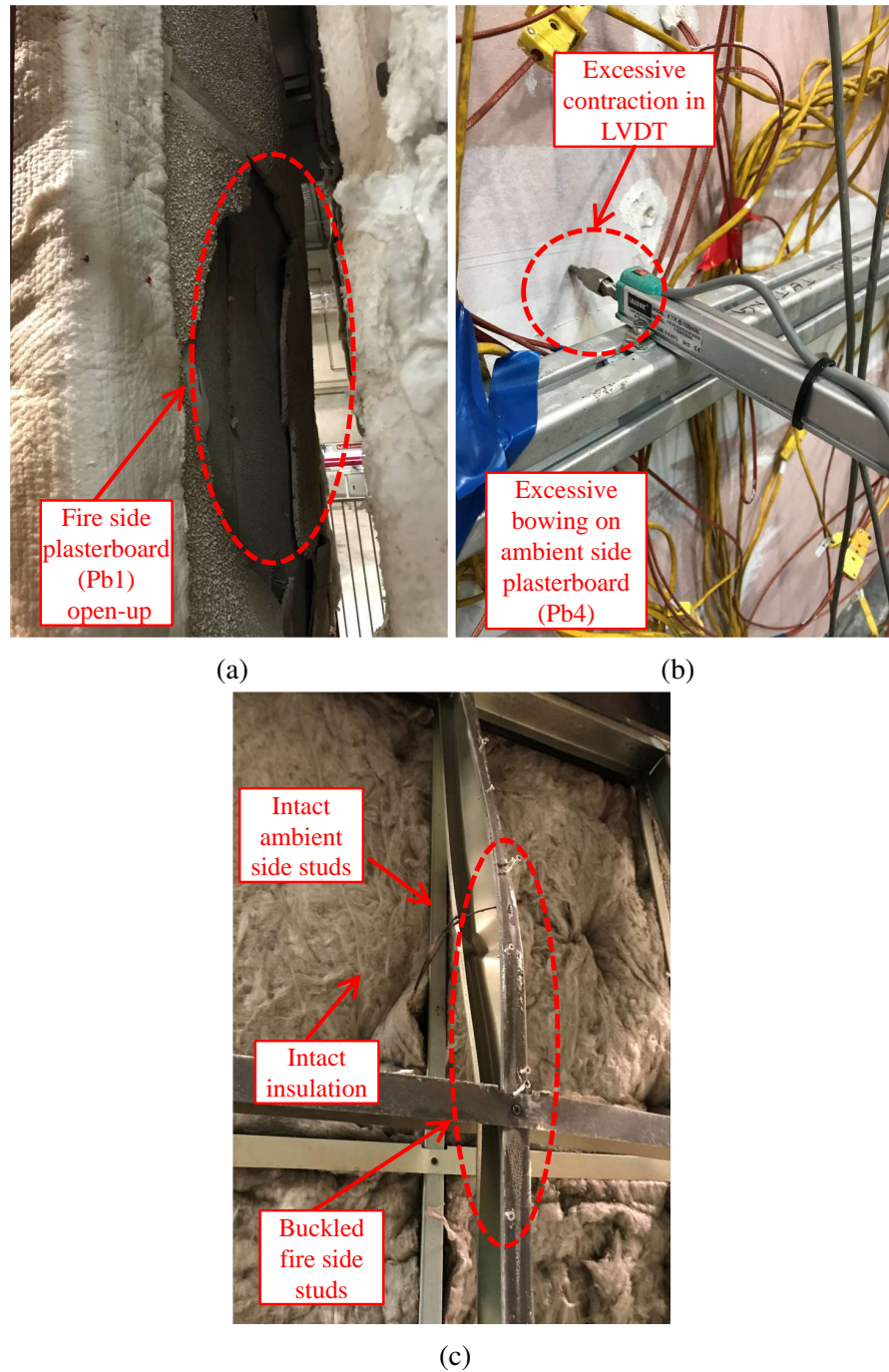


Figure 4.36: Failure of Test-T7 wall (a) Fire exposed side (b) Excessive bowing on ambient side plasterboard (c) Local compressive failure of stud

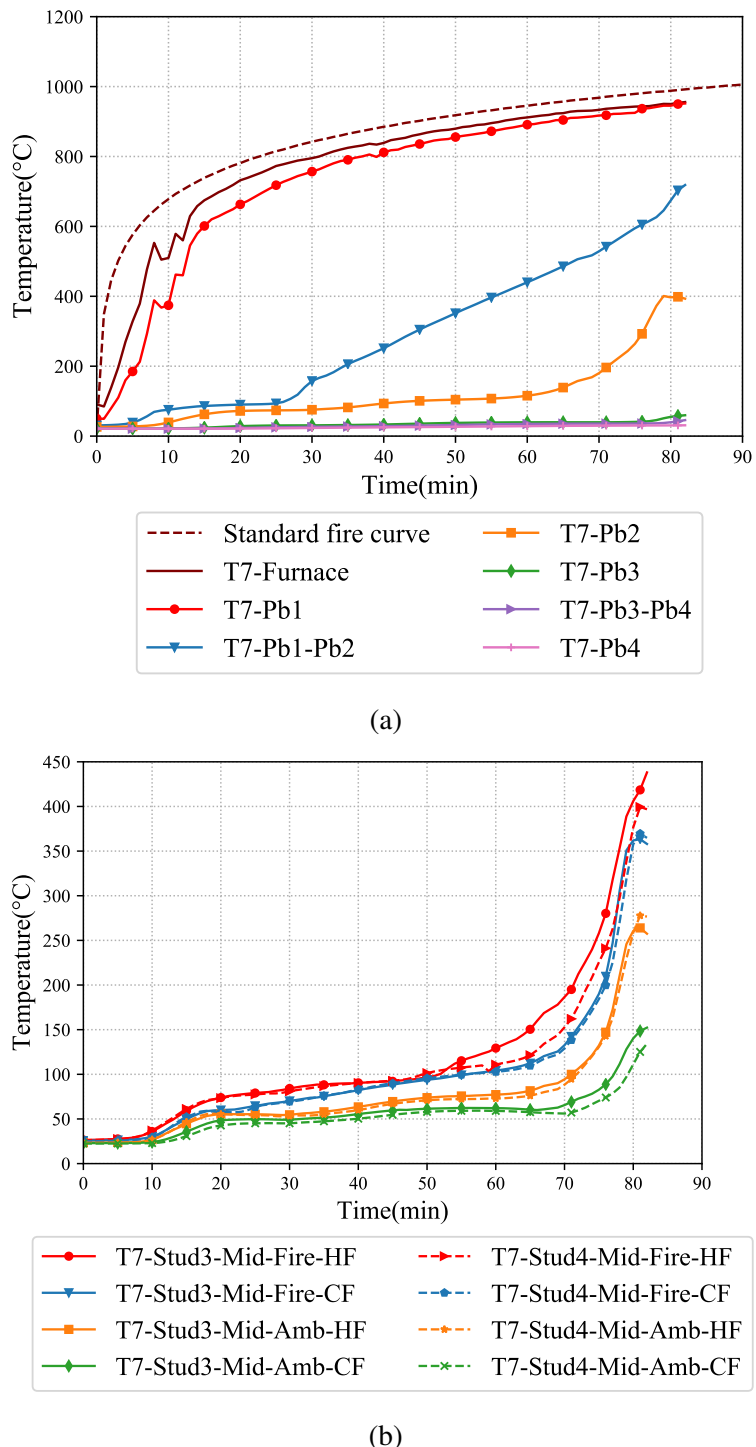


Figure 4.37: Plasterboard and stud time-temperature curves of Test-T7 (a) Average plasterboard temperatures (b) Stud3 and 4 temperatures

The time-temperature curve on the studs as shown in Figure 4.37 (b) also exhibited a similar behaviour in comparison with Test-T5. All the hot and cold flange temperatures of the studs were well below 100°C till 50 min of fire test. After 50 min the fire side hot flange (T7-Stud3-Mid-Fire-HF) time-temperature curve upsurged rapidly to attain a maximum of 438°C at the end of fire test. The corresponding cold flange T7-Stud3-Mid-Fire-HF recorded a maximum of 363°C. The ambient side hot and cold flanges were well below 100°C till 70 min of fire test after which the time-temperature curve T7-Stud3-Mid-Amb-HF gradually increased to reach a maximum of 263°C at the end of fire test. However, the T7-Stud3 and Stud4-Mid-Amb-CF recorded temperatures well below 200°C till the end of fire test.

The axial displacement and lateral deflection versus time plots are presented in Figures 4.38 (a) and (b). There was no significant axial displacement in the studs till 65 min of the fire test. This is in correlation with the low time-temperature profile in the studs. The maximum axial displacement due to thermal expansion was -4.26 mm only at 80 min of fire test after which load reversal occurred resulting in an axial shortening of +10.52 mm at the end of fire test. The fire test was concluded after 81 min due to structural inadequacy as the test wall could not withstand the applied axial compression load. A maximum lateral deflection of -26.91 mm was recorded at the end of the fire test.

4.12 Fire Test-T8

4.12.1 Test-T8 Failure Time and Mode, and Observations

Test-T8 was conducted on a double stud LSF wall made of 90 mm deep studs with noggings at 1 m spacing and a plasterboard layer between the two rows of stud (effective cavity depth of 90 mm) as shown in Figure 4.39 (also known as shaftliner). Figure 4.40 shows the construction sequence of test wall. The fire test was conducted for 240 min under non-load bearing conditions. Water droplets were visible in the top left corner of the ambient side plasterboard (Pb4) after 35 min of fire exposure. The fire side plasterboard layers were completely calcinated, however, the plasterboard layer between the studs (Pb3) and those on the ambient side (Pb4 and Pb5) were intact until the end of the fire test (Figure 4.41 (a)). Neither an insulation failure nor an integrity failure

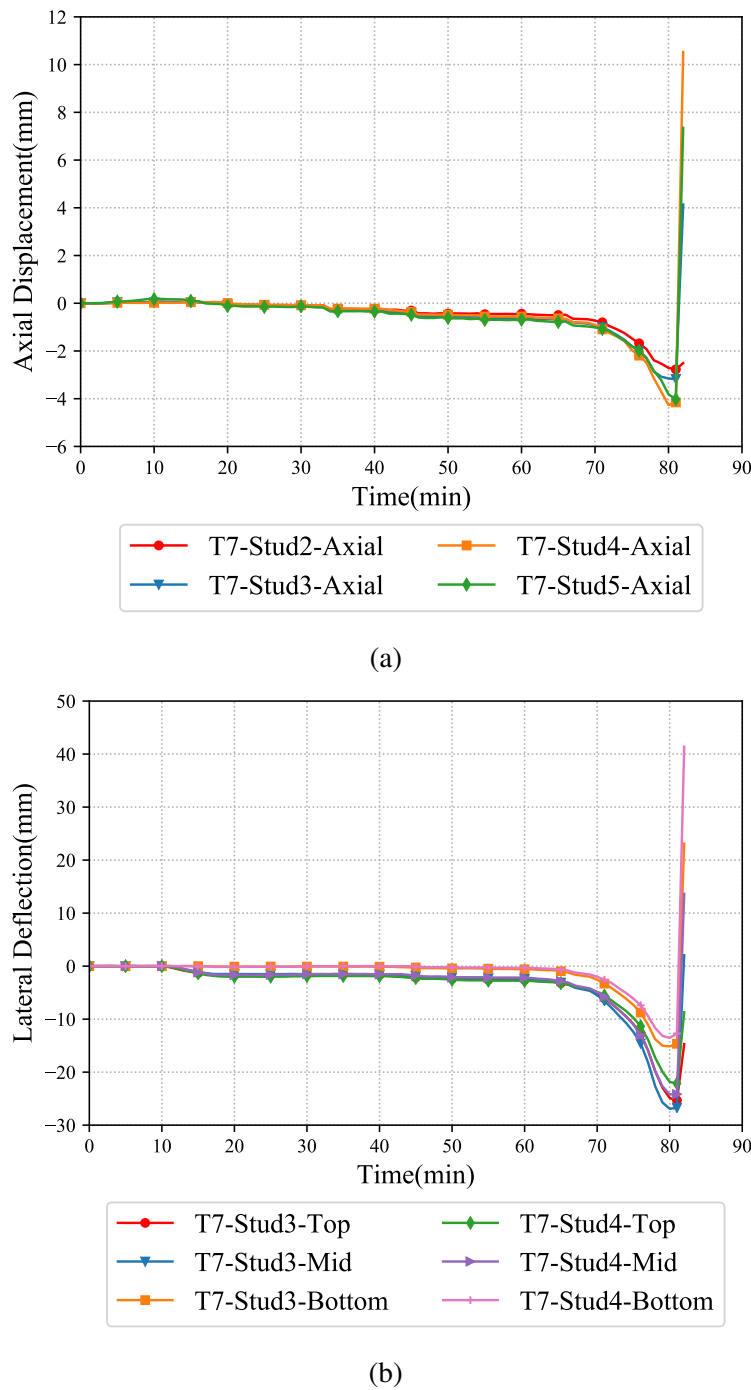


Figure 4.38: Axial displacement and lateral deflection curves from Test-T7 (a) Axial displacement versus time (b) Lateral deflection versus time curves

occurred until 240 min.

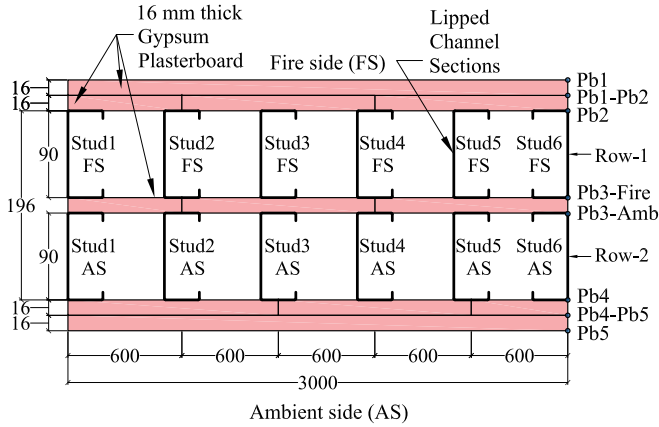


Figure 4.39: Plan view of shaftliner LSF wall panel used in Test-T8

4.12.2 Test-T8 Results and Discussion

Figure 4.42 (a) shows the average plasterboard time-temperature curves from Test-T8. The fire side plasterboard temperature (Pb1) agreed reasonably well with the standard fire curve until about 180 min of the fire test. Excessive plasterboard fall-off on the fire side after 164 min is evident from the sudden rise in the T8-Pb1-Pb2 time-temperature curve, reaching the fire side curve. The ambient side plasterboard temperatures were less than 100°C till the end of the fire test, as evident from the T8-Pb5 curves shown in Figure 4.42 (c). This confirms the absence of insulation failure in the test wall.

The stud time-temperature curves from Test-T8 are shown in Figure 4.42 (b). The fire side hot flange (T8-Stud3-Mid-Amb-HF) recorded a maximum temperature of 985°C at 240 min while the ambient side hot flange T8-Stud3-Mid-Amb-HF recorded a maximum temperature of 718°C at 240 min. The corresponding cold flange temperatures (T8-Stud3-Mid-Fire-CF and T8-Stud3-Mid-Amb-CF) were 968°C and 674°C. Such high stud temperatures are unlikely to be reached in load bearing fire tests as confirmed by many load bearing fire tests (Feng and Wang (2005), Chen et al. (2012), and Kodur et al. (2013)). Although this test wall was tested under non-load bearing conditions, local buckling of hot and cold flange elements was observed on both fire and ambient side studs (Figure 4.41 (c)). The local buckling was due to the high temperatures experienced on all the stud hot and cold flanges where the intact ambient side plasterboard acted as an additional load. Maximum axial displacement of 14.89

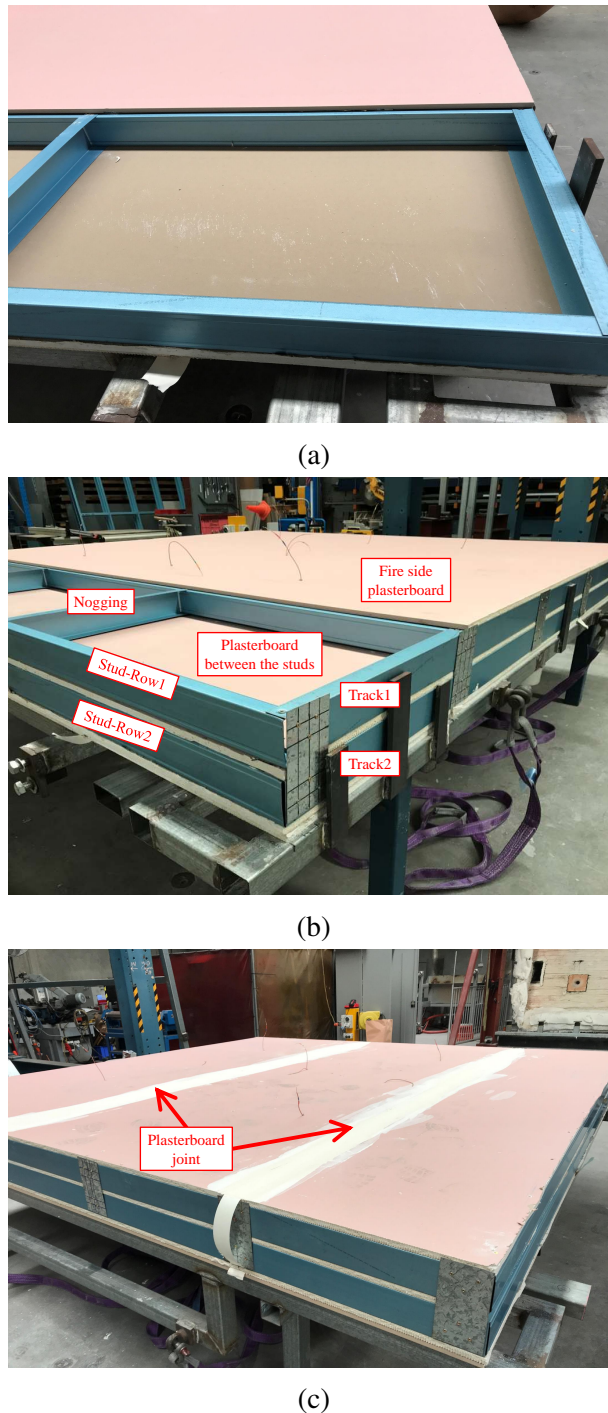


Figure 4.40: Test-T8 wall construction sequence (a) Test frame assembly (b) Plasterboard installation (c) Constructed test wall

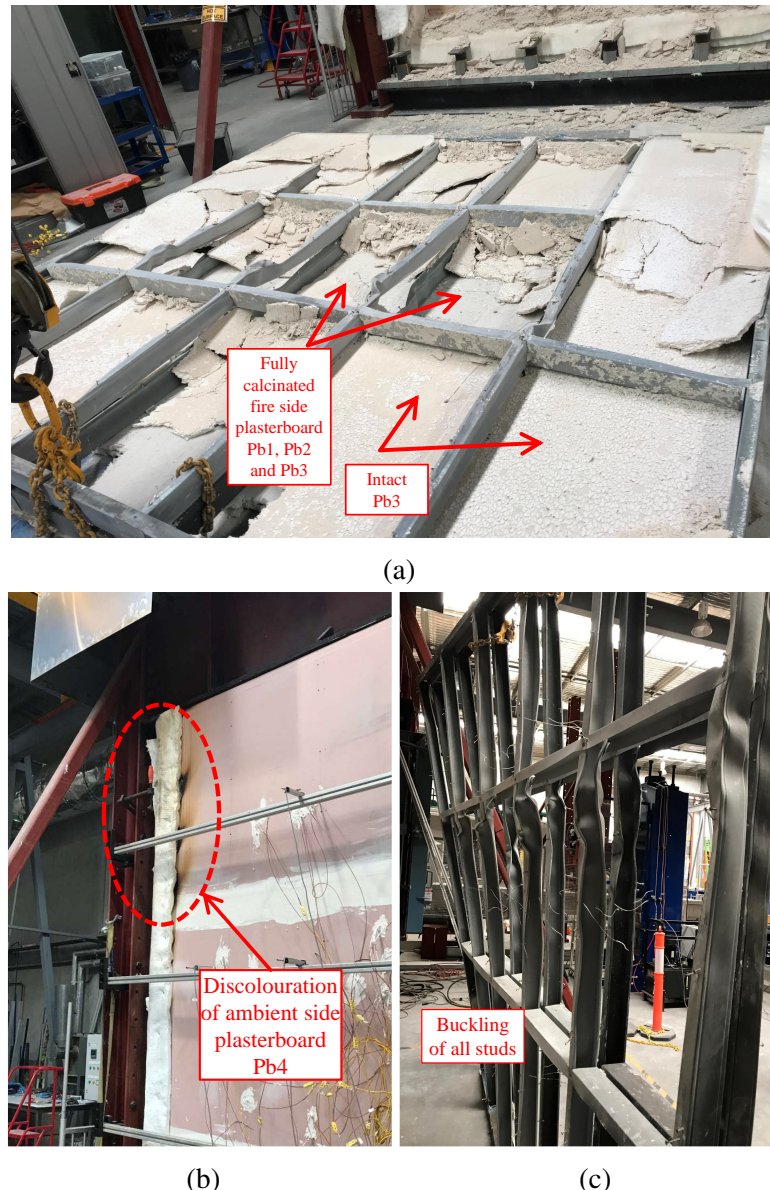


Figure 4.41: Failure of Test-T8 wall (a) Fire exposed side (b) Discolouration of ambient side plasterboard (c) Local compressive failure of studs

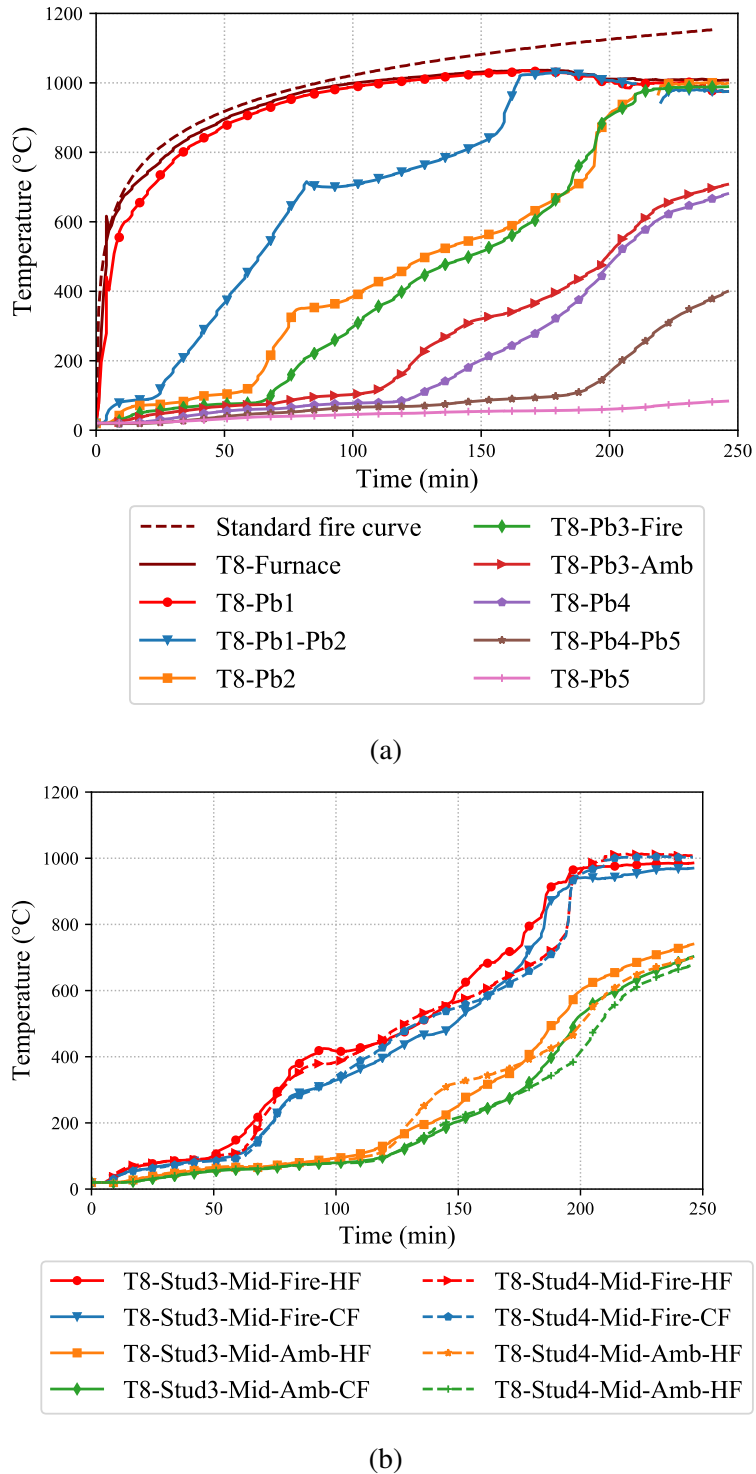
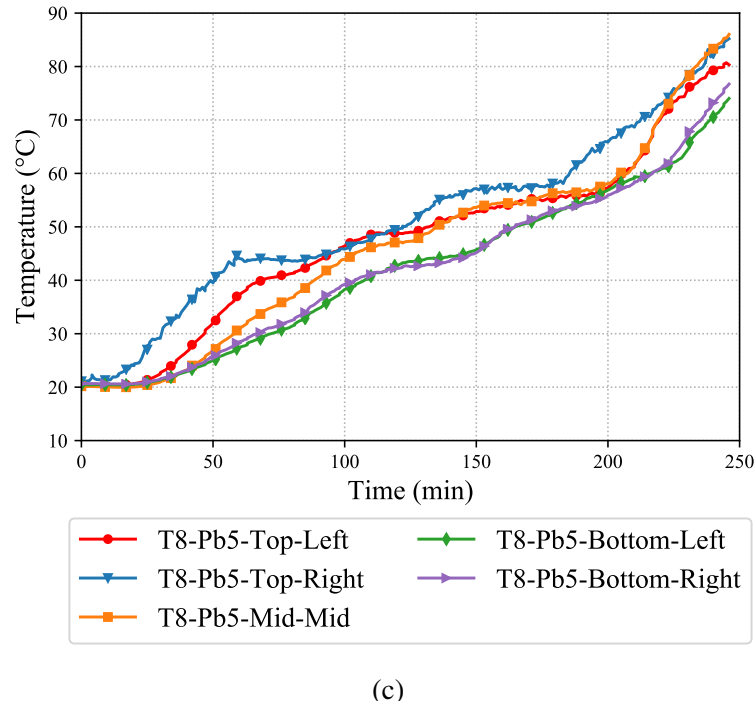


Figure 4.42: Plasterboard and stud time-temperature curves of Test-T8 (a) Average plasterboard temperatures (b) Studs 3 and 4 temperatures (c) Ambient side plasterboard temperatures (Pb5)



(c)

Figure 4.42: Plasterboard and stud time-temperature curves of Test-T8 (a) Average plasterboard temperatures (b) Studs3 and 4 temperatures (c) Ambient side plasterboard temperatures (Pb5)

mm was recorded on Stud4 as shown in Figure 4.43 (a). The lateral deflection versus time curve was nearly flat and recorded -7 mm at 100 min of fire test. It then increased to a maximum of -30 mm after 200 min and reversed back to -3 mm as shown in Figure 4.43 (b).

4.13 Fire Test-T9

4.13.1 Test-T9 Failure Time and Mode, and Observations

Test-T9 was conducted on a staggered stud LSF wall with 90 mm deep studs (cavity depth of 150 mm) and lined with two layers of 16 mm gypsum plasterboards. The studs are arranged in a staggered pattern with every alternative stud at 600 mm centres. The staggered stud LSF wall configuration used in Test-T9 is shown in Figure 4.44. Figure 4.45 shows the construction of test wall. This test was conducted under non-load bearing conditions as staggered stud LSF walls are commonly used as non-load bearing walls. After 20 min, mild smoke was observed on the top right corner of the test wall. Water droplets were visible due to the process of plasterboard calcination in the

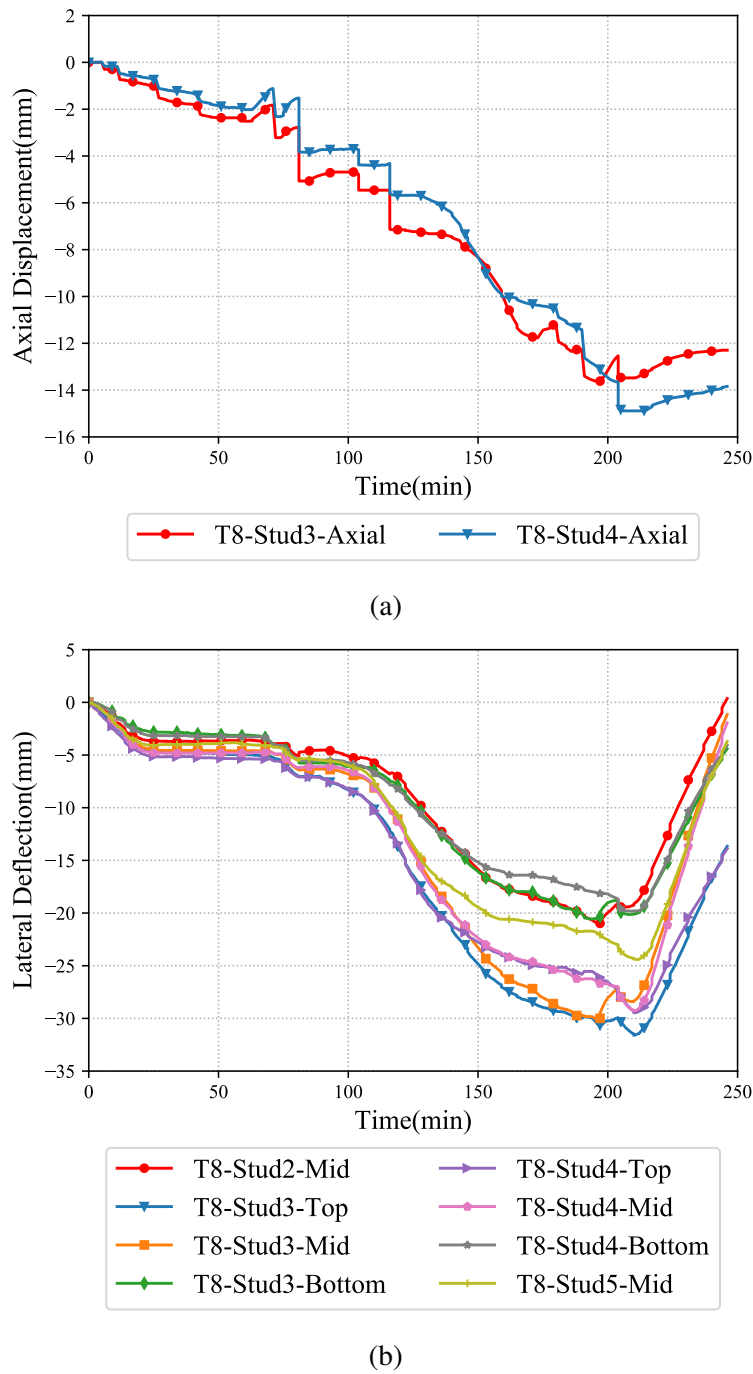


Figure 4.43: Axial displacement and lateral deflection versus time curves from Test-T8
(a) Axial displacement versus time (b) Lateral deflection versus time curves

top left corner on the ambient side. This test was concluded after 191 min of fire exposure, but there was no insulation or integrity failure until then. Figure 4.46 (a) shows the fire side (Pb1) of test wall after the test, which reveals a significant plasterboard fall-off on the fire side, whereas Figure 4.46 (b) shows the ambient side plasterboard (Pb4). Local compressive failure of studs can be seen in Figure 4.46 (c) even though this was a non-load bearing wall.

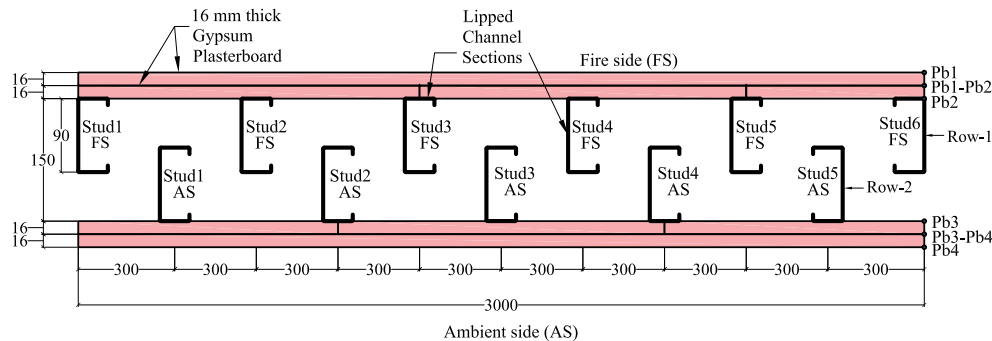


Figure 4.44: Plan view of staggered stud LSF wall panel used in Test-T9

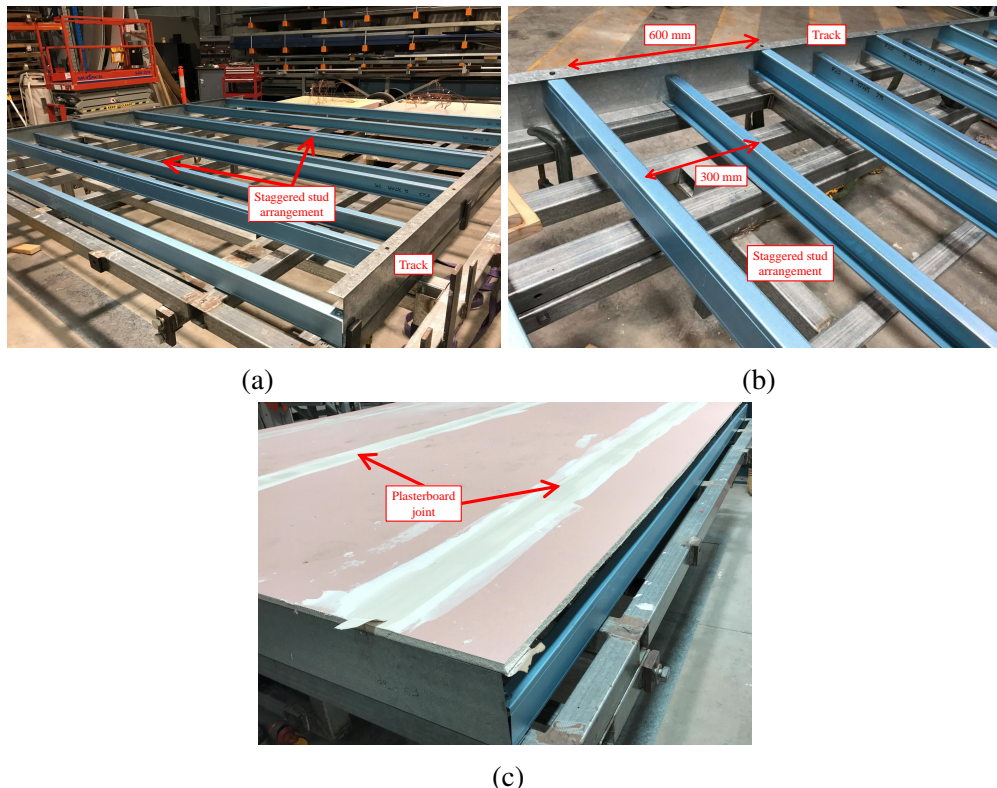


Figure 4.45: Test-T9 wall construction sequence (a) Test wall frame construction (b) Test frame end connection (c) Constructed test wall

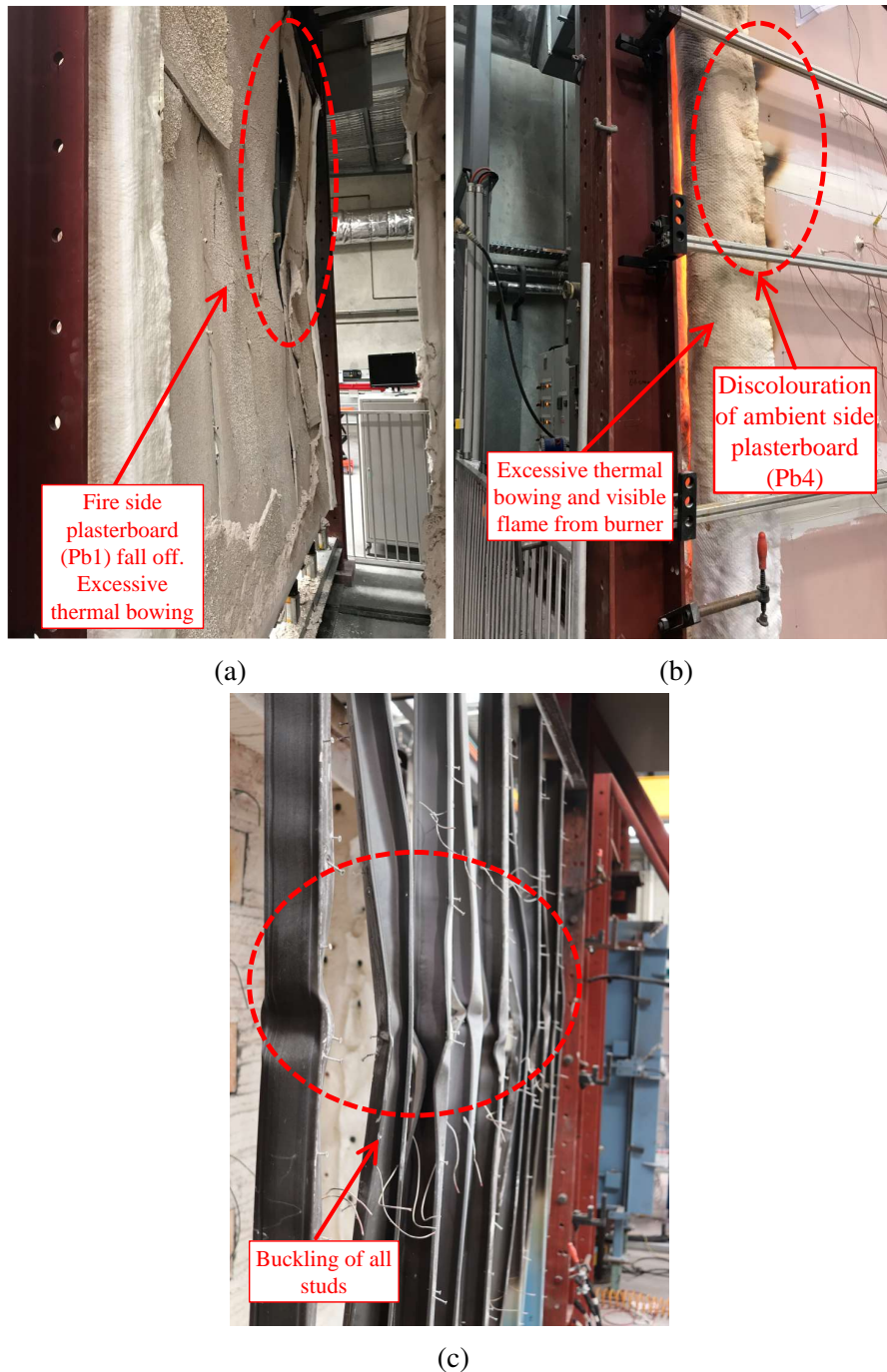


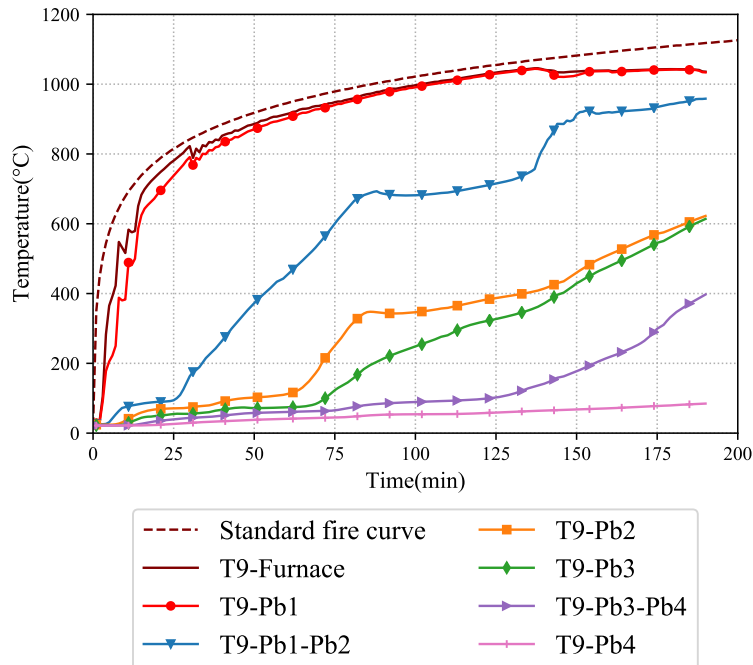
Figure 4.46: Failure of Test-T9 wall (a) Fire exposed side (b) Discolouration of ambient side plasterboard and excessive thermal bowing (c) Local compressive failure of studs

4.13.2 Test-T9 Results and Discussion

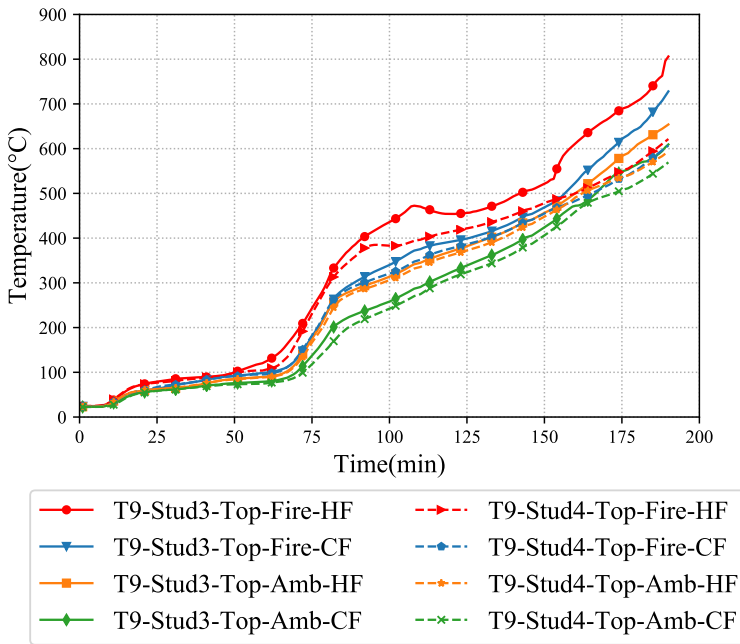
The average time-temperature curves of the plasterboard and stud surfaces from Test-T9 are summarised in Figures 4.47 (a) to (c). The time-temperature curve of fire side plasterboard interface T9-Pb1-Pb2 was nearly flat for the initial 25 min after which the curve exhibited a steep rise, reaching 693°C at 88 min. Then the curve became a plateau and showed only a gradual increase during 80 to 120 min. This observation is caused by the wider cavity (150 mm) producing a natural convection within the cavity. A reduced time-temperature profile is also visible on the fire side cavity T9-Pb2. This behaviour is also caused by the discontinuous stud arrangement in staggered stud wall. The plateau region observed in Test-T1 on non-cavity insulated double stud wall was also present in the plasterboard T9-Pb1-Pb2 and T9-Pb2 time-temperature curves confirming the earlier claim. However, the duration of the plateau region was shorter in comparison with Test-T1. This is partly due to the increased cavity depth of 200 mm used in Test-T1 in comparison with the cavity depth of 150 mm used in this test.

The highest temperature recorded on the fire side hot flange (T9-Stud3-Mid-Fire-HF) was 840°C at 187 min. As the plasterboard provides no passive protection to the hot flange of every alternative stud this worsens the situation resulting in excessive inward thermal bowing of -18 mm at 155 min. From 155 min to the end of the fire test the test wall deformed outwards resulting in a lateral deflection of 6 mm at 190 min. This means that a total of 24 mm thermal bowing deformation occurred within the last 35 min. The temperatures of the ambient side Pb4 were less than 100°C till the end of the fire test as shown in Figure 4.47 (c), i.e., no insulation failure.

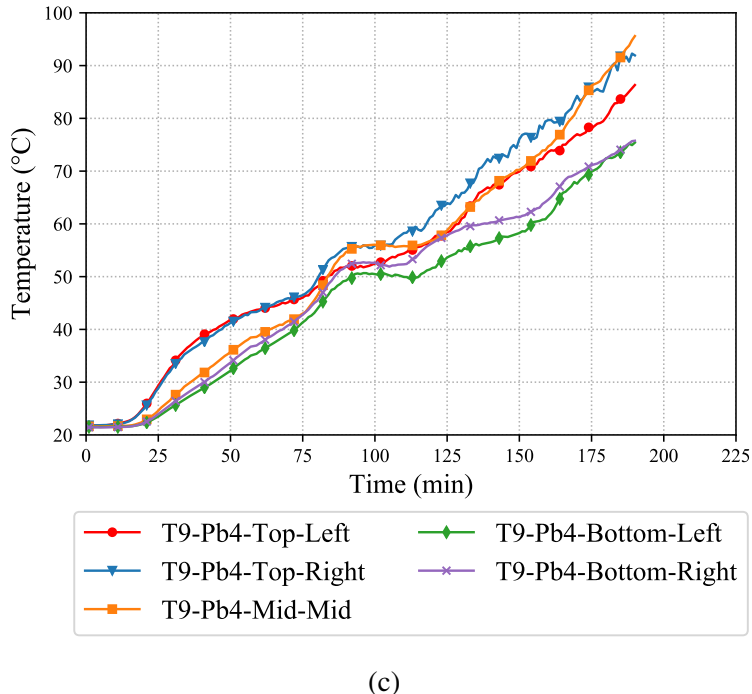
The fire test was conducted for 191 min after which the test was concluded because of the structural failures of studs (Figure 4.46 (c)). Maximum axial displacement of -11.16 mm was recorded in Stud3 as shown in Figure 4.48 (a). The lateral deflection versus time curves also show higher lateral deflection of -19.20 mm at about 190 min (Figure 4.48 (b)). In staggered stud walls the plasterboard is screw fastened to only one flange of the studs. This reduces the in-plane lateral restraint offered by the plasterboards to the studs in comparison with the studs restrained on both flanges. Although this is a non-load bearing wall fire test, the ambient side gypsum plasterboard did not soften and remained in position until the end of the fire test. This meant the self weight



(a)



(b)



(c)

Figure 4.47: Plasterboard and stud time-temperature curves of Test-T9 (a) Average plasterboard temperatures (b) Studs3 and 4 temperatures (c) Ambient side plasterboard temperatures (Pb5)

of the boards acting as a load on the much weakened studs led to their local buckling failures shown in Figure 4.46 (c).

The stud time-temperature curves from Test-T9 are shown in Figure 4.47 (a). The first peak temperature of 470°C was recorded at 107 min on the fire side stud hot flange (T9-Stud3-Top-Fire-HF). It reduced to 449°C at 123 min, i.e., 21°C drop in 16 min after which the temperature increased gradually. This effect is because of the fire side stud hot flange losing heat into the wider cavity. This plateau in the hot flange time-temperature curve is also visible in the fire side cavity plasterboard temperature curve (Figure 4.47 (b)). This is evident from the increased slope in the ambient side cavity (T9-Pb3) time-temperature curve as shown in Figure 4.47 (a). Further, the standard fire curve is also nearly flat during this period resulting in the fire side plasterboard surface to lose heat to the ambient side of the test wall.

The ambient side stud hot flanges (T9-Stud3-Top-Amb-HF) did not have the temperature plateau as observed for the fire side stud hot flanges. The peak temperature of T9-Stud3-Mid-Amb-HF was 687°C at 190 min. Since the temperatures of the hot and cold flanges were high, even the self-weight of the ambient side plasterboards was sufficient to cause local buckling failures of studs at mid-height (Figure 4.46 (c)).

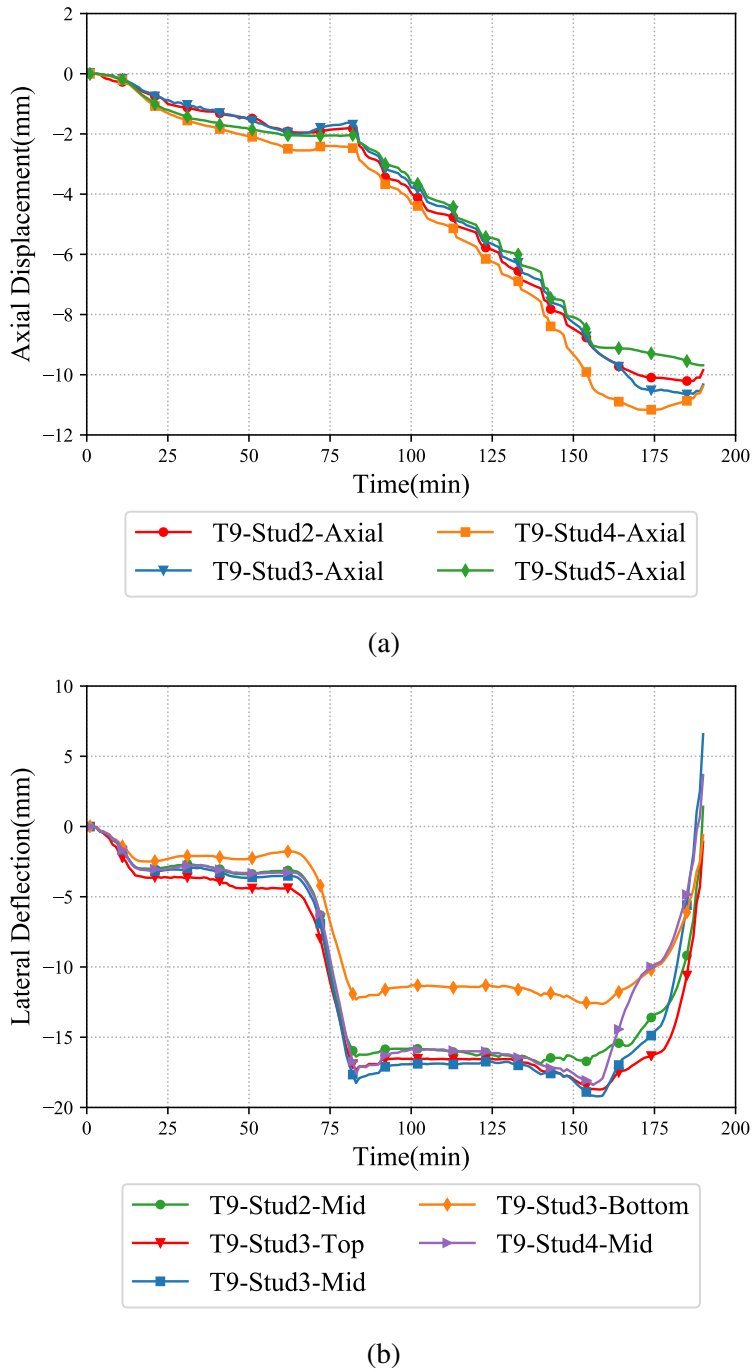


Figure 4.48: Axial displacement and lateral deflection versus time curves from Test-T9
(a) Axial displacement versus time (b) Lateral deflection versus time curves

4.14 Fire Test-T10

4.14.1 Test-T10 Failure Time and Mode, and Observations

Test-T10 was also conducted on a staggered stud LSF wall shown in Figure 4.49. However, this test was conducted under load bearing conditions with glass fibre cavity insulation as shown in Figure 4.50. From the ambient capacity Test-AT5 discussed in Chapter 3, the axial compression capacity of the test wall was determined to be 68.89 kN. In this fire test 40% of the load (27.55 kN) was applied to the test wall panel and then a full-scale fire test was conducted. It is to be noted that, intermittent omega noggings were provided at 1 m intervals to provide lateral restraints. Conventional LCS noggins are connected through the stud flanges, however the omega noggings were connected through the stud webs to maintain the discontinuous stud arrangements. Details of the omega nogging connections are given in Chapter 3, Figure 3.19 (a). The test wall configuration and construction details are also shown in Figures 4.49 and 4.50. Unlike the standard insulation installation process in single stud LSF walls, the cavity insulation was staggered between the studs as shown in Figure 4.50 (b). This was done to meet the acoustic requirements for the test wall. However, the acoustic rating for the wall was not investigated as the research focus was to investigate the fire performance of cavity insulated staggered stud LSF wall.

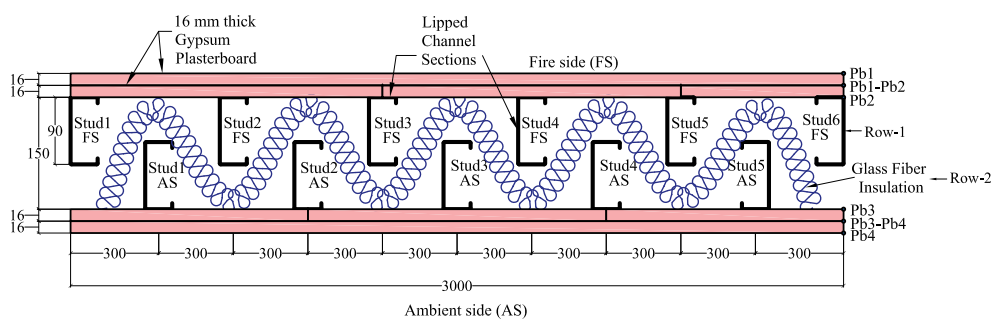


Figure 4.49: Plan view of staggered stud LSF wall panel with cavity insulation used in Test-T10

After 7 min from the start of the fire test, smoke was visible on the top right corner of the test wall panel. Water droplets were also found to be dripping near the origin of smoke indicating the start of evaporation of free water content from gypsum plasterboard. Mild smoke was visible at 34 min of fire test, which then lasted till 74 min of the fire test at the top left and right corners of the test wall panel. The test wall

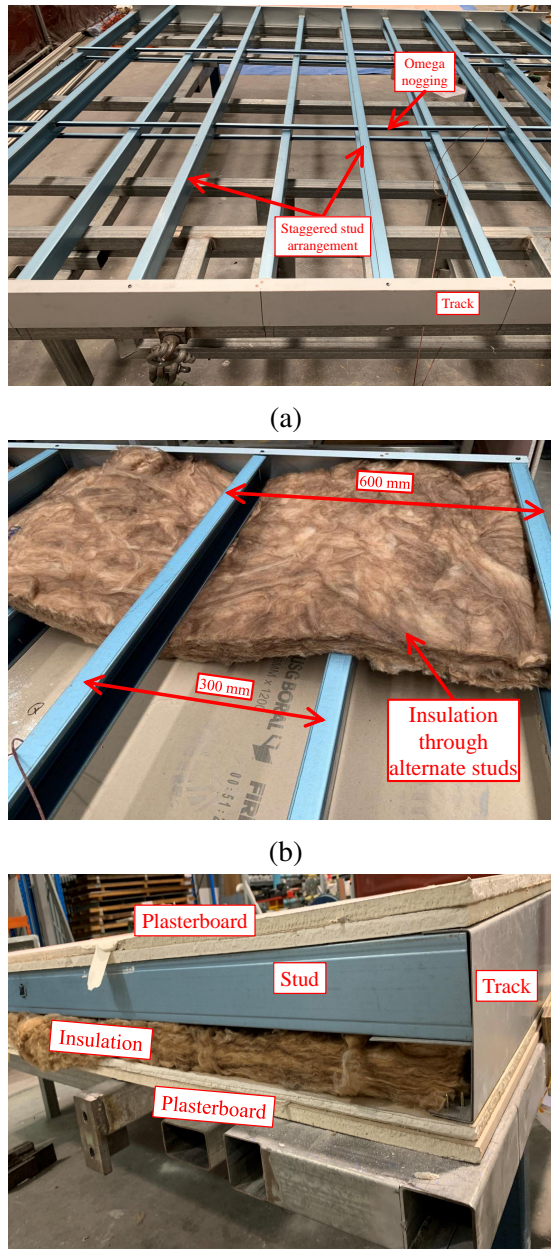


Figure 4.50: Test-T10 wall construction sequence (a) Test frame construction (b) Cavity insulation installation (c) Constructed test wall

could not withstand the applied axial compression load after 85 min and failed due to structural inadequacy of the studs.

Post fire test investigation showed small plasterboard fall-off at mid-height of the test panel on the fire exposed surface. The fire side plasterboard Pb1 experienced localised fall-off while the second plasterboard layer on the fire side (Pb2) was intact. However, significant joint open-up was noticeable on the fire side as shown in Figure 4.51 (a). It is to be noted that, the insulation was burnt only on the fire exposed side. However, due to higher temperature concentration near the studs, discolouration of the insulation was noticeable as shown in Figure 4.51 (c). Severe local buckling of fire side studs was observed, while no significant buckling was seen on the ambient side studs as shown in Figure 4.51 (d). This implies that the heat transfer within the cavity is blocked by the glass fibre insulation trapping the heat on the fire side studs only. This is also evident from the intermittent discolouration visible near the stud locations.

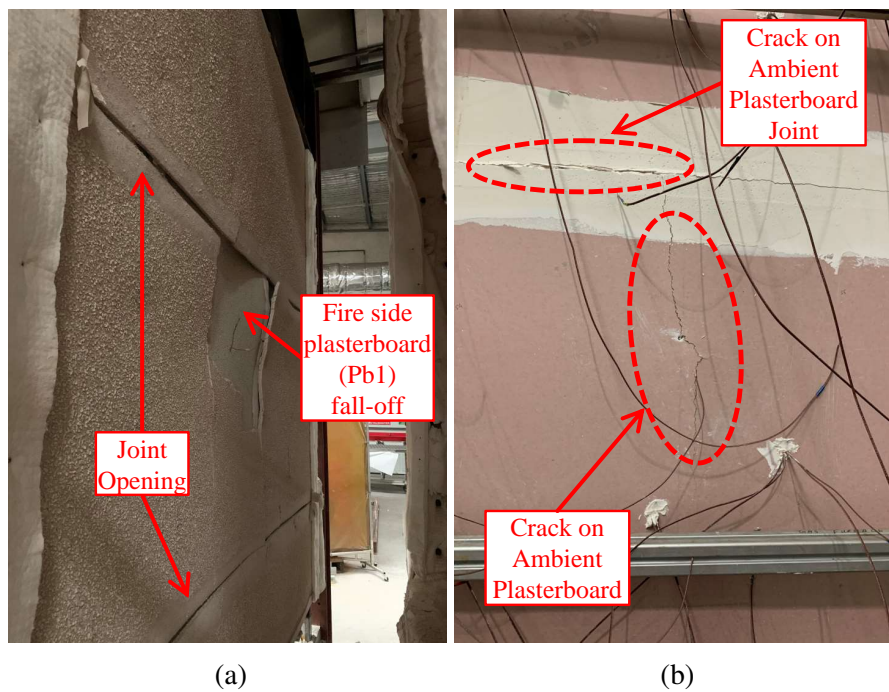


Figure 4.51: Failure of Test-T9 wall (a) Fire exposed side (b) Crack on ambient side plasterboard and joint (c) Discolouration of glass fibre insulation (d) Buckling of fire side studs

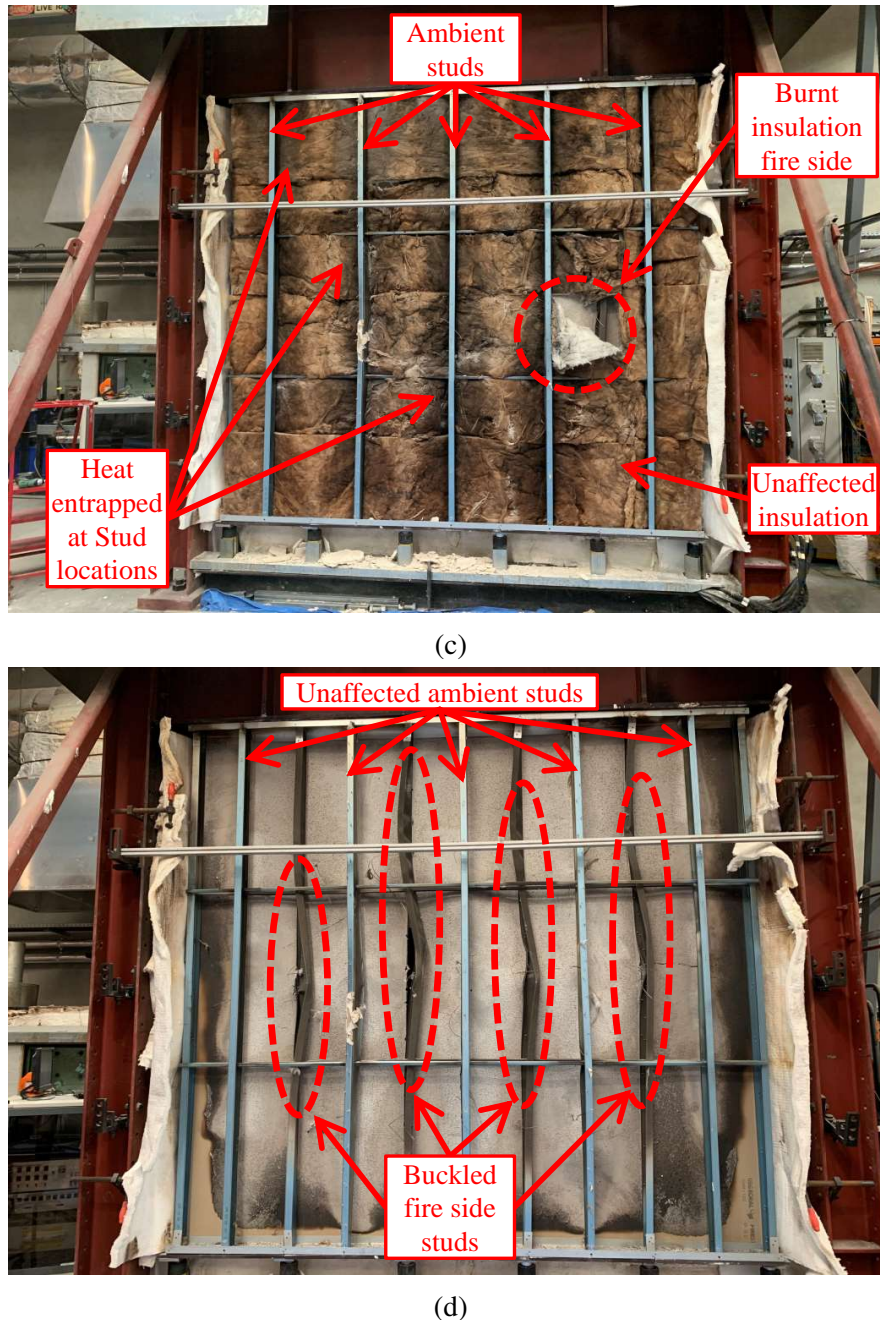


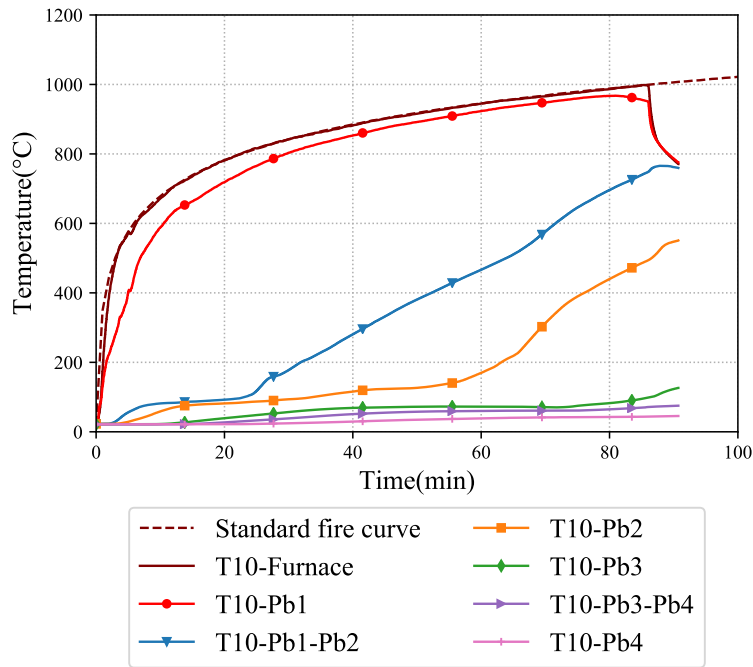
Figure 4.51: Failure of Test-T9 wall (a) Fire exposed side (b) Crack on ambient side plasterboard and joint (c) Discolouration of glass fibre insulation (d) Buckling of fire side studs

4.14.2 Test-T10 Results and Discussion

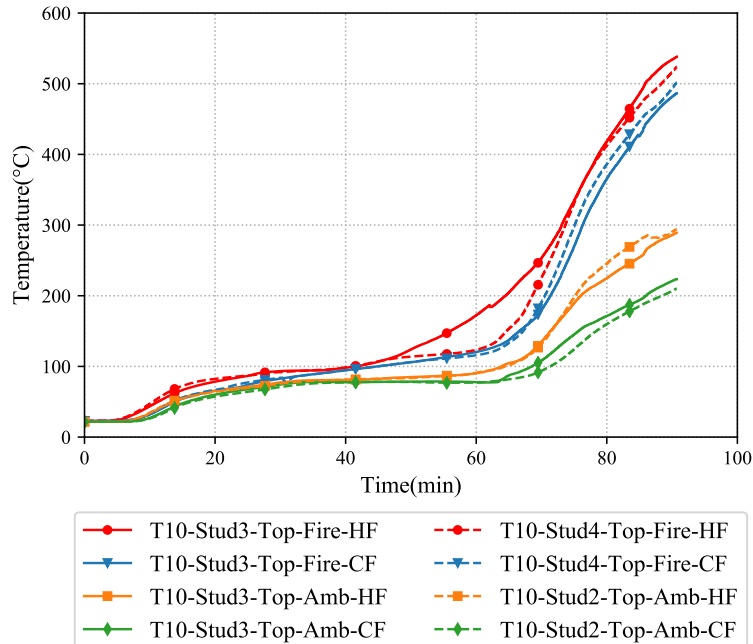
The plasterboard time-temperature curves are shown in Figure 4.52. A similar trend in the time-temperature curve was observed in comparison with the results from Test-T5 to T7 (cavity insulated walls). Fire side plasterboard interface time-temperature curve (Pb1-Pb2) exhibited a flat region for the initial 20 min of the fire test and then resulting in a steep increase in the curve. This behaviour was noticeable in previous fire test results with cavity insulation. A sudden peak in the curve at the end of the fire test similar to the previous tests was not noticeable because of the absence of significant plasterboard fall-off in the test wall. However, the fire side plasterboard had the joints open-up, which is evident form Figure 4.51 (a). The maximum temperatures recorded on the fire side interface (Pb1-Pb2) and fire side cavity (Pb2) surfaces were 748°C and 489°C. However, the ambient side plasterboard temperatures such as Pb3, Pb3-Pb4 and Pb4 recorded temperatures less than 200°C at the end of the fire test, signifying the absence of insulation failure.

The critical hot and cold flange temperature of 494°C and 432°C were recorded at T10-Stud3-Top-Fire-HF and CF at stud locations 750 mm from the top of the test wall panel. The difference between the fire side hot and cold flange temperatures was only 62°C and the time-temperature profile was almost similar amongst them as shown in Figure 4.52 (b). This behaviour was also noticed in previously discussed cavity insulated fire Tests-T5,T6 and T7. However, the ambient side hot and cold flanges (T10-Stud3-Top-Amb-HF and CF) recorded temperatures of 257°C and 197°C, respectively. The ambient side temperatures are considerably lower than the corresponding hot flange temperatures, which is different from cavity insulated double stud wall fire test results. This behaviour is because of the staggered stud arrangement in Test-T10. Also, the ambient side studs are completely covered by the cavity insulation, whereby the cavity insulation prevents the passage of heat to the ambient side hot and cold flanges.

The axial displacement and lateral deflection curves from Test-T10 are shown in Figure 4.53. Gradual axial expansion from the start of the fire test was observed reaching a maximum expansion of -7.78 mm at 76 min on T10-Stud3-Axial after which the studs started to contract. The load reversal resulted in a maximum axial contraction of -4.55 mm recorded at 85 min after which the test panel could not survive the applied



(a)



(b)

Figure 4.52: Plasterboard and stud time-temperature curves of Test-T10 (a) Average plasterboard temperatures (b) Stud3 temperatures

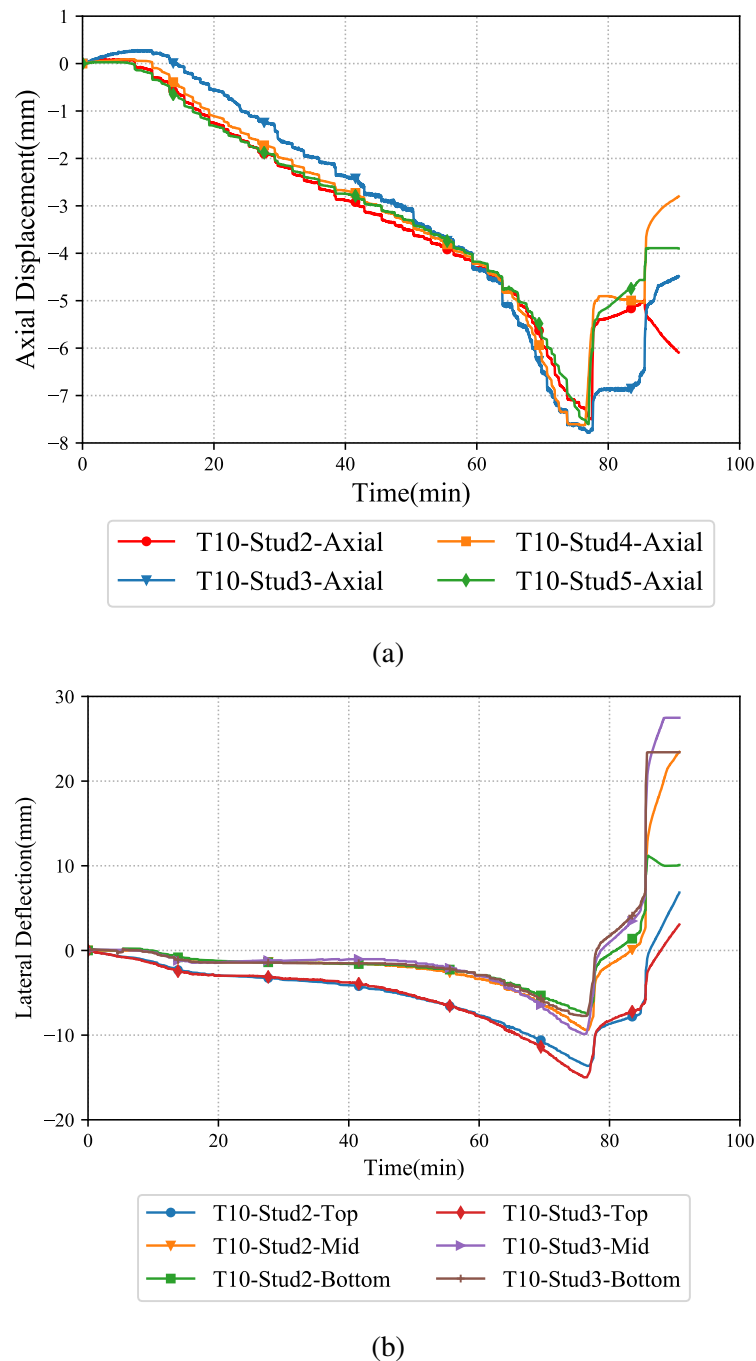


Figure 4.53: Axial displacement and lateral deflection versus time curves from Test-T10 (a) Axial displacement versus time (b) Lateral deflection versus time curves

axial load marking the end of fire test due to structural inadequacy failure criterion. A maximum lateral deflection of -9.87 mm was observed at 76 min after which the curves reversed and resulted a lateral deflection of 27.48 mm at the end of fire test.

4.15 Summary of Full-Scale Fire Tests

This section presents a summary of the results from the 10 full-scale fire tests conducted on double, staggered and shaftliner LSF walls. Table 4.2 presents the important results from these fire tests. Tests-T1 to T4 were conducted on non-cavity insulated double stud LSF walls. Tests-T1 to T3 were conducted on double stud walls with 90 mm studs and a cavity depth of 200 mm while Test-T4 was conducted on double stud wall with 70 mm studs and a cavity depth of 160 mm. Tests-T5 to T7 were conducted on double stud LSF walls with glass fibre cavity insulation. However, Test-T5 was conducted with cavity insulation on both rows of studs while Test-T7 was conducted with cavity insulation on the ambient side row of studs. Test-T6 was conducted as a repeat test for Test-T5 to verify the accuracy of the results attained from Test-T5. Tests-T8 and T9 were conducted under non-load bearing conditions. Test-T8 was conducted on a double stud LSF wall with a plasterboard between the two stud rows (shaftliner), while Test-T9 was conducted on a staggered stud LSF wall. Test-10 was also conducted on a staggered stud LSF wall but with cavity insulation curved to match the staggered stud arrangement and also under load bearing conditions. Among the 10 full-scale fire tests, eight tests were conducted under load bearing conditions and two tests were conducted under non-load bearing conditions.

Tests-T1 and T2 were conducted under the same LR of 0.4 wherein, Test-T1 wall survived 176 while Test-T2 wall survived 132 min. This difference may be due to various reasons such as the earlier plasterboard fall-off and higher thermal bowing effects on the fire side in Test-T2. Test-T2 was conducted with 0.75 mm thick stud sections in comparison to Test-T1 with 0.95 mm thick stud sections. A unique behaviour was observed in Tests-T1,T2 and T4, where the time-temperature curve on the fire side plasterboard interface (Pb1-Pb2) became almost flat from 80 to 120 min of fire exposure as shown in Figure 4.54 (a). This behaviour was observed in Test-T4 (with 70 mm studs) as well, where the time-temperature curve followed a similar pattern in

Table 4.2: Fire test results

Test Name	Description	Stud Depth (mm)	Cavity Depth (mm)	Stud Thickness (mm)	Cavity Insulation	Load Ratio	Critical HF °C	Critical CF °C	Failure Time	Failure Criteria
T1	Double Stud	90	200	0.95	No	0.4	459	411	176	Structural adequacy
T2	Double Stud	90	200	0.75	No	0.4	593	514	132	Structural adequacy
T3	Double Stud	90	200	0.75	No	0.6	332	226	81	Structural adequacy
T4	Double Stud	70	160	0.95	No	0.4	505	380	171	Structural adequacy
T5	Double Stud	90	200	0.95	Both ⁺	0.4	447	361	76	Structural adequacy
T6*	Double Stud	90	200	0.95	Both ⁺	0.4	547	471	91	Structural adequacy
T7	Double Stud	90	200	0.95	Ambient ⁺⁺	0.4	438	363	81	Structural adequacy
T8	Shaftliner	90	196	0.75	No	NLB	985	969	240	No insulation failure
T9	Staggered Stud	90	150	0.75	No	NLB	806	728	191	Structural adequacy
T10	Staggered Stud	90	150	0.95	Full**+	0.4	538	486	85	Structural adequacy

* Repeat of Test-T5

+ Cavity insulation on both stud rows

++ Cavity insulation on ambient stud rows only

** Cavity insulation staggered alongside the studs

NLB - Non-Load Bearing

comparison with Test-T1 despite the smaller cavity depth of 160 mm as shown in Figure 4.54 (b). However, both Tests-T1 and T4 had the same stud thickness of 0.95 mm. The failure time was also similar to Test-T1 (176 min) whereby Test-T4 survived 171 min.

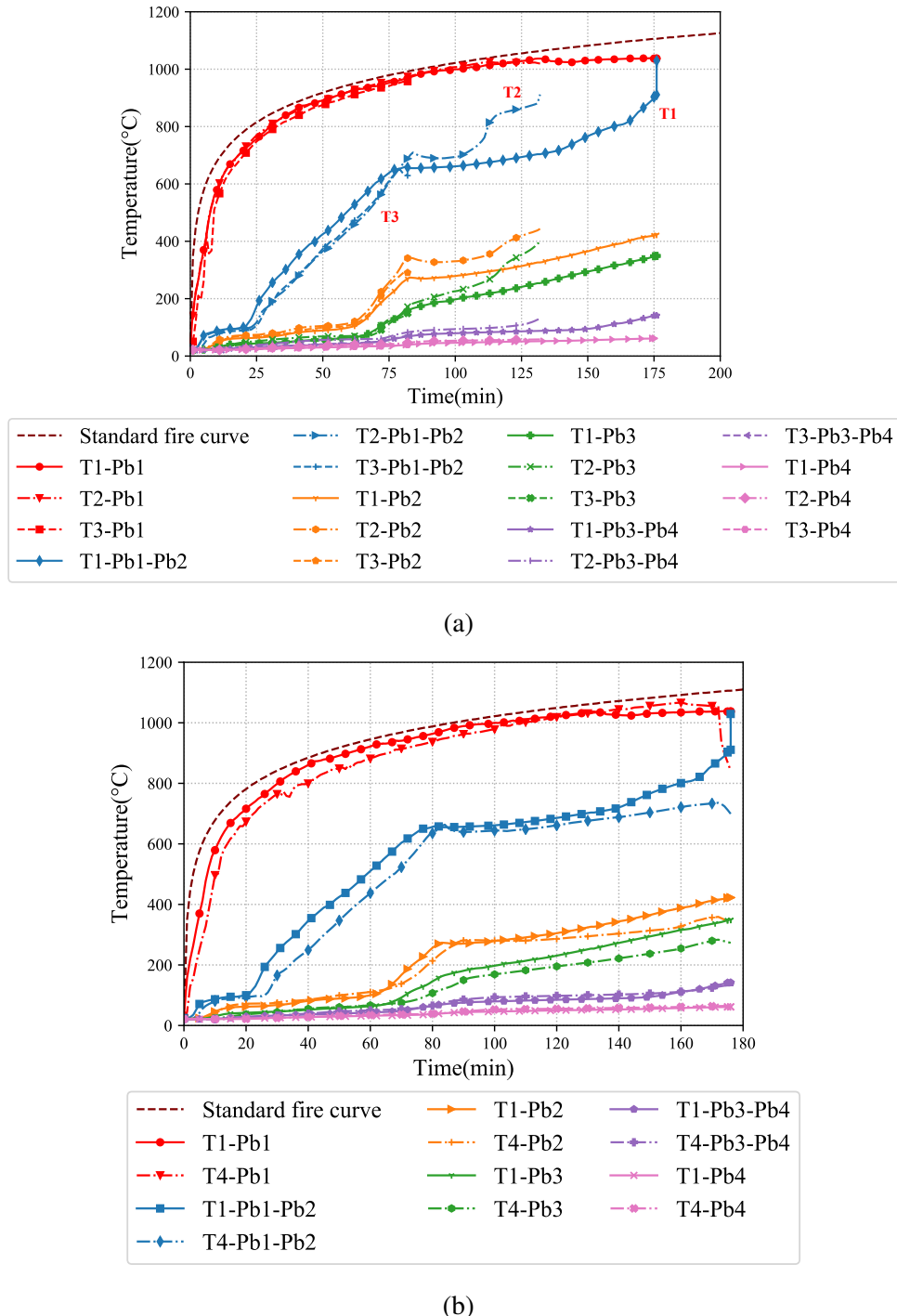


Figure 4.54: Comparison of average plasterboard time-temperature curves from Tests (a) T1, T2 and T3 (b) T1 and T4

This trend was reflected in the ambient side plasterboard time-temperature curve

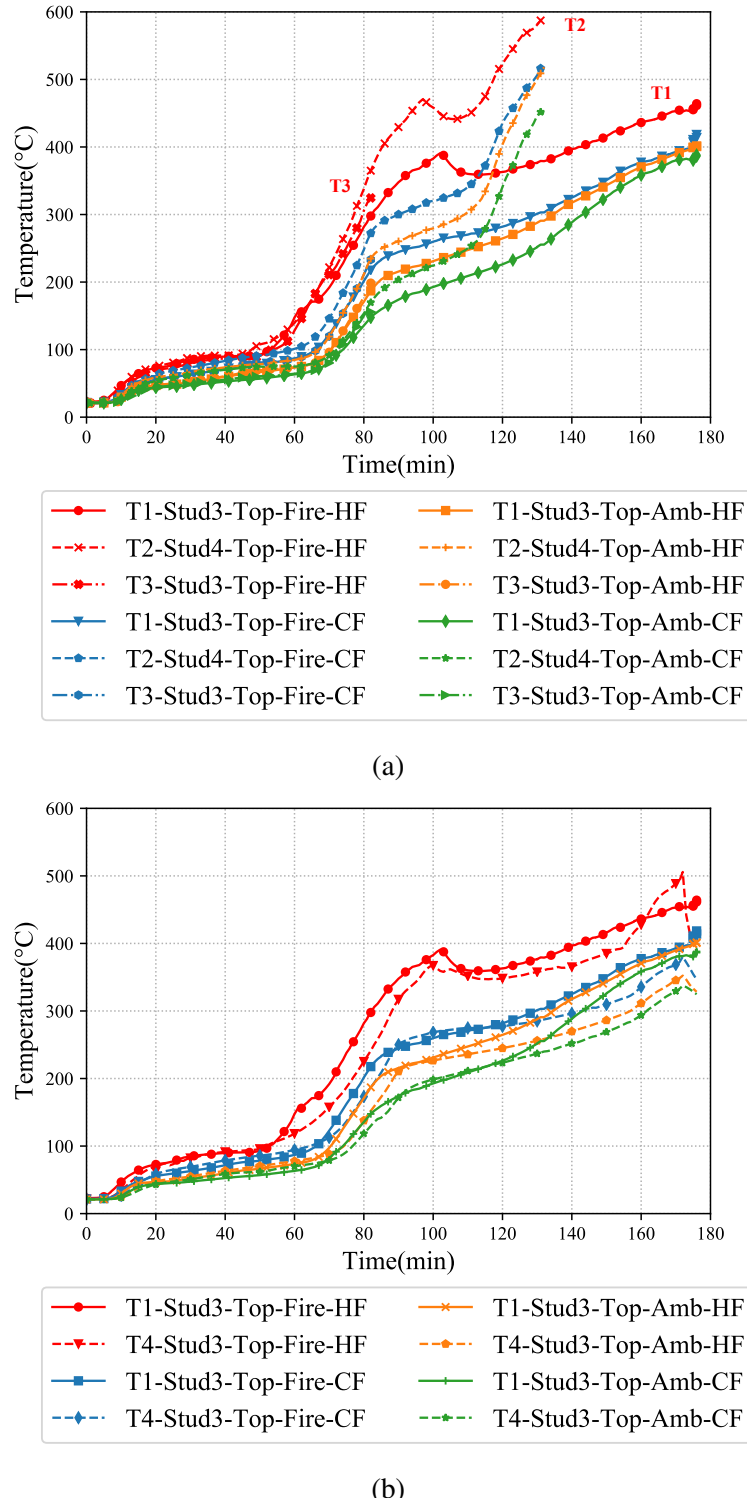


Figure 4.55: Comparison of critical stud time-temperature curves from (a) T1, T2 and T3 (b) T1 and T4

also. This behaviour also contributed to the unique pattern in the fire side hot flange time-temperature curves of studs in Tests-T1, T2 and T4. These effects were minimal in Test-T3 because it failed at 81 min (higher LR). Therefore it is evident that there is a state of equilibrium between 80 and 120 min of fire exposure in double stud LSF walls. The time-temperature curves of Tests-T1, T2 and T3 are compared against each other as shown in Figure 4.54 (a). All the non-cavity insulated double stud wall fire tests plasterboard time-temperature curves exhibit a similar trend throughout the respective fire test indicating that the heat transfer mechanism in double stud walls remains unaffected by the stud thickness. The effect of change in cavity depth from 160 to 200 mm is also negligible for double stud LSF walls as shown in Figure 4.54 (b). The stud time-temperature curves are compared in Figures 4.55 (a) and (b). A small dip in the time-temperature curve is noticeable at the time period where the plasterboard time-temperature curves exhibit a plateau region during the fire test. However, the recorded fire side hot flange temperature was higher in Test-T2 (T2-Stud4-Top-Fire-HF) in comparison with Tests-T1 and T3. This may be attributed to the higher lateral deflection, shown earlier in Figure 4.18 (b). Also, the plasterboard fall-off and open-up observed in Test-T2 (Figure 4.16 (a)) contributed to the sudden increase in stud hot flange temperatures. Comparison of stud time-temperature curves between Tests-T1 and T4 as shown in Figure 4.55 (b) exhibits similar behaviour on all the flanges. It is to be noted that the studs used in Test-T1 were 90 mm deep while the studs used in Test-T4 were 70 mm deep. Difference in cavity depth was 40 mm between Tests-T1 (200 mm cavity depth) and T4 (160 mm cavity depth), but with the same stud configuration and thickness. This indicates that the effect of cavity depth did not significantly affect the stud hot and cold flange time-temperature curves in double stud LSF walls.

In the comparison of Tests-T8 and T9 results, the time-temperature curves exhibited a different behaviour as shown in Figure 4.56. Test-T8 was conducted on double stud walls with a 16 mm plasterboard between the two stud rows while Test-T9 was conducted on staggered stud walls. In these two tests, the stud depth of 90 mm and the thickness of 0.75 mm were the same. However, the cavity depth was 196 mm (2×90 mm + 16 mm) in Test-T8 while it was 150 mm in Test-T9 due to the staggered stud arrangement. Fire side cavity surface (Pb2) time-temperature curve followed a similar trend for the initial 80 min in all the fire tests. However, after 80 min a plateau region

was observed in T9-Pb2 as shown in Figure 4.56. This behaviour is due to the wider cavity in Test-T9 (cavity depth 150 mm). There prevails a natural convection within the cavity thereby introducing a plateau region on the time-temperature curve. This behaviour was not evident on the fire side cavity surface (Pb2) of Test-T8 as the cavity depth was only 90 mm and the Pb2 temperatures were higher than those in Test-T9. In Test-T8, due to the cavity being split into two by the middle plasterboard layer, which absorbs the heat from Pb2 surface, the effect of natural convection within the cavity was reduced. This behaviour is evident in the stud time-temperature curve comparison as shown in Figure 4.57. Hot flange time-temperature curves of the studs in Test-T8 also show a linear increase in the trend after 100 min of fire test. The plateau region exhibited in the stud time-temperature curves from Test-T1 was not present in Test-T8 but was evident in Test-T9. This is because of the single 150 mm wider cavity in comparison with 90 mm cavity split into two in Test-T8. Also, the ambient side hot and cold flange temperatures were significantly less in comparison with Test-T1 and T9 as shown in Figure 4.57 because of the middle plasterboard layer in Test-T8.

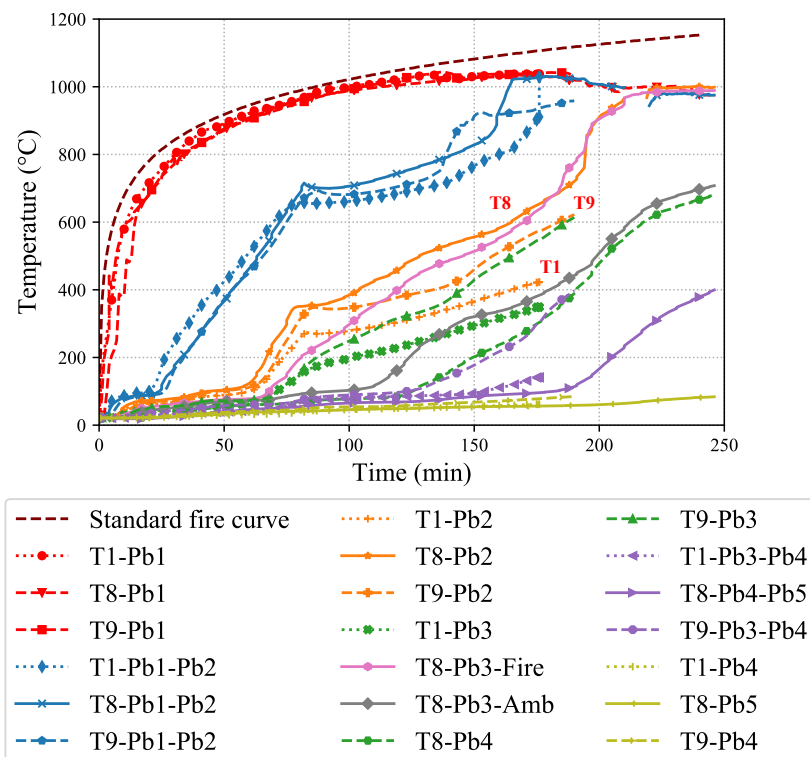


Figure 4.56: Comparison of average plasterboard time-temperature curves from Tests-T1, T8 and T9

Similarly the time-temperature curves from Tests-T5,T6,T7 and T10 exhibited a

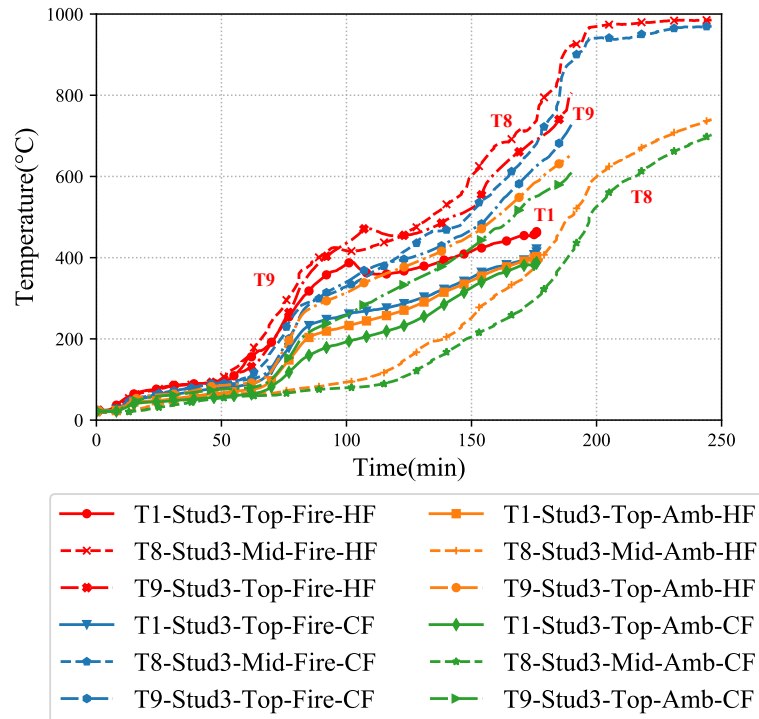


Figure 4.57: Critical stud time-temperature curve comparison between Tests-T1, T8 and T9

similar behaviour. As these tests were conducted with cavity, insulation the failure times of the tests were significantly reduced in comparison with the counterparts without cavity insulation. Irrespective of the LSF wall stud configuration, the fire side plasterboard interface time-temperature curve Pb1-Pb2 exhibited a similar behaviour in all the cavity insulated fire tests. The recorded temperatures were well below 100 °C for the initial 20 min of the fire test after which a steep rise in the time-temperature curve is noticed till the end of the fire test as shown in Figure 4.58. This behaviour indicates the entrapment of heat within the fire side of the test wall irrespective of the stud configuration. This behaviour is evident from the steep increase in the fire side cavity (Pb2) time-temperature curves after 60 min in all the cavity insulated fire tests.

Effects of heat entrapment is also visible on the stud time-temperature curves as shown in Figure 4.59, where the fire side hot flange temperatures increase steeply in comparison with the temperatures of other flanges. This causes a large variation of temperature distribution in studs resulting in premature failure of studs due to structural inadequacy in cavity insulated complex LSF wall Tests-T5, T6, T7 and T10. Despite positioning the insulation away from the fire side cavity as in Test-T7, the heat entrapment was still evident resulting in a similar time-temperature pattern in compar-

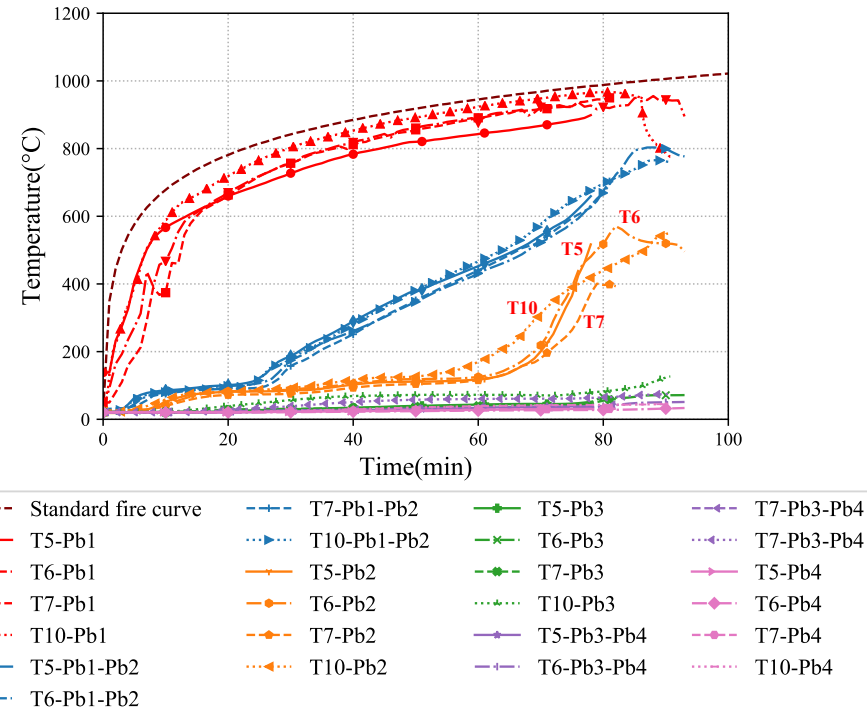


Figure 4.58: Comparison of average plasterboard time-temperature curves from Tests-T5, T6, T7 and T10

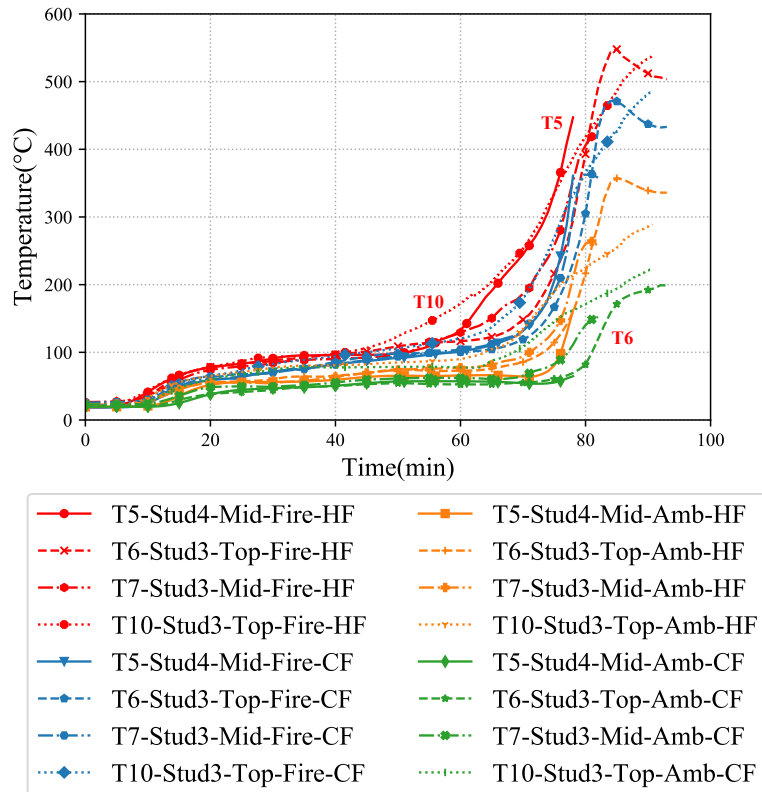


Figure 4.59: Comparison of critical stud time-temperature curves from Tests-T5, T6, T7 and T10

ison with other cavity insulated fire test results as shown in Figures 4.58 and 4.59. To understand this unique heat transfer mechanism in complex LSF walls it becomes important to compare these fire test results with those of conventional single stud walls. The following section provides a comparison of fire test results of single and double stud walls.

4.16 Comparison with Single Stud Wall Test Results

The time-temperature curves from the fire tests of single stud LSF walls with 92 mm and 150 mm stud depths conducted at 0.4 LR by past researchers are compared with the double stud LSF wall test results from this study. This includes both the non-cavity insulated and cavity insulated LSF walls. The non-cavity insulated 92 mm and 150 mm single stud wall tests are referred to as Tests-SS-T1 and SS-T2 while the cavity insulated single stud wall is referred to as SS-T3. Non-cavity insulated single stud wall tested under non-load bearing conditions (NLB) is referred as SS-T4. Details about the construction and testing procedures of the non-cavity insulated LSF wall can be found in Ariyanayagam and Mahendran (2018b). Likewise, details about the cavity insulated LSF walls can be found in Gunalan et al. (2013). However, Test-SS-T3 wall was tested under 0.2 LR. It is also considered here since the effect of load ratio does not have a significant effect on the time-temperature curves. Table 4.3 presents the details of the fire tests considered in the comparison.

Comparisons of the fire test results are made in three groups. Firstly the non-cavity insulated double studs walls are compared against the respective single stud LSF walls. Secondly, the cavity insulated LSF walls which include double and staggered stud walls are compared. Lastly, the staggered and shaft liner non-cavity insulated walls are compared against the single stud LSF walls. The important comparison results and corresponding discussions are presented next.

4.16.1 Comparison of Non-Cavity Insulated Fire Test Results - Tests-T1, T2, T4, SS-T1 and SS-T2

The time-temperature curves of Pb1 from Tests-T1, T4, SS-T1 and SS-T2 exhibited similar behaviour and agreed well with the standard fire curve. The time-temperature

Table 4.3: Details of single and double stud wall tests considered for comparison

Test Name	Description	Stud Depth (mm)	Cavity Depth (mm)	Stud Thickness (mm)	Failure Time (min)	Load Ratio	Critical HF (°C)	Critical CF (°C)
T1	Double Stud	90	0.95	200	176	0.4	459	411
T2	Double Stud	90	0.75	200	132	0.4	593	514
T4	Double Stud	70	0.95	160	171	0.4	505	380
T5*	Double Stud	90	0.95	200	76	0.4	447	361
T7 ⁺	Double Stud	90	0.95	200	81	0.4	438	363
T8	Shaftliner	90	0.75	196	240	NLB	985	969
T9	Staggered Stud	90	0.75	150	191	NLB	806	728
T10 ⁺⁺	Staggered Stud	90	0.95	150	85	0.4	538	486
SS-T1**	Single Stud	92	1.15	92	127	0.4	477	389
SS-T2**	Single Stud	150	1.15	150	162	0.4	500	425
SS-T3**+	Single Stud	92	1.15	92	101	0.2	700	357
SS-T4**	Single Stud	92	1.15	92	197	NLB	987	94

* Cavity insulation on both stud rows - Double stud wall

+ Cavity insulation on ambient stud rows only - Double stud wall

++ Staggered cavity insulation- Staggered stud wall

*+ Cavity insulation single stud wall

** Non-cavity insulated single stud wall

curve for Pb1-Pb2 interface on the fire side of the double stud wall (Test-T1) was flat from 80 to 110 min of fire exposure while that of Test-SS-T1 showed a steep rise as shown in Figure 4.60. A flat Pb1-Pb2 curve was observed in Test-SS-T2 with 150 mm cavity depth only for a shorter time period as shown in comparison to Test-T1. This difference is due to the presence of a larger cavity in double stud LSF wall Test-T1. Therefore, it can be inferred that larger the cavity the time-temperature curve becomes flatter during the 80 to 110 min period of fire exposure (200 vs 150 mm cavity depth). This pattern is not noticeable in Test-SS-T1 as the cavity depth is only 92 mm. The reduced heat transfer is reflected across all the plasterboards from the fire side cavity (Pb2) to the ambient side (Pb4) in Tests-T1 and SS-T2, but the time-temperature curves kept rising in Test-SS-T1. Due to the increased heat transfer rate and smaller cavity depth Test-SS-T1 wall panel survived only 127 min while Test-SS-T2 survived 162 min (Table 4.3).

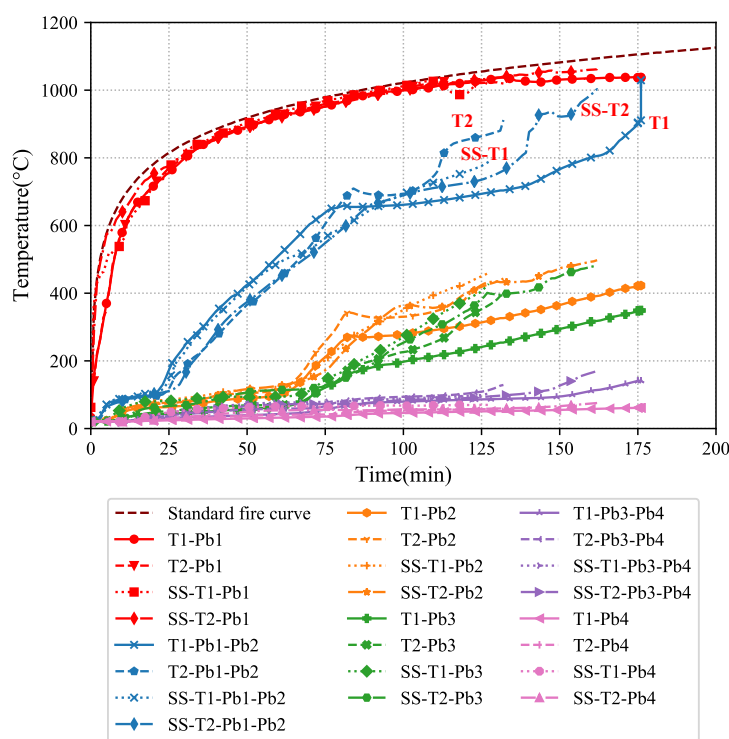


Figure 4.60: Comparison of average plasterboard time-temperature curves from Tests-T1, T2, SS-T1 and SS-T2

The plasterboard time-temperature curve from Test-T2 with thinner studs (0.75 mm) also exhibited a similar behaviour when compared with the results of Tests-SS-T1 and SS-T2 as shown in Figure 4.60. The plateau length was shorter for Test-T2 than for Test-T1 because there was a significant plasterboard fall-off in Test-T2. The

plasterboard fall-off on the fire side caused by higher lateral deflection in thinner (0.75 mm) stud wall contributed to the premature rise in the Pb1-Pb2 time-temperature curve in Test-T2 at 110 min resulting in a reduced failure time of 132 min in Test-T2. Test-T3 was not considered in the comparisons because it was conducted at a higher LR of 0.6.

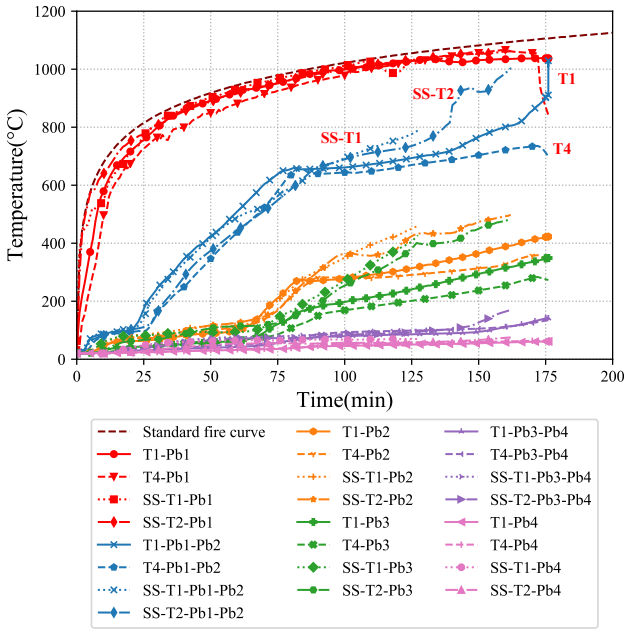


Figure 4.61: Comparison of average plasterboard time-temperature curves from Tests-T1, T4, SS-T1 and SS-T2

In the fire tests the temperatures were measured at quarter heights in Studs3 and 4 and at mid-height in Studs2 and 5. However, only the critical (failed) stud time-temperature curves are used, i.e. Stud3-Top curve for the comparisons of Tests-T1 and T4, Stud4-Top for Test-T2, and Stud4-Mid for Test-SS-T1 and Stud4-Top curve for the comparisons of Test-SS-T2. The stud time-temperature curves of Tests-T1, T2, SS-T1 and SS-T2 are compared in Figure 4.62 and the curves of Tests-T1, T4, SS-T1 and SS-T2 are compared in Figure 4.63. The hot flanges of all tests exhibited a similar behaviour until 60 min of fire exposure after which there was an increase in the slope of the curves. The T1-Stud3-Top-Fire-HF curve became flat after 80 min whereas the SS-T1-Stud4-Mid-HF kept on increasing rapidly. The cold flange time-temperature curves followed a similar pattern until 80 min after which the T1-Stud4-Mid-Fire-CF curve exhibited only a gradual increase while the SS-T1-Stud4-Mid-CF increased rapidly as shown in Figure 4.62. This is because of the unique plasterboard time-temperature

curve pattern observed in double stud walls. Further there is no contact between the fire and ambient side stud rows due to the presence of a 20 mm air gap in Tests-T1 and T4. This prevents the heat transfer through conduction and the heat energy in the fire side cold flange radiates and convects into the air cavity thereby influencing the unique heat transfer mechanism in double stud LSF walls. The unique behaviour was also evident in double stud wall Test-T4 where the T4-Stud3-Top-Fire-HF time-temperature curve exhibited a flat region despite the usage of 70 mm studs with a reduced cavity depth as shown in Figure 4.63.

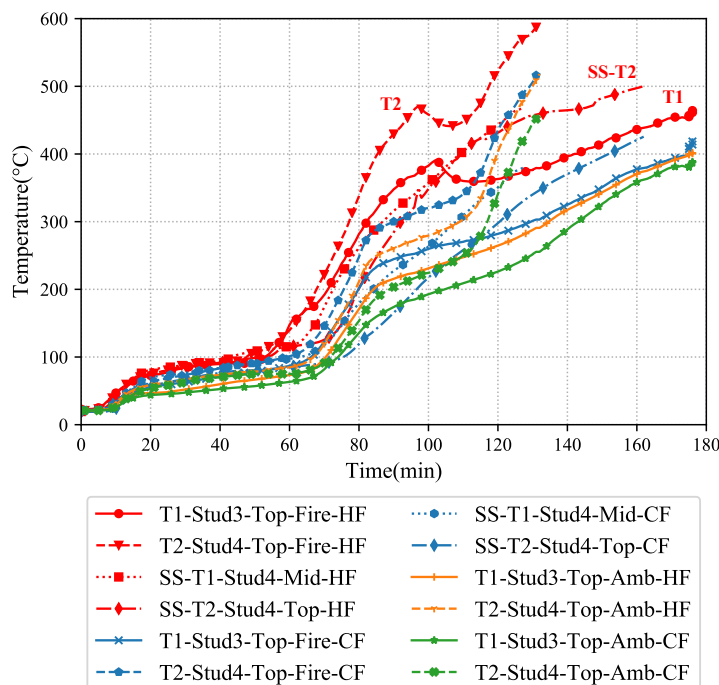


Figure 4.62: Comparison of critical stud time-temperature curves from Tests-T1, T2, SS-T1 and SS-T2

The time-temperature curves of T1-Stud3-Top and SS-T2-Stud4-Top are also compared in Figure 4.62. The hot flange temperatures in Test-SS-T2 were less than those in Test-T1 (SS-T2-Stud4-Top-HF vs T1-Stud3-Top-Fire-HF) in the initial stages till 100 min despite the cavity depth being less than that in Test-T1 (150 vs 200 mm). In double stud walls, the heat transfer cannot happen to the ambient side row of studs through pure conduction whereas in a single stud wall, it is possible up to the ambient side cold flange. This further explains the reason for the lower hot flange temperatures of Test-SS-T2. But due to the increased cavity depth and discontinuity between the two rows of studs in double stud walls, a flat region develops in the time-temperature curves of

Test-T1, resulting in higher stud failure times. This behaviour is similar in double stud walls with lesser cavity depth of 150 mm as in Test-T4. The stud time-temperature curve T4-Stud3-Top-Fire-HF exhibits the flat region confirming the assumptions.

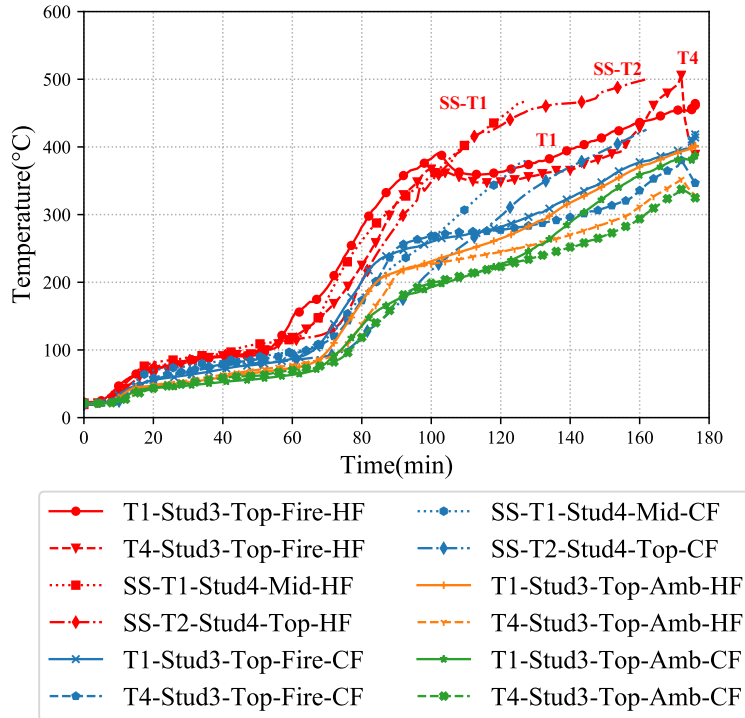


Figure 4.63: Comparison of critical stud time-temperature curves from Tests-T1, T4, SS-T1 and SS-T2

The time-temperature curves of T2-Stud4-Top and SS-T1-Stud4-Mid are also compared in Figure 4.62. These are similar to those of Test-T1. The hot flange temperatures were similar for Tests-T2 and SS-T1 until 95 min after which the curve T2-Stud4-Top-Fire-HF exhibited a flat region similar to Test-T1. But the SS-T1-Stud4-Mid-HF curve increased rapidly. This confirms the unique heat transfer phenomenon in double stud walls. In the case of cold flange time-temperature curves the SS-T1-Stud4-Mid-CF temperature was less than that of T2-Stud4-Top-Amb-CF because of the thinner stud (0.75 mm) used in Test-T2. But a flat region was not observed in Test-SS-T1 as the cavity depth was only 92 mm and the stud thickness was 1.15 mm. However, the hot flange temperature of Test-T2 was higher than in Test-SS-T2 (T2-Stud4-Top-Fire-HF vs SS-T2-Stud4-Top-HF) as shown in Figure 4.62. This is because of the higher stud thickness of 1.15 mm in Test-SS-T2 compared to 0.75 mm in Test-T2. The cold flange temperature SS-T2-Stud4-Top-CF recorded a lower temperature in comparison with T2-Stud4-Top-Amb-CF. The 150 mm single stud wall in Test-SS-T2 survived 162 min

while the double stud wall in Test-T2 survived only 132 min due to the more slender studs used in Test-T2. There was also a significant plasterboard fall-off on the fire side, resulting in an early failure in Test-T2. As mentioned earlier, Test-T3 was not considered in the comparisons (higher LR and thus reduced failure time).

4.16.2 Comparison of Cavity Insulated Fire Test Results - Tests-T5, T7, T10 and SS-T3

Comparison between the cavity insulated wall fire test results are presented in Figures 4.64 and 4.65. Average plasterboard time-temperature curves compared in Figure 4.64 shows that the flat region exhibited by the non-cavity insulated double stud LSF walls were not noticeable in the cavity insulated wall fire test results. Cavity insulated single stud tests results also matched this behaviour wherein no flat region was observed in the time-temperature curves of plasterboard. This shows the entrapment of heat on the fire side in cavity insulated LSF walls. The plasterboard interface time-temperature curve Pb1-Pb2 in single stud wall (SS-T3-Pb1-Pb2) recorded temperatures higher than its competitors. However, the pattern exhibited by plasterboard time-temperature curves of single, double and staggered stud LSF walls with cavity insulation were mostly similar wherein, the plasterboard interface time-temperature curve Pb1-Pb2 exhibited a steep increase after 20 min in all fire tests. Likewise, the fire side cavity surface time-temperature curved Pb2 was flat till 50 min in all fire tests, after which a steep increase in the curve was noticed. Also, similar to the SS-T3-Pb1-Pb2 curve the SS-T3-Pb2 curve was higher in comparison with other cavity insulated fire test results. This proves that, despite the difference in LSF wall configuration, the presence of cavity insulation results in similar time-temperature curves due to the entrapment of heat on the fire side of the test wall.

Heat entrapment on the fire side of the test wall results in increased temperatures on the stud hot flanges as shown in Figure 4.65. As a result, there arises a huge difference in temperatures between the stud hot and cold flanges in cavity insulated LSF walls in comparison with non-cavity insulated LSF walls. This causes larger lateral deflection thereby resulting in fire side plasterboard open-up. Plasterboard open up causes hot gases from the furnace to enter the cavity. This results in sudden rise of temperatures on the cold flanges of studs as well in double stud LSF walls. As the fire side cold

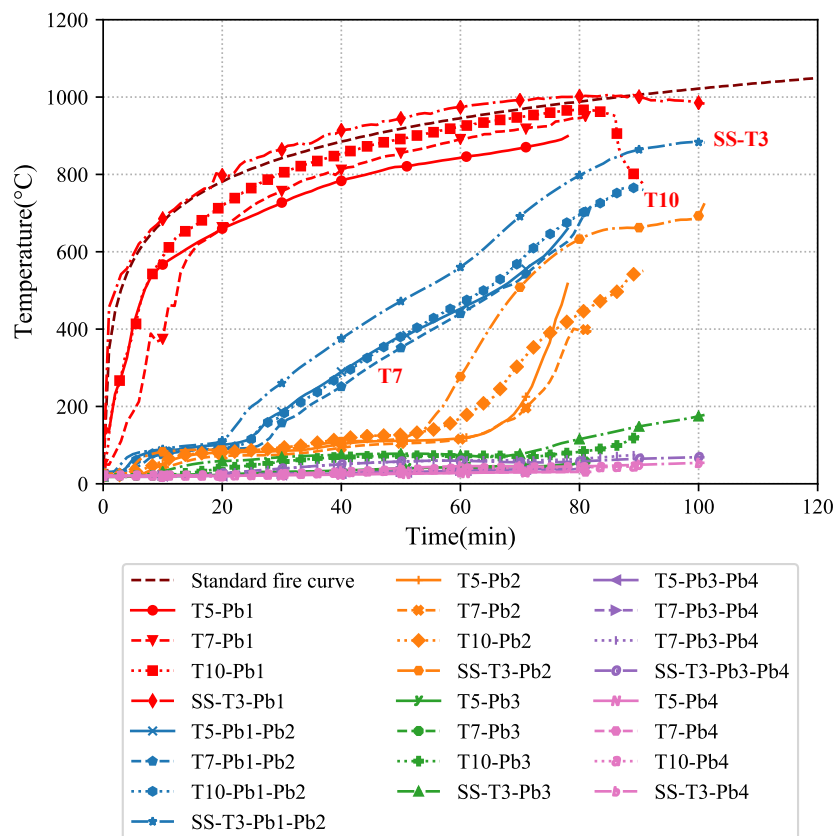


Figure 4.64: Comparison of average plasterboard time-temperature curves from Tests-T5, T7, T10 and SS-T3

flanges do not have contact with the ambient side plasterboards, the heat gained by the cold flanges could not be transferred to the adjacent plasterboards. Whereas, in the case of single stud LSF wall, the SS-T3-Stud2-Mid-CF temperatures were well below the double stud wall cold flange T5-Stud3-Top-Fire-CF temperature.

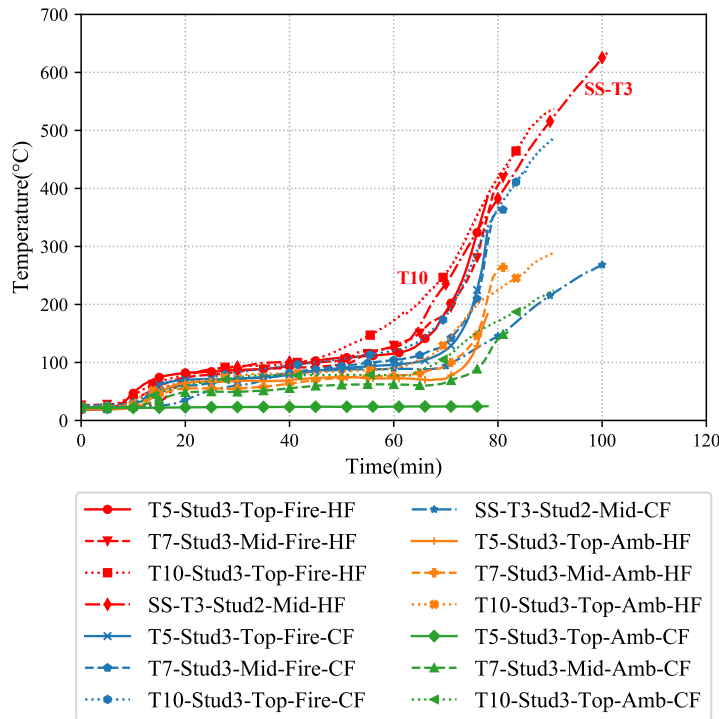


Figure 4.65: Comparison of critical stud time-temperature curves from Tests-T5, T7, T10 and SS-T3

In single stud LSF walls the cold flanges are in contact with the ambient side plasterboard cavity, thereby transferring the heat to the ambient side plasterboards. This is also evident from the higher SS-T3-Pb4 ambient side temperatures as shown in Figure 4.64. The ambient side hot flange temperatures T5-Stud3-Top-Amb-HF and T7-Stud3-Mid-Amb-HF also increase significantly in double stud LSF walls due to the plasterboard open up. However, in staggered stud LSF wall Test-T10, the ambient side hot flange (T10-Stud3-Top-Fire-HF) recorded temperatures less than double stud wall temperatures. In staggered stud wall system the ambient side hot flanges are 60 mm away from the fire side plasterboard cavity influencing the reduced ambient side hot flange temperatures.

4.16.3 Comparison of Non-Cavity Insulated Shaftliner and Staggered Stud Fire Test Results - Tests T8, T9 and SS-T4

Non-load bearing fire Tests-T8 and T9 are compared against single stud wall fire Test-T4 tested also tested under non-load bearing conditions to understand the temperature profile in complex LSF wall configurations in comparison with single stud wall configurations. Fire side cavity surface (Pb2) time-temperature curve followed a similar trend for the initial 80 min in all the fire tests. However, after 80 min a plateau region was observed in T9-Pb2 (staggered stud wall) as shown in Figure 4.66. This behaviour is due to the wider cavity in Test-T9 (cavity depth 150 mm). There prevails a natural convection within the cavity thereby introducing a plateau region on the time-temperature curve. This behaviour was not evident on the fire side cavity surface of Tests-T8 and SS-T4 as the cavity depth was only 90/92 mm and the Pb2 temperatures were higher than those in Test-T3. In Test-T8, due to the cavity being split into two by the middle plasterboard layer which absorbs the heat from Pb2 surface, the effect of natural convection within the cavity was reduced.

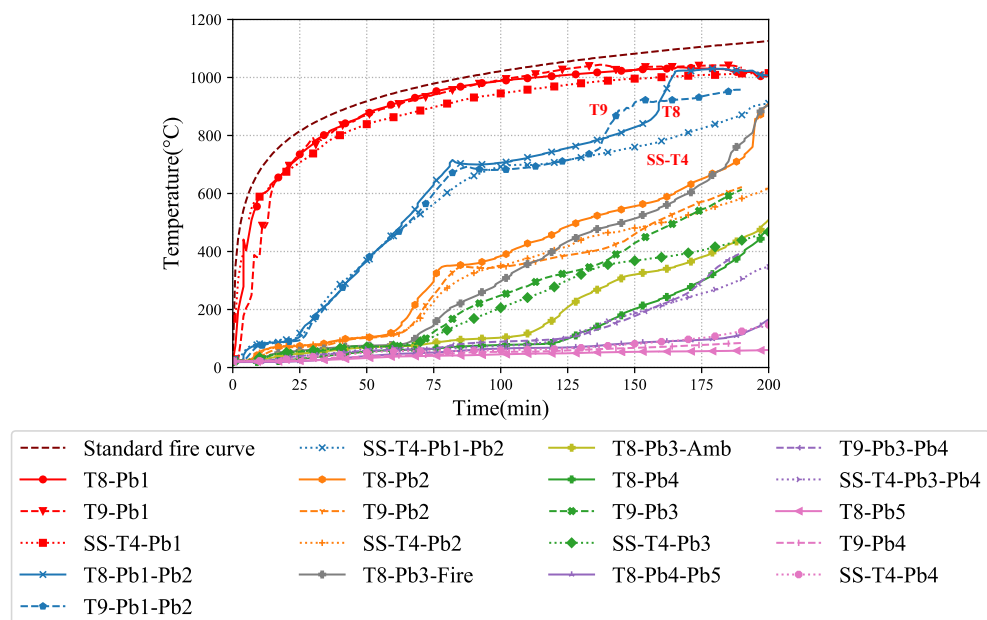


Figure 4.66: Comparison of average plasterboard time-temperature curves from Tests-T8, T9 and SS-T4

The plasterboard time-temperature curve on the ambient side cavity (T9-Pb3) in Test-T9 (150 mm staggered stud) recorded temperatures significantly higher in comparison with Test-T8 (T8-Pb4). In Test-T8, the presence of an additional plasterboard

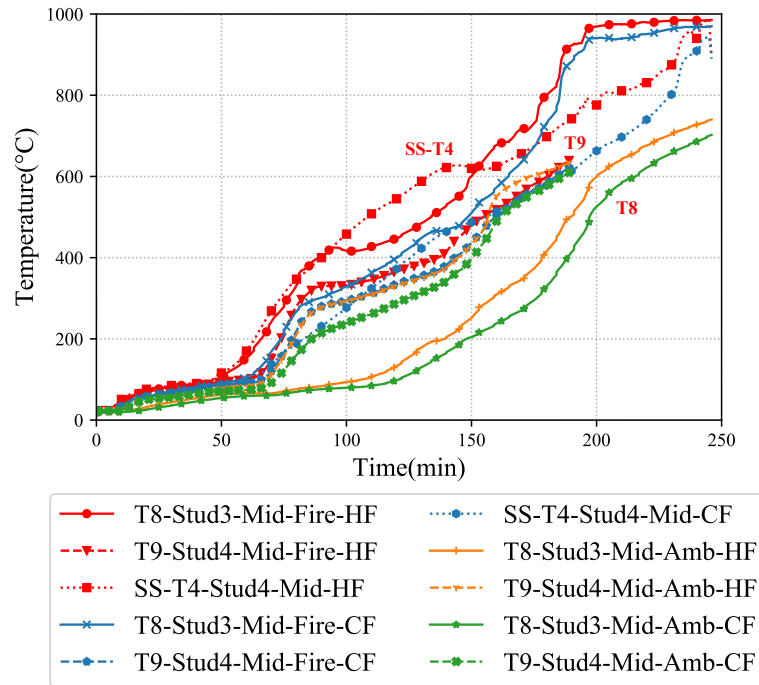


Figure 4.67: Comparison of critical stud time-temperature curves from Tests-T8, T9 and SS-T4

splits the cavity into two resulting in lower temperatures in the ambient side cavity. This is also evident from the lower ambient side plasterboard time-temperature curve (T8-Pb5) in comparison with T9-Pb4 as shown in Figure 4.66. However, the ambient side plasterboard temperature in Test-T9 (T9-Pb4) was lower than that in Test-SS-T4 (SS-T4-Pb4). This is due to the wider cavity in Test-T9 (150 mm) than in Test-SS-T4 (92 mm).

Similar observations can be made regarding the stud time-temperature curves of Tests-T8, T9 and SS-T4. The hot flange temperatures recorded in Test-T9 (T9-Stud4-Mid-Fire-HF) were lower than those in Tests-T8 and SS-T4 because of the wider cavity in Test-T9. This shows that the heat conducted through the studs was lost into the cavity due to the presence of large air volume within the wider cavity. The natural convection prevailing within the cavity significantly contributes to this behaviour. Non-load bearing walls are mostly governed by the insulation failure criterion and the ambient side plasterboard temperatures determine this failure. But the failure of staggered stud wall in Test-T9 was due to structural inadequacy criterion (stud failure). This is because the plasterboard lining provided lateral restraint to only one flange of the stud due to the staggered stud arrangement used. However, in Tests-T8 and SS-T4,

both flanges of the studs were effectively restrained by plasterboard lining. This shows that non-load bearing LSF walls also need effective lateral restraints via plasterboard lining.

4.16.4 Comparison of Axial Displacement and Lateral Deflection Versus Time Curves

The axial displacements and lateral deflections of the critical studs with respect to time are compared in Figures 4.68 and 4.69. This includes comparison between non-cavity insulated and cavity insulated walls.

In non-cavity insulated wall tests, the maximum axial displacements recorded by the non-cavity insulated walls in Tests-T1, T2, T4, SS-T1 and SS-T2 were -6.79, -6.83, -5.59, -12 and -14.86 mm, respectively as shown in Figure 4.68 (a). Likewise, the maximum lateral deflections recorded were -14.44, -18.84, -24.74, -30.56 and -13.47 mm, respectively, and are shown in Figure 4.68 (b). The axial displacements were higher in single stud wall Tests-SS-T1 and SS-T2 while the lateral deflections were higher in Test-SS-T1. The axial displacements for double stud wall Tests-T1, T2 and T4 followed a similar pattern till 65 min. The axial displacement curves in Tests-SS-T1 and SS-T2 were higher throughout the compared time frame for other double stud wall fire tests. But the lateral deflections were similar in all the fire tests. The lateral deflection curve exhibited a rapid increase after 80 min in Test-SS-T1 while it increased gradually in other fire tests. It is to be noted that the studs in single stud LSF walls are effectively restrained laterally on both flanges by plasterboards at 300 mm intervals. But in the case of double stud walls the plasterboards provide lateral restraint only on the fire side hot flange and ambient side cold flange at 300 mm intervals. Instead, lateral restraints are provided through noggings at 1000 mm intervals but the flanges are not fully restrained. Despite the reduced lateral restraint conditions, the non-cavity insulated double stud walls exhibit better fire performance over single stud LSF walls.

In cavity insulated wall tests, the maximum axial displacements recorded by Tests-T5, T6, T7, T10 and SS-T3 were 15.86, 5.98, 4.13, -7.78 and 16.01 mm, respectively. However, in double stud walls the maximum axial displacement occurred at the end of the fire test while in staggered and single stud wall Tests-T10 and SS-T3 the axial

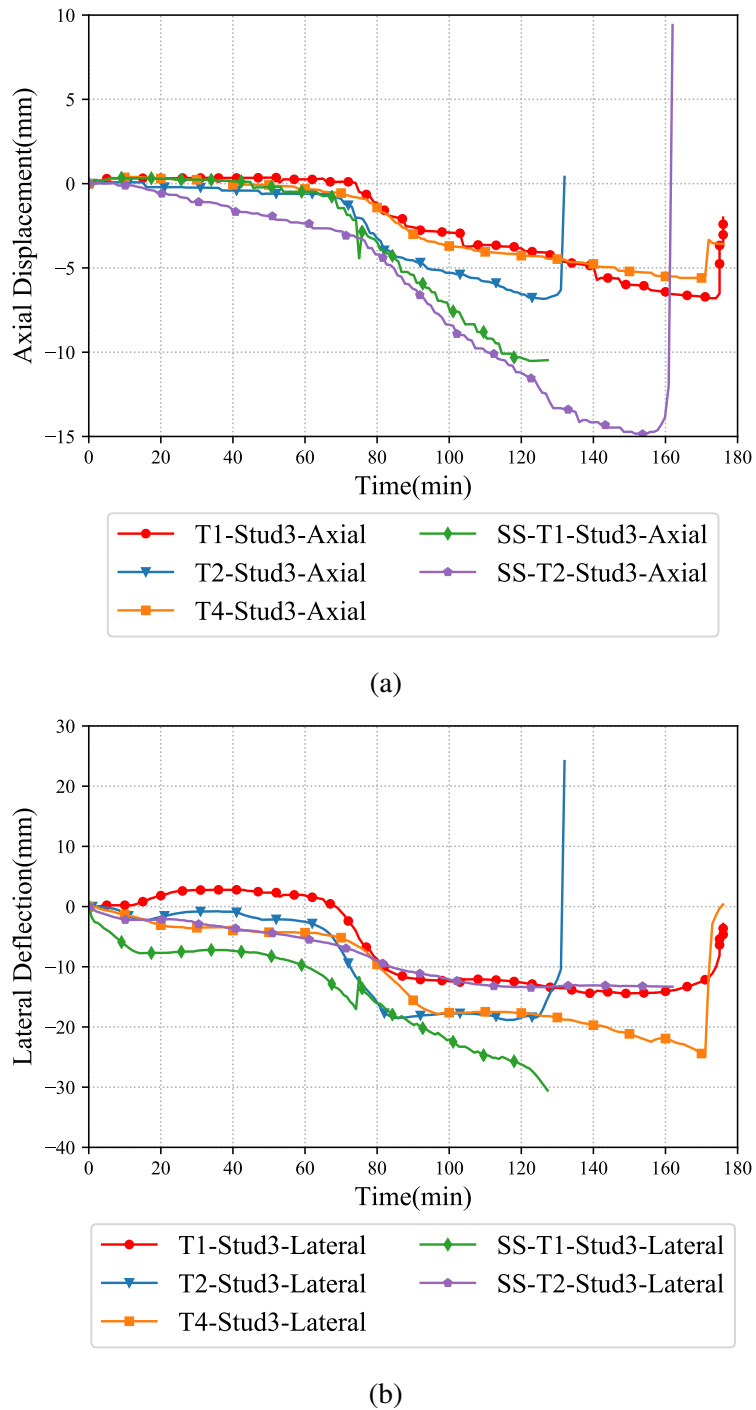


Figure 4.68: Comparison of axial displacement and lateral deflection versus time curves from Tests-T1, T2, T4, SS-T1 and SS-T2 results - (a) Axial displacement versus time and (b) Lateral deflection versus time

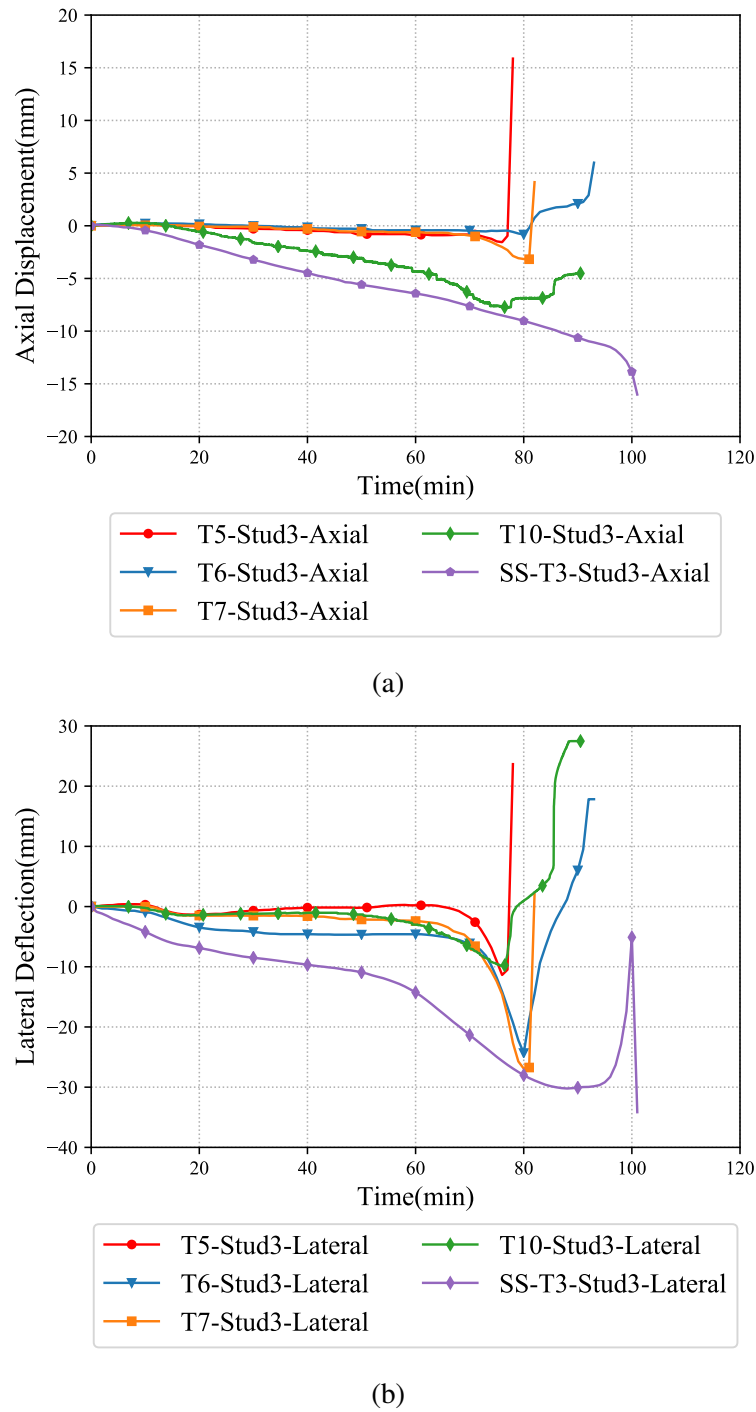


Figure 4.69: Comparison of axial displacement and lateral deflection versus time curves from Tests-T5, T6, T7 and SS-T3 results - (a) Axial displacement versus time and (b) Lateral deflection versus time

shortening was progressive throughout the fire test as shown in Figure 4.69 (a). But, the maximum axial displacement was recorded in single stud wall Test-SS-T3. Likewise, the maximum lateral deflections recorded were 23.65, -24.33, -26.91, 27.48 and -34.15 mm as shown in Figure 4.69 (b). Similar to axial displacement, the lateral deflection was higher for the single stud wall Test-T3. However, the lateral deflection was not significant during the double and staggered stud wall tests and occurred at the end of the fire test. This shows the superior performance of cavity insulated double and staggered stud walls in comparison with single stud LSF walls. Also, it is to be noted that the nogging restraints provided to the staggered stud wall Test-T10 was through omega noggings, and not through conventional unclipped channel section noggings.

4.17 Conclusions

This chapter has described the experimental investigation conducted on a series of the complex LSF wall configurations under fire conditions. Using standard fire tests a detailed investigation was conducted to study the effects of various LSF wall configurations in fire. Single stud LSF wall test results from previous research at the QUT Wind and Fire Engineering Laboratory were also compared with the results of double and staggered stud walls to further understand the effects of double and staggered stud wall configurations. The following conclusions can be drawn from this experimental study.

- A delayed heat transfer mechanism was observed in double stud walls in comparison with single stud walls. This is because of the wider cavity and the discontinuity in double stud walls caused by the 20 mm air gap.
- The time-temperature curve of the fire side plasterboard interface becoming a plateau was identified as the reason for the increased failure times of double stud walls in Tests-T1, T2 and T4. This causes a reduction in the temperature of the fire side hot flange in double stud walls.
- The plateau region in the time-temperature curve was not observed in the hot flange of single stud wall in Test-SS-T2 even with a larger cavity of 150 mm. This infers that the unique time-temperature profile of hot flanges exhibiting a

plateau region is caused by the discontinuous stud arrangement in double stud LSF walls.

- Cavity depth of the LSF wall was also found to have a significant influence on the time-temperature curves. In addition to the discontinuous stud arrangement, the plateau region in the time-temperature curve was also influenced by the wider cavity as the time taken by the large air volume within the cavity to attain equilibrium increases with increasing cavity depth. This is dependent on the air volume causing natural convection within the cavity. The heat dissipated by the studs through radiation into the cavity also contributed to the plateau region, which was evident in the time-temperature curves of plasterboards and studs.
- In non-cavity insulated double stud walls, the fire side row of studs tend to lose heat into the larger cavity due to the 20 mm gap between the ambient stud rows resulting in delayed heat transfer mechanism, thereby increasing the failure time of the test wall under fire conditions.
- Despite the absence of plasterboard restraint at 300 mm screw locations on one flange, the axial displacements and lateral deflections were lower in double stud walls (Test-T1 and T2) in comparison with single stud walls (Tests-SS-T1 and SS-T3), confirming the presence of thermal bowing, which has a significant influence on the fire performance of load bearing LSF walls.
- In the cavity insulated double stud wall Tests-T5 and T6, heat entrapment on the fire side stud rows was observed, resulting in premature failure of the test wall under load bearing conditions. This is because of the heat accumulation on the fire side due to the cavity insulation trapping the heat flow, thereby increasing the stud hot flange temperatures. The heat entrapment causes a relatively large temperature gradient on the stud flanges in comparison with non-cavity insulated double stud walls, resulting in premature failures.
- The plateau region in the time-temperature curve was not observed in the shaft-liner LSF wall Test-T8. However, a delayed heat transfer was noticed from the fire side to ambient side resulting in better temperature gradient along the plasterboards and studs in comparison with double stud walls. This is because of the

cavity split into two by the middle plasterboard layer. Due to the limitations in the experimental set-up, load bearing test could not be conducted for shaftliner walls and will be investigated through structural numerical models in Chapter 7.

- Staggered stud LSF wall fire Test-T9 conducted under non-load bearing conditions failed due to structural inadequacy. Failure of non-load bearing LSF wall under structural inadequacy criterion is unusual and has not been investigated before. However, this unusual failure was due to the absence of adequate lateral restraints from plasterboard on one flange and also partially due to the absence of intermittent nogging restraints resulting in excessive thermal bowing. Intact ambient side plasterboard acting as an additional loads on the studs subjected to higher temperatures also contributed to this structural failure.
- Cavity insulated staggered stud wall Test-T10 under load bearing conditions with the addition of omega noggings and end cleats resulted in better structural fire performance in comparison with cavity insulated double stud wall Tests-T5 and T6 conducted under the same load ratio. This infers that the usage of omega noggings and end cleats can significantly improve the structural fire performance of staggered stud LSF wall in comparison with the double stud wall counterparts.
- Currently used heat transfer Finite Element (FE) models to predict the thermal behaviour of LSF walls assume only radiation effects to be predominant within the cavity facing surfaces with an emissivity co-efficient of 0.9 for the cavity facing surfaces, neglecting the convective heat transfer component inside the cavity. This assumption represents nearly a black body surface and their FE models were found to be adequate for LSF walls with a cavity depth up to 90 mm. However, in wider cavity LSF walls, due to the presence of large air volume, the existing heat transfer model might not be able to simulate the plateau region in non-cavity insulated walls or the sudden increase in the stud time-temperature curves in the cavity insulated wall fire tests. Therefore, the fire test results from this chapter will be useful to develop and validate the thermal numerical models to simulate the observed heat transfer effects. Based on the thermal models, structural models will also be developed to predict the failure times of the complex LSF wall systems.

Chapter 5

Thermal FE Modelling of Complex LSF Walls

5.1 Introduction

Experimental investigation on LSF walls under fire conditions can be used to determine the FRL under different load ratios. However, the experimental approach is time consuming and expensive. To overcome this shortcoming, numerical methods are used to predict the same. This chapter focuses on developing a robust thermal model to predict the temperature distribution in LSF wall in fire. Several numerical models using Finite Element (FE) techniques have been developed by past researchers to simulate the heat transfer in single stud LSF walls (Feng et al., 2003a; Keerthan and Mahendran, 2012a; Ariyanayagam and Mahendran, 2019). This includes 2D and 3D models using different FE software packages. Majority of the thermal FE models assumed the heat transfer by conduction through plasterboards and studs from fire side to the ambient side. The cavity region was assumed to be closed and corresponding boundary conditions were specified in the FE model. Cavity radiation was considered as the predominant mode of heat transfer within the cavity to simulate the heat transfer mechanism in LSF walls (Rusthi et al., 2017b; Ariyanayagam and Mahendran, 2019). However, this assumption holds good only to LSF walls with single row of studs as the stud flanges are in contact with the adjoining plasterboard. Also, the previous models were created by considering a closed cavity which does not precisely represent the experimental fire tests. These assumptions did not significantly affect the time-temperature curves due

to the presence of single row of studs resulting in a continuous contact within the cavity from fire side to the ambient side in previous research studies. However, in the case of complex LSF walls such as double stud, staggered stud and shaftliner LSF walls, there prevails a discontinuous stud arrangement, resulting in a different heat transfer mechanism within the cavity in comparison with single stud LSF wall as shown in Figure 5.1.

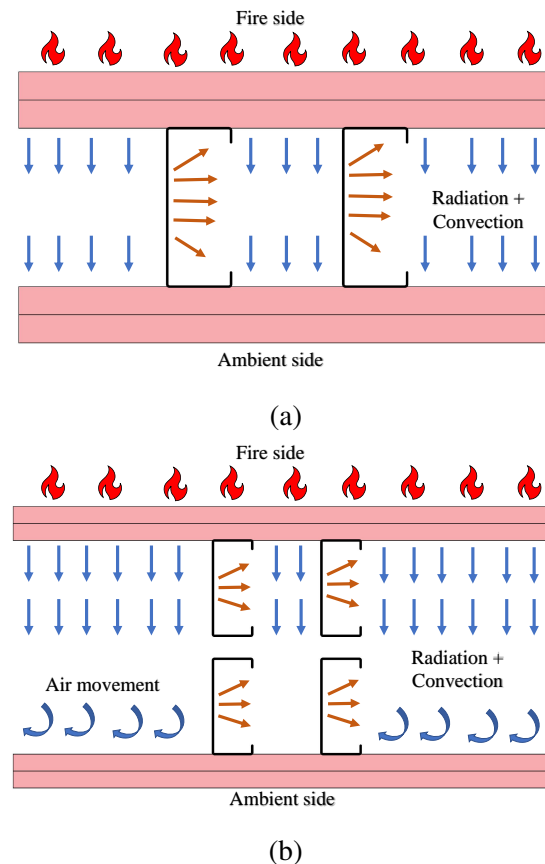


Figure 5.1: Heat transfer mechanism in (a) Single stud (b) Double stud LSF walls

Therefore, to address these issues, a detailed literature review was first undertaken and the most suitable thermal models were considered to predict the temperature profiles of the conducted full-scale fire tests in Chapter 4. The developed numerical model was then used to perform thermal analysis for all the conducted full-scale fire tests to predict the time-temperature curves of studs and plasterboards. The predicted time-temperature curves of stud hot and cold flanges were then be used to determine the structural failure times of the complex LSF wall systems and also to validate against the conducted full-scale fire tests. To solve the above-mentioned advanced numerical models it was essential to utilize the availability of the computational resources

efficiently.

The advent of high performance computing has helped to address problems of higher order numerical complexity with the advanced processing power. The speed of a computer is determined by the quantum of parallel operations that can be performed in any given time. Computers used for general activities have processing power in a range up to 12 GHz (Giga Hertz), whereas in a high-performance computing facility many nodes will be linked to parent hub forming a cluster. As a result, the processing speed that can be practically achieved can reach up to Tera-Hertz. Finite Element Analysis (FEA) by default uses single point precision memory for solving the numerical analysis as this memory is extracted from the processor in the local node of the computer. Graphical processing unit (GPU) is also called for the analysis in some of the FEA packages (for example ABAQUS), which can then utilize the double point precision memory to solve the numerical problem. Numerical solving time for a problem in the High Performance Computing (HPC) can be exponentially increased by deploying GPU vector parallelization technique. This is generally achieved by clustering the CPU processing cores with the GPU processing cores to minimize the solver time of the FEA package. High-performance computing facility available at the Queensland university of Technology (QUT) was used in this research to develop and analyse the thermal numerical models. ABAQUS and FDS thermal were run in the HPC cluster which operates on Linux operating system. However the source code of SAFIR was modified to make it run in the Linux HPC cluster available at QUT. This chapter presents the details of the thermal modelling of complex LSF walls and the results.

5.2 Thermal modelling in SAFIR

SAFIR is a finite element program developed in FORTRAN programming language by the University of Liege to model the behaviour of structures in fire (Franssen and Gerney (2017)). Past researchers have extensively used SAFIR to determine the thermal behaviour of LSF walls with various stud sections in fire. This includes research studies of Keerthan and Mahendran (2012b) and Keerthan and Mahendran (2013) wherein the LSF wall assemblies were modelled in 2D and the thermal analyses were carried out to determine the temperature evolution across the cross-section to simulate the time-

temperature curves from full-scale fire tests. Considering the 2D nature of solving the heat transfer problem for computational efficiency, SAFIR was first considered for creating the thermal FE models. GiD, a universal pre and post-processor software, was used to create the model in 2D for this research study. Temperature dependent thermal properties for steel and gypsum plasterboard in LSF walls were extracted from Dodangoda (2018), which were later confirmed by Steau et al. (2020). Although, the temperature dependant material properties were preloaded in SAFIR for steel and gypsum plasterboard, the apparent thermal properties proposed by Dodangoda (2018) (Figures 5.2 to 5.4) were used in the analysis to better represent the full-scale fire tests. SAFIR solves the heat exchange problem mainly through conduction, which is based on Fourier equation. Firstly, attempt was made to simulate the full-scale fire Test-T1 of a double stud wall from the experimental investigation detailed in Chapter 4.

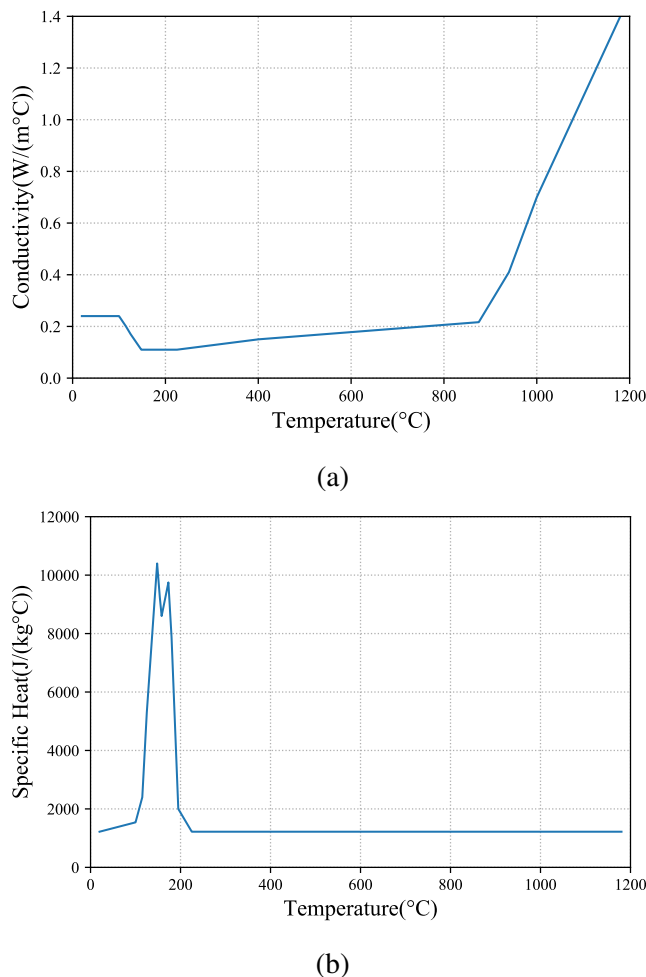
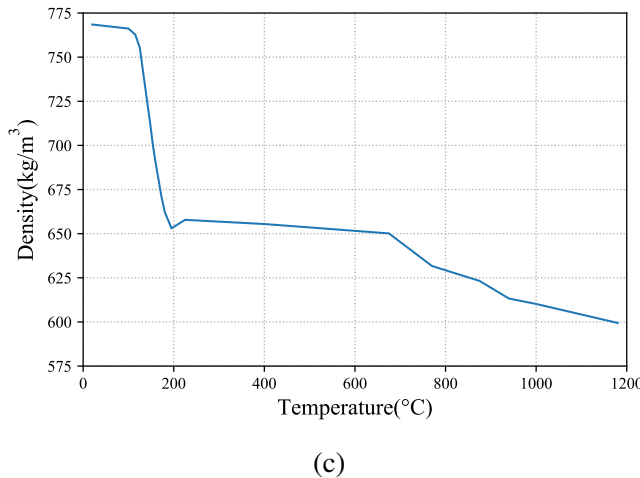
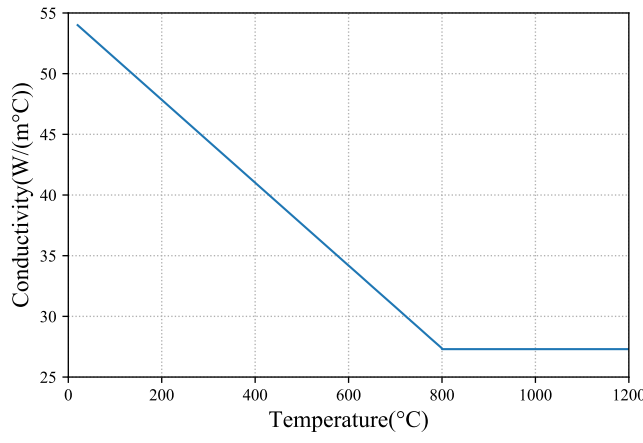


Figure 5.2: Elevated temperature thermal properties of plasterboard from Dodangoda (2018) (a) Conductivity versus temperature (b) Specific heat versus temperature (c) Density versus temperature

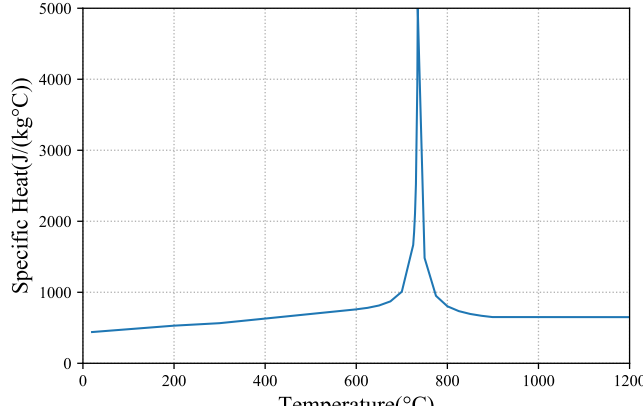


(c)

Figure 5.2: Elevated temperature thermal properties of plasterboard from Dodangoda (2018) (a) Conductivity versus temperature (b) Specific heat versus temperature (c) Density versus temperature

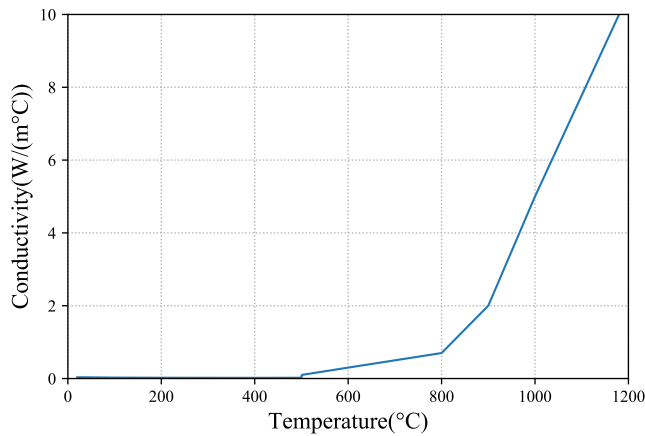


(a)



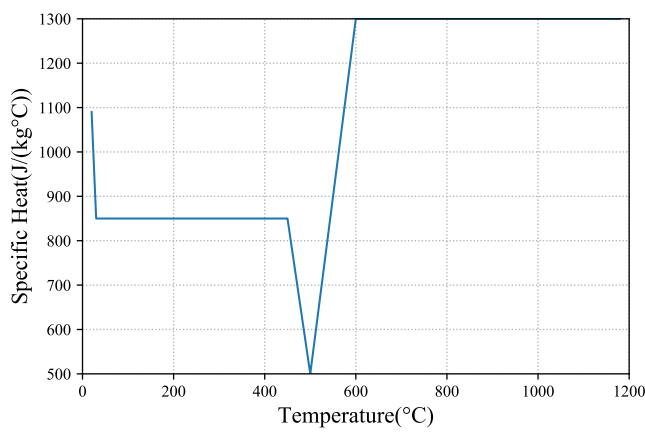
(b)

Figure 5.3: Elevated temperature thermal properties of steel from Dodangoda (2018) (a) Conductivity versus temperature (b) Specific heat versus temperature



(a)

Figure 5.4: Elevated temperature thermal properties of glass fibre insulation from Do-dangoda (2018) (a) Conductivity versus temperature (b) Specific heat versus temperature



(b)

Figure 5.4: Elevated temperature thermal properties of glass fibre insulation from Do-dangoda (2018) (a) Conductivity versus temperature (b) Specific heat versus temperature

The 2D model was created with a width of 0.6 m based on past literature (Keerthan and Mahendran (2012b) and Keerthan and Mahendran (2013)) and the depth of the model was 264 mm representing the overall wall configuration used in Test-T1 (Figure 5.5). Due to symmetry, the models consisted of one set of studs only with 300 mm cavity width on either side of the geometry. Sides of the model were closed with gypsum plasterboard to create a closed cavity. This is because of the limitations in SAFIR to solve models with open cavity. After model creation, Non-uniform rational basis spline (NURB) surfaces were assigned to the 2D model geometry. Frontier conditions were given to the fire and ambient surfaces to specify the ISO 834 standard time-temperature curve on the fire side and “F20” condition on the ambient side to simulate ambient room temperature condition. No frontier conditions were provided to the side plasterboards to simulate adiabatic conditions, wherein assumption of no heat transfer through the sides was considered. Mesh density was maintained globally at 10 mm throughout the model based on initial sensitivity investigations and from past literature. However, the mesh density is automatically adjusted by the GiD pre-processor near the stud and plasterboard contact as SAFIR allows unstructured meshing for 2D thermal analysis. Triangular meshes were used for the thermal model. Figure 5.5 shows the details of the developed double stud model to represent Test-T1 in SAFIR for thermal behaviour prediction. Details about the meshes are shown in Figure 5.6

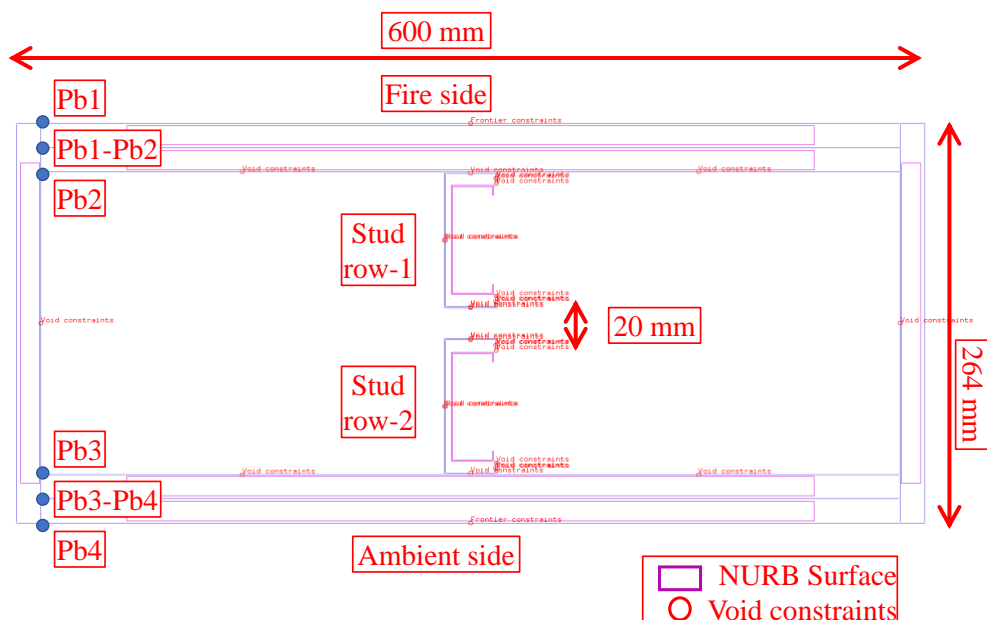


Figure 5.5: 2D model of Test-T1 in SAFIR using GiD interface

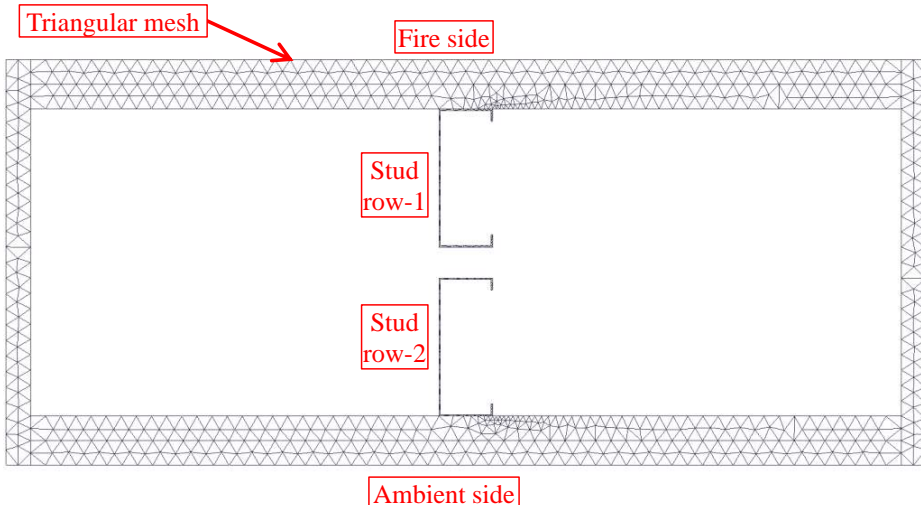


Figure 5.6: 2D model mesh of Test-T1 in SAFIR using GiD interface

The thermal properties were applied to the corresponding surfaces through the input file as GiD-SAFIR interface does not have the ability to assign multiple user defined material properties through graphical input methods. Convective heat transfer coefficient of $25 \text{ W/m}^2\text{ }^\circ\text{C}$ was assigned to the fire side while $10 \text{ W/m}^2\text{ }^\circ\text{C}$ was assigned to the ambient side plasterboard surface. Relative emissivity of 0.9 was specified to the cavity. ISO 834 standard time-temperature curve was used as the fire side boundary condition and was preloaded in the SAFIR package. The boundary condition on the ambient side was assigned to be at room temperature by using the “F20 Frontier condition”. The sides of the model were assumed to be adiabatic. All the models were analysed for a time period of 240 min. The thermal analysis results were post-processed with the help of DIAMOND, a software package specifically designed to view and post process SAFIR analysis results. Thermal analysis output from the models are shown in Figures 5.7 and 5.8.

Some general notations will be followed throughout this paper, to easily identify the surfaces on which thermocouple measurements were taken and considered for comparison as shown in Figures 5.8 and 5.9. Pb1 and Pb4 refer to the fire side and the ambient side plasterboard surfaces. Fire side and ambient side plasterboard cavity surfaces are referred to as Pb2 and Pb3. The interface between the two plasterboard layers on the fire side is referred to as Pb1-Pb2 while the interface between the ambient side plasterboards is referred to as Pb3-Pb4 for all fire tests except Test-T4. The hot and cold flanges of single stud walls are referred to as HF and CF. Also, the average plaster-

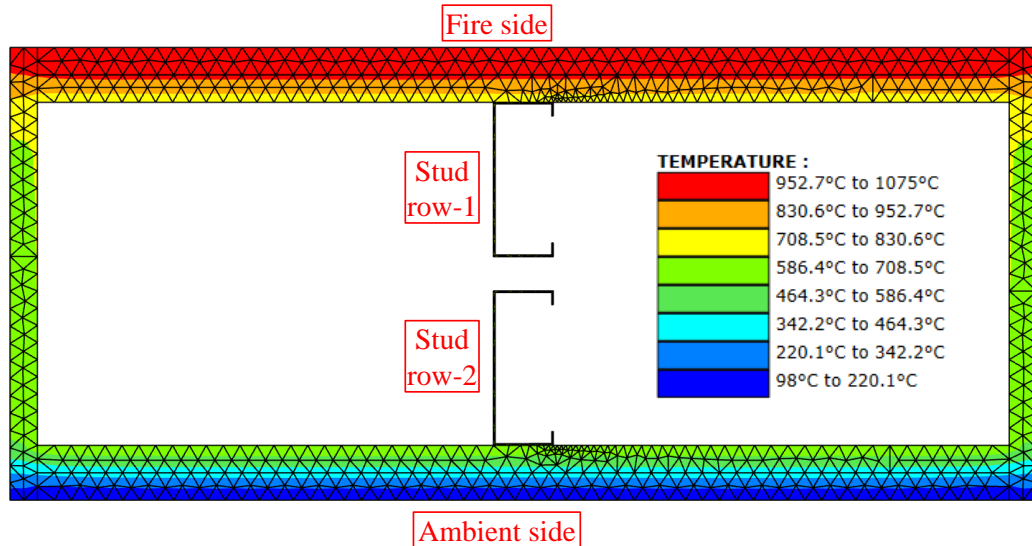
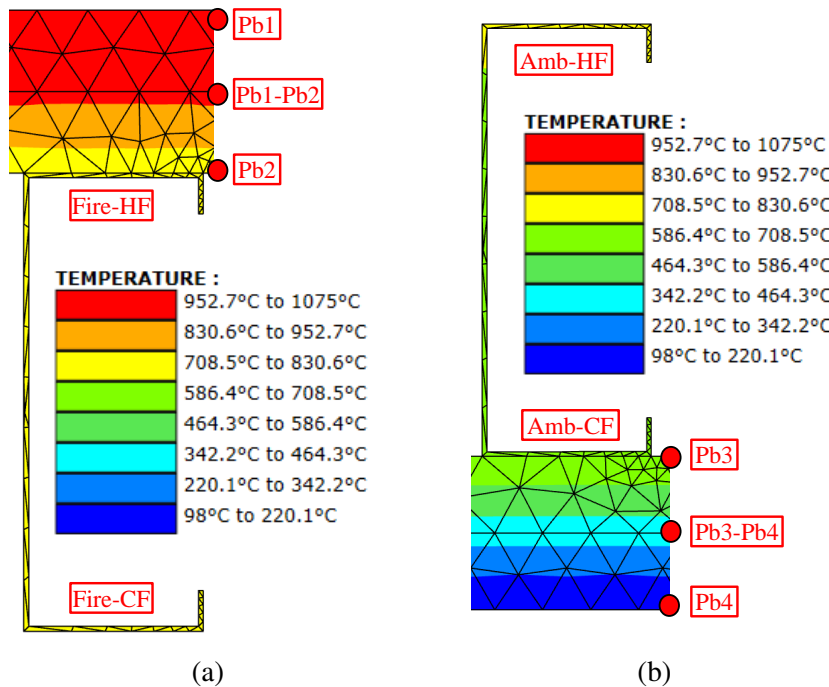


Figure 5.7: Thermal analysis output from SAFIR 2D model

Figure 5.8: Thermal analysis output of studs from SAFIR 2D model (a) Fire side stud
(b) Ambient side stud

board time-temperature curves from the experiments will be used for the comparison against the thermal model predictions. This is because of the large surface area of the specimen in the full-scale fire test resulting in different temperatures along the height of the test wall. However, the stud time-temperature curves measured at mid-height of the test wall (1500 mm) will be considered for comparison as the surface area of the studs is low in comparison with the plasterboards. The mid-height thermocouple is selected instead of average thermocouple measurements along the height because the temperature measurements at the top will be hotter and at the bottom will be cooler. Computing the average would not be ideal for comparison due to the temperature gradient along the stud height. Figure 5.9 (a) compares the plasterboard time-temperature curves from SAFIR thermal analysis against experimental results. The fire side plasterboard temperatures (Pb1) show good agreement in comparison with the experimental results. It is to be noted that the Pb1 time-temperature curve is given as the fire side “Frontier condition” to the thermal model to better simulate the experiments. The fire side plasterboard interface (Pb1-Pb2) time-temperature curve exhibited a plateau region in the experiments. This behaviour is attributed to various factors such as increased convection and moisture transfer. However, simulating these effects are challenging and is beyond the scope of this study. The Pb1-Pb2 time-temperature curve from SAFIR thermal analysis exhibited reasonable agreement with the experimental results till 60 min after which the predictions from SAFIR were higher. Likewise, the fire side cavity (Pb2) and the ambient side cavity (Pb3) time-temperature curves agreed well with the experimental results till 60 and 80 min, respectively, after which a steep increase in the time-temperature curve is observed. This results in increased time-temperature curve on the ambient side plasterboard interface (Pb3-Pb4) and the ambient side plasterboard surface (Pb4).

Figure 5.9 (b) compares the time-temperature curves of the studs. The stud time-temperature curves of all the hot and cold flanges agree reasonably well till 60 min in comparison with the experimental results. However, the predictions after 60 min from SAFIR thermal analysis were higher in comparison with the experimental results. The maximum temperature recorded by T1-Stud4-Fire-HF was 385°C at 176 min while the Fire-HF temperature predicted by SAFIR was 544°C at 176 min. The temperature of the corresponding cold flange from the experiment was 329°C while it was 521°C from

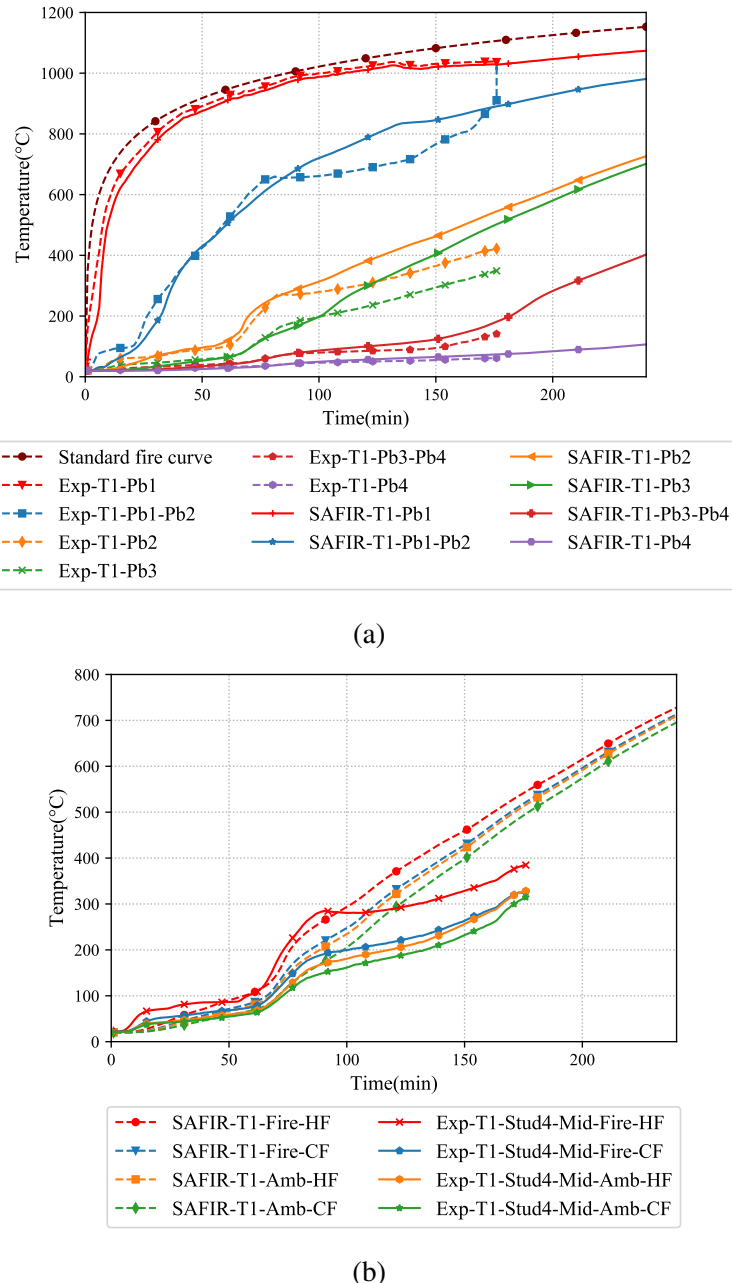


Figure 5.9: Comparison of the time temperature curves from SAFIR thermal analysis and experiments (a) Average plasterboard temperatures (b) Stud4-Mid temperatures

SAFIR thermal model. The ambient side hot and cold flange temperature predictions were also high from the SAFIR thermal model in comparison with the experimental results. It is to be noted that the difference in temperatures between the hot and cold flanges was small in the thermal model predictions. This results in over estimation of the time-temperature curve predictions in comparison with the experiments. The presence of wider cavity in double stud LSF walls (200 mm) in comparison with conventional single stud LSF wall with 90 mm cavity might have attributed to this reduced temperature profile. The discontinuous stud arrangement in double stud LSF wall fire Test-T1 along with the wider cavity was identified as the prime reason for the reduced temperatures on the studs and these effects could not be predicted by the SAFIR thermal model. The effect of convection is also higher due to the wider cavity in complex LSF walls and this effect has to be accounted for the thermal model. SAFIR solves the conduction problem for a cartesian system of coordinates based on Fourier equation as shown in Equation (5.1).

$$\frac{\partial}{\partial_x} \left(k \frac{\partial T}{\partial_x} \right) + \frac{\partial}{\partial_y} \left(k \frac{\partial T}{\partial_y} \right) + \frac{\partial}{\partial_z} \left(k \frac{\partial T}{\partial_z} \right) + Q = c\rho \frac{\partial T}{\partial t} \quad (5.1)$$

Where,

x, y, z = vector of cartesian coordinates (m),

T = temperature (K),

k = thermal conductivity (W/mK),

Q = term to account for internal generation of heat (W/m³),

ρ = specific mass (kg/m³)

c = specific heat(J/kgK),

t = time (s).

Heat exchange on the surfaces and internal cavities is based on linear convection shown in Equation (5.2). The law of grey bodies is used for radiative flux calculations as shown in Equation (5.3)

$$h_c = h(T_g - T_s) \quad (5.2)$$

Where,

h_c = convective heat flux between solid and gas (W/m²),

h = coefficient of convection (W/m²K),

T_g = temperature of gas (K),

T_s = temperature of solid surface (K).

$$h_r = \sigma \epsilon T_s^4 \quad (5.3)$$

Where,

h_r = radiative heat flux emitted by a solid (W/m²),

σ = Stefan-Boltzman constant (5.67×10^{-8} W/mK⁴),

ϵ = emissivity of the solid,

T_s = temperature of solid surface (K).

As mentioned in Equation (5.2) the effect of convection is linearized within the cavity in SAFIR heat transfer calculations. Simulating the effect of natural convection by approximation within the cavity is not well documented in SAFIR and hence could not be used in the developed model to predict these effects resulting in higher temperature predictions in the studs. As the failure time of the test wall is based on the critical hot flange temperature, the temperature predictions of the stud hot flanges from SAFIR will result in premature structural failure time predictions in comparison with the test wall failure times. Therefore, it becomes a necessity to develop a thermal model to accurately predict the temperature evolution of studs in complex LSF wall systems in fire. Considering the above-mentioned limitations in SAFIR with respect to predicting the time-temperature curves of complex LSF walls exposed to standard fire curve, investigations were then conducted using the most commonly used FEA package ABAQUS and the corresponding discussions are given next.

5.3 Thermal modelling in ABAQUS

ABAQUS is one of the commonly used FE packages to solve structural and heat transfer problems. Three-dimensional heat transfer brick element (DC3D8) was used to create the plasterboard and studs for the FE thermal model. SI units were followed in model creation wherein the studs and plasterboards were modelled in 3D. The model was 1200 mm wide and 600 mm high considering the symmetry of LSF wall based on past research conducted by Rusthi et al. (2017b) and Ariyanayagam and Mahendran

(2019). Mesh density was kept at 10 mm throughout the studs and 20 mm along the length of the wall for plasterboards. Across the width of the wall near the plasterboards, a mesh density of 4 mm was adopted based on past research and sensitivity analysis. Figures 5.10 and 5.11 show typical model and mesh details used for thermal analysis in ABAQUS. Temperature dependent thermal properties based on past research from Dodangoda (2018) were used in the analysis. The FE model for thermal analysis consisted of one stud only connected to the plasterboards at the centre. A cavity width of 300 mm was maintained on both sides of the studs. The cavity was closed on the top and bottom and the sides in the model for the thermal analysis as simulating open cavity with symmetry boundary conditions results in extensive computational cost. Tie conditions were provided as constraints on the interface between the stud flanges and the plasterboard surfaces facing the cavity. Radiation was assumed to be predominant within the cavity. An emissivity of 0.9 was specified within the cavity. Convection and radiation boundary conditions were given to the fire and ambient side surfaces. Convective heat transfer coefficient of $25 \text{ W/m}^2\text{C}$ was applied to the fire side while $10 \text{ W/m}^2\text{C}$ was specified on the ambient side plasterboard surface. The tracks and noggings were not considered in the thermal analysis as their effect on the thermal behaviour was insignificant. ISO 834 Standard fire curve was specified as the input boundary condition to the thermal model. Thermal analysis was carried out for a time period of 240 min to simulate the thermal behaviour of double stud wall Test-T1.

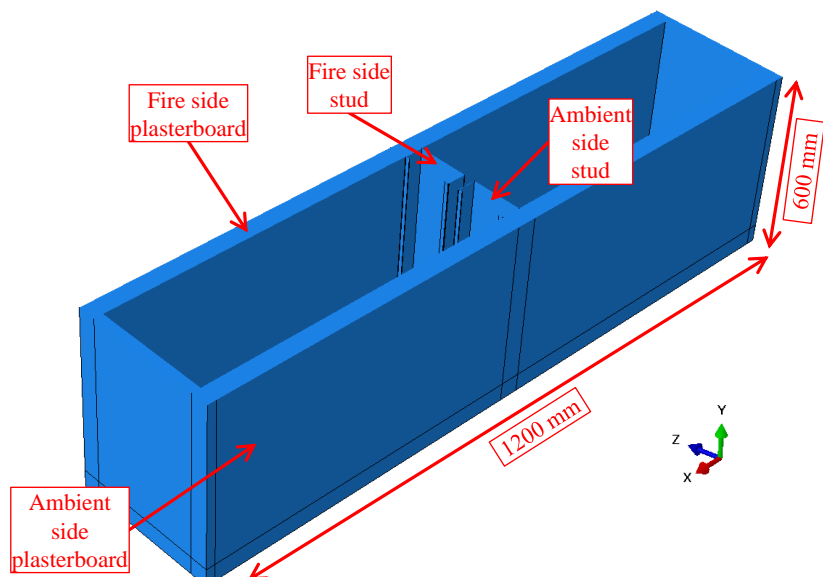


Figure 5.10: 3D model of double stud wall in ABAQUS

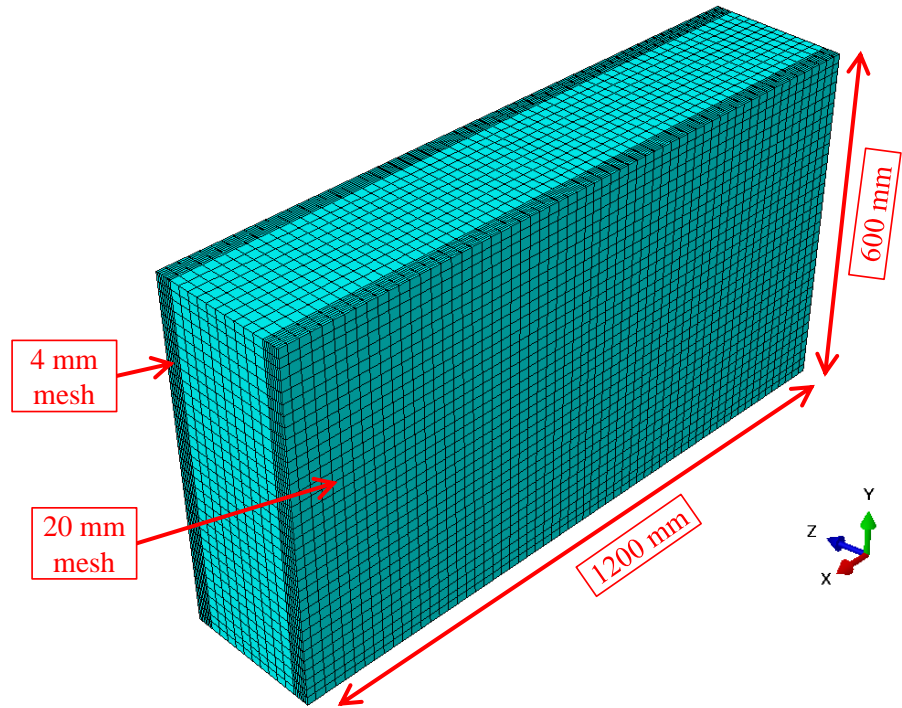


Figure 5.11: Mesh arrangement in the thermal model from ABAQUS

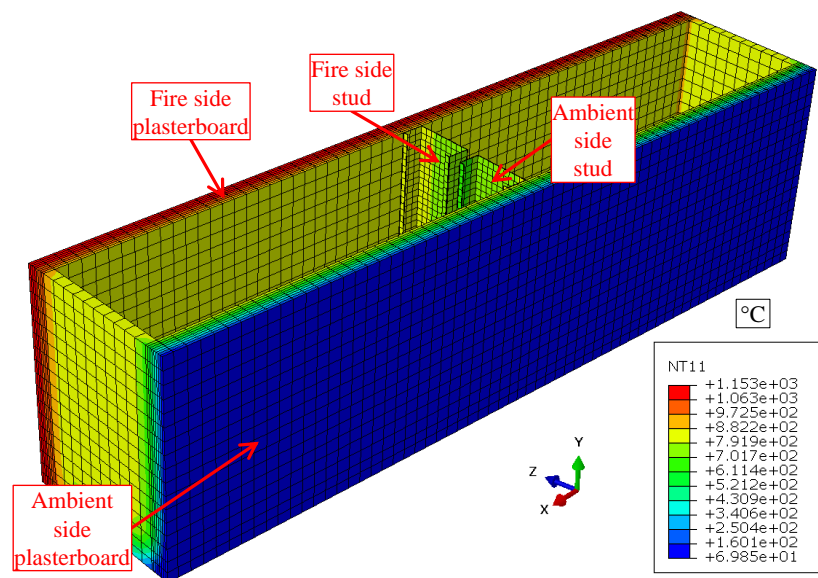


Figure 5.12: Thermal analysis output from ABAQUS for wall

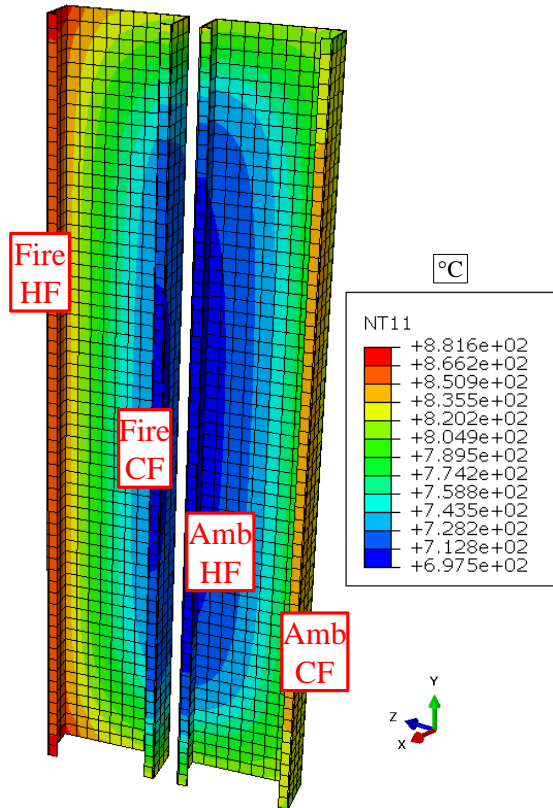


Figure 5.13: Thermal analysis output from ABAQUS for studs

Figures 5.12 and 5.13 show the thermal analysis output from ABAQUS. It is to be noted that from Figure 5.13 the temperature distribution is concentrated on the fire side hot flange (Fire-HF) and ambient side cold flange (Amb-CF). This temperature distribution in the studs is unusual in comparison with the time-temperature curves from the experimental studies. The ambient side cold flange is hotter than the ambient side hot flange which means that the heat is transferred to the ambient side plasterboards and then is conducted to the stud flanges as the effect of radiation is considered predominant within the cavity. This assumption does not hold good in the case of non-cavity insulated double stud LSF walls as the order of temperature distribution will be Fire-HF, Fire-CF, Amb-HF and Amb-CF. This hierarchy is clearly evident from the conducted full-scale fire test results in Chapter 4. Further comparisons were made against the time-temperature curves of plasterboards and studs and the discussions are presented next to understand the thermal model predictions.

Figure 5.14 presents the time-temperature curves of plasterboard from ABAQUS heat transfer analysis. The fire side plasterboard time-temperature curves (Pb1) agree reasonably well with the experimental results. The plateau region present in the time-

temperature curve on the fire side plasterboard interface Pb1-Pb2 was not visible in the ABAQUS thermal model predictions. The plateau region in the time-temperature curve present in the experiments is because of the combined effects of radiation and natural convection within the cavity. As the thermal analysis was conducted by assuming only radiation effects within the closed cavity, the thermal model time-temperature curves predicted temperatures higher than the experiments. Both fire and ambient side plasterboard curves (Pb2 and Pb3) from ABAQUS were also higher than the experimental results as they are influenced by the plasterboard interface (Pb1-Pb2) time-temperature curve. The ambient side plasterboard time-temperature curve prediction was also higher in comparison with the experimental results. However, the time-temperature curves of the ambient side plasterboard (Pb4) matched reasonably well with the experimental results as shown in Figure 5.14 (a).

The stud time-temperature curves are presented in Figure 5.14 (b). The hot and cold flanges matched reasonably well till 60 min of the fire test. However, the time-temperature curves exhibited steep rise after 60 min. This indicates that the cooling effect experienced in the stud hot and cold flanges from experiments could not be simulated by the developed ABAQUS thermal model. The ambient side cold flange (T1-Abaqus-Amb-CF) time-temperature curve was higher than the ambient side hot flange (T1-Abaqus-Amb-HF) as shown in Figure 5.14 (b), which is unusual. However, this discrepancy was not present in SAFIR thermal analysis Figure 5.9 (b). This is also partly because the stud rows in Test-T1 are located 20 mm apart, resulting in no heat transfer through conduction during the fire test. As the heat transfer within the cavity is assumed to be dominated by radiation in the ABAQUS heat transfer model, the time-temperature curves on the ambient side hot and cold flanges mismatch in comparison with the experimental results. Similar to SAFIR heat transfer analysis results, the time-temperature curves of studs from ABAQUS thermal analysis were significantly higher than the experimental results. The complex heat transfer effects of convection combined with radiation within the cavity were not accounted for in the single stud wall thermal models developed using SAFIR and ABAQUS. Therefore, it becomes a necessity to develop a thermal model which can account for the combined convection and radiation effects within the cavity and simulate more accurately the thermal behaviour of the complex LSF walls systems.

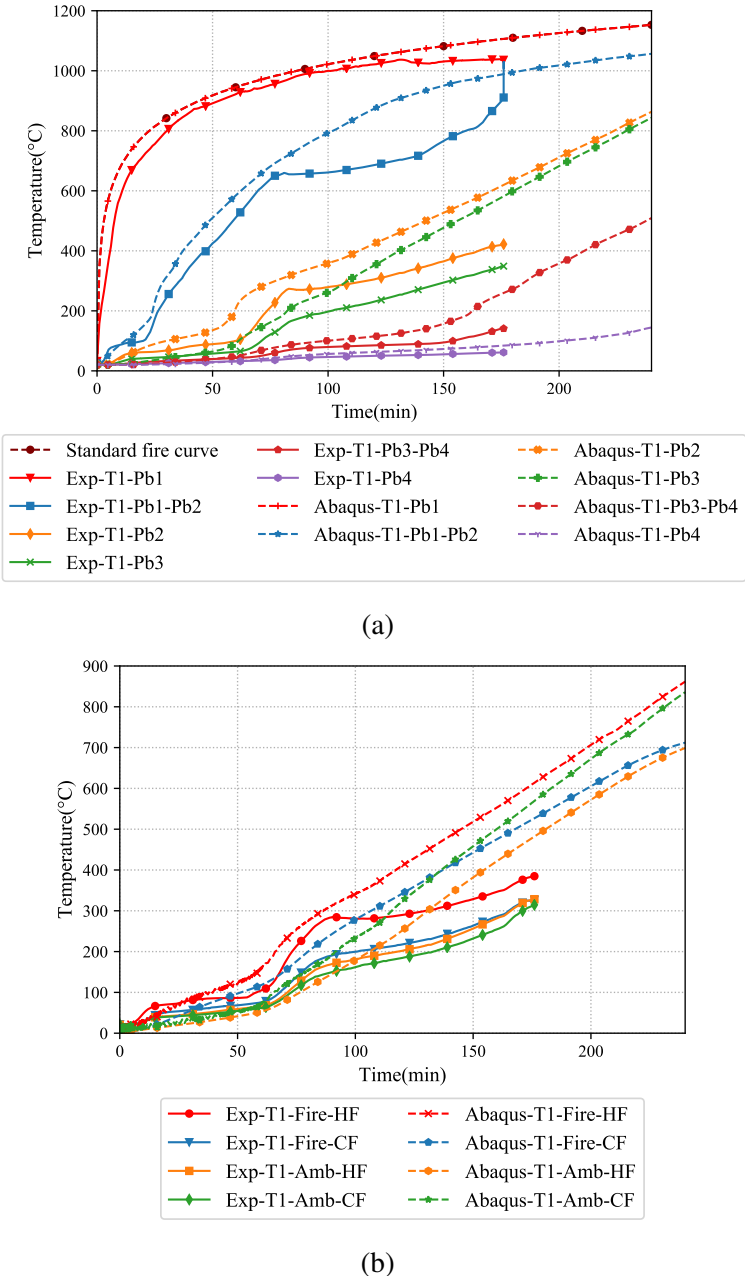


Figure 5.14: Comparison of time-temperature curves from ABAQUS thermal analysis and experiments (a) Average plasterboard temperatures (b) Stud4-Mid temperatures

5.4 Thermal modelling in FDS

Unlike other FE packages in which the thermal models of LSF walls are readily available, very limited literature is available on the thermal models of LSF walls developed in FDS except in research studies conducted by Lázaro et al. (2016), Lázaro et al. (2018), and Nguyen et al. (2018). Thermal FE models in FDS are needed in this research study to predict the time-temperature profiles of the complex LSF walls. The previous FDS model considered in the literature assumed the LSF wall as a homogeneous entity and the thermal models were created with single obstruction (&OBST) comprising of studs and plasterboards. However, this approach cannot be employed in this study as the individual time-temperature curves from the studs are necessary to predict the structural behaviour of the LSF wall in fire. Therefore, the plasterboards and studs were modelled separately to depict the experimental set-up.

Past literature considered different model dimensions based on their experimental set-up. The model dimensions varied form 50×50 mm to 3×3 m. Likewise, the mesh density also varied from 5 to 50 mm (Lázaro et al. (2018) and Nguyen et al. (2018)). This assumption was best suitable as the time-temperature curves were measured on the fire exposed and ambient sides only in the above-mentioned research studies. However, these studies did not model the structural behaviour of the wall. To develop the current thermal model based on past literature, a sensitivity analysis was conducted initially to determine the effects of the model dimensions. Also, in the sensitivity analyses the obstructions (&OBST) were modelled as solid entity, which was found to add complexity to the model resulting in higher computational time. Therefore, a simplistic approach of modelling the obstructions as 2D entity was chosen in this research study to model the complex LSF walls.

5.4.1 Thermal model description in FDS

The models were created in the command line interface using Notepad ++ a general purpose text editor. However, PyroSim was used for pre-processing the models in certain instances to consolidate meshes in the boundary. SmokeView was used for post-processing and visualising the thermal model results. Output from the thermal models were saved on to a CSV file, which was later used for plotting the time-temperature

curves. Certain assumptions were used in creating the FDS thermal model. The models were created with the appropriate depth of the test wall used in the experiments. However, the height and width of the model were restricted to 200 mm. The variation in heat transfer along the height of the test wall was ignored in order to simplify the model. This is because, the standard time-temperature curve is specified as the input boundary condition to the entire fire exposed surface (Pb1) using the vent function (&VENT) in FDS. This implies that, the temperature input is uniform throughout the surface and the variation in temperature which occurs in the experiments due to difference in furnace burner temperatures can be assumed insignificant and ignored in the current model, as the comparison is made against the average time-temperature curve achieved in the furnace. It is to be noted that the ISO 834 time-temperature curve is specified as the input boundary condition on the fire side plasterboard in ABAQUS and SAFIR thermal models. However, in FDS it is specified through a &VENT surface, which provides the leverage to simulate the standard fire curve from furnace similar to the full-scale fire tests. This might result in a small difference between the incident fire side plasterboard (Pb1) temperature and the standard fire curve due to the small distance between the &VENT surface and the Pb1 surface. This small difference in temperatures will still be within the permissible limits of 100°C as per AS 1530.4 (SA (2014)) and can be ignored.

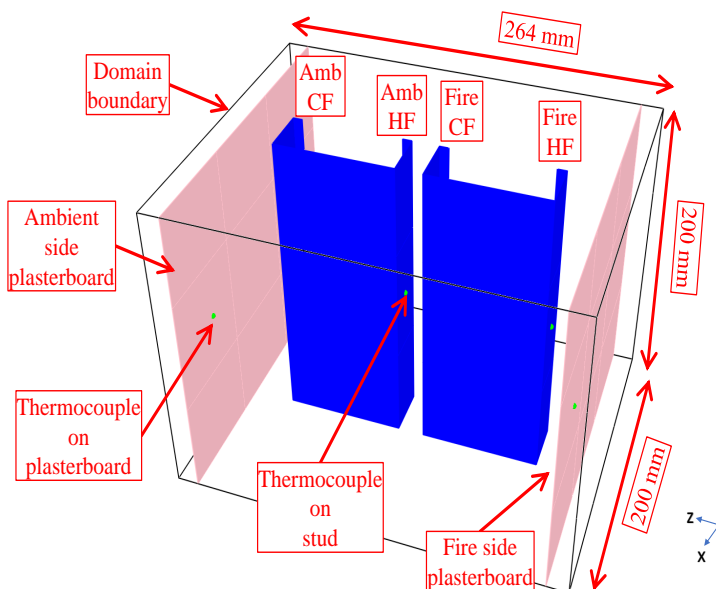


Figure 5.15: Model of Double Stud LSF Wall Panel

Considering the above mentioned findings, the obstructions in the model followed

“1 cell thick” rule of FDS as shown in Figure 5.15. The temperature dependent material properties for gypsum plasterboards, steel studs and glass fibre insulation for the thermal analysis were taken from Dodangoda (2018). The temperature dependent material properties were used for conductivity and specific heat only. Temperature-dependant material properties were specified to the model using &RAMP function in the FDS input file. The density was kept constant at 768.5kg/m³ for plasterboard, 7850 kg/m³ for steel and 11 kg/m³ for glass fibre insulation. An emissivity of 0.9 was used for the plasterboards while the emissivity used for the steel stud was 0.7. The model was enclosed in a domain boundary with 16 mm mesh based on the sensitivity analyses, matching the plasterboard thickness. Convective heat transfer co-efficient of 25 W/m²°C was considered for the fire side plasterboard surface while it was 10 W/m²°C for the ambient side plasterboard surface. AS 1530.4 (SA, 2014) standard fire curve (identical to ISO 834 (2014) curve) was specified as the input boundary condition to replicate the fire side using &VENT function. The domain boundary was created in close contact with the model to prevent any heat loss around the model sides during simulation. The domain boundary was closed in all directions and adiabatic boundary conditions were specified representing no heat transfer through the sides. The boundary facing the ambient side was alone kept open to simulate the natural convection from the ambient side plasterboard surface. As “1-cell thick” modelling technique was used, the contact between the studs and plasterboards was achieved by specifying the material thickness of plasterboard and studs. The corresponding thickness was specified on the surface line using the &SURF function. Temperatures were measured across the model using the &DEVC function at various locations similar to thermocouples and the corresponding time-temperature curves were plotted. The thermal model analysis was carried out for a time period of 240 min for all the conducted full-scale fire test configurations. The time-temperature curves from the FDS model and experiment are compared and discussed in the next section.

5.4.2 Thermal model validation - Non-cavity insulated Tests-T1, T2, T3, T4, T8 and T9

The thermal model was created with its height and width of 200 mm while its depth of the model was 264 mm similar to the full-scale fire Test-T1 of a double stud wall made

of 90×0.95 mm studs with a load ratio of 0.4. The thermal analysis was carried out for a time period of 240 min. Figure 5.16 shows the thermal model of Test-T1 with 16 mm meshes. The boundary domain was subdivided to nine regions to facilitate parallel processing in the HPC cluster. Through this the thermal model could be solved in 26 min, which is a considerable optimisation in the computational time in comparison with SAFIR and ABAQUS thermal models.

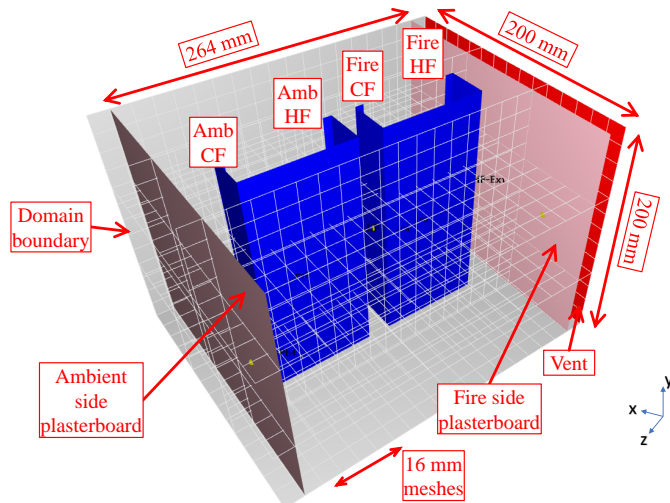


Figure 5.16: Thermal model of Test-T1 wall

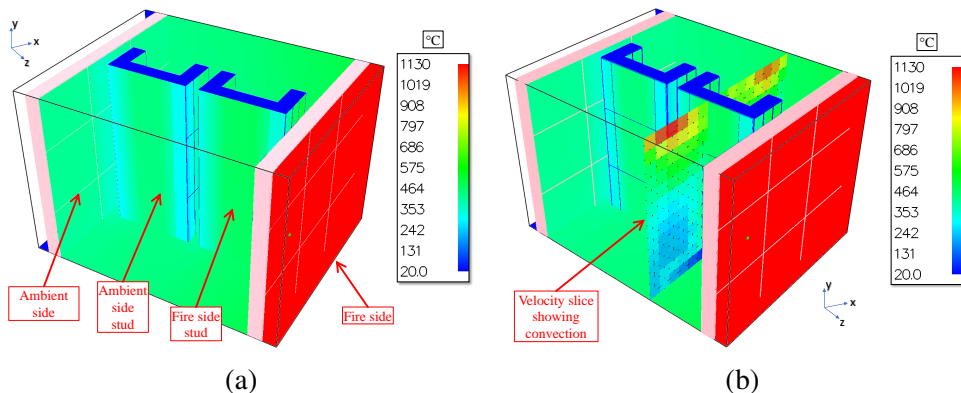


Figure 5.17: Output from FDS thermal analysis (a) Temperature profile (b) Velocity slice for convection

Temperature profile and velocity slice from FDS thermal model are shown in Figures 5.17 (a) and (b). Time-temperature curves of plasterboard from FDS thermal analysis are compared against experimental results and are presented in Figure 5.18 (a). Fire side time-temperature curve (Fds-T1-Pb1) exhibited good agreement with the ISO 834 time-temperature curve. Plasterboard interface time-temperature curve (Fds-T1-Pb1-Pb2) exhibited a reasonable agreement with the experimental results till 75 min

of fire test. The plateau region experienced in the fire test time-temperature curve was not significantly noticeable in the FDS thermal analysis prediction. The occurrence of plateau region between the plasterboard interface is attributed to the factors such as wider cavity depth, natural convection together with radiation effects, discontinuous stud arrangement, and moisture movement within the plasterboard. Except for the effects of moisture movement, all the other effects were accounted for in the current thermal model. However, the combined effects along with the moisture movement between the plasterboard interface could not be simulated due to the complexity in the modelling technique and is beyond the scope of this research study. But, the model was able to successfully incorporate the effects of convection within the cavity due to the change in the air temperature within the cavity. This is evident from the time-temperature curve of fire side plasterboard interface surfaces as shown in Figure 5.18 (a). Unlike a steep increase in the Pb1-Pb2 time-temperature from SAFIR and ABAQUS a change in slope is noticeable from the FDS thermal analysis prediction as shown in Figure 5.19. This confirms that the developed FDS model could better predict the thermal behaviour of non-cavity insulated double stud LSF walls. The time-temperature curve of the fire side cavity surface from the thermal model (Fds-T1-Pb2) was higher than the experimental curve. However, the ambient side cavity (Pb3), the ambient side plasterboard interface (Pb3-Pb4) and the ambient side plasterboard surface time-temperature curve predictions exhibited reasonable agreement with the experimental results.

Stud time-temperature curves shown in Figure 5.18 (b) also exhibited good agreement with the experimental results till 75 min of the fire test. The increase in slope experienced in the time-temperature curves from 50 min of the experimental results could also be simulated by the developed thermal model with reasonable accuracy. However, as the predicted fire side cavity (Pb2) plasterboard temperatures were higher than those in the experiments Figure 5.18 (b)s, similar effects were noticeable in the stud hot and cold flanges wherein the predicted hot and cold flange time-temperature curves were marginally higher than the experimental results. The maximum temperature recorded by the fire side hot flange on Stud4-Mid (Exp-T1-Fire-HF) at the end of the fire test at 176 min was 395°C while the predictions from FDS thermal model was 431°C. i.e., a difference of 8.35% (36°C). This can be considered as small in relation

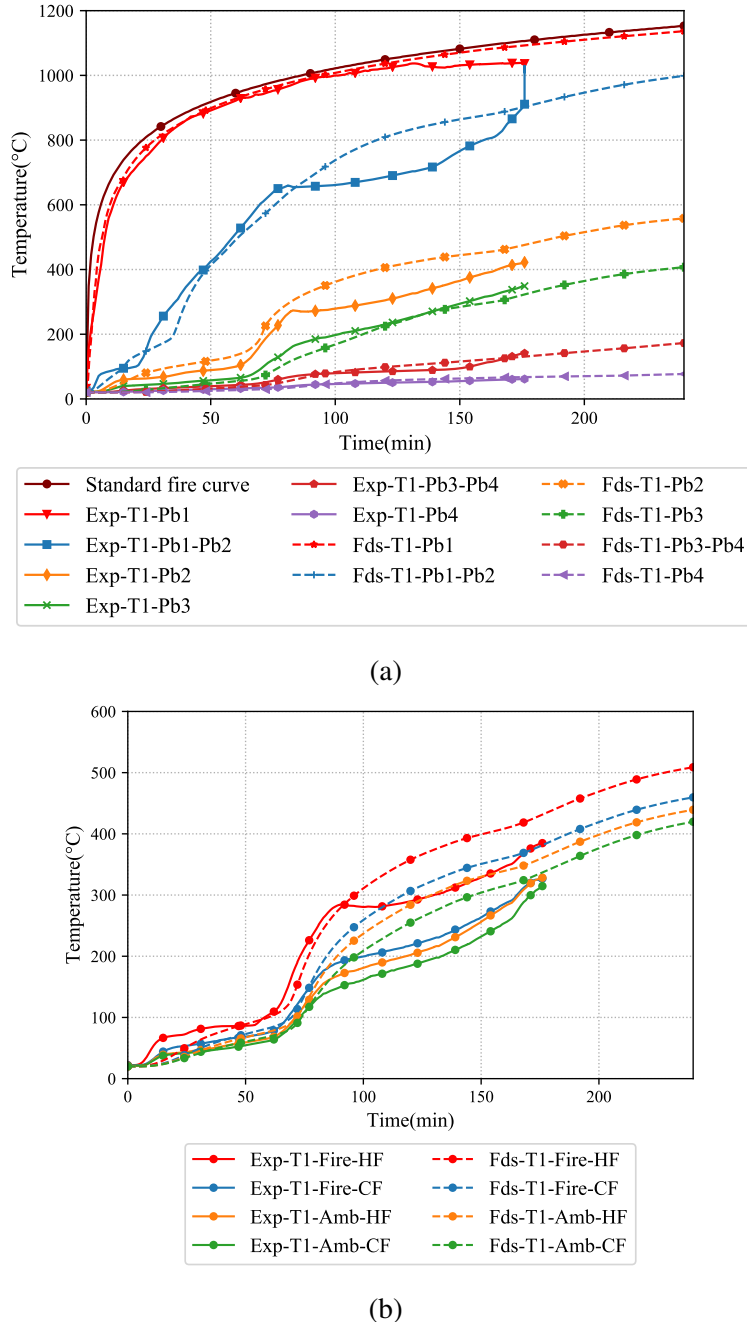


Figure 5.18: Comparison of time-temperature curves from experiment and FDS model for Test-T1 (a) Average Plasterboard (b) Stud4-Mid

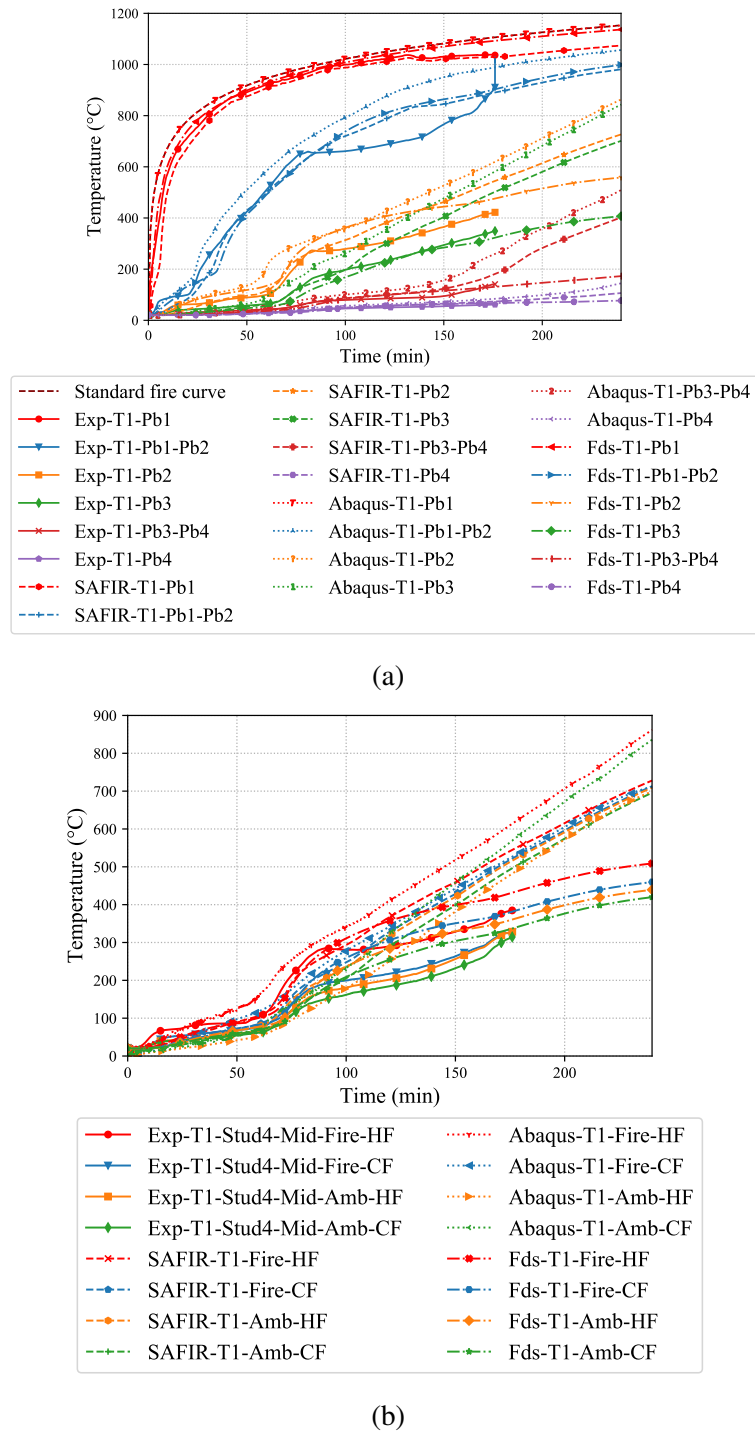


Figure 5.19: Comparison of time-temperature curves from experiment, SAFIR, FDS and ABAQUS models for Test-T1 (a) Average Plasterboard (b) Stud4-Mid

to the use of stud hot flange temperatures in structural failure time predictions.

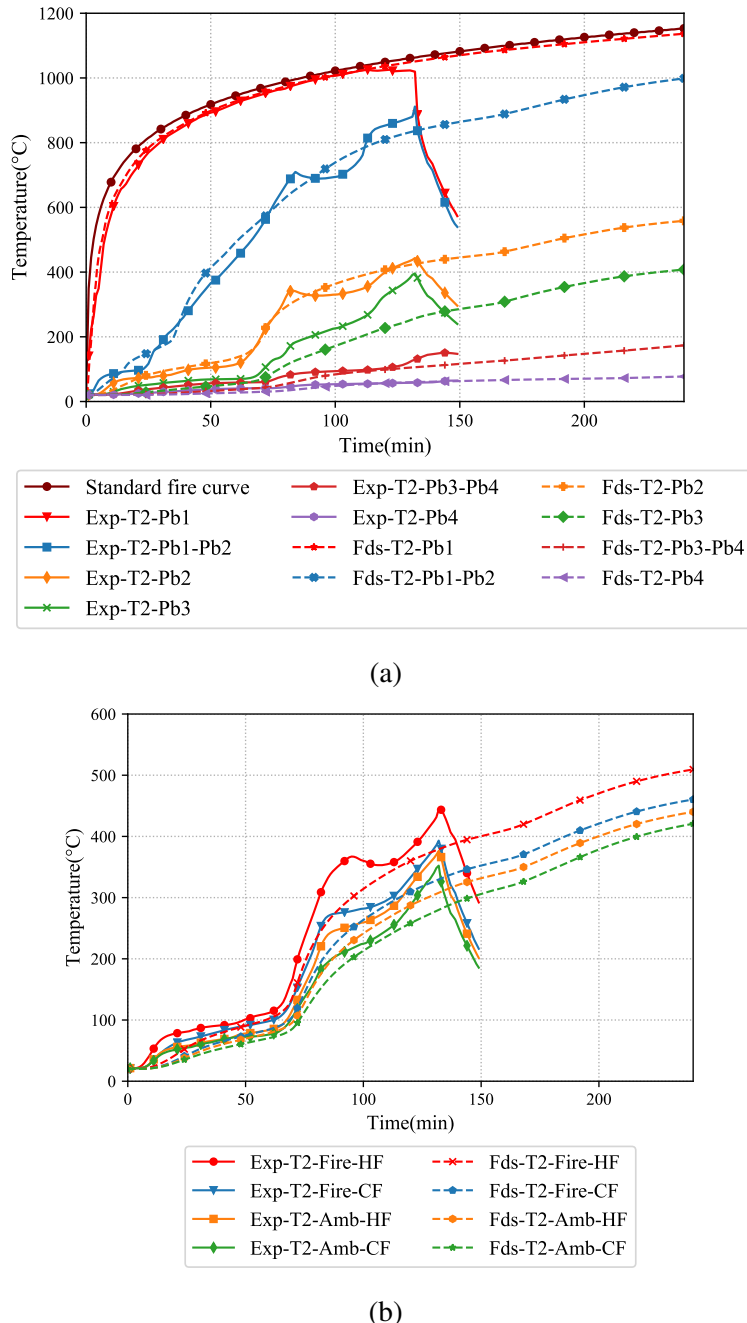


Figure 5.20: Comparison of time-temperature curves from experiment and FDS model for Test-T2 (a) Average Plasterboard (b) Stud3-Mid

Figure 5.20 (a) compares the plasterboard time-temperature curves for Test-T2 of a double stud wall made of 90×0.75 mm studs with a load ratio of 0.4. The plasterboard time-temperature curves exhibited reasonable agreement except for T2-Pb3 where the FDS model predictions were less than the experimental results. However, the ambient side plasterboard surface time-temperature curves also agreed reasonably

well. Stud time-temperature curves agreed well till 60 min of the fire test as shown in Figure 5.20 (b). The steep increase experienced in the Exp-T2-Fire-HF could not be simulated in the FDS model as this was a result of localised plasterboard open-up in the fire test. The temperature recorded at 132 min in Exp-T2-Fire-HF was 444°C while it was 380°C from the FDS model, i.e., FDS model prediction of the stud hot flange temperature was 64 °C less than the experimental results. Similarly, the difference in the fire side cold temperature was 62°C (393-331°C). The fire side hot and cold flange temperatures are 14.4% and 15.77% less than the corresponding experimental results of Test-T2. This may be partly due to the plasterboard fall-off on the fire side plasterboard during the fire test as reported in Section 4.6.2 of Chapter 4.

As Test-T3 was conducted on a double stud wall made of 90×0.75 mm studs but with a higher load ratio of 0.6, the time-temperature curves from the experiment are limited to 81 min. However, the FDS thermal analysis predictions were carried out for 240 min. Figure 5.21 (a) shows a good comparison of the plasterboard time-temperature curves from FDS model and experiment. All the plasterboard time-temperature curves exhibit good agreement with the experimental results. This is further evident from the stud time-temperature curves shown in Figure 5.21 (b).

Test-T4 was conducted on a double stud wall made of 70×0.95 mm studs under a load ratio of 0.4. Figure 5.22 (a) compares the plasterboard time-temperature curves from FDS thermal analysis and experiment. The plasterboard time-temperature curves predicted by the FDS thermal model were higher than the experimental results from Test-T4 till the fire side cavity surface. However, the ambient side plasterboard time-temperature curves matched reasonably well with the experimental results. Stud hot and cold flange time-temperature curves shown in Figure 5.22 (b) also exhibited good agreement. The ambient side hot and cold flange time-temperature curves from FDS thermal analysis (Fds-T4-Amb-HF and CF) were marginally less in comparison with the experimental results (Exp-T4-Amb-HF and CF).

Test-T8 was conducted on a shaftliner LSF wall where a plasterboard was placed within the cavity thereby splitting the cavity into two as shown in Figure 5.23. The temperature output from the FDS model is also shown in Figure 5.24. Figure 5.25 (a) compares the plasterboard time-temperature curves from FDS model and experiment for Test-T8. The time-temperature curves of the plasterboard from FDS thermal model

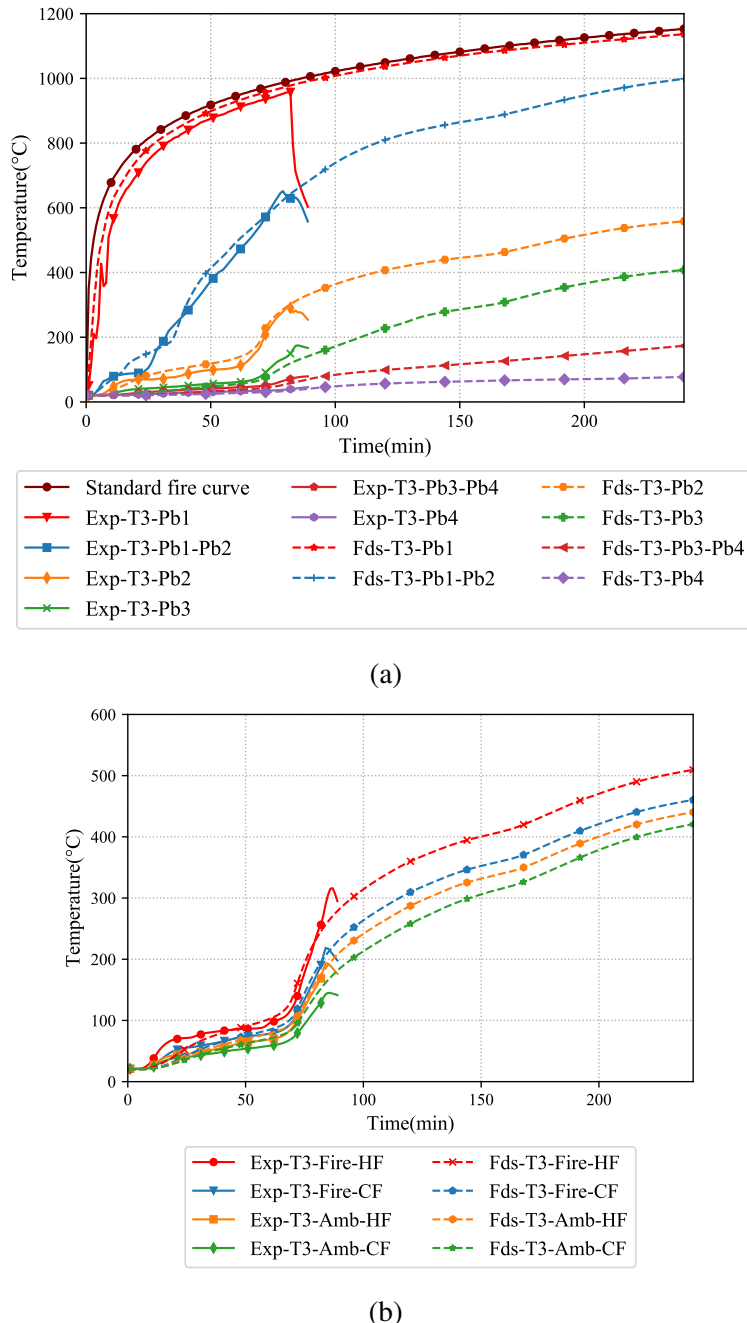


Figure 5.21: Comparison of time-temperature curves from experiment and FDS model for Test-T3 (a) Average Plasterboard (b) Stud4-Mid

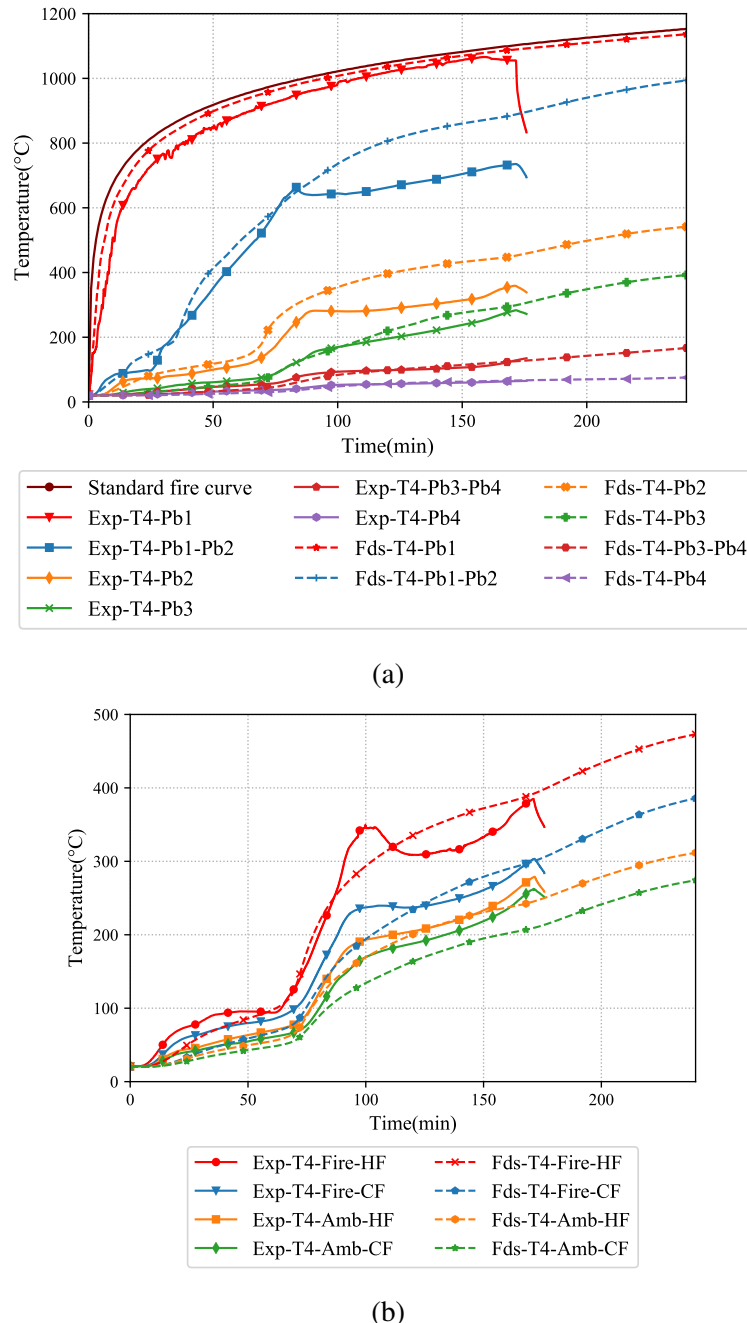


Figure 5.22: Comparison of time-temperature curves from experiment and FDS model for Test-T4 (a) Average Plasterboard (b) Stud3-Mid

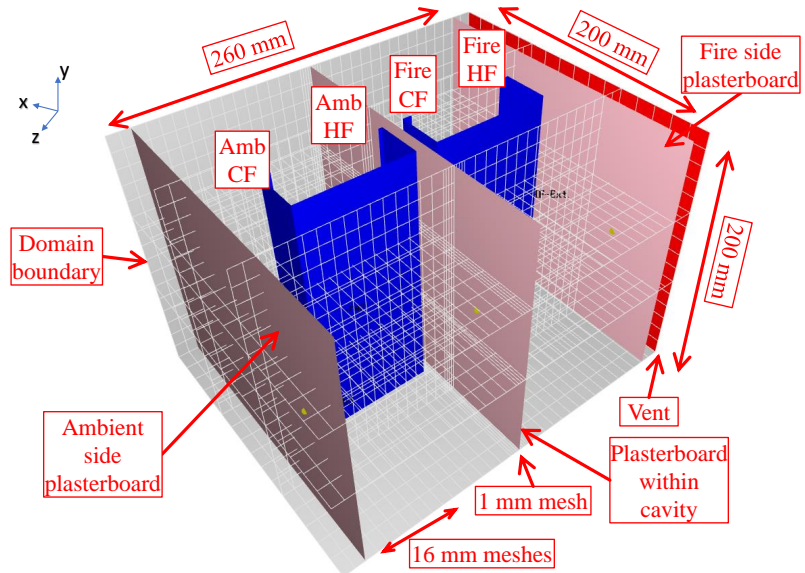


Figure 5.23: Thermal model of Test-T8 wall

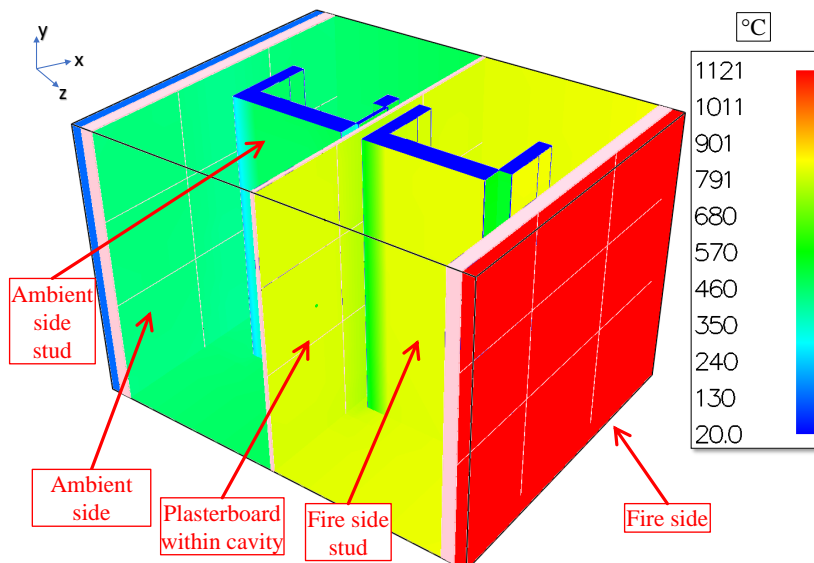


Figure 5.24: Thermal model output for Test-T8 wall

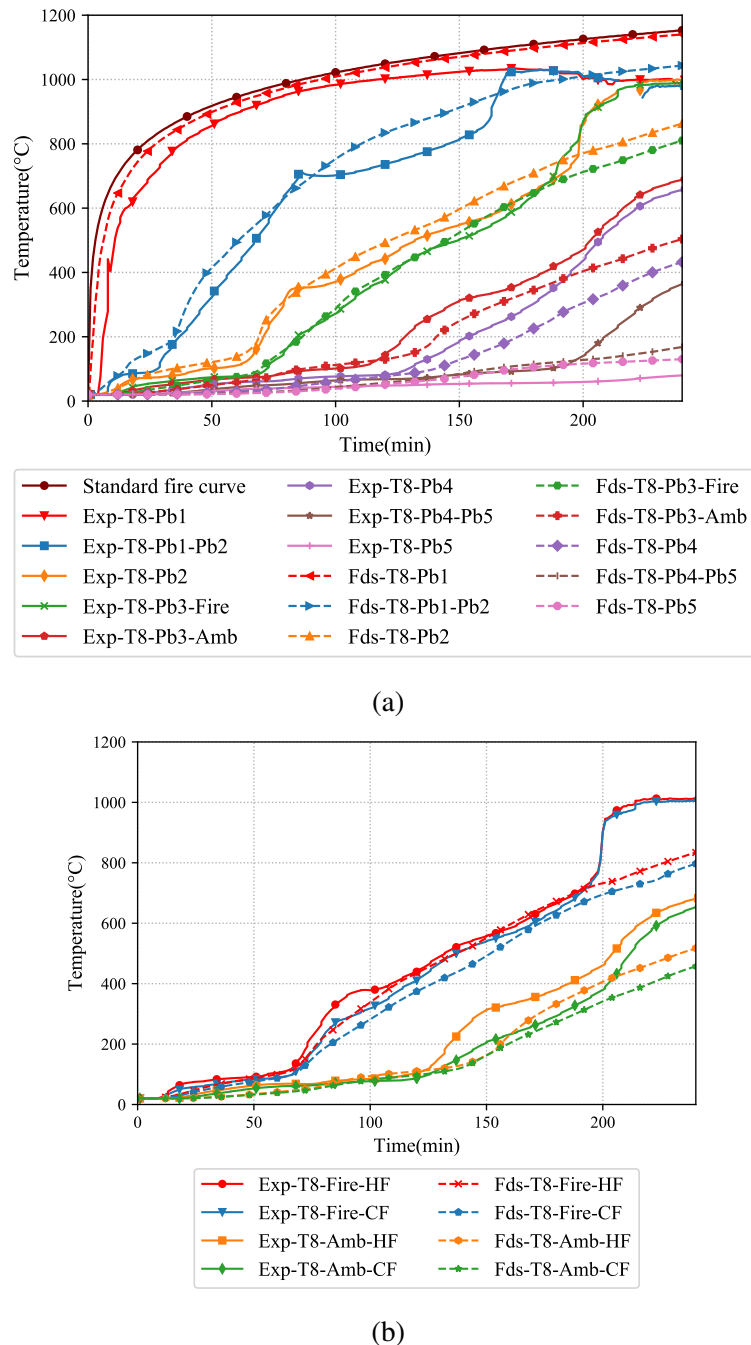


Figure 5.25: Comparison of time-temperature curves from experiment and FDS model for Test-T8 (a) Average Plasterboard (b) Stud4-Mid

match reasonably well with the experimental results till 160 min of the fire test. Due to the occurrence of significant plasterboard fall-off in the experiment, the resulting steep increase in the time-temperature curve near the end could not be simulated by the FDS thermal model. This was also reflected in the stud time-temperature curves shown in Figure 5.25 (b). The hot and cold flanges match reasonably well till the plasterboard fall-off time in the experiment.

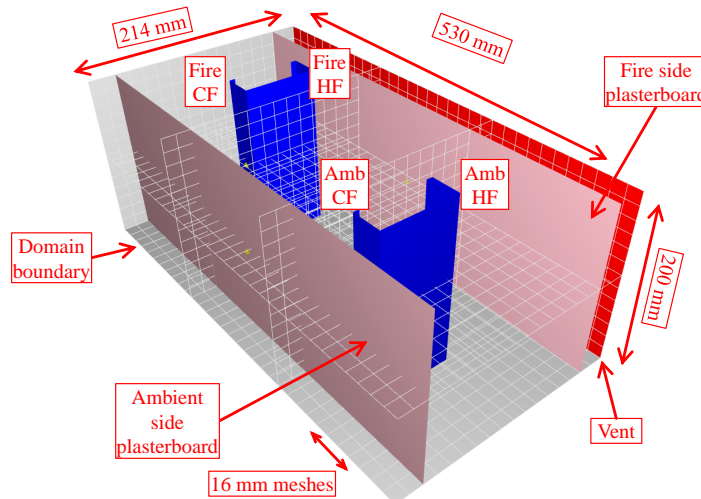


Figure 5.26: Thermal model of Test-T9 wall

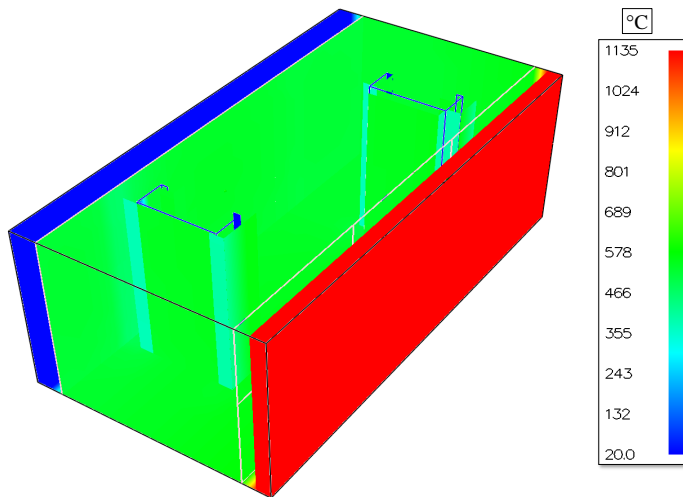
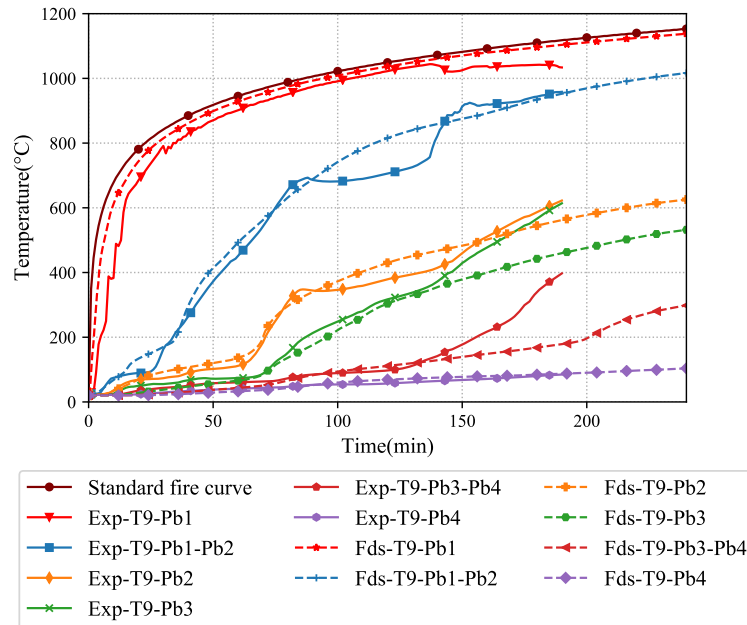
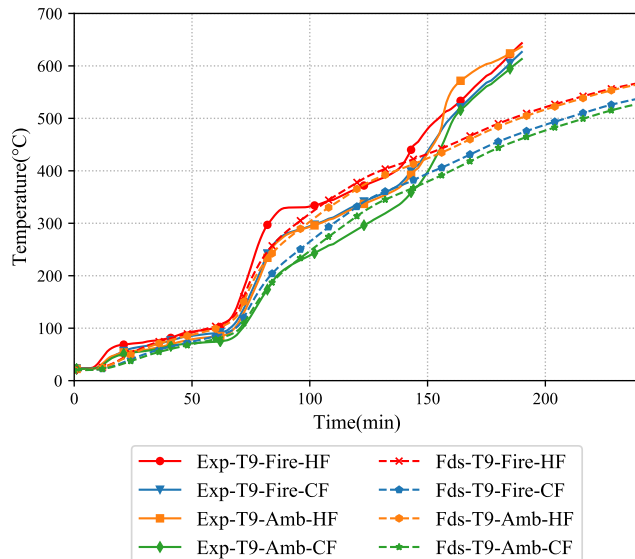


Figure 5.27: Thermal output for Test-T9 wall

Test-T9 was conducted on staggered stud LSF wall with a cavity depth of 150 mm. The studs in the test wall were arranged in a staggered manner wherein the hot flange of the ambient side stud does not have direct contact with the plasterboard as shown in Figure 5.26. Figure 5.27 shows the temperature output from the FDS model. The



(a)



(b)

Figure 5.28: Comparison of time-temperature curves from experiment and FDS model for Test-T9 (a) Average Plasterboard (b) Stud4-Mid

plasterboard time-temperature curves from the experiment and FDS thermal model are compared in Figure 5.28 (a). A reasonable agreement is observed in the time-temperature curve comparison between the experiment and the FDS thermal model. The thermal model predictions were marginally above the experimental results till 120 min of the time-temperature curve. After 150 min significant plasterboard fall-off was observed in the fire Test-T9, which resulted in a higher time-temperature curve as shown in Figure 5.28 (a). This is also evident in the stud time-temperature curves as shown in Figure 5.28 (b). The stud time-temperature curves from the FDS thermal model were also in close agreement with the experimental results till 150 min. However, the FDS stud time-temperature curve exhibited a gradual rise after 150 min, while the experimental curves exhibited a steep rise. Ambient side hot flange facing the plasterboard recorded temperatures higher than the fire side cold flange in the experiments as this was close to the fire side plasterboard. This behaviour was also captured by the FDS thermal model. Based on the above-mentioned comparison it is evident that the FDS thermal model developed in this study can be used to predict thermal behaviour of non-cavity insulated complex LSF wall systems.

5.4.3 Thermal model validation - Cavity insulated Tests-T5, T6, T7 and T10

FDS model similar to the non-cavity insulated test wall was used to predict the time-temperature profile for cavity insulated test walls also. The use of cavity insulation was also achieved with “1-cell thick” rule in FDS. The obstruction (&OBST) for cavity insulation was modelled without intersecting with the other &OBST such as plasterboard or stud to avoid numerical instability in the thermal model. FDS thermal model representing Test-T5 of a cavity insulated double stud wall made of 90×0.95 mm studs is shown in Figure 5.29.

Figure 5.30 (a) compares the plasterboard time-temperature curves from FDS thermal model and experiment. An important observation in the case of cavity insulated wall is the sudden increase of the fire side cavity time-temperature curve (Exp-T5-Pb2). This indicates the presence of severe plasterboard open-up and was also reported in Chapter 4. Plasterboard open-up occurs predominantly in the plasterboard joints or in the weakest portion of the test wall. However, in the present model the plasterboard

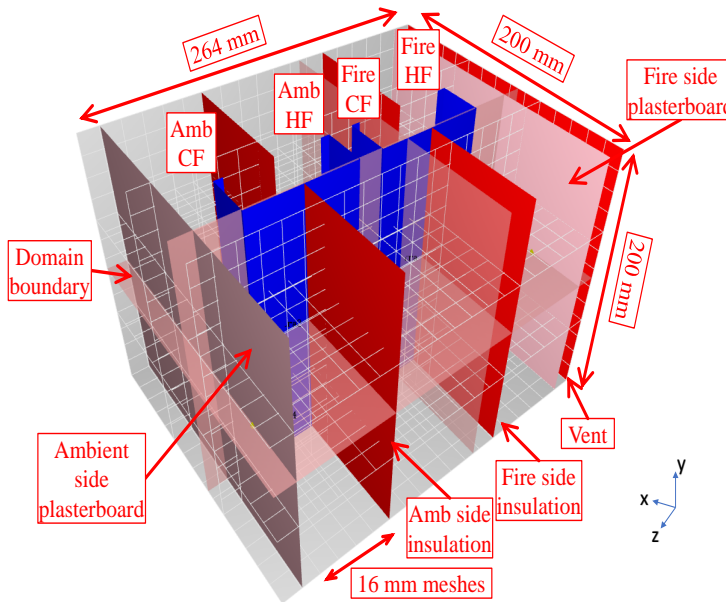


Figure 5.29: Thermal model of Test-T5 wall

open-up is considered by removing the middle portion as shown in Figure 5.31 (b) to all the models for simplification. To achieve the plasterboard open-up effect on FDS thermal model, the concept of “set-point” temperature was used in the fire side plasterboard interface (Pb1-Pb2). Once the thermocouple Pb1-Pb2 reaches the set point temperature a portion of the plasterboard ($67 \text{ mm} \times 67 \text{ mm}$) was removed during the analysis and the thermal analysis was continued till 240 min with a hole in the fire side plasterboard as shown Figure 5.31. A “set-point” temperature of 640°C was used at the plasterboard interface (Pb1-Pb2) to initiate the plasterboard open-up based on based on ASTM 1588 (Sultan (2015)).

The FDS thermal model was able to simulate the steep rise in time-temperature curve experienced in thermocouple Exp-T5-Pb2 as shown in Figure 5.30 (a) to a reasonable accuracy and was also able to predict the temperature profile till 240 min. Reasonable agreement was observed on all the plasterboard time-temperature curves. Stud time-temperature curves shown in Figure 5.30 (b) also exhibited good agreement with the experimental results. Test-T6 was conducted as a repeat test and the corresponding model validation for time-temperature curves are shown in Figures 5.32 (a) and (b). Time-temperature curve agreement between FDS thermal model and the experimental results is good for Test-T6 also.

Test-T7 was conducted on double stud LSF wall with $90 \times 0.95 \text{ mm}$ studs wherein the cavity insulation was placed only within the ambient side row of studs (0.4 Load

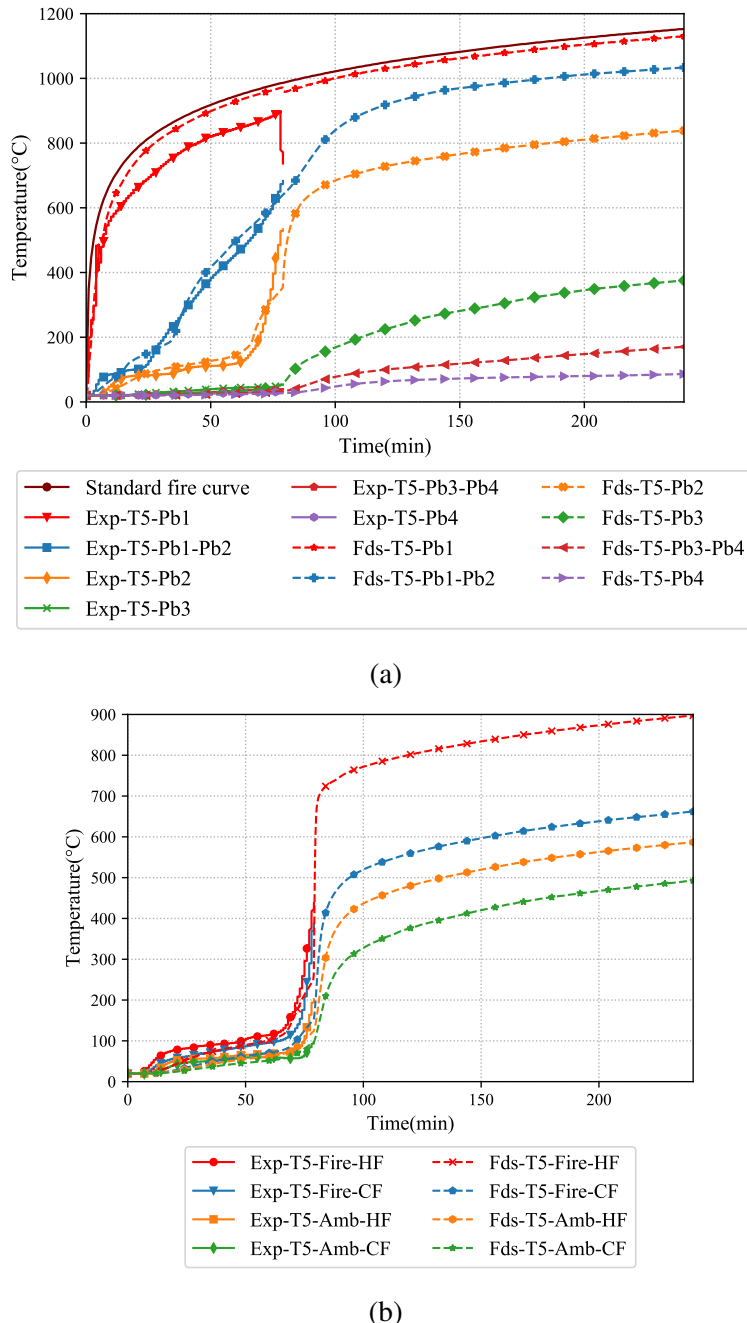


Figure 5.30: Comparison of time-temperature curves from experiment and FDS model for Test-T5 (a) Average Plasterboard (b) Stud3-Mid

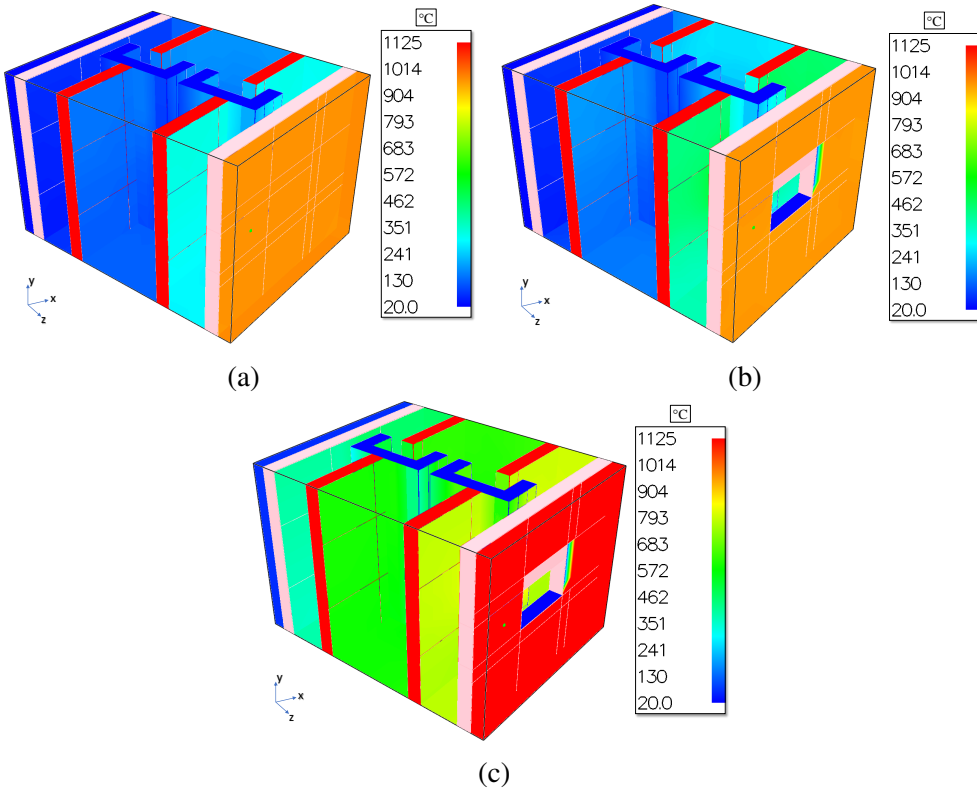


Figure 5.31: Temperature output for Test-T5 from FDS thermal analysis (a) Before plasterboard open-up at 78 min (b) After plasterboard open-up at 79 min (c) At 240 min (End of Simulation)

Ratio). Figure 5.33 shows the FDS model with ambient side cavity insulation considered for the thermal analysis. Figure 5.34 (a) compares the time-temperature curves from FDS thermal analysis and experiment. Sudden increase in the plasterboard time-temperature curve (Exp-T7-Pb2) was observed in this fire test also. This behaviour was also predicted by the developed FDS thermal model and is evident from the comparison in Figure 5.34 (a). Increase in the plasterboard time-temperature curves also affects the corresponding stud hot and cold flange temperatures. The developed FDS thermal model was able to predict the sudden increase in the stud hot and cold flange time-temperature curves as shown in Figure 5.34 (b) with a reasonable agreement. The temperature output predicted by the FDS thermal model considering plasterboard open-up is shown in Figure 5.35.

Cavity insulated staggered stud wall Test-T10 made of 90×0.95 mm studs (0.4 Load Ratio) was modelled as shown in Figure 5.36. Cavity insulation was curved through the studs in the test wall. However, to increase the computational efficiency the cavity insulation is staggered linearly between the studs with two horizontal and

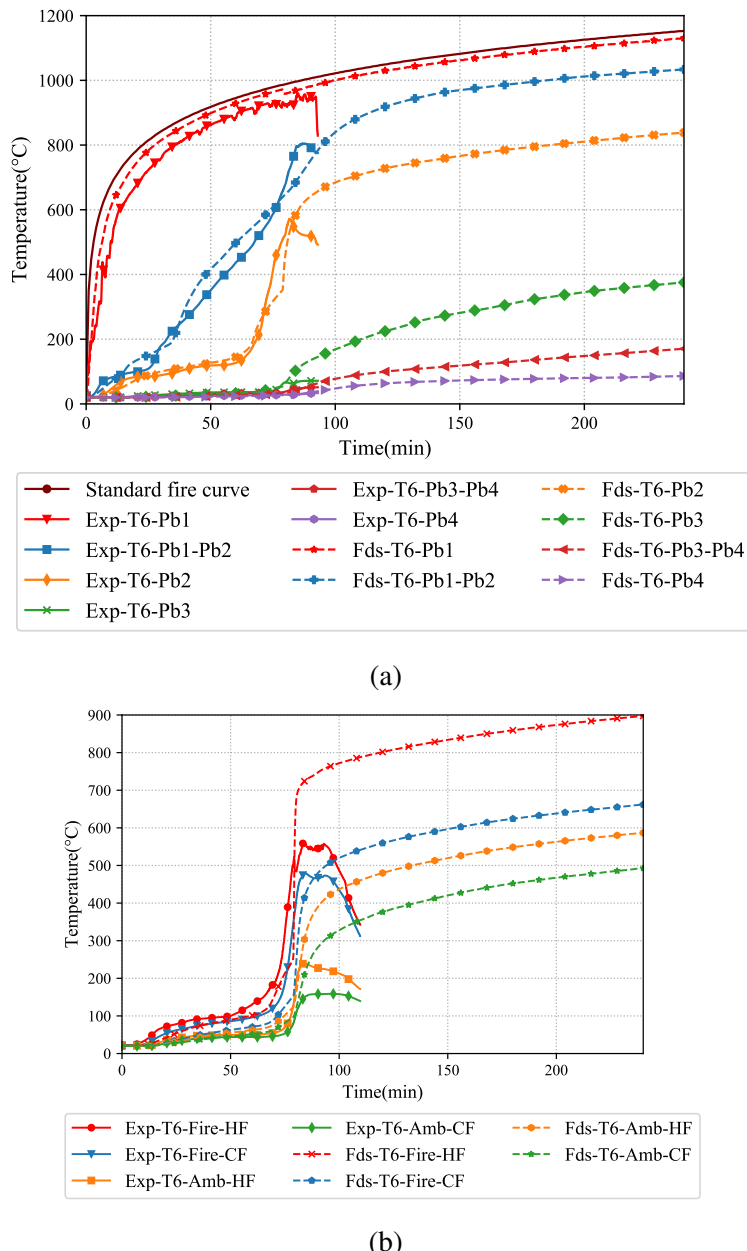


Figure 5.32: Comparison of time-temperature curves from experiment and FDS model for Test-T6 (a) Average Plasterboard (b) Stud4-Mid

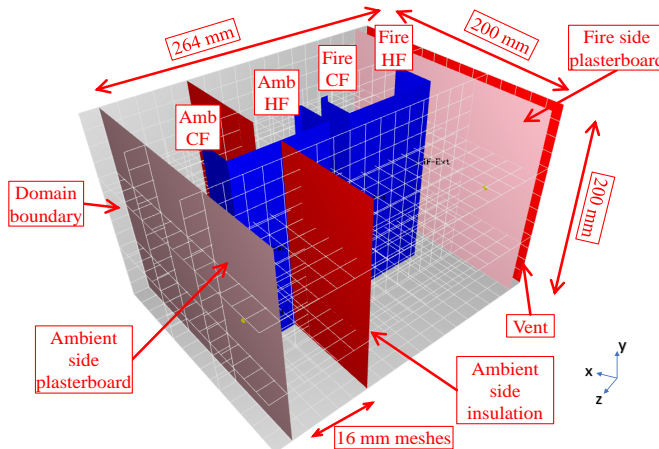
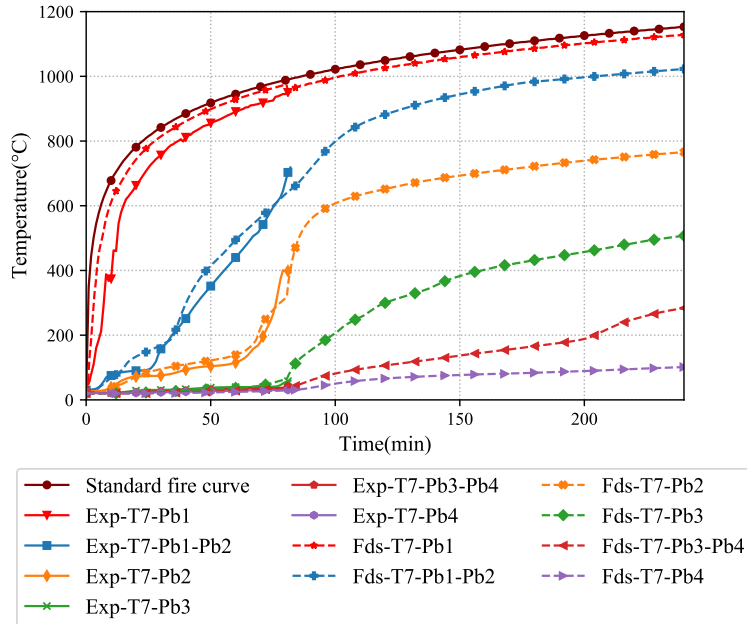


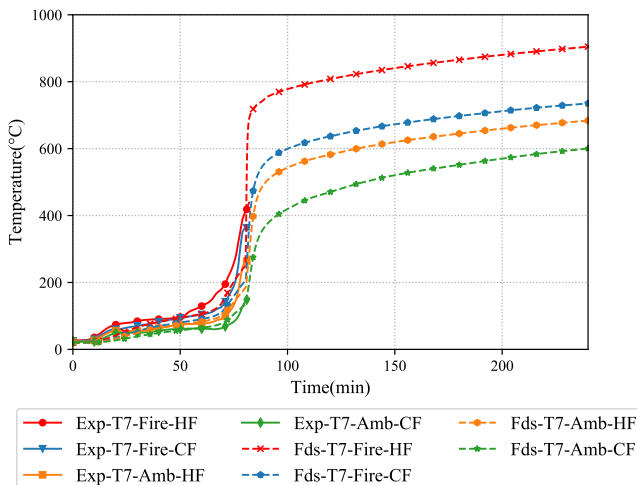
Figure 5.33: Thermal model of Test-T7 wall

one vertical obstruction (&OBST) as shown in Figure 5.36. Time-temperature curves from FDS thermal model are compared against the corresponding experimental results in Figures 5.37 (a) and (b).

Plasterboard open-up was observed in the full-scale fire Test-T10 leading to the sudden temperature rise in the fire side cavity plasterboard surface (Exp-T10-Pb2) similar to other test walls with cavity insulation. The developed FDS thermal model was able to predict this behaviour to a reasonable accuracy for both plasterboard and stud time-temperature curves as shown in Figure 5.38. Fire side plasterboard time-temperature curves matched reasonably well with the experimental results as shown in Figure 5.37 (a). However, the ambient side plasterboard temperatures were lower than the experimental results. This was observed for the stud hot and cold flanges as well. The fire side hot and cold flange temperatures (Fds-T10-Fire-HF and CF) matched reasonably well with the experiments as shown in Figure 5.37 (b). However, the ambient side hot and cold flange temperatures (Fds-T10-Amb-HF and CF) were lower than the experimental results. The increase in the slope of the time-temperature curves on the ambient side hot and cold flanges occurred at a later time period in comparison with the experiments because of the position of temperature measurement by the thermocouples between the FDS model and the experiment. This may lead to unconservative results in the structural model.



(a)



(b)

Figure 5.34: Comparison of time-temperature curves from experiment and FDS model for Test-T7 (a) Average Plasterboard (b) Stud3-Mid

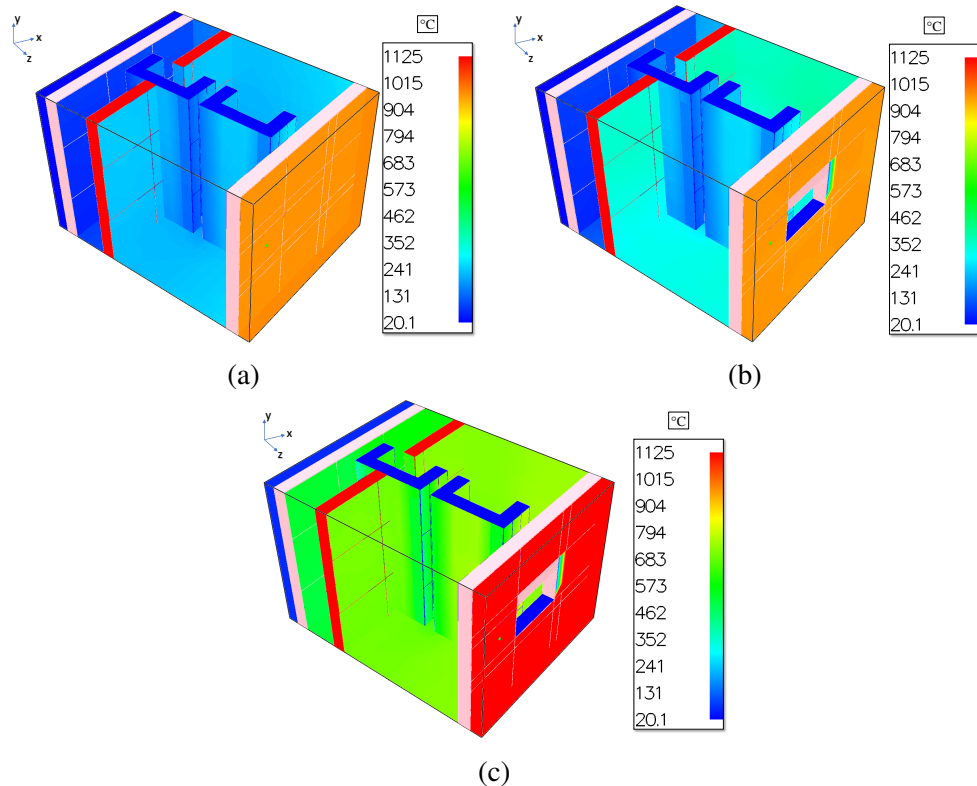


Figure 5.35: Temperature output for Test-T7 from FDS thermal analysis (a) Before plasterboard open-up at 79 min (b) After plasterboard open-up at 80 min (c) At 240 min (End of Simulation)

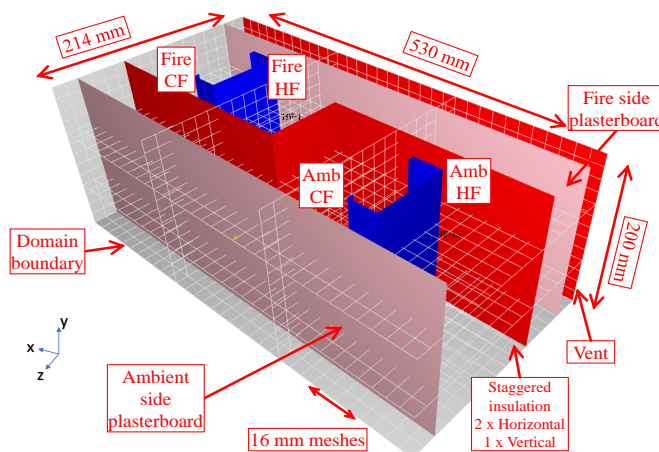


Figure 5.36: Thermal model of Test-T10 wall

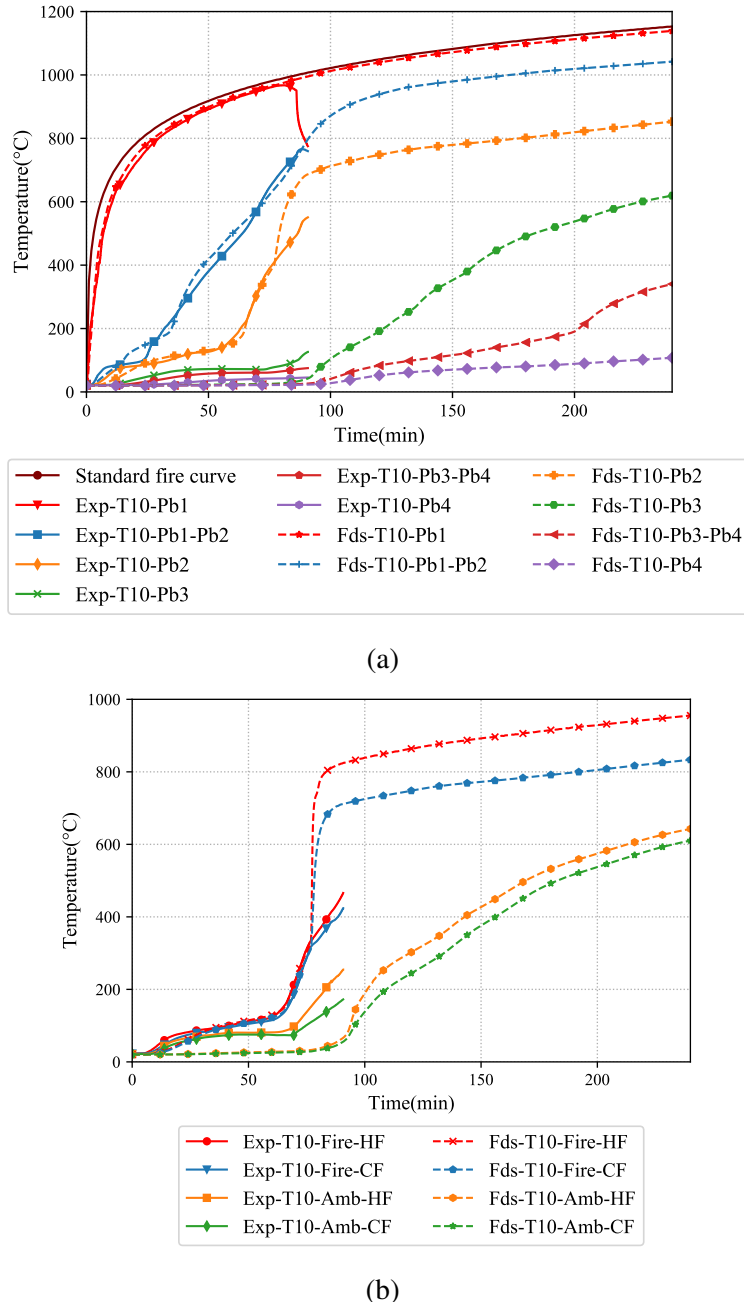


Figure 5.37: Comparison of time-temperature curves from experiment and FDS model for Test-T10 (a) Average Plasterboard (b) Stud3-Mid

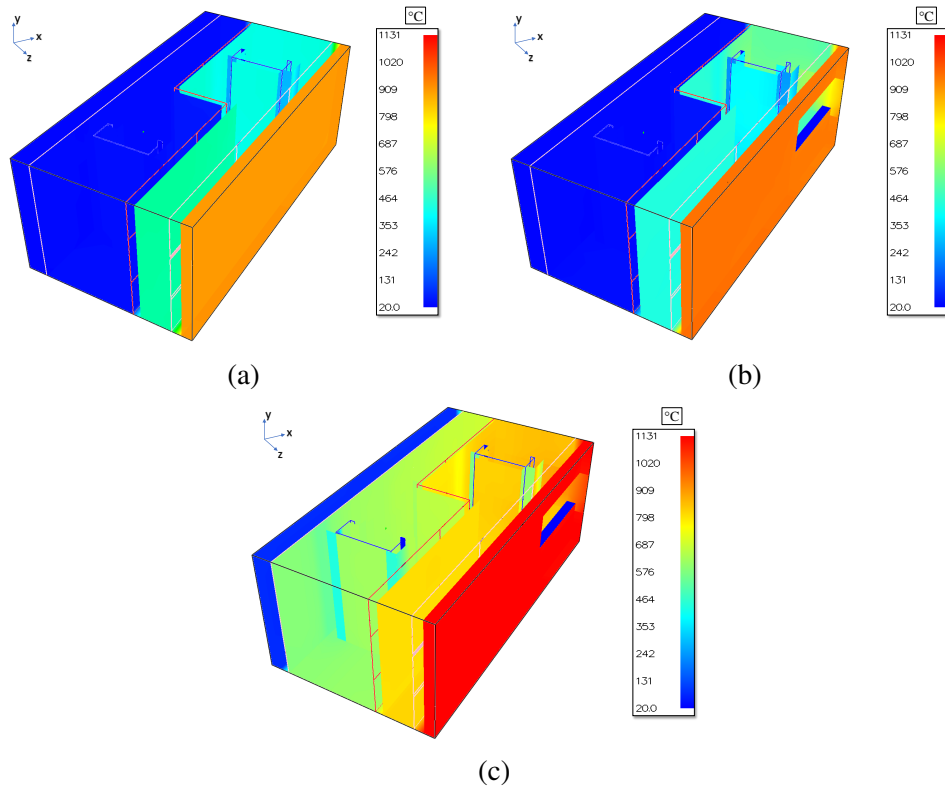


Figure 5.38: Temperature output for Test-T10 from FDS thermal analysis (a) Before plasterboard open-up at 79 min (b) After plasterboard open-up at 80 min (c) At 240 min (End of Simulation)

5.4.4 Thermal model validation - Non-cavity insulated Tests-T1, T2, T3, T4, T8 and T9 with plasterboard open-up

As the plasterboard open-up in fire tests contributes significantly to the prediction of time-temperature curves, the non-cavity insulated test models were also analysed with the plasterboard openings in them. Similar technique used for cavity insulated wall tests as described in Section 5.4.3 were used for the developed thermal models. The set-point temperature was increased to 900°C for non-cavity insulated LSF walls based on Sultan (2015). The plasterboard open-up temperatures corresponding to the fire tests also match this assumption of 900°C in all the conducted non-cavity insulated fire tests. Determining the plasterboard open-up and predicting the corresponding stud hot flange temperatures is important, as these temperatures will be used in the structural FE model. The time-temperature curves from FDS thermal analysis pertaining to the tested wall configurations are presented and discussed next.

Figure 5.39 shows the plasterboard and stud time-temperature curves from FDS thermal model with plasterboard open-up for double stud wall Test-T1. The sudden

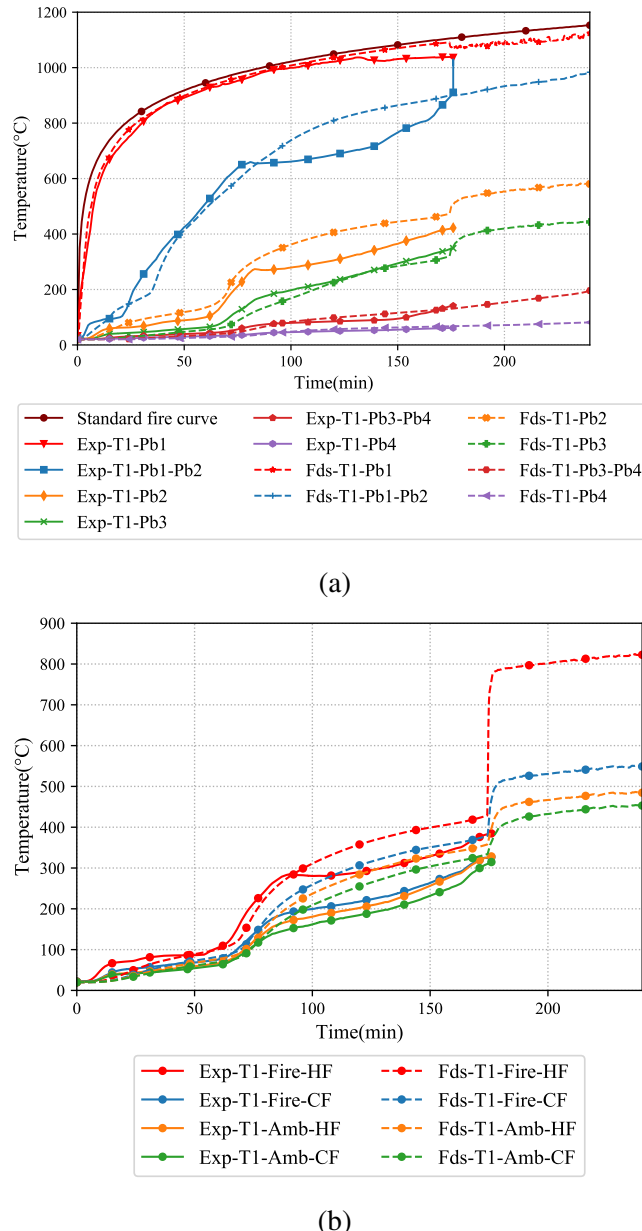


Figure 5.39: Comparison of time-temperature curves from experiment and FDS model with plasterboard open-up for Test-T1 (a) Average Plasterboard (b) Stud4-Mid

increase in the plasterboard time-temperature curve at 176 min can be simulated reasonably as shown in Figure 5.39 (a). This sudden increase is also noticeable in the stud time-temperature curves comparison shown in Figure 5.39 (b). The fire side hot flange temperatures also agree reasonably well with the experimental results which will be used in the structural FE model for predicting the failure time of the wall configuration.

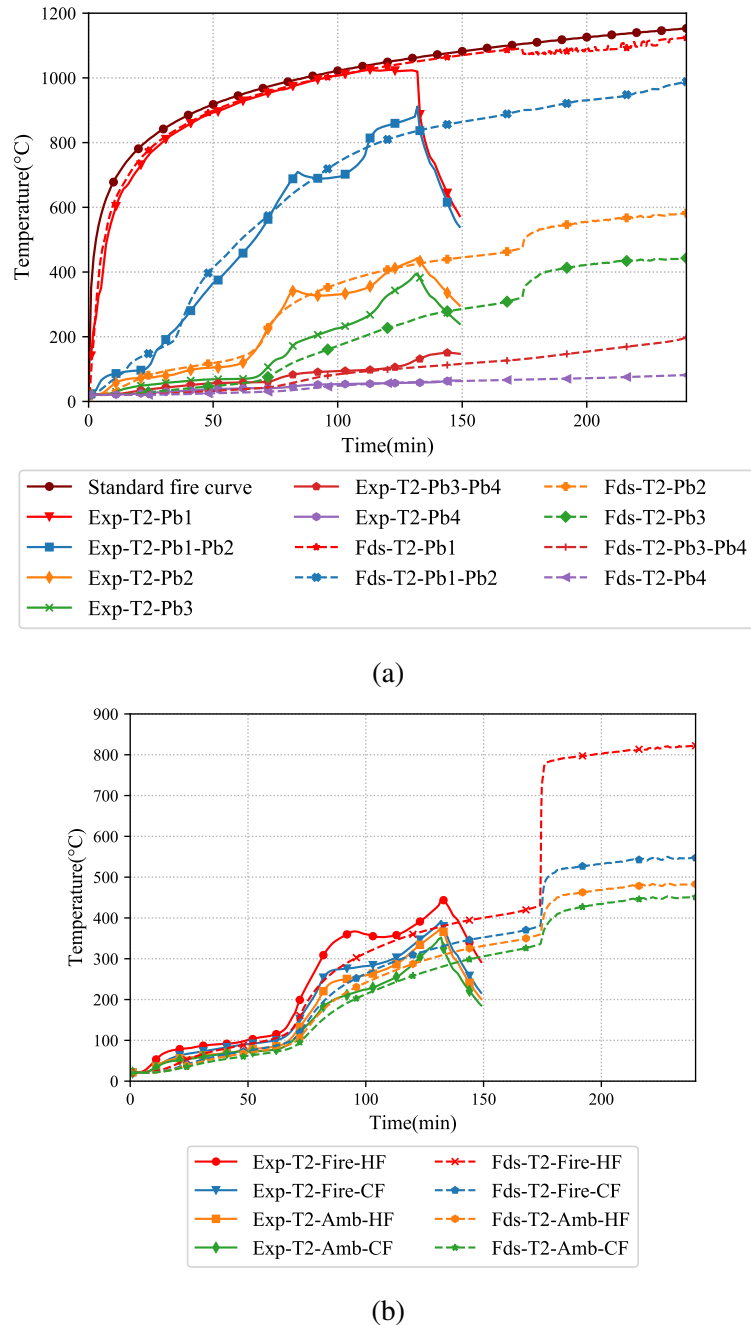


Figure 5.40: Comparison of time-temperature curves from experiment and FDS model with plasterboard open-up for Test-T2 (a) Average Plasterboard (b) Stud4-Mid

Figure 5.40 shows the time-temperature curve comparison for Test-T2. The sudden increase in the plasterboard time-temperature curve as shown in Figure 5.40 (a) was noticeable from 120 min. However, the FDS thermal model predictions shows the sudden increase after 175 min. This is reflected in the stud time-temperature curves also as shown in Figure 5.40 (b). The delay in sudden temperature rise in the hot flange may lead to increased structural failure time which may lead to unconservative results. Test-T2 was conducted with 0.75 mm thick studs unlike Test-T1 with 0.95 mm studs. The set-point temperature of 900°C may be higher for thinner stud section as Tests-T2 and T3 had higher lateral deflection in comparison with Tests-T1 and T4. This was because of the use of thinner studs in the test wall. Severe plasterboard fall-off was also observed in Test-T2 causing premature failure and was discussed in Section 4.6 of Chapter 4. However, this will be further discussed in Chapter 6. Also, during fire tests under load bearing conditions, the furnace is stopped once the test wall fails due to structural inadequacy criterion. The time-temperature curves of plasterboard and studs dip after this time and is evident by the cooling face of the time-temperature curves as shown in Figure 5.40. However, the FDS models are analysed for a time period of 240 min. The behaviour of the test wall post-fire test can be determined through this which will help in determining the structural failure time of the test wall under different load ratios. As Test-T3 was conducted with the same configuration as Test-T2 under a higher load ratio (0.6 LR) the time-temperature curves from the experimental results are available only till 81 min. Comparison of the time-temperature curves of the plasterboards and studs are shown in Figure 5.41, but will not be considered for detailed discussion.

The FDS thermal model results for double stud wall Test-T4 with 70×0.95 mm studs are presented in Figure 5.42. Plasterboard open-up was noticeable at the test wall failure time of 171 min for Test-T4 from the FDS thermal analysis results. FDS thermal model was able to predict the open-up time to a reasonable accuracy and is noticeable by the sudden increase in the plasterboard time-temperature curve in Figure 5.42 (a). The sudden increase in the stud time-temperature curves was also evident in the FDS model predictions and is shown in Figure 5.42 (b). Test-T4 was conducted on 0.95 mm and the time-temperature curves of the plasterboards and studs match reasonably well considering 900°C as the set-point temperature.

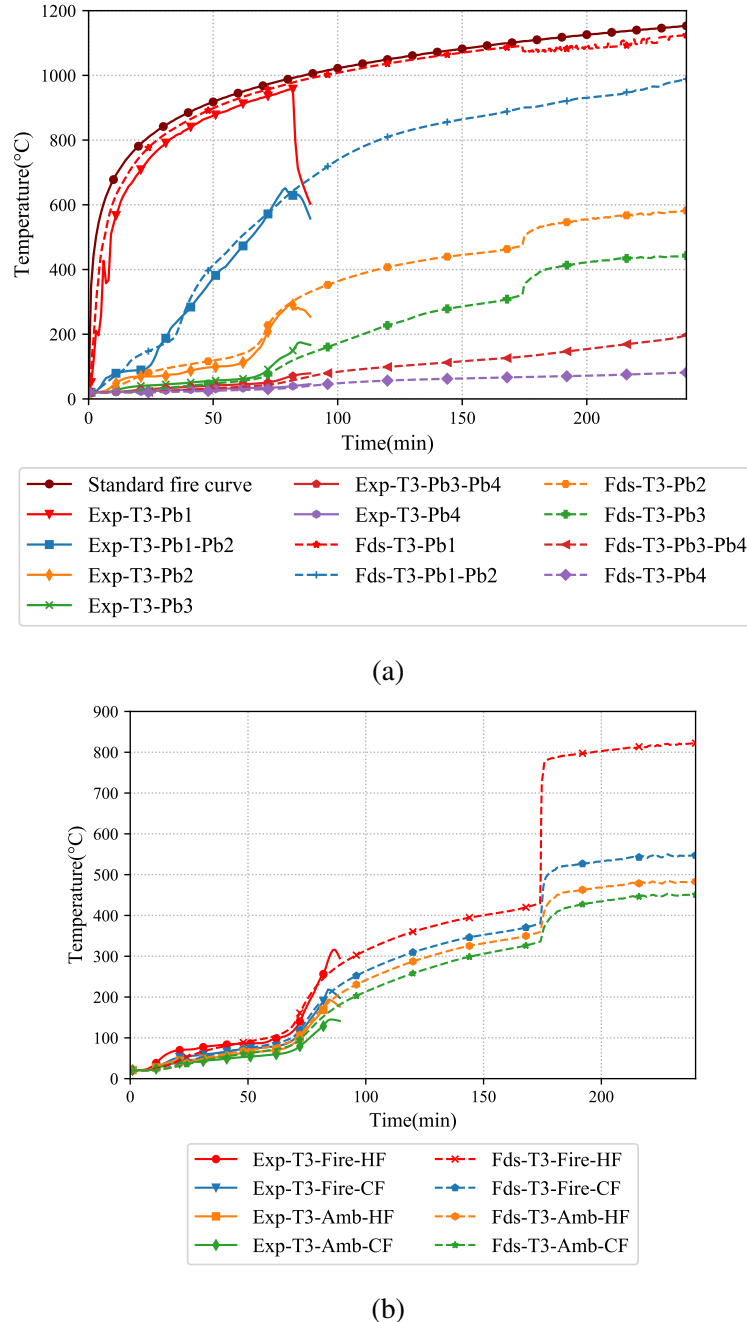
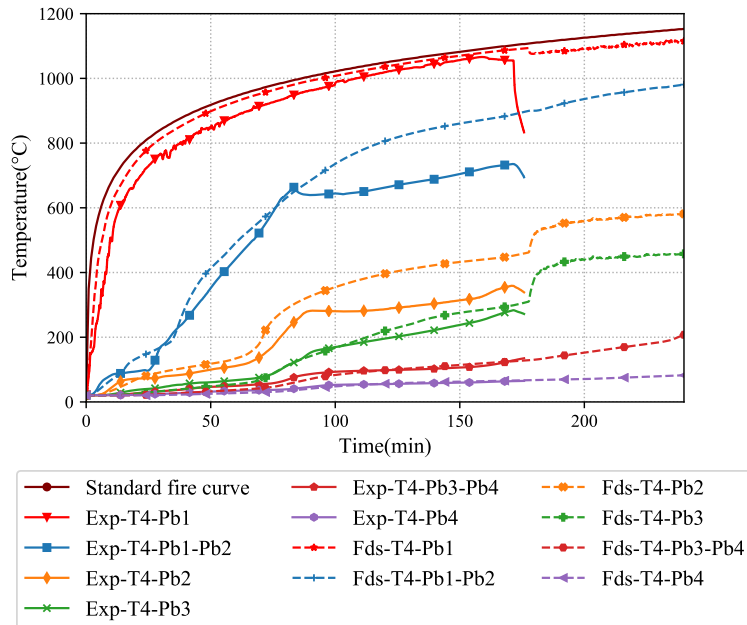
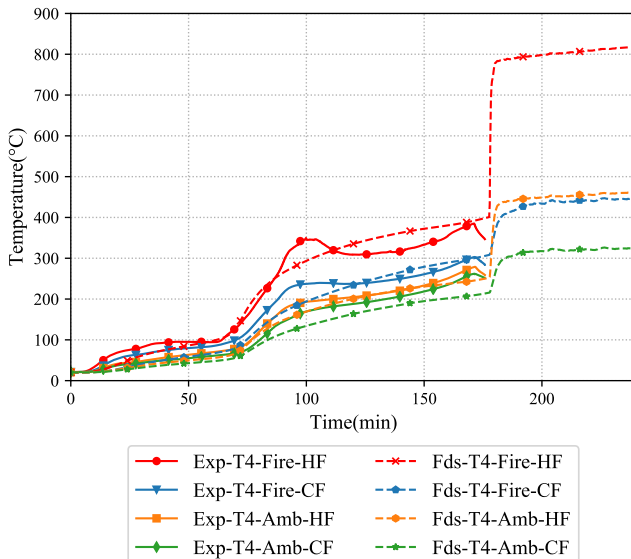


Figure 5.41: Comparison of time-temperature curves from experiment and FDS model with plasterboard open-up for Test-T3 (a) Average Plasterboard (b) Stud4-Mid



(a)



(b)

Figure 5.42: Comparison of time-temperature curves from experiment and FDS model with plasterboard open-up for Test-T4 (a) Average Plasterboard (b) Stud3-Mid

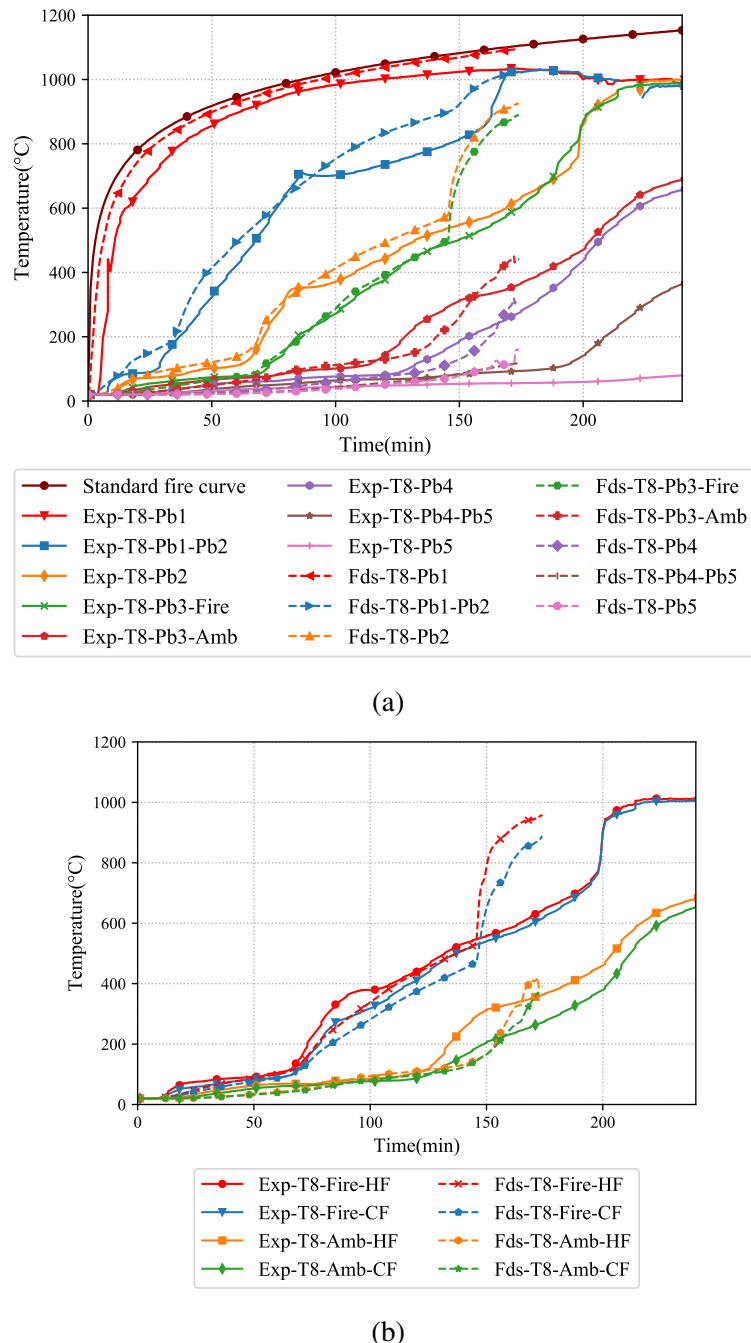


Figure 5.43: Comparison of time-temperature curves from experiment and FDS model with plasterboard open-up for Test-T8 (a) Average Plasterboard (b) Stud4-Mid

Test-T8 FDS thermal model analysis was conducted on shaftliner LSF walls. As this test was conducted under non-load bearing conditions experimental results were available till 240 min. The FDS thermal model without plasterboard open-up showed reasonable agreement with the experimental results and the thermal model was able to predict the time-temperature profiles of the test wall till 240 min as shown in Figures 5.43 (a) and (b). However, the FDS thermal model with plasterboard open-up experienced severe instability and was able to predict the time-temperature profile till 174 min only. However, the time-temperature curves exhibited reasonable accuracy till this time. Temperatures reached by the stud hot flanges were over 800°C after 174 min in the fire test. This is a very high thermal load on the studs and the studs cannot carry any axial compression load at this very high temperature which exceeds the limiting stud flange temperatures stated by Gunalan and Mahendran (2013a) under all load ratios. Therefore, no further iterations were conducted for the Test-T8 FDS thermal model as the stud hot flange temperatures predicted by the FDS thermal model were over 800°C at 174 min.

Test-T9 was conducted on staggered stud LSF wall under non-load bearing conditions. The time-temperature curves of the plasterboard and studs matched reasonably well with the experimental results and are shown in Figure 5.44. The plasterboard open-up time could also be predicted with reasonable accuracy by the FDS thermal model which is evident from the sudden increase in the plasterboard time-temperature curve as shown in Figure 5.44 (a). The stud hot and cold flange time-temperature curves also exhibited reasonable agreement with the experimental results considering the plasterboard open-up as shown in Figure 5.44 (b). In staggered stud walls the ambient side hot flange temperature (Fds-T9-Amb-HF) as shown in Figure 5.44 (b) is higher than the fire side cold flange (Fds-T9-Fire-CF) temperature.

5.4.5 Influence of Plasterboard Open-Up

The thermal FDS models were created with and without plasterboard open-up and thermal analysis was conducted for all the LSF wall configurations considered for experimental investigation. It is evident that the plasterboard open-up is significant in all the LSF walls with cavity insulation (Models-T5, T6, T7 and T10) resulting in the sudden temperature increase resulting in premature failure times. However, in the case of non-

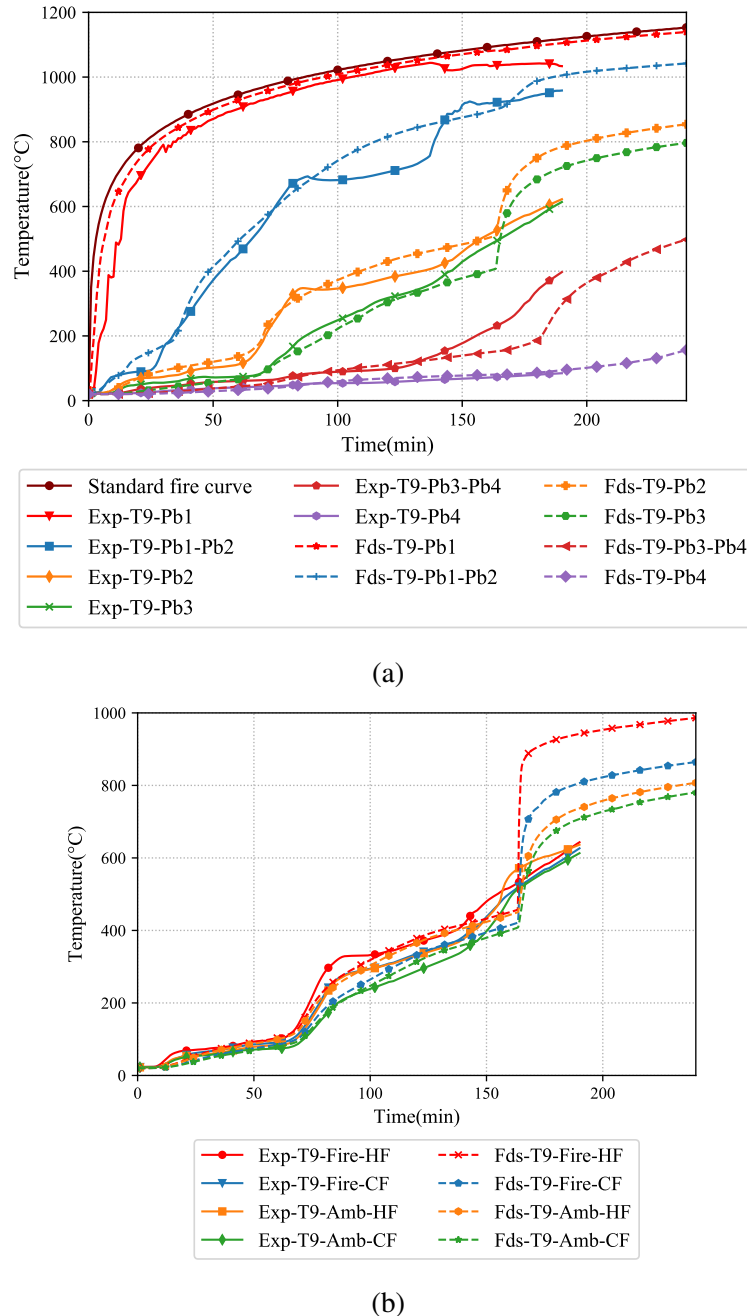


Figure 5.44: Comparison of time-temperature curves from experiment and FDS model with plasterboard open-up for Test-T9 (a) Average Plasterboard (b) Stud4-Mid

cavity insulated LSF wall models such as T1, T2, T3, T4, T8 and T9 the plasterboard open-up occurred in later stages of the fire test and the same was considered for thermal analysis. To determine the influence of the plasterboard open-up in the FDS thermal models the time-temperature curves of plasterboards and studs corresponding to the models with and without plasterboard open-up are compared in Figures 5.45 to 5.50. The comparison between the plasterboard open-up and non plasterboard open-up models show that the plasterboard and stud time-temperature curves are similar till the time when open-up “set-point” temperature is reached. Considering the plasterboard time-temperature curves the difference is minimal for at fire side, fire side interface (Pb1, Pb1-Pb2) and ambient side and ambient side interface surfaces (Pb3, Pb3-Pb4). The time-temperature curves show a sudden rise in the fire and ambient side cavity surfaces (Pb3, Pb4). This behaviour of the time-temperature curve is evident in all the non-cavity insulated models except Test-T8. In Test-T8 the difference in plasterboard time-temperature curves is higher in comparison with the other models.

The sudden increase in the plasterboard and stud time-temperature curves in the non-cavity insulated wall models were noticeable around 170 min in the case of double and staggered stud LSF walls. However, the sudden increase was observed at around 140 min for shaftliner wall model. This is attributed to the varying cavity depth along with the middle plasterboard layer retaining the heat. But in double stud wall the heat is convected within the cavity thereby resulting in reduced heat transfer mechanism. The non-cavity insulated double stud wall fire tests were conducted for nearly 180 min in the case of Test-T1 and T4 while it was 132 min in the case of Test-T2 due to premature plasterboard fall-off. The common observation in all the non-cavity insulated fire tests was the plasterboard open-up irrespective of the load ratio. Therefore, it is evident that the plasterboard open-up happens to be the initiation of the failure in the test walls. Also, in the fire tests the intensity of heat incident on the fire side plasterboard is high as the time of exposure to the standard fire curve on these surfaces is over 120 min in all the fire tests but for T3. The plasterboards become soft after this time period due to complete dehydration, initiating the plasterboard open-up on the fire side of the test wall. The plasterboard open-up is considered to occur at a set-point temperature of 900°C in the developed FDS thermal model. This corresponds to a time period of around 170 min in the FDS thermal model.

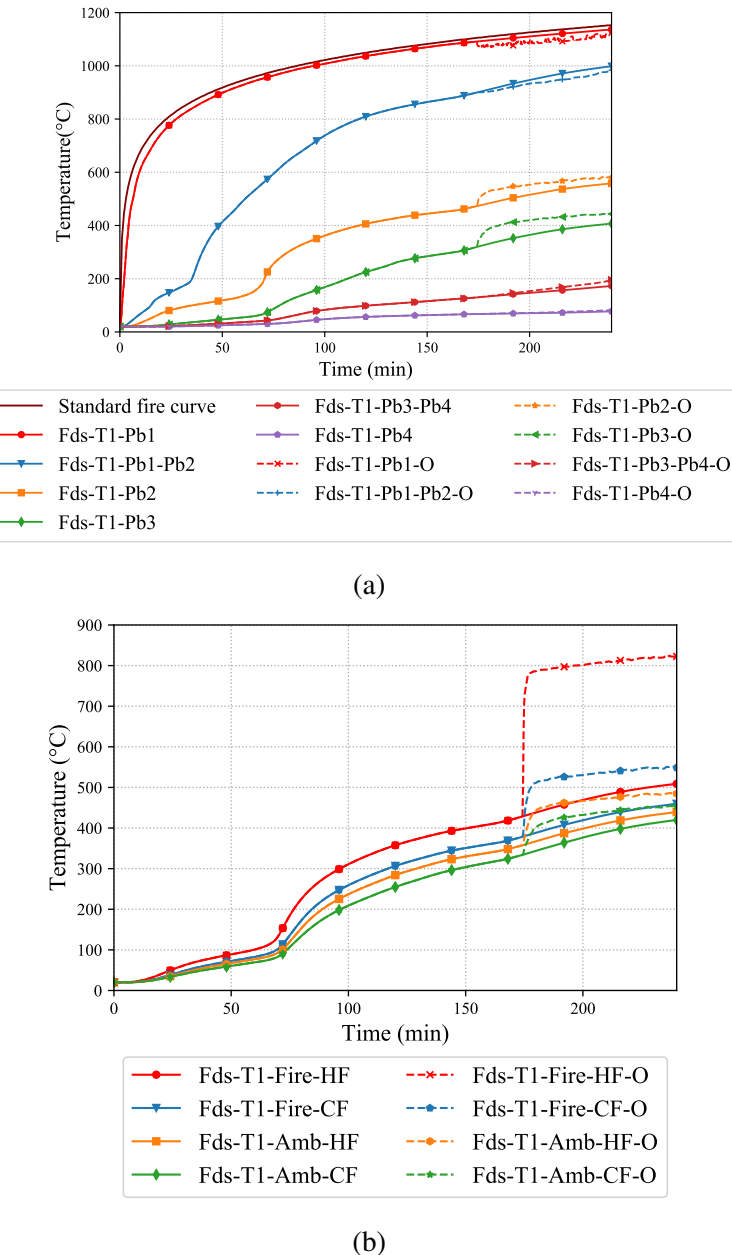


Figure 5.45: Comparison of time-temperature curves from FDS model with and without plasterboard open-up for Test-T1 (a) Plasterboard (b) Studs

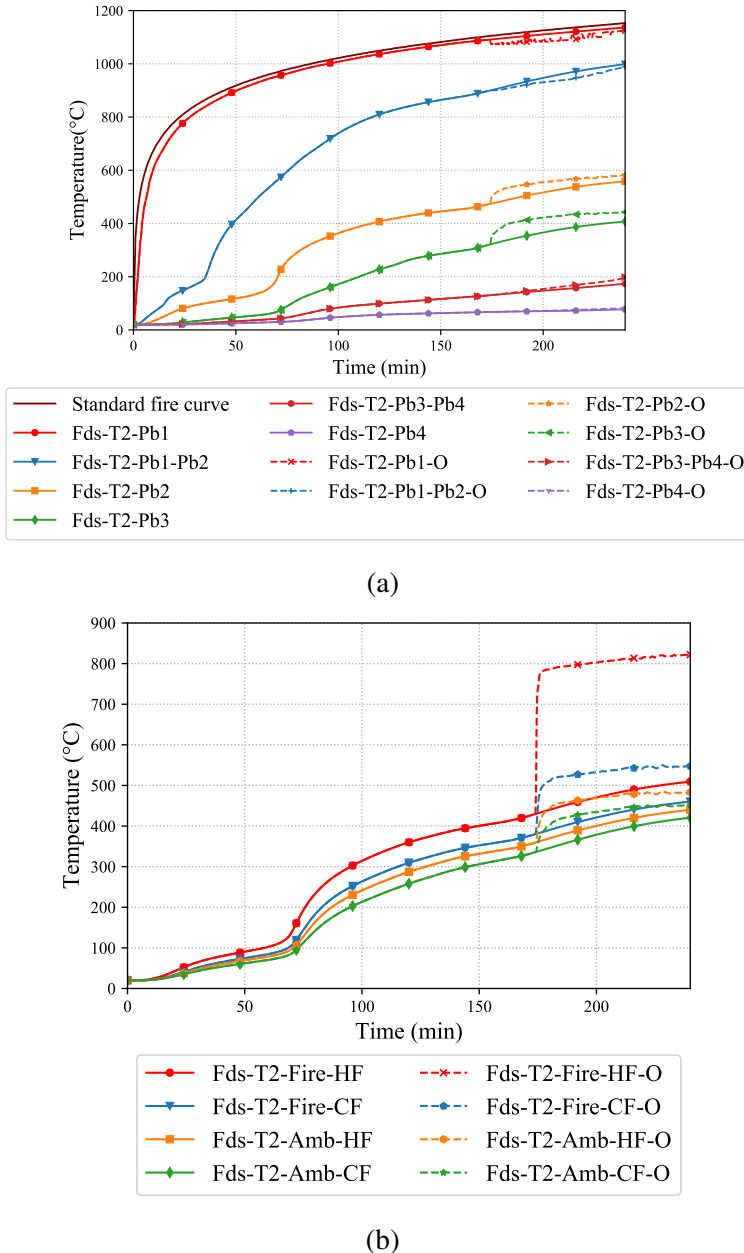


Figure 5.46: Comparison of time-temperature curves from FDS model with and without plasterboard open-up for Test-T2 (a) Plasterboard (b) Studs

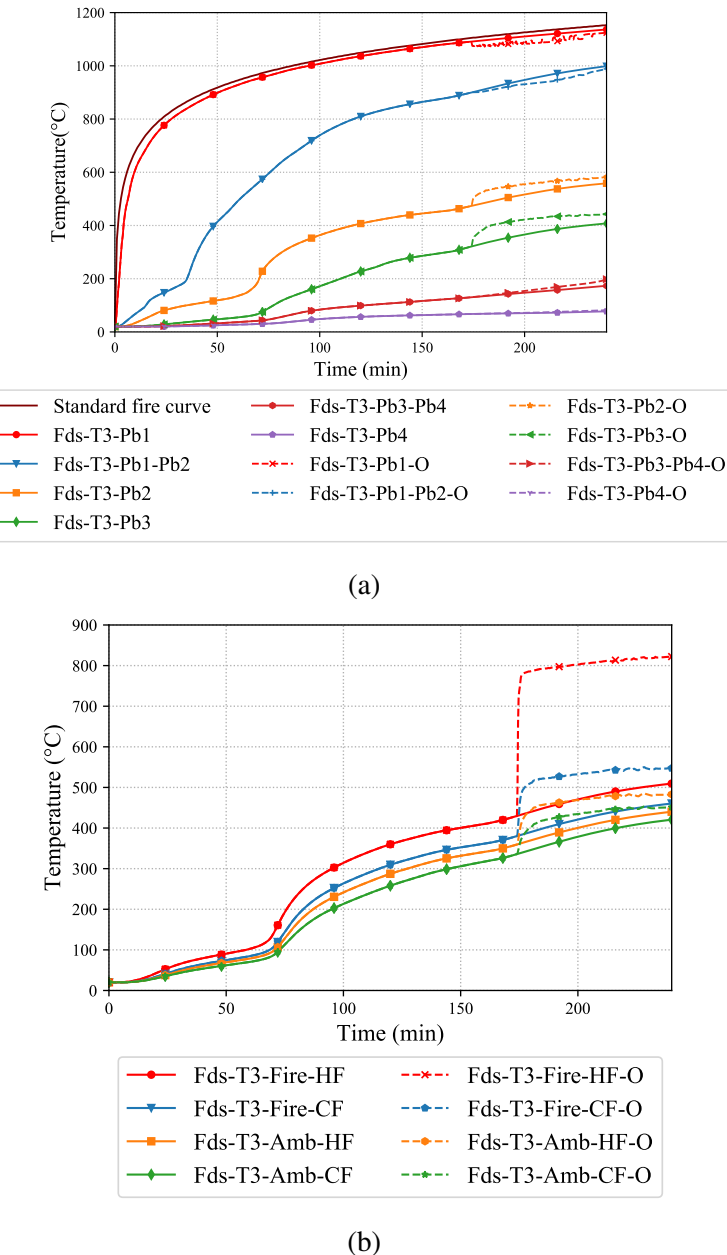


Figure 5.47: Comparison of time-temperature curves from FDS model with and without plasterboard open-up for Test-T3 (a) Plasterboard (b) Studs

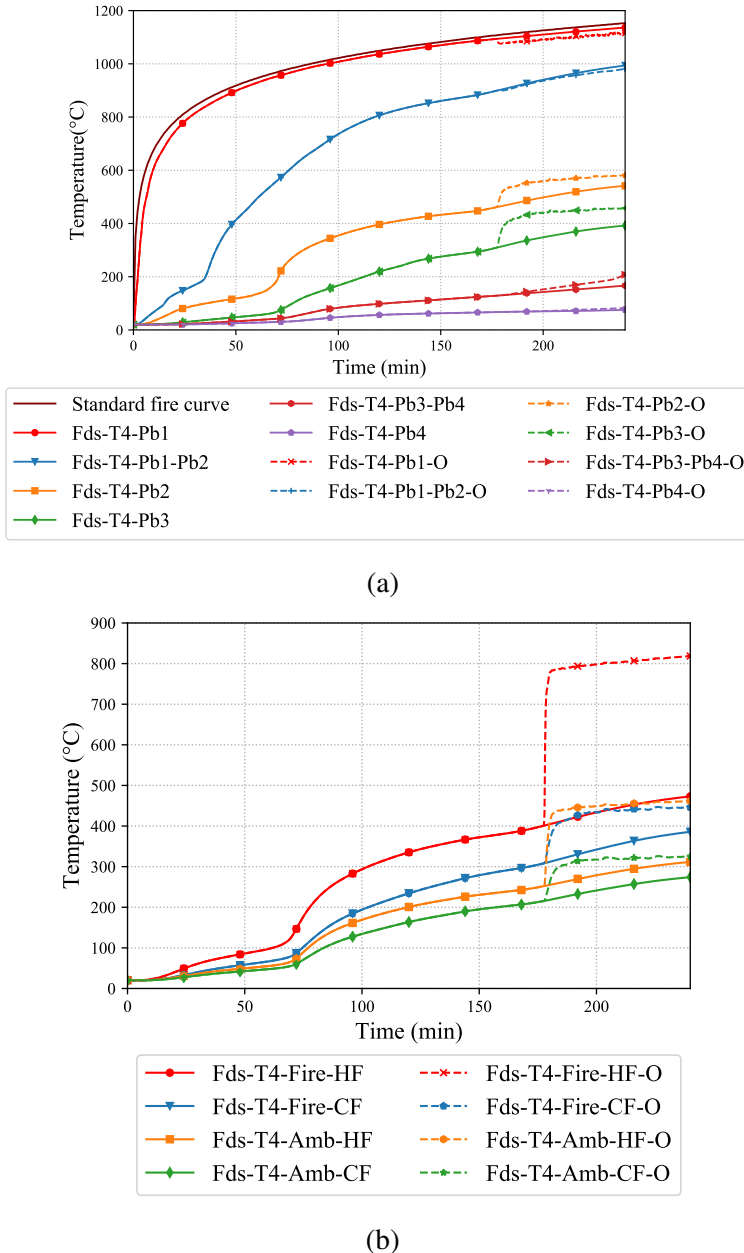


Figure 5.48: Comparison of time-temperature curves from FDS model with and without plasterboard open-up for Test-T4 (a) Plasterboard (b) Studs

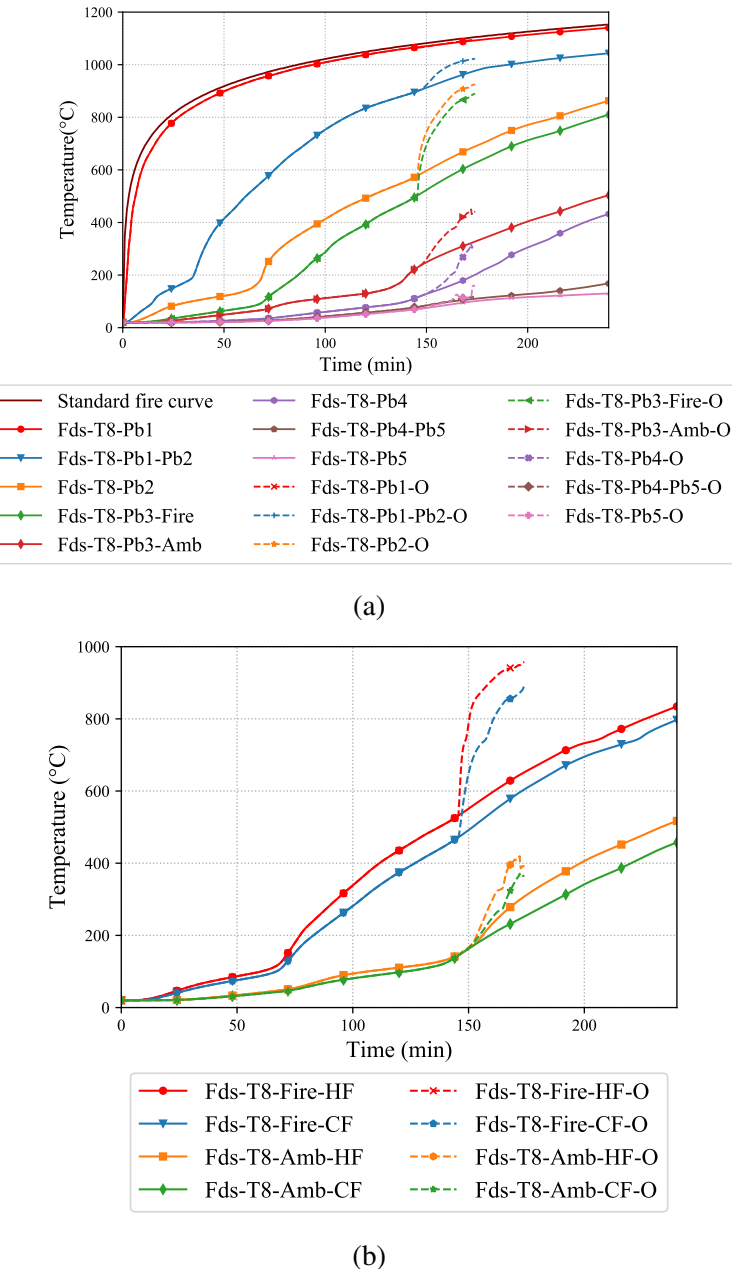


Figure 5.49: Comparison of time-temperature curves from FDS model with and without plasterboard open-up for Test-T8 (a) Plasterboard (b) Studs

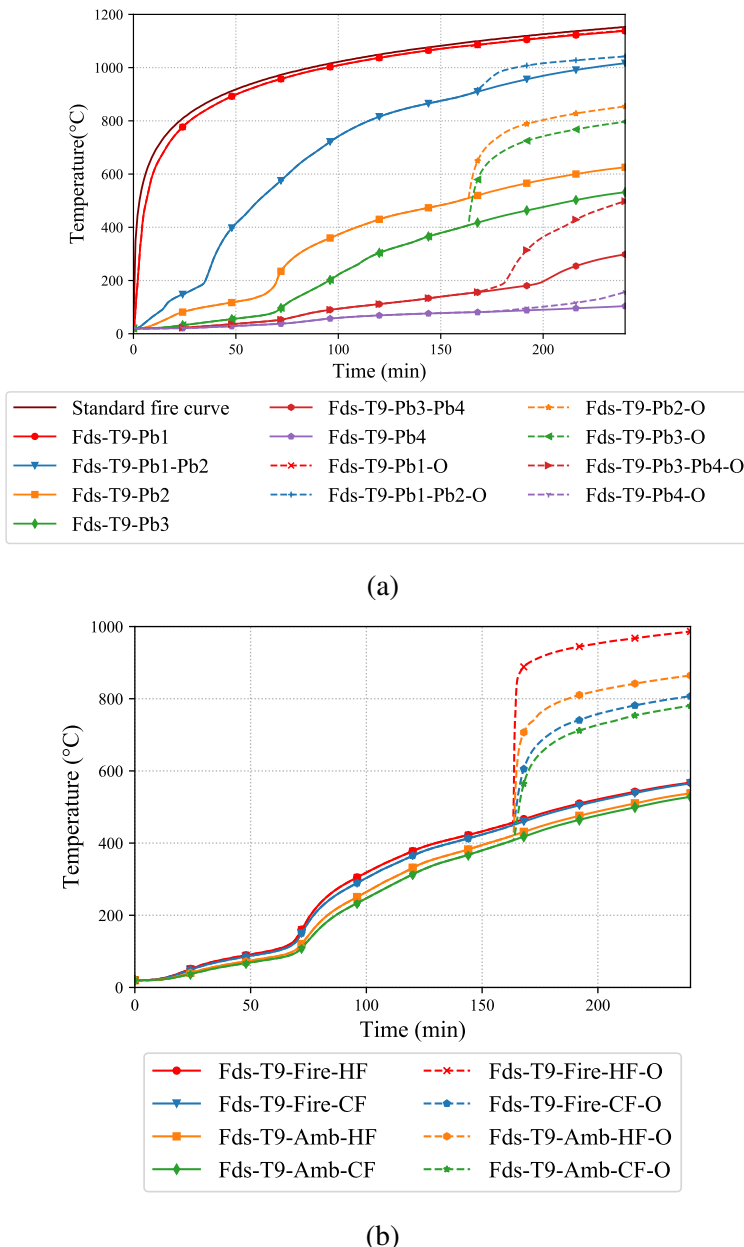


Figure 5.50: Comparison of time-temperature curves from FDS model with and without plasterboard open-up for Test-T9 (a) Plasterboard (b) Studs

The stud critical hot flange temperatures at the considered plasterboard open-up time is over 400°C. This critical stud temperature corresponds to a load ratio of 0.4 and below as stated by Gunalan and Mahendran (2013a). Generally, the fire designs for the LSF walls are conducted for a LR of 0.5 to 0.6. Therefore considering the plasterboard open-up in the non-cavity insulated models might not significantly affect the failure time of the non-cavity insulated load bearing complex LSF walls above 0.5 LR. However, the plasterboard open-up can result in conservative results for LR less than 0.4. But the situation where these LSF walls will be used under these lower LR is unlikely and therefore the time-temperature curves from the plasterboard open-up FDS thermal model will be considered for the structural models and parametric study in Chapters 6 and 7.

5.5 Conclusions

Detailed investigations were conducted using thermal FE modelling techniques and the results were compared with experimental results reported in Chapter 4. Following conclusions are drawn from these investigations.

- Firstly, 2D thermal FE model was created using SAFIR and the results were compared against the experimental results from the full-scale fire Test-T1. Despite using the measured thermal material properties, the model predictions of the time-temperature curves were significantly higher than the corresponding experimental results. Similar modelling techniques used in the past literature for single stud LSF wall were adapted, but the thermal profile predictions were over-conservative in comparison with the experimental results. This may be attributed to the linear computation of radiation and convection within the cavity by SAFIR. However, the runtime of the thermal model was considerably low and did not require the use of high performance computing due to the use of 2D model.
- Due to the over-conservative results from SAFIR FE thermal analysis, investigations were then carried out by creating a 3D solid model in ABAQUS, which was the widely used FE package to predict the thermal behaviour of single stud LSF walls among past research studies. The model was created by considering

all the factors reported in the literature for thermal analysis of single stud LSF walls.

- The assumptions such as closed cavity within the model and radiation being the dominant mode of heat transfer within the cavity similar to single stud LSF wall were also incorporated in the FE thermal model developed in ABAQUS. This led to reasonable time-temperature curve predictions of the plasterboard. However, the temperatures were significantly higher than the experimental results. Also, the ambient side hot flange temperature was higher than the fire side cold flange temperature, which contradicts the experimental results in the case of double stud wall Test-T1. The runtime of the ABAQUS thermal FE model was significantly higher than that of the SAFIR thermal FE model despite the use of HPC. This is attributed to the use of 3D solid elements. Therefore, the thermal FE model developed in ABAQUS with the given assumptions was not considered further.
- 3D thermal models were then created in FDS using “1-cell thick” rule and the time-temperature curves were predicted for all the full-scale fire tests. The shortcomings faced in the SAFIR and ABAQUS thermal FE models such as simulating the effects of convection within the cavity was addressed in the FDS thermal model. Also, previous ABAQUS models considered apparent thermal properties to simulate the plasterboard open-up in cavity insulated LSF walls. However, this technique was not suitable in simulating the sudden increase in the plasterboard and stud time-temperature curves, for instance, in Test-T5. This issue was also addressed in the developed FDS thermal model, wherein a portion (67 mm × 67 mm) of the plasterboard was removed based on a given set-point temperature. Through this, the steep rise in the time-temperature curve experienced in the cavity and non-cavity insulated double, shaftliner and staggered stud LSF walls could be predicted to reasonably accuracy.
- In the previous thermal models, the input ISO 834 time-temperature curve is specified on the fire side plasterboard as a boundary condition. This technique was used to simplify the thermal model by past researchers. However, this does not simulate the exact behaviour of the LSF wall during the fire test. In the full-

scale fire tests, the ISO 834 time-temperature curve is incident on the fire side plasterboard (Pb1) from the furnace through the combined effects of radiation and convection. But, specifying the ISO 834 time-temperature curve as the input boundary condition in SAFIR and ABAQUS will restrict the model to not delete the elements during thermal analysis as the boundary condition is applied on the entire fire side plasterboard surface. This results in conservative results and also becomes difficult to simulate plasterboard open-up, which is common in the LSF walls considered in this study. However, this shortcoming was also addressed in the FDS model developed in this study.

- Despite the use of HPC in solving the FDS thermal model, the runtime of the models was significantly lower in comparison with SAFIR and ABAQUS thermal models. The developed FDS thermal models predicted the experimental time-temperature curves to a reasonable accuracy for all the full-scale fire tests. Therefore, the developed FDS thermal model is considered suitable to predict the thermal behaviour of the shaftliner, double and staggered stud wall systems and will be used in detailed parametric studies.

[This page is intentionally left blank]

Chapter 6

Structural FE Modelling of Complex LSF Walls

6.1 Numerical Analysis of Complex LSF Walls-Ambient Conditions

Finite element method (FEM) is a numerical technique to arrive at a solution for a boundary value problem using partial differential equation to the nearest approximation. The analysis carried out with this methodology is termed as Finite Element Analysis (FEA). FEA works with the logic of minimising the error function in the given boundary value problem by employing variations methods from calculus. Many numerical validation methods prevail till date, but FEM is one of the easiest methods of solving the given problem. The major advantages of using FEM is that any complex problem can be discretised into a simpler problem and analysed in parts to arrive at the result.

There are many FEA packages commercially available in the market. Packages that are widely used by researchers and engineers are ANSYS, ABAQUS, NASTRAN, PATRAN, LS-Dyna etc. Each package has its own unique features and varies in their utility with respect to time and release of the software patches. The decision to use a specific FEA package depends on the necessity of the end user. ABAQUS is proposed for use in this research for structural FE analysis. ABAQUS originally got its name from the calculation tool abacus. Major modules of the software are CAE (Complete ABAQUS environment), explicit, standard, CFD (Computational Fluid Mechanics)

and Electromagnetic. The CAE module is generally used to develop the models in a GUI (Graphical user interface) environment. Other methods of importing the model from other FEA packages are also readily available. Programming languages such as Fortran and Python are embedded within the ABAQUS environment so that the end user is left with endless customization options depending upon their requirements. The standard module in ABAQUS is used for addressing problems related to general structural and multiphysics. As the name suggests the explicit module addresses the contact problems in an efficient manner. The CFD module is used for computational fluid dynamics problems involving liquid flow or thermal flow problems and the Electromagnetic environment is meant for problems related to computational electromagnetics. Since this research focuses on the structural behaviour of LSF walls CAE module will be used for numerical modelling and analysis.

6.2 ABAQUS Modelling Set-up

The numerical models were created in ABAQUS within the CAE environment. Despite the ambient capacity experiments consisting of 4 and 6 studs the numerical models were created with single stud only to achieve maximum computational efficiency. As the stud arrangements are symmetric in the ambient temperature capacity tests of LSF walls, modelling and analysing the single stud was considered as the efficient approach. This consideration was based on past literature on the structural FE models developed by Shahbazian and Wang (2011), Gunalan and Mahendran (2013b), Kessawan and Mahendran (2016b), and Ariyanayagam and Mahendran (2019). The FEA simulation for predicting the ambient temperature capacity of double and staggered stud walls comprises of two steps. Firstly, linear buckling analysis was performed on the studs to determine the buckling load under ambient conditions. After determining the buckling load, local imperfections were included in the model ($d/150$) based on Gunalan and Mahendran (2013b) and static non-linear analysis was carried out to determine the ultimate capacity of LSF wall. The following steps were carried out to determine the buckling load of the studs. As ABAQUS does not have any system of units built in, it is left to the discretion of the user to follow consistent units throughout the model. The International System of Units (SI) was used throughout the modelling

and analysis of the complex LSF walls in this research study. The first step was to create the sketch of the lipped channel section (LCS) studs in the GUI windows as shown in Figure 6.1.

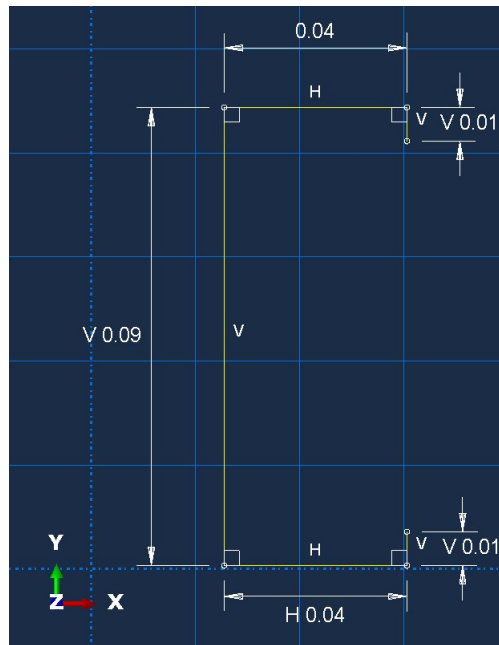


Figure 6.1: Input screen for sketching showing typical LCS stud - ABAQUS

Centreline dimensions were used in the modelling as shell modelling technique was used in the simulation. 3D shell elements were used for the linear buckling and static non-linear analysis under ambient temperature conditions using S4R (4-node shell) element with reduced integration. After completing the section sketch, the model was extruded to 3 m length, depicting studs in the experimental set-up. The extruded section sketch forms a FEATURE in the FE model. The FEATURE forms the PART with additional components and are discussed next. A PART can have single or multiple FEATURES. Some of the additional components of a PART includes, SETS, Section Assignments and Engineering Features such as Inertia and Spring Constants. However, only SETS and Section Assignment will be used in the current structural FE model. For FEA the material properties plays a major role in determining the structural capacity of the developed model. The material properties of steel such as yield stress and elastic modulus were extracted from Kankamge and Mahendran (2011) which were later confirmed by Rokilan and Mahendran (2019). The measured yield strength and elastic modulus are entered in the true stress-strain form as Engineering stress-strain curves are not an accepted form of input in the ABAQUS CAE environment. Yield

strength of 610 MPa and elastic modulus of 200 GPa were used in the ambient temperature structural analysis. The density of steel was kept constant at 7850 kg/m^3 . Once the material properties of steel are keyed in, they are assigned to the corresponding PART through Section Assignment. The PART is then imported into the assembly, wherein two independent INSTANCES of the stud are created. Multiple point constraints (MPCs) using beam element were used at the top and bottom of the model on a reference point replicating the centre of gravity (CG) of the model and appropriate boundary conditions were assigned to it. This is achieved by tying all the edges at the top and bottom of the model to their corresponding reference points as shown in Figure 6.2 (a). Translations along the x, y and z-axes were fixed at the bottom of the model while the model was free to move along the z-axis at the top. The model was fixed against rotation along the z-axis only at the top and bottom. Translation along the x-axis was fixed on the stud flanges at screw locations (300 mm) to simulate the lateral restraints provided by plasterboards on the exterior flanges. Individual plasterboards were not modelled to improve the computational efficiency. Lateral restraints provided by the noggings were specified at 1 m intervals on all the flanges. A mesh density of 4 mm was adopted throughout the model based on past literature and initial sensitivity study as shown in Figure 6.2 (b). A concentric unit load was applied at the top reference point and the buckling analysis was carried out by specifying linear perturbation in the step option. Figure 6.3 shows a typical double stud wall model in ABAQUS. Ten eigen modes were requested for each model to investigate the buckling modes of the studs. The input file was modified with “*NODE FILE U” argument to collect the buckling modes as a data file and to be used in the non-linear analysis. The buckling analysis results were viewed with the in-built data visualization tool in ABAQUS CAE environment.

The second step was to conduct non-linear structural analysis and to determine the ultimate load carrying capacity of the studs. The model used for the buckling analysis was imported to a new file to conduct the analysis. The analysis step option was replaced with static general option and the “NLgeom” feature was turned on to include the nonlinear effects as a result of large deformation in the model. Maximum increments needed for the analysis are specified depending on the model and also the initial, minimum and maximum increment size. Specific dissipated energy fraction was used

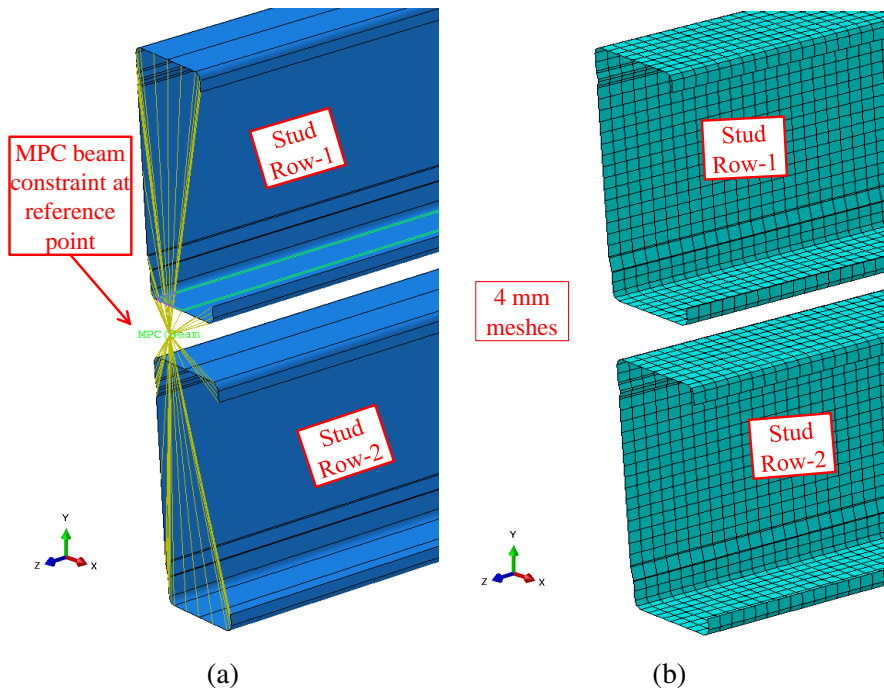


Figure 6.2: Typical double stud model in ABAQUS (a) Support condition (b) Mesh density

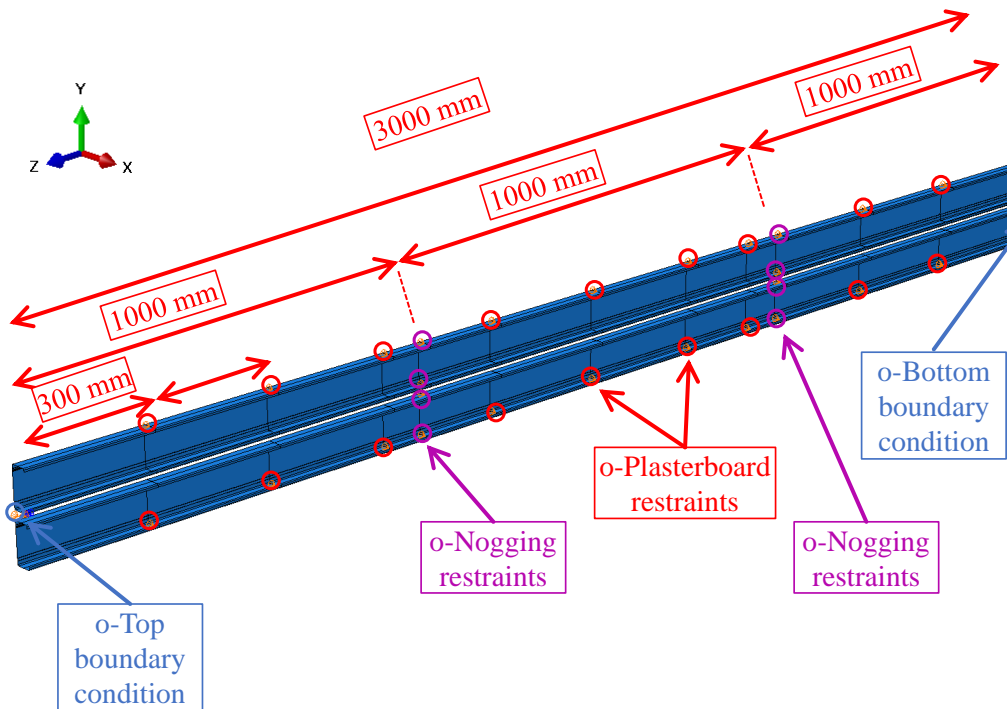


Figure 6.3: Support and restraint conditions of double stud wall model in ABAQUS

for automatic stabilization in the model for better convergence. History output requests were specified at the top reference point to monitor the axial displacement and at the bottom reference point to monitor the support reactions throughout the analysis. These history outputs are stored in the output database (ODB) file for every n^{th} increment in the analysis. Maximum principal stresses in all the elements throughout the model were also extracted from the analysis. Structural model validation and comparison with the experimental results are discussed next.

6.3 Structural FE Model Prediction - Ambient Temperature Capacity Tests

Structural FE models were developed for all the tested LSF wall configurations listed in Chapter 3. This includes wall configurations such as single and double stud LSF walls. The load versus axial displacement results from the developed structural FE models are presented and compared with the experimental results next.

Test-AT1

Test-AT1 was conducted on a double stud LSF wall with 90×0.95 mm lipped channel studs as shown in Figure 6.4. The applied axial compression load versus axial displacement results from finite element analysis (FEA) and experiments are shown in Figure 6.5. Finite element analysis of Test-AT1 wall resulted a maximum axial compression capacity of 71.97 kN while it was 73.0 kN from the experimental results, a good agreement. However, the gradients of the axial load versus displacement curves from structural FE analysis and experiment do not match well. This is because of the difference in the plasterboard lateral restraint and the end restraint conditions between FE model and experiment. The MPC beam restraint constraints to simulate end supports and the intermittent lateral restraint provided as boundary conditions in the FE model contributes to the difference in slope of the applied load versus axial displacement curve. Modelling the stud to track and stud to plasterboard connection with the appropriate lateral lateral stiffness from the screws in the FE model can eliminate this issue. However, this was beyond the scope of this study.

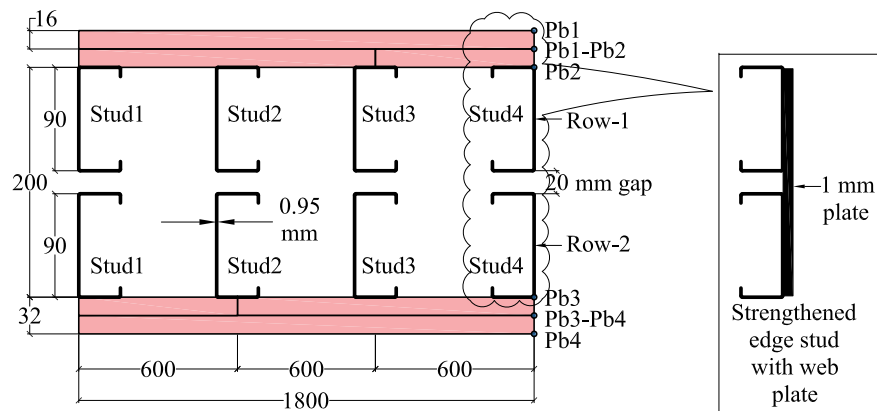


Figure 6.4: Test-AT1 wall configuration

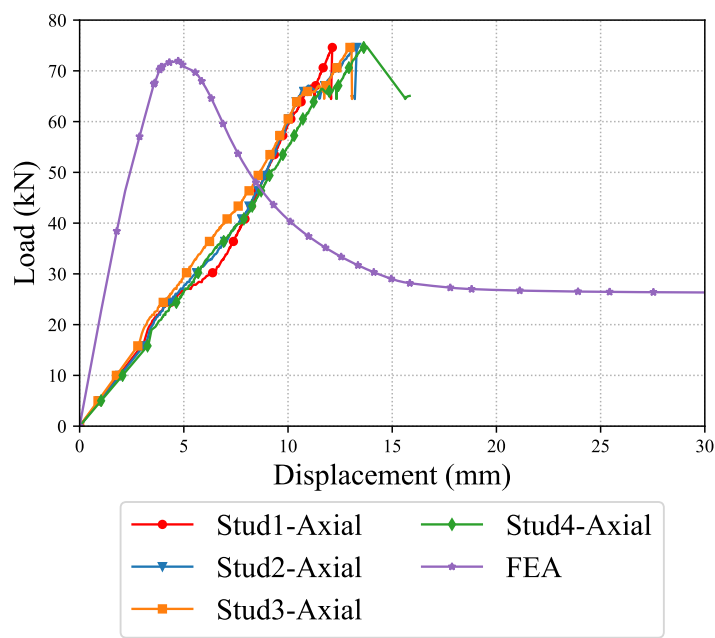


Figure 6.5: Comparison of load versus displacement curves of Test-AT1 wall from FEA and experiment

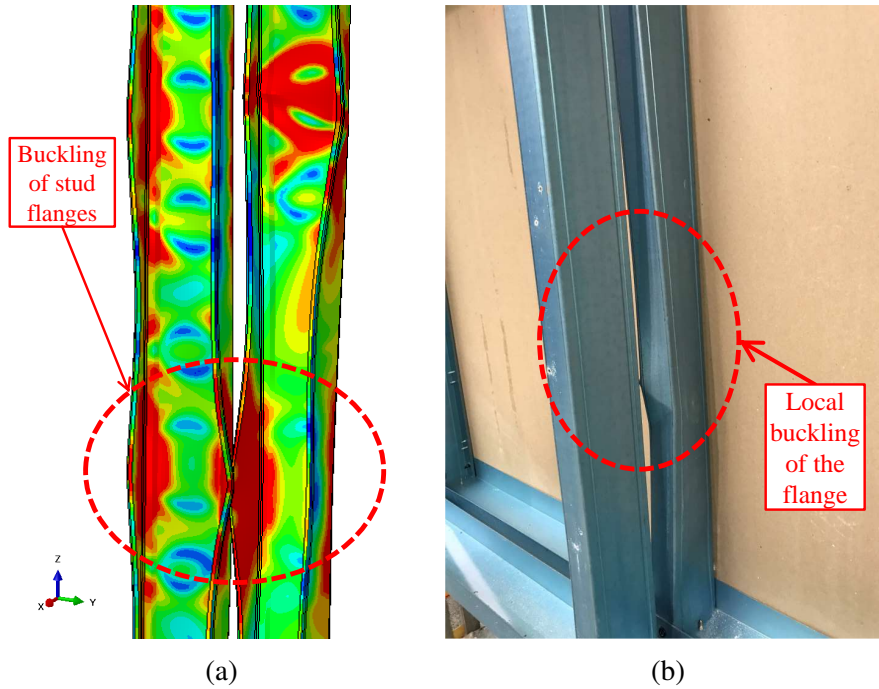


Figure 6.6: Buckling failure of studs in Test-AT1 wall (a) FEA (b) Experiment

Since a general static method of analysis was adopted in FEA the axial compression load was applied instantaneously by load control technique in predefined small increments. This might also contribute to the change in the slope of the applied load versus axial displacement curve. The lateral deflections from the FEA are not considered for comparison as local buckling was the dominant mode of failure of studs. The failure mode predicted by FEA is compared with the experimental results in Figure 6.6. Buckling of the stud flanges observed in the experiments was also simulated by the developed FE model.

Test-AT2

Test-AT2 was conducted on a double stud LSF walls with 90×0.75 mm lipped channel studs as shown in Figure 6.7. The structural FE model gave an axial compression capacity of 46.25 kN while the experimental axial compression capacity was 47.08 kN as shown in Figure 6.8, a good agreement. The local compressive failure of the stud web and flanges shown in Figure 6.9 (a) was well simulated by the developed FE model as shown in Figure 6.9 (a). It is to be noted that the buckling was significant on one flange of the stud in test wall. However, the stud buckling mode simulation from the FE structural model resulted in the buckling of the flanges and web. This

is attributed to the post-ultimate failure behaviour experienced by the stud in the FE model. During the full-scale ambient capacity test after the test wall (first stud) failure, the applied load is transferred to the other studs. As, the edge studs were strengthened the test wall could withstand this excess load for a short time within which the load application was stopped. Therefore, depending upon the time taken to stop the load application after test wall failure is attributed to the post-failure behaviour of the studs in the ambient temperature capacity tests. Also, the stabilization criterion used for Test-T2 was capable of predicting the post-buckling failure. However, determining these factors are based on a trial and error method and varies with the models as stated in the ABAQUS documentation manual (Simulia Corporation, 2017).

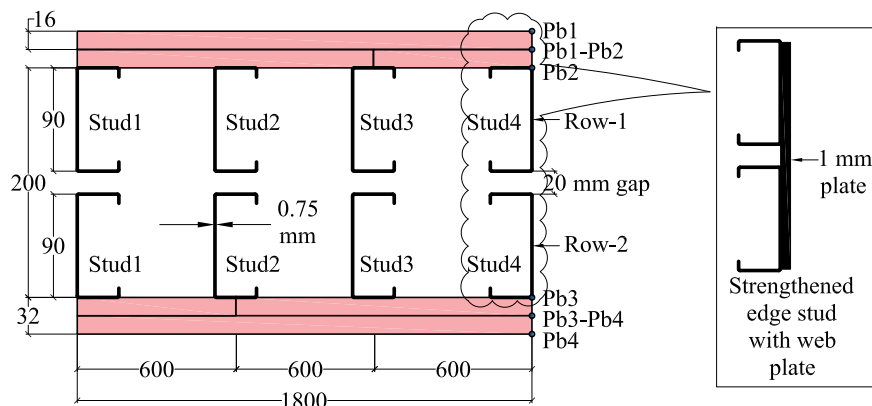


Figure 6.7: Test-AT2 wall configuration

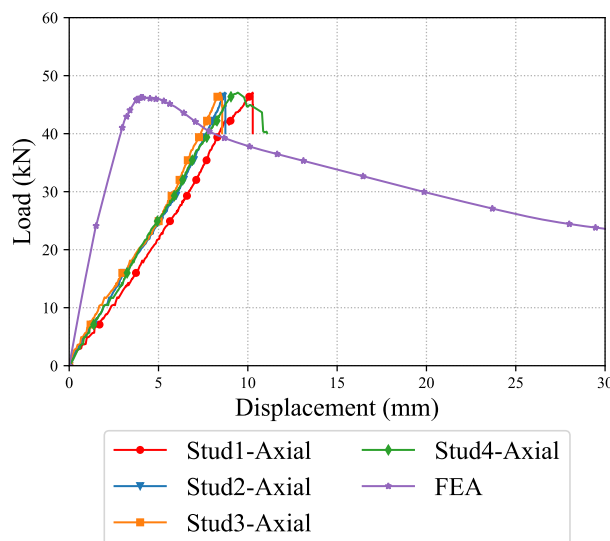


Figure 6.8: Comparison of load versus displacement curves of Test-AT2 wall from FEA and experiment

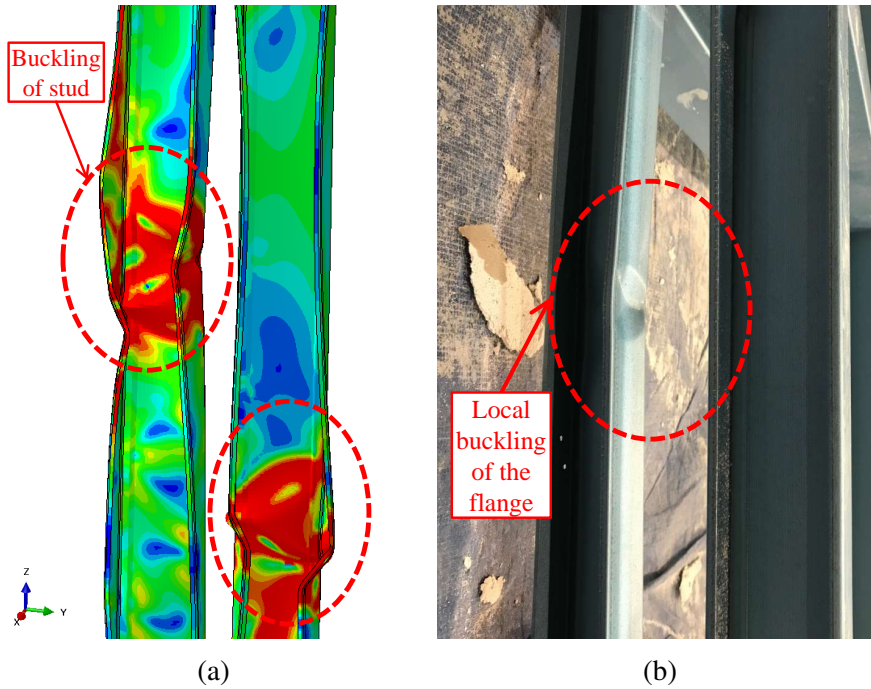


Figure 6.9: Buckling failure of studs in Test-AT2 wall (a) FEA (b) Experiment

The ambient temperature tests were conducted on LSF walls with either four or six studs. However, in the developed structural FE models single stud was used for computational efficiency. As discussed in Section 3.6 of Chapter 3, the screw fastened connection of studs with plasterboards and tracks were not considered in the FE model. However, the nodes at the screw locations were provided with full restraints. This was achieved through MPC beam constraints on the end supports and through boundary conditions to simulate intermittent plasterboard restraint on the stud flanges. This assumption holds good as global buckling in the major axis direction was not the dominant failure mode in the ambient temperature capacity tests of double stud walls.

Test-AT3

As stated earlier Test-AT3 was conducted with six studs unlike four studs in Test-AT2 as shown in Figure 6.10. Figure 6.11 compares the axial compression load versus axial displacement curves from FEA and experiment. The experiment gave an ambient temperature compression capacity of 39.42 kN while the structural FE models prediction was 46.25 kN. However, as stated earlier in Section 3.6 of Chapter 3 the reduction in axial compression capacity from the experiment was attributed to the weak plasterboard minor axis restraints provided to the edge studs (Studs1 and 6). As the test wall

failed due to the bearing of the edge studs no further comparisons were made for the Test-AT3 with the FE model.

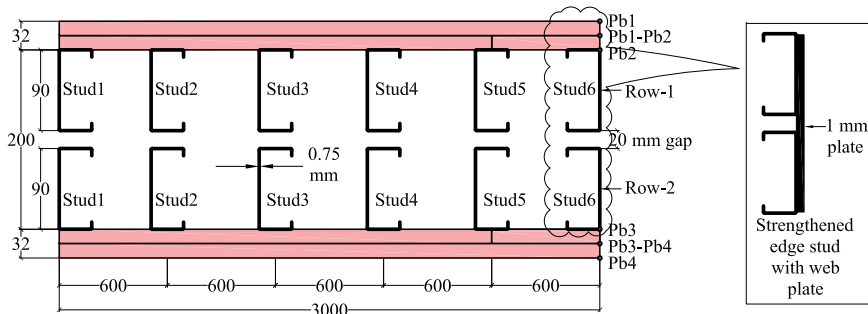


Figure 6.10: Test-AT3 wall configuration

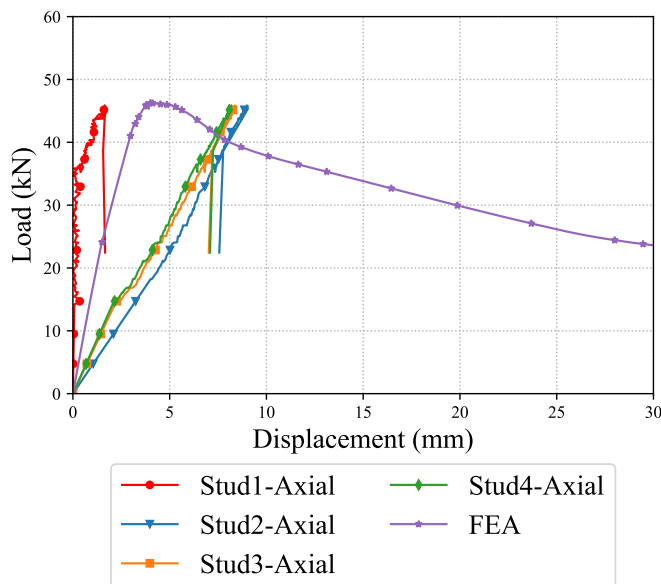


Figure 6.11: Comparison of load versus displacement curves of Test-AT3 wall from FEA and experiment

Test-AT4

Test-AT4 was conducted on a double stud LSF wall with 70×0.95 mm lipped channel studs as shown in Figure 6.12. In this test, the edge studs (Stud1 and 4) were strengthened to avoid premature failures. The structural FE model gave an axial compression capacity of 71.81 kN as shown in Figure 6.13. However, the experimental axial compression capacity was 86.21 kN. This higher ambient temperature stud capacity might be due to the higher yield strength of the studs used in the test wall. This was possible because the steel studs for Test-AT4 were procured from a different batch of studs.

However, the yield strength used in the structural FE model was the same. Another reason for the higher axial compression capacity from the experiment may be because of the load sharing by the strengthened edge studs. This could have also influenced the applied load versus axial displacement curve exhibiting an intermittent slope as shown in Figure 6.13. The buckling of web and flanges observed in the studs in the experiment was simulated well by the developed structural FE model as shown in Figure 6.14.

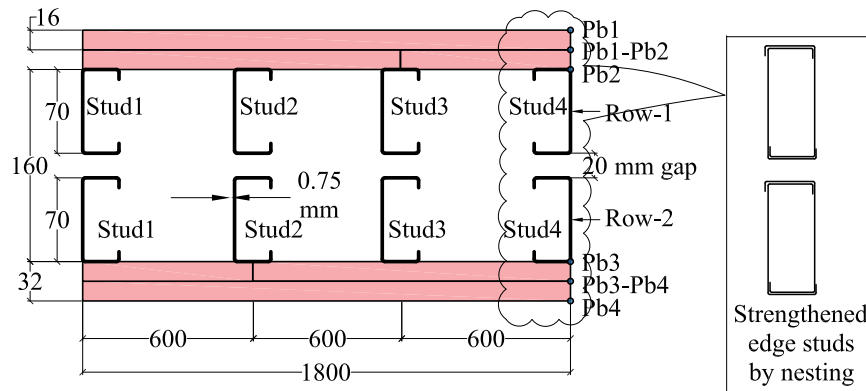


Figure 6.12: Test-AT4 wall configuration

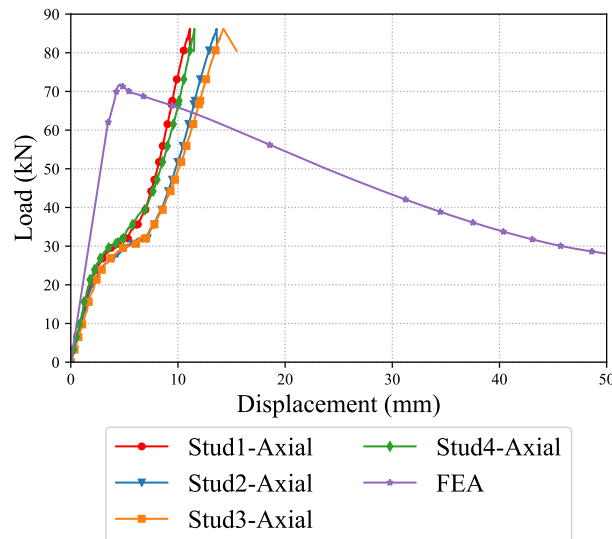


Figure 6.13: Comparison of load versus displacement curves of Test-AT4 wall from FEA and experiment

Local buckling of the web was noticeable in Stud3 Row-1 from the experiment while local buckling was observed in both studs from the FE simulation. This is as a result of post-ultimate failure response simulated by the FE model. The snapshot of the local buckling in the FE model was captured in the last time step of the simulation

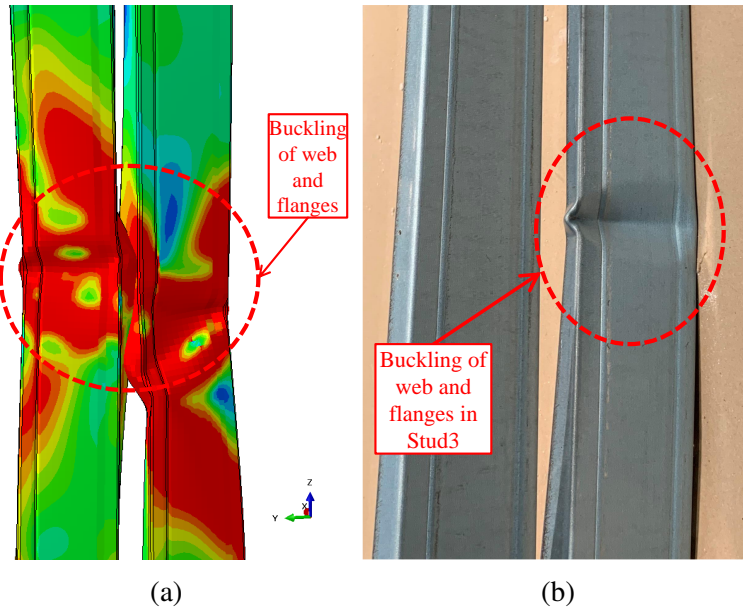


Figure 6.14: Buckling failure of studs in Test-AT4 wall (a) FEA (b) Experiment

corresponding to the axial displacement of 40 mm from load versus displacement curve shown in Figure 6.13.

Test-AT5

Test-AT5 was conducted on a staggered stud LSF wall made of 90×0.95 mm lipped channel studs as shown in Figure 6.15. The modelling technique adapted to simulate the ambient capacity Test-AT5 was different in comparison with the other four ambient capacity tests. This is because of the use of omega noggings in the experimental set-up. As the noggings were connected through the webs instead of flanges in the experimental test wall, similar set-up was adapted in the structural FE model. Firstly, service holes were made on the studs at 1 m interval. The studs were arranged at 300 mm apart in the ASSEMBLY. A Reference Point (RP) was created at the top and bottom centroid of the wall system as shown in Figure 6.16 (a). Top and bottom boundary conditions along with the axial load were applied through these RPs. Partitions were created around the service holes to facilitate the application of MPC beam constraints. This was done by selecting the edges of the service holes as the slave edges connecting to a master node at the centre of service hole through MPC beam constraint as shown in Figure 6.16 (b). A RP was created at the centre of all the service holes and the noggings restraints were provided as boundary condition. Translation along the x-axis

was fixed at the RP to simulate the minor axis restraint provided by the omega nogging on the stud web. Details about the MPC-constraints on the service holes of the studs are shown in Figure 6.16 (b). Meshing near the stud service holes is critical in the structural FE model. Therefore, partitions were created around the stud service holes in the ASSEMBLY to create a sweep mesh around the service holes as shown in Figure 6.16 (c). The structural analysis was conducted using a similar procedure to that of Tests-AT1 to AT4 incorporating the above-mentioned changes in the model.

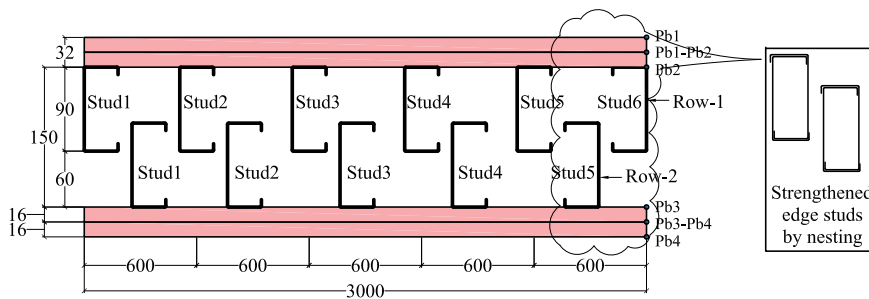


Figure 6.15: Test-AT5 wall configuration

Figure 6.17 compares the axial compression load versus axial displacement curves from structural FE model and experiment. The structural FE model gave an axial compression capacity of 60.98 kN in comparison with the experimental capacity of 68.49 kN. Buckling of the stud web and flanges near the service holes observed in the experiment was simulated well by the developed structural FE model as shown in Figure 6.18.

6.4 Summary of Ambient Temperature Capacity Predictions

A summary of the ambient temperature capacities predicted by the structural FE model is shown in Table 6.1. Comparison with experimental capacities show that the developed structural FE model could determine the structural failure capacity of the double and staggered stud LSF walls under ambient temperature conditions to a reasonable accuracy except for Test-AT4 (16.7% lower prediction). The buckling failure modes corresponding to all the ambient capacity tests were also simulated to a reasonable accuracy in all the ambient temperature capacity models. Therefore, this structural FE

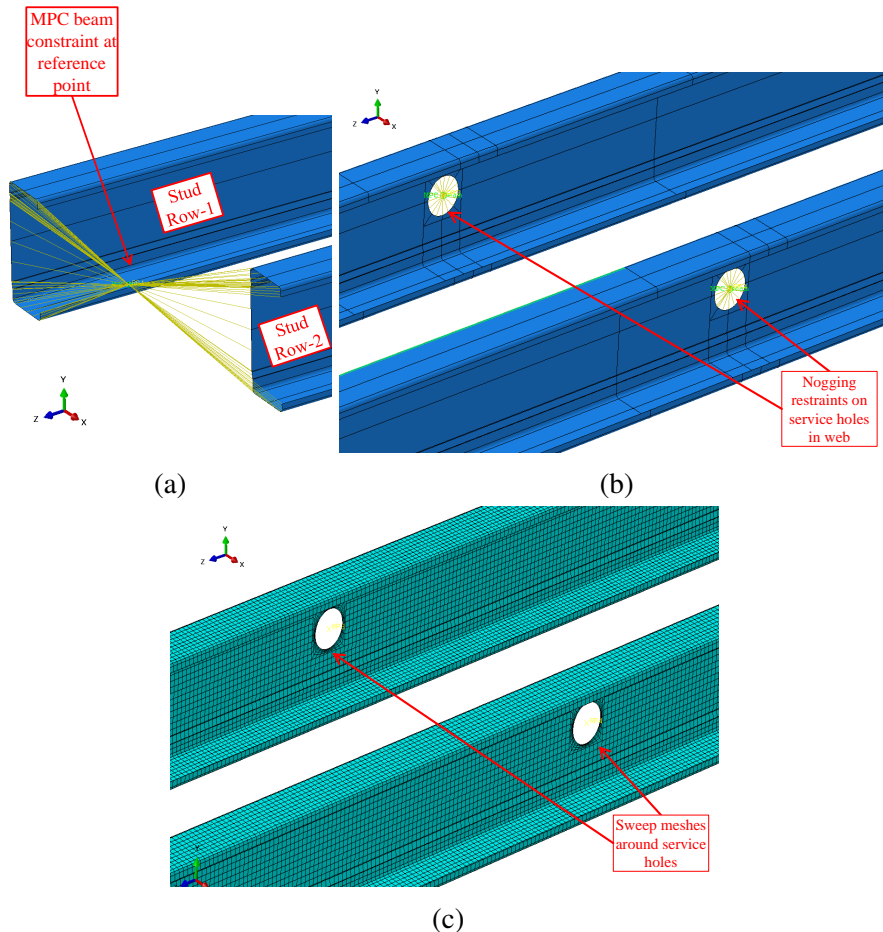


Figure 6.16: Test-AT5 - Staggered stud model (a) MPC beam constraints to simulate end restraints (b) MPC beam constraints at service holes to simulate nogging restraints (c) Sweep meshes around service holes

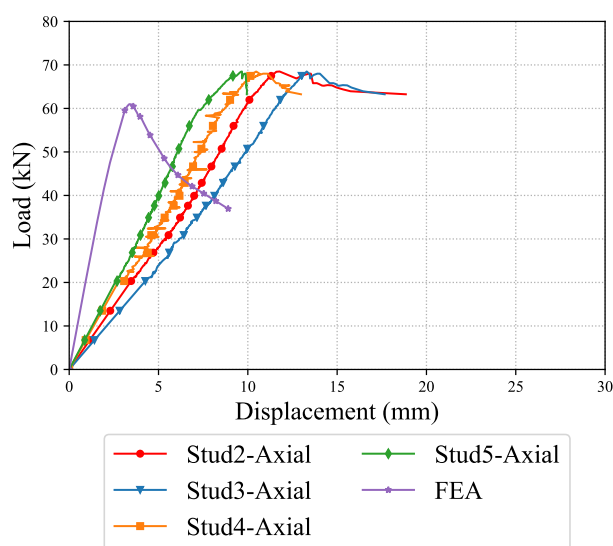


Figure 6.17: Comparison of load versus displacement curves of Test-AT5 wall from FEA and experiment

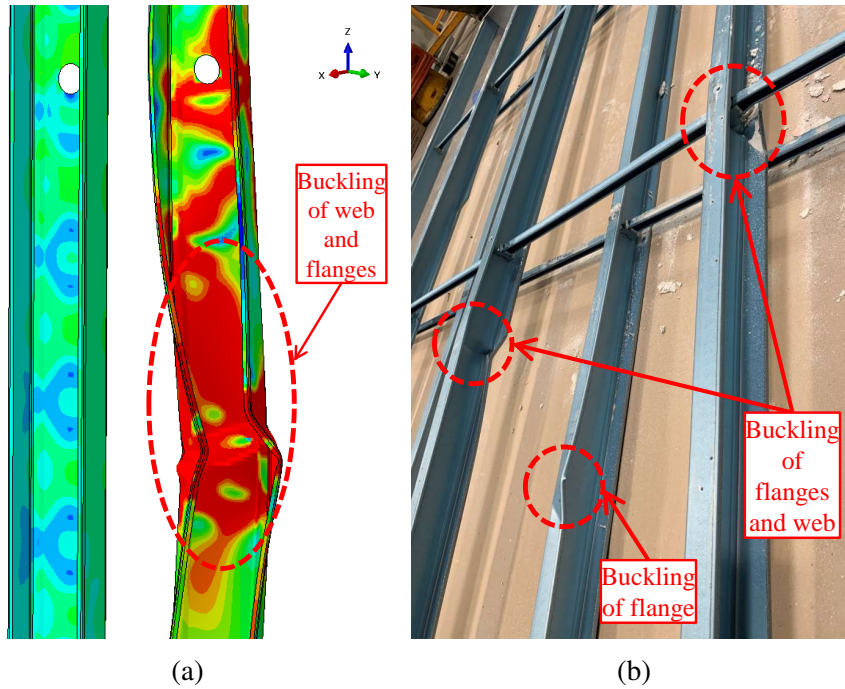


Figure 6.18: Buckling failure of studs in Test-AT5 wall (a) FEA (b) Experiment

model was further extended to include temperature boundary conditions in studs to predict the failure time of these complex LSF walls exposed to fire conditions.

Table 6.1: Ambient temperature capacity predictions by FEA and comparison with experimental capacities

Test Name	Description	Failure capacity (kN)		Ratio of FEA/Test capacity
		Test	FEA	
AT1	Double Stud - 90 × 0.95 - 4 studs	73.00	71.97	-1.03
AT2	Double Stud - 90 × 0.75 - 4 studs	47.08	46.25	-0.83
AT3	Double Stud - 90 × 0.75 - 6 studs	39.42	46.25	6.83
AT4	Double Stud - 70 × 0.95 - 4 studs	86.21	71.81	-14.40
AT5	Staggered Stud - 90 × 0.95 - 11 studs	68.49	60.98	-7.51

6.5 Coupled Temperature Displacement Structural Analysis

After determining the ambient temperature capacities in Chapter 3, the failure times of the tested LSF walls in fire from Chapter 4 were considered for investigation.

Full-scale fire Tests-T1 to T7 and T10 conducted under load-bearing conditions were considered in the numerical investigation of this chapter. The non-load bearing fire Tests-T8 and T9 were investigated in Chapter 7. The aim of the coupled temperature displacement structural analysis was to determine the failure times of the tested wall configurations under specified temperature boundary conditions along with axial compression load. 3D shell elements were used in the analysis using S4RT element which supports temperature degree of freedom. Temperatures on the hot and cold flanges were extracted from the FDS thermal models from Chapter 5 and were incorporated as boundary conditions on to the stud hot and cold flanges in the structural model. Attempts were also made to extract the stud hot and cold flange temperatures from Test-T1 wall and the degree of agreement in the failure time between the developed FE model and experiment was investigated. This technique was employed to investigate the credibility of the developed structural FE model using sequentially coupled-temperature displacement analysis. Temperature boundary conditions on the stud webs was assumed to vary linearly based on the hot and cold flange temperatures and applied to the stud nodes along the length as shown in Figure 6.19. Linear temperature variation along the web is governed by the number of mesh nodes on the stud web. However, the fire and ambient side hot and cold flanges had no variations in the input temperature boundary condition. Concentrated force from the initial non-linear structural ambient temperature analysis was applied at the reference point on the top of the FE model. This assumption was based on Ariyanayagam and Mahendran (2018c) to model the structural response of single stud LSF walls in fire. A similar approach was followed in this investigation as well.

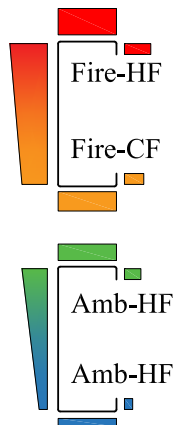


Figure 6.19: Temperature variation of studs in double stud LSF walls

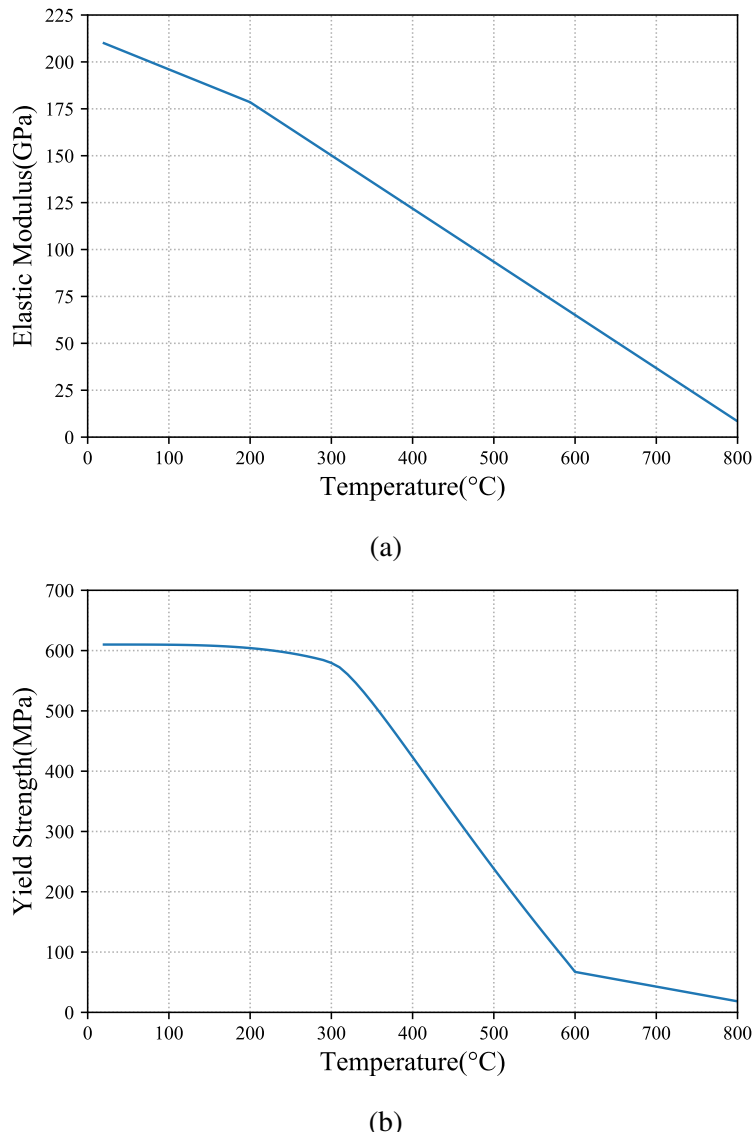


Figure 6.20: Elevated temperature mechanical properties of G550 steel from Kankamage and Mahendran (2011)

A coupled-temperature displacement analysis was conducted to determine the structural response of studs under axial compression along with temperature boundary conditions. The applied axial compression load in the FE model was equal to the applied load in the full-scale fire test in Chapter 4. Transient mode of analysis was adapted and all the models were analysed for a time-period of 240 min (14400 s). The effects of non-linearity were considered in the coupled temperature-displacement analysis. This method of structural analysis is generally referred to as sequentially coupled analysis wherein thermal analysis is conducted first followed by structural analysis. The output from thermal analysis acts as input to the structural analysis. The reactions were monitored on the bottom reference point and the axial displacement was monitored on the top reference point of the model at the centroid using history output feature in ABAQUS. The monitored data was stored in an output database file (ODB) and later used for post-processing.

As the coupled temperature-displacement structural analysis includes the effects of temperatures, the material properties used in the model had to account for the variations caused by elevated temperatures. Therefore, the elevated temperature mechanical properties of cold-formed steel were extracted from Kankamge and Mahendran (2011) which were verified by Rokilan and Mahendran (2019). The elevated temperature mechanical properties of steel such as elastic modulus and yield strength used in the FE model are shown in Figure 6.20. As the coupled-temperature displacement analysis involves solving two boundary conditions such as temperature and axial compression load at the same time, severe convergence issues arise with the FE model. This is because of the non-linear nature of the problem resulting in large deformations in the model. The non-linear nature of the model is largely due to the usage of thin-walled elements as studs. Treating these instabilities with a global solution might not best fit the problem. This was addressed by the introduction of automatic damping factor and adaptive stabilization factor during the analysis. This helps the models to converge to the desired solution. However, as stated earlier in the previous section, determining these factors are based on a trial and error method and varies with the models as stated in the ABAQUS documentation manual (Simulia Corporation, 2017). Therefore, the failure criteria of a model is determined either by comparing the reduction in the applied axial load with respect to time or with respect to axial displacement

or with lateral deflection or a combination of the aforesaid. The selection of the failure criteria in the FE model depends on the convergence achieved in the given model based on the temperature boundary condition and applied axial loads.

Test-T1

Test-T1 was conducted on a non-cavity insulated double stud LSF wall with 90×0.95 mm lipped channel studs as shown in Figure 6.21. Ambient temperature capacity FE model gave an ultimate compression capacity of 71.97 kN. As the full-scale fire Test-T1 was conducted under 0.4 LR (load ratio) an axial compression capacity of 28.76 kN was applied to the model and a coupled temperature displacement analysis was carried out.

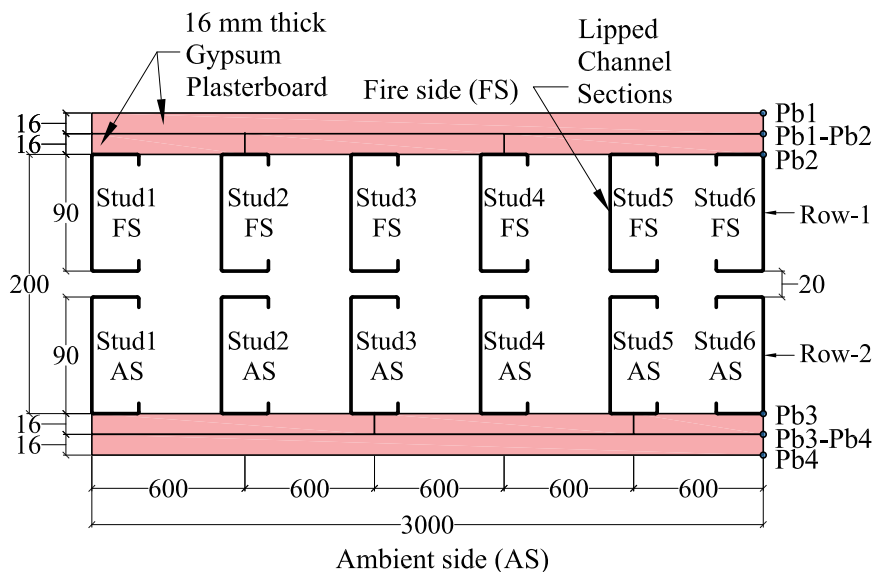


Figure 6.21: Test-T1 wall configuration

To determine the level of agreement in predicting the failure time of the developed structural model, the stud time-temperature curve from Test-T1 was used as boundary condition to the FE model and sequentially coupled temperature-displacement analysis was conducted. The failure of the coupled temperature displacement model of Test-T1 wall was determined using the time versus axial displacement and lateral deflection curves extracted from the model as shown in Figure 6.22. The failure time predicted by the FE model was 176 min, which matches accurately with the experimental failure time of 176 min.

Buckling failure mode extracted from the FE model is shown in Figure 6.23 (a). The local buckling experienced in the stud hot flanges shown in Figure 6.23 (b) was simulated by the developed structural FE model as shown in Figure 6.23 (a). However, the buckling deformation in the hot flange of the stud predicted by the developed structural model was less in comparison with that observed in the experiment. This is attributed to the post-buckling behaviour experienced by the test wall. During fire test, once the limiting hot flange temperature is reached under the applied axial load, the test wall fails due to the buckling failure in studs. However, the application of load to the test wall could not be stopped instantaneously as the load application was controlled manually due to the limitation in the test set-up. This results in excessive buckling deformation of the failed studs in the test wall. In the structural FE model, the coupled temperature-displacement analysis is automatically terminated once convergence is achieved in the model. This may lead to termination of the analysis even before the stud enters the post-ultimate failure phase. Therefore, capturing the post-ultimate failure effects in the FE model is challenging in sequentially coupled-temperature displacement analysis. Generally, altering the stabilization factors in the coupled temperature displacement analysis can result in good predictions of the post-ultimate failure behaviour of the thin-walled steel studs, but might not always result in accurate predictions due to converge issues in the FE model.

As the developed structural FE model was able to predict the failure time based on the stud temperatures from experiments, attempts were made to incorporate the stud temperature predictions from the FDS model into the structural FE model to predict the failure time for Test-T1. Figure 6.24 shows the comparison of axial displacement and lateral deflection curves from FE model based on stud temperatures from FDS thermal analysis output and the experimental results. Comparison with the buckling modes from experimental result in Figure 6.25 (b) reveals that the local buckling of studs observed in the full-scale fire test could not be predicted by the developed FE model. This was due to severe instability in the model causing convergence issue. However, the axial displacement and lateral deflection versus time curves could predict the failure time reasonably well. The failure time predicted by the structural FE model was 174 min while the experiment gave a failure time of 176 min. The maximum axial displacement recorded in the fire Test-T1 was -8 mm while it was 12.75 mm from the

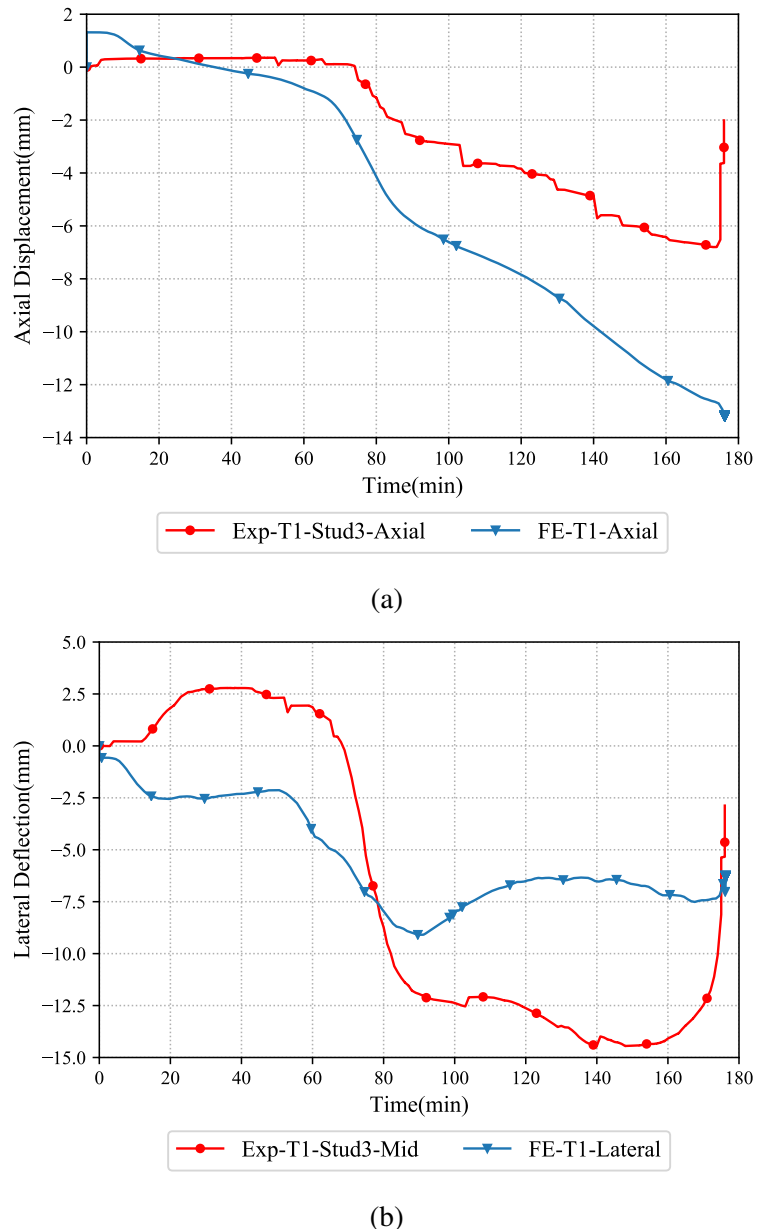


Figure 6.22: Comparison of displacement versus time curves of Test-T1 from FEA based on stud flange temperatures from experiment and experimental results (a) Axial displacement versus time (b) Lateral deflection versus time curves

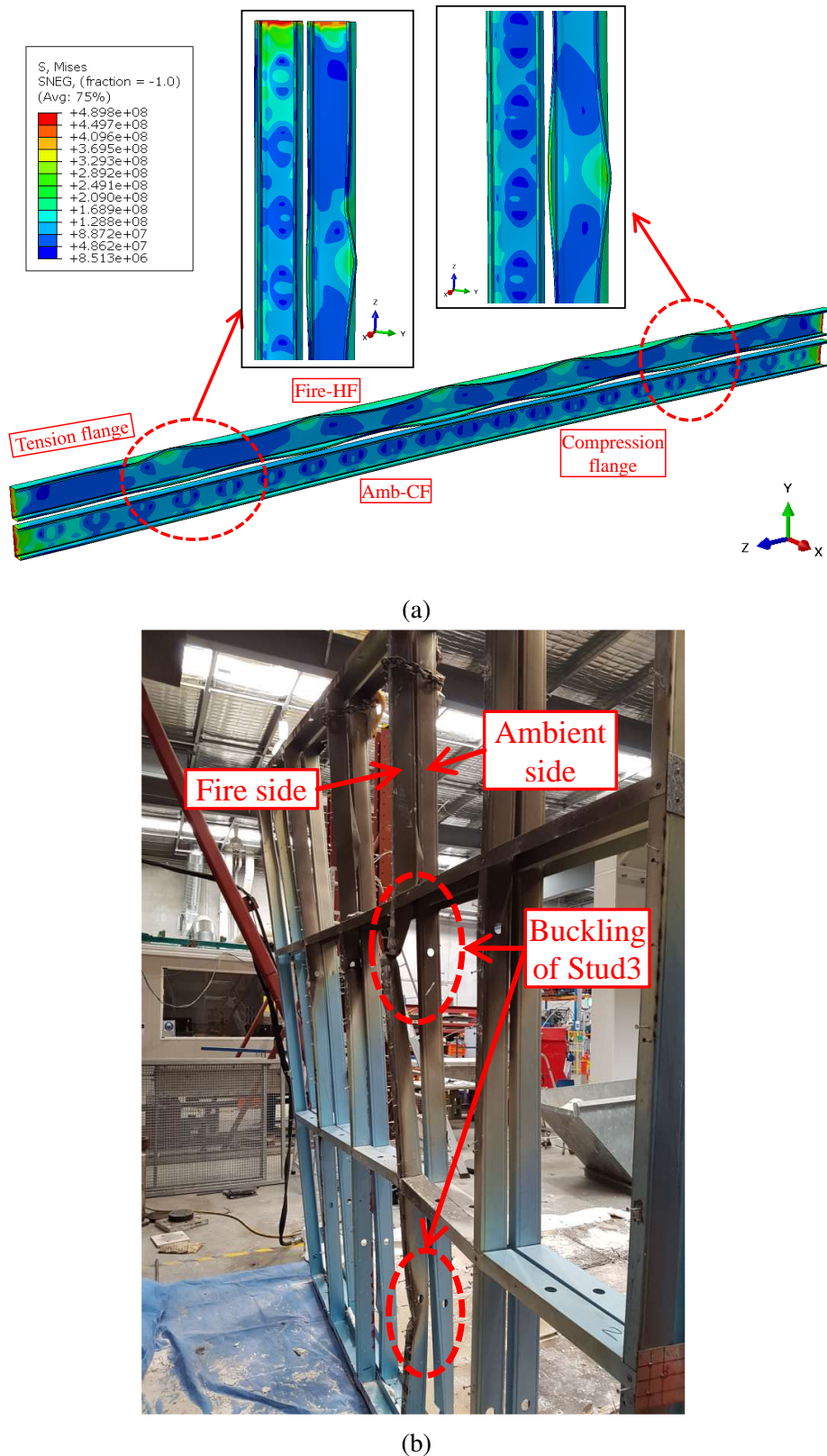


Figure 6.23: Buckling failure of studs in Test-T1 wall (a) FEA based on stud temperatures from experiment (b) Experiment

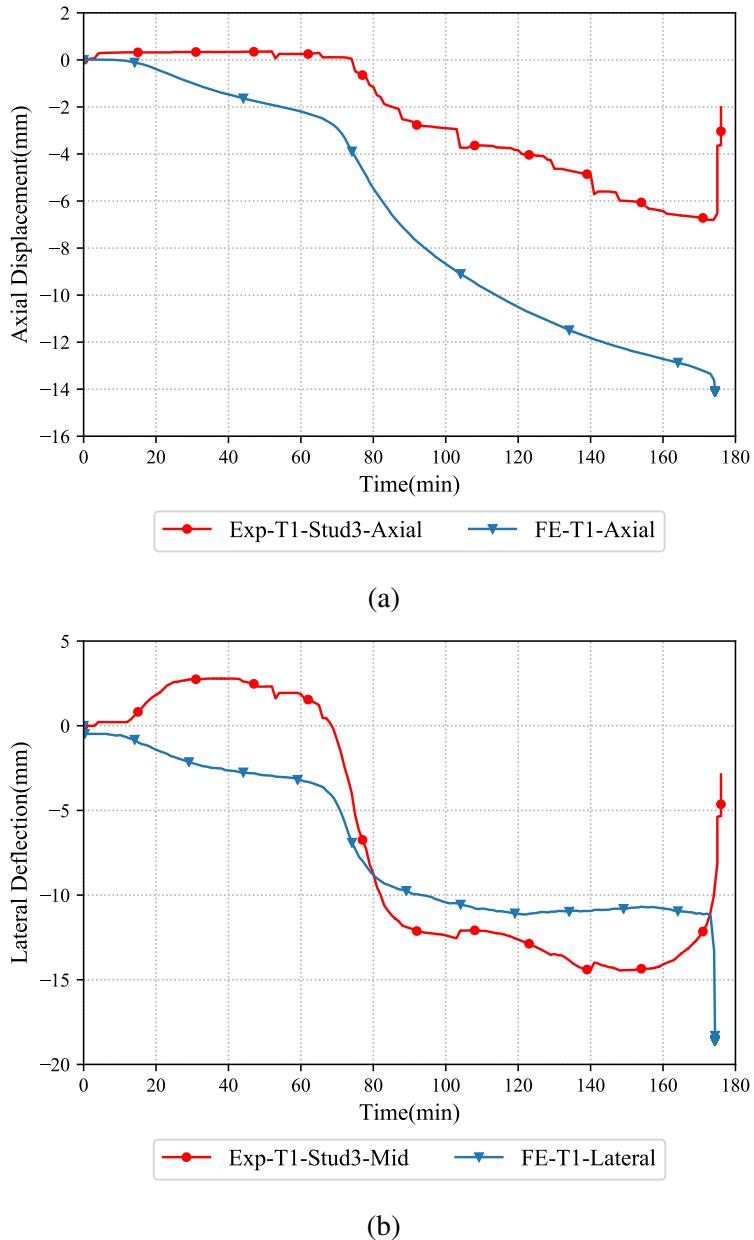


Figure 6.24: Comparison of displacement versus time curves of Test-T1 from FEA based on stud flange temperatures from FDS and experiment (a) Axial displacement versus time (b) Lateral deflection versus time curves

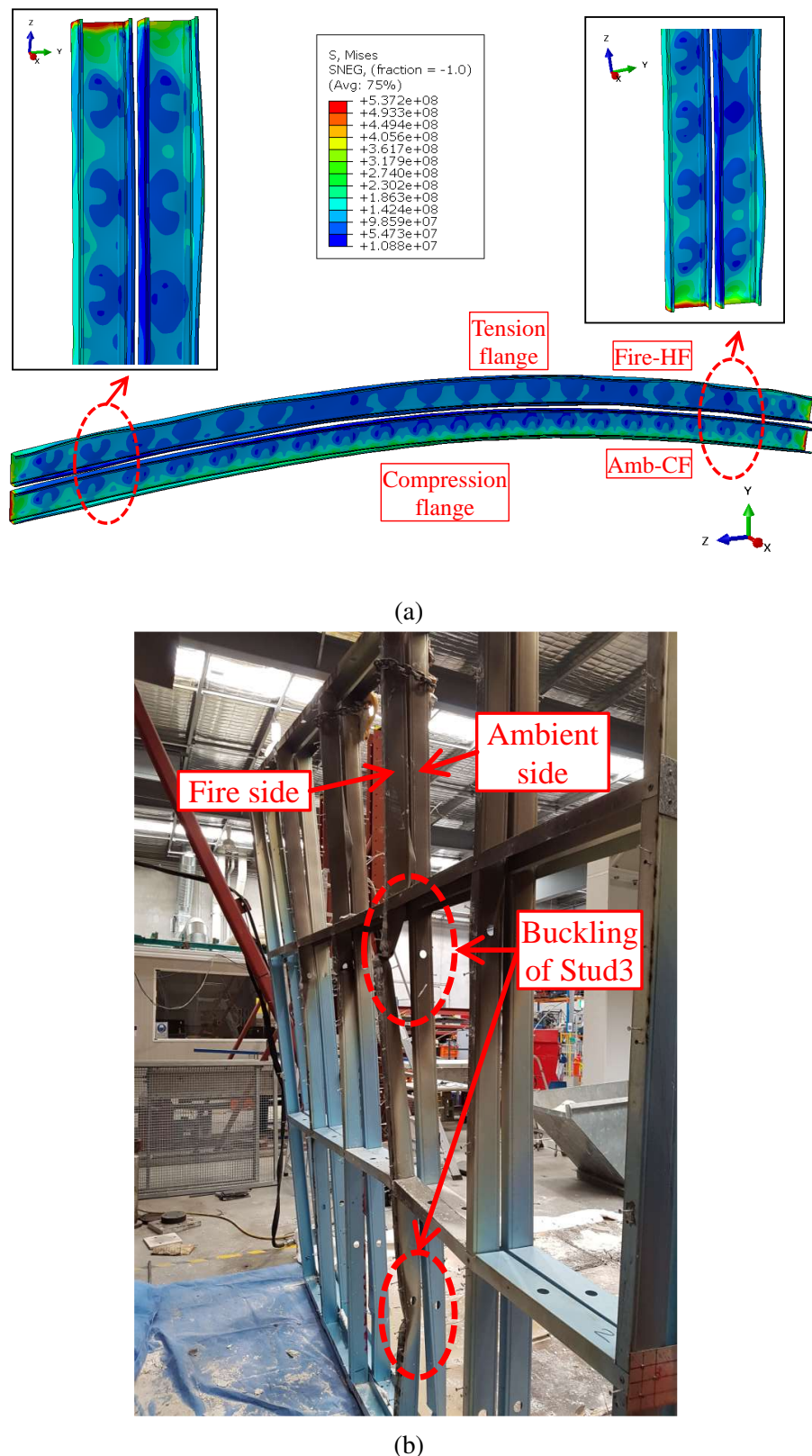


Figure 6.25: Buckling failure of studs in Test-T1 wall (a) FEA based on stud flange temperatures from FDS (b) Experiment

FE model predictions. Likewise, the experiment resulted a lateral deflection of -14.44 mm while the FE model gave 18.6 mm.

Test-T2

Test-T2 was conducted on a non-cavity insulated double stud LSF wall similar to the configuration shown in Figure 6.21 but with thinner lipped channel studs (90×0.75 mm) under 0.4 LR. The axial compression capacity under ambient temperature conditions from FEA was 46.25 kN. Structural analysis for Test-T2 was carried out with an axial compression load of 18.5 kN, representing 0.4 LR. The axial displacement and lateral deflection versus time curves from FEA corresponding to Test-T2 are compared against experimental results in Figure 6.26. The axial displacement versus time curve from experiment shows no significant variation for the initial 70 min. However, the predictions from FEA shows a gradual increase in the curve as shown in Figure 6.26 (a). The axial displacement curve is steep after 70 min in both experimental and FEA cases. A sudden increase in the curve at failure witnessed in the experimental curve could also be predicted by the developed structural FE model. The maximum axial displacement recorded from the experiment was 7.13 mm while it was 13.11 mm from the FE model prediction. Figure 6.26 (b) compares the lateral deflection versus time curves from experiment and FEA. The flat region in the lateral deflection curve till 60 min from the experiment was also observed in the FE model prediction. However, the maximum lateral deflection reported in the experiment was larger from the experiment resulting -20.25 mm while it was -16.56 mm from the FE model prediction. Failure time from the FE model prediction was 174 min while it was 132 min from the experiment. This difference in failure time prediction is because of the premature plasterboard fall-off in the fire Test-T2 as reported in Section 4.6.2.

Figure 6.27 shows the comparison of the buckling modes of studs from FE model predictions and experiments. Local buckling was noticeable only on the flanges from the FE model predictions as shown in Figure 6.27 (a) while severe local buckling was noticeable on the stud web and flanges from the experiment as shown in Figure 6.27 (b). This was because of the post-failure deformations experienced by the test wall during the full-scale fire test. The FE model experience convergence issues

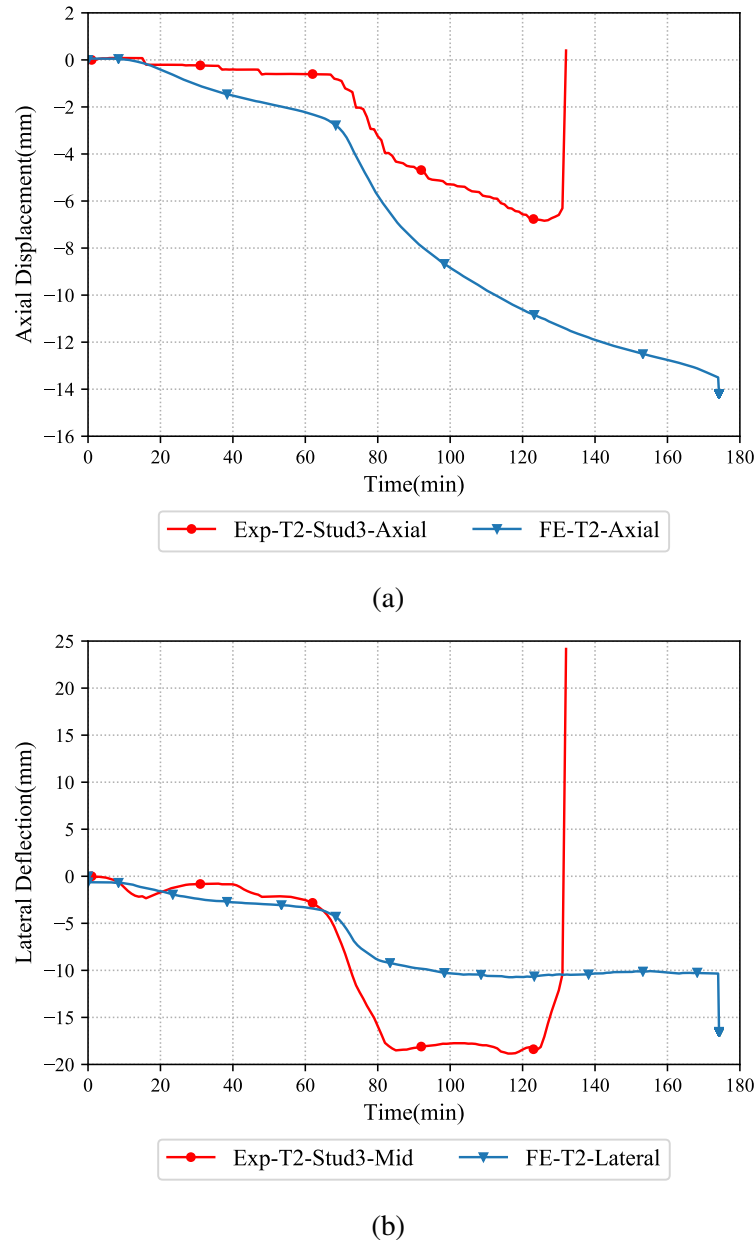


Figure 6.26: Comparison of displacement versus time curves of Test-T2 from FEA and experiment (a) Axial displacement versus time (b) Lateral deflection versus time curves

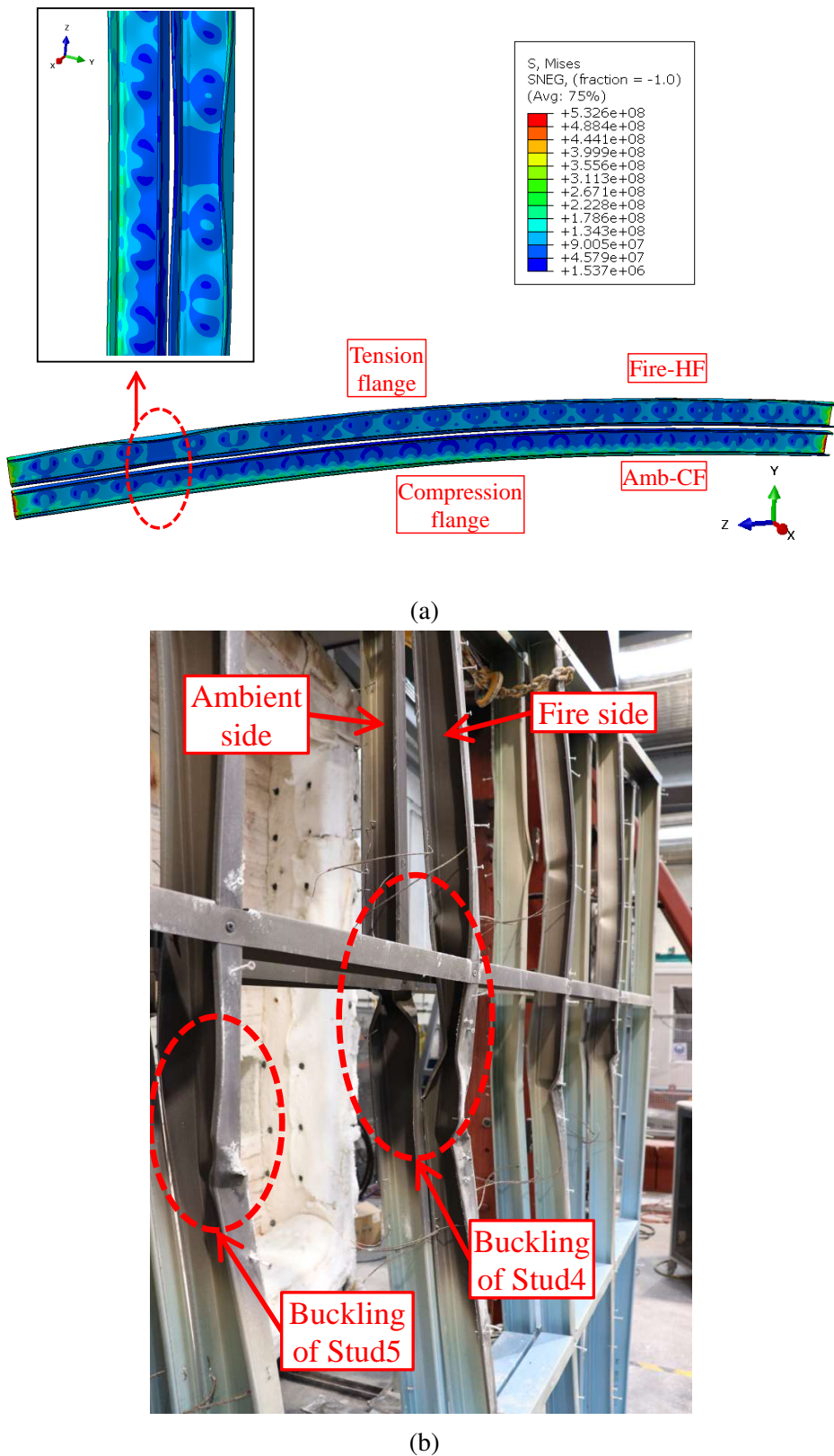


Figure 6.27: Buckling failure of studs in Test-T2 wall (a) FEA (b) Experiment

in simulating the post-failure behaviour of the studs thereby resulting in local buckling failure of the flanges corresponding to the failure time as shown in Figure 6.27 (a).

Test-T3

Test-T3 was conducted on a non-cavity insulated double stud LSF wall similar to the configuration shown in Figure 6.21 with 90×0.75 mm lipped channel studs but under a higher load ratio of 0.6. The axial displacement and lateral deflection versus time curves from FEA and experiment are shown in Figure 6.28. The gradual increase in slope exhibited by the axial displacement curve from experiment was also noticeable in the FE predictions as shown in Figure 6.28 (a). The lateral deflection was nearly flat and reached a sudden increase at the end of the fire test. This behaviour in the lateral deflection could also be predicted by the structural FE model as shown in Figure 6.28 (b). The failure time predicted by the FE model was 82 min compared to that of 81 min from the fire test. The agreement in failure time between the FE model prediction and experimental result was good in Test-T3 as no significant plasterboard fall-off was noticeable in this fire test unlike in Test-T2.

Local buckling of the flange was the predominant failure mode in the experiment as shown in Figure 6.29 (b) and was noticed at mid-height in the 3 m test wall. No significant buckling of the web was noticed in the experiment. Similar observations were observed from the FE model simulations. However, the buckling on the fire side stud was noticeable near the ends while the local buckling of the flange at mid-height was noticeable on the ambient side stud. This is because of the load sharing to the ambient side post-failure of the fire side stud which was simulated by the developed structural FE model. The local buckling of flanges near mid-height on the fire side stud in experiment may also be attributed to the localised plasterboard joint open-up in the experiment. Joint open-ups in the test wall could result in localised temperature concentration on the stud fire side hot flange thereby causing localised buckling as witnessed in Test-T3. The plasterboard joint open-up is more susceptible in Test-T3 as the fire test was conducted under higher load ratio.

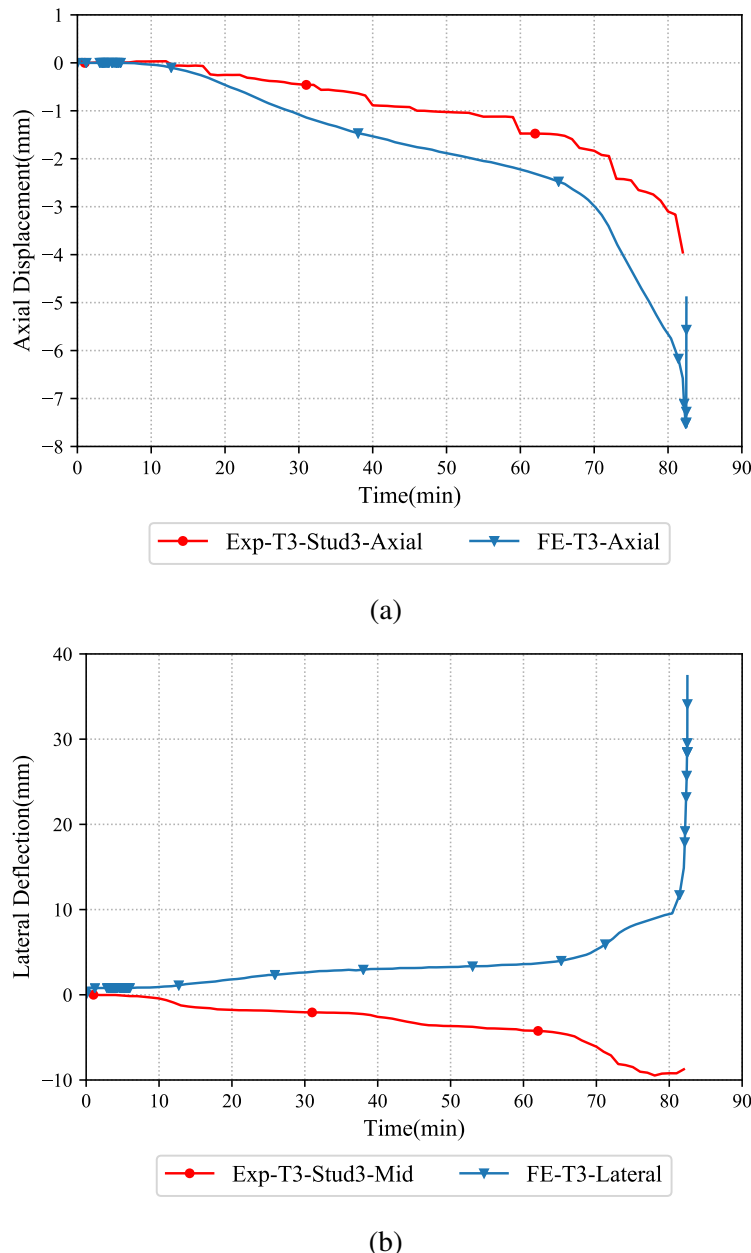


Figure 6.28: Comparison of displacement versus time curves of Test-T3 from FEA and experiment (a) Axial displacement versus time (b) Lateral deflection versus time curves

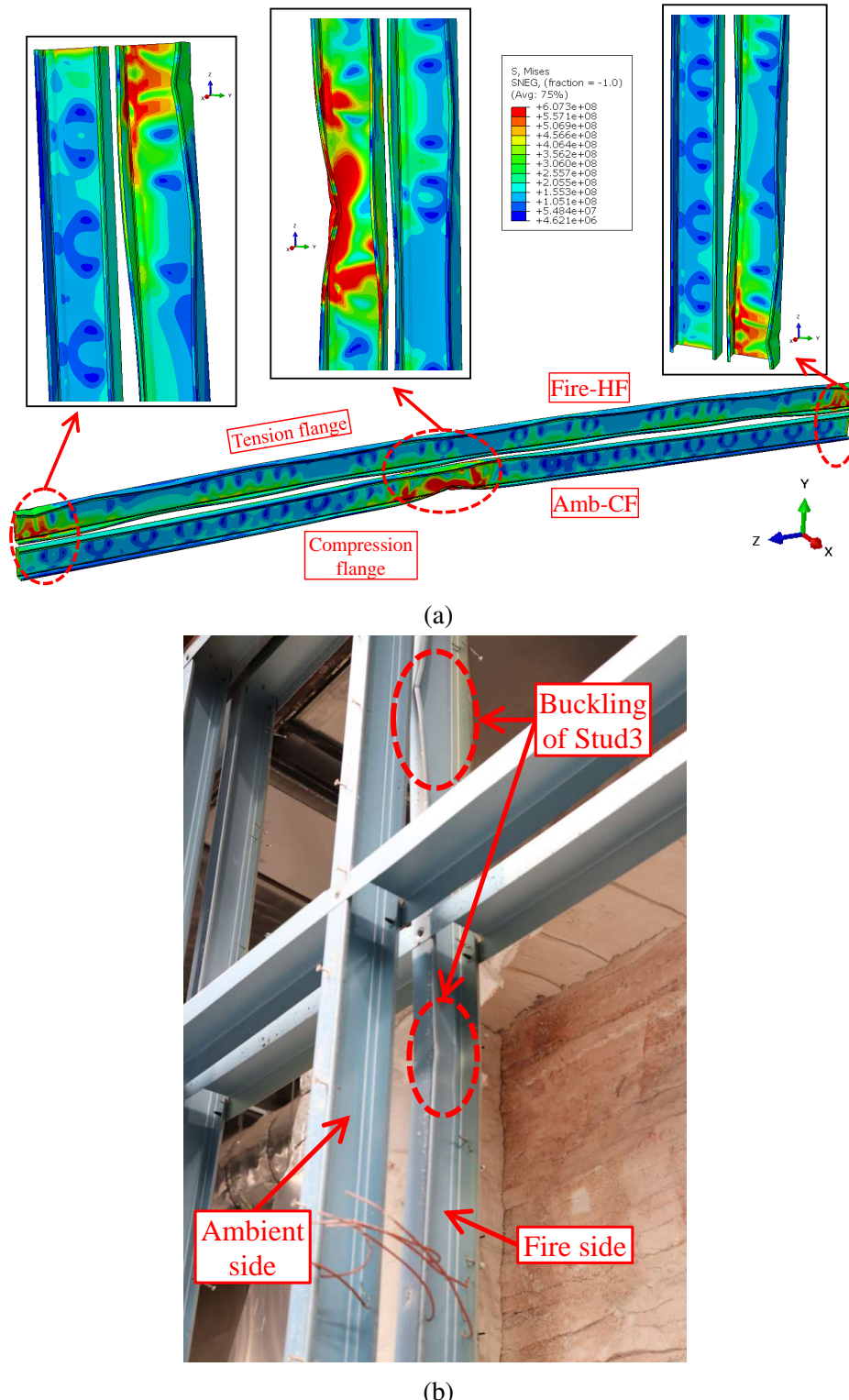


Figure 6.29: Buckling failure of studs in Test-T3 wall (a) FEA (b) Experiment

Test-T4

Test-T4 was conducted on a non-cavity insulated double stud LSF wall with 70×0.95 mm studs based on the wall configuration shown in Figure 6.30. The axial compression capacity under ambient temperature conditions from FEA was 71.81 kN. Structural analysis for Test-T4 was carried out with an axial compression load of 28.7 kN, representing 0.4 LR. The axial displacement and lateral deflection versus time curves from experiment and FE predictions are compared against each other in Figure 6.31. The axial displacement versus time curve from the experiment as shown in Figure 6.31 (a) exhibited a flat region till 60 min of fire test after which it progressively increased to a maximum of -5.95 mm at the end of the fire test. This behaviour was also reflected in the structural FE model prediction wherein a maximum axial displacement of 15 mm was recorded at the end of the fire test. The axial displacement versus time curve then changed sign indicating structural failure in the model similar to the experiment. Lateral deflection versus time curve shown in Figure 6.31 (b) also exhibited reasonable agreement between the FE model prediction and the experimental result. The change in slope experienced in the lateral deflection versus time curve after 60 min was also reflected in the FE model prediction. The maximum lateral deflection predicted by the FE model at the time of failure was 19 mm while it was -24.43 mm from the experiment.

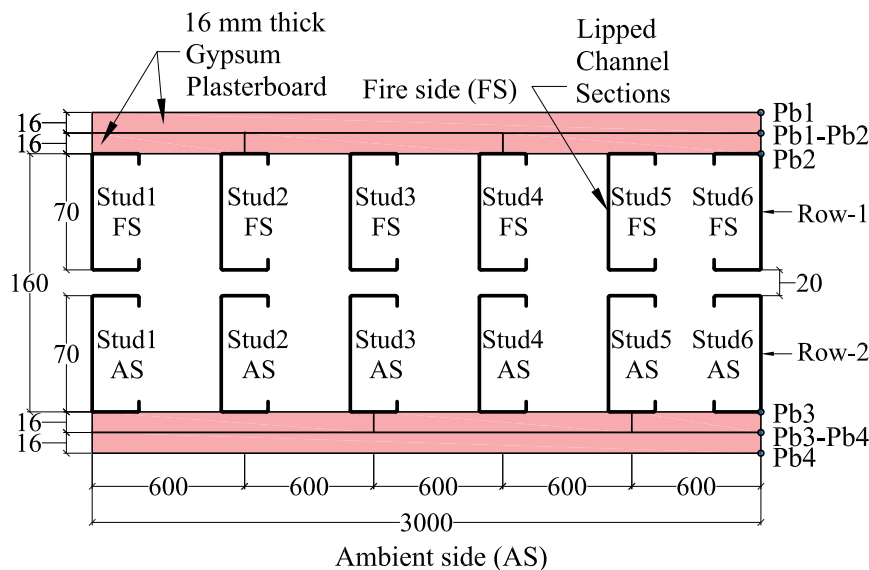


Figure 6.30: Test-T4 wall configuration

The failure time predicted by the FE model was 178 min while it was 171 min from

the experiment. Local compressive failure on the fire side hot flange of studs observed in the full-scale fire test could also be simulated by the developed FE model as shown in Figure 6.32. The axial compression load given to the structural FE model was based on the predictions from Chapter 3 where the ambient compression capacity predicted by the ambient structural model was less than the ambient capacity experimental result. When the non-dimensional load ratio is taken for consideration, the failure time prediction for the full-scale fire test matched reasonably well with the experimental failure time for Test-T4. The local buckling of the flanges in the fire side studs was observed at the top of the specimen as shown in Figure 6.32 (b). Similar behaviour was simulated by the FE model as shown in Figure 6.32 (a). This infers that the buckling failure behaviour of the studs in Test-T4 wall could be simulated by the developed FE model considering the stud temperatures from FDS thermal model.

Test-T5

Test-T5 was conducted on a double stud LSF wall with glass fibre cavity insulation and 90×0.95 mm studs as shown on Figure 6.33. The difference between the cavity insulated wall tests in comparison with the non-cavity insulated wall tests is the large temperature difference between the hot and cold flanges. This was also predicted by the developed FDS thermal model as discussed in Section 5.4.3 of Chapter 5. The input boundary conditions of the structural FE models also incorporated these effects. The axial displacement and lateral deflection versus time curves from the structural FE analysis are compared against the experimental results in Figure 6.34. Similar to the experimental results of the axial displacement versus time curve in Figure 6.34 (a), FE analysis predicted curve was flat till the end of the fire test simulation.

The maximum axial displacement was 5 mm from the FE model prediction, while it was -1.55 mm in the experiment. Similar trend was observed in the lateral deflection versus time curve comparison shown in Figure 6.34 (b). The lateral deflection versus time curve was flat in both the FE model prediction and experiment. Maximum lateral deflection at the failure time was -11.35 mm in the experiment while it was -16.87 mm in the FE model prediction. However, the flat region in the lateral deflection curve was similar in both the FE model prediction and the experiment. This is in correlation with

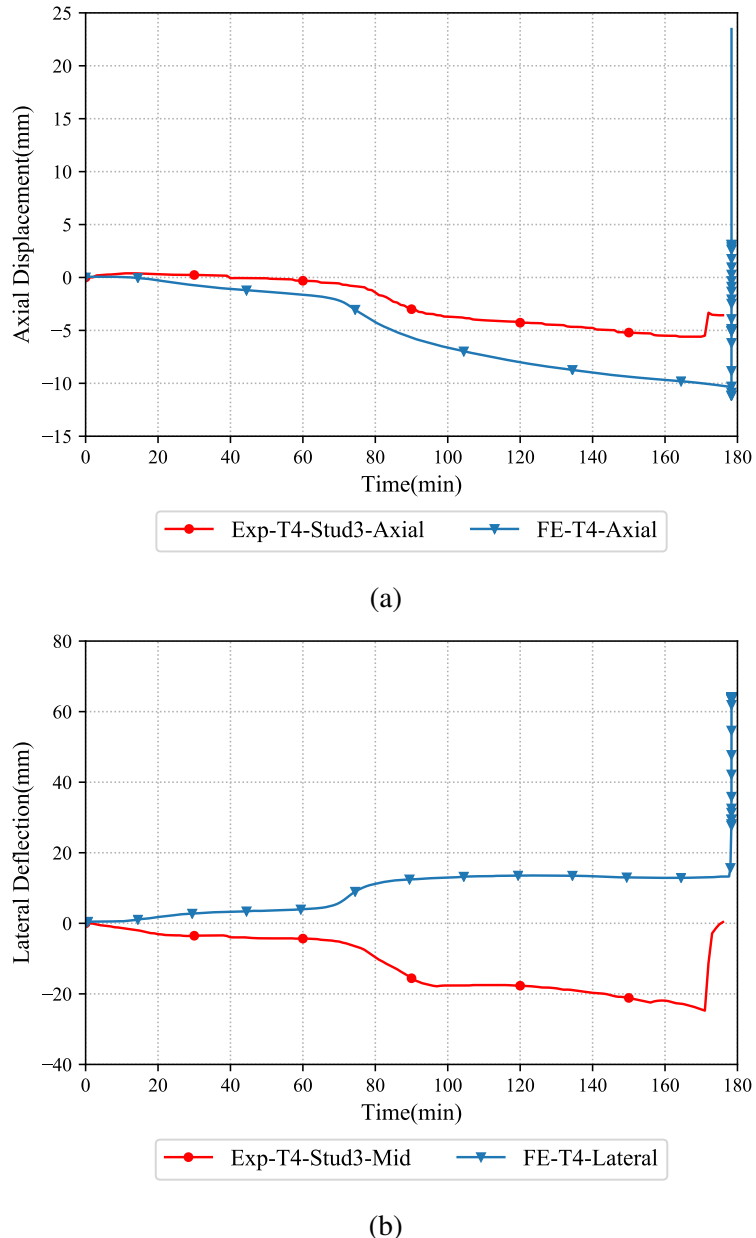


Figure 6.31: Comparison of displacement versus time curves of Test-T4 from FEA and experiment (a) Axial displacement versus time (b) Lateral deflection versus time curves

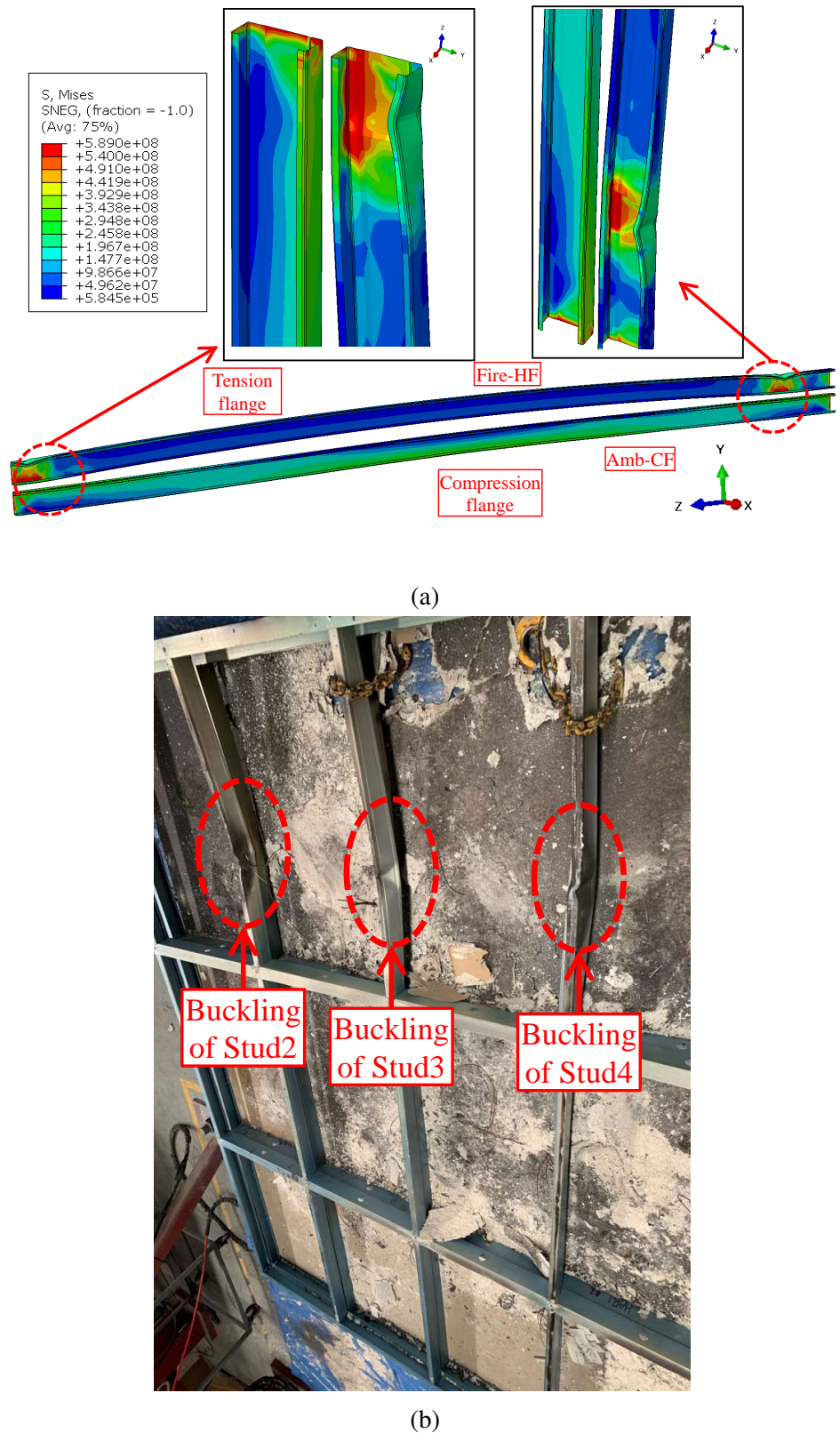


Figure 6.32: Buckling of studs in Test-T4 wall (a) FEA (b) Experiment

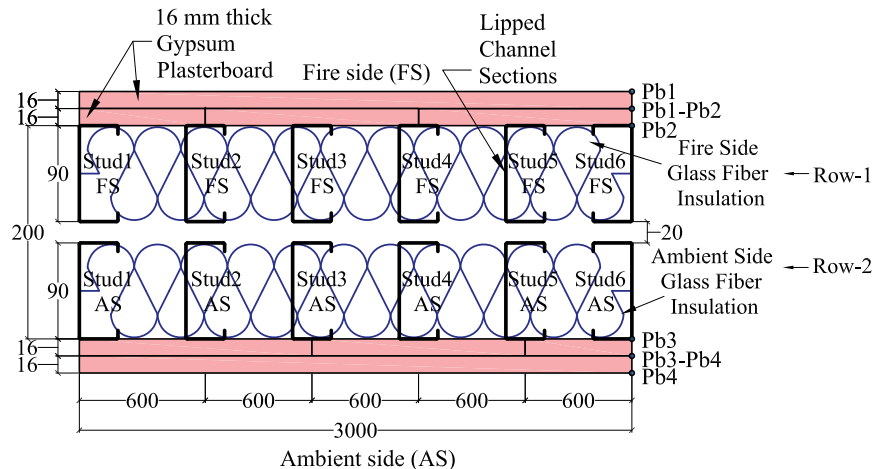


Figure 6.33: Test-T5 wall configuration

the earlier finding from the experimental study in Chapter 4 that the lateral deflection due to thermal bowing is less in cavity insulated double stud LSF walls in comparison with the non-cavity insulated double stud walls. The failure time predicted by the FE model was 80 min while it was 76 min from the experiment.

Figure 6.35 shows the buckling of flanges on the fire side along with global buckling about the major axis. But the global buckling should have occurred during the post-failure stage in the experiment as the time versus lateral deflection curve shown in Figure 6.34 (b) exhibits no significant deflection till the end of the fire test. The sudden increase noticed in the Exp-T5-Stud3-Mid lateral deflection curve infers that the major axis global buckling in studs should have occurred post-failure. This effect could be captured by the developed FE model as shown in the curve FE-T5-Lateral in Figure 6.34 (b). Also, the local buckling of the fire side hot flanges progressing to global buckling in the major axis could be simulated by the developed FE structural model using coupled temperature-displacement analysis technique as shown in Figure 6.35 (b). This infers that the FE model could simulate the post-failure behaviour in cavity insulated double stud walls accurately.

Test-T6

Test-T6 was conducted as a repeat test to that of Test-T5 on cavity insulated double stud LSF walls. Therefore, the same structural FE model was used for the comparison. The experiment gave a failure time of 91 min while the FE model gave a failure time

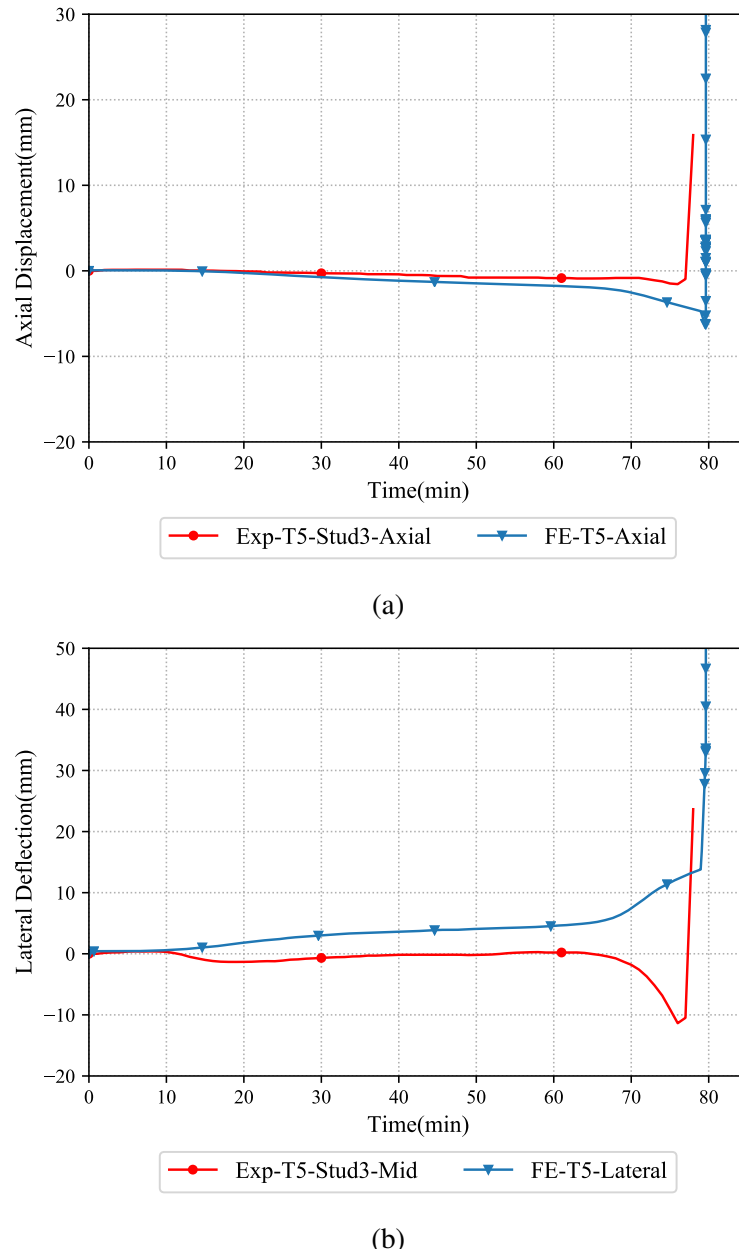


Figure 6.34: Comparison of displacement versus time curves of Test-T5 from FEA and experiment (a) Axial displacement versus time (b) Lateral deflection versus time curves

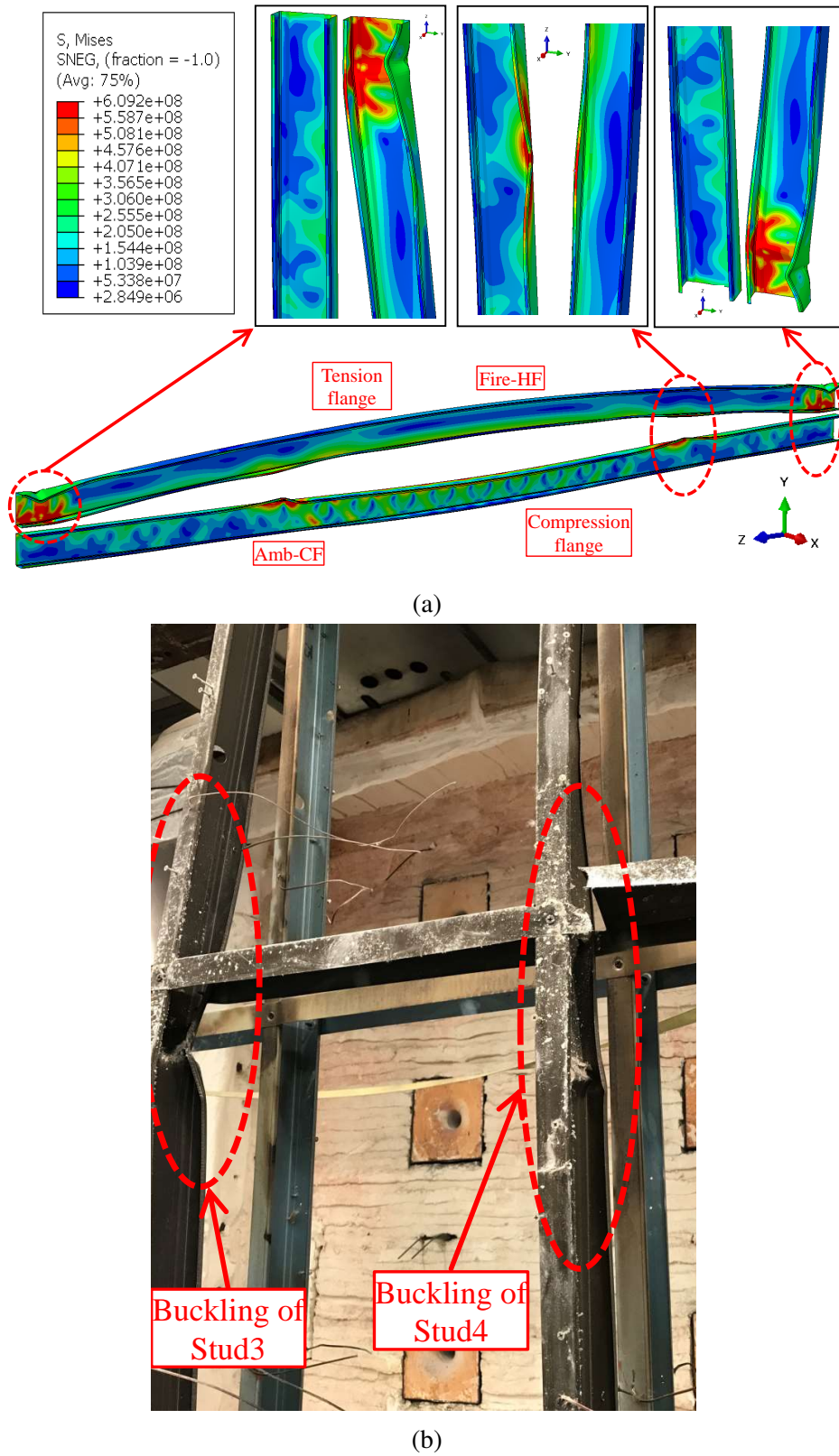


Figure 6.35: Buckling failure of studs in Test-T5 wall (a) FEA (b) Experiment

of 80 min. Figure 6.36 compares the axial displacement and lateral deflection versus time curves from FEA and experiment are shown in Figure 6.36. Similar trends were observed in the axial displacement and lateral deflection versus time curves from FEA and experiment. However, the failure time prediction from FEA was lower in comparison with the experimental result for Test-T6. However, the difference in failure times is small and can be neglected.

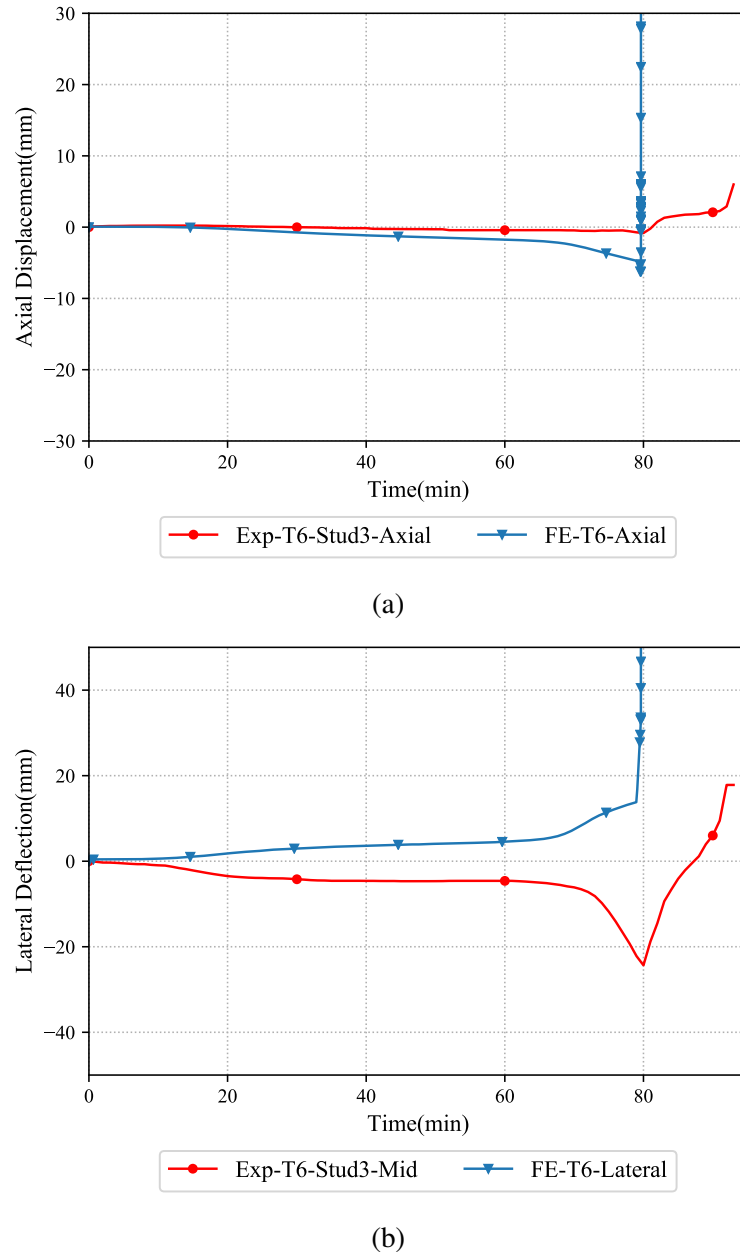


Figure 6.36: Comparison of displacement versus time curves of Test-T6 from FEA and experiment (a) Axial displacement versus time (b) Lateral deflection versus time curves

It is to be noted that the FE model corresponding to Test-T5 and T6 were the same.

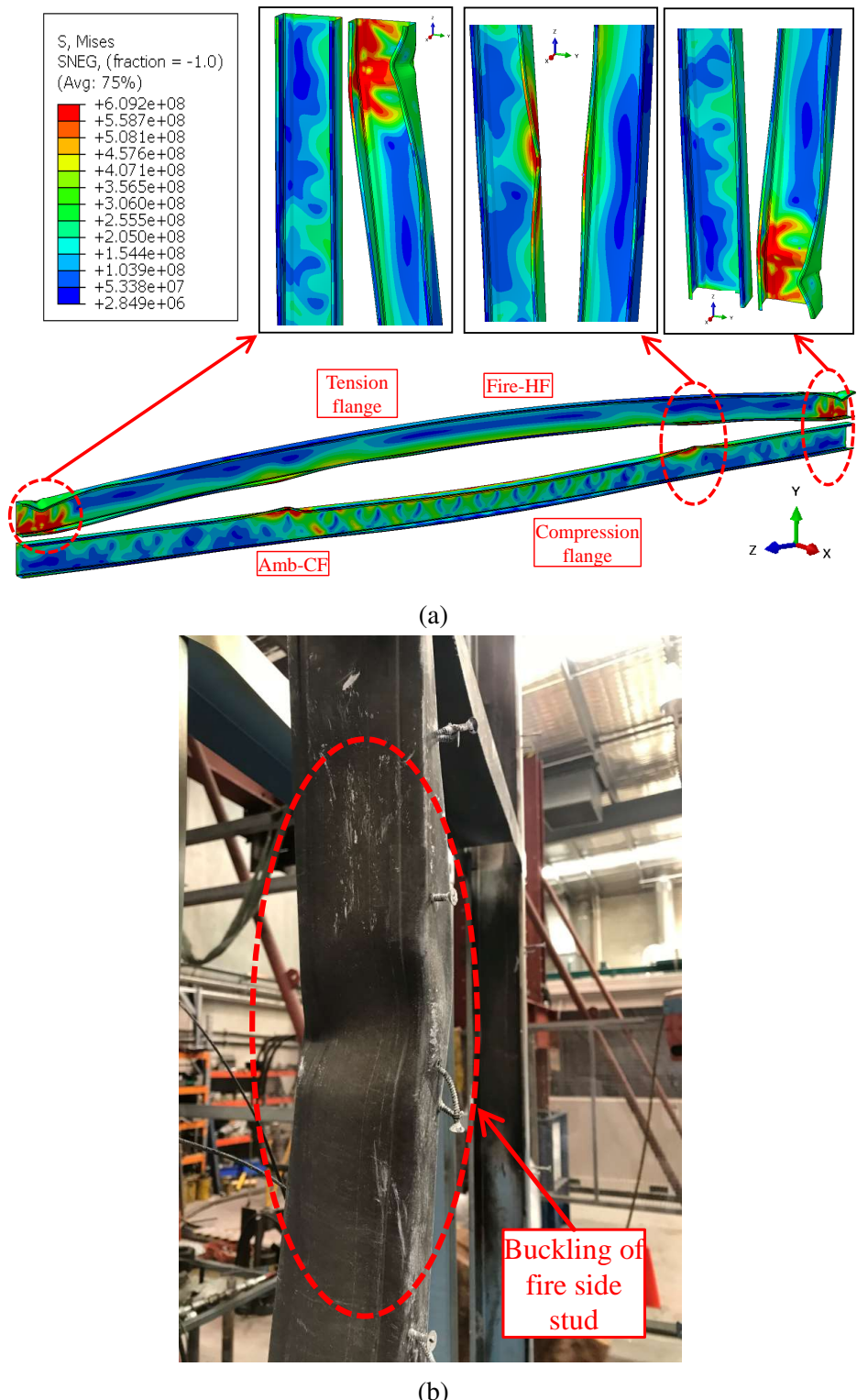


Figure 6.37: Buckling failure of studs in Test-T6 wall (a) FEA (b) Experiment

Local buckling of the fire side stud web and flange was noticeable at mid-height of the test wall as shown in Figure 6.37 (b) which progressed to global buckling similar to Test-T5. However, the FE model could simulate the local buckling of the fire side web and flanges near the end of the model. The global buckling was also simulated by the FE model. This infers good agreement between the experiment and the FE model prediction as the position of the buckling in the specimen is attributed by many factors which include plasterboard open-up and localised temperature concentration. This may not be considered as the inefficiency of the developed FE model and can be neglected.

Test-T7

Test-T7 was also conducted on a cavity insulated double stud wall with 90×0.95 mm studs under 0.4 LR as shown in Figure 6.38. But, the glass fibre cavity insulation was placed only on the ambient side of the test wall in the full-scale fire test. Through this the effect of cavity insulation position in the time-temperature profile was investigated. However, the difference in stud hot and cold flange temperatures was large in comparison with the non-cavity insulated double stud walls similar to Test-T5. This effect could also be simulated by the FDS thermal model in Section 5.4.3, of Chapter 5 and the corresponding time-temperature curves were used as the stud hot and cold flange boundary conditions in the structural FE model. The axial displacement and lateral deflection versus curves from the structural FE model are compared against the experimental results in Figure 6.40. The developed structural FE model was able to predict the gradual increase in the axial displacement curve observed in the experiment as shown in Figure 6.40 (a). An axial displacement of -3.15 mm was observed in the experiment at failure while it was 7.9 mm from the structural FE model prediction. The lateral deflection versus time curve was nearly flat in both the experimental result and FE model prediction till stud failure after which the curve exhibits a steep increase as shown in Figure 6.40 (b). This infers that the lateral deflection due to thermal bowing is less in cavity insulated double stud walls in comparison to non-cavity insulated double stud walls irrespective of the position of the insulation within the cavity. The failure time predicted by the FE model was 81 min which was the same as the experimental

failure time of Test-T7.

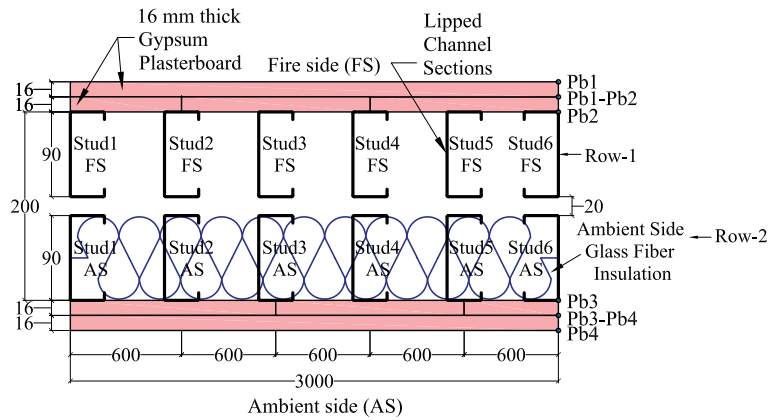


Figure 6.38: Test-T7 wall configuration

Local buckling of the fire side studs at the top of the test wall propagating to global buckling in the major axis was noticeable in the ambient cavity insulated Test-T7 wall as shown in Figure 6.39 (b). This buckling behaviour was similar to that of Tests-T5 and T6 with full cavity insulation. The axial displacement and lateral deflection curves also show the occurrence of major axis global buckling at the end of the fire test. The structural FE model was also able to simulate the local buckling of the web and flanges and was also able to predict the major axis global buckling at the end of simulation as shown in Figure 6.39 (a). The global buckling experienced in the studs is because of the post-failure effects in the test wall and the same could be simulated by the developed FE model.

Test-T10

Test-T10 was conducted on a staggered stud LSF wall with glass fibre cavity insulation and 90×0.95 mm studs under 0.4 LR as shown in Figure 6.41. The axial displacement and lateral deflection versus time curves comparison between the FE model prediction and the experimental result is shown in Figure 6.42. The gradual increase in the axial displacement versus time curve noticeable in the experimental results could be simulated by the developed structural FE model as shown in Figure 6.42 (a). The maximum axial displacement was 6.36 mm from the FE model simulation while it was -7.78 mm from the experimental result. The flat behaviour of the lateral deflection versus time curve exhibited in the experiment could be simulated to a reasonable agreement by

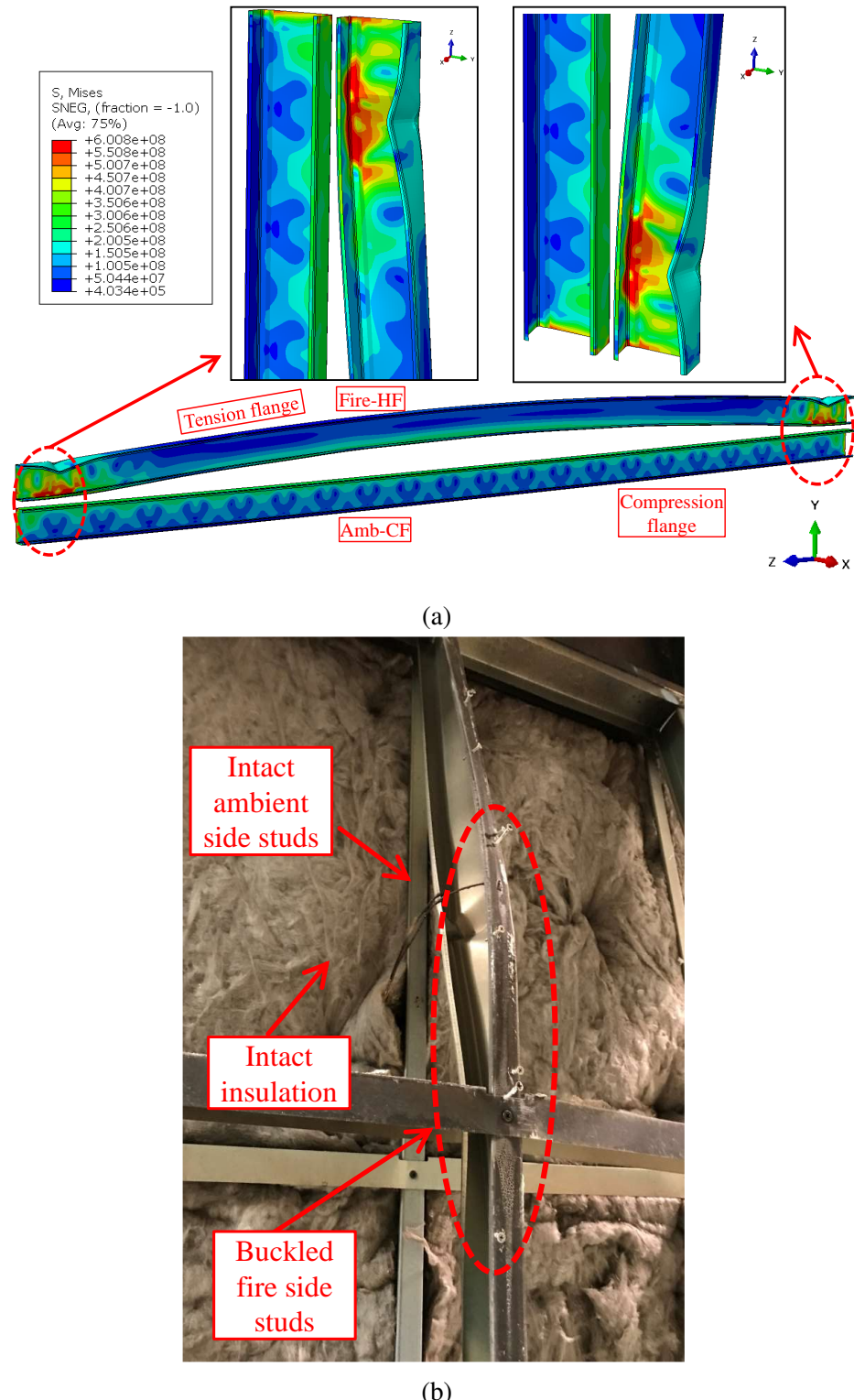


Figure 6.39: Buckling of studs in Test-T7 wall (a) FEA (b) Experiment

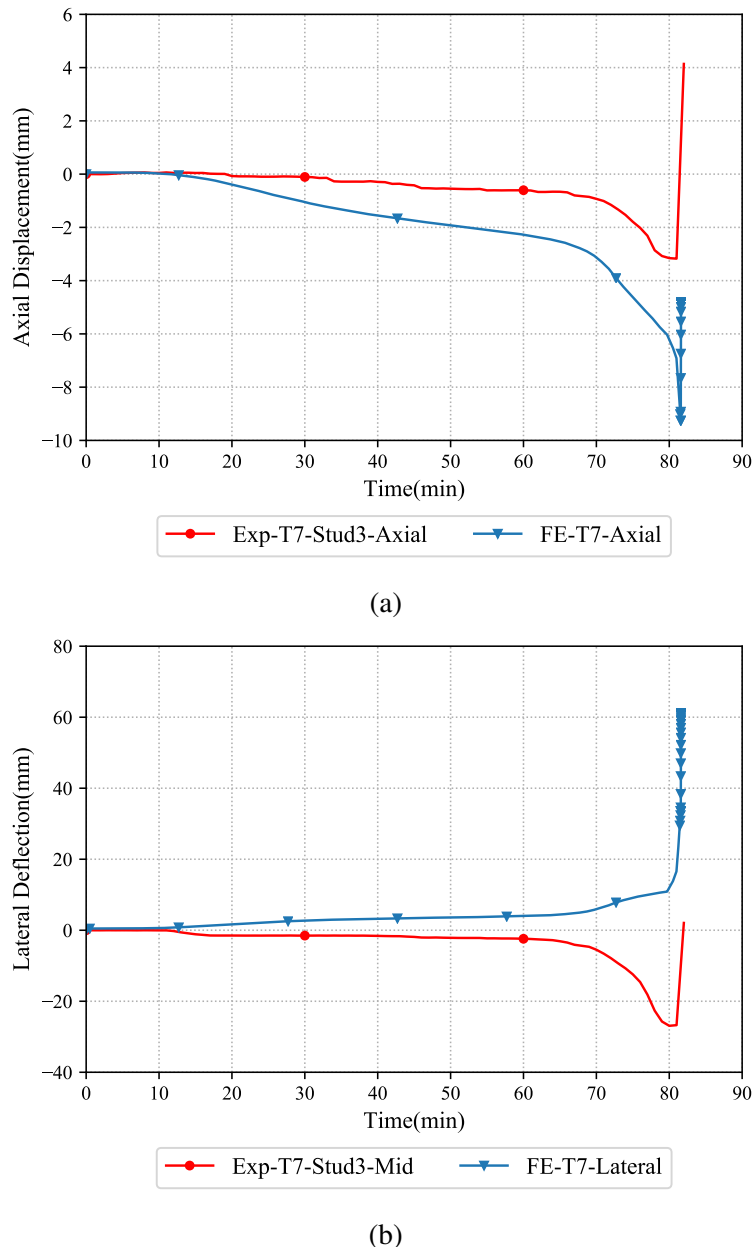


Figure 6.40: Comparison of displacement versus time curves of Test-T7 from FEA and experiment (a) Axial displacement versus time (b) Lateral deflection versus time curves

the developed FE model till 55 min. The dip in the lateral deflection curve from the experiment was sudden in comparison to the gradual increase in the curve from the FE model. Buckling of the studs was noticeable on the fire side studs in the experiment while the ambient side studs were intact. The experimental failure time was 85 min while the FE model predicted a failure time of 92 min.

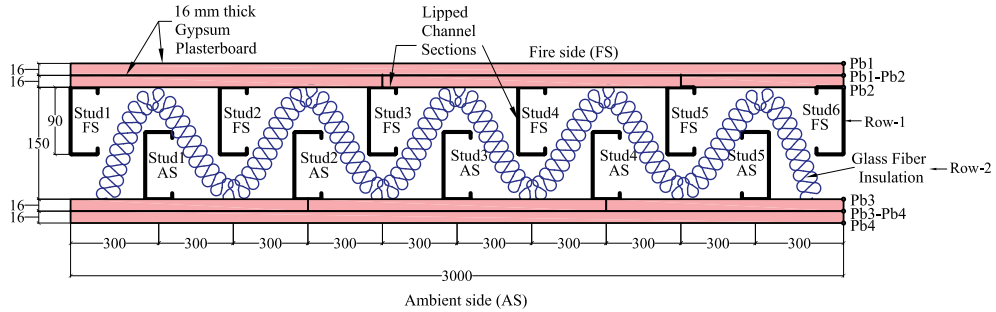


Figure 6.41: Test-T10 plan view

Local buckling of the flanges was the dominant failure mode in the Test-10 wall. However, the major axis global buckling visible in the experiment is from the post-buckling behaviour of the test wall as shown in Figure 6.43 (b). This is evident from the lateral deflection versus time curve (Exp-T10-Stud3-Mid) shown in Figure 6.42 (b). The developed FE structural model could simulate the local buckling of the fire side stud flange, but could not simulate the major axis global effects. This is because the model experienced convergence issues and could not simulate the post-buckling effects.

6.6 Summary and Conclusions

This chapter has presented the results of structural FE modelling of double and staggered stud LSF walls tested under ambient (refer Chapter 3) and fire (refer Chapter 4) conditions. Firstly, the ambient temperature axial compression capacity tests conducted in Chapter 3 were considered and the results were used to validate the developed FE model. Conventional FE modelling techniques developed in past research studies were adopted to predict the ambient temperature capacity of the tested walls to determine the suitability of the structural FE model based on two double and staggered studs with appropriate support and restraint conditions to predict the ambient temperature axial load carrying capacities of double and staggered stud LSF walls.

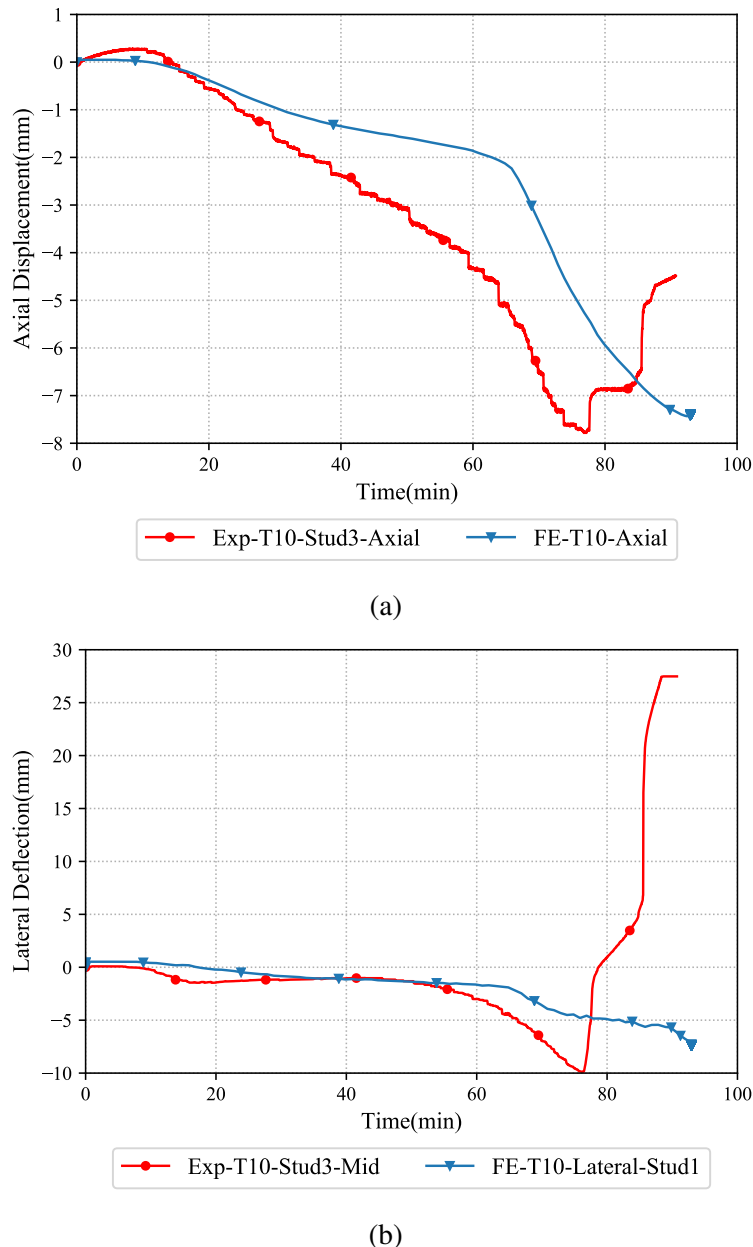


Figure 6.42: Comparison of displacement versus time curves of Test-T10 from FEA and experiment (a) Axial displacement versus time (b) Lateral deflection versus time curves

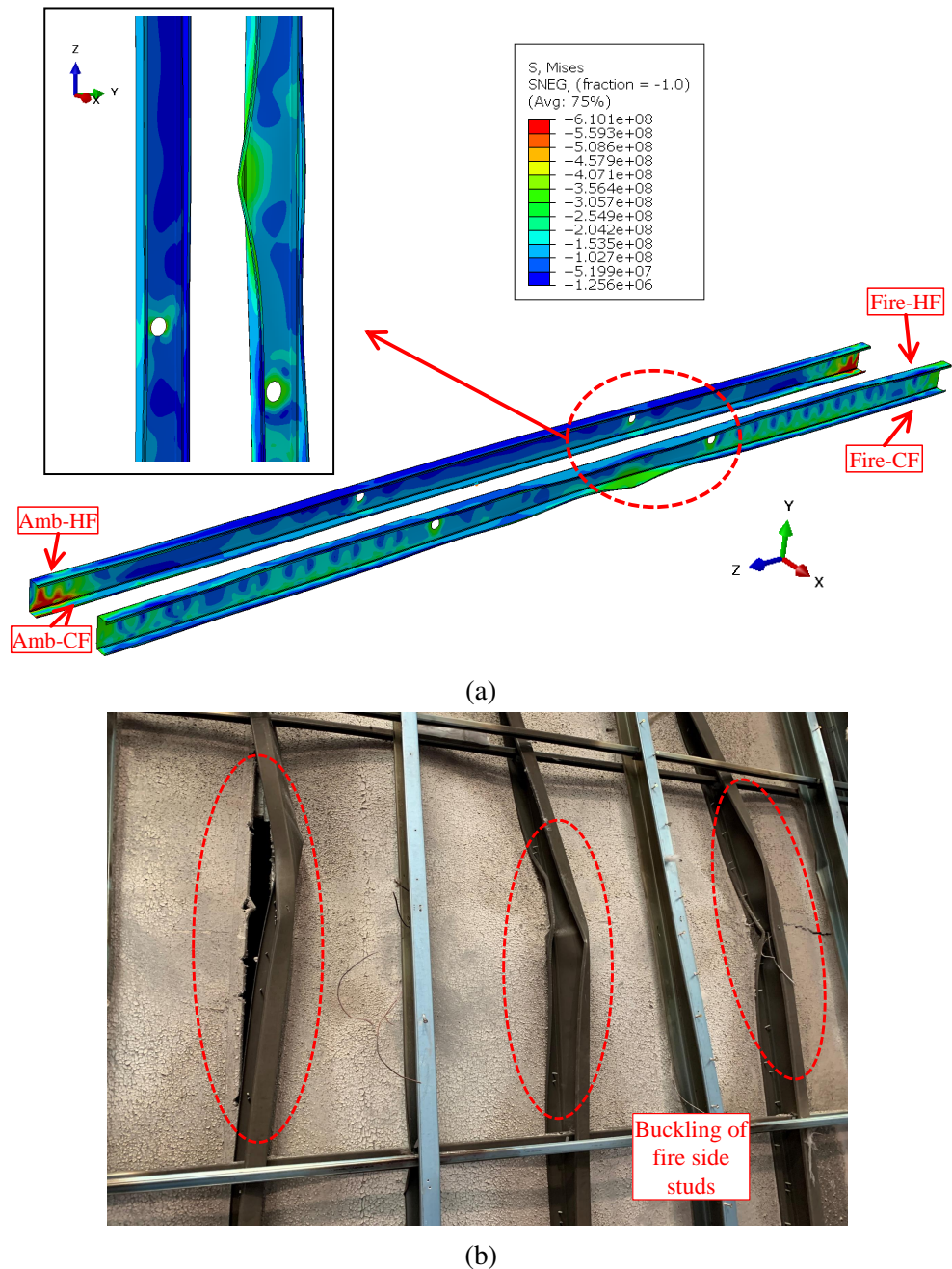


Figure 6.43: Buckling failure of studs in Test-T10 wall (a) FEA (b) Experiment

3D shell models were used for this purpose and the results from the structural analyses were then compared against the experimental results. The structural FE model was used to include temperature boundary conditions and sequentially coupled temperature displacement analyses were conducted on single stud models along with the required axial load. The failure times from the FE modelling were then compared against those from full-scale fire tests. Based on the conducted structural FE analyses, the following conclusions can be made and is summarised next.

- Ambient temperature structural FE models of single studs developed using ABAQUS were able to predict the ambient temperature axial load carrying capacities of the tested double and staggered stud walls to a reasonable agreement except for Test-AT4. The failure modes predicted by the ambient temperature structural FE models also exhibited reasonable agreement with the results from the ambient temperature axial compression capacity tests.
- The sequentially coupled temperature-displacement FE analyses of the tested full-scale LSF walls gave reasonably accurate failure time predictions in comparison with the experiments except for Test-T2. This is attributed to the premature plasterboard fall-off leading to earlier failure time in the fire test. However, the effects of premature plasterboard fall-off was not considered in the structural FE model, which gave longer failure time predictions for Test-T2 only. The axial displacement and lateral deflection versus time curves were compared with the experimental results, which exhibited reasonable agreement with the full-scale fire test results. The axial displacement and lateral deflection versus time curve predictions were over-estimated in some cases. Also, the failure mode predictions of the studs were not always in good correlation with the experimental results. This is because of the severe non-linearity causing convergence issue in the FE model. This may be overcome by adopting techniques such as dynamic explicit coupled temperature displacement analysis, but was not considered in this research.
- Despite the severe non-linearity causing convergence issues and numerical instability in the coupled temperature displacement model analysis, after multiple iterations by altering the stabilization factor the sequentially coupled temper-

ature displacement analysis technique was able to predict the failure times of the load bearing full-scale LSF walls with reasonable accuracy. Therefore, the current modelling technique will be adopted in a numerical parametric study in Chapter 7. Fully coupled temperature displacement analysis may be a viable option by considering the coupled nature of the full-scale fire tests as stated by Rusthi et al. (2018) and Dias et al. (2019b) but is not deemed worthy due to computational inefficiency.

[This page is intentionally left blank]

Chapter 7

Thermal and Structural FE Modelling

Parametric Study

7.1 Introduction

Chapter 5 discussed about the FDS thermal model predictions for the full-scale fire tests conducted in Chapter 4. However, the thermal model predictions were limited to the selected double, staggered and shaftliner wall configurations chosen for the full-scale fire tests. Likewise, Chapter 6 discussed the structural FE models to predict the ambient temperature axial load carrying capacity of the complex LSF wall tests in Chapter 3 which included double and staggered stud walls but was limited to shaftliner LSF walls under ambient temperature and fire conditions. Attempts were therefore made in this Chapter to determine the thermal and structural performance of other complex LSF wall configurations which were not considered for in the full-scale fire and ambient temperature capacity tests. Full-scale fire tests are time consuming and expensive to conduct which necessitates this parametric study on other complex LSF wall systems. Thermal modelling techniques validated through FDS and structural modelling techniques validated through ABAQUS were considered in this parametric study. The structural models include ambient temperature axial capacity prediction and the sequentially coupled temperature-displacement analysis. The parameters considered for the thermal and structural modelling studies are discussed next.

7.2 Parameters considered

Based on the conducted ambient temperature axial compression capacity tests and full-scale fire tests the LSF configurations for the parametric study were limited to double, staggered and shaftliner LSF walls. Stud depths of 70 and 90 mm with 0.75 and 0.95 mm thicknesses which are widely used in the Australian market for load bearing LSF wall were considered for investigation in this study. However, the cavity depth of the wall varied based on the wall configuration. Two layers of 16 mm plasterboards were considered for all the LSF wall configurations. Glass fibre insulation was considered for the wall configurations with cavity insulation. G550 grade steel was considered for all the studs in structural analysis. The parametric FDS thermal models were based on with single stud model for computational efficiency. As the input ISO 834 time-temperature curve is specified uniformly to the fire exposed surface in the model, there arises no significant temperature variation occurs along the width of the test wall. Therefore, the single stud model was found suitable and was adapted in the parametric study. This also results in no significant temperature variation along the height of the test wall. Therefore, variation in temperature along the wall height was also not considered in the parametric study based on the FDS thermal analysis conducted in Chapter 5. Plasterboard open-up was considered in all the thermal model analysis with "SETPOINT" temperatures depending on the wall configuration. In the case of ambient temperature structural capacity analysis in ABAQUS, unsheathed 3 m long shell model with appropriate lateral restraint conditions was considered most suitable based on the analysis in Chapter 6. The 3 m long unsheathed shell model was also used for the sequentially coupled temperature displacement analysis to determine the failure time of LSF wall configurations.

The LSF wall configurations considered in the parametric study are shown in Figures 7.1 to 7.3. Table 7.1 lists the complex LSF wall configurations selected for the thermal parametric study. Some general notations will be followed to represent the models in the parametric study. DS represents Double stud wall, SL represents Shaftliner wall and ST represents Staggered stud wall with respect to the complex LSF wall configurations. AI represents ambient side cavity insulation, BI represents both sides cavity insulation and FI represents full cavity insulation.

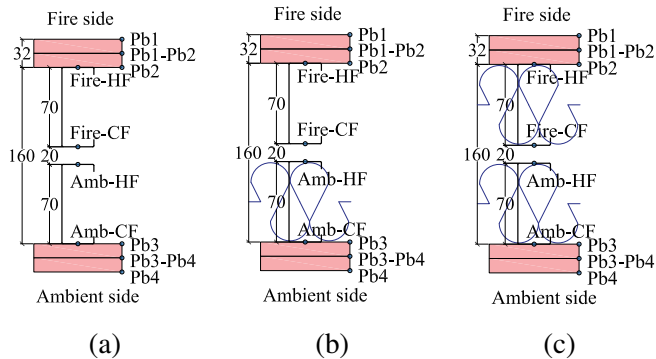


Figure 7.1: Double Stud Wall with 70 mm studs (a) No insulation (b) Ambient side cavity insulation (c) Both sides cavity insulation

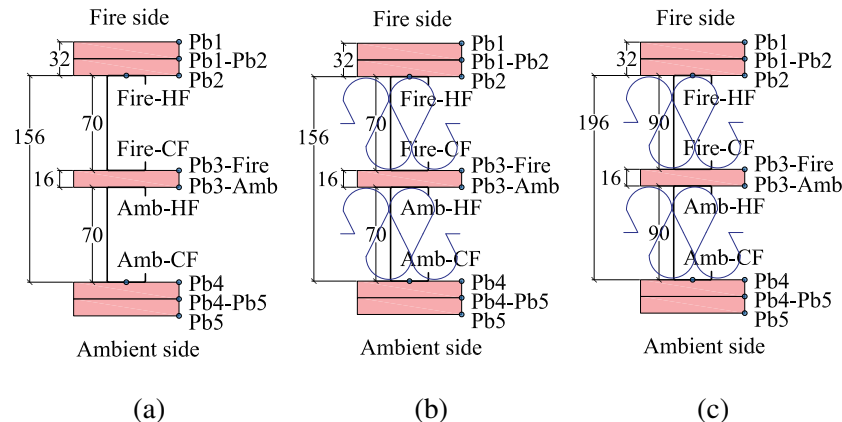


Figure 7.2: Shaftliner Wall with 70 and 90 mm studs (a) 70 mm wall no cavity insulation (b) 70 mm wall full cavity insulation (c) 90 mm wall full cavity insulation

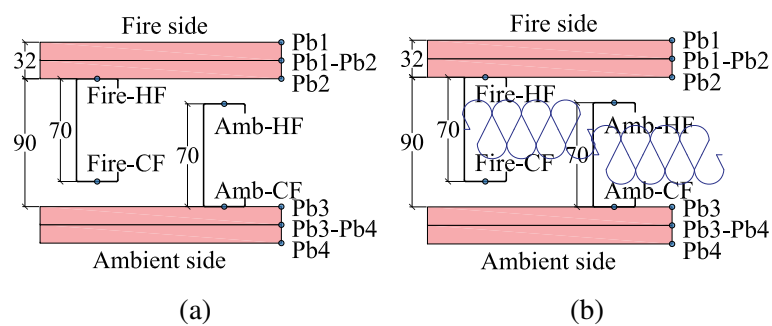


Figure 7.3: Staggered Stud Wall with 70 mm studs (a) No insulation (b) Full cavity insulation

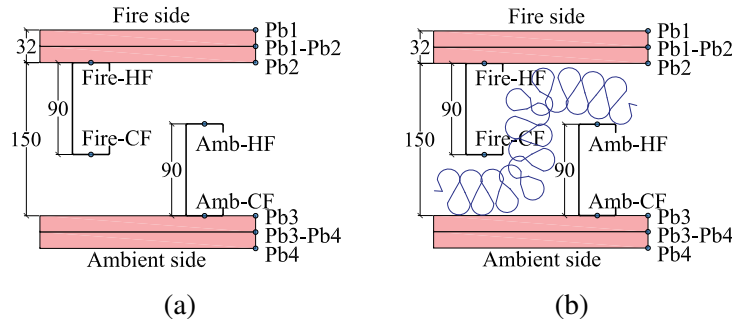


Figure 7.4: Staggered Stud Wall with 90 mm studs (a) No insulation (b) Full cavity insulation

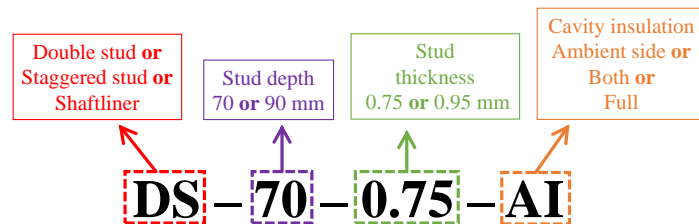


Figure 7.5: General notation for thermal parametric models

Table 7.1: FDS Thermal models considered in the parametric study

Model Name	Wall Type	Stud Depth	Stud Thickness	Insulation
DS-70-0.75	Double stud	70	0.75	Nil
DS-70-0.75-AI			0.75	Ambient side
DS-70-0.75-BI			0.75	Both sides
DS-70-0.95-AI			0.95	Ambient side
DS-70-0.95-BI			0.95	Both sides
DS-90-0.75-AI	Double stud	90	0.75	Ambient side
DS-90-0.75-BI			0.75	Both sides
SL-70-0.75	Shaftliner	70	0.75	Nil
SL-70-0.75-FI			0.75	Full
SL-70-0.95			0.95	Nil
SL-70-0.95-FI			0.95	Full
SL-90-0.75-FI			0.75	Full
SL-90-0.95	Staggered stud	90	0.95	Nil
SL-90-0.95-FI			0.95	Full
ST-70-0.75	Staggered stud	70	0.75	Nil
ST-70-0.75-FI			0.75	Full
ST-70-0.95			0.95	Nil
ST-70-0.95-FI			0.95	Full
ST-90-0.95			0.95	Nil
ST-90-0.75-FI			0.75	Full

7.3 Thermal Parametric Models

This section details the thermal analyses conducted on the selected complex LSF wall configurations listed in Table 7.1. The time-temperature curves of plasterboards and studs were extracted from the FDS thermal analysis output and corresponding discussions are made. Considering the repetitive nature of the problem statement, snippets were created using PYTHON programming language for data extraction and plotting of the time-temperature curves from the FDS thermal analysis output. All the thermal models were analysed under two conditions. Firstly the model was analysed without considering plasterboard open-up. Then plasterboard open-up was accounted based on the "SETPOINT" temperature depending on the LSF wall configuration grouped into non-cavity insulated and cavity insulated walls. In general construction practice, LSF wall configurations can be used under load bearing and non-load bearing conditions. Therefore, predicting the thermal behaviour under load bearing and non-load bearing conditions will yield better understanding on the thermal performance of these complex LSF walls. Some general notations along with those previously mentioned will be followed to represent the time-temperature curves of the models with and without plasterboard open-up. "Fds-O" represents the time-temperature curves with plasterboard open-up while "Fds" in the legend represents time-temperature curve corresponding to model without plasterboard open-up.

7.3.1 Double stud wall with 70 mm studs

FDS thermal analysis conducted on 70 mm double stud walls with and without cavity insulation are discussed in this section. Figure 7.6 shows the time-temperature curves from FDS thermal analysis conducted on non-cavity insulated double stud LSF walls with 70×0.75 mm studs (DS-70-0.75 as shown in Figure 7.1 (a)). The effective cavity depth in the considered model was 160 mm ($70 \times 2 + 20 = 160$). The fire side plasterboard time-temperature curve (Fds-Pb1) exhibited reasonable agreement with the input ISO 834 standard time-temperature curve as shown in Figure 7.6 (a). A small dip in the Fds-O-Pb1 time-temperature curve is noticeable at 175 min. However, this was not observed in the Fds-Pb1 time-temperature curve. This is a resultant of the plasterboard open-up simulated in the FDS thermal model. The fire side plasterboard interface Fds-

O-Pb1-Pb2 exhibited a steady increase in the time-temperature curve till 120 min of the simulation after which the curve tends to exhibit a plateau. However, the fire side cavity (Fds-O-Pb2) time-temperature curve recorded temperatures significantly less than the fire side interface (Pb1-Pb2). The sudden increase in the Fds-O-Pb2 curve at 175 min confirms the plasterboard open-up. But the Fds-Pb2 continues till the end of simulation by exhibiting a gradual increase. Similar trend is followed by the ambient side cavity (Fds-O-Pb3) time-temperature curve. The ambient side plasterboard interface (Fds-O-Pb3-Pb4) time-temperature curve recorded temperature less than 200°C till 220 min of simulation. Likewise, the ambient side plasterboard (Fds-Pb4) temperatures were less than 100°C till the end of simulation despite considering the plasterboard open-up. This infers the absence of insulation failure in the selected double stud wall configuration. The sudden increase in the time-temperature curves in the plasterboard open-up model is because the heat from the fire side is let into the cavity thereby exposing the studs and plasterboard directly to the input ISO 834 time-temperature curve.

The stud hot and cold flange temperatures from the DS-70-0.75 model is shown in Figure 7.6 (b). The stud fire side hot flange temperature Fds-O-Fire-HF showed a gradual increase till plasterboard open-up after which a sudden increase in the curve is noticed. This is reflected in the corresponding fire side cold flange (Fds-O-Fire-CF) and the ambient side hot and cold flanges (Fds-O-Amb-HF and CF). It is to be noted that the difference in the Fds-O-Fire-HF and CF time-temperature curve is minimal in the early stages of simulation and continues till the plasterboard open-up. This minimal difference in the time-temperature curve is also noticed on the Fds-O-Amb-HF and CF curves. However, post plasterboard open-up the difference in the hot and cold flange temperatures becomes large. This may be due to the fire side hot flange getting directly exposed to the input ISO 834 time-temperature curve. Also as the corresponding cold flange (Fds-O-Fire-CF) is separated by 20 mm gap there prevails no heat transfer through conduction similar to full-scale fire Test-T1 in Chapter 4. However, the difference between the other flanges apart from the Fds-O-Fire-HF is minimal. This is because of the non exposure of the other flanges to the ISO 834 time-temperature curve. Due to the absence of insulation within the cavity there is significant loss of heat from the stud surfaces into the cavity resulting this unique behaviour in the time-temperature curve. The steep increase during plasterboard open-up was not witnessed

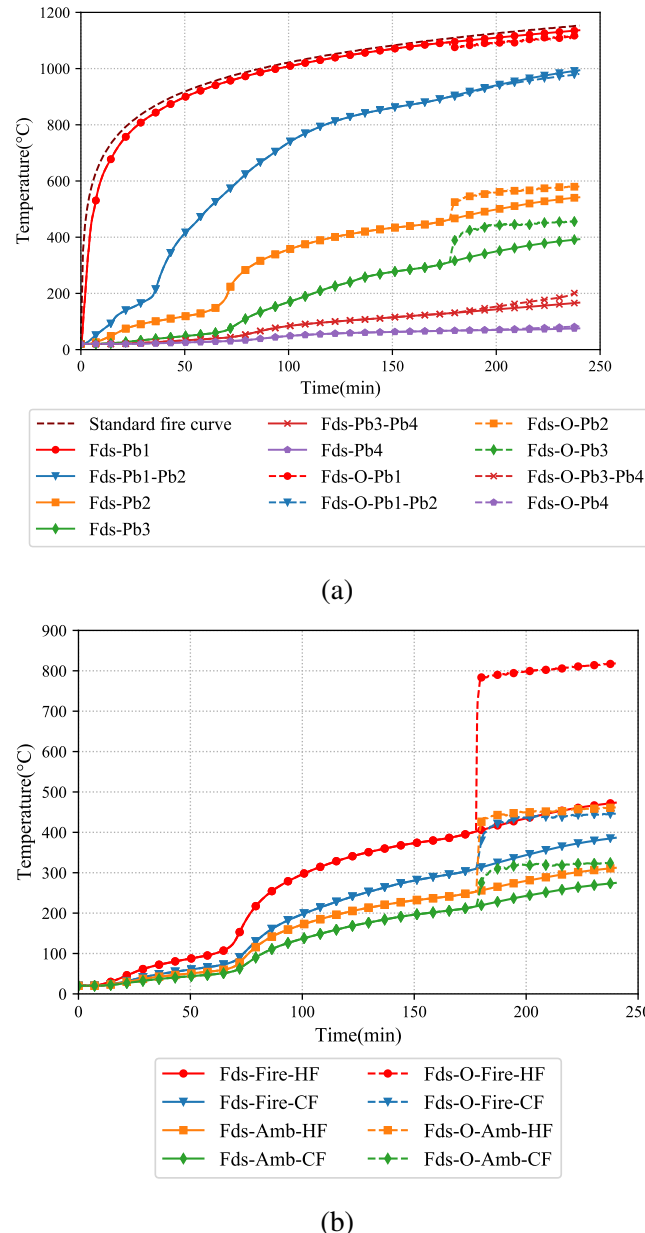


Figure 7.6: Model DS-70-0.75 - Plasterboard and stud time-temperature curves of non-cavity insulated double stud wall with 70×0.75 mm studs - (a) Plasterboard temperatures (b) Stud temperatures

on the Fds-Fire-HF time-temperature curve. The maximum temperature achieved by the model with plasterboard open-up was 829°C while it was 497°C for the model without plasterboard open-up.

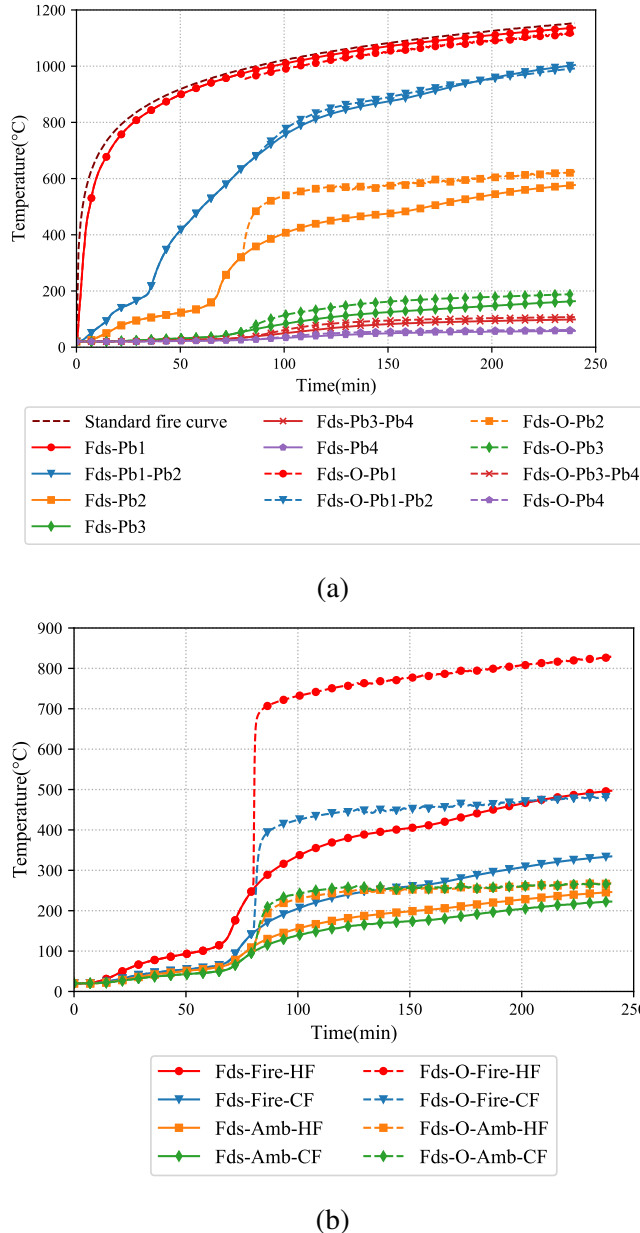


Figure 7.7: Model DS-70-0.75-AI - Plasterboard and stud time-temperature curves of ambient cavity insulated double stud wall with 70 × 0.75 mm studs - (a) Plasterboard temperatures (b) Stud temperatures

Insulating the ambient side cavity as in Figure 7.1 (b) exhibits a different time-temperature curve behaviour as shown in Figure 7.7. Based on fire Test-T7 in Chapter 4 the model DS-70-0.75-AI had cavity insulation only on the ambient side. The fire side plasterboard interface (Fds-O-Pb1-Pb2) shown in Figure 7.7 (a) exhibited a

similar behaviour to the that of the non-cavity insulated model. It is to be noted that the Fds-O-Pb1-Pb2 exhibited a similar trend in comparison with the Fds-Pb1-Pb2. This infers that the time-temperature curve behaviour on the fire side plasterboard interface of cavity insulated 70 mm double stud models are similar irrespective of the plasterboard open-up. However, the fire side cavity time-temperature curve (Fds-O-Pb2) exhibited a steep rise after 60 min of simulation unlike the non-cavity insulated model. This is attributed to the difference in "SETPOINT" temperature for plasterboard open-up initiation in the thermal model. Despite the plasterboard open-up all the ambient side time-temperature curves which include Fds-O-Pb3, Fds-O-Pb3-Pb4 and Fds-O-Pb4 recorded temperatures less than 200°C till the end of simulation. Models without plasterboard open-up also exhibited similar behaviour. This infers that the glass fibre cavity insulation on the ambient side has trapped the heat from the fire side resulting in lower ambient side plasterboard temperatures confirming the absence of insulation failure in the models. The lower time-temperature curves exhibited by the ambient side hot and cold flanges for model DS-70-0.75-AI confirm the behaviour of heat entrapment on the fire side surfaces only as shown in Figure 7.7 (b). The effect of heat entrapment is further evident from the increased stud fire side hot flange temperatures (Fire-HF). This was evident in the model without plasterboard open-up wherein the Fds-Fire-HF recorded temperatures higher than the other flanges.

Providing cavity insulation on both the stud rows resulted in similar behaviour in the plasterboard and stud time-temperature curves similar to model DS-70-0.75-AI. Time-temperature curves of plasterboard and studs corresponding to model DS-70-0.75-BI are shown in Figure 7.8. The sudden increase in the plasterboard and stud time-temperature curves at plasterboard open-up is evident in the model with cavity insulation on both sides. Due to severe numerical instability the analysis was terminated at 160 min and could not be conducted for 240 min. However, the model without plasterboard open-up could be simulated for 240 min. Open-up in the FDS thermal model causes severe numerical instability as explained in the FDS software manual (McGrattan et al., 2013) and requires multiple iterations in the case of non-convergence to arrive at the solution. As the model with plasterboard open-up resulted in temperatures above the limiting criteria, no further iterations were conducted.

To determine the effect of cavity insulation on thicker studs, the model DS-70-

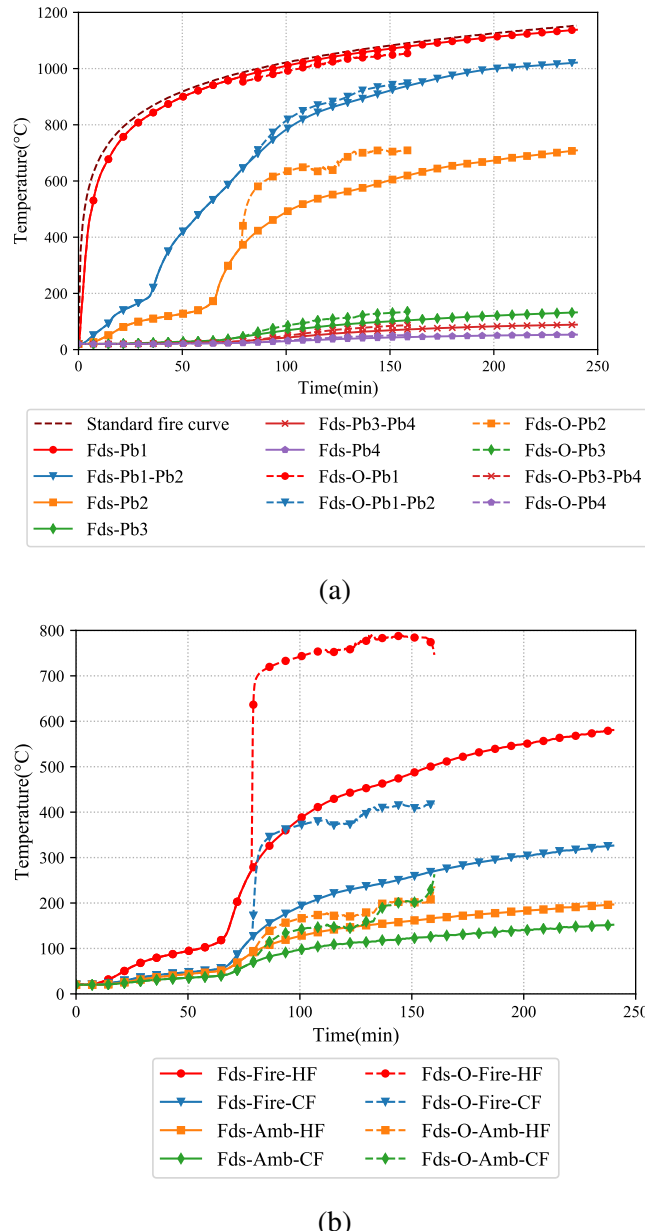


Figure 7.8: Model DS-70-0.75-BI - Plasterboard and stud time-temperature curves of both sides cavity insulated double stud wall with 70×0.75 mm studs - (a) Plasterboard temperatures (b) Stud temperatures

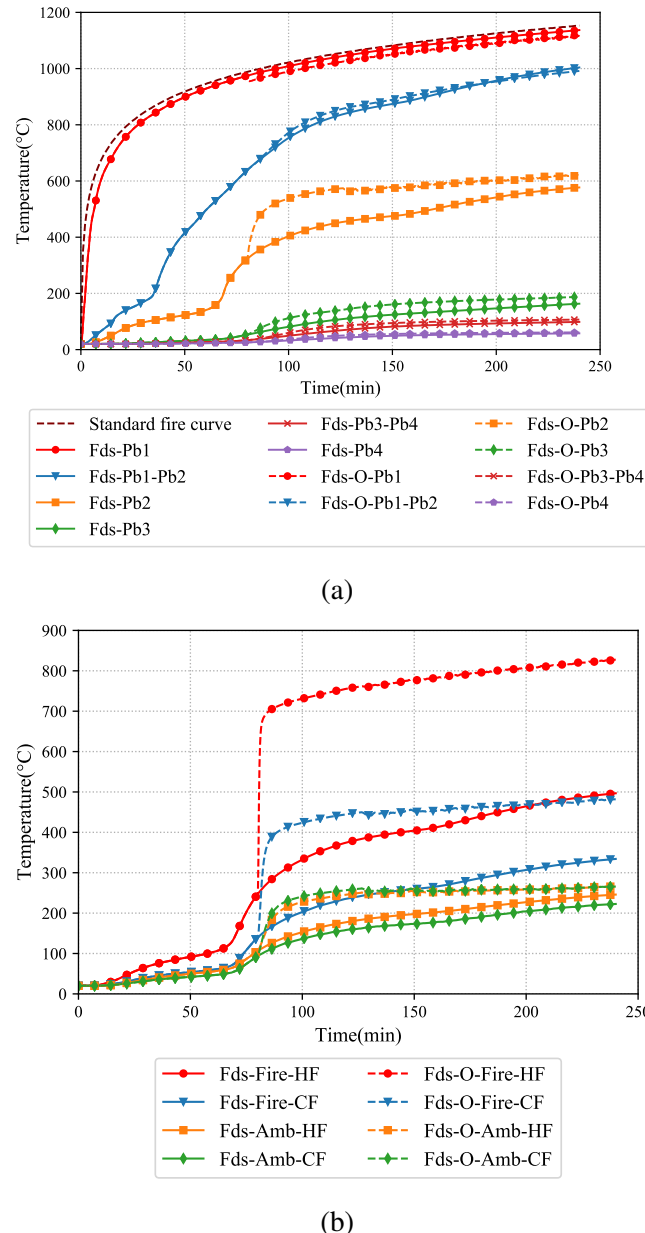


Figure 7.9: Model DS-70-0.95-AI - Plasterboard and stud time-temperature curves of both sides cavity insulated double stud wall with 70×0.95 mm studs - (a) Plasterboard temperatures (b) Stud temperatures

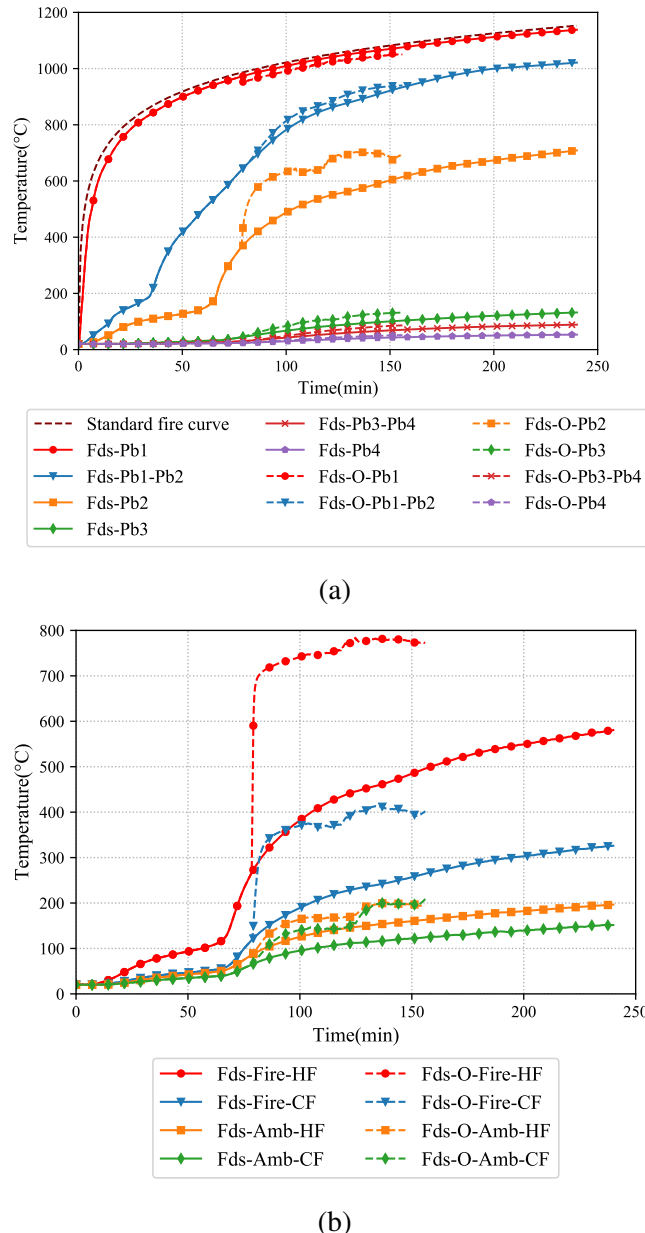


Figure 7.10: Model DS-70-0.95-BI - Plasterboard and stud time-temperature curves of both cavity insulated double stud wall with 70×0.95 mm studs - (a) Plasterboard temperatures (b) Stud temperatures

0.95-BI was then created with 70×0.95 mm studs as shown in Figure 7.1 (c). It is to be noted that fire Test-T4 was conducted with the same configuration as this model but without the cavity insulation. Similar to model DS-70-0.75-BI this model also suffered numerical instabilities leading to convergence issues and the thermal analysis could be simulated for 156 min only. However, the behaviour exhibited by the plasterboard and stud time-temperature curves as shown in ?? was similar to those exhibited by the DS-70-0.75-BI model. This infers that the effect of stud thickness does not result in significant changes in the time-temperature curves of cavity insulated double stud walls with 70 mm studs. This may be partly attributed by the effective cavity depth also. The effective cavity depth is 160 mm in this case which is less than the cavity depth of 200 mm generally available in double stud walls with 90 mm studs. Reduced cavity depth may result in faster heat transfer within the cavity from fire side to ambient side. Therefore the effect of stud thickness might not play a significant role in the temperature profile of the LSF wall. The model without the plasterboard open-up to simulate the non-load bearing conditions could be simulated for 240 min and is also shown in Figure 7.10. Similar to other models the time-temperature curves of the model without plasterboard open-up recorded temperatures less than the plasterboard open-up model.

7.3.2 Double stud walls with 90 mm studs

Like the double stud wall models with 70 mm studs attempts were made to predict the temperature profiles of double stud walls with 90 mm studs. An effective cavity depth of 200 mm was considered in the model ($90 \times 2 + 20 = 200$). Time-temperature curves of plasterboards and studs corresponding to double stud walls with 90 mm studs are discussed in this section. Figure 7.11 shows the time-temperature curves of plasterboards and studs corresponding to double stud wall with 90×0.75 mm studs (DS-90-0.75-AI) with cavity insulation on the ambient stud rows. The non-cavity insulated models with the same configuration was considered for investigation through full-scale fire test in Chapter 4 as Test-T2 and the thermal model predictions of the same was presented in Section 5.4.4 of Chapter 5.

The fire side interface plasterboard time-temperature curve (Fds-O-Pb1-Pb2) from model DS-90-0.75-AI shown in Figure 7.11 (a) exhibits a steep increase in the curve

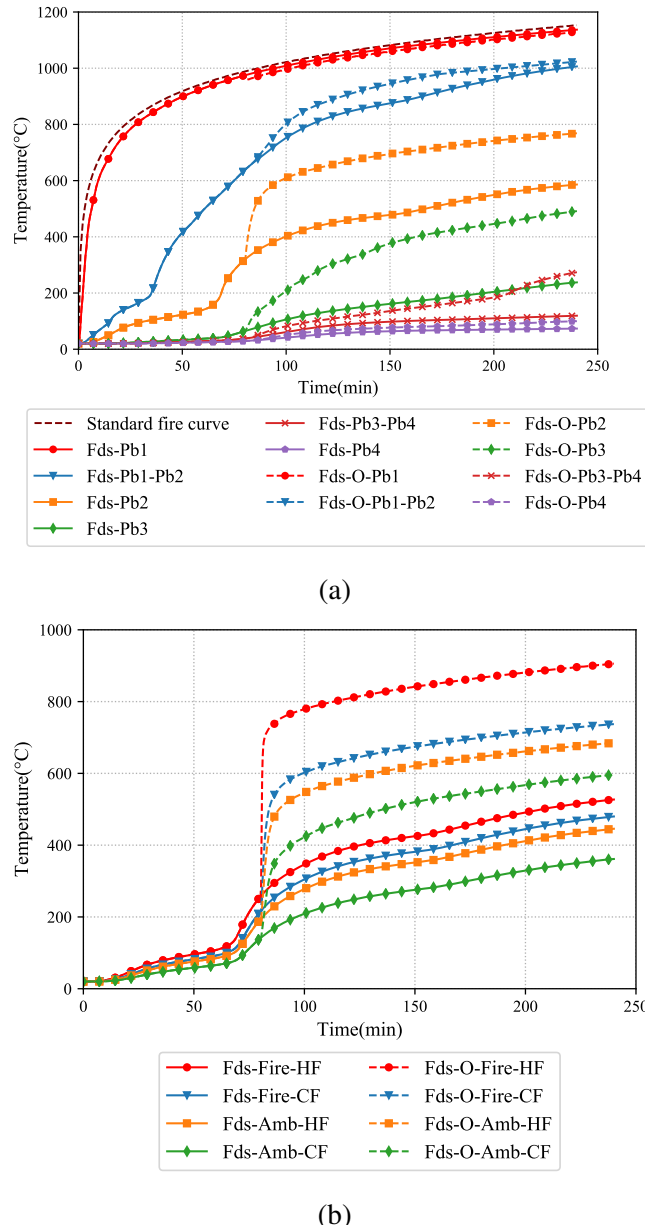


Figure 7.11: Model DS-90-0.75-AI - Plasterboard and stud time-temperature curves of ambient side cavity insulated double stud wall with 90×0.75 mm studs - (a) Plasterboard temperatures (b) Stud temperatures

similar to the double stud wall models with 70 mm studs. This is witnessed in the model with plasterboard open-up (Fds-O-Pb1-Pb2). But the ambient side plasterboard temperatures (Fds-O-Pb3) are more in comparison with the double stud models with 70 mm studs. This is attributed by the glass fibre cavity insulation in the wall entrapping the heat flow within the cavity confirming the earlier claim. In the case of double stud wall with cavity insulation on the ambient side, there is no contact between the glass fibre insulation and the fire side plasterboards. This allows the heat to be transferred to the ambient side plasterboards and the insulation resulting in higher time-temperature curves in comparison with double stud wall with 70 mm studs. This is evident from the stud time-temperature curve shown in Figure 7.11 (b). The difference in the hot and cold flanges are minimal in the case of DS-90-0.75-AI. However, in the case of 70 mm double stud wall with ambient cavity insulation model DS-90-0.75-AI, the ambient side stud time-temperature curves shows very less difference and record similar temperatures as shown in Figure 7.9 (b). The maximum fire side hot flange temperature of Fds-Fire-HF was 527°C while it was 905°C for Fds-O-Fire-HF.

In the case of 90 mm double stud wall with both cavity insulation model DS-90-0.75-BI, the time-temperature curves on the ambient side plasterboards were less than 200°C till the end of simulation as shown in Figure 7.12 (a). This is in correlation with the time-temperature curves of both cavity insulated 70 mm double stud wall. Also, the differences between the fire side hot flange temperatures and the corresponding cold flange temperatures are significantly high in comparison with the ambient side cavity insulated walls and are shown in Figure 7.12 (b). The difference between fire side hot and cold flanges (Fds-O-Fire-HF and CF) is 136°C (551°–416°C) in the model without plasterboard open-up while the difference is 317°C (814°–497°C) in the model with plasterboard open-up. This shows the intensity of thermal load incident on the stud hot flange due to plasterboard open-up in cavity insulated 90 mm double stud LSF walls.

7.3.3 Shaftliner stud walls with 70 mm studs

Due to the limitations in the testing set-up, shaftliner LSF walls could not be tested under load bearing conditions during experimental investigation. To overcome this limitation, shaftliner LSF walls systems with 70 and 90 mm deep studs were consid-

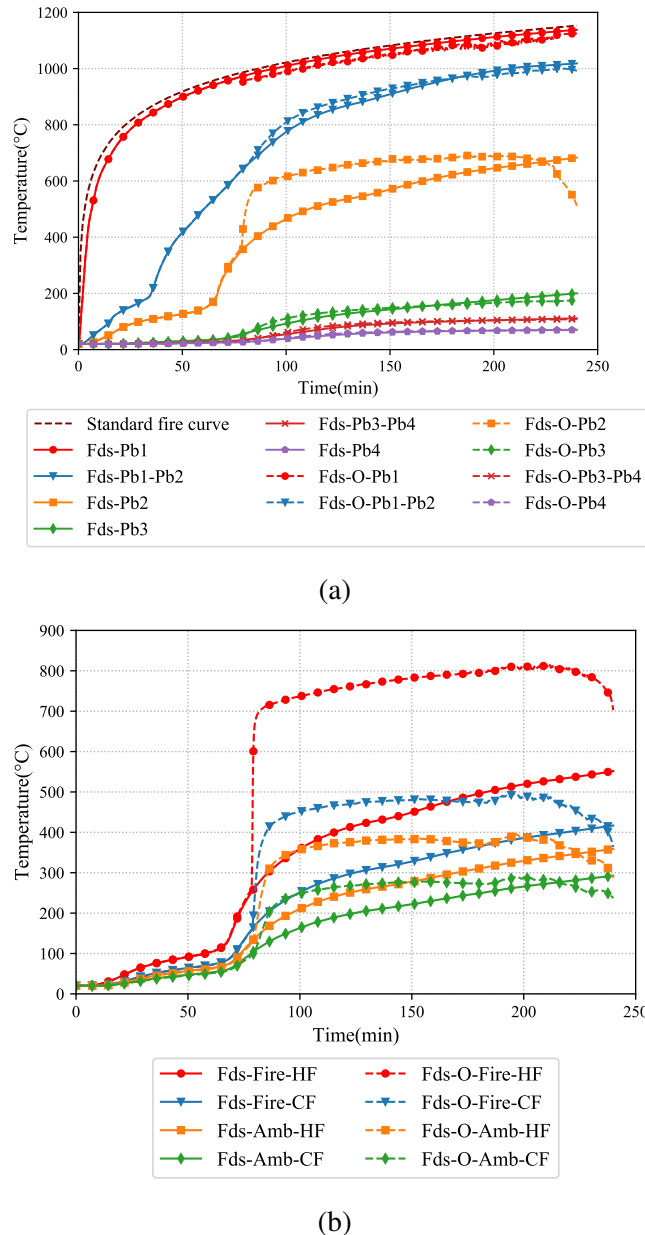


Figure 7.12: Model DS-90-0.75-BI - Plasterboard and stud time-temperature curves of both cavity insulated double stud wall with 90×0.75 mm studs - (a) Plasterboard temperatures (b) Stud temperatures

ered and the results of shaftliner walls with 70 mm studs are discussed in this section. Firstly, the results from the FDS thermal analysis are discussed. Later, the stud temperatures were used to determine the failure time of the test wall under load bearing conditions through the sequentially coupled temperature displacement analysis which was validated in Chapter 6. This sections details the thermal analysis results on shaftliner LSF walls with 70 mm studs as shown in Figures 7.2 (a) and (b).

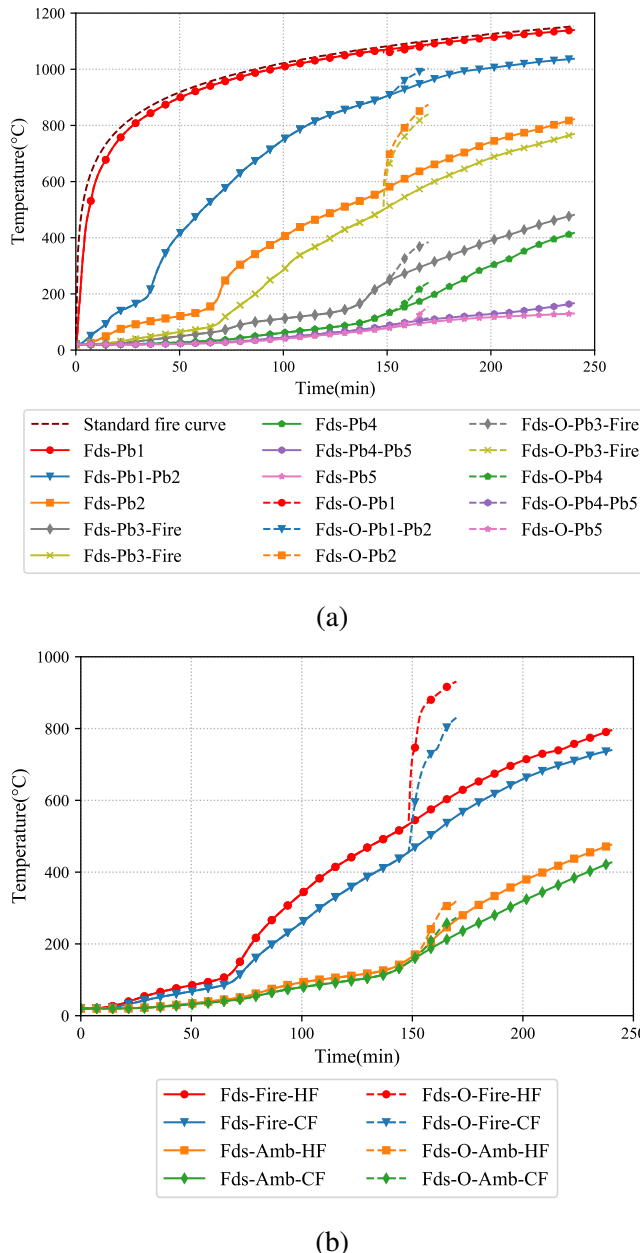


Figure 7.13: Model SL-70-0.75 - Plasterboard and stud time-temperature curves of non-cavity insulated shaftliner wall with 70 x 0.75 mm studs - (a) Plasterboard temperatures (b) Stud temperatures

Figure 7.13 (a) shows the plasterboard time-temperature curve from non-cavity in-

sulated shaftliner model SL-70-0.75 similar to the configuration shown in Figure 7.2 (a). Severe non-linearity was experienced during thermal analysis leading to convergence issues and the model was simulated for 170 min. This is because of the consideration of plasterboard open-up in the model similar to the double stud walls. However, the plasterboard open-up has resulted in a steep inclination after 150 min as evident in the fire and ambient side plasterboard time temperature curves (Fds-O-Pb1 and Fds-O-Pb3-Fire and Amb) shown in Figure 7.13 (a). The plasterboard interface time-temperature curve Fds-O-Pb1-Pb2 tend to reach the input fire curve after 150 min of simulation because of the small effective cavity depth of 70 mm. This is also visible in the corresponding fire side cavity Fds-O-Pb2 time-temperature curve and in the plasterboard between the cavity Fds-O-Pb3-Fire and Fds-O-Pb3-Amb. The steep increase in the time-temperature curve is also visible on the ambient side plasterboards (Fds-O-Pb4 and Pb5) but is subtle in comparison with the fire side. The model without plasterboard open-up did not experience convergence issue and was able to be simulated for 240 min. The corresponding time-temperature curves are also compared along those from plasterboard open-up models. The stud time-temperature curves exhibit a steep rise in the fire side hot flange temperatures as shown in Figure 7.13 (b). The fire side hot and cold flange temperatures (Fds-Fire-HF and CF) exceeded 800°C after 160 min which is higher than the limiting temperature for stud failure under all load ratios proposed by Gunalan and Mahendran (2013a). Considering the critical hot flange temperature no further iterations were conducted for the model SL-70-0.75. However, the model without plasterboard open-up could be simulated for 240 min.

Figure 7.14 shows the time-temperature curves from model SL-70-0.75-FI. The model was simulated with full cavity insulation as shown in Figure 7.2 (b). Models with cavity insulation only on the fire side cavity was not considered for the FDS thermal parametric analysis. This is because in general construction practice shaftliner walls are used with full cavity insulation to achieve the desired acoustic ratings. Also, providing cavity insulation only on the fire side cavity will make the shaftliner wall behave like a single stud wall because of the heat entrapment in cavity insulated LSF walls. Figure 7.14 (a) shows the time-temperature curves of plasterboards from the model SL-70-0.75-FI. The Fds-Pb1-Pb2 curve exhibits a steep rise tending to match the input ISO 834 time-temperature curve. This infers the entrapment of heat by the

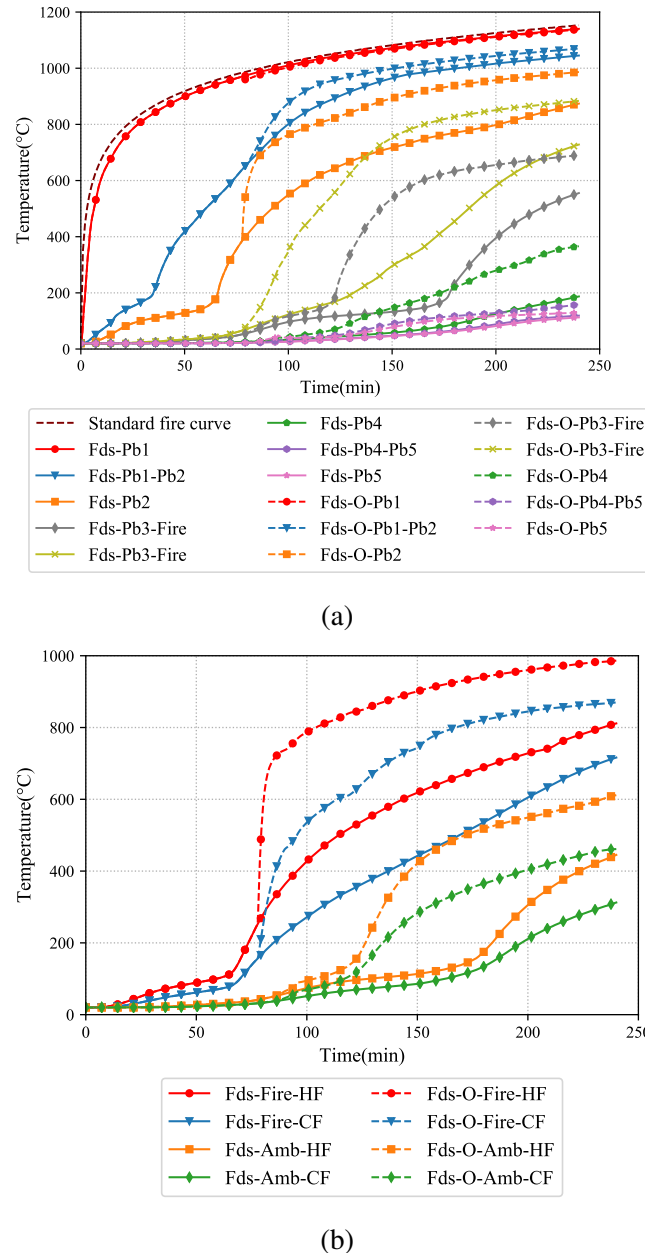
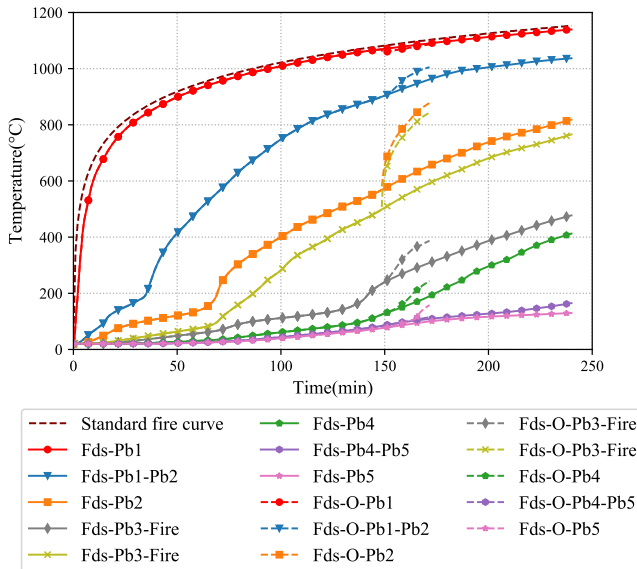
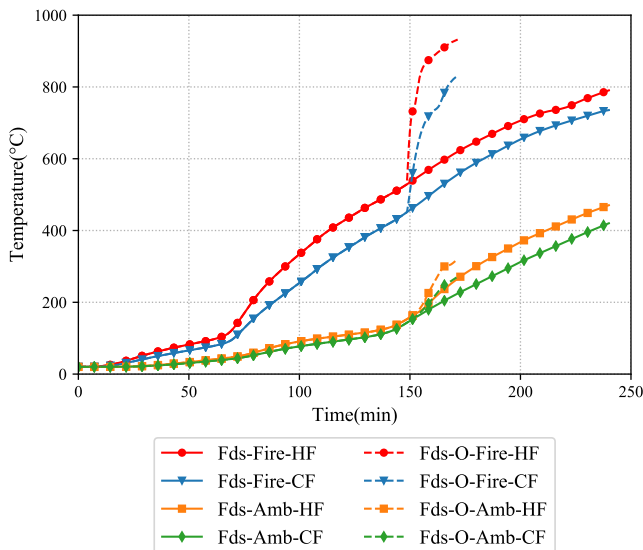


Figure 7.14: Model SL-70-0.75-FI - Plasterboard and stud time-temperature curves of cavity insulated shaftliner wall with 70×0.75 mm studs - (a) Plasterboard temperatures (b) Stud temperatures

cavity insulation within the fire side plasterboards. This behaviour is exhibited by the Fds-O-Pb1-Pb2 curve which confirms the earlier claim in double stud wall models that the time-temperature curve on the fire side plasterboard interface is similar to the cavity insulated double stud walls irrespective of the plasterboard open-up.



(a)



(b)

Figure 7.15: Model SL-70-0.95 - Plasterboard and stud time-temperature curves of non-cavity insulated shaftliner wall with 70×0.95 mm studs - (a) Plasterboard temperatures (b) Stud temperatures

Similar trend was observed on the middle plasterboard layer within the cavity. However, the non-plasterboard open-up model exhibited a gradual increase till the end of simulation. The ambient side plasterboard interface Fds-O-Pb4-Pb5 and am-

bient side plasterboard Fds-O-Pb5 time-temperature curves were less than 200°C till the end of simulation. The stud time-temperature curves shown in Figure 7.14 (b) also exhibited a steep gradient on the fire side hot and cold flanges (Fire-HF and CF). The difference between the fire side hot and cold flanges (Fds-O-Fire-HF and CF) in comparison with the ambient side hot and cold flanges (Fds-O-Amb-HF and CF) was large as a result of cavity insulation. This behaviour was also observed in the double stud wall models. The stud time-temperature curves were also similar in the models without plasterboard open-up till the open-up time. The large difference in the fire and ambient side studs was also evident in the Fds-Fire-HF and CF and Fds-Amb-HF and CF time-temperature curves. It is to be noted that, in the case of double stud wall model, steep inclination in the time-temperature curve was predominant in the fire side hot flange(Fds-O-Fire-HF) only. The inclinations in Fds-O-Fire-CF, Fds-O-Amb-HF and CF time-temperature curves were not large in comparison with the Fds-O-Fire-HF in the case of double stud LSF walls. But, in the case of shaftliner walls, both the Fds-O-Fire-HF and CF exhibit a steep inclination in the time-temperature curve. This is influenced by the middle plasterboard layer absorbing the heat within the fire side cavity. This effect of steep inclination in the fire side stud time-temperature curves is further influenced by the presence of cavity insulation and is also present in the models without plasterboard open-up.

The thickness of the 70 mm deep stud shaftliner model was changed from 0.75 mm to 0.95 mm and FDS thermal analyses were conducted. Time-temperature curves of plasterboard and stud from the models SL-70-0.95 and SL-70-0.95-FI are shown in Figures 7.15 and 7.16. The non-cavity insulated model also experienced numerical instability and thus the thermal analysis was conducted for 172 min. It is evident from the time-temperature curves that there is no significant difference in comparison with the time-temperature curves from the cavity insulated model SL-70-0.75-FI. This infers that the effect of stud thickness did not significantly influence the heat transfer within the wall cavity in shaftliner LSF walls. This inference also holds good in the case of models without plasterboard open-up. No further iterations were conducted on the plasterboard open-up model as the critical fire side stud hot flange temperature (Fds-O-Fire-HF) has already exceeded 800°C, which is more than the limiting temperatures under the general LR range of 0.2 to 0.7.

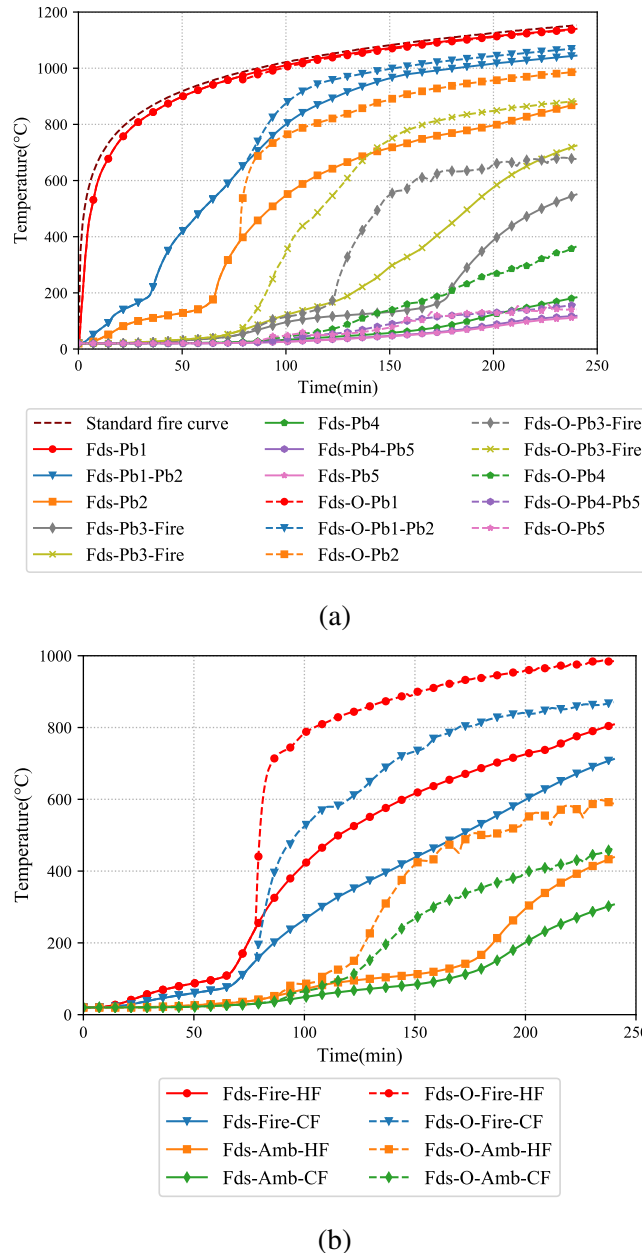


Figure 7.16: Model SL-70-0.95-FI - Plasterboard and stud time-temperature curves of cavity insulated shaftliner wall with 70 × 0.95 mm studs - (a) Plasterboard temperatures (b) Stud temperatures

7.3.4 Shaftliner stud walls with 90 mm studs

Shaftliner wall models were created with 90 mm deep 0.75 and 0.95 mm thick studs as shown in Figure 7.2 (c) and are discussed in this section. Figure 7.17 shows the time-temperature curves of studs and plasterboard from the cavity insulated shaftliner model with 90×0.75 mm studs. Non-cavity insulated shaftliner wall 90×0.75 mm studs was investigated in the experimental study as Test-T8 in Chapter 4 and thermal model predictions for the same were discussed in Chapter 5. The steep increase in the plasterboard interface time-temperature curve (Fds-O-Pb1-Pb2) was observed in the model with plasterboard open-up tending to reach the input ISO 834 time-temperature curve as shown in Figure 7.17 (a). Non-cavity insulated shaftliner model (SL-90-0.75) with plasterboard open-up experienced severe instability similar to the previous plasterboard open-up models. However, the model without plasterboard open-up could be simulated for 240 min. The Fds-O-Pb3-Fire plasterboard time-temperature curve corresponding to the middle fire side plasterboard surface exhibited a steep increase on the curve which was similar to the shaftliner models with 70 mm deep studs. This infers that irrespective of the stud depth used in the shaftliner LSF wall configuration, plasterboard open-up will result in direct exposure of heat into the cavity despite the provision of cavity insulation. This results in sudden increase in the fire side hot flange (Fds-O-Fire-HF and CF) time-temperature curves as shown in Figure 7.17 (b). However, in the case of the model without plasterboard open-up the hot flange temperature increases steadily. It is to be noted that the slope of the Fds-Fire-HF is higher in the case of shaftliner walls in comparison with the double stud walls as shown in Figure 5.20 in Chapter 5. This increased slope in the time-temperature curve is contributed by the middle plasterboard layer absorbing the heat within the cavity thereby increasing the fire side stud hot and cold flange temperatures. This phenomenon was also reported in the experimental investigation in Chapter 4 and was also simulated by the developed FDS thermal model in Chapter 5. Parametric model results also agree with this claim confirming the accuracy of the developed FDS thermal model.

Figures 7.18 and 7.19 show the time-temperature curves from thermal models of non-cavity insulated and cavity insulated shaftliner walls with 90×0.95 mm studs. Numerical instability was observed on both the models leading to a simulation time of 174 min for non-cavity insulated shaftliner model SL-90-0.95 and 122 min for cav-

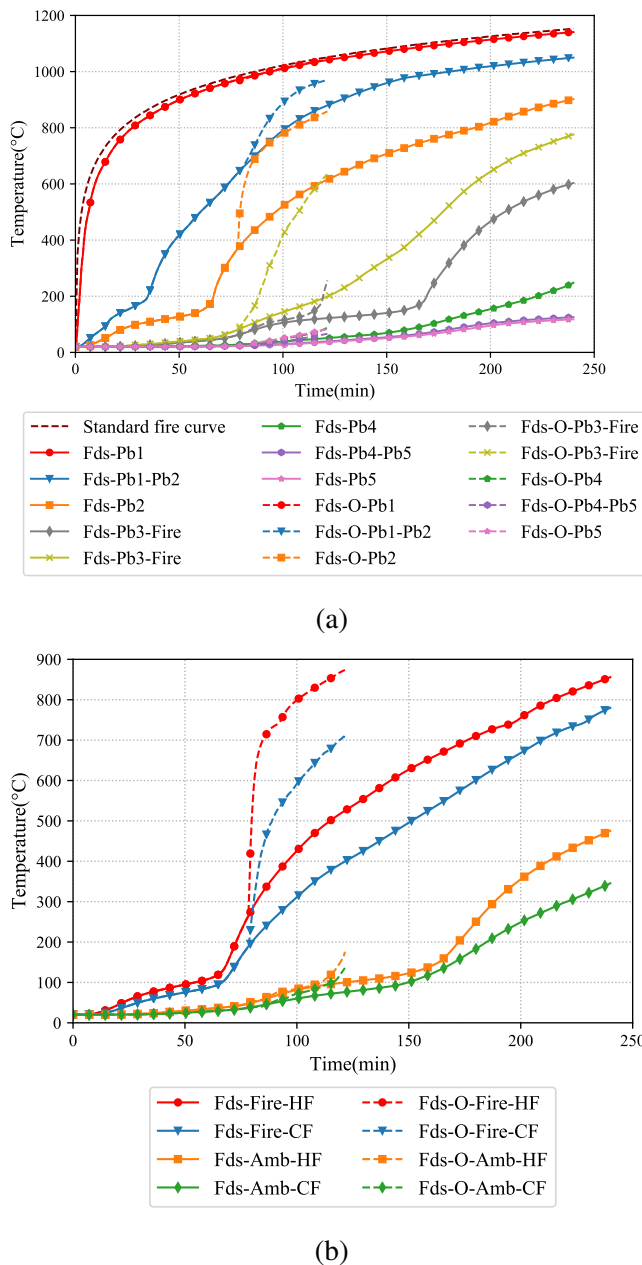


Figure 7.17: Model SL-90-0.75-FI - Plasterboard and stud time-temperature curves of cavity insulated shaftliner wall with 90×0.75 mm studs - (a) Plasterboard temperatures (b) Stud temperatures

ity insulated shaftliner model SL-90-0.95-FI. Plasterboard time-temperature curves of non-cavity insulated model are similar till the plasterboard open-up after which a steep increase in the time-temperature curves are observed as shown in Figure 7.18 (a). Despite the plasterboard open-up the ambient side plasterboard interface (Fds-O-Pb3-Pb4) and the ambient side plasterboard (Fds-O-Pb4) recorded temperatures less than 200°C which confirms the absence of insulation failure in the model SL-90-0.95. This observation was also similar in the cavity insulated shaftliner model SL-90-0.95-FI. As the "SETPOINT" temperatures are lower in the case of cavity insulated wall models the steep increase in the time-temperature curve is noticed earlier during simulation in comparison with the non-cavity insulated model.

In the case of stud time-temperature curves for non-cavity insulated model SL-90-0.95 the fire side hot and cold flanges (Fds and Fds-O-Fire-HF and CF) are closer irrespective of the plasterboard open up as shown in Figure 7.18 (b). The ambient side hot and cold flanges also recorded similar temperatures in the case of non-cavity insulated model SL-90-0.95. But in the cavity insulated model SL-90-0.95-FI the difference between the fire side hot and cold flange (Fds-Fire-HF and CF) was large as shown in Figure 7.19 (b). The difference between the flanges was larger in the case of model SL-90-0.95-FI considering plasterboard open-up (Fds-O-Fire-HF and CF) as shown in Figure 7.19 (b). This confirms the entrapment of heat by the glass fibre cavity insulation. Despite the cavity being split by the middle plasterboard layer, the heat entrapment is significant in cavity insulated shaftliner LSF walls with 90 mm deep studs.

7.3.5 Staggered stud walls with 70 mm studs

Thermal models were created to predict the thermal behaviour of the staggered stud walls. This section presents the results from the staggered stud wall models with 70 mm studs shown in Figure 7.3. An effective cavity depth of 90 mm was maintained for the models with 70 mm deep studs arranged in a staggered pattern. In the case of cavity insulated models the glass fibre insulation is placed in a linear pattern as shown in Figure 7.3 (b). As the distance between the free stud edge and the plasterboard is 20 mm, compressing the insulation is not the preferred option to achieve the required acoustic rating. Therefore, linear arrangement of the glass fibre insulation was used in

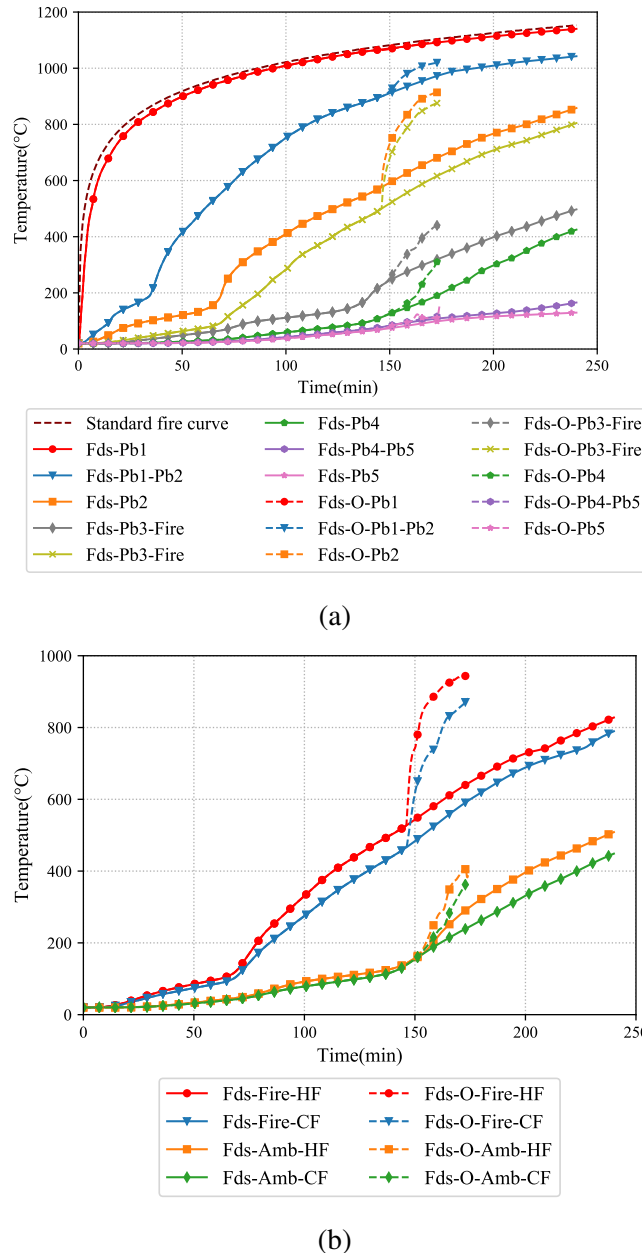


Figure 7.18: Model SL-90-0.95 - Plasterboard and stud time-temperature curves of non-cavity insulated shaftliner wall with 90 × 0.95 mm studs - (a) Plasterboard temperatures (b) Stud temperatures

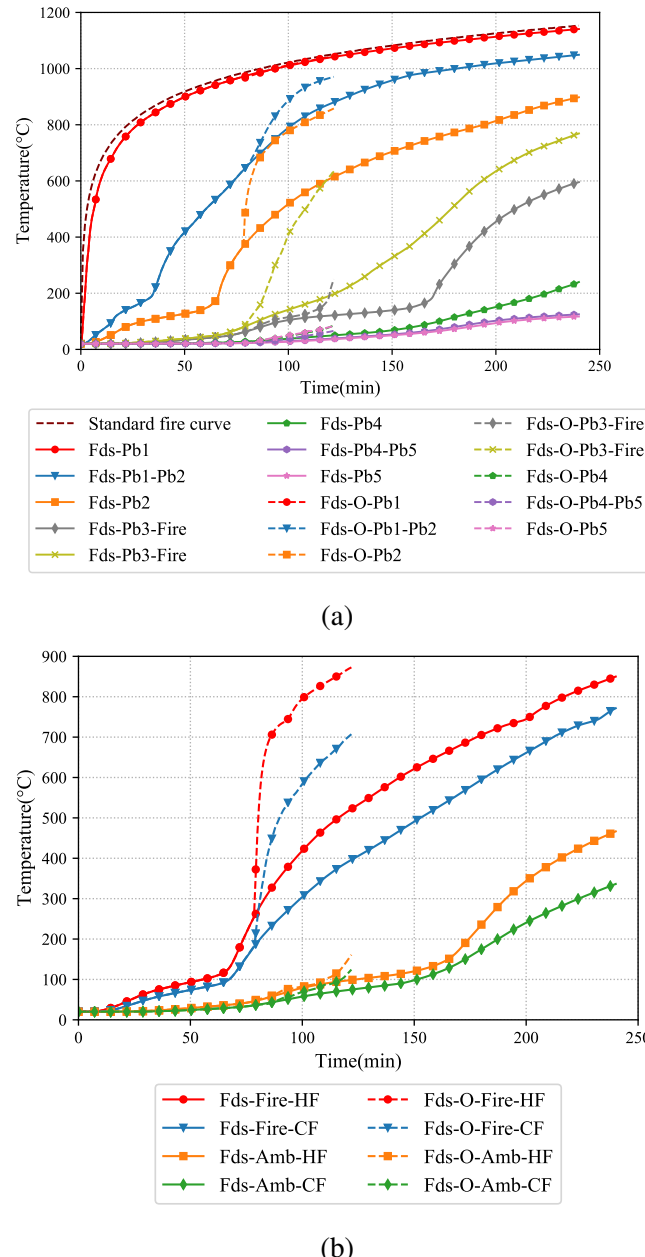


Figure 7.19: Model SL-90-0.95-FI - Plasterboard and stud time-temperature curves of cavity insulated shaftliner wall with 90×0.95 mm studs - (a) Plasterboard temperatures (b) Stud temperatures

the thermal models.

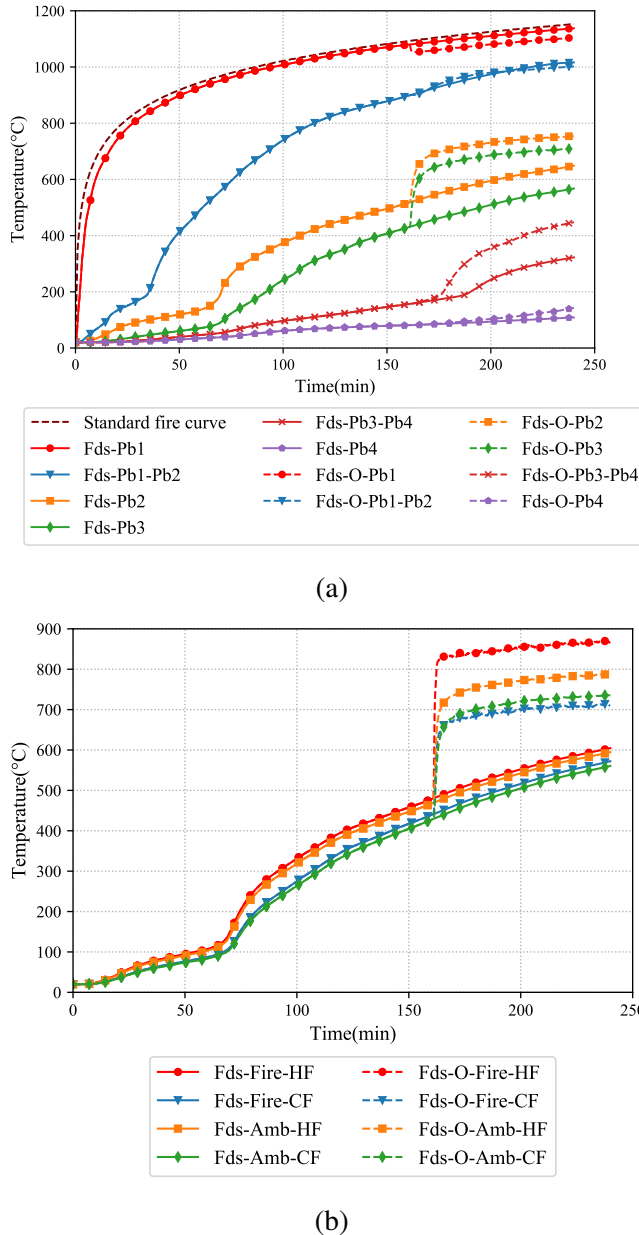


Figure 7.20: Model ST-70-0.75 - Plasterboard and stud time-temperature curves of non-cavity insulated staggered stud wall with 70×0.75 mm studs - (a) Plasterboard temperatures (b) Stud temperatures

The plasterboard time-temperature curves from the non-cavity insulated staggered stud model ST-70-0.75 are shown in Figure 7.20 (a). All the plasterboard time-temperature curves follow similar pattern till the plasterboard open-up. In the staggered stud LSF walls the ambient side hot flange (Fds-Amb-HF) is hotter than the fire side cold flange (Fds-Fire-CF) because of the staggered stud arrangement within the wall cavity. The ambient side cold flange is located closer to the fire side plasterboards resulting in

this behaviour. This is also visible on the ambient side hot flange (Fds-O-Amb-HF) of model ST-70-0.75 considering plasterboard open-up as shown in Figure 7.20 (b). Also, the temperatures exhibited by the fire and ambient side hot and cold flanges are similar in comparison with each other. In other words, the temperature gradient of the stud flanges in the case of non-cavity insulated staggered stud LSF wall is less in comparison with other wall configurations such as double stud and shaftliner LSF walls. However, the temperature gradient is significant if plasterboard open-up is taken into consideration as shown in Figure 7.20 (b).

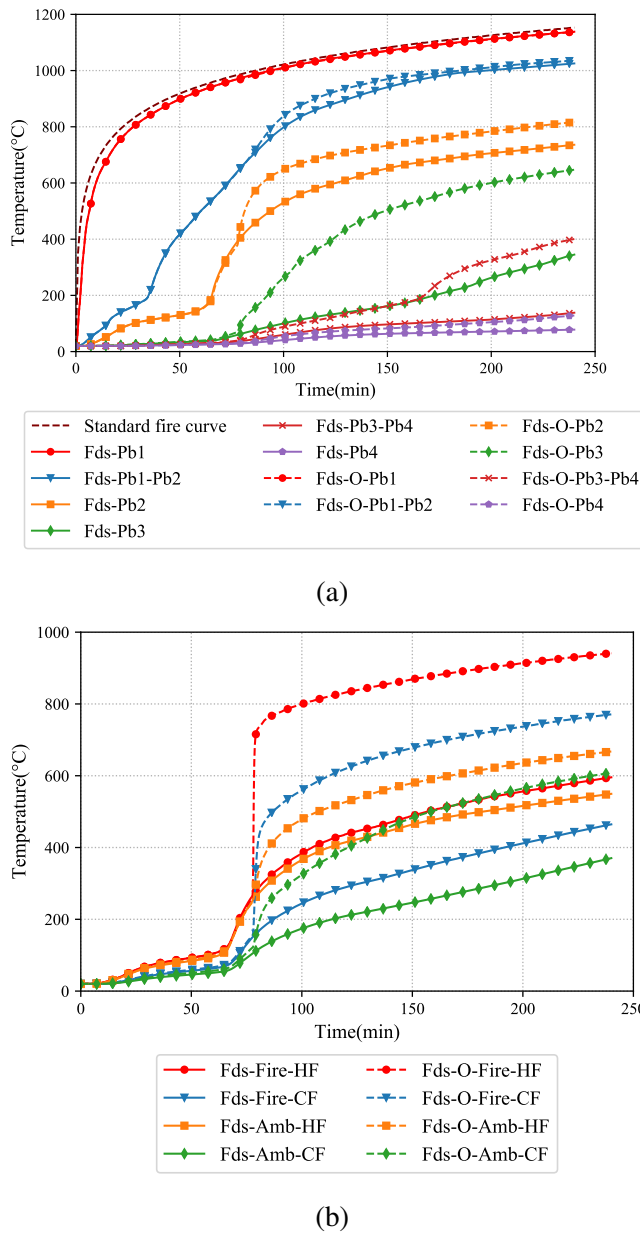


Figure 7.21: Model ST-70-0.75-FI - Plasterboard and stud time-temperature curves of cavity insulated staggered stud wall with 70×0.75 mm studs - (a) Plasterboard temperatures (b) Stud temperatures

Plasterboard time-temperature curves from the staggered stud model with cavity insulation (ST-70-0.75-FI) are shown in Figure 7.21 (a). The steep increase in the fire side plasterboard interface (Fds-Pb1-Pb2) time-temperature curve is observed at a similar time to that of the non-cavity insulated model. This is attributed to the reduced cavity depth of 90 mm used in the model. The ambient side plasterboard curves (Fds and Fds-O-Pb3-Pb4 and Pb4) recorded temperatures less than 200°C inferring the absence of insulation failure in the model irrespective of the plasterboard open-up as shown in Figure 7.21. Also, in the cavity insulated model ST-70-0.75-FI with plasterboard open-up the fire side cold flange (Fds-O-Fire-CF) is hotter than the ambient side hot flange (Fds-O-Amb-HF). This is because, in the thermal model, the plasterboard open-up was assumed to occur near the fire side studs causing the temperatures of the flanges to be higher than the ambient side studs where the plasterboard was intact. The cavity insulation entraps the heat on the fire side due to the linear arrangement within the cavity thus causing this time-temperature profile in studs.

The staggered stud model was continued with 70×0.95 mm studs. Time-temperature curves of stud and plasterboard from the non-cavity insulated model ST-70-0.95 are shown in Figure 7.22. They are similar in comparison to the results for 0.75 mm thick studs. The phenomenon of fire side cold flange in stud (Fire-CF) was hotter in comparison with ambient side hot flange (Amb-HF) irrespective of the plasterboard open-up was noticeable in the ST-70-0.95-FI.

7.3.6 Staggered stud walls with 90 mm studs

This section presents the thermal model results of staggered stud walls with 0.75 and 0.95 mm thick 90 mm deep studs with 0.75 and 0.95 mm thickness. An effective cavity depth of 150 mm was maintained in the staggered stud model. Unlike the staggered stud model with 70 mm deep studs with linear cavity insulation the staggered stud model with 90 mm deep studs had the cavity insulation staggered around the studs. Non-cavity insulated staggered stud walls with 90×0.75 mm studs and cavity insulated staggered stud wall with 90×0.95 mm studs have already been investigated using experiments (Chapter 4) and FDS thermal analysis (Chapter 5) and will not be considered in this section. The plasterboard interface time-temperature curve (Fds and Fds-O-Pb1-Pb2) exhibited a similar behaviour in the model ST-90-0.75-FI irrespective

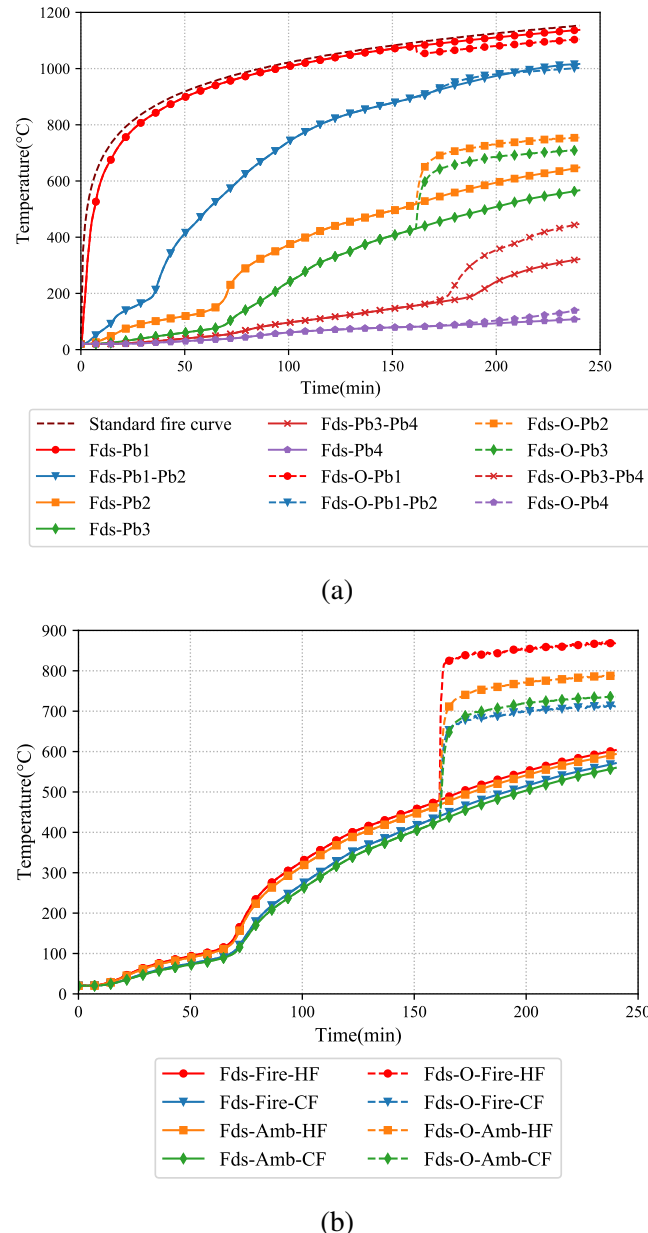


Figure 7.22: Model ST-70-0.95 - Plasterboard and stud time-temperature curves of non-cavity insulated staggered stud wall with 70×0.95 mm studs - (a) Plasterboard temperatures (b) Stud temperatures

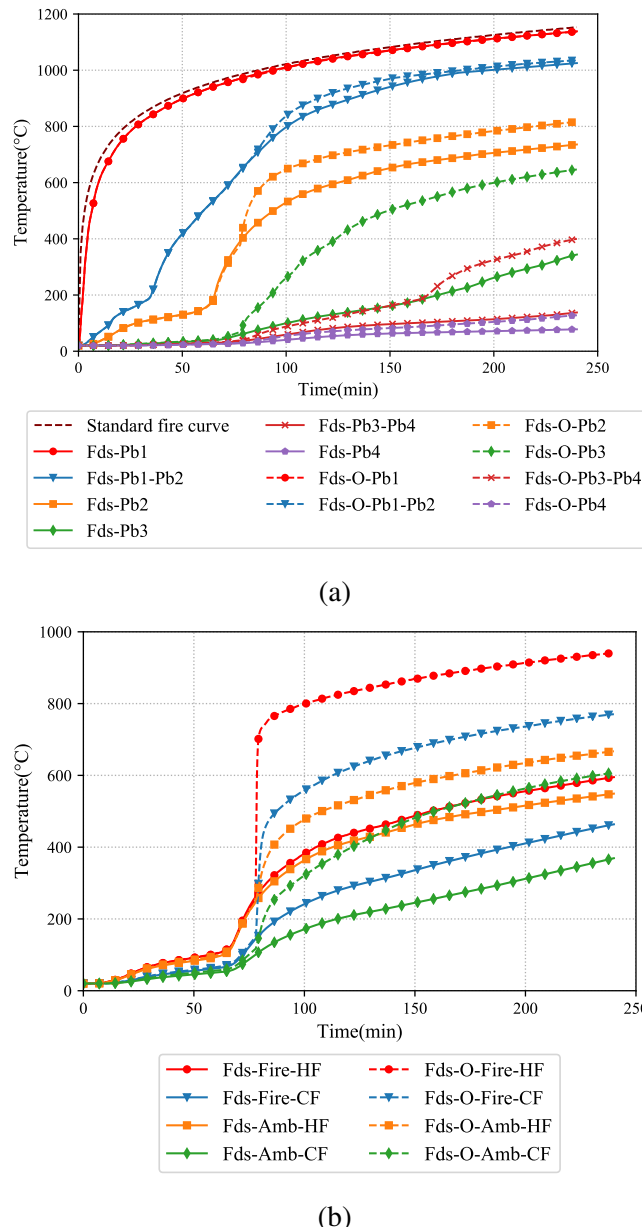


Figure 7.23: Model ST-70-0.95-FI - Plasterboard and stud time-temperature curves of cavity insulated staggered stud wall with 70 × 0.95 mm studs - (a) Plasterboard temperatures (b) Stud temperatures

of the plasterboard open-up. The fire side cavity time-temperature curve in the plasterboard open-up model exhibited a sudden increase in the curve in comparison with the other ambient side time-temperature curves. However, the ambient side plasterboard time-temperature curve was less than 200°C in both the thermal model simulation indicating the absence of insulation failure in models.

Likewise, the plasterboard time-temperature curves of the non-cavity insulated thermal model (ST-90-0.95) with 90 × 0.95 mm studs are shown in Figure 7.25 (a). The plasterboard interface time-temperature curve (Fds and Fds-O-Pb1-Pb2) was similar in both the models with and without plasterboard open-up. However, a sudden increase in the fire and ambient side cavity (Fds-O-Pb2 and Pb3) time-temperature curves were noticed in the ST-90-0.95 model considering plasterboard open-up as shown in Figure 7.25 (a). This might lead to higher temperatures on the ambient side plasterboard. However, similar to other non cavity insulated models the temperatures on the ambient side plasterboards (Fds and Fds-O-Pb) was less than 200°C inferring the absence of insulation failure in the model.

Stud time-temperature curves for the thermal model ST-90-0.75-FI is shown in Figure 7.24 (b). The fire side hot and cold flange temperatures (Fds-O-Fire-HF and CF) recorded similar temperatures in the ST-90-0.75-FI model without plasterboard open-up. The gradient in temperature between the fire side hot and cold flanges was minimal in the fire side hot and cold flanges. However, the temperature gradient was smaller in the ambient side hot and cold flanges (Fds-O-Amb-HF and CF) in the model considering the plasterboard open-up. The difference in temperatures between the stud hot and cold flanges of the fire and ambient side in the model ST-90-0.75-FI was higher in models irrespective of the plasterboard open-up. This is attributed by the glass fibre insulation staggered within the cavity entrapping the heat on the fire side of the model. This observation was noticed in all the thermal models with cavity insulation. Stud time-temperature curves for the non-cavity insulated model ST-90-0.95 is shown in Figure 7.25 (b). The observations in the stud curves are similar irrespective of the plasterboard open-up and replicated the behaviour observed in staggered stud walls with 70 mm deep studs. This includes the resemblance of the time-temperature curve pattern exhibited by all the stud flanges. However, the sudden increase in the time-temperature curve of the stud flanges was noticeable in the model with plasterboard

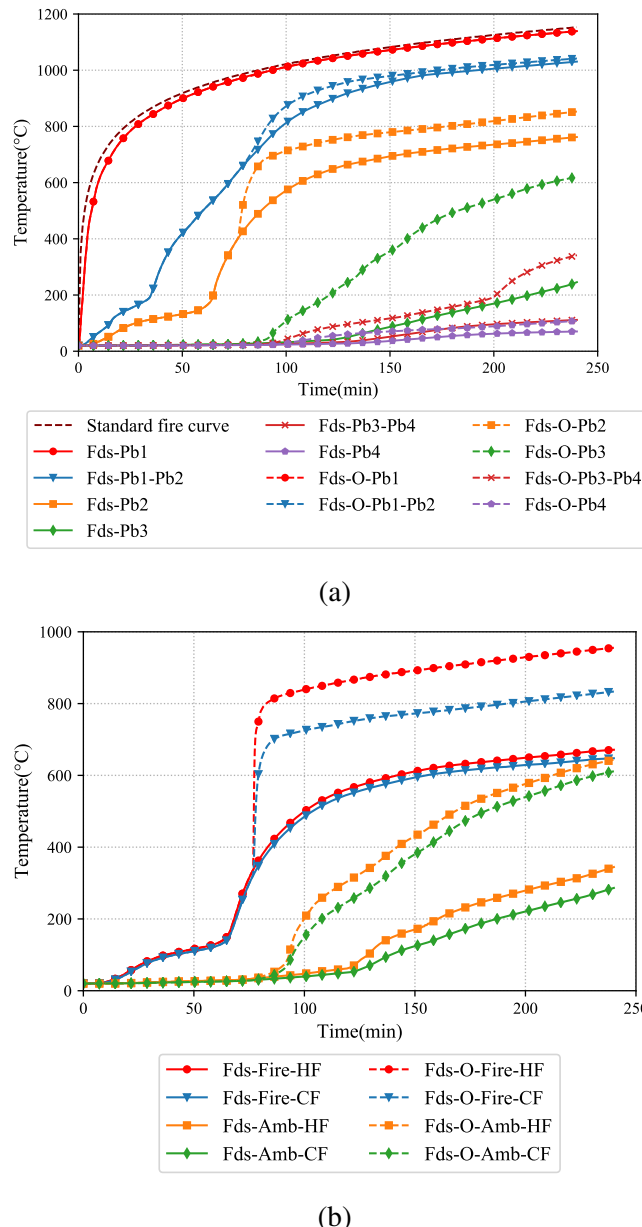


Figure 7.24: Model ST-90-0.75-FI - Plasterboard and stud time-temperature curves of cavity insulated staggered stud wall with 70×0.75 mm studs - (a) Plasterboard temperatures (b) Stud temperatures

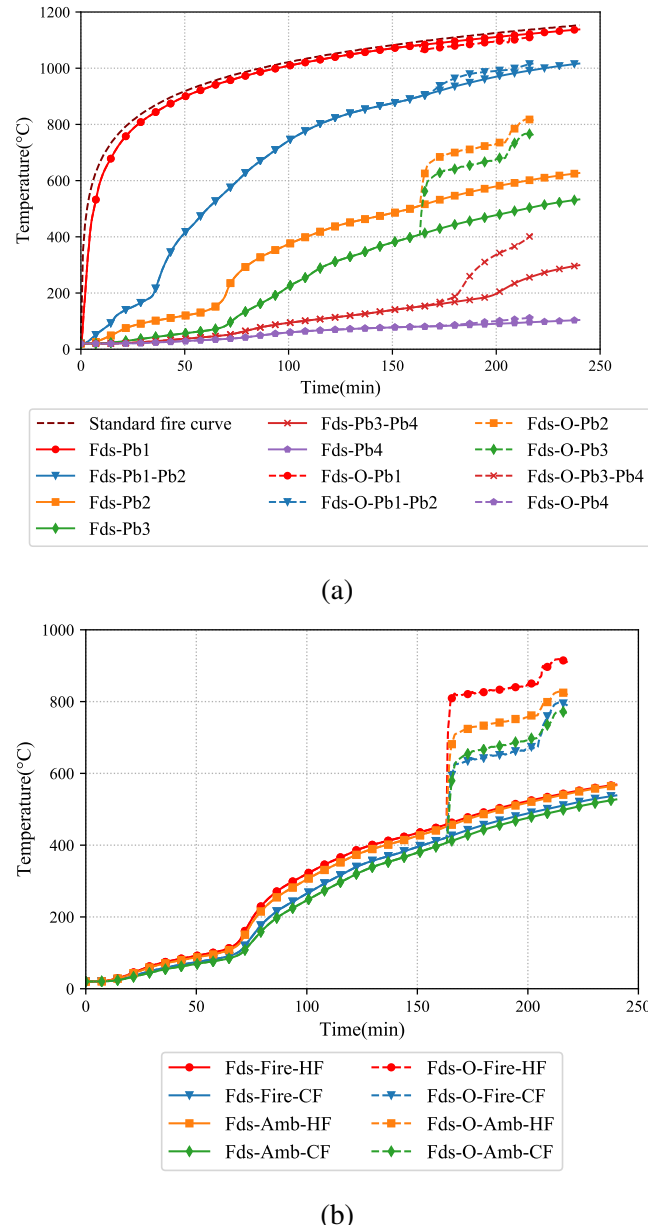


Figure 7.25: Model ST-90-0.95 - Plasterboard and stud time-temperature curves of non-cavity insulated staggered stud wall with 90×0.95 mm studs - (a) Plasterboard temperatures (b) Stud temperatures

open-up due to the direct exposure of heat on the studs.

7.4 Ambient Temperature Structural Models

To determine the failure time of the selected wall configurations, the ambient temperature axial compression capacity of the studs is needed. Therefore, based on the validated ambient capacity structural FE model in ABAQUS from Chapter 6 for the experimental investigations conducted in Chapter 3, new structural models were created and analysed for the selected wall configurations. 3D shell models were created with single stud set and the ambient temperature axial compression capacity predictions were derived. The structural FE models were created for the following wall configurations DS-70-0.75, SL-70-0.75, SL-70-0.95, SL-90-0.75, SL-90-0.95, ST-70-0.75, ST-70-0.95, ST-90-0.75 listed in Table 7.1. The applied axial compression load versus axial displacement curves from the conducted structural analyses are shown in Figure 7.26 while Table 7.2 presents the failure loads.

Amongst the selected complex LSF wall configurations, the model SL-90-0.95 gave the maximum axial compression capacity of 85.83 kN as shown in Table 7.2. This is attributed to lower the slenderness ratio of the thick 0.95 mm studs along with the effective plasterboard lateral restraints provided to both the stud flanges in the case of shaftliner LSF wall configuration. However, the staggered stud wall model with 70 × 0.95 mm studs (ST-70-0.95) resulted in the third highest axial compression capacity of 65.87 kN. Likewise the axial compression capacity of the staggered stud wall model with 70 × 0.75 mm studs (ST-70-0.75) resulted an axial capacity of 48.03 kN which is higher than the axial compression capacity of the double stud wall model DS-70-0.75. However, in the case of double stud wall effective restraints are provided on one flange of the stud. In the case of staggered stud wall effective restraints are provided on the stud flange through plasterboard and on the web service holes through omega nogging. This difference in restraint arrangement might have attributed to the superior axial compression capacity performance in staggered stud LSF walls.

To understand the behaviour of the complex LSF wall configurations further the structural FE model results of the tested walls from Chapter 6 are compared from this study. Comparison of the axial compression capacity in terms of applied axial

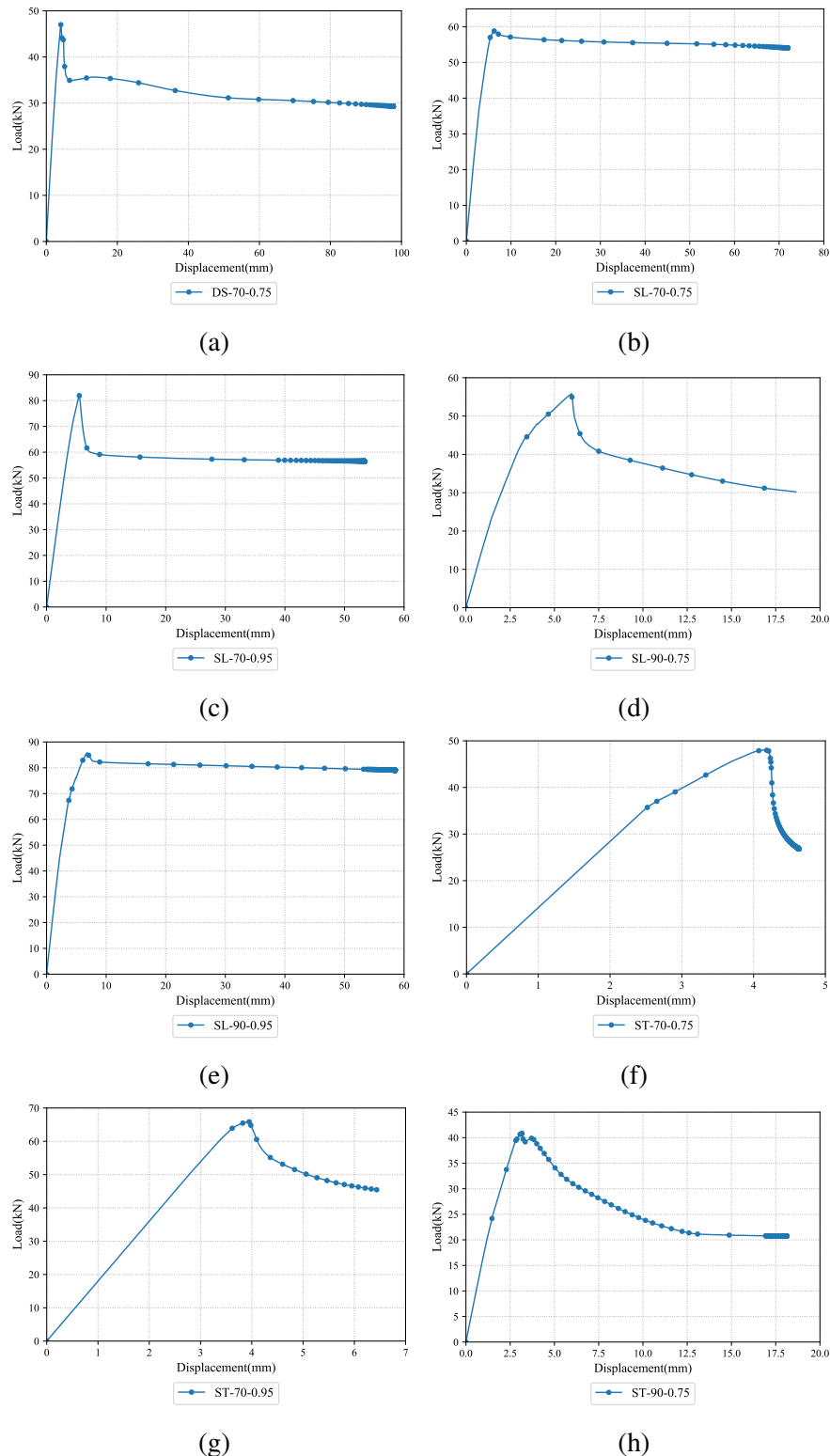


Figure 7.26: Ambient temperature axial compression capacity of complex LSF walls considered in the parametric study (a) DS-70-0.75, (b) SL-70-0.75, (c) SL-70-0.95, (d) SL-90-0.75, (e) SL-90-0.95, (f) ST-70-0.75, (g) ST-70-0.95, (h) ST-90-0.75

Table 7.2: Ambient temperature axial compression capacities from structural FE models

Model	Description	Failure Load (kN)
DS-70-0.75	Double stud - 70×0.75	47.05
DS-70-0.95	Double stud - 70×0.95 (AT4)*	71.81
DS-90-0.75	Double stud - 90×0.75 (AT2)*	46.25
DS-90-0.95	Double stud - 90×0.95 (AT1)*	71.97
SL-70-0.75	Shaftliner - 70×0.75	58.81
SL-70-0.95	Shaftliner - 70×0.95	81.97
SL-90-0.75	Shaftliner - 90×0.75	55.85
SL-90-0.95	Shaftliner - 90×0.95	85.83
ST-70-0.75	Staggered stud - 70×0.75	48.03
ST-70-0.95	Staggered stud - 70×0.95	65.87
ST-90-0.75	Staggered stud - 90×0.75	40.9
ST-90-0.95	Staggered stud - 90×0.95 (AT5)*	60.98

* FE model predictions from Chapter 6, Table 6.1

load versus axial displacement curves between the experimental model from Chapter 6 and results from the models considered for the parametric study are presented in Figure 7.27.

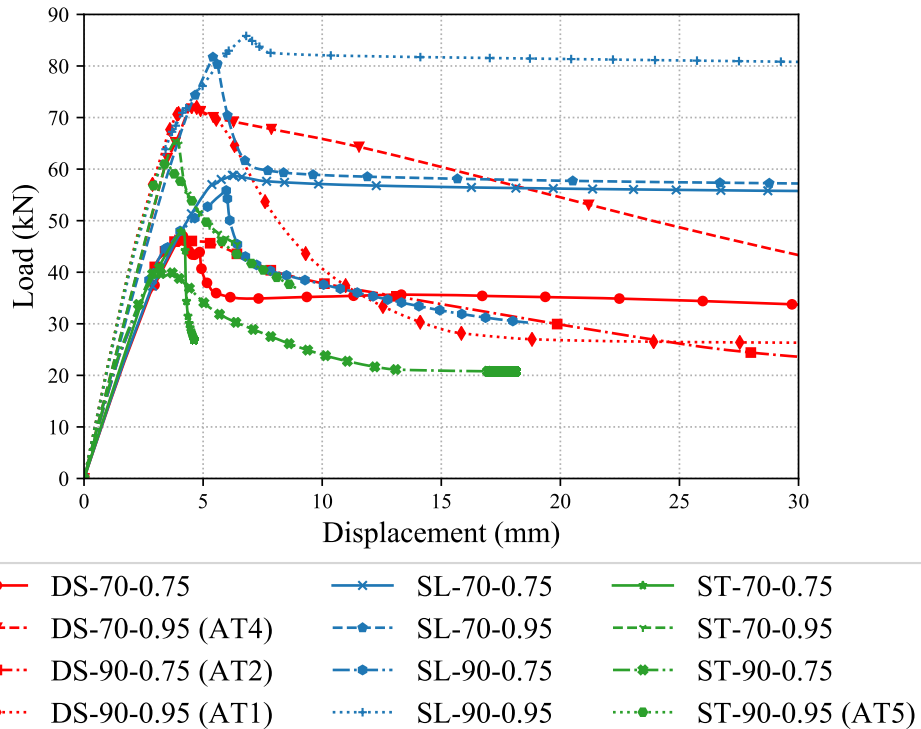


Figure 7.27: Comparison of axial compression load-displacement curves from experiment and parametric FE model

Comparison of the ambient temperature axial load carrying capacity from FE model

shows that the shaftliner model SL-90-0.95 resulted in the maximum capacity of 85.83 kN in comparison with other models. This is attributed by the lateral restraint on both the stud flanges. However, the double stud model resulted in a capacity of 71.97 kN and the staggered stud model resulted in a capacity of 60.98 kN with the same stud geometry of 90×0.95 . But in the case of complex wall configurations with 70×0.75 mm studs the staggered stud wall model ST-70-0.75 resulted a higher capacity of 48.03 kN in comparison with the double stud wall model DS-70-0.75 resulting 47.05 kN. This infers that, the staggered stud wall with 70×0.75 mm studs performs better in comparison with a similar double stud wall.

It is to note that, for a double stud wall with 70 mm deep studs the effective cavity width will be 160 mm while it is 90 mm in the case of staggered stud wall. This might result in considerable savings in the floor space in a building. Also, no wall configuration with 0.75 mm thick studs resulted in higher axial compression load in comparison with the 0.95 mm thick stud wall configurations. If the floor space in a building is considered as the governing criteria, staggered stud wall with 70×0.95 mm studs (ST-70-0.95) would be the optimal choice under load bearing condition based on the conducted parametric investigation under ambient temperature conditions. However, performance of these walls under fire conditions needs further investigation and are discussed next.

7.5 Elevated Temperature Structural Models

To determine the failure time of the selected wall configurations in the parametric study under fire conditions, sequentially coupled temperature displacement analyses were conducted under different load ratios (LRs). Typically, the design load on the LSF wall varies between 20% and 70% of the ambient temperature axial compression capacity of the wall. Therefore, the parametric study was limited to the selected LSF wall configurations under LRs in the range of 0.2 to 0.7. The ambient temperature capacities detailed in Table 7.2 were used to determine the loads corresponding to the required LR. The procedure for the coupled temperature displacement structural analysis was similar to those detailed in Section 6.5 of Chapter 6. Sequentially coupled temperature displacement analyses were conducted in ABAQUS for all the configurations listed in

Table 7.1.

7.5.1 FRL Predictions for Wall Configurations from Experimental Study

This section presents the failure time and corresponding FRL (30, 60, 90, 120, 180, 240 min) for the wall configurations considered in the experimental study in Section 4.4.1 of Chapter 4 (Table 4.1). The failure time for a load ratio in the range of 0.2 to 0.7 is presented as load ratio versus failure time curves while the corresponding FRLs are given in tables to represent the FRL in min for the structural adequacy criterion. As per the National Construction Code of Australia (ABCB (2019)) the minimum FRL required for the complex LSF walls used as internal partitions should satisfy a minimum structural adequacy criterion of 60 min in fire. Therefore, the FE models which resulted in a structural failure time of 60 min was taken for investigation irrespective of the applied load ratio and is represented as 60/-/. Likewise, models which did not satisfy this criteria were given a neutral FRL and is represented as -/-/.

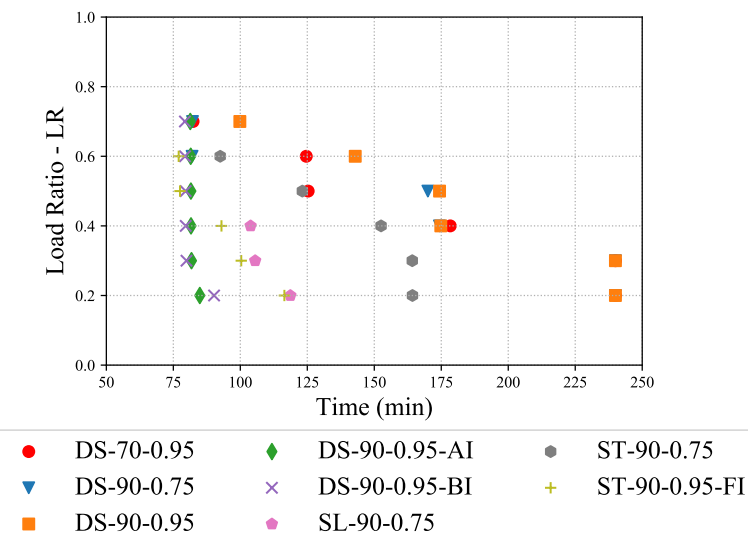


Figure 7.28: FRL of LSF wall configurations from experimental study

The failure time of the configurations considered for the experimental investigation from 0.2 to 0.7 load ratios are shown in Figure 7.28 and is also detailed in Table 7.3. The FRL of the considered wall configurations were determined by conducting sequentially coupled temperature-displacement analysis based on the stud temperatures from the FDS thermal models from Sections 5.4.3 and 5.4.4 of Chapter 5. This includes

the double stud, staggered stud and shaftliner LSF walls configurations conducted as Tests-T1 to T10.

Table 7.3: FRL predictions of 70 mm and 90 mm deep studs configuration based on experiments

Configuration	LR	Failure Time (min)	FRL
DS-70-0.95	0.2	240	240/-/-
	0.3	240	240/-/-
	0.4	178	120/-/-
	0.5	125	60/-/-
	0.6	124	90/-/-
	0.7	82	60/-/-
DS-90-0.75	0.2	240	240/-/-
	0.3	240	240/-/-
	0.4	174	120/-/-
	0.5	170	120/-/-
	0.6	82	60/-/-
	0.7	82	60/-/-
DS-90-0.95	0.2	240	240/-/-
	0.3	240	240/-/-
	0.4	174	120/-/-
	0.5	174	120/-/-
	0.6	142	120/-/-
	0.7	87	60/-/-
DS-90-0.95-AI	0.2	85	60/-/-
	0.3	81	60/-/-
	0.4	81	60/-/-
	0.5	81	60/-/-
	0.6	81	60/-/-
	0.7	81	60/-/-
DS-90-0.95-BI	0.2	90	90/-/-
	0.3	79	60/-/-
	0.4	79	60/-/-
	0.5	79	60/-/-
	0.6	79	60/-/-
	0.7	79	60/-/-
SL-90-0.75	0.2	119	90/-/-
	0.3	105	90/-/-
	0.4	104	90/-/-
	0.5	*	*
	0.6	*	*
	0.7	*	*

The FRL of the non-cavity insulated double stud walls (DS-70-095, DS-90-075 and

Table 7.3: Continued...

Configuration	LR	Failure Time (min)	FRL
ST-90-075	0.2	164.25	120/-/-
	0.3	164.18	120/-/-
	0.4	152.53	120/-/-
	0.5	123.16	120/-/-
	0.6	92.5	90/-/-
	0.7	*	*
ST-90-095-FI	0.2	116.45	90/-/-
	0.3	100.35	90/-/-
	0.4	92.97	90/-/-
	0.5	77.5	60/-/-
	0.6	77	60/-/-
	0.7	*	*

DS-90-095) resulted an FRL of 240 min up to 0.3 LR. However, the maximum FRL achieved by the cavity insulated double stud walls (DS-90-095-AI, DS-90-095-BI) was 90 min. This is in correlation with the experimental findings from Chapter 4. The non-cavity insulated shaftliner LSF wall (SL-90-075) resulted an FRL of 90 min for 0.2 to 0.4 LR. However, due to sever numerical instabilities causing convergence issues in the FE model the FRL of the shaftliner wall SL-90-075 above 0.4 LR could not be determined. But it can be inferred that the FRL beyond 0.4 LR could not be higher than 90 min based on the FRL predictions up to 90 min. The non-cavity insulated staggered stud wall configuration (ST-90-075) resulted an FRL of 120 min for LR 0.2 to 0.5. However, the FRL was reduced to 90 min for configuration ST-90-075 under 0.6 LR. The FRL of the configuration ST-90-075 under 0.7 LR could not be determined due to convergence issues with the FE model. From the non-cavity insulated wall configurations considered in this section the double stud wall with 90×0.95 mm studs (DS-90-095) performed better even under high load ratios of 0.6 LR. In the case of cavity insulated walls the staggered stud wall with 90×0.95 mm studs (ST-90-095-FI) performed better till 0.5 LR. As plasterboard open-up was considered in the thermal analysis, the stud hot flange temperatures rapidly increases at the open up time in the complex LSF wall configurations. The fire side hot flange temperatures governs the structural failure in load bearing LSF walls. Therefore, this sudden increase in the temperatures will result in similar failure times of the LSF wall irrespective of the load ratio. Further wall configurations considered in the parametric study are discussed

next.

7.5.2 FRL Predictions for Wall Configurations from Parametric Study

This section presents the FRL of all the configurations considered for the parametric study in this research. Twelve double stud wall, eight shaftliner wall and eight staggered stud wall configurations were considered for the parametric study. Each wall configuration was analysed for load ratios from 0.2 to 0.7 accounting to 168 FE structural models. The parameters included 70 and 90 mm deep studs with 0.75 and 0.95 mm thicknesses corresponding to the configurations considered in the parametric thermal analysis. This also includes non-cavity insulated and cavity insulated wall configurations.

7.5.2.1 FRL Predictions of Double Stud LSF Wall Configurations

The double stud LSF wall configurations considered for the parametric analysis are discussed in this section. Figure 7.29 shows the load ratio versus time scattered plots for the considered double stud LSF wall configurations. The FRLs of the double stud wall configurations are presented in Table 7.4.

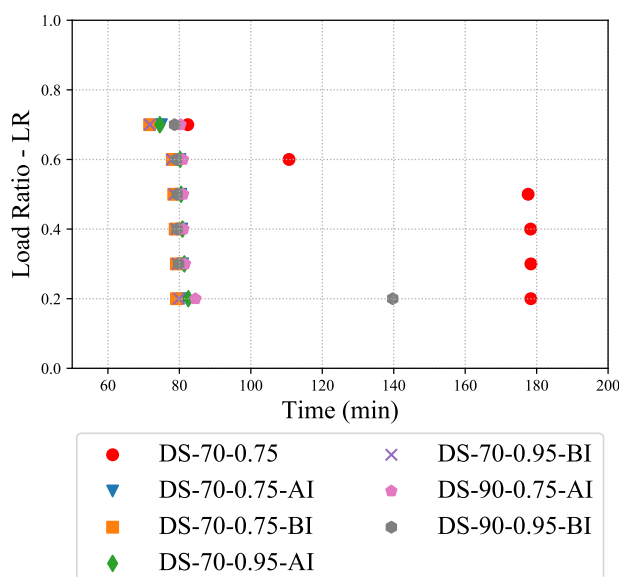


Figure 7.29: FRLs of double stud wall configurations from parametric study

Table 7.4: FRL of double stud walls with 70 mm deep studs

Configuration	LR	Failure Time (min)	FRL
DS-70-0.75	0.2	178.38	120/-/-
	0.3	178.4	120/-/-
	0.4	178.31	120/-/-
	0.5	*	*
	0.6	110.69	90/-/-
	0.7	82.36	60/-/-
DS-70-0.75-AI	0.2	80.9	60/-/-
	0.3	80.9	60/-/-
	0.4	80.65	60/-/-
	0.5	80.38	60/-/-
	0.6	80.15	60/-/-
	0.7	74.97	60/-/-
DS-70-0.75-BI	0.2	79.18	60/-/-
	0.3	79.16	60/-/-
	0.4	78.83	60/-/-
	0.5	78.43	60/-/-
	0.6	78.04	60/-/-
	0.7	71.67	60/-/-
DS-70-0.95	0.2	240	240/-/-
	0.3	240	240/-/-
	0.4	178.36	120/-/-
	0.5	125.33	120/-/-
	0.6	124.62	120/-/-
	0.7	82.37	60/-/-
DS-70-0.95-AI	0.2	82.51	60/-/-
	0.3	81.4	60/-/-
	0.4	80.87	60/-/-
	0.5	80.48	60/-/-
	0.6	80.21	60/-/-
	0.7	74.52	60/-/-
DS-70-0.95-BI	0.2	79.9	60/-/-
	0.3	79.56	60/-/-
	0.4	79.19	60/-/-
	0.5	78.64	60/-/-
	0.6	77.92	60/-/-
	0.7	71.72	60/-/-

* Model with convergence issues

The stud time-temperature curves from the thermal models of double stud wall configurations were extracted from Section 7.3.1 and coupled temperature-displacement analysis was conducted. The non-cavity insulated double stud LSF wall with 70×0.95 mm stud (DS-70-095) resulted in the highest FRL of 240 min for 0.2 and 0.3 LR. However, the same non-cavity insulated double stud wall configuration resulted in an FRL of 120 min as shown in Table 7.4. This is because of the thinner stud sections used in the model (DS-70-0.95). The model DS-70-0.75 under 0.5 LR suffered convergence issue and the corresponding FRL could not be predicted. The double stud models with cavity insulation resulted an FRL of 60 irrespective of the position of the cavity insulation in all load ratios. This is because of the heat entrapment in the fire side studs experienced by the test wall in Chapter 4 resulting in premature failure.

The FRL of double stud walls with 90 mm studs are shown in Table 7.5. Similar to the non-cavity double stud walls with 70 mm deep studs the non-cavity insulated double stud wall with 90×0.95 mm (DS-90-0.95) studs resulted in the highest FRL of 240 min for load ratios 0.2 and 0.3. The DS-90-0.95 wall could result an FRL of 120 min even under a higher LR of 0.6 while a similar configuration with 0.75 mm (DS-90-0.75) studs resulted an FRL of 60 min. The model DS-90-0.75-BI under 0.2 LR suffered convergence issues and the FRL could not be predicted. Based on the predicted FRLs it can be inferred that the thickness of the studs significantly influence the FRL of double stud LSF walls. When the applied axial load is non-dimensionalised to load ratio the effect of cavity depth do not significantly affect the FRL, however has a moderate influence on the failure time of the test wall. As the FRLs are rounded to the nearest 30 min, the influence of cavity depth on the failure time of the double stud LSF walls can be neglected.

7.5.2.2 FRL Predictions of Shaftliner LSF Wall Configurations

FRLs predictions of the shaftliner LSF walls considered for the parametric analysis are presented in this section. Figure 7.30 shows the load ratio versus failure time scattered plots. The shaftliner walls were also modelled with 70 and 90 mm deep studs with 0.75 and 0.95 thickness. In the case of cavity insulated shaftliner walls, the cavity insulation was positioned throughout the cavity. The model with ambient side cavity insulation was not considered for investigation. This is because from the experimental

Table 7.5: FRLs of double stud walls with 90 mm deep studs

Configuration	LR	Failure Time (min)	FRL
DS-90-0.75	0.2	240	240/-/-
	0.3	240	240/-/-
	0.4	174.32	120/-/-
	0.5	170	120/-/-
	0.6	82	60/-/-
	0.7	82	60/-/-
DS-90-0.75-AI	0.2	84.5	60/-/-
	0.3	81.58	60/-/-
	0.4	81.15	60/-/-
	0.5	81.07	60/-/-
	0.6	81	60/-/-
	0.7	80.33	60/-/-
DS-90-0.75-BI	0.2	*	*
	0.3	79.79	60/-/-
	0.4	79.35	60/-/-
	0.5	79.34	60/-/-
	0.6	79.16	60/-/-
	0.7	78.66	60/-/-
DS-90-0.95	0.2	240	240/-/-
	0.3	240	240/-/-
	0.4	174.83	120/-/-
	0.5	174.36	120/-/-
	0.6	142.89	120/-/-
	0.7	87.33	60/-/-
DS-90-0.95-AI	0.2	84.88	60/-/-
	0.3	81.78	60/-/-
	0.4	81.6	60/-/-
	0.5	81.56	60/-/-
	0.6	81.49	60/-/-
	0.7	81.33	60/-/-
DS-90-0.95-BI	0.2	90.21	90/-/-
	0.3	79.91	60/-/-
	0.4	79.63	60/-/-
	0.5	79.61	60/-/-
	0.6	79.36	60/-/-
	0.7	79.33	60/-/-

* Model with convergence issues

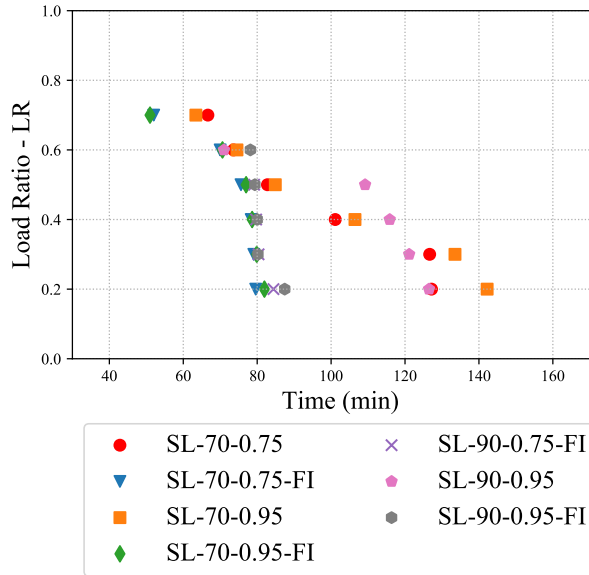


Figure 7.30: FRLs of shaftliner wall configurations from parametric study

Table 7.6: FRL of shaftliner walls with 70 mm deep studs

Configuration	LR	Failure Time (min)	FRL
SL-70-0.75	0.2	127.17	120/-/-
	0.3	126.67	120/-/-
	0.4	101.12	90/-/-
	0.5	82.78	60/-/-
	0.6	73.6	60/-/-
	0.7	66.66	60/-/-
SL-70-0.75-FI	0.2	79.6	60/-/-
	0.3	79.09	60/-/-
	0.4	78.38	60/-/-
	0.5	75.62	60/-/-
	0.6	69.98	60/-/-
	0.7	52	-
SL-70-0.95	0.2	142.22	120/-/-
	0.3	133.52	120/-/-
	0.4	106.46	90/-/-
	0.5	84.9	60/-/-
	0.6	74.53	60/-/-
	0.7	63.41	60/-/-
SL-70-0.95-FI	0.2	81.96	60/-/-
	0.3	79.88	60/-/-
	0.4	78.64	60/-/-
	0.5	77	60/-/-
	0.6	70.61	60/-/-
	0.7	51	-

investigations conducted in Chapter 4 it was found that the position of cavity insulation did not significantly influence the thermal behaviour as the heat entrapment occurred in the walls with ambient side cavity insulation also. This was evident in the FDS thermal models investigated in Section 7.3 of this chapter.

Table 7.7: FRLs of shaftliner walls with 90 mm deep studs

Configuration	LR	Failure Time (min)	FRL
SL-90-0.75	0.2	118.68	90/-/-
	0.3	105.55	90/-/-
	0.4	103.84	90/-/-
	0.5	*	*
	0.6	*	*
	0.7	*	*
	0.2	84.4	60/-/-
SL-90-0.75-FI	0.3	80.37	60/-/-
	0.4	79.71	60/-/-
	0.5	79.16	60/-/-
	0.6	*	*
	0.7	*	*
	0.2	126.5	120/-/-
	0.3	121.12	120/-/-
SL-90-0.95	0.4	115.86	90/-/-
	0.5	109.2	90/-/-
	0.6	71	60/-/-
	0.7	*	*
	0.2	87.44	60/-/-
	0.3	80.2	60/-/-
	0.4	80	60/-/-
SL-90-0.95-FI	0.5	79.36	60/-/-
	0.6	78.16	60/-/-
	0.7	*	*

* Model with convergence issues

FRLs from shaftliner LSF walls with 70×0.75 and 0.95 studs are shown in Table 7.6. Despite separating the cavity into two with the middle plasterboard layer the 70 mm deep shaftliner walls with 0.75 mm and 0.95 mm thick studs could not result an FRL of 240 min under any load ratio. This is attributed by the plasterboard open-up which acts as a critical influencing factor in the stud time-temperature curves which greatly influences the FRL. Due to the presence of middle plasterboard layer, there arises very less cooling affect within the cavity and the stud temperatures are more in comparison with the double stud walls. Despite having plasterboard restraints on

both the stud flanges, due to the high temperatures on the stud hot and cold flanges, the shaftliner LSF walls could not perform better in comparison with the double stud walls with 70 mm deep studs. From this it is inferred that the contact between the stud flanges and the plasterboard influences the stud time-temperature curves, thereby affecting the FRL. In the case of cavity insulated walls the heat entrapment was more in comparison with double stud LSF walls with both cavity insulated. This results in a larger temperature gradient between the stud hot and cold flanges. This had attributed to the early failure times resulting in lower FRLs in cavity insulated shaftliner LSF walls.

FRLs of Shaftliner LSF walls with 90 mm \times 0.75 and 0.95 studs are presented in Table 7.7. Due to sever non-linearity resulting in convergence issues some of the FRLs of shaftliner wall with 90 mm deep studs could not be determined and are also shown in Table 7.7. Similar to shaftliner LSF walls with 70 mm deep studs, the shaftliner liner LSF walls with 90 mm deep studs could not result an FRL of 240 min for any load ratio irrespective of the thickness of the studs. Also, the maximum FRL achieved by the 90 mm deep shaftliner LSF walls was 120 min from shaftliner wall model with 90 \times 0.95 mm stud (SL-90-095) under 0.2 and 0.3 LR. This was lower than 120 min from the shaftliner LSF walls with 70 mm studs. This is attributed to the slenderness of the studs and partly due to the heat entrapment on the fire side cavity causing the stud hot flanges to absorb more heat in comparison with the other flanges, thereby resulting in large temperature gradient. The larger temperature gradients have significant influence of the FRLs under load bearing conditions.

7.5.2.3 FRL Predictions of Staggered Stud LSF Wall Configurations

Parametric study conducted on staggered stud LSF wall models are discussed in this section. The load ratio versus failure time scattered plots for all the considered staggered stud wall configuration is shown in Figure 7.31. Table 7.8 presents the details of FRLs of staggered stud LSF wall conducted on 70 mm \times 0.75 and 0.95 mm studs. The maximum FRL achieved by the staggered stud LSF walls with 70 mm deep studs was 120 min. This is attributed to the lateral restraint conditions provided to the studs in the model. As discussed earlier in Chapter 6 the staggered stud wall studs are effectively restrained on one flange.

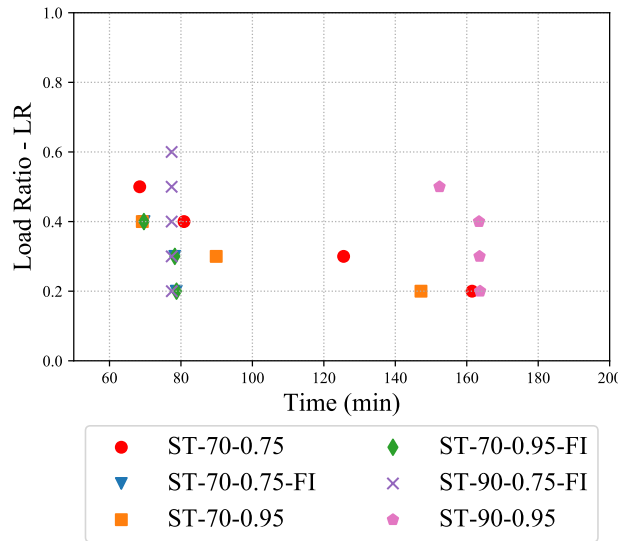


Figure 7.31: FRL of staggered stud wall configurations from parametric study

Table 7.8: FRLs of staggered stud walls with 70 mm deep studs

Configuration	LR	Failure Time (min)	FRL
ST-70-0.75	0.2	161.49	120/-/-
	0.3	125.53	120/-/-
	0.4	80.86	60/-/-
	0.5	68.46	60/-/-
	0.6	19.6	-
	0.7	-	-
ST-70-0.75-FI	0.2	78.69	60/-/-
	0.3	78.28	60/-/-
	0.4	69.67	60/-/-
	0.5	44.44	-
	0.6	15.54	-
	0.7	0.8274	-
ST-70-0.95	0.2	147.19	120/-/-
	0.3	89.87	60/-/-
	0.4	69.18	60/-/-
	0.5	17.16	-
	0.6	-	-
	0.7	-	-
ST-70-0.95-FI	0.2	78.76	60/-/-
	0.3	78.29	60/-/-
	0.4	69.63	60/-/-
	0.5	33.18	-
	0.6	12.91	-
	0.7	-	-

Table 7.9: FRLs of staggered stud walls with 90 mm deep studs

Configuration	LR	Failure Time (min)	FRL
ST-90-0.75	0.2	164.25	120/-/-
	0.3	164.18	120/-/-
	0.4	152.53	120/-/-
	0.5	123.16	120/-/-
	0.6	92.5	90/-/-
	0.7	*	*
ST-90-0.75-FI	0.2	77.45	60/-/-
	0.3	77.41	60/-/-
	0.4	77.41	60/-/-
	0.5	77.4	60/-/-
	0.6	77.4	60/-/-
	0.7	*	*
ST-90-0.95	0.2	163.73	120/-/-
	0.3	163.58	120/-/-
	0.4	163.43	120/-/-
	0.5	152.38	120/-/-
	0.6	*	*
	0.7	*	*

* Model with convergence issues

The staggered restraints provided on the stud flanges results in reduction in the axial load carrying capacities under ambient and fire conditions. This results in reduced failure times under load bearing conditions under fire. The cavity insulated staggered stud LSF walls resulted an FRL of 60 min irrespective of the stud thickness. However, this 60 min FRL was corresponding to LR of 0.2 to 0.4 after which the models resulted in FRLs less than 60 min as shown in Table 7.8. This is attributed to the heat entrapment on the fire side studs similar to that of double stud and shaftliner LSF walls. It is to be noted that in shaftliner walls with 70 mm deep studs the FDS models was conducted by considering linear cavity insulation arrangement as staggering the cavity insulation was practically not feasible considering the 90 mm effective cavity width. As 75 mm thick glass fibre cavity insulation was considered in the model the 90 mm cavity was not suitable to stagger the insulation within the cavity. However, this did not change the heat entrapment issue in cavity insulated walls, thereby resulting in reduced FRL.

The FRLs corresponding to staggered stud LSF walls with 90×0.75 and 0.95 mm studs are shown in Table 7.9. The maximum FRL from the non-cavity insulated

staggered stud models ST-90-0.75 and 0.95 was 120 min for LRs from 0.2 to 0.5. This was equivalent to non-cavity insulated double stud LSF walls. The FRLs of the non-cavity insulated staggered stud LSF walls with 90×0.75 and 0.95 mm studs were higher in comparison with shaftliner LSF walls. This infers that the air gap between the stud rows significantly influences the FRL of complex LSF walls under load bearing conditions. All the models suffered numerical instabilities causing convergence issues at 0.7 LR and the corresponding FRLs could not be determined. However, all the staggered models with 90 mm studs resulted a minimum FRL of 60 min.

7.6 Summary and Conclusions

This chapter presents the results from the conducted parametric study. Firstly, FDS thermal analyses were conducted to determine the time-temperature profiles of the selected complex LSF wall configurations apart from those considered in the experimental and thermal FDS investigations reported in Chapters 4 and 6. The structural response of these complex wall configurations, double stud, shaftliner and staggered stud wall systems, were determined under ambient temperature conditions and their corresponding axial compression capacities were determined. These were then used to determine the failure times using sequentially coupled temperature displacement structural analyses under 0.2 to 0.7 LR. The failure times and the FRLs of the complex LSF wall configurations were determined from the conducted parametric study. Following conclusions can be drawn from the conducted parametric study.

- Effective cavity depth of the LSF wall models had significant influence on the plasterboard time-temperature curves thereby reflecting in the stud hot and cold flange time-temperature curves.
- The stud thickness had less influence on the time-temperature profiles of the complex LSF wall systems. But, the presence of cavity insulation significantly influenced the stud time-temperature profiles. The temperature gradients of the stud were higher in the cavity insulated wall models. However, the difference in stud flange temperatures were less in staggered stud walls.
- The effect of plasterboard open-up could be successfully simulated by the devel-

oped FDS thermal model, but further investigation is required to determine the appropriate set-point temperatures to initiate the open-up in different wall configurations. This can further be extended to investigate the difference in opening at different places on the model by developing a full-scale FDS thermal model but was beyond the scope of this research.

- The absence of contact between the stud rows in the case of double and staggered stud walls and the contact between studs and plasterboard in shaftliner LSF walls was found to have significant influence on the time-temperature profiles of the stud and plasterboard. The presence of discontinuous stud arrangement resulted in cooler hot and cold flange temperatures. This cooling effect or the plateau region was not noticed in the shaftliner LSF walls configurations.
- The ambient temperature structural models using 3D shell elements was able to predict the axial compression capacities of all the considered complex LSF wall configurations. However, the sequentially coupled temperature displacement models exhibited convergence issues in many cases. The stabilization parameters considered in the models were based on trial and error method and did not tend to best fit the problem and needs further investigation.

[This page is intentionally left blank]

Chapter 8

Conclusions

8.1 Summary

Complex LSF wall systems are an integral part of cold-formed steel construction, which includes the double stud, shaftliner and staggered stud LSF wall systems. However, past research studies conducted throughout the globe have always been limited to the investigation of conventional single stud LSF wall systems. Although, extensive research has been conducted on single stud LSF walls systems, there has been very limited research data available on the above-mentioned complex LSF wall systems. Therefore, this research investigated the fire performance of the complex LSF wall systems through experimental and numerical studies. Their fire resistance levels (FRL) were determined based on full-scale fire tests and advanced numerical analysis, thereby facilitating the usage of these complex LSF walls in cold-formed steel construction. In particular, the staggered stud wall systems which were preferably used under non-load bearing conditions, were tested under full-scale load bearing conditions with omega noggings and end cleat connections, to enable their use as load bearing walls. Numerical thermal models were developed using a CFD program, FDS, in predicting the thermal behaviour of the complex LSF wall systems in fire. The sequentially coupled-temperature displacement structural FE models were then developed and used to predict the failure times of these LSF wall systems by incorporating the time-temperature inputs from the FDS thermal analysis. This research has yielded important experimental and numerical results, which can be used by engineers and designers in safely and cost-effectively designing the three types of complex LSF wall

systems for various applications using cold-formed steel construction.

8.2 Research Outcomes

The aim of this research were detailed in Section 1.5 of Chapter 1. The aims achieved as the outcome of this research are detailed next.

8.2.1 Selection of Complex LSF wall Systems

Conducting full-scale fire tests are cumbersome, time-consuming and expensive. Therefore, the initial literature review conducted in Chapter 2 not only investigated the research studies conducted on the fire performance of LSF wall systems but also investigated the availability and suitability of the most commonly used complex LSF walls systems. The ground work conducted as a part of this research included leading expert opinions in the cold-formed steel industry in Australia and research consideration of the wall configurations were narrowed down to double stud, shaftliner and staggered stud LSF wall systems. As determination of fire performance was the motto of this research fire rated plasterboards were only used for this research. Also, the steel stud sections used for this research were locally procured to better understand the behaviour of the LSF walls currently used in the cold-formed steel industry. Unlike past research in which the steel stud sections were folded in-house through press break, the studs used in this research were procured from a roll-form manufacturer. This ensured the frames used for experimental investigations were precise to the nearest mm. Also the pre-punch holes in the studs and tracks for screw fastening facilitated easier assembly of the wall frame during construction of the test wall.

8.2.2 Ambient Temperature Structural Performance of Complex LSF Walls

- Full-scale ambient temperature axial compression capacity tests were conducted on double stud and staggered stud LSF wall systems. The behaviour of the studs under axial compression and the ultimate compression capacities of the test wall were determined. Local buckling of studs were the predominant failure mode in

both the LSF wall configurations.

- The effective plasterboard restraints provided to the studs in combination with the nogging restraints were capable to provide the required lateral restraints to the stud preventing minor axis (in-plane) buckling in the test wall. In the case of staggered stud LSF wall system, the provision of omega nogging along with the end cleats facilitated the staggered stud wall system to withstand axial compression load similar to a double stud LSF wall system, making them suitable for load bearing applications under fire.
- Experimental investigations revealed that strengthening the edge studs in a test wall was necessary to avoid bearing failures and to accurately determine the axial compression capacity of the test wall. Nesting the edge studs was found to be the better alternative under ambient capacity tests.
- Axial compression capacity predictions using the new AS 4600 design equations based on Direct Strength Method (DSM), was able to predict the capacities of the test wall with reasonable accuracy.

8.2.3 Fire Performance of Complex LSF Walls

Ten full-scale fire tests on complex LSF walls were conducted for this research. Detailed analyses of the fire test results of double stud walls were undertaken by comparing them against the fire test results of conventional single stud LSF walls. The differences in heat transfer mechanism between the single and double stud walls were clearly identified. Following conclusions are drawn from the conducted full-scale fire tests.

- The combined presence of wider cavity and discontinuous stud rows was identified as the reason for the observed delayed heat transfer mechanism in double stud walls. Comparison with a single stud wall of wider cavity proves that the existence of wider cavity alone does not influence the delayed heat transfer mechanism. The presence of a discontinuous stud arrangement is the main contributor to the delayed heat transfer.

- The presence of thinner studs did not affect the unique heat transfer mechanism in double stud walls as the plateau region in the time-temperature curve was clearly visible in non-cavity insulated double stud wall fire tests.
- Comparison of the time-temperature curves of double stud walls under different load ratios showed that the heat transfer mechanism was unaffected by the higher load ratio.
- Despite the difference in lateral restraints to the studs due to the discontinuous rows of studs, the fire test results showed that the failure time of double stud walls was higher than that of similar single stud walls under the same load ratio. This shows that the discontinuous stud arrangement does not affect the structural performance of double stud walls in fire.

The conducted fire tests also included two full-scale fire tests on non-load bearing LSF walls with varying cavity depth. Shaftliner and staggered stud LSF walls with varying cavity depth were also tested under non-load bearing conditions. The following specific conclusions are discussed next.

- Increasing the cavity depth of LSF walls improved the fire performance significantly.
- The temperature distribution across the wall depth decreased with increasing cavity depth. This is due to the presence of air movement within the wider cavity resulting in natural convection. Radiation from the plasterboards and studs into the cavity also contributed to this behaviour. This is evident from the unique plateau region observed in the plasterboard time-temperature curves of staggered stud wall. This plateau region is also due to the discontinuous stud arrangement in staggered stud wall. However, this was not experienced in shaftliner wall as the effective cavity depth was 90 mm. Continuous stud arrangement with a middle plasterboard layer was identified as the reason behind the absence of plateau region in the time-temperature curves of shaftliner wall tested in this study.
- Regardless of the cavity depth, plasterboard fall-off also significantly governed the fire resistance of single plasterboard lined walls as it exposed the thin-walled

steel studs and the remaining plasterboard layers to higher temperatures.

- In LSF walls with double plasterboard linings, plasterboard fall-off did not significantly affect the fire resistance. The calcination process of the fire side plasterboards was delayed in this situation thereby resulting in lower temperature gradient across the wall depth. The lower ambient side temperatures allowed the ambient side plasterboards to remain intact till the end of the fire test.
- In the staggered stud wall fire test, the absence of lateral restraints to both flanges of the studs resulted in the structural failure of studs, whereas in the shaftliner wall fire test with a middle plasterboard layer, the presence of effective plasterboard restraints increased the fire resistance. These results show the importance of plasterboard restraints to both flanges of the thin-walled steel studs in LSF walls.
- Although increasing the cavity depth resulted in higher fire resistance, splitting the cavity of shaftliner LSF wall with a middle plasterboard layer was found to be more beneficial in terms of fire resistance. In the fire test of shaftliner LSF wall, lower ambient side temperatures were observed in comparison with the fire test of staggered stud LSF wall. Shaftliner wall arrangement can eliminate the structural inadequacy failures of steel studs and provide higher fire resistance under non-load bearing conditions.
- As the unique thermal behaviour of the double stud, shaftliner and staggered stud walls are adequately identified including their overall fire performance, these walls can be used in the construction industry where single stud LSF walls could not satisfy the FRL and acoustic requirements.
- The fire test data from this research were also used to develop and validate numerical models to predict the fire performance of double stud LSF walls.

Considering the importance of cavity insulation in LSF walls for sound insulation, this research study has also investigated the response of cavity insulated double stud and staggered stud LSF walls in fire. Three full-scale fire tests out of the ten were conducted with cavity insulation for this research study and valuable time-temperature

data for the cavity insulated double and staggered stud LSF walls were determined. The corresponding conclusions are discussed next.

- Despite the presence of wider cavity depth in double stud LSF walls, the presence of cavity insulation entraps the heat on the fire exposed side of the double stud LSF wall. This causes the heat to accumulate on the fire side sides only, thereby increasing the corresponding hot flange temperatures significantly. This is a detrimental effect if the cavity insulation is provided on both the studs rows in double stud wall Tests-T5 and T6.
- In Test-T7 the cavity insulation was provided in the ambient stud rows only to allow the heat within the cavity thereby moving the cavity insulation away from the fire exposed side. However, this did not provide beneficial results as the heat was still entrapped on the fire side studs thereby resulting in a similar time-temperature profile in comparison with Tests-T5 and T6.
- Comparison with a non-cavity insulated LSF wall revealed that the plateau region in the time-temperature curves on the plasterboard and studs are not evident in the cavity insulated LSF walls. The constructive effect provided by the discontinuous stud arrangement and the wider cavity did not result in delayed heat transfer mechanism experienced in non-cavity insulated double stud LSF walls.
- Plasterboard open up in the fire tests of cavity insulated double and staggered stud LSF walls was found to be the major contributor in sudden temperature increase of the studs under load bearing conditions. Also, the additional pressure developed within the cavity due to the temperature entrapment may have influenced the plasterboard open up and needs further detailed investigation.
- Buckling of the fire side row studs was observed in the cavity insulated staggered stud wall Test-T10 further affirming the claim of heat entrapment in cavity insulated complex LSF walls. This shows that the heat entrapment is a major contributor in premature failure of the steel studs irrespective of the wall configuration in complex LSF walls and needs further investigation.

8.2.4 Thermal modelling of Complex LSF Walls

- Detailed investigations were conducted to develop suitable thermal numerical models and to investigate the fire performance of the complex LSF wall configurations.
- Initial investigation on the developed thermal models in SAFIR software package resulted in conservative time-temperature predictions of the conducted full-scale fire test.
- Attempts were then made to develop the thermal models in ABAQUS. Comparison of the thermal model results from ABAQUS with the conducted full-scale fire test on double stud LSF wall did not agree well. The plasterboard time-temperatures curves agreed reasonably well in all fire tests up to a certain time period. However, the stud time-temperature curves in double stud walls did not agree with the available experimental results. The cause was identified as the effect of natural convection within the cavity, and the same could not be simulated in the existing ABAQUS thermal model.
- Even though the thermal models in ABAQUS were validated for single stud walls, the same could not be used for double stud walls. This clearly showed that the assumption of only the radiation heat transfer within the cavity to be the dominant mode of heat transfer does not hold good for double stud LSF walls.
- Finally, thermal models using FDS were developed to predict the thermal response of these LSF walls in fire. This included the effects of convection within the cavity and was able to predict the time-temperature curves of the conducted full-scale fire tests with good agreement.
- Obstruction removal technique at specified setpoint temperature was employed to simulate the plasterboard open up on the fire exposed side through which the sudden rise in the time-temperature curve experienced in some fire tests could be simulated with reasonable accuracy. However, the setpoint temperatures were extracted from past research study and needs further investigation to determine the suitability in other complex LSF wall configurations.

- The thermal model results from the developed FDS thermal models were then used in structural FE models to predict the failure times of the tested and other similar double stud, shaftliner and staggered stud LSF walls configurations.

8.2.5 Structural modelling of Complex LSF Walls

- Structural models developed initially in ABAQUS to predict the ambient temperature capacity tests resulted in good agreement in regards to the ultimate failure load predictions. The buckling modes of the studs from the ambient temperature capacity test walls were also simulated with good agreement.
- Based on the developed ambient temperature capacity models, sequentially coupled thermal-structural analysis was carried out using ABAQUS by importing the temperatures from the FDS thermal analysis. Through this, the structural response of the steel studs in LSF walls exposed to fire were simulated. The failure times of all the walls configurations considered for the experimental investigation were predicted with good agreement through the developed structural models. Considering the plasterboard open up in the thermal analysis has resulted in increased hot flange temperatures causing premature structural failure in comparison with non-cavity insulated double stud LSF walls. Irrespective to the position in LSF wall, cavity insulation causes detrimental effects on the fire performance of cavity insulated double stud LSF walls.
- However, the developed sequentially coupled temperature displacement model suffered convergence issue in many cases and the failure modes of the studs could not be simulated well. This was attributed to the dissipated energy factor in the analysis and determining the same for every model was challenging. Further investigation on this might solve the convergence issues with the developed structural model.

8.3 Future Research and Recommendations

This research has presented with valuable results from the full-scale fire tests on complex LSF walls. Also, the developed numerical models to predict the thermal and

structural performance of the complex LSF walls exhibited good agreement in most cases. However, based on the current research findings and limitations, following recommendations are worthwhile for further investigation in future.

- Although full-scale fire tests are expensive and time-consuming, these are inevitable in determining the fire performance of new LSF wall configurations. For instance, the staggered stud LSF walls with different stud spacing and arrangement is worth investigating to arrive at the optimal staggered stud wall configuration. This also holds true for double stud LSF walls.
- Fire test on shaftliner LSF walls was conducted under non-load bearing conditions in this research due to the limitations in the experimental set-up. Conducting full-scale fire tests on the shaftliner LSF wall with a C-H stud instead of conventional lipped channel section (LCS) under load bearing conditions can improve the understanding on the fire performance of shaftliner LSF walls.
- The developed FDS thermal model was small-scale in nature and the plasterboard open-up was considering by removing a portion of the obstruction. However, this approach can be conservative in some cases, especially in LSF walls where the open-up and fall-off of plasterboard is minimal. Furthermore, models to simulate joint open ups near studs in particular may improve the predictions rather than partial obstruction removal.
- FDS may be considered as an alternative to predict the thermal behaviour of LSF walls by considering all the modes of heat transfer, but the results from the thermal models are not visually pleasing and easy to understand. Creating thermal models using other commercially available computational fluid dynamics (CFD) software packages may deemed worthwhile considering the present limitations.
- The structural shell modelling with sequentially coupled temperature displacement analysis technique is considered as the best fit to determine the structural behaviour of LSF walls under fire. However, in full-scale fire tests the problem statement is fully coupled. A robust fully-coupled model may be considered as an alternative but may not be the optimal solution in all circumstances considering the computational efficiency of the fully-coupled models.

- The DSM predictions were limited to the ambient temperature axial capacities in this research. This can be extended to determine the failure times under fire conditions and also investigate the suitability of the existing design equations for different LSF wall configurations.

Appendix A

FDS code

FDS code representing a typical double stud LSF wall model is shown below.

```
.....  
  
&HEAD CHID='r0', TITLE='double stud wall'  
&TIME T_END=14400/  
  
&DUMP RENDER_FILE='r0.ge1', COLUMN_DUMP_LIMIT=.TRUE., DT_RESTART=300.0,  
DT_SL3D=0.25/  
  
!&MESH ID='cube', IJK=15,19,13, XB=0.0,0.232,-0.016,0.28,0.0,0.2/  
  
&OBST ID='fire', XB=0,0.232,0,0,0,0.2, SURF_ID='ADIABATIC GYPSUM_FIRE'/  
&OBST ID='amb', XB=0,0.232,0.264,0.264,0,0.2, SURF_ID='ADIABATIC  
GYPSUM_AMB'/  
&OBST ID='lip-fhf', XB=0.1335,0.1335,0.0320,0.0390,0,0.2 , SURF_ID='  
ADIABATIC STEEL' /  
&OBST ID='flange-fhf', XB=0.0985,0.1335,0.032,0.032,0,0.2 , SURF_ID='  
ADIABATIC STEEL' /  
&OBST ID='web-fhf', XB=0.0985,0.0985,0.032,0.122,0,0.2 , SURF_ID='  
ADIABATIC STEEL' /  
&OBST ID='flange-fcf', XB=0.0985,0.1335,0.122,0.122,0,0.2 , SURF_ID='  
ADIABATIC STEEL' /  
&OBST ID='lip-fcf', XB=0.1335,0.1335,0.1150,0.1220,0,0.2 , SURF_ID='
```

```
ADIABATIC STEEL' /
&OBST ID='lip-ahf', XB=0.1335,0.1335,0.1420,0.1490,0,0.2 , SURF_ID='
ADIABATIC STEEL' /
&OBST ID='flange-ahf', XB=0.0985,0.1335,0.1420,0.1420,0,0.2 , SURF_ID='
ADIABATIC STEEL' /
&OBST ID='web-ahf', XB=0.0985,0.0985,0.1420,0.2320,0,0.2 , SURF_ID='
ADIABATIC STEEL' /
&OBST ID='flange-acf', XB=0.0985,0.1335,0.2320,0.2320,0,0.2 , SURF_ID='
ADIABATIC STEEL' /
&OBST ID='lip-acf', XB=0.1335,0.1335,0.2250,0.2320,0,0.2 , SURF_ID='
ADIABATIC STEEL' /
```



```
!&MISC SOLID_PHASE_ONLY=TRUE/
&MISC THICKEN_OBSTRUCTIONS=.TRUE./
&RADI RADIATION=TRUE/
```



```
&DEVC XYZ = 0.048,0,0.1, IOR = 2, ID='Pb1', QUANTITY = 'INSIDE WALL
TEMPERATURE', DEPTH=0.001 /
&DEVC XYZ = 0.048,0,0.1, IOR = 2, ID='Pb1-Pb2', QUANTITY = 'INSIDE WALL
TEMPERATURE', DEPTH=0.016 /
&DEVC XYZ = 0.048,0,0.1, IOR = 2, ID='Pb2', QUANTITY = 'INSIDE WALL
TEMPERATURE', DEPTH=0.032 /
&DEVC XYZ = 0.048,0.264,0.1, IOR = -2, ID='Pb3', QUANTITY = 'INSIDE
WALL TEMPERATURE', DEPTH=0.001 /
&DEVC XYZ = 0.048,0.264,0.1, IOR = -2, ID='Pb3-Pb4', QUANTITY = 'INSIDE
WALL TEMPERATURE', DEPTH=0.016 /
&DEVC XYZ = 0.048,0.264,0.1, IOR = -2, ID='Pb4', QUANTITY = 'INSIDE
WALL TEMPERATURE', DEPTH=0.032 /
&DEVC XYZ = 0.1160,0.032,0.1, IOR = 2, ID='FHF', QUANTITY = 'INSIDE
WALL TEMPERATURE', DEPTH=0 /
&DEVC XYZ = 0.1160,0.0323,0.1, IOR = 2, ID='FHF-Extra', QUANTITY = '
INSIDE WALL TEMPERATURE', DEPTH=0.00094 /
&DEVC XYZ = 0.1160,0.032,0.1, IOR = 2, ID='FHF-Extra2', QUANTITY = '
INSIDE WALL TEMPERATURE', DEPTH=0.03294 /
```

```

&DEVC XYZ = 0.1160,0.122,0.1, IOR = 2, ID='FCF', QUANTITY = 'INSIDE
    WALL TEMPERATURE', DEPTH=0 /

&DEVC XYZ = 0.1160,0.122,0.1, IOR = 2, ID='FCF-Extra', QUANTITY = '
    INSIDE WALL TEMPERATURE', DEPTH=0.00094 /

&DEVC XYZ = 0.1160,0.142,0.1, IOR = 2, ID='AHF', QUANTITY = 'INSIDE
    WALL TEMPERATURE', DEPTH=0 /

&DEVC XYZ = 0.1160,0.142,0.1, IOR = 2, ID='AHF-Extra', QUANTITY = '
    INSIDE WALL TEMPERATURE', DEPTH=0.00094 /

&DEVC XYZ = 0.1160,0.232,0.1, IOR = 2, ID='ACF', QUANTITY = 'INSIDE
    WALL TEMPERATURE', DEPTH=0 /

&DEVC XYZ = 0.1160,0.232,0.1, IOR = 2, ID='ACF-Extra', QUANTITY = '
    INSIDE WALL TEMPERATURE', DEPTH=0.00094 /

&DEVC XYZ = 0.1160,0.232,0.1, IOR = 2, ID='ACF-Extra2', QUANTITY = '
    INSIDE WALL TEMPERATURE', DEPTH=0.03294 /


&SURF ID='ADIABATIC ', ADIABATIC=.TRUE./
&SURF ID='ADIABATIC GYPSUM', COLOR='PINK', ADIABATIC=.TRUE./
&SURF ID='ADIABATIC GYPSUM_FIRE', COLOR='PINK', THICKNESS=0.032,
    MATL_ID='GYPSUM', HEAT_TRANSFER_COEFFICIENT_BACK=25, BACKING=
        EXPOSED'/

&SURF ID='ADIABATIC GYPSUM_AMB', COLOR='PINK', THICKNESS=0.032, MATL_ID
    ='GYPSUM', HEAT_TRANSFER_COEFFICIENT_BACK=10, BACKING='VOID'/

&SURF ID='ADIABATIC STEEL', COLOR='BLUE', THICKNESS=0.00095, MATL_ID=
    STEEL'/

&SURF ID='HOT STEEL', COLOR='RED', TMP_FRONT=1153.0, RAMP_T='standard'/
&RAMP ID='standard', T=0.0, F=0.0173/
&RAMP ID='standard', T=60.0, F=0.3029/
&RAMP ID='standard', T=120.0, F=0.3856/
&RAMP ID='standard', T=180.0, F=0.4357/
&RAMP ID='standard', T=240.0, F=0.4718/
&RAMP ID='standard', T=300.0, F=0.5/
&RAMP ID='standard', T=360.0, F=0.5232/
&RAMP ID='standard', T=420.0, F=0.5428/
&RAMP ID='standard', T=480.0, F=0.5599/

```

```
&RAMP ID='standard', T=540.0, F=0.575/
&RAMP ID='standard', T=600.0, F=0.5885/
&RAMP ID='standard', T=660.0, F=0.6007/
&RAMP ID='standard', T=720.0, F=0.6119/
&RAMP ID='standard', T=780.0, F=0.6222/
&RAMP ID='standard', T=840.0, F=0.6318/
&RAMP ID='standard', T=900.0, F=0.6407/
&RAMP ID='standard', T=960.0, F=0.649/
&RAMP ID='standard', T=1020.0, F=0.6568/
&RAMP ID='standard', T=1080.0, F=0.6642/
&RAMP ID='standard', T=1140.0, F=0.6712/
&RAMP ID='standard', T=1200.0, F=0.6778/
&RAMP ID='standard', T=1260.0, F=0.6841/
&RAMP ID='standard', T=1320.0, F=0.6901/
&RAMP ID='standard', T=1380.0, F=0.6958/
&RAMP ID='standard', T=1440.0, F=0.7013/
&RAMP ID='standard', T=1500.0, F=0.7066/
&RAMP ID='standard', T=1560.0, F=0.7117/
&RAMP ID='standard', T=1620.0, F=0.7166/
&RAMP ID='standard', T=1680.0, F=0.7213/
&RAMP ID='standard', T=1740.0, F=0.7258/
&RAMP ID='standard', T=1800.0, F=0.7302/
&RAMP ID='standard', T=1860.0, F=0.7345/
&RAMP ID='standard', T=1920.0, F=0.7386/
&RAMP ID='standard', T=1980.0, F=0.7425/
&RAMP ID='standard', T=2040.0, F=0.7464/
&RAMP ID='standard', T=2100.0, F=0.7502/
&RAMP ID='standard', T=2160.0, F=0.7538/
&RAMP ID='standard', T=2220.0, F=0.7574/
&RAMP ID='standard', T=2280.0, F=0.7608/
&RAMP ID='standard', T=2340.0, F=0.7642/
&RAMP ID='standard', T=2400.0, F=0.7675/
&RAMP ID='standard', T=2460.0, F=0.7707/
&RAMP ID='standard', T=2520.0, F=0.7738/
```

```
&RAMP ID='standard', T=2580.0, F=0.7768/
&RAMP ID='standard', T=2640.0, F=0.7798/
&RAMP ID='standard', T=2700.0, F=0.7827/
&RAMP ID='standard', T=2760.0, F=0.7856/
&RAMP ID='standard', T=2820.0, F=0.7884/
&RAMP ID='standard', T=2880.0, F=0.7911/
&RAMP ID='standard', T=2940.0, F=0.7938/
&RAMP ID='standard', T=3000.0, F=0.7964/
&RAMP ID='standard', T=3060.0, F=0.799/
&RAMP ID='standard', T=3120.0, F=0.8015/
&RAMP ID='standard', T=3180.0, F=0.8039/
&RAMP ID='standard', T=3240.0, F=0.8064/
&RAMP ID='standard', T=3300.0, F=0.8087/
&RAMP ID='standard', T=3360.0, F=0.8111/
&RAMP ID='standard', T=3420.0, F=0.8134/
&RAMP ID='standard', T=3480.0, F=0.8156/
&RAMP ID='standard', T=3540.0, F=0.8178/
&RAMP ID='standard', T=3600.0, F=0.82/
&RAMP ID='standard', T=3660.0, F=0.8222/
&RAMP ID='standard', T=3720.0, F=0.8243/
&RAMP ID='standard', T=3780.0, F=0.8264/
&RAMP ID='standard', T=3840.0, F=0.8284/
&RAMP ID='standard', T=3900.0, F=0.8304/
&RAMP ID='standard', T=3960.0, F=0.8324/
&RAMP ID='standard', T=4020.0, F=0.8343/
&RAMP ID='standard', T=4080.0, F=0.8363/
&RAMP ID='standard', T=4140.0, F=0.8382/
&RAMP ID='standard', T=4200.0, F=0.84/
&RAMP ID='standard', T=4260.0, F=0.8419/
&RAMP ID='standard', T=4320.0, F=0.8437/
&RAMP ID='standard', T=4380.0, F=0.8455/
&RAMP ID='standard', T=4440.0, F=0.8472/
&RAMP ID='standard', T=4500.0, F=0.849/
&RAMP ID='standard', T=4560.0, F=0.8507/
```

```
&RAMP ID='standard', T=4620.0, F=0.8524/
&RAMP ID='standard', T=4680.0, F=0.8541/
&RAMP ID='standard', T=4740.0, F=0.8557/
&RAMP ID='standard', T=4800.0, F=0.8573/
&RAMP ID='standard', T=4860.0, F=0.859/
&RAMP ID='standard', T=4920.0, F=0.8606/
&RAMP ID='standard', T=4980.0, F=0.8621/
&RAMP ID='standard', T=5040.0, F=0.8637/
&RAMP ID='standard', T=5100.0, F=0.8652/
&RAMP ID='standard', T=5160.0, F=0.8667/
&RAMP ID='standard', T=5220.0, F=0.8682/
&RAMP ID='standard', T=5280.0, F=0.8697/
&RAMP ID='standard', T=5340.0, F=0.8712/
&RAMP ID='standard', T=5400.0, F=0.8726/
&RAMP ID='standard', T=5460.0, F=0.8741/
&RAMP ID='standard', T=5520.0, F=0.8755/
&RAMP ID='standard', T=5580.0, F=0.8769/
&RAMP ID='standard', T=5640.0, F=0.8783/
&RAMP ID='standard', T=5700.0, F=0.8797/
&RAMP ID='standard', T=5760.0, F=0.881/
&RAMP ID='standard', T=5820.0, F=0.8824/
&RAMP ID='standard', T=5880.0, F=0.8837/
&RAMP ID='standard', T=5940.0, F=0.885/
&RAMP ID='standard', T=6000.0, F=0.8863/
&RAMP ID='standard', T=6060.0, F=0.8876/
&RAMP ID='standard', T=6120.0, F=0.8889/
&RAMP ID='standard', T=6180.0, F=0.8901/
&RAMP ID='standard', T=6240.0, F=0.8914/
&RAMP ID='standard', T=6300.0, F=0.8926/
&RAMP ID='standard', T=6360.0, F=0.8939/
&RAMP ID='standard', T=6420.0, F=0.8951/
&RAMP ID='standard', T=6480.0, F=0.8963/
&RAMP ID='standard', T=6540.0, F=0.8975/
&RAMP ID='standard', T=6600.0, F=0.8987/
```

```
&RAMP ID='standard', T=6660.0, F=0.8999/
&RAMP ID='standard', T=6720.0, F=0.901/
&RAMP ID='standard', T=6780.0, F=0.9022/
&RAMP ID='standard', T=6840.0, F=0.9033/
&RAMP ID='standard', T=6900.0, F=0.9045/
&RAMP ID='standard', T=6960.0, F=0.9056/
&RAMP ID='standard', T=7020.0, F=0.9067/
&RAMP ID='standard', T=7080.0, F=0.9078/
&RAMP ID='standard', T=7140.0, F=0.9089/
&RAMP ID='standard', T=7200.0, F=0.91/
&RAMP ID='standard', T=7260.0, F=0.9111/
&RAMP ID='standard', T=7320.0, F=0.9121/
&RAMP ID='standard', T=7380.0, F=0.9132/
&RAMP ID='standard', T=7440.0, F=0.9142/
&RAMP ID='standard', T=7500.0, F=0.9153/
&RAMP ID='standard', T=7560.0, F=0.9163/
&RAMP ID='standard', T=7620.0, F=0.9173/
&RAMP ID='standard', T=7680.0, F=0.9184/
&RAMP ID='standard', T=7740.0, F=0.9194/
&RAMP ID='standard', T=7800.0, F=0.9204/
&RAMP ID='standard', T=7860.0, F=0.9214/
&RAMP ID='standard', T=7920.0, F=0.9224/
&RAMP ID='standard', T=7980.0, F=0.9233/
&RAMP ID='standard', T=8040.0, F=0.9243/
&RAMP ID='standard', T=8100.0, F=0.9253/
&RAMP ID='standard', T=8160.0, F=0.9262/
&RAMP ID='standard', T=8220.0, F=0.9272/
&RAMP ID='standard', T=8280.0, F=0.9281/
&RAMP ID='standard', T=8340.0, F=0.9291/
&RAMP ID='standard', T=8400.0, F=0.93/
&RAMP ID='standard', T=8460.0, F=0.9309/
&RAMP ID='standard', T=8520.0, F=0.9318/
&RAMP ID='standard', T=8580.0, F=0.9327/
&RAMP ID='standard', T=8640.0, F=0.9337/
```

```
&RAMP ID='standard', T=8700.0, F=0.9346/
&RAMP ID='standard', T=8760.0, F=0.9354/
&RAMP ID='standard', T=8820.0, F=0.9363/
&RAMP ID='standard', T=8880.0, F=0.9372/
&RAMP ID='standard', T=8940.0, F=0.9381/
&RAMP ID='standard', T=9000.0, F=0.939/
&RAMP ID='standard', T=9060.0, F=0.9398/
&RAMP ID='standard', T=9120.0, F=0.9407/
&RAMP ID='standard', T=9180.0, F=0.9415/
&RAMP ID='standard', T=9240.0, F=0.9424/
&RAMP ID='standard', T=9300.0, F=0.9432/
&RAMP ID='standard', T=9360.0, F=0.944/
&RAMP ID='standard', T=9420.0, F=0.9449/
&RAMP ID='standard', T=9480.0, F=0.9457/
&RAMP ID='standard', T=9540.0, F=0.9465/
&RAMP ID='standard', T=9600.0, F=0.9473/
&RAMP ID='standard', T=9660.0, F=0.9481/
&RAMP ID='standard', T=9720.0, F=0.9489/
&RAMP ID='standard', T=9780.0, F=0.9497/
&RAMP ID='standard', T=9840.0, F=0.9505/
&RAMP ID='standard', T=9900.0, F=0.9513/
&RAMP ID='standard', T=9960.0, F=0.9521/
&RAMP ID='standard', T=1.002E4, F=0.9529/
&RAMP ID='standard', T=1.008E4, F=0.9537/
&RAMP ID='standard', T=1.014E4, F=0.9544/
&RAMP ID='standard', T=1.02E4, F=0.9552/
&RAMP ID='standard', T=1.026E4, F=0.956/
&RAMP ID='standard', T=1.032E4, F=0.9567/
&RAMP ID='standard', T=1.038E4, F=0.9575/
&RAMP ID='standard', T=1.044E4, F=0.9582/
&RAMP ID='standard', T=1.05E4, F=0.959/
&RAMP ID='standard', T=1.056E4, F=0.9597/
&RAMP ID='standard', T=1.062E4, F=0.9604/
&RAMP ID='standard', T=1.068E4, F=0.9612/
```

```
&RAMP ID='standard', T=1.074E4, F=0.9619/
&RAMP ID='standard', T=1.08E4, F=0.9626/
&RAMP ID='standard', T=1.086E4, F=0.9634/
&RAMP ID='standard', T=1.092E4, F=0.9641/
&RAMP ID='standard', T=1.098E4, F=0.9648/
&RAMP ID='standard', T=1.104E4, F=0.9655/
&RAMP ID='standard', T=1.11E4, F=0.9662/
&RAMP ID='standard', T=1.116E4, F=0.9669/
&RAMP ID='standard', T=1.122E4, F=0.9676/
&RAMP ID='standard', T=1.128E4, F=0.9683/
&RAMP ID='standard', T=1.134E4, F=0.969/
&RAMP ID='standard', T=1.14E4, F=0.9697/
&RAMP ID='standard', T=1.146E4, F=0.9703/
&RAMP ID='standard', T=1.152E4, F=0.971/
&RAMP ID='standard', T=1.158E4, F=0.9717/
&RAMP ID='standard', T=1.164E4, F=0.9724/
&RAMP ID='standard', T=1.17E4, F=0.973/
&RAMP ID='standard', T=1.176E4, F=0.9737/
&RAMP ID='standard', T=1.182E4, F=0.9744/
&RAMP ID='standard', T=1.188E4, F=0.975/
&RAMP ID='standard', T=1.194E4, F=0.9757/
&RAMP ID='standard', T=1.2E4, F=0.9763/
&RAMP ID='standard', T=1.206E4, F=0.977/
&RAMP ID='standard', T=1.212E4, F=0.9776/
&RAMP ID='standard', T=1.218E4, F=0.9783/
&RAMP ID='standard', T=1.224E4, F=0.9789/
&RAMP ID='standard', T=1.23E4, F=0.9795/
&RAMP ID='standard', T=1.236E4, F=0.9802/
&RAMP ID='standard', T=1.242E4, F=0.9808/
&RAMP ID='standard', T=1.248E4, F=0.9814/
&RAMP ID='standard', T=1.254E4, F=0.982/
&RAMP ID='standard', T=1.26E4, F=0.9827/
&RAMP ID='standard', T=1.266E4, F=0.9833/
&RAMP ID='standard', T=1.272E4, F=0.9839/
```

```
&RAMP ID='standard', T=1.278E4, F=0.9845/
&RAMP ID='standard', T=1.284E4, F=0.9851/
&RAMP ID='standard', T=1.29E4, F=0.9857/
&RAMP ID='standard', T=1.296E4, F=0.9863/
&RAMP ID='standard', T=1.302E4, F=0.9869/
&RAMP ID='standard', T=1.308E4, F=0.9875/
&RAMP ID='standard', T=1.314E4, F=0.9881/
&RAMP ID='standard', T=1.32E4, F=0.9887/
&RAMP ID='standard', T=1.326E4, F=0.9893/
&RAMP ID='standard', T=1.332E4, F=0.9899/
&RAMP ID='standard', T=1.338E4, F=0.9905/
&RAMP ID='standard', T=1.344E4, F=0.991/
&RAMP ID='standard', T=1.35E4, F=0.9916/
&RAMP ID='standard', T=1.356E4, F=0.9922/
&RAMP ID='standard', T=1.362E4, F=0.9928/
&RAMP ID='standard', T=1.368E4, F=0.9933/
&RAMP ID='standard', T=1.374E4, F=0.9939/
&RAMP ID='standard', T=1.38E4, F=0.9945/
&RAMP ID='standard', T=1.386E4, F=0.995/
&RAMP ID='standard', T=1.392E4, F=0.9956/
&RAMP ID='standard', T=1.398E4, F=0.9962/
&RAMP ID='standard', T=1.404E4, F=0.9967/
&RAMP ID='standard', T=1.41E4, F=0.9973/
&RAMP ID='standard', T=1.416E4, F=0.9978/
&RAMP ID='standard', T=1.422E4, F=0.9984/
&RAMP ID='standard', T=1.428E4, F=0.9989/
&RAMP ID='standard', T=1.434E4, F=0.9995/
&RAMP ID='standard', T=1.44E4, F=1.0/
```

```
&MATL ID = 'GYPSUM'
DENSITY = 768.5
EMISSIVITY=0.9
SPECIFIC_HEAT_RAMP = 'c_ramp'
```

```
CONDUCTIVITY_RAMP = 'k_ramp' /
&RAMP ID='c_ramp', T = 20 , F = 1.22 /
&RAMP ID='c_ramp', T = 100 , F = 1.54 /
&RAMP ID='c_ramp', T = 115 , F = 2.4 /
&RAMP ID='c_ramp', T = 125 , F = 5.294 /
&RAMP ID='c_ramp', T = 148 , F = 10.4 /
&RAMP ID='c_ramp', T = 154 , F = 9.232 /
&RAMP ID='c_ramp', T = 158 , F = 8.6 /
&RAMP ID='c_ramp', T = 173 , F = 9.75 /
&RAMP ID='c_ramp', T = 180 , F = 7.885 /
&RAMP ID='c_ramp', T = 195 , F = 2 /
&RAMP ID='c_ramp', T = 225 , F = 1.22 /
&RAMP ID='c_ramp', T = 400 , F = 1.22 /
&RAMP ID='c_ramp', T = 675 , F = 1.22 /
&RAMP ID='c_ramp', T = 770 , F = 1.22 /
&RAMP ID='c_ramp', T = 875 , F = 1.22 /
&RAMP ID='c_ramp', T = 940 , F = 1.22 /
&RAMP ID='c_ramp', T = 1000, F = 1.22 /
&RAMP ID='c_ramp', T = 1180, F = 1.22 /
&RAMP ID='k_ramp', T = 20 , F = 0.24 /
&RAMP ID='k_ramp', T = 100 , F = 0.24 /
&RAMP ID='k_ramp', T = 115 , F = 0.2 /
&RAMP ID='k_ramp', T = 125 , F = 0.17 /
&RAMP ID='k_ramp', T = 148 , F = 0.11 /
&RAMP ID='k_ramp', T = 154 , F = 0.11 /
&RAMP ID='k_ramp', T = 158 , F = 0.11 /
&RAMP ID='k_ramp', T = 173 , F = 0.11 /
&RAMP ID='k_ramp', T = 180 , F = 0.11 /
&RAMP ID='k_ramp', T = 195 , F = 0.11 /
&RAMP ID='k_ramp', T = 225 , F = 0.11 /
&RAMP ID='k_ramp', T = 400 , F = 0.15 /
&RAMP ID='k_ramp', T = 675 , F = 0.1885 /
&RAMP ID='k_ramp', T = 770 , F = 0.2018 /
&RAMP ID='k_ramp', T = 875 , F = 0.2165 /
```

```
&RAMP ID='k_ramp', T = 940 , F = 0.41 /
&RAMP ID='k_ramp', T = 1000, F = 0.7 /
&RAMP ID='k_ramp', T = 1180, F = 1.4 /

&MATL ID = 'STEEL'
DENSITY = 7850
EMISSIVITY=0.7
SPECIFIC_HEAT_RAMP = 'a_ramp'
CONDUCTIVITY_RAMP = 'b_ramp' /

&RAMP ID='a_ramp', T = 20 , F = 0.44 /
&RAMP ID='a_ramp', T = 200 , F = 0.53 /
&RAMP ID='a_ramp', T = 300 , F = 0.565 /
&RAMP ID='a_ramp', T = 599 , F = 0.759 /
&RAMP ID='a_ramp', T = 600 , F = 0.76 /
&RAMP ID='a_ramp', T = 625 , F = 0.781 /
&RAMP ID='a_ramp', T = 650 , F = 0.814 /
&RAMP ID='a_ramp', T = 675 , F = 0.872 /
&RAMP ID='a_ramp', T = 700 , F = 1.008 /
&RAMP ID='a_ramp', T = 725 , F = 1.666 /
&RAMP ID='a_ramp', T = 727 , F = 1.848 /
&RAMP ID='a_ramp', T = 729 , F = 2.111 /
&RAMP ID='a_ramp', T = 731 , F = 2.523 /
&RAMP ID='a_ramp', T = 734 , F = 3.917 /
&RAMP ID='a_ramp', T = 735 , F = 5 /
&RAMP ID='a_ramp', T = 750 , F = 1.483 /
&RAMP ID='a_ramp', T = 775 , F = 0.95 /
&RAMP ID='a_ramp', T = 799 , F = 0.809 /
&RAMP ID='a_ramp', T = 800 , F = 0.803 /
&RAMP ID='a_ramp', T = 825 , F = 0.735 /
&RAMP ID='a_ramp', T = 850 , F = 0.695 /
&RAMP ID='a_ramp', T = 875 , F = 0.669 /
&RAMP ID='a_ramp', T = 899 , F = 0.651 /
&RAMP ID='a_ramp', T = 1200, F = 0.65 /
&RAMP ID='b_ramp', T = 20 , F = 54 /
```

```

&RAMP ID='b_ramp', T = 200 , F = 47.85 /
&RAMP ID='b_ramp', T = 300 , F = 44.43 /
&RAMP ID='b_ramp', T = 599 , F = 34.22 /
&RAMP ID='b_ramp', T = 600 , F = 34.19 /
&RAMP ID='b_ramp', T = 625 , F = 33.34 /
&RAMP ID='b_ramp', T = 650 , F = 32.48 /
&RAMP ID='b_ramp', T = 675 , F = 31.63 /
&RAMP ID='b_ramp', T = 700 , F = 30.78 /
&RAMP ID='b_ramp', T = 725 , F = 29.92 /
&RAMP ID='b_ramp', T = 727 , F = 29.85 /
&RAMP ID='b_ramp', T = 729 , F = 29.79 /
&RAMP ID='b_ramp', T = 731 , F = 29.72 /
&RAMP ID='b_ramp', T = 734 , F = 29.61 /
&RAMP ID='b_ramp', T = 735 , F = 29.58 /
&RAMP ID='b_ramp', T = 750 , F = 29.07 /
&RAMP ID='b_ramp', T = 775 , F = 28.21 /
&RAMP ID='b_ramp', T = 799 , F = 27.4 /
&RAMP ID='b_ramp', T = 800 , F = 27.3 /
&RAMP ID='b_ramp', T = 825 , F = 27.3 /
&RAMP ID='b_ramp', T = 850 , F = 27.3 /
&RAMP ID='b_ramp', T = 875 , F = 27.3 /
&RAMP ID='b_ramp', T = 899 , F = 27.3 /
&RAMP ID='b_ramp', T = 1200, F = 27.3 /


&VENT ID='Hburner' SURF_ID='HOT STEEL' XB
    =0.0,0.232,-0.016,-0.016,0.0,0.2 /
&VENT MB='YMAX', SURF_ID='OPEN' /
&VENT MB='XMAX', SURF_ID='ADIABATIC' /
&VENT MB='XMIN', SURF_ID='ADIABATIC' /
&VENT MB='ZMAX', SURF_ID='ADIABATIC' /
&VENT MB='ZMIN', SURF_ID='ADIABATIC' /


&SLCF QUANTITY='TEMPERATURE', VECTOR=.TRUE., CELL_CENTERED=.TRUE., PBX
    =0.1/

```

Appendix A. FDS code

```
&SLCF QUANTITY='TEMPERATURE', VECTOR=.TRUE., CELL_CENTERED=.TRUE., PBY  
=0.1/  
&SLCF QUANTITY='TEMPERATURE', VECTOR=.TRUE., CELL_CENTERED=.TRUE., PBZ  
=0.1/  
  
&BNDF QUANTITY='WALL TEMPERATURE' /  
&BNDF QUANTITY='NET HEAT FLUX' /  
  
&TAIL /
```

Appendix B

Axial Compression Capacity Prediction based on DSM

The procedures to determine the ambient temperature axial compression capacity of stud based on Direct Strength Method is shown below.

Nominal External Dimensions

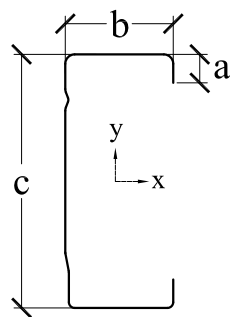


Figure B.1: Nominal external dimensions of stud

$A = 7 \text{ mm}$, $B = 36 \text{ mm}$ and $C = 89 \text{ mm}$; Thickness (BMT) = 0.95 mm

Effective length about the major axis of bending $L_x = 3,000 \text{ mm}$

Effective length about the minor axis of bending $L_x = 1,000 \text{ mm}$

Section Properties of Stud from CUFSM

Gross area of section $A_g = 160.34 \text{ mm}^2$

Second moment of area about the major axis $I_{xx} = 202,187 \text{ mm}^4$

Second moment of area about the minor axis $I_{yy} = 26,513 \text{ mm}^4$

$$\text{Radius of gyration about major axis } r_x = \sqrt{\frac{I_{xx}}{A_g}} = \sqrt{\frac{202,187}{160.34}} = 35.51 \text{ mm}$$

$$\text{Radius of gyration about minor axis } r_y = \sqrt{\frac{I_{yy}}{A_g}} = \sqrt{\frac{26,513}{160.34}} = 12.86 \text{ mm}$$

Mechanical Properties of the Stud

Yield strength at ambient temperature (measured) $f_y = 617.5 \text{ MPa}$

Elastic modulus at ambient temperature (measured) $E_{20} = 215,500 \text{ MPa}$

Elastic flexural buckling stress (f_{oc}) - Cl 3.4 AS/NZS (SA (2018))

Plasterboard provides torsional and flexural-torsional buckling restraints to the studs in gypsum plasterboard lined walls, thus the stud sections are not subjected to torsional or flexural-torsional buckling.

Elastic flexural buckling stress about the major axis f_{ox}

$$f_{ox} = \frac{\pi^2 E}{\left(\frac{l_{ex}}{r_x}\right)^2} = \frac{\pi^2 \times 215,500}{\left(\frac{3000}{35.51}\right)^2} = 297.99 \text{ MPa}$$

Elastic flexural buckling stress about the minor axis f_{oy}

$$f_{ox} = \frac{\pi^2 E}{\left(\frac{l_{ex}}{r_y}\right)^2} = \frac{\pi^2 \times 215,500}{\left(\frac{1000}{12.86}\right)^2} = 351.68 \text{ MPa}$$

Elastic flexural buckling stress f_{oc} = Lesser of f_{ox} and f_{oy} = 297.99 MPa

Flexural buckling capacity of the stud N_{ce}

Elastic flexural buckling load $N_{oc} = A_g f_{oc} = 160.34 \times 297.99 = 47.78 \text{ kN}$

Nominal yield load $N_y = A_g f_y = 160.34 \times 617.5 = 99.01 \text{ kN}$

$$\lambda_c = \sqrt{\frac{N_y}{N_{oc}}} = \sqrt{\frac{99.01}{47.78}} = 1.440 < 1.5$$

Flexural buckling capacity $N_{ce} = (0.658 \lambda_c^2) N_y = 0.658^{1.44^2} \times 99.01 = 41.59 \text{ kN}$

Local buckling capacity of the stud

Local buckling factor = 0.22 (From CUFSM signature curve)

Critical local buckling load $N_{ol} = A_g \times (\text{Locl buckling load factor}) \times f_y$

$$N_{ol} = 160.34 \times (0.22 \times 617.5) = 21.85kN$$

$$\lambda_l = \sqrt{\frac{N_{ce}}{N_{ol}}} = \sqrt{\frac{41.59}{21.85}} = 1.379 > 0.776$$

$$\text{Local buckling capacity of the stud } N_{cl,1} = \left(1 - 0.15 \left(\frac{N_{ol}}{N_{ce}} \right)^{0.4} \right) \left(\frac{N_{ol}}{N_{ce}} \right)^{0.4} N_{ce}$$

$$N_{cl,1} = \left(1 - 0.15 \left(\frac{21.85}{41.59} \right)^{0.4} \right) \left(\frac{21.58}{41.59} \right)^{0.4} \times 41.59 = 28.43kN$$

Ultimate local buckling capacity of the stud at ambient temperature = **28.43 kN**

[This page is intentionally left blank]

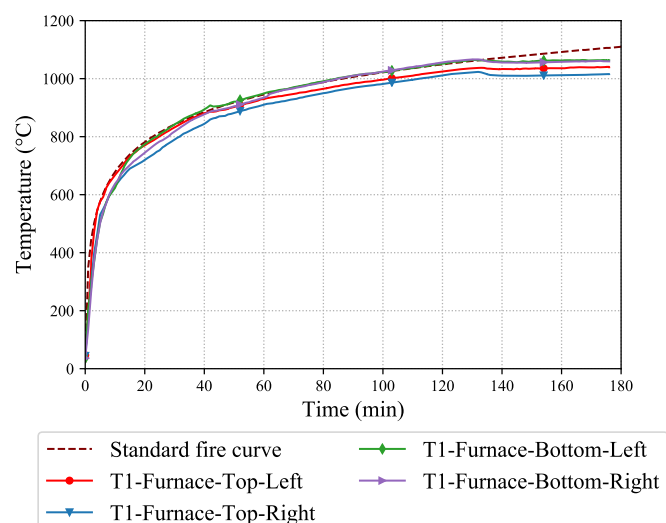
Appendix C

Full-scale fire test results

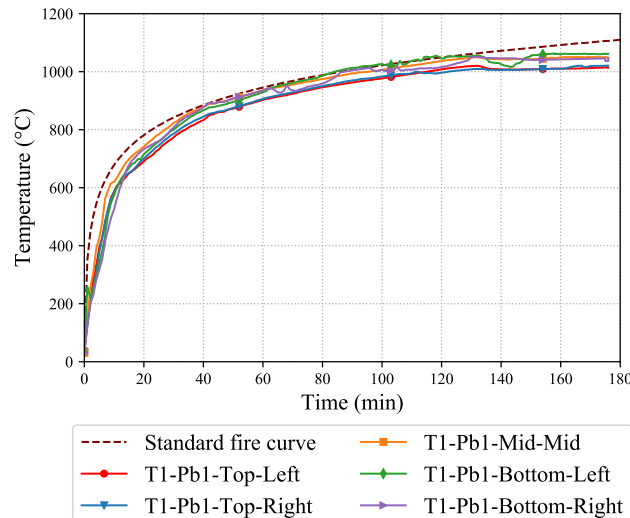
Individual time-temperature curves from the full-scale fire tests conducted in Chapter 4 are presented below.

Test-T1

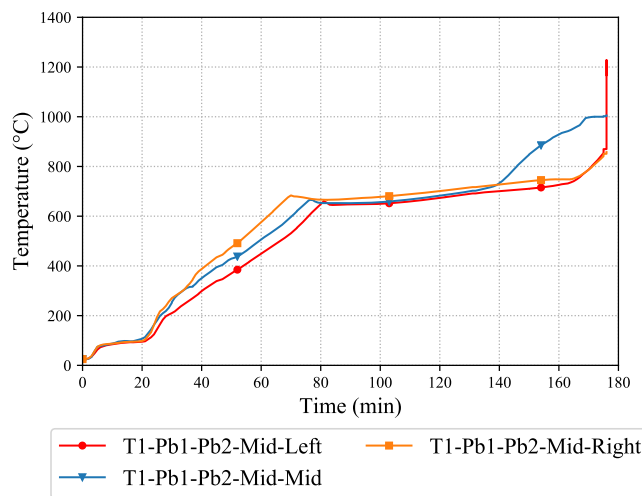
Test-T1 Plasterboard Time-Temperature Curves



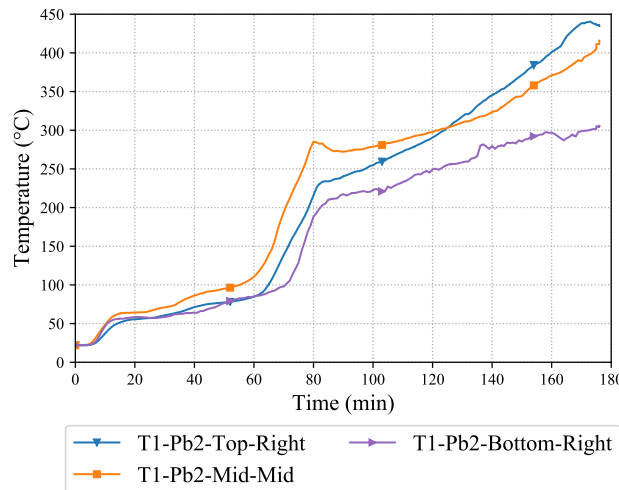
T1-Furnace



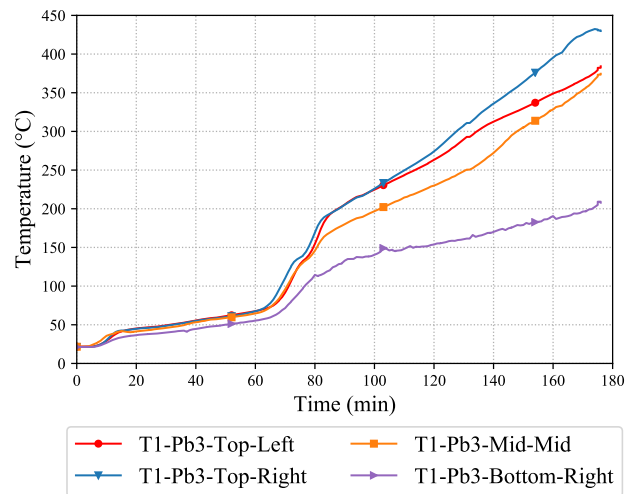
T1-Pb1



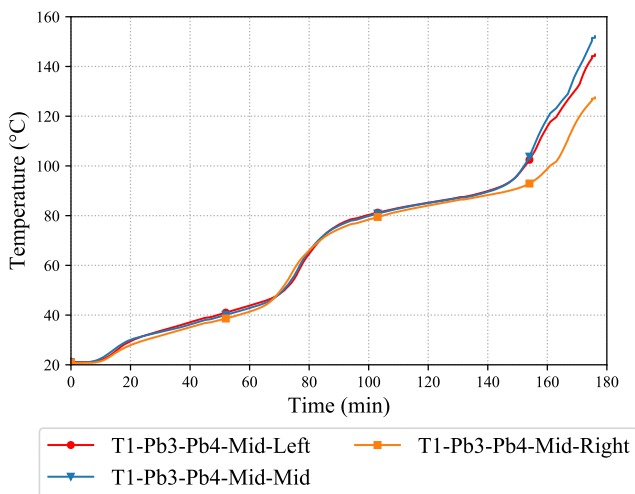
T1-Pb1-Pb2



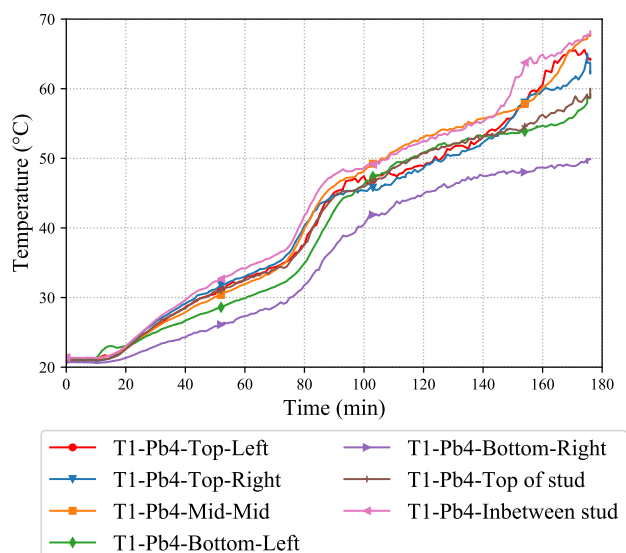
T1-Pb2



T1-Pb3

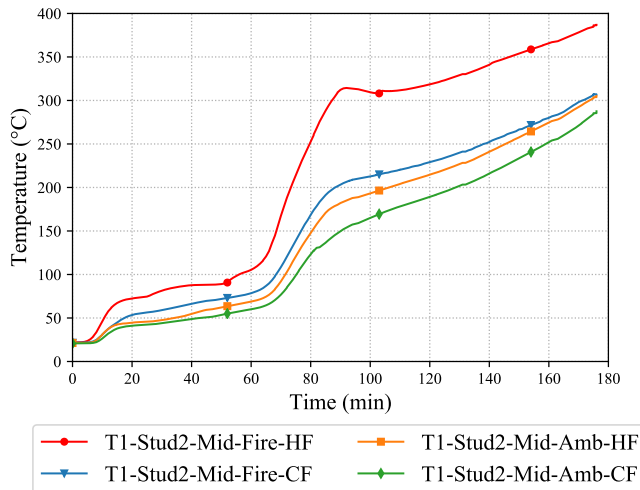


T1-Pb3-Pb4

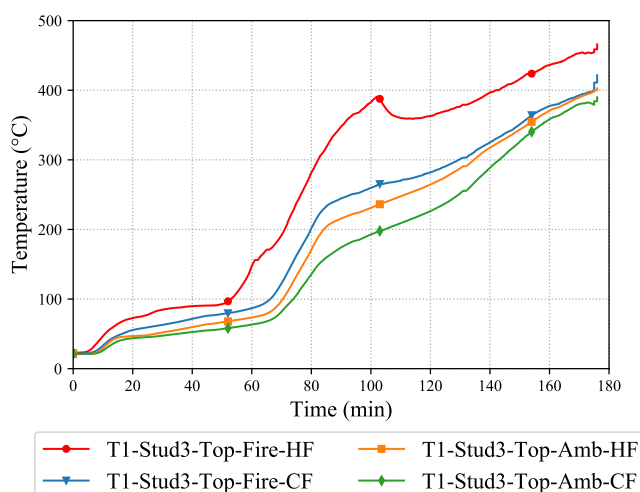


T1-Pb4

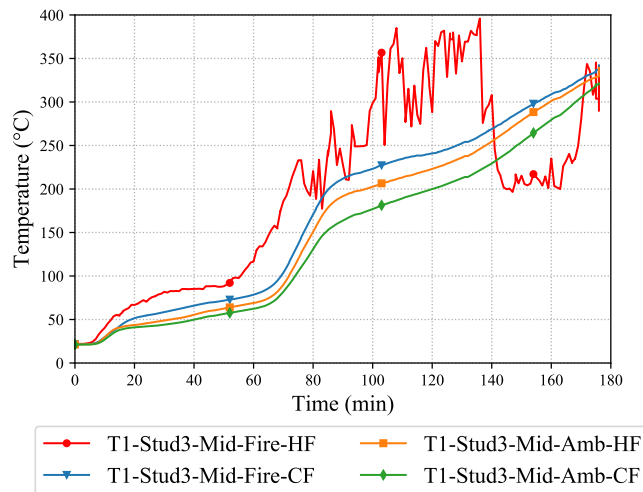
T1-Stud Time-Temperature Curves



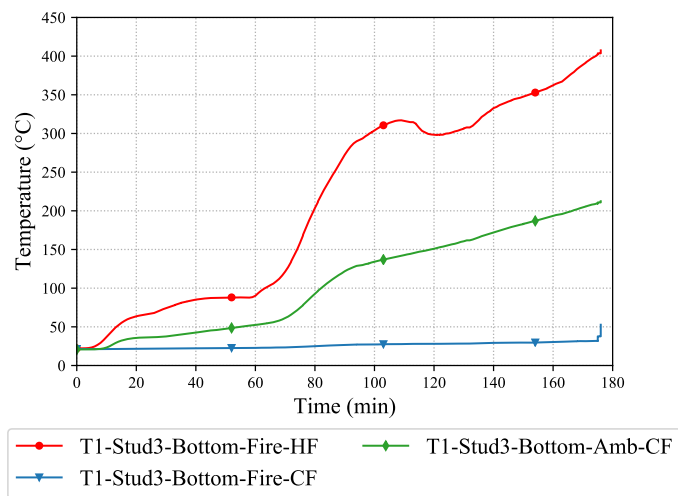
T1-Stud2-Mid



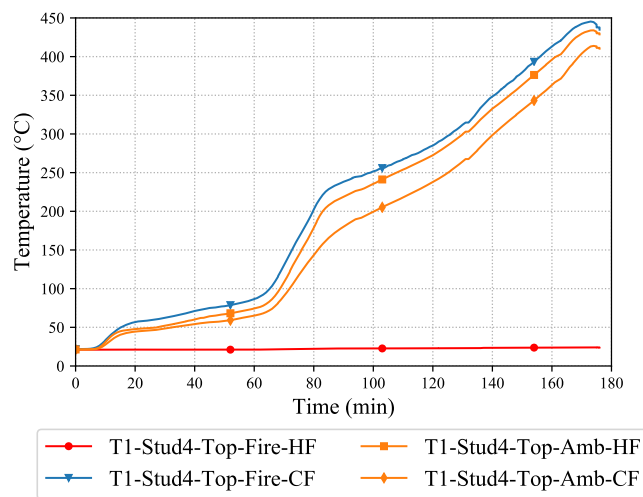
T1-Stud3-Top



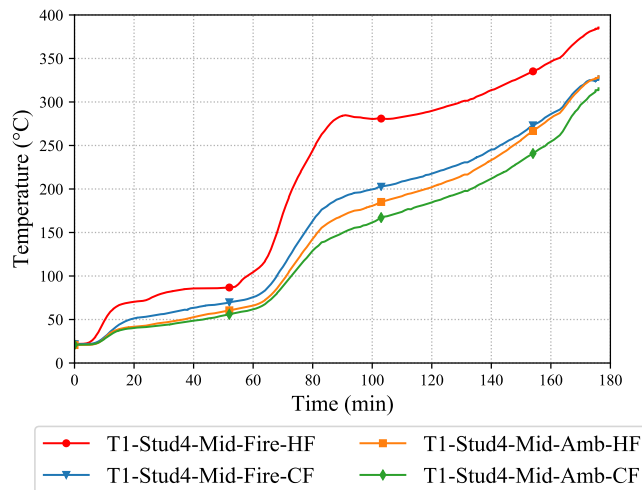
T1-Stud3-Mid



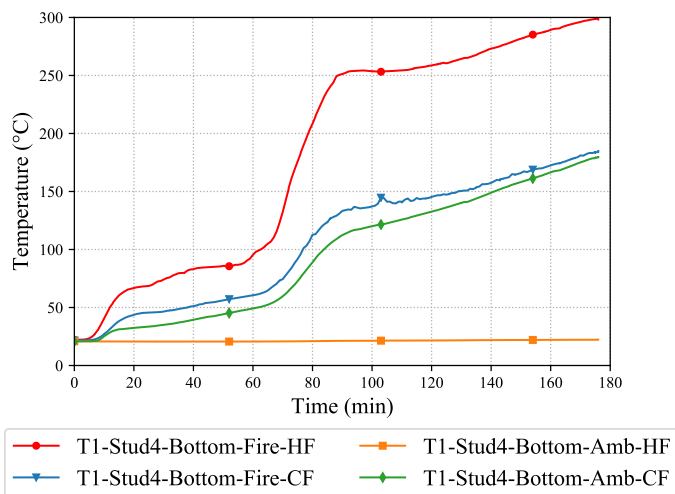
T1-Stud3-Bottom



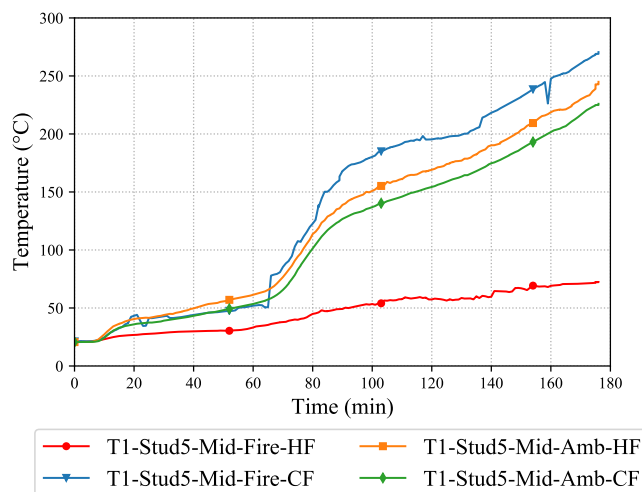
T1-Stud4-Top



T1-Stud4-Mid



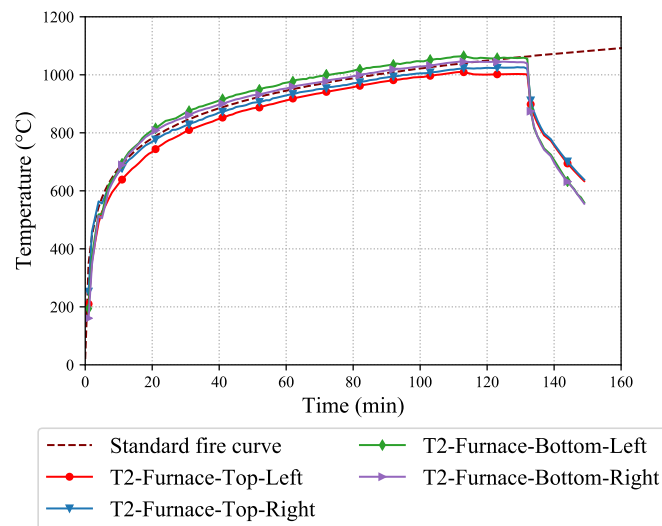
T1-Stud4-Bottom



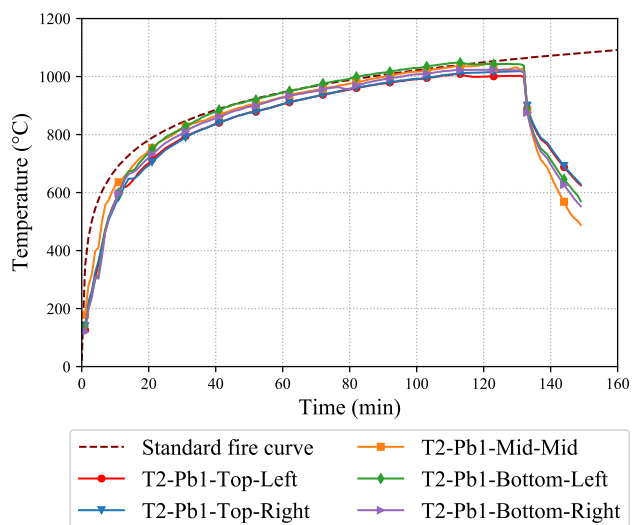
T1-Stud5-Mid

Test-T2

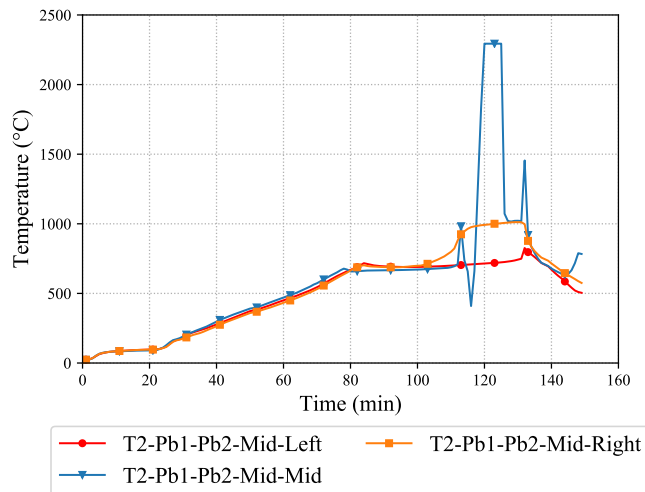
Test-T2 Plasterboard Time-Temperature Curves



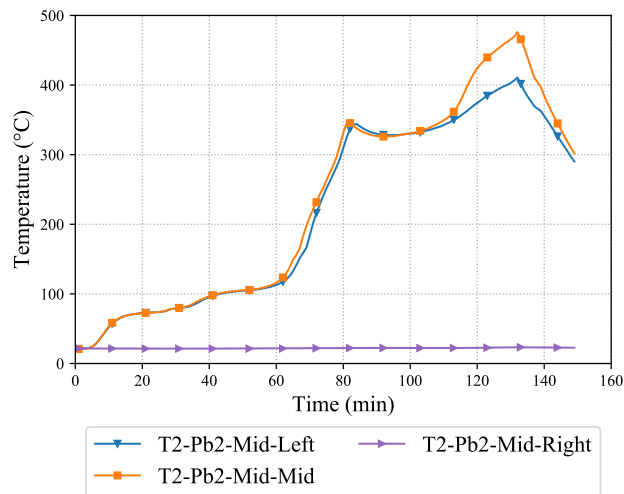
T2-Furnace



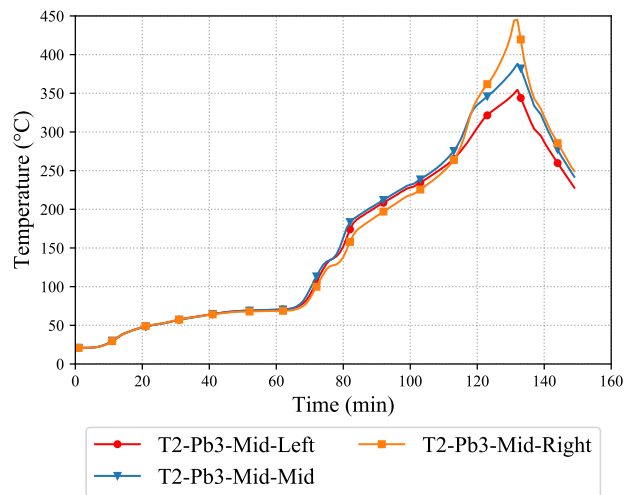
T2-Pb1



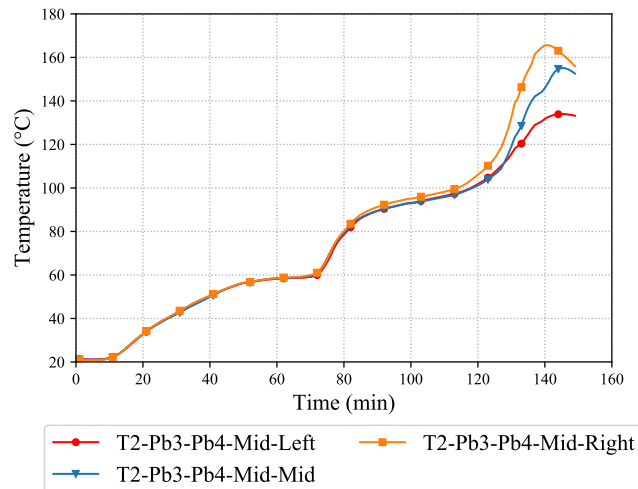
T2-Pb1-Pb2



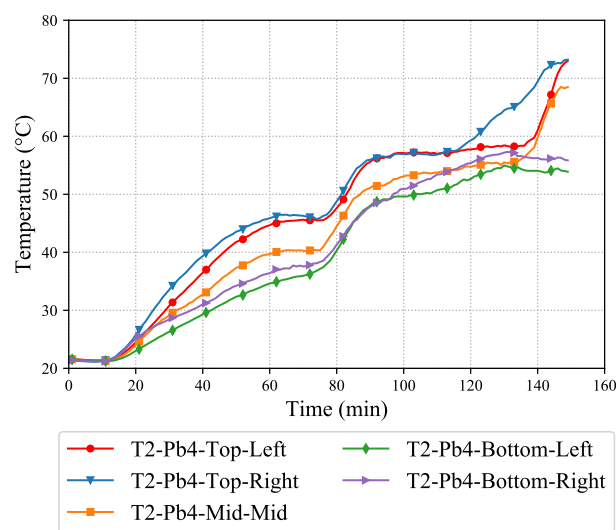
T2-Pb2



T2-Pb3

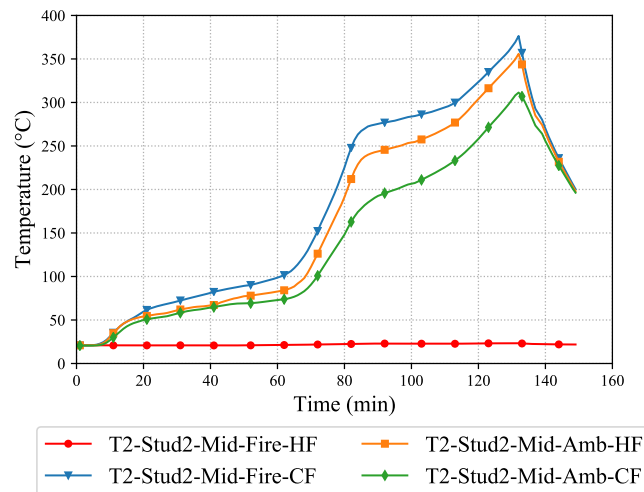


T2-Pb3-Pb4

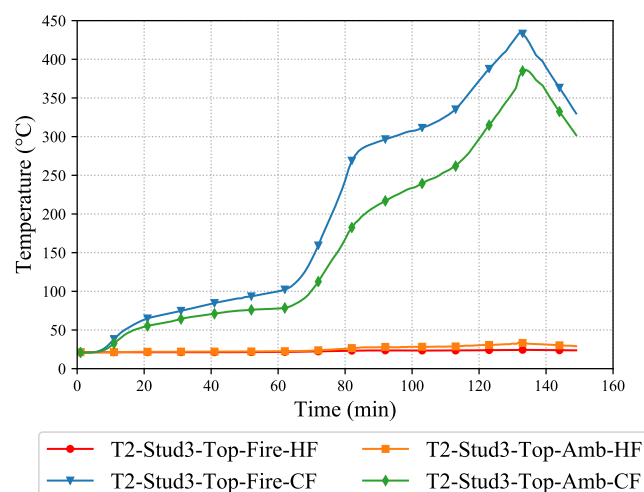


T2-Pb4

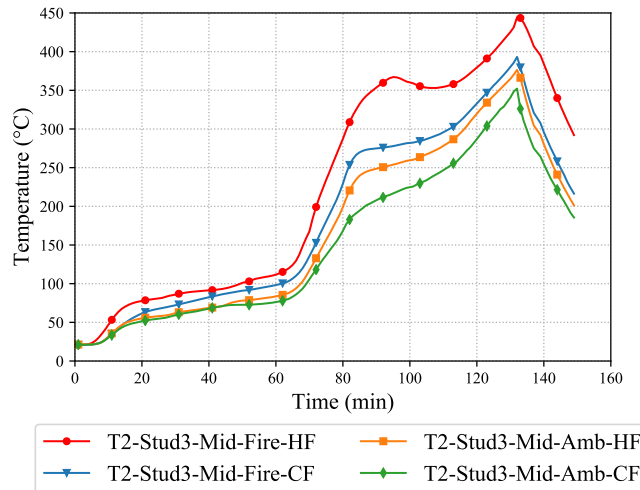
T2-Stud Time-Temperature Curves



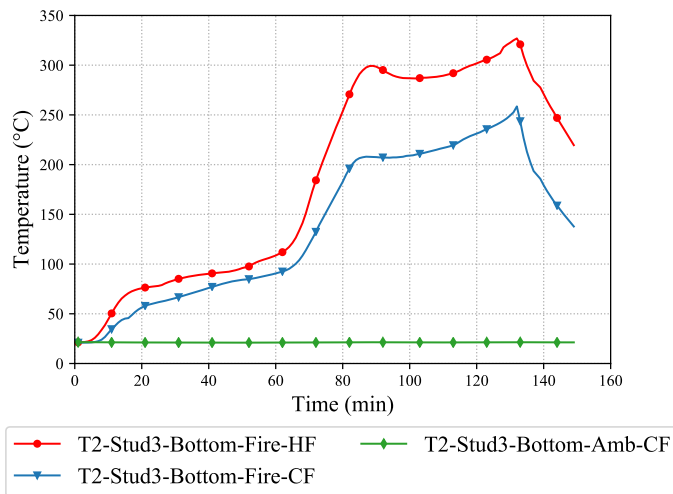
T2-Stud2-Mid



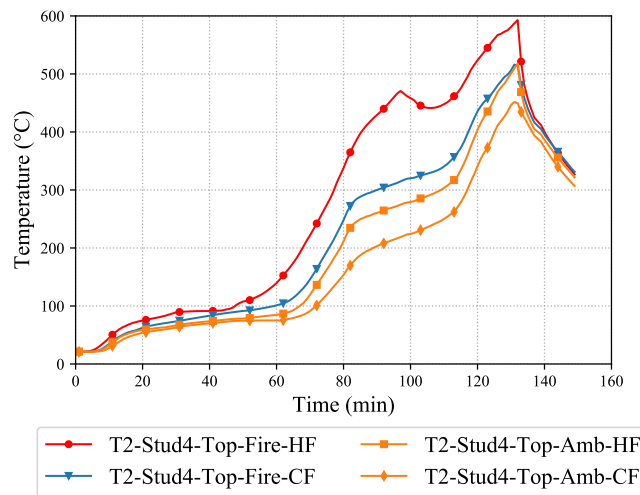
T2-Stud3-Top



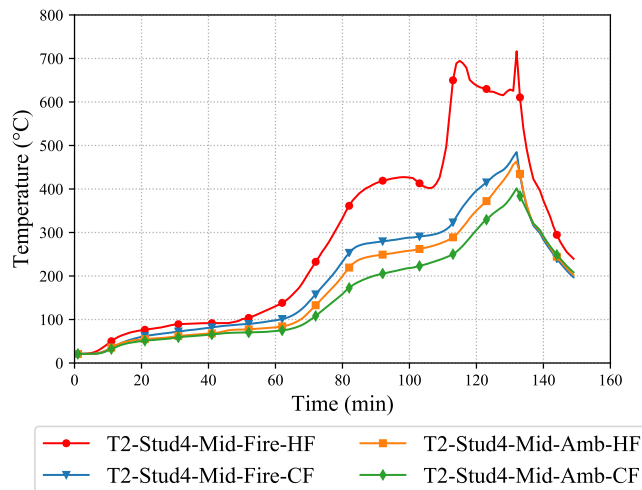
T2-Stud3-Mid



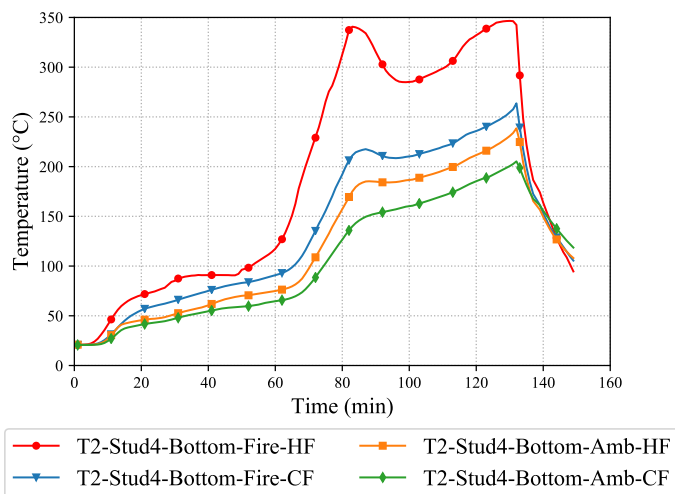
T2-Stud3-Bottom



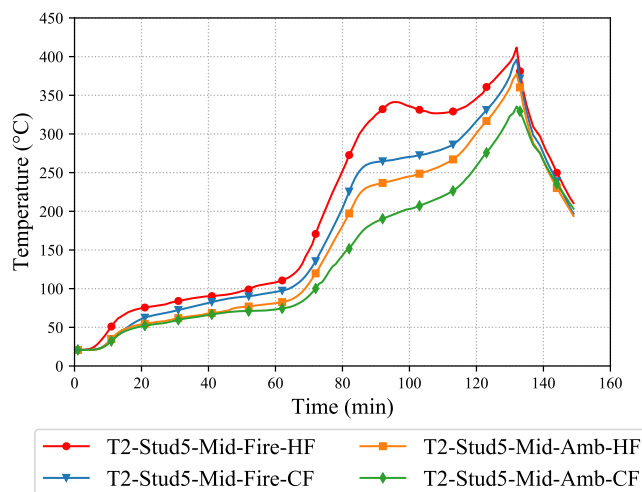
T2-Stud4-Top



T2-Stud4-Mid



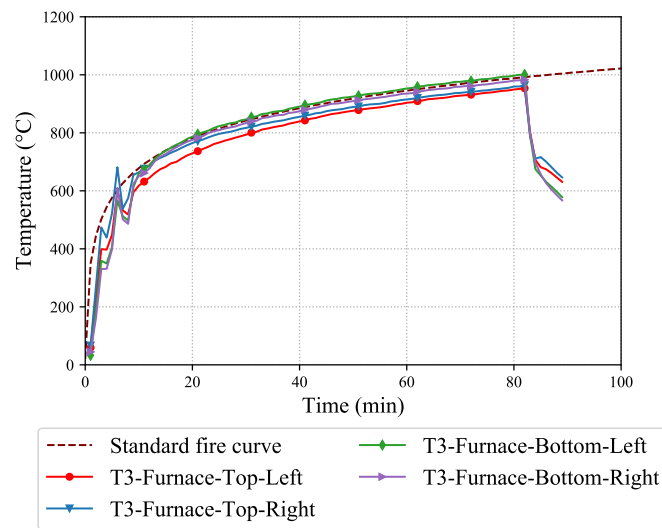
T2-Stud4-Bottom



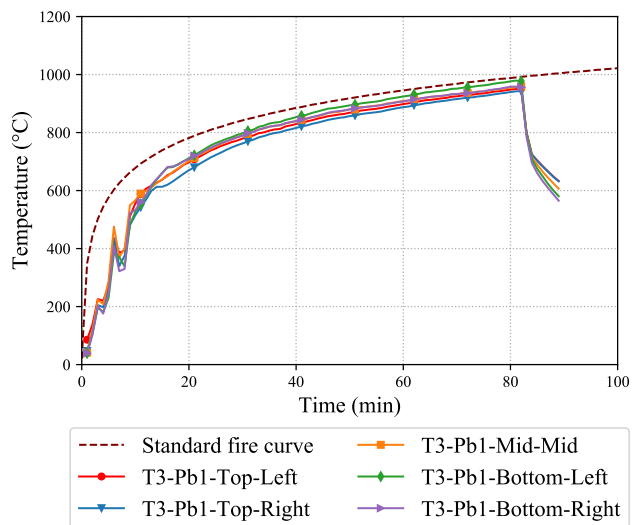
T2-Stud5-Mid

Test-T3

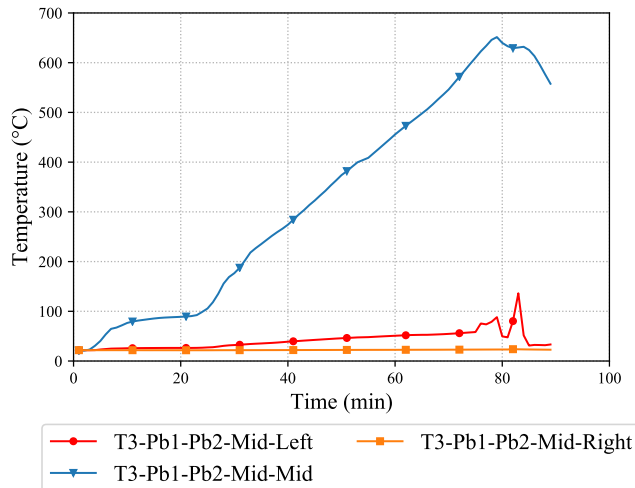
Test-T3 Plasterboard Time-Temperature Curves



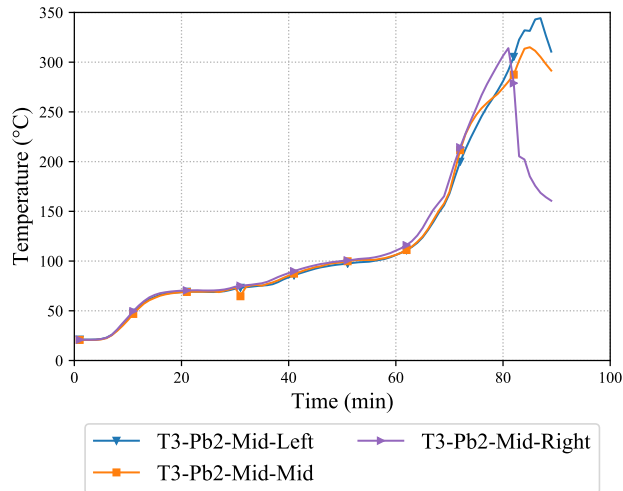
T3-Furnace



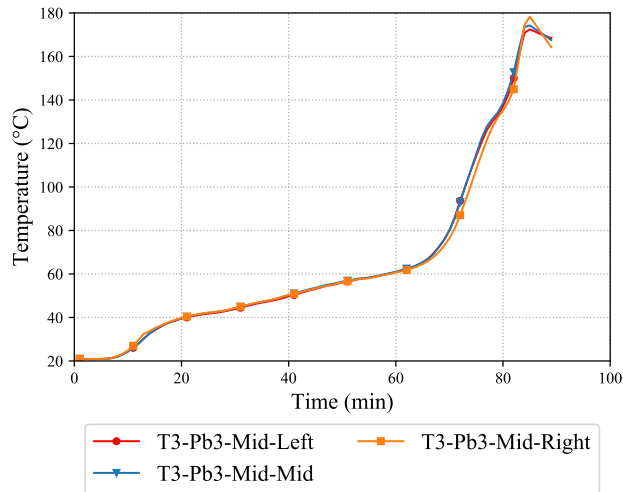
T3-Pb1



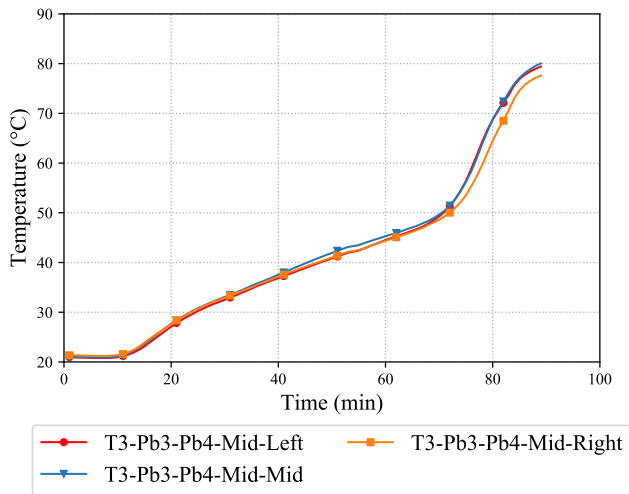
T3-Pb1-Pb2



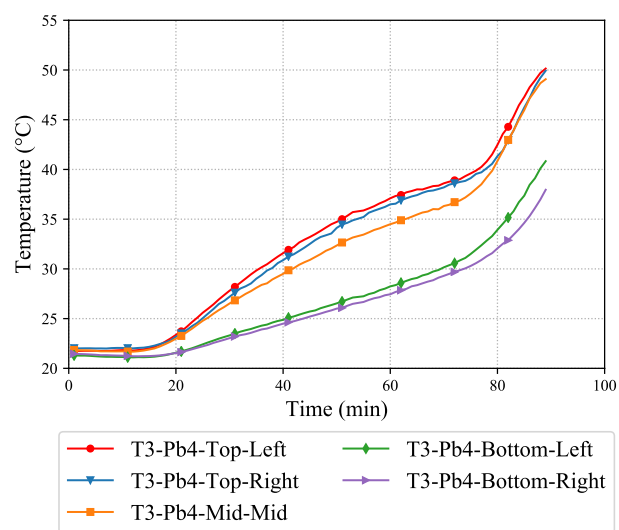
T3-Pb2



T3-Pb3

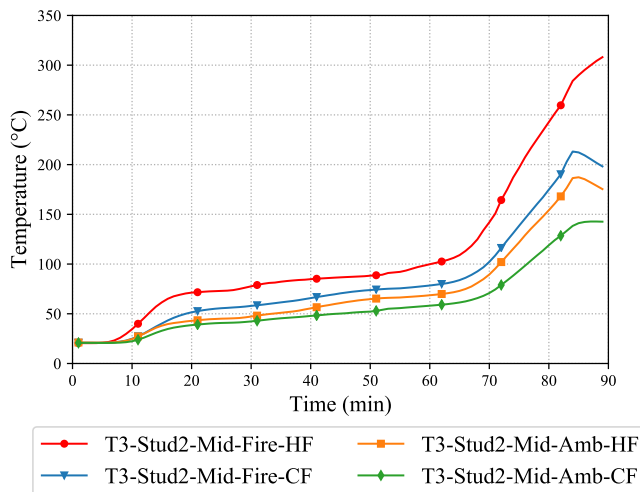


T3-Pb3-Pb4

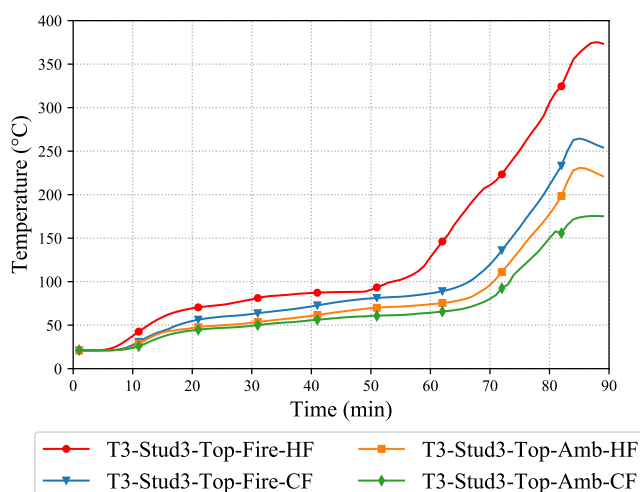


T3-Pb4

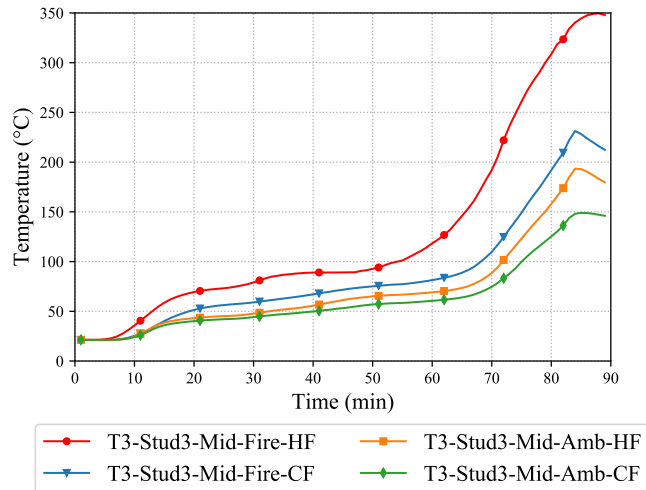
T3-Stud Time-Temperature Curves



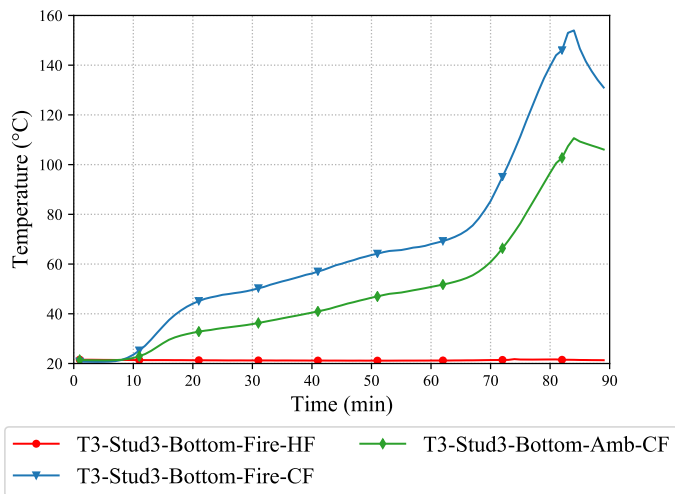
T3-Stud2-Mid



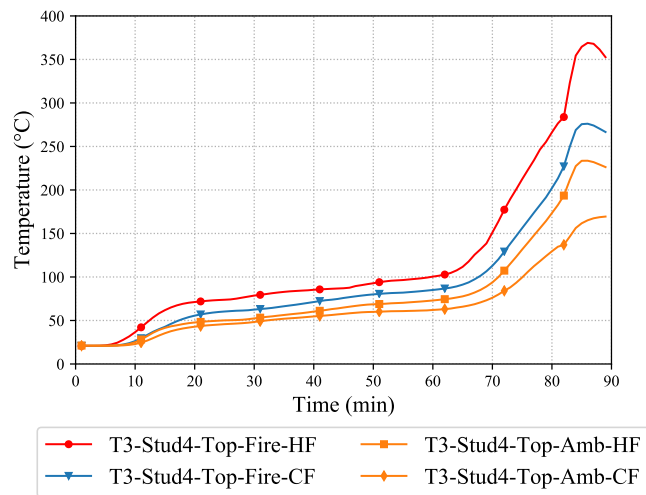
T3-Stud3-Top



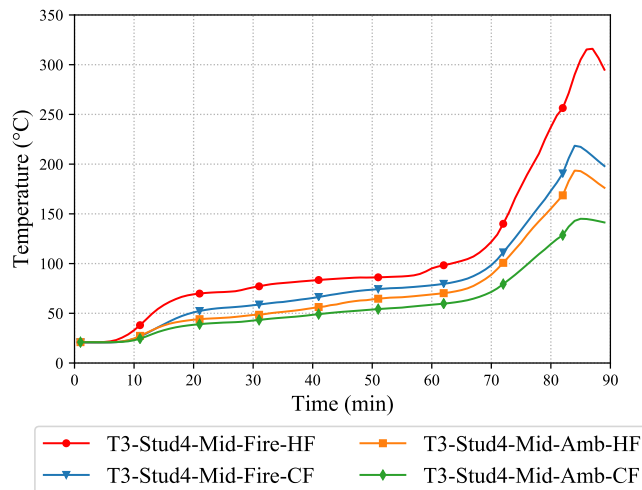
T3-Stud3-Mid



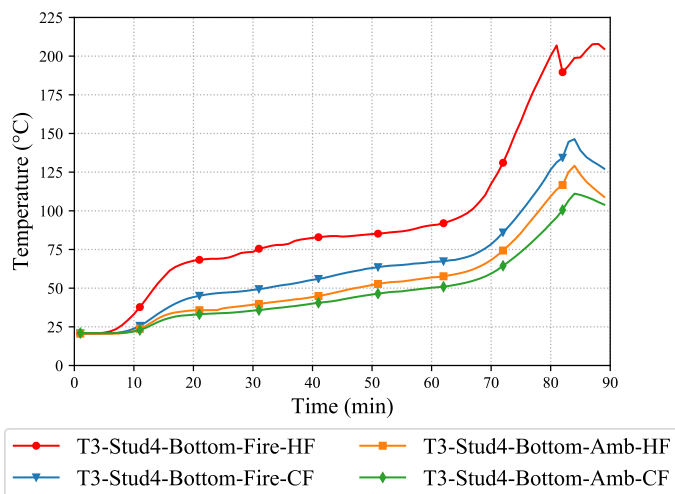
T3-Stud3-Bottom



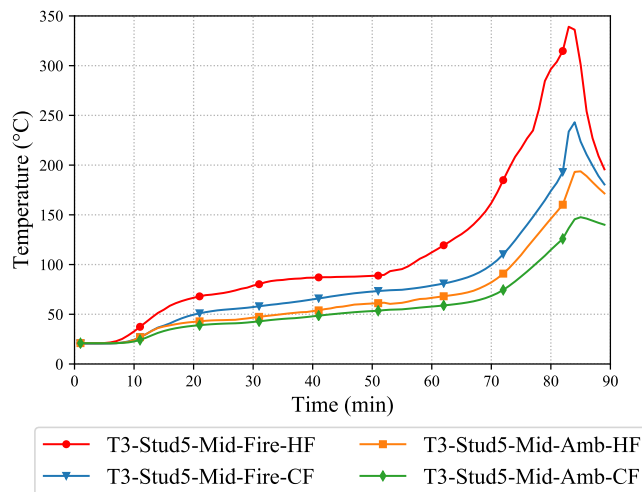
T3-Stud4-Top



T3-Stud4-Mid



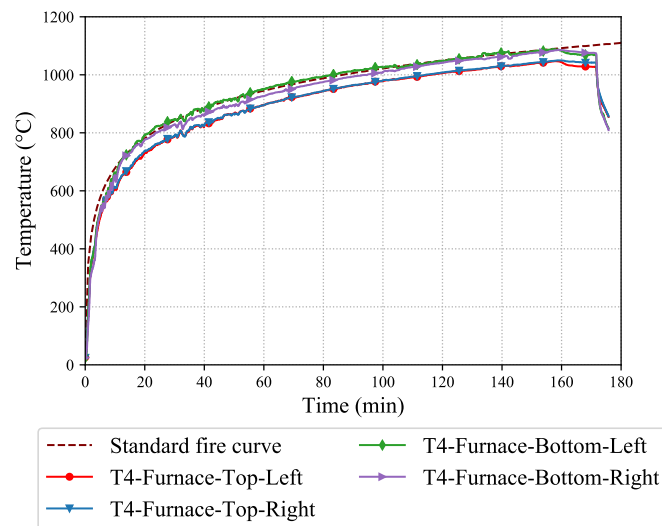
T3-Stud4-Bottom



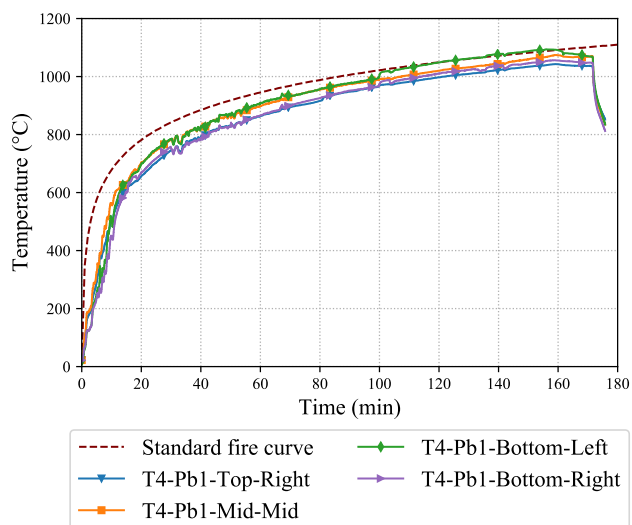
T3-Stud5-Mid

Test-T4

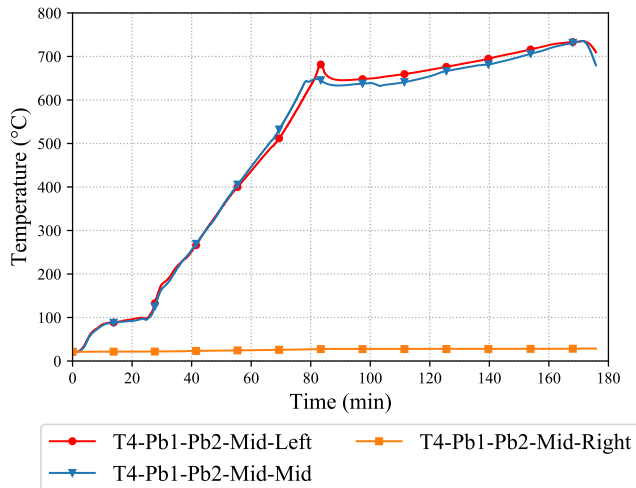
Test-T4 Plasterboard Time-Temperature Curves



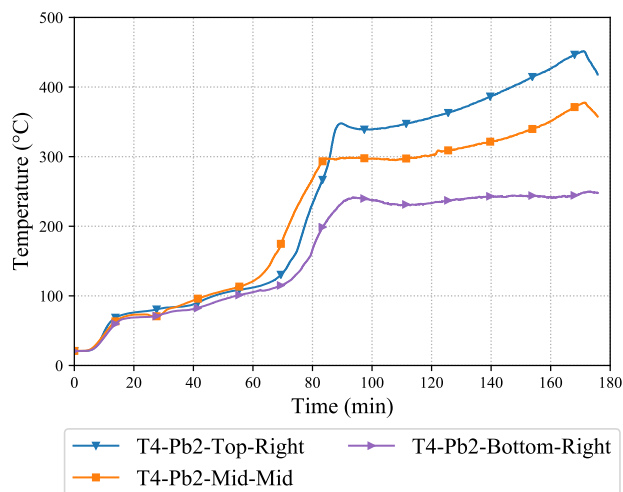
T4-Furnace



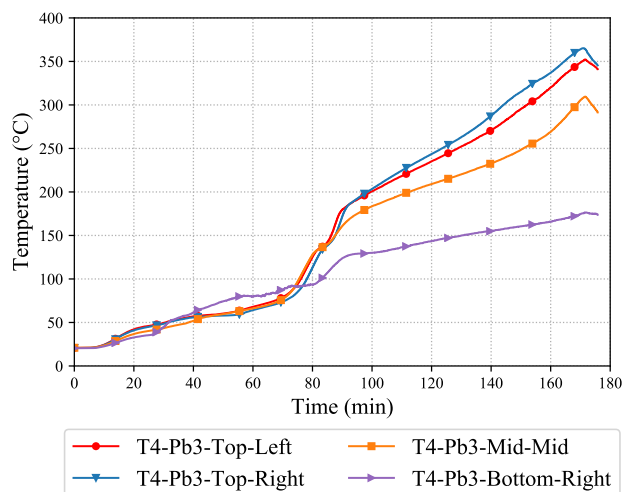
T4-Pb1



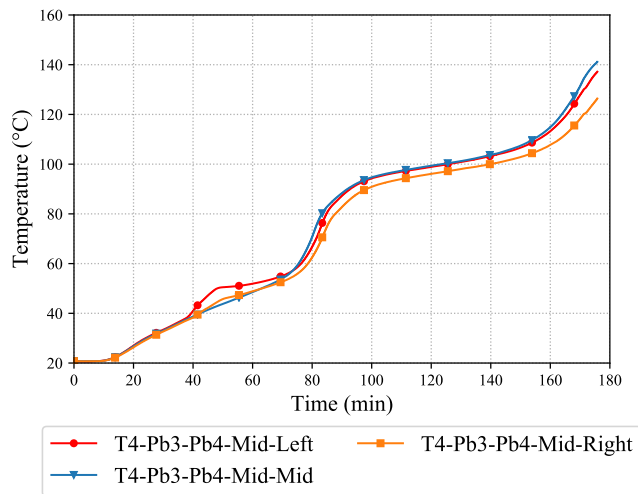
T4-Pb1-Pb2



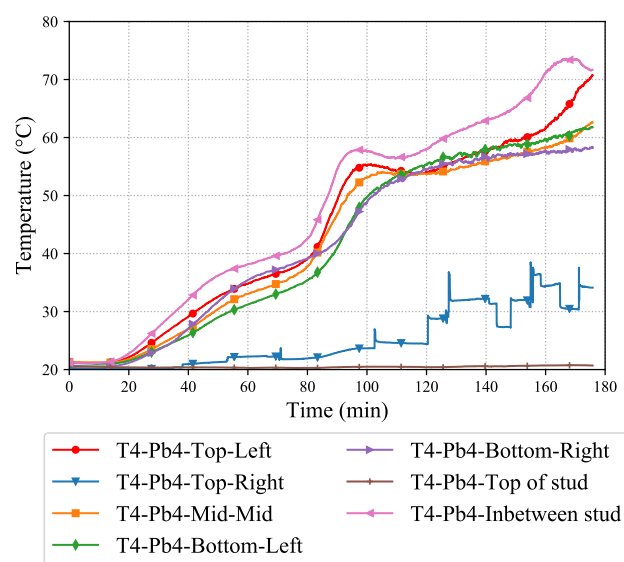
T4-Pb2



T4-Pb3

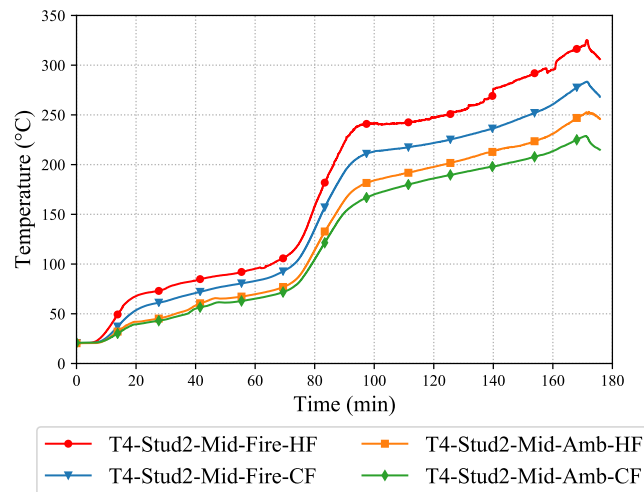


T4-Pb3-Pb4

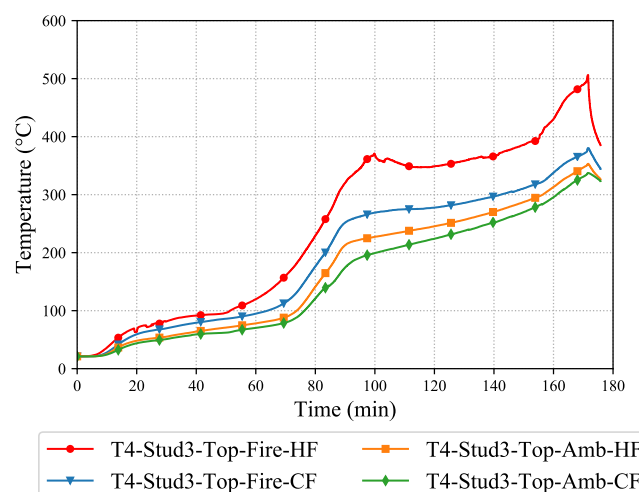


T4-Pb4

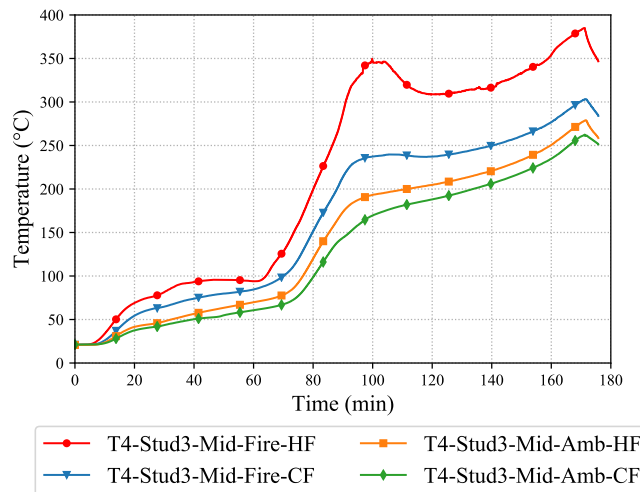
T4-Stud Time-Temperature Curves



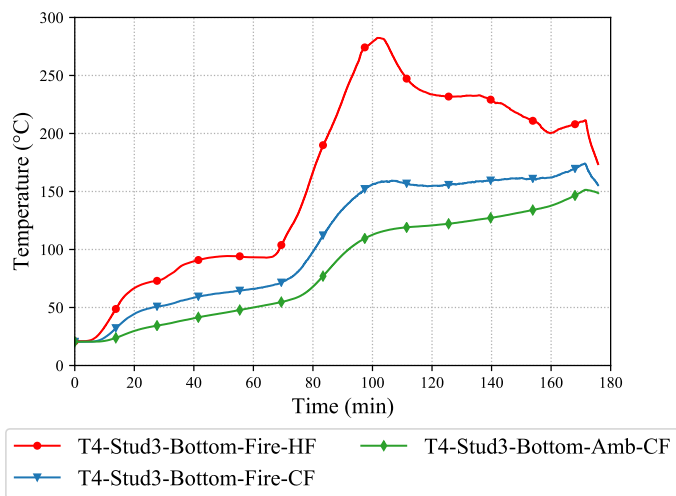
T4-Stud2-Mid



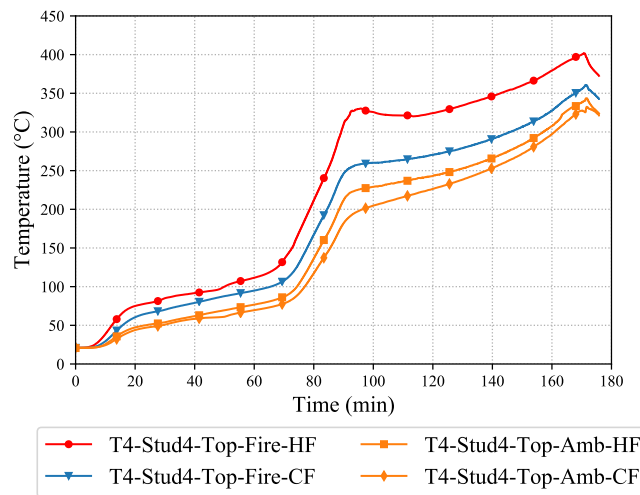
T4-Stud3-Top



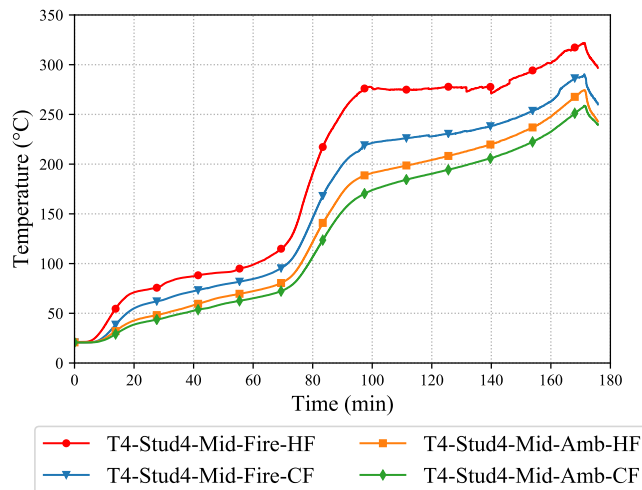
T4-Stud3-Mid



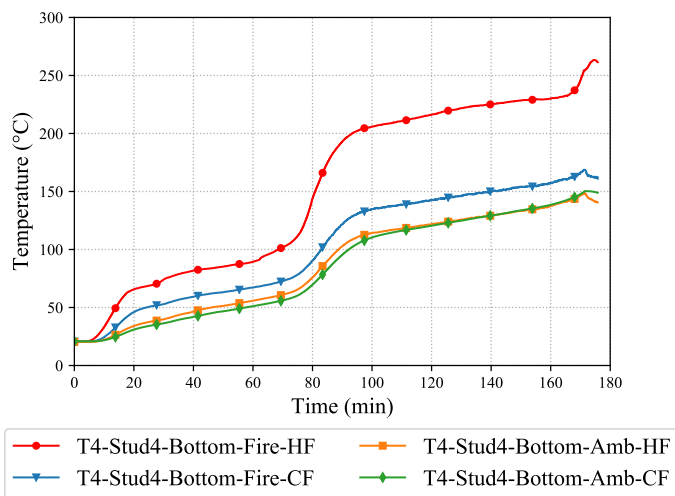
T4-Stud3-Bottom



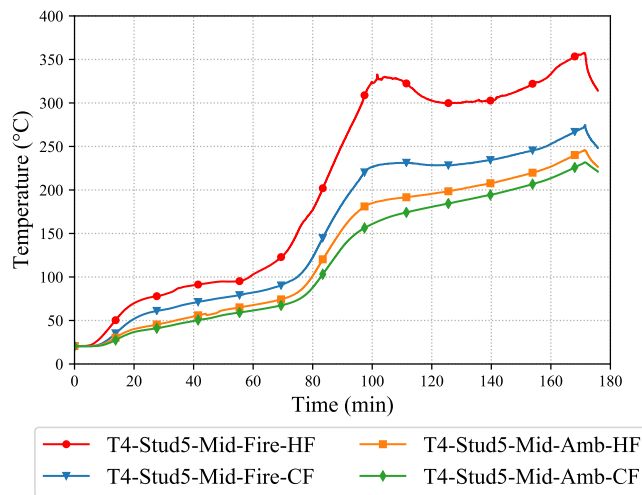
T4-Stud4-Top



T4-Stud4-Mid



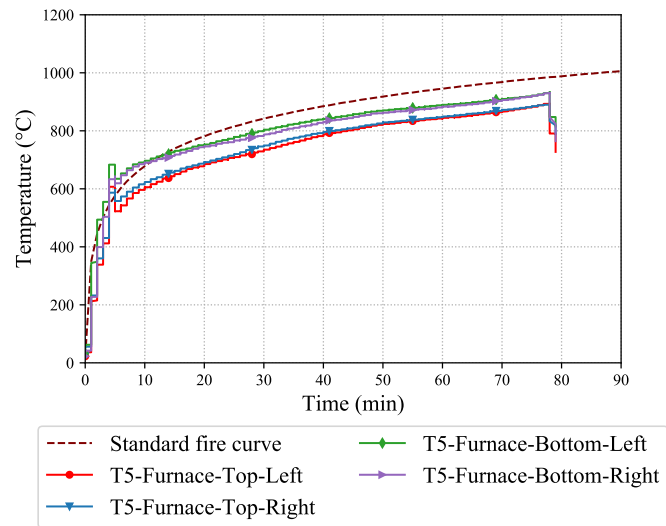
T4-Stud4-Bottom



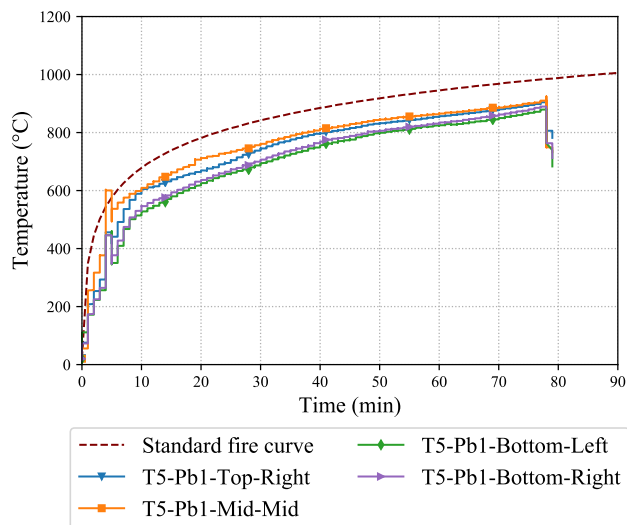
T4-Stud5-Mid

Test-T5

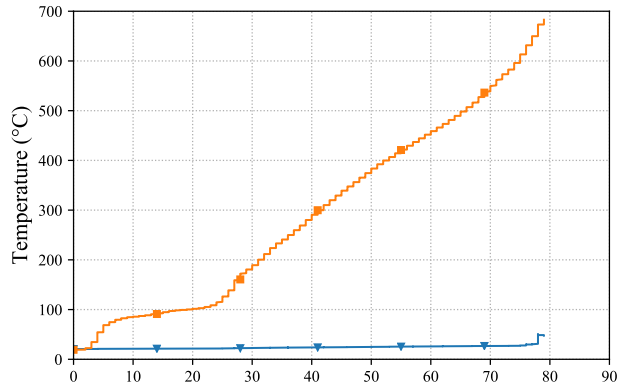
Test-T5 Plasterboard Time-Temperature Curves



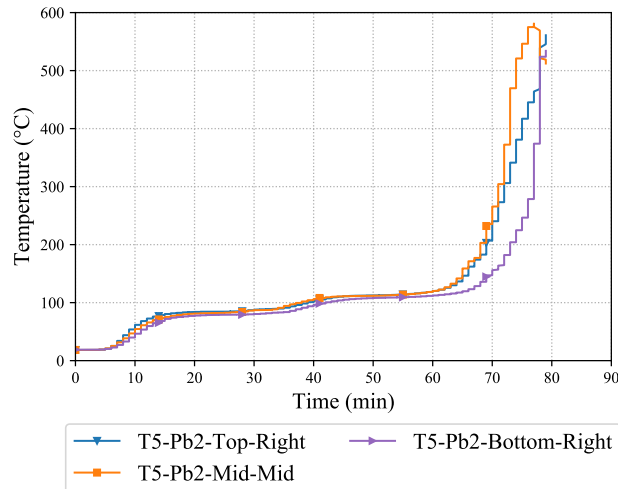
T5-Furnace



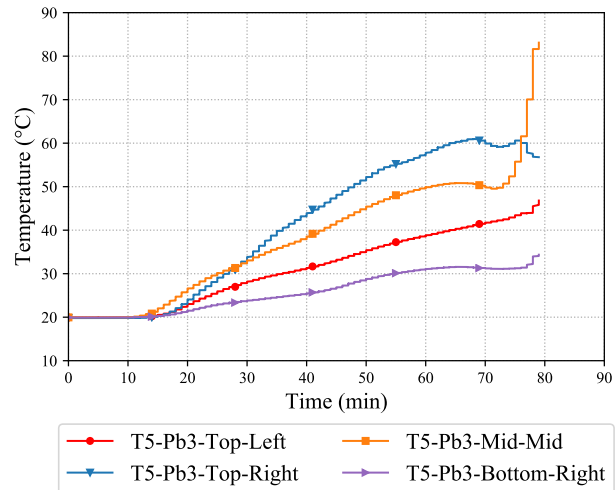
T5-Pb1



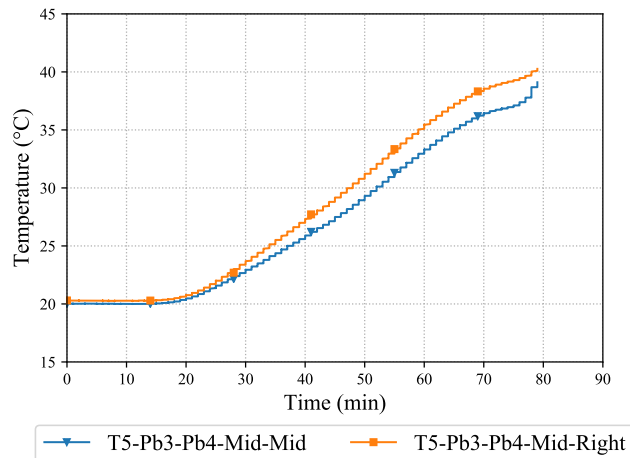
T5-Pb1-Pb2



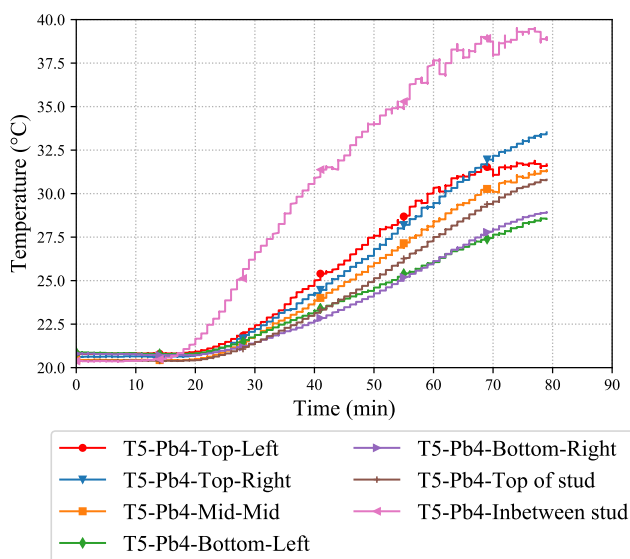
T5-Pb2



T5-Pb3

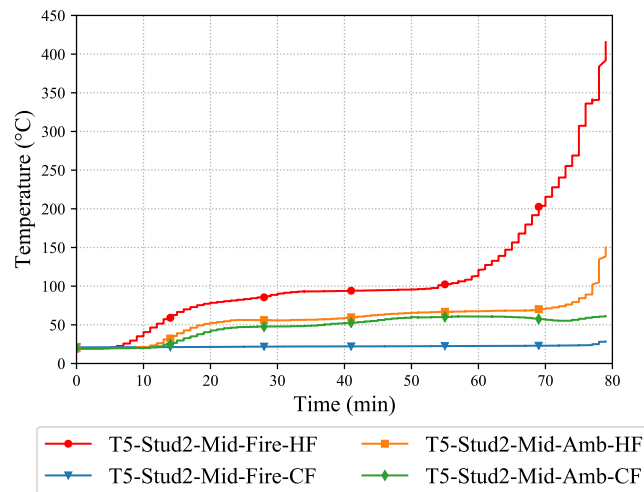


T5-Pb3-Pb4

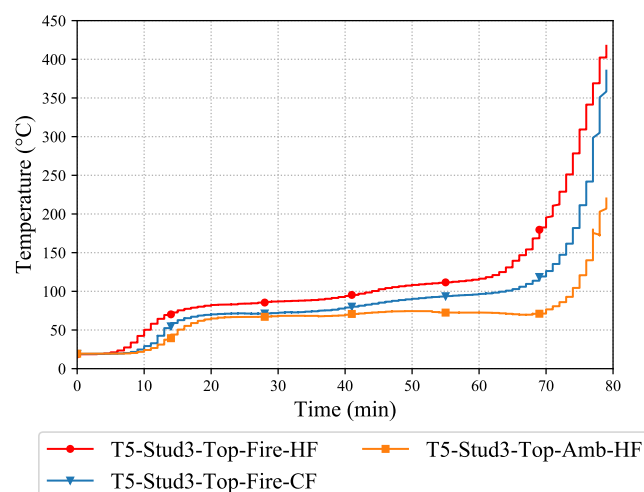


T5-Pb4

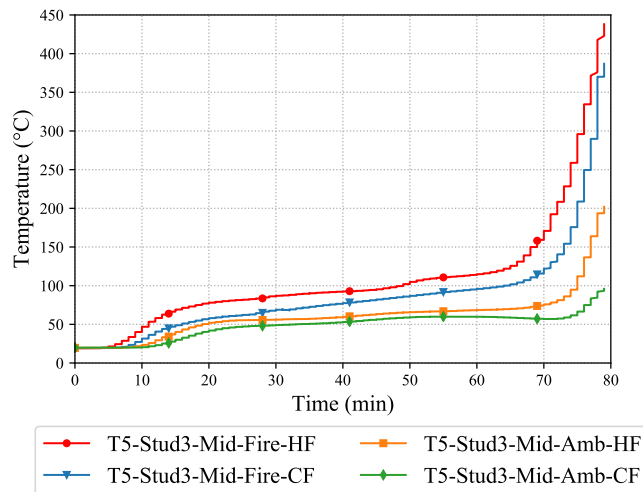
T5-Stud Time-Temperature Curves



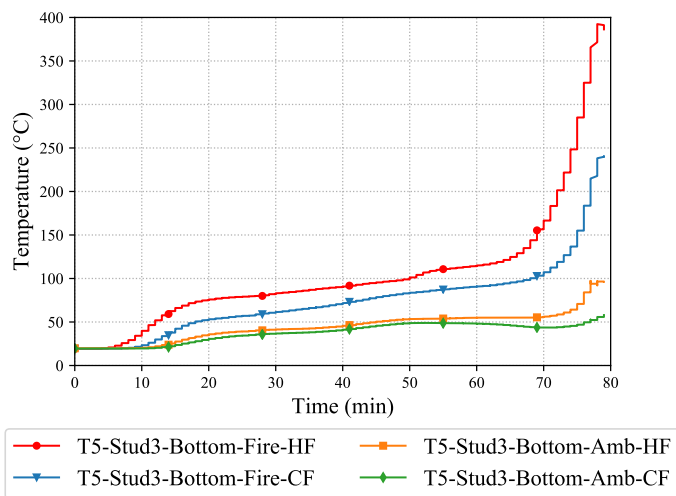
T5-Stud2-Mid



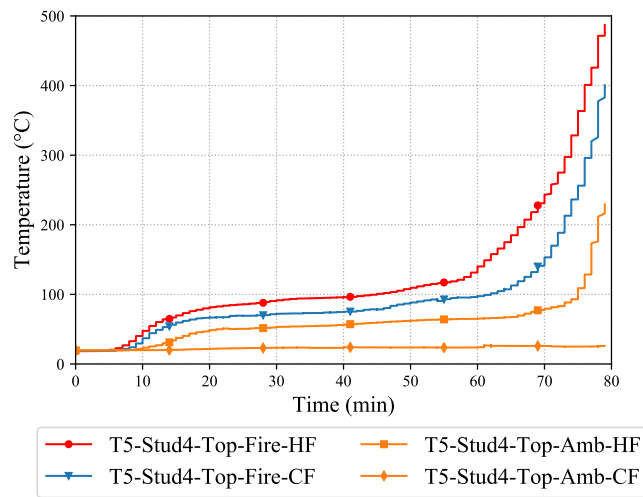
T5-Stud3-Top



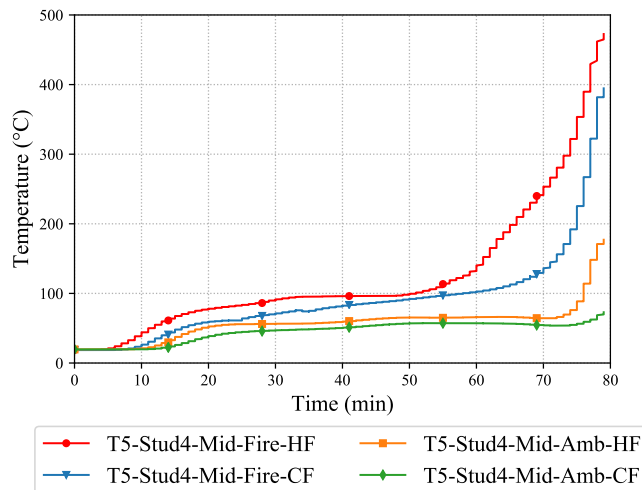
T5-Stud3-Mid



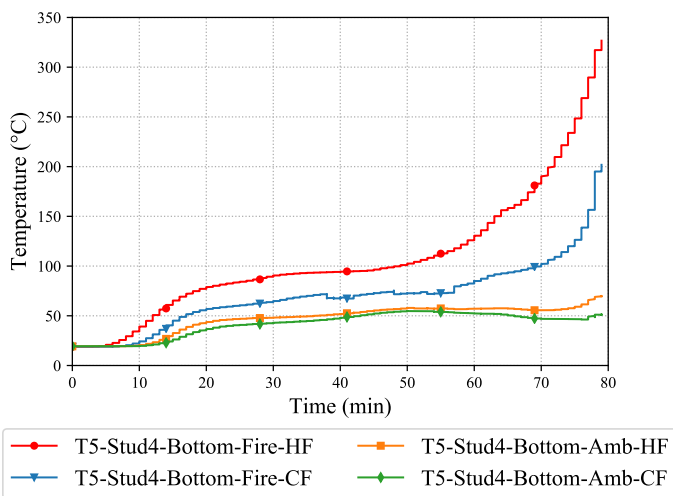
T5-Stud3-Bottom



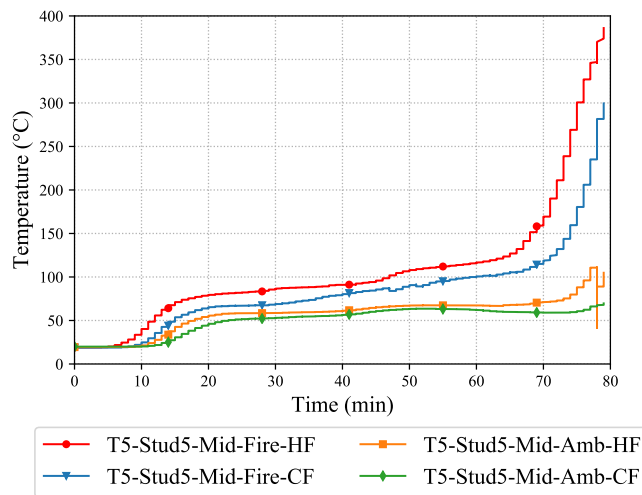
T5-Stud4-Top



T5-Stud4-Mid



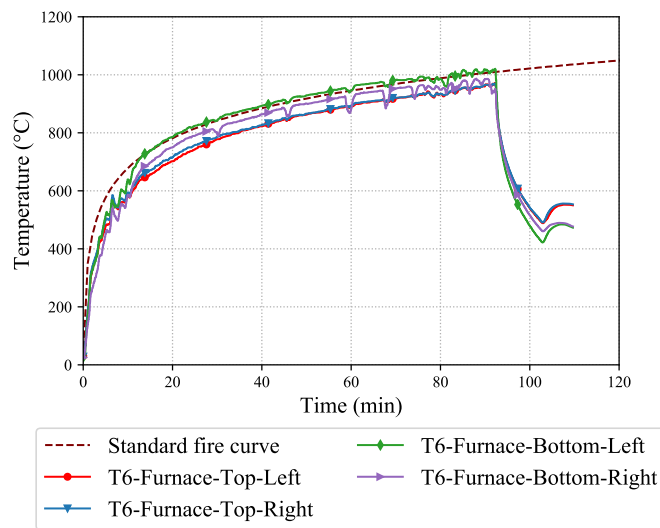
T5-Stud4-Bottom



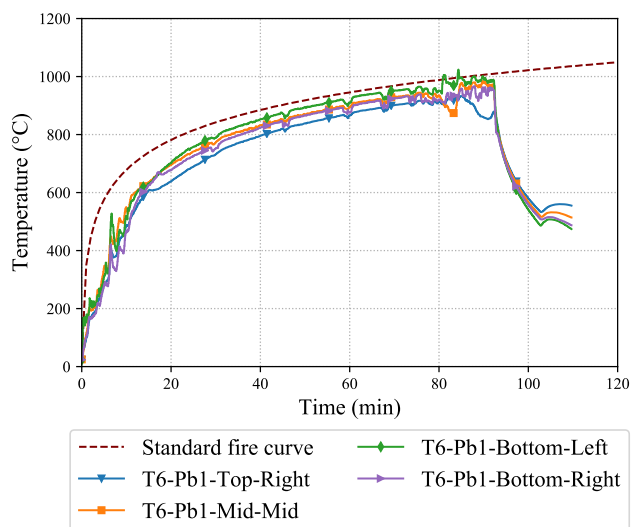
T5-Stud5-Mid

Test-T6

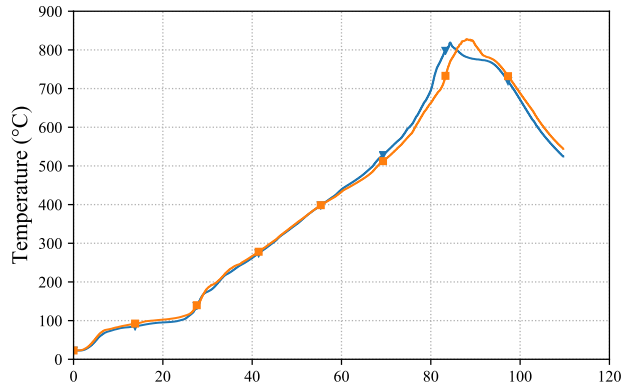
Test-T6 Plasterboard Time-Temperature Curves



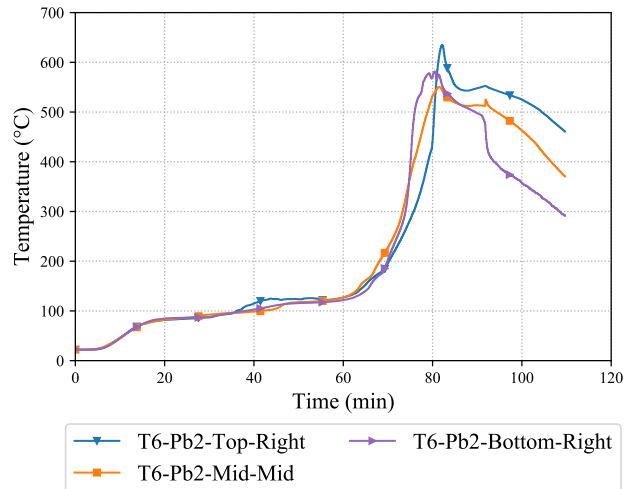
T6-Furnace



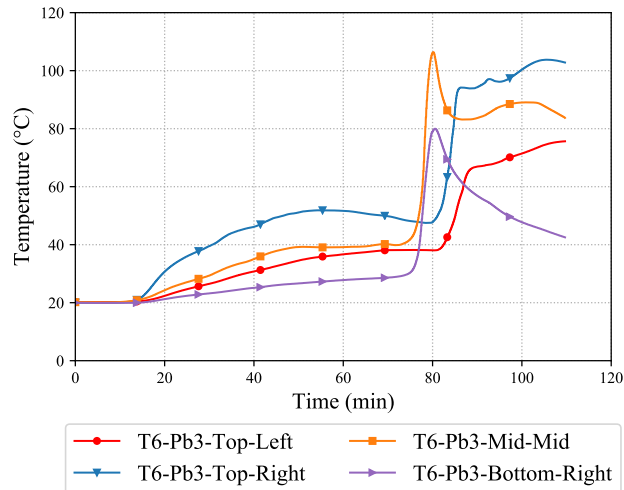
T6-Pb1



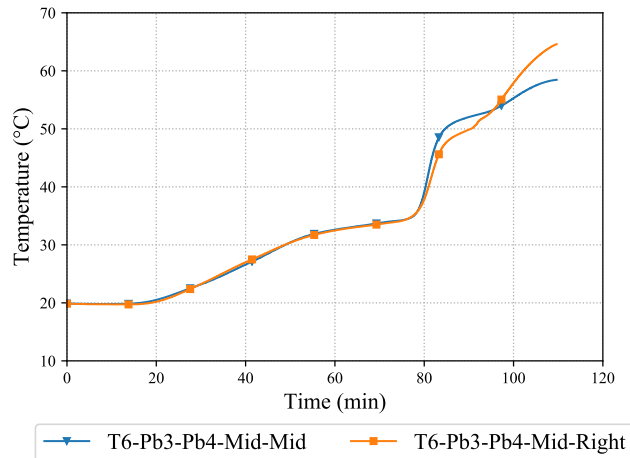
T6-Pb1-Pb2



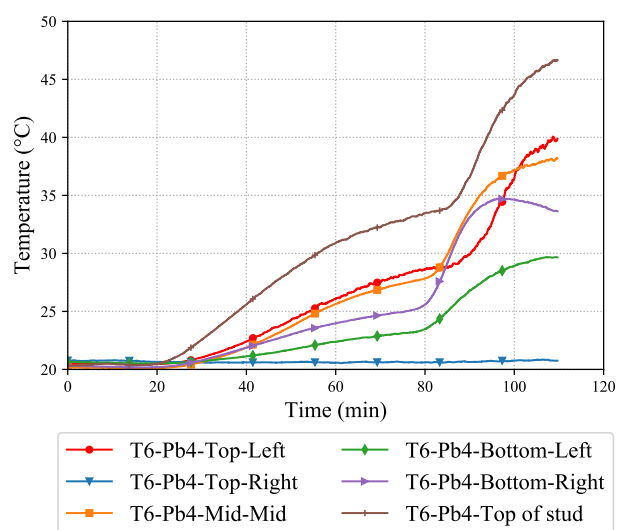
T6-Pb2



T6-Pb3

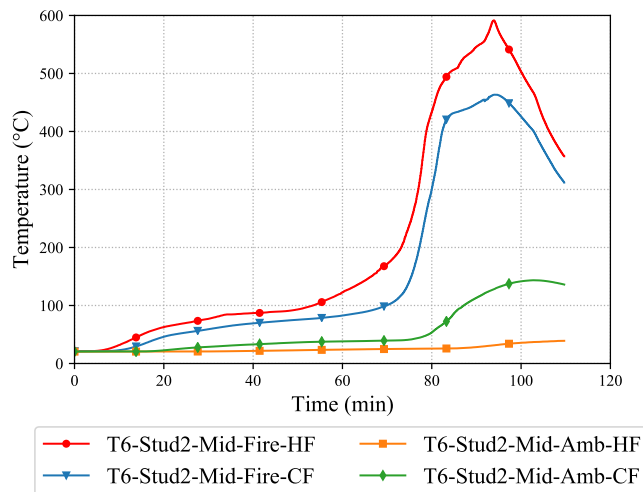


T6-Pb3-Pb4

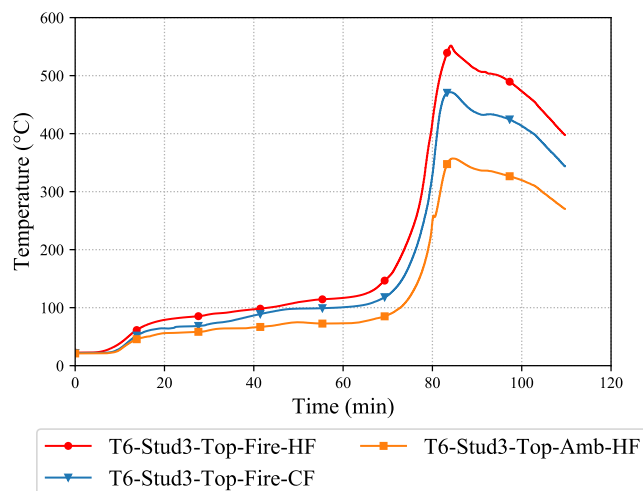


T6-Pb4

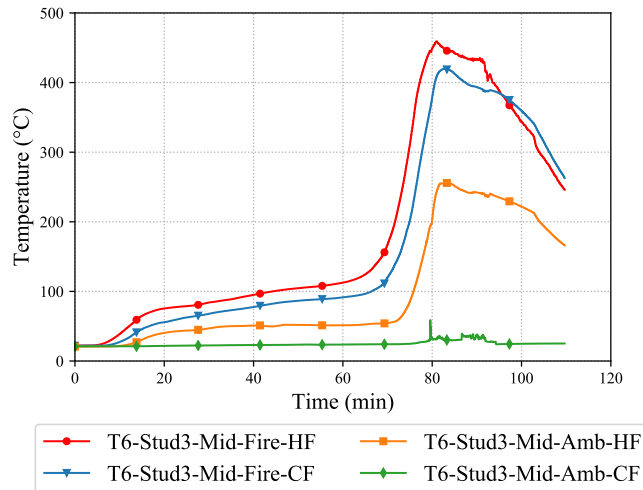
T6-Stud Time-Temperature Curves



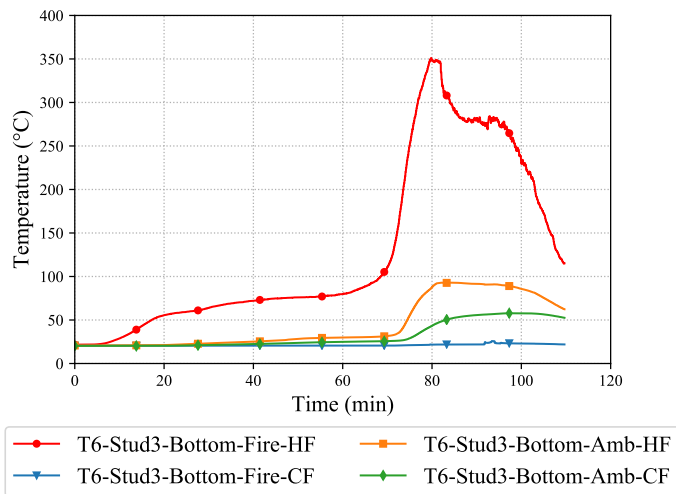
T6-Stud2-Mid



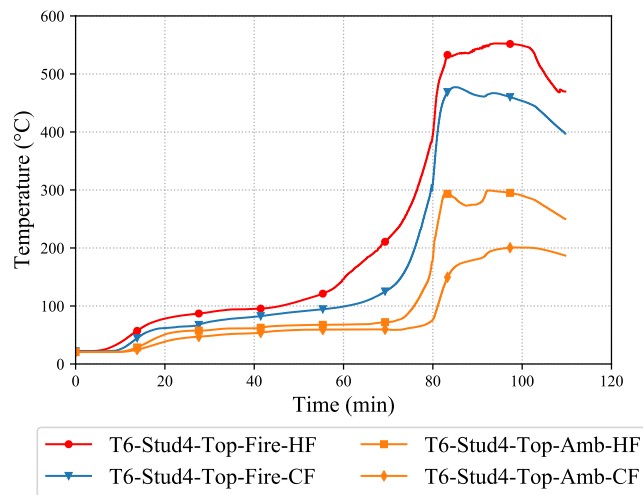
T6-Stud3-Top



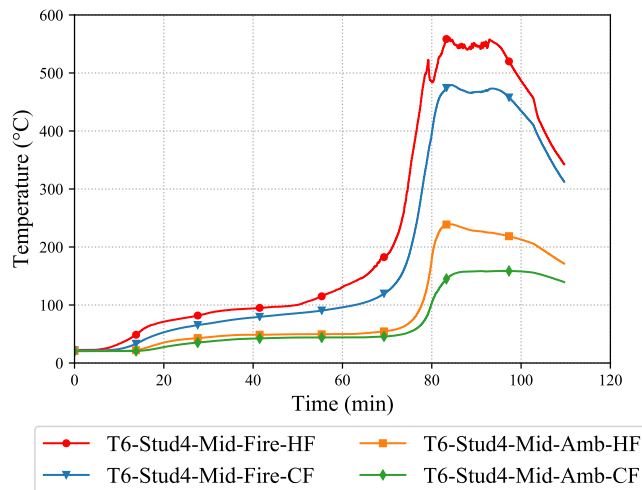
T6-Stud3-Mid



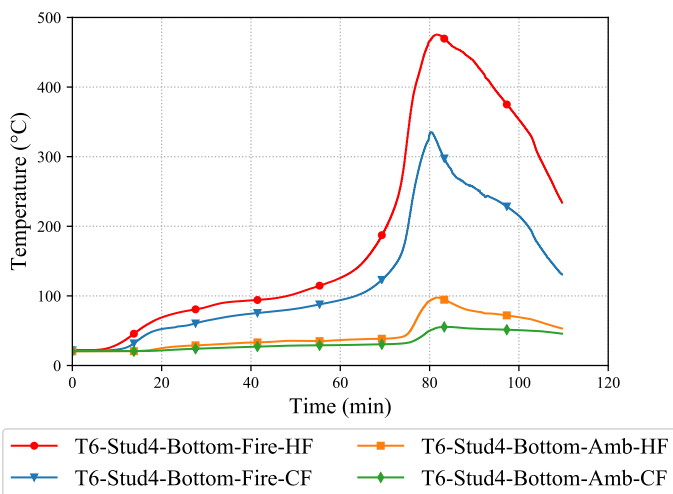
T6-Stud3-Bottom



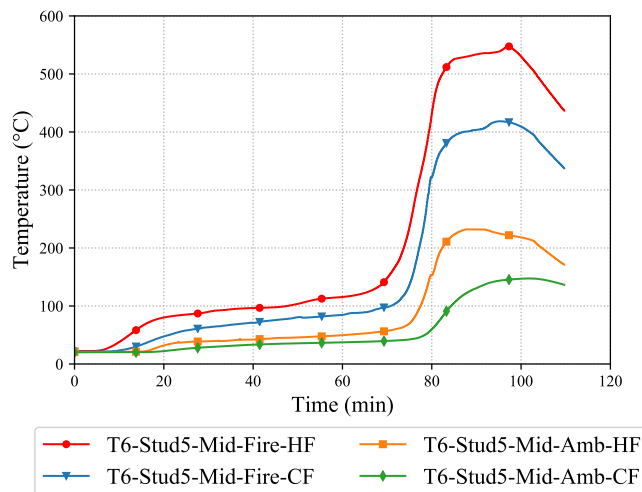
T6-Stud4-Top



T6-Stud4-Mid



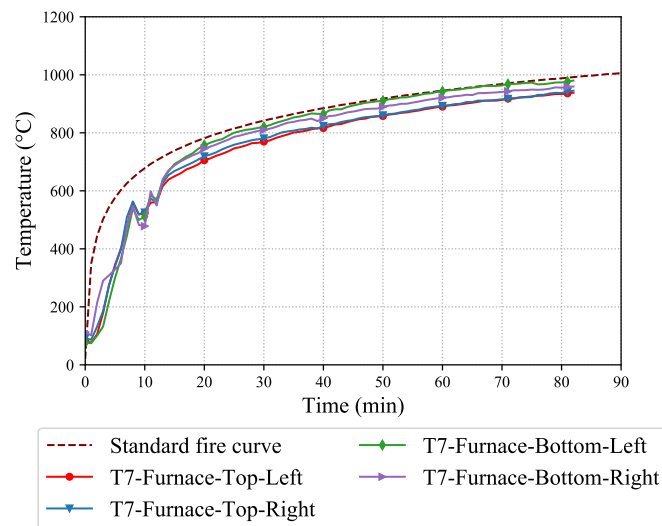
T6-Stud4-Bottom



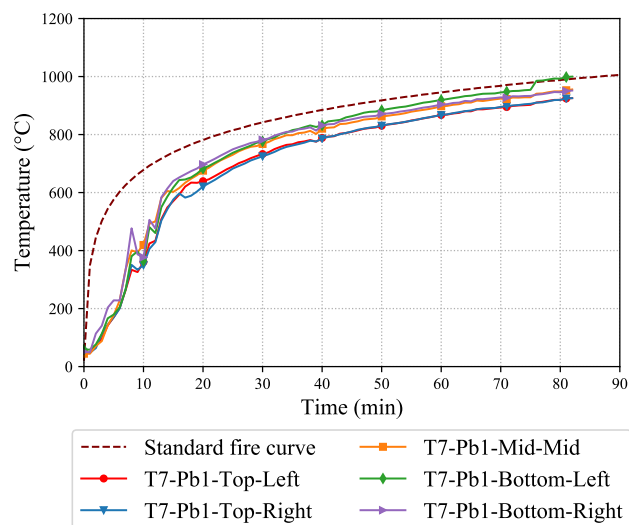
T6-Stud5-Mid

Test-T7

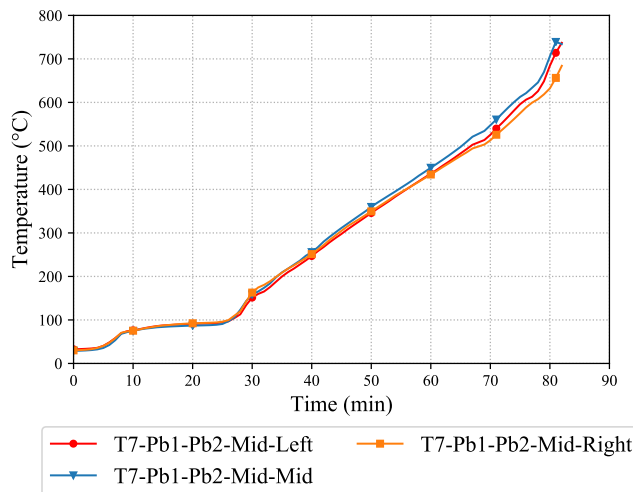
Test-T7 Plasterboard Time-Temperature Curves



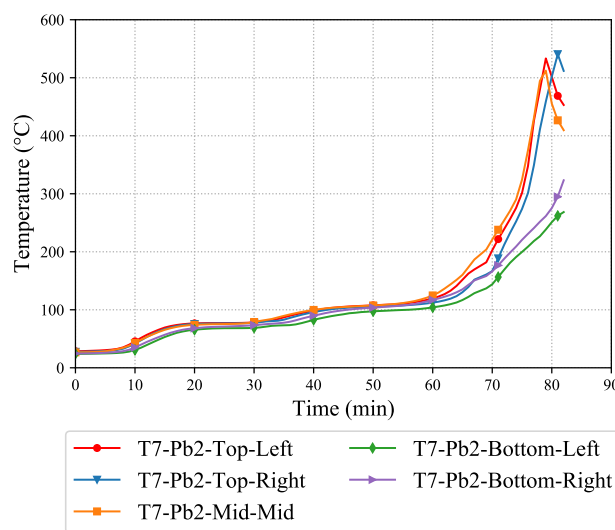
T7-Furnace



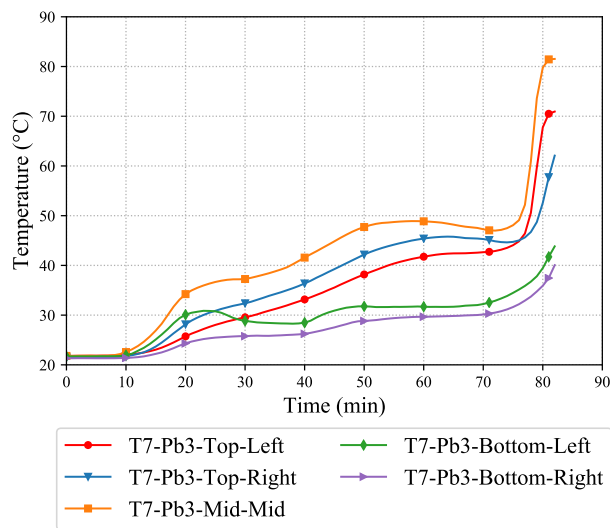
T7-Pb1



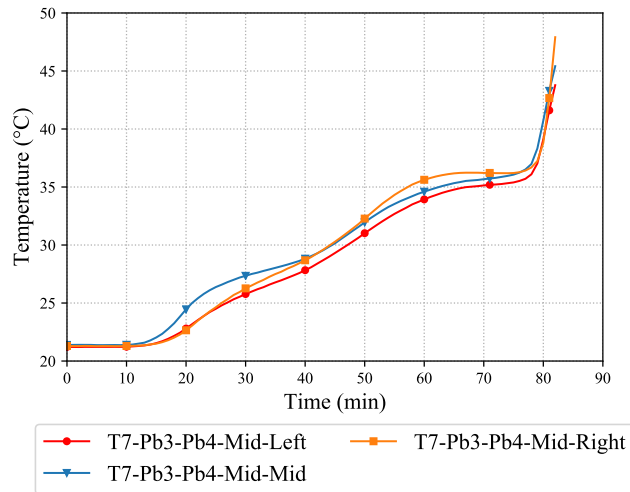
T7-Pb1-Pb2



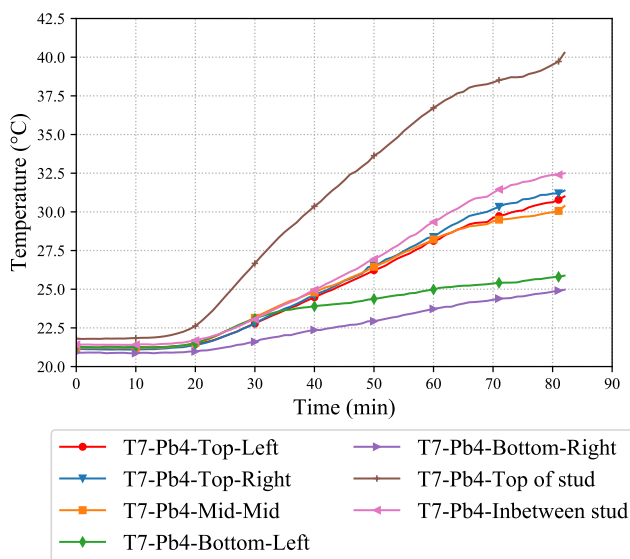
T7-Pb2



T7-Pb3

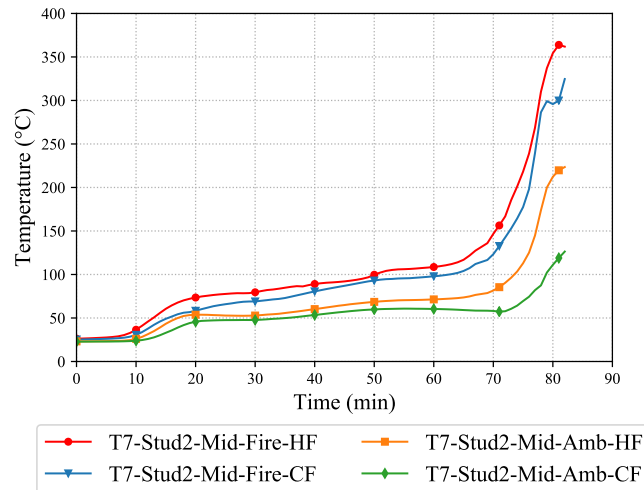


T7-Pb3-Pb4

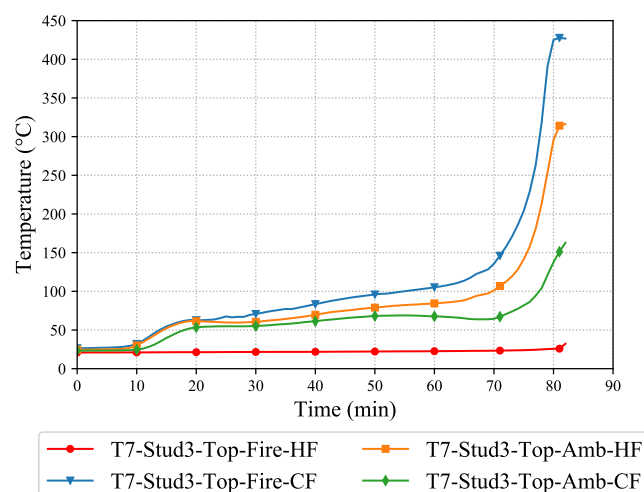


T7-Pb4

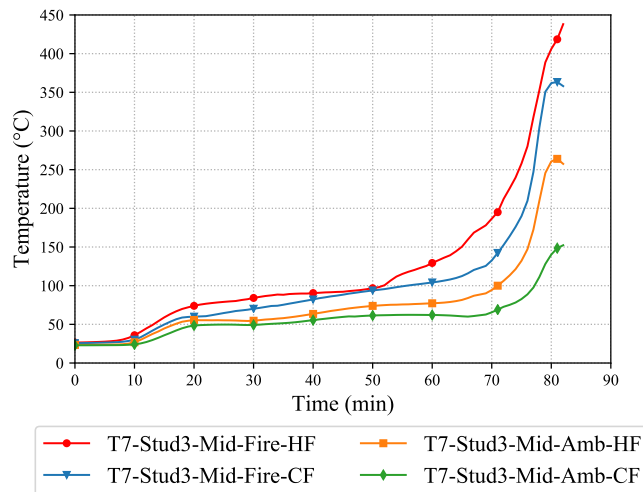
T7-Stud Time-Temperature Curves



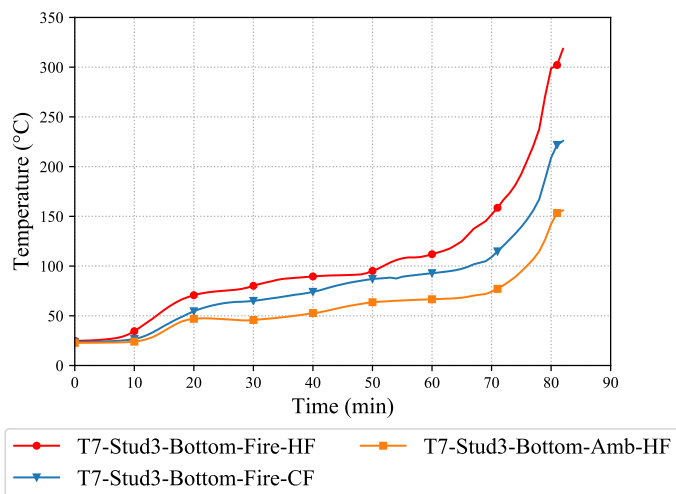
T7-Stud2-Mid



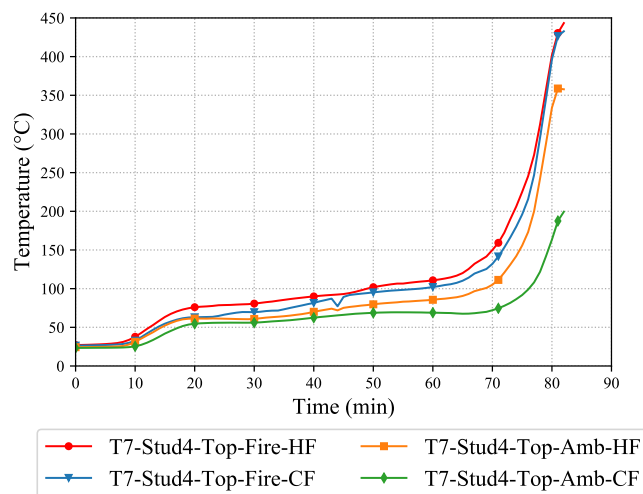
T7-Stud3-Top



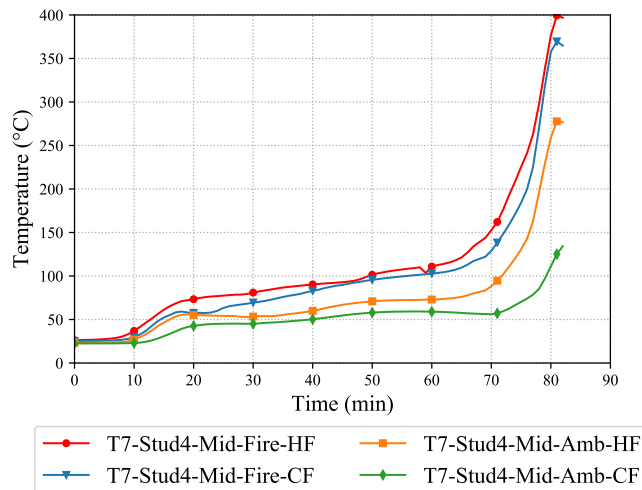
T7-Stud3-Mid



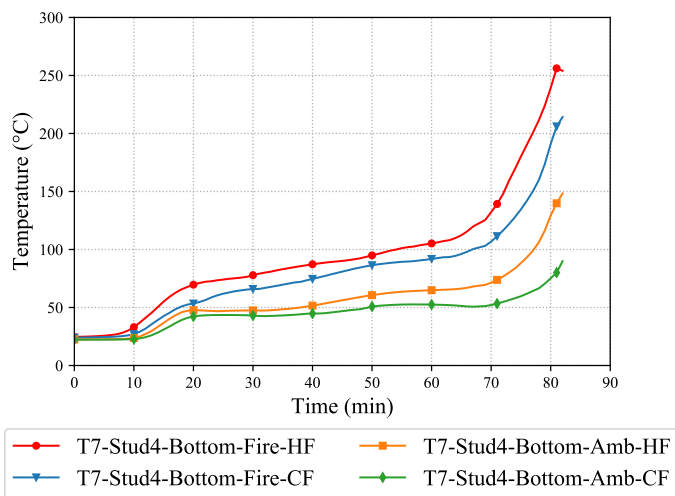
T7-Stud3-Bottom



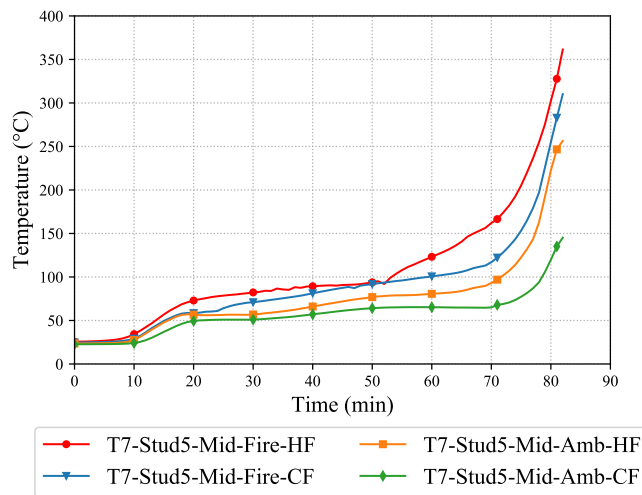
T7-Stud4-Top



T7-Stud4-Mid



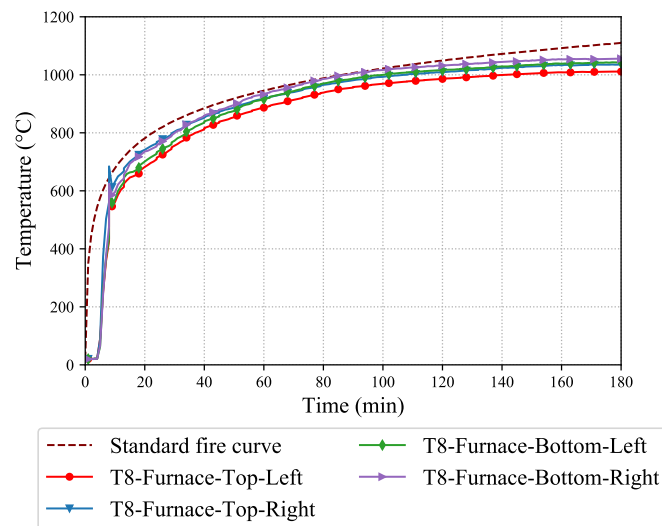
T7-Stud4-Bottom



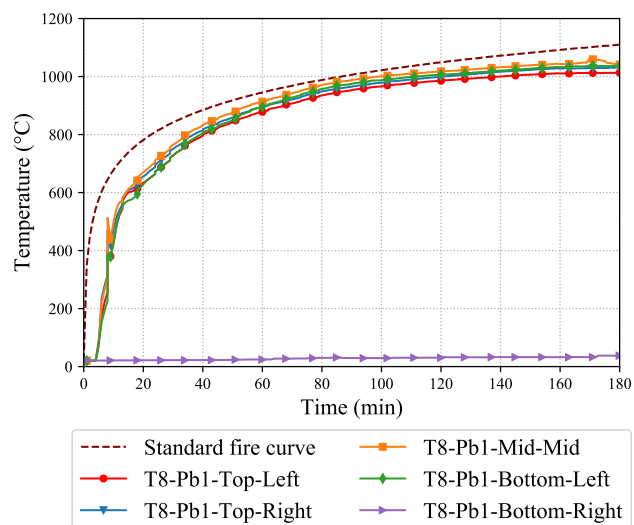
T7-Stud5-Mid

Test-T8

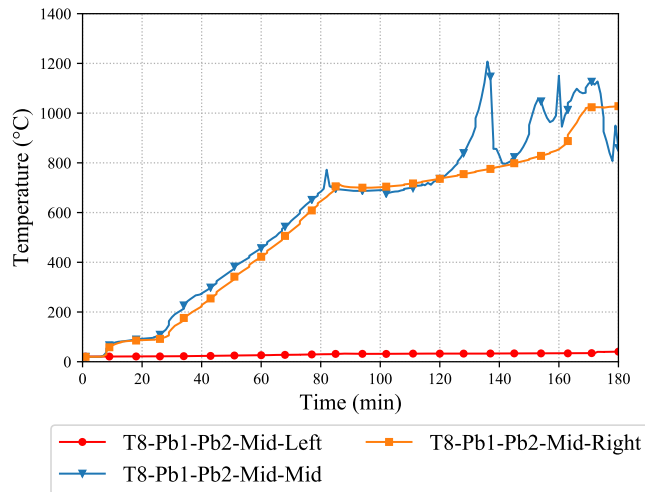
Test-T8 Plasterboard Time-Temperature Curves



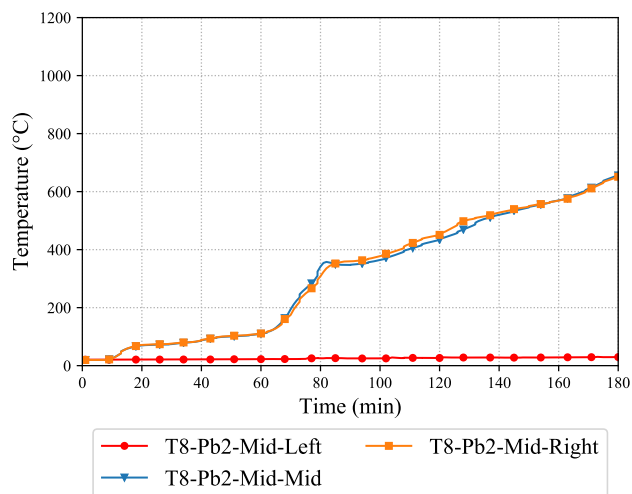
T8-Furnace



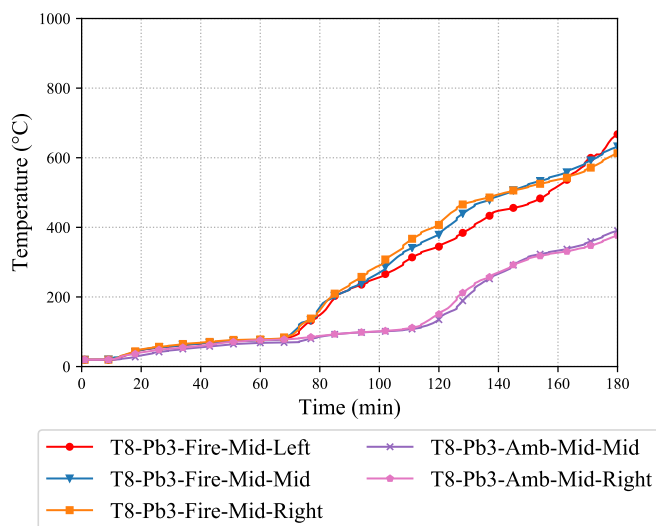
T8-Pb1



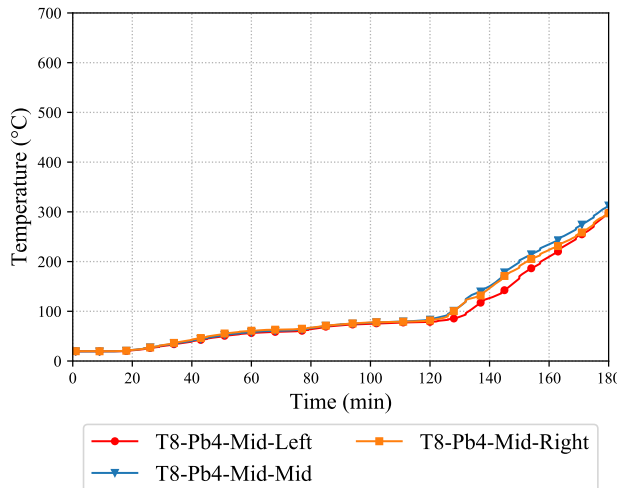
T8-Pb1-Pb2



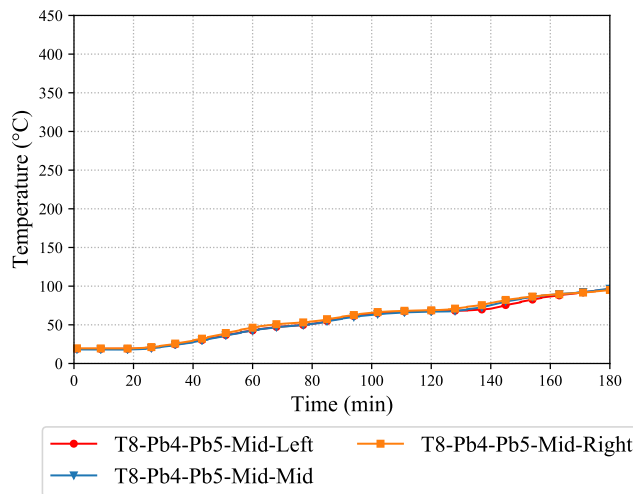
T8-Pb2



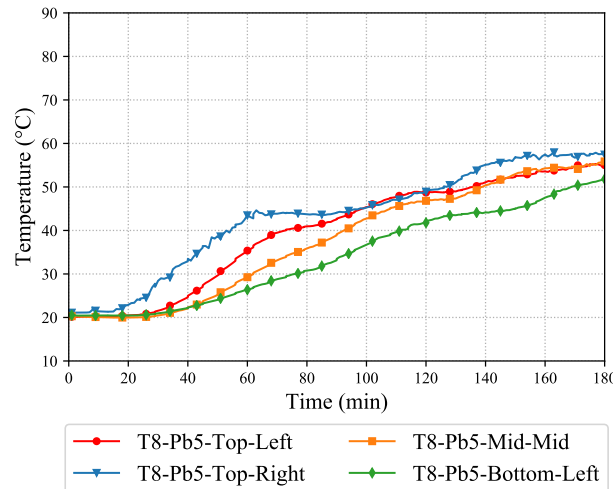
T8-Pb3



T8-Pb3

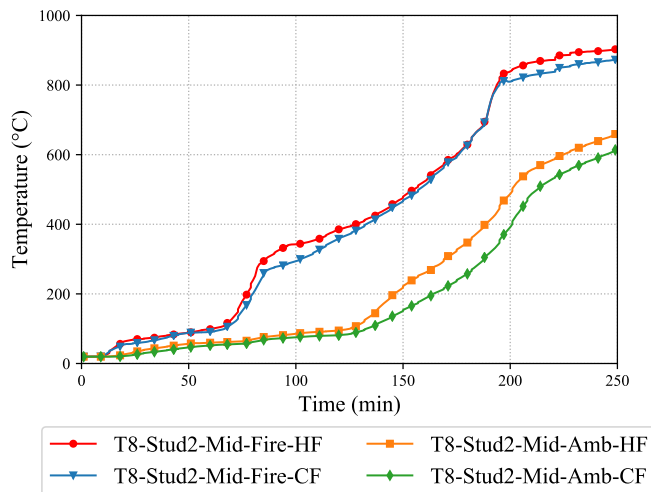


T8-Pb3-Pb4

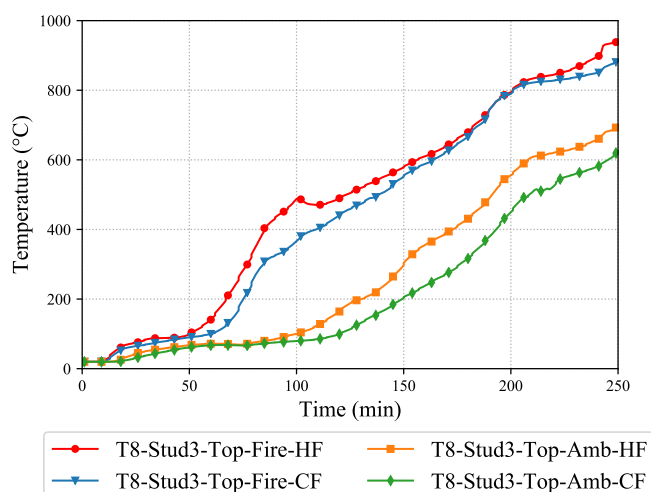


T8-Pb4

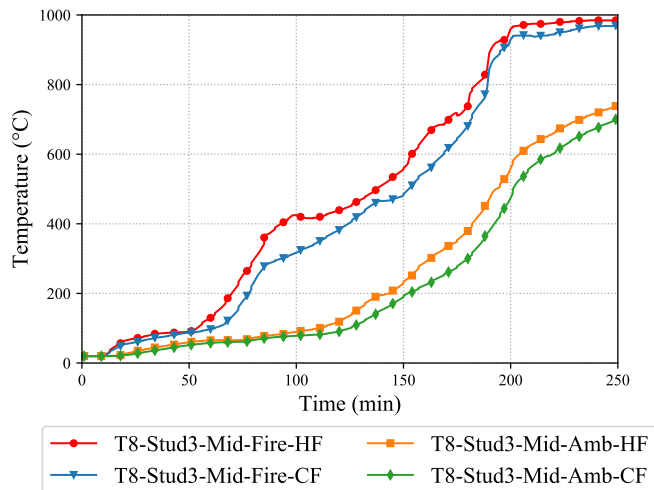
T8-Stud Time-Temperature Curves



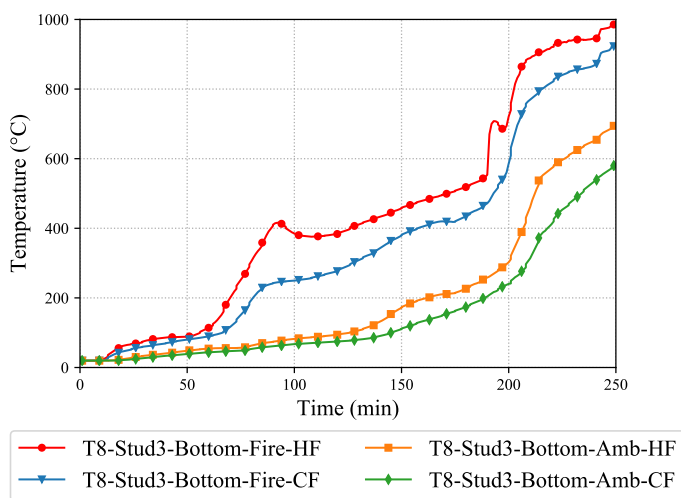
T8-Stud2-Mid



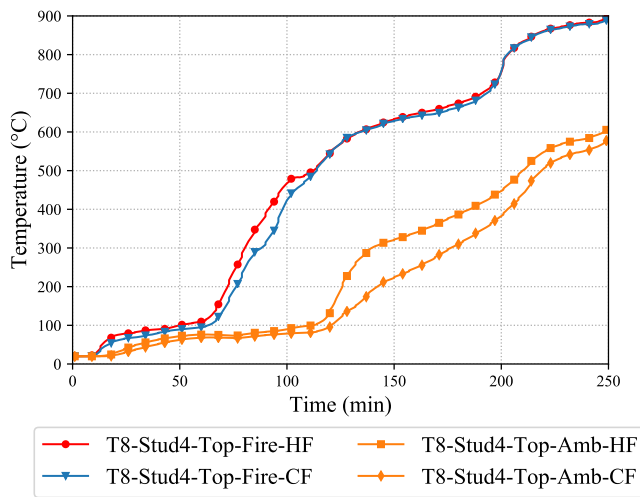
T8-Stud3-Top



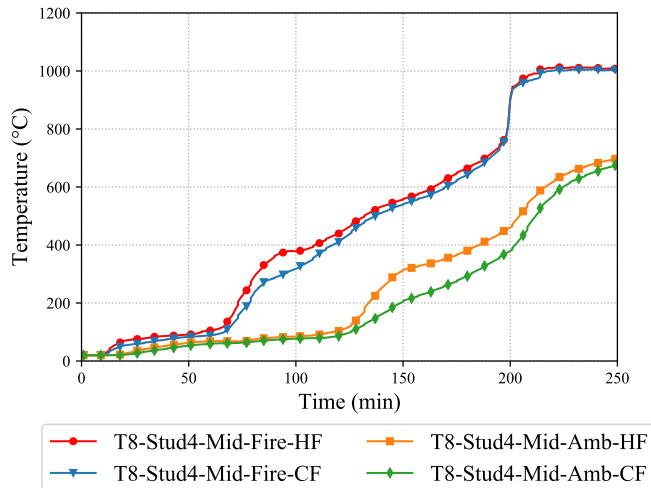
T8-Stud3-Mid



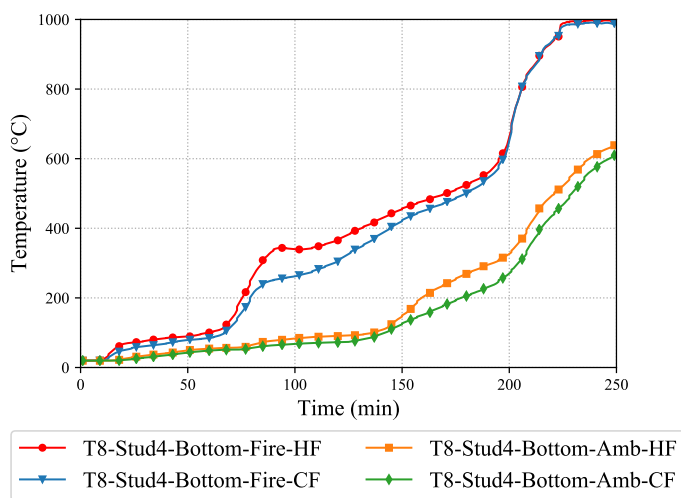
T8-Stud3-Bottom



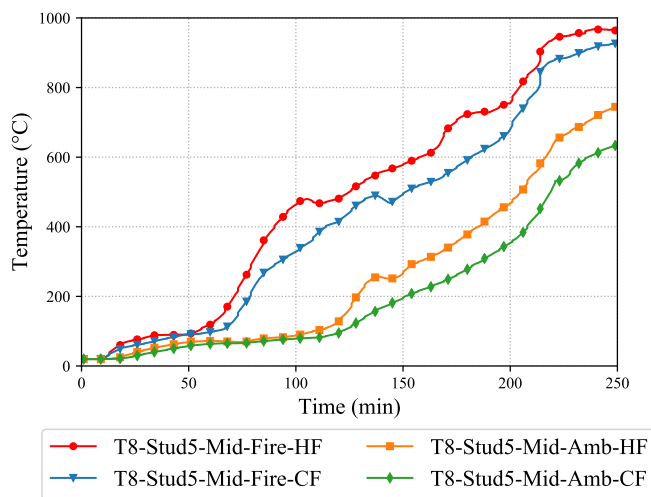
T8-Stud4-Top



T8-Stud4-Mid



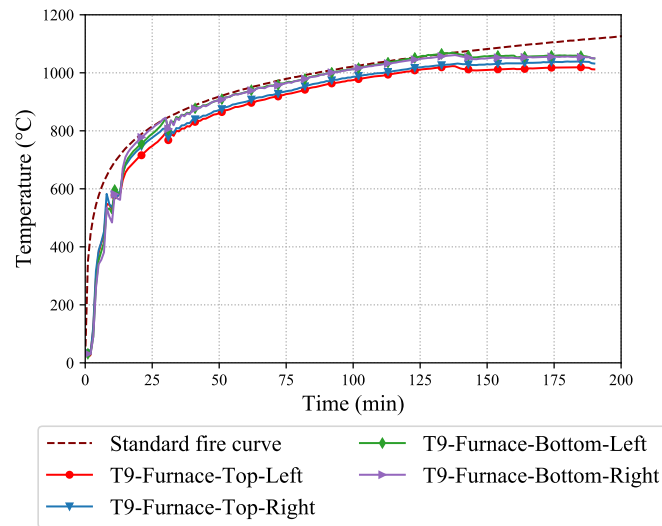
T8-Stud4-Bottom



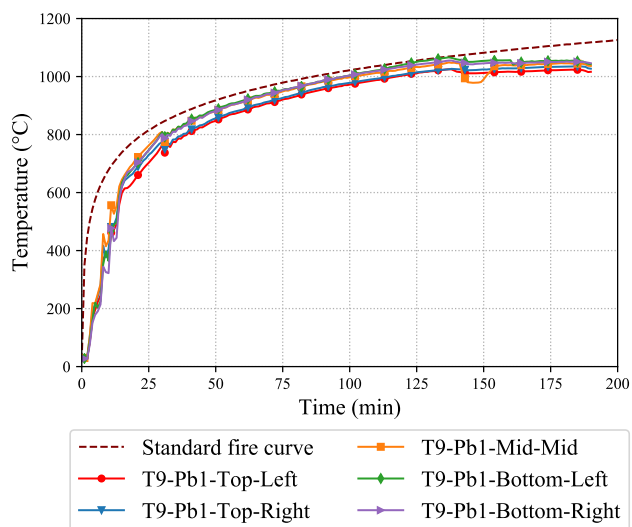
T8-Stud5-Mid

Test-T9

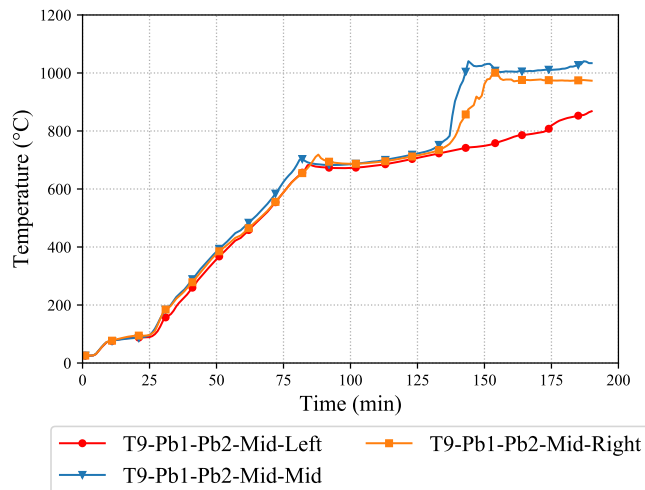
Test-T9 Plasterboard Time-Temperature Curves



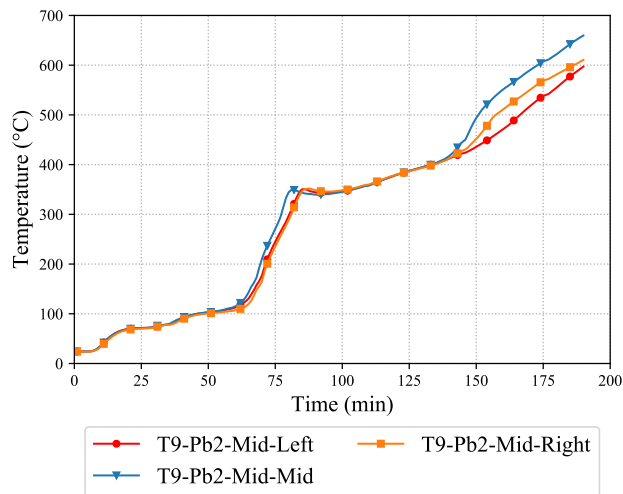
T9-Furnace



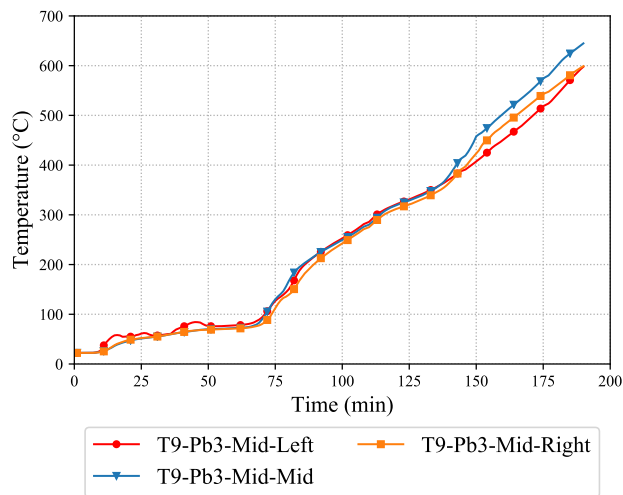
T9-Pb1



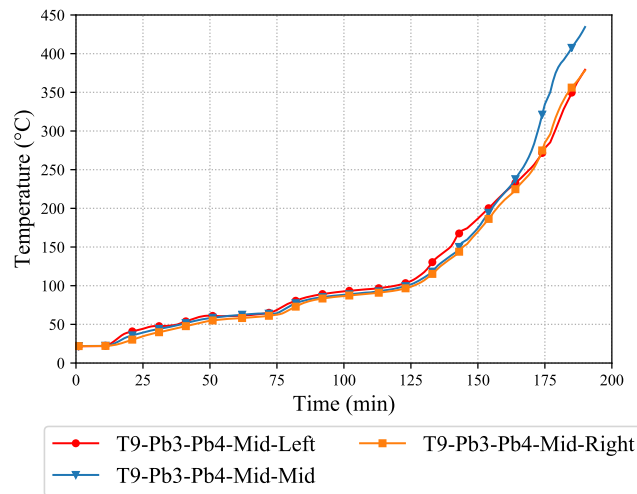
T9-Pb1-Pb2



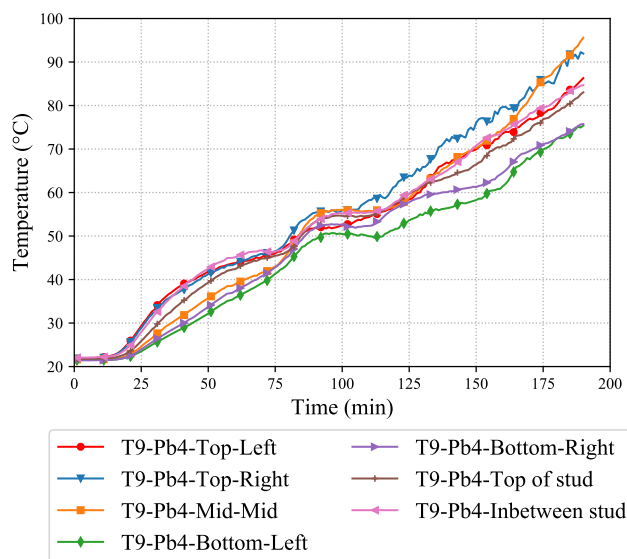
T9-Pb2



T9-Pb3

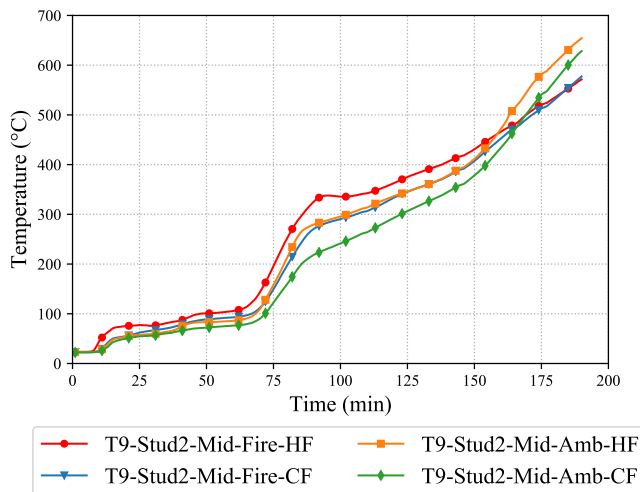


T9-Pb3-Pb4

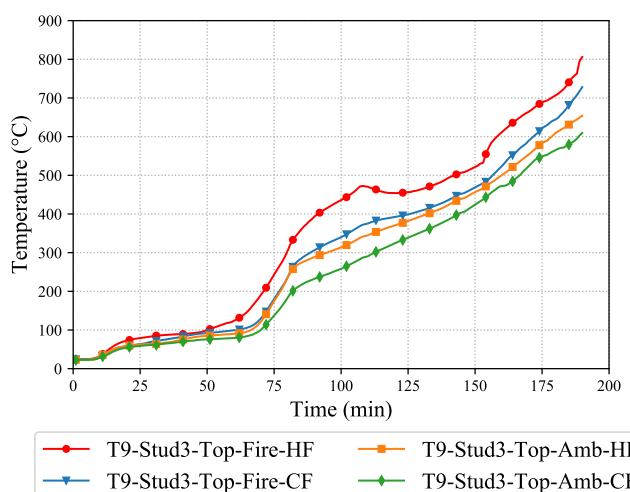


T9-Pb4

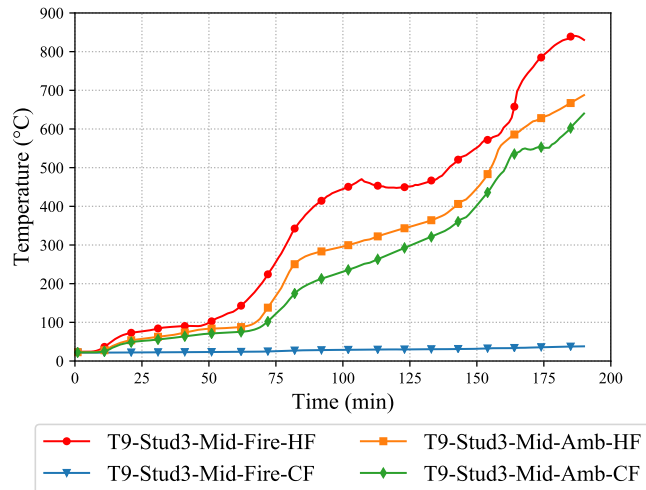
T9-Stud Time-Temperature Curves



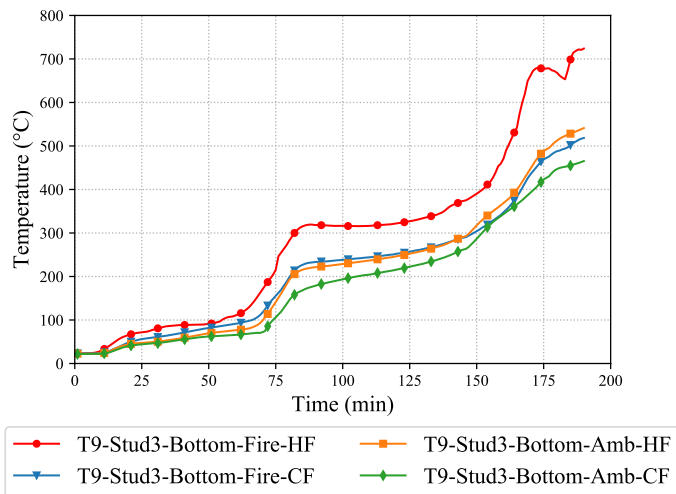
T9-Stud2-Mid



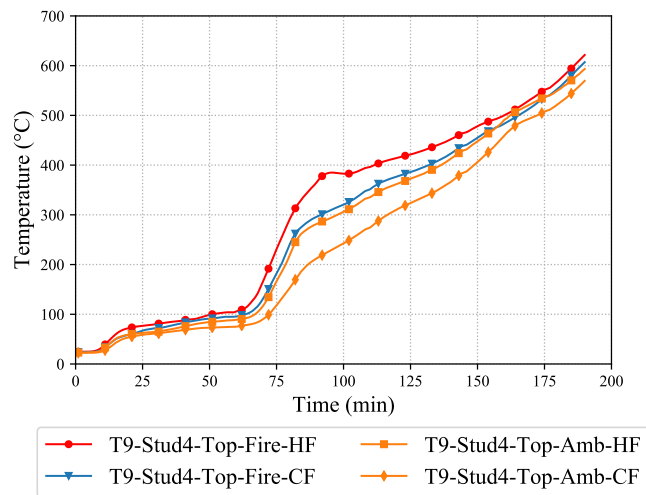
T9-Stud3-Top



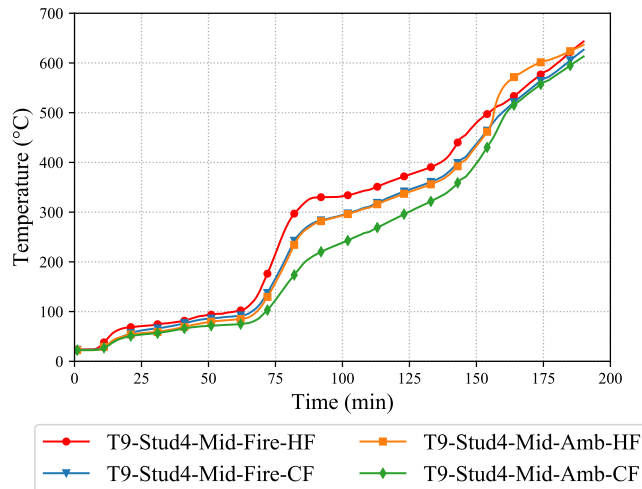
T9-Stud3-Mid



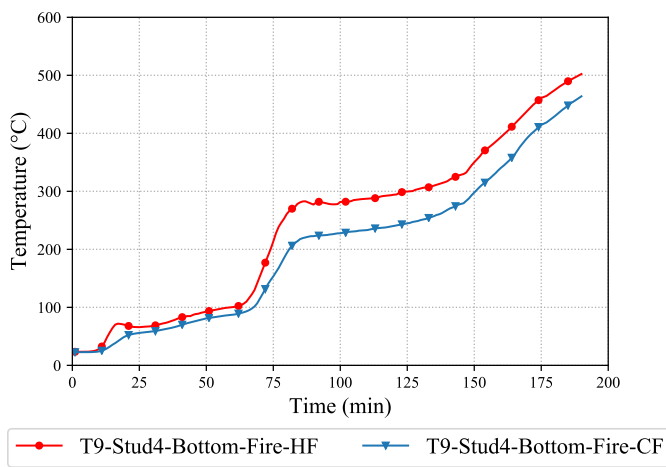
T9-Stud3-Bottom



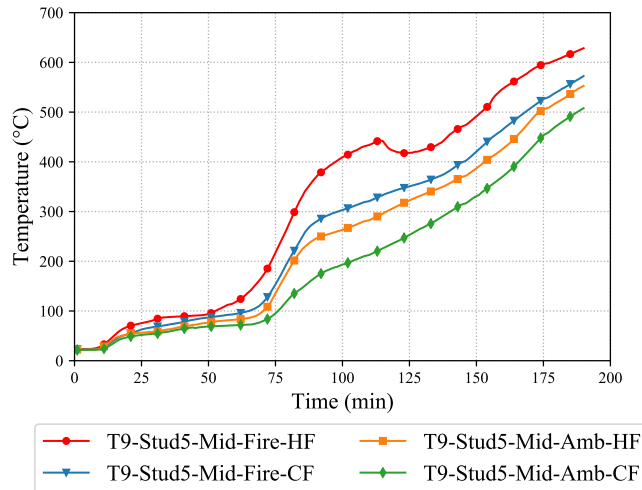
T9-Stud4-Top



T9-Stud4-Mid



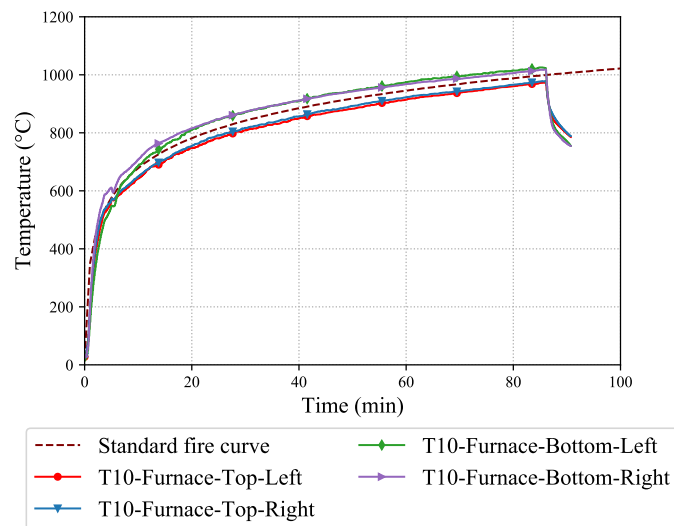
T9-Stud4-Bottom



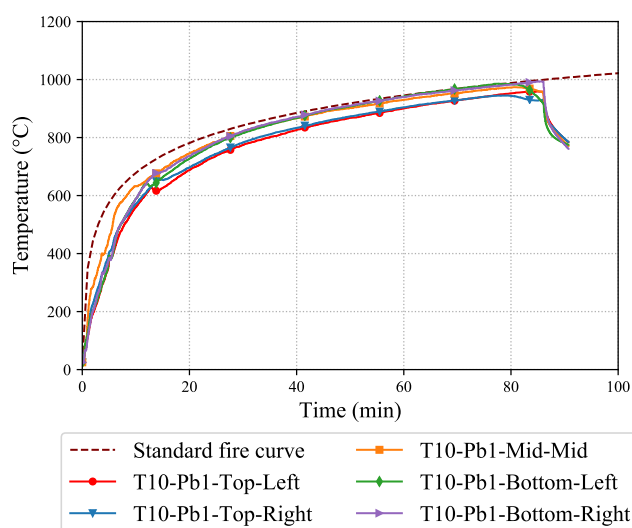
T9-Stud5-Mid

Test-T10

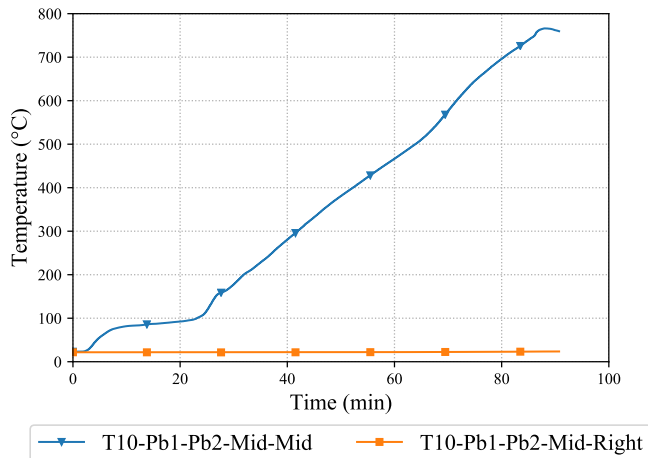
Test-T10 Plasterboard Time-Temperature Curves



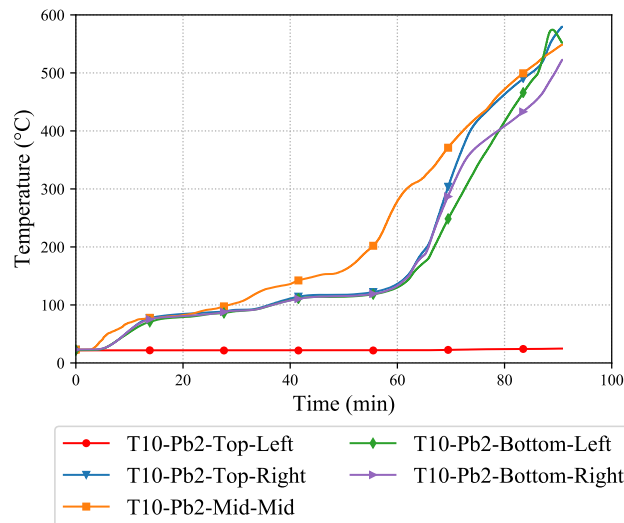
T10-Furnace



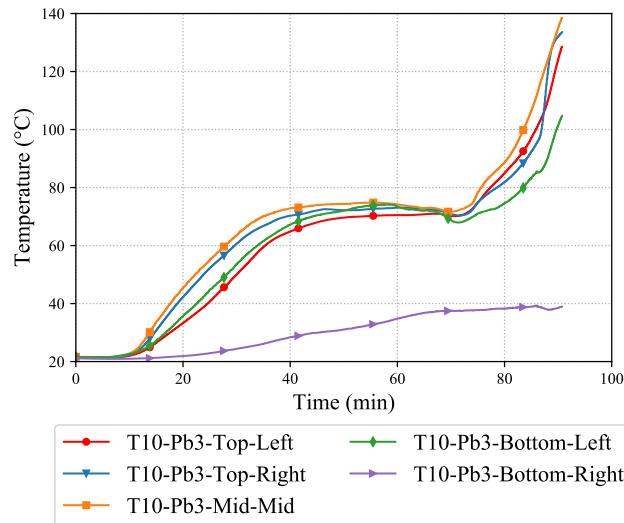
T10-Pb1



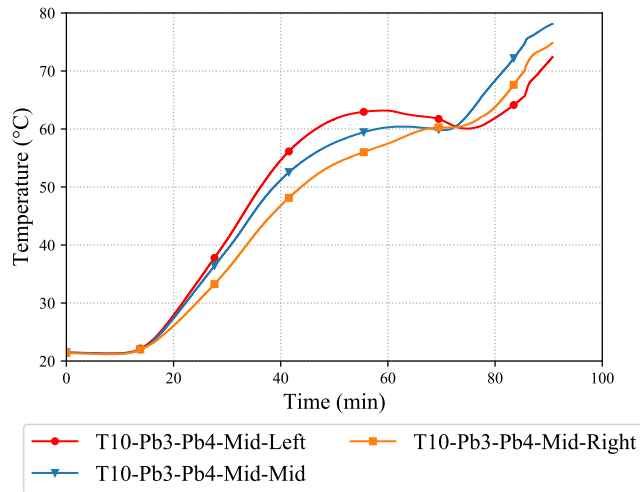
T10-Pb1-Pb2



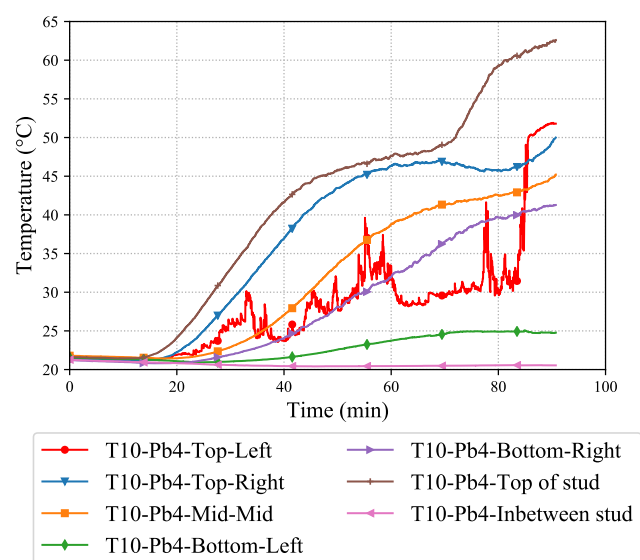
T10-Pb2



T10-Pb3

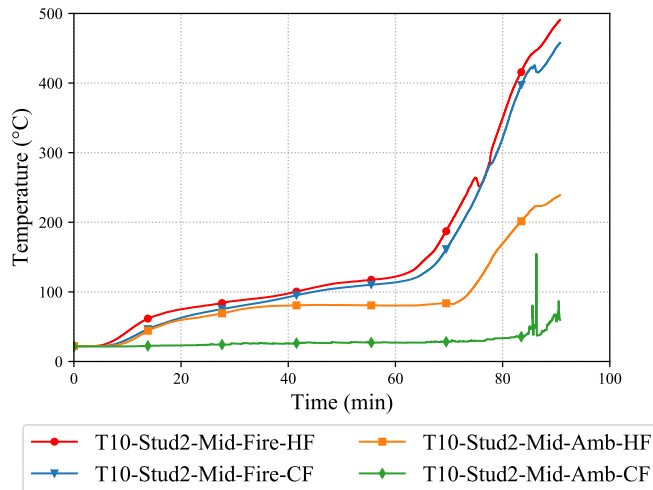


T10-Pb3-Pb4

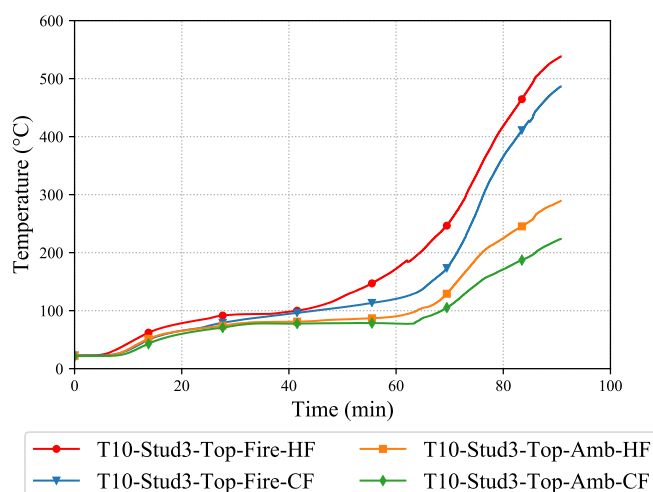


T10-Pb4

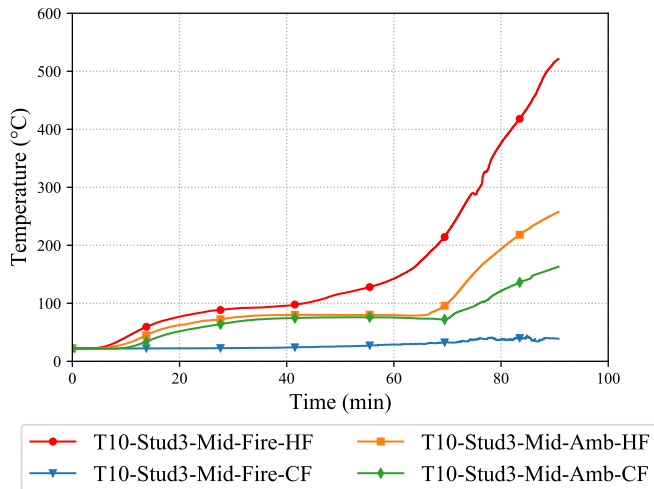
T10-Stud Time-Temperature Curves



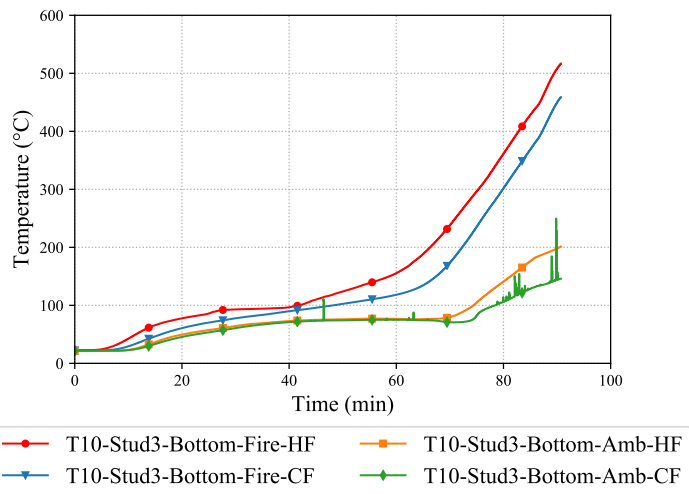
T10-Stud2-Mid



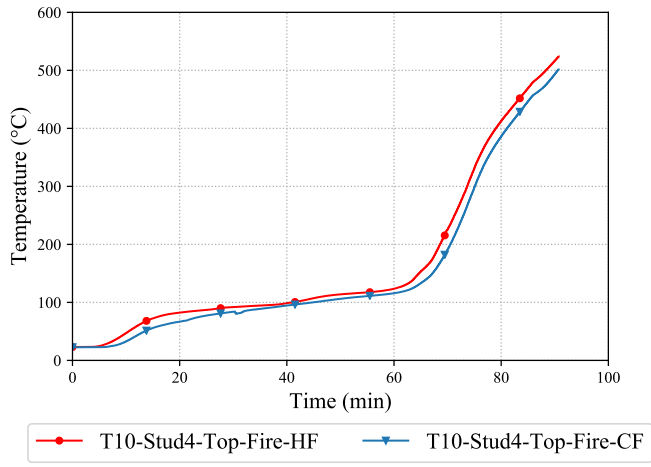
T10-Stud3-Top



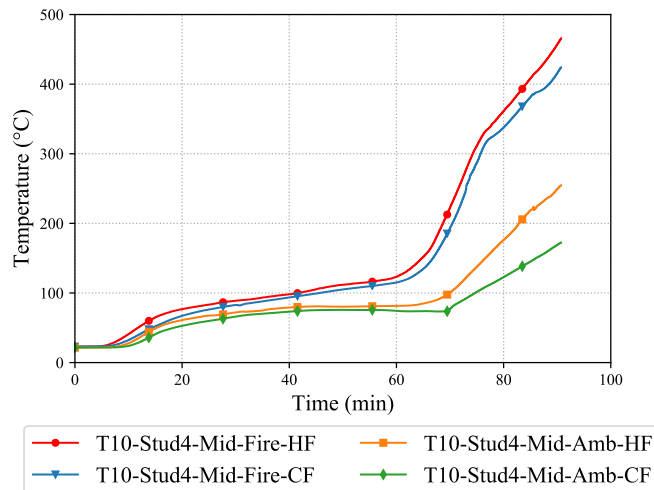
T10-Stud3-Mid



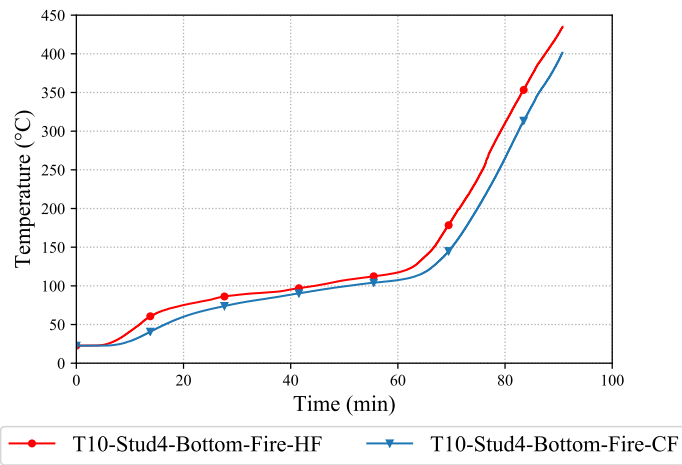
T10-Stud3-Bottom



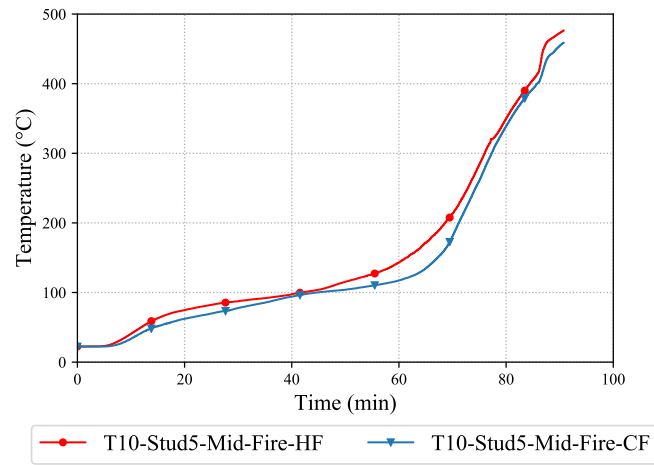
T10-Stud4-Top



T10-Stud4-Mid



T10-Stud4-Bottom



T10-Stud5-Mid

Bibliography

- ABCB, A. B. C. B. (2019). *Building Code of Australia / National Construction Code (NCC)*. Tech. rep.
- Alfawakhiri, F., M. A. Sultan, and D. H. MacKinnon (1999). “Fire Resistance of Load-bearing Steel-Stud Wall Protected with Gypsum Board: A Review”. English. In: *Fire Technology* 35.4, pp. 308–335. DOI: <http://dx.doi.org/10.1023/A:1015401029995>.
- Andreozzi, A., N. Bianco, M. Musto, and G. Rotondo (2013). “Influence of wall emissivity and convective heat transfer coefficient on the adiabatic surface temperature as thermal/structural parameter in fire modeling”. In: *Applied Thermal Engineering* 51.1–2, pp. 573–585. DOI: <https://doi.org/10.1016/j.applthermaleng.2012.09.024>.
- Ang, C. N. and Y. C. Wang (2009). “Effect of moisture transfer on specific heat of gypsum plasterboard at high temperatures”. In: *Construction and Building Materials* 23.2, pp. 675–686. DOI: <https://doi.org/10.1016/j.conbuildmat.2008.02.016>.
- Arendt, K. and M. Krzaczek (2014). “Co-simulation strategy of transient CFD and heat transfer in building thermal envelope based on calibrated heat transfer coefficients”. In: *International Journal of Thermal Sciences* 85, pp. 1–11. ISSN: 12900729. DOI: <10.1016/j.ijthermalsci.2014.06.011>.
- Ariyanayagam, A., G. Kyoungsoo, and M. Mahendran (2016a). *Ambient Temperature Axial Compressive Capacity of Peer Stud Walls Lined with Gypsum Plasterboards*. Tech. rep. QUT.
- Ariyanayagam, A. D., S. Kesawan, and M. Mahendran (2016b). “Detrimental effects of plasterboard joints on the fire resistance of light gauge steel frame walls”. In:

- Thin-Walled Structures* 107, pp. 597–611. ISSN: 02638231. DOI: [10.1016/j.tws.2016.07.003](https://doi.org/10.1016/j.tws.2016.07.003).
- Ariyanayagam, A. D. and M. Mahendran (Dec. 2014). “Experimental study of load-bearing cold-formed steel walls exposed to realistic design fires”. In: *Journal of Structural Fire Engineering* 5.4, pp. 291–329. ISSN: 20402325. DOI: [10.1260/2040-2317.5.4.291](https://doi.org/10.1260/2040-2317.5.4.291).
- Ariyanayagam, A. D. and M. Mahendran (June 2018a). “Experimental study of non-load bearing light gauge steel framed walls in fire”. In: *Journal of Constructional Steel Research* 145, pp. 529–551. ISSN: 0143974X. DOI: [10.1016/j.jcsr.2018.02.023](https://doi.org/10.1016/j.jcsr.2018.02.023).
- Ariyanayagam, A. D. and M. Mahendran (2018b). “Fire performance of load bearing LSF wall systems made of low strength steel studs”. In: *Thin-Walled Structures* 130, pp. 487–504. ISSN: 0263-8231. DOI: <https://doi.org/10.1016/j.tws.2018.05.018>.
- Ariyanayagam, A. D. and M. Mahendran (Mar. 2018c). “Residual capacity of fire exposed light gauge steel frame walls”. In: *Thin-Walled Structures* 124, pp. 107–120. ISSN: 02638231. DOI: [10.1016/j.tws.2017.11.048](https://doi.org/10.1016/j.tws.2017.11.048).
- Ariyanayagam, A. D. and M. Mahendran (Apr. 2019). “Influence of cavity insulation on the fire resistance of light gauge steel framed walls”. In: *Construction and Building Materials* 203, pp. 687–710. ISSN: 0950-0618. DOI: [10.1016/J.CONBUILDMAT.2019.01.076](https://doi.org/10.1016/J.CONBUILDMAT.2019.01.076).
- B.C. Son; H. Shoub (1973). *Fire Endurance Tests of Double Module Walls of Gypsum Board and Steel Studs*. Tech. rep. April, p. 27. DOI: [10.6028/NBS.IR.73-173](https://doi.org/10.6028/NBS.IR.73-173).
- Babrauskas, V. and R. B. Williamson (Aug. 1978). “The historical basis of fire resistance testing — Part I”. In: *Fire Technology* 14.3, pp. 184–194. ISSN: 1572-8099. DOI: [10.1007/BF01983053](https://doi.org/10.1007/BF01983053).
- Baleshan, B. and M. Mahendran (2016). “Fire design rules to predict the moment capacities of thin-walled floor joists subject to non-uniform temperature distributions”. In: *Thin-Walled Structures* 105, pp. 29–43. ISSN: 02638231. DOI: [10.1016/j.tws.2016.01.006](https://doi.org/10.1016/j.tws.2016.01.006).
- Batista Abreu, J. C. and B. W. Schafer (2015). “Fire performance of cold-formed steel walls”. English. PhD thesis. Ann Arbor, p. 243. ISBN: 9781369474626.

- Camotim, D., N. Silvestre, R. Gonçalves, and P. B. Dinis (2006). “GBT-based Structural Analysis of Thin-walled members: Overview, Recent Progress and Future Developments”. In: *Advances in Engineering Structures, Mechanics & Construction*. Ed. by Pandey, M., Xie, W.-C., and Xu, L. Dordrecht: Springer Netherlands, pp. 187–204. ISBN: 978-1-4020-4891-3. DOI: [10.1007/1-4020-4891-2_16](https://doi.org/10.1007/1-4020-4891-2_16).
- Chen, J. and B. Young (2007). “Experimental investigation of cold-formed steel material at elevated temperatures”. In: *Thin-Walled Structures* 45.1, pp. 96–110. DOI: <http://dx.doi.org/10.1016/j.tws.2006.11.003>.
- Chen, W., J. Ye, Y. Bai, and X. L. Zhao (2012). “Full-scale fire experiments on load-bearing cold-formed steel walls lined with different panels”. In: *Journal of Constructional Steel Research* 79, pp. 242–254. ISSN: 0143974X. DOI: [10.1016/j.jcsr.2012.07.031](https://doi.org/10.1016/j.jcsr.2012.07.031).
- Chen, W., J. Ye, Y. Bai, and X. L. Zhao (2014). “Thermal and mechanical modeling of load-bearing cold-formed steel wall systems in fire”. In: *Journal of Structural Engineering (United States)* 140.8, A4013002. ISSN: 07339445. DOI: [10.1061/\(ASCE\)ST.1943-541X.0000862](https://doi.org/10.1061/(ASCE)ST.1943-541X.0000862).
- Chen, W., J. Ye, Y. Bai, and X.-L. Zhao (2013). “Improved fire resistant performance of load bearing cold-formed steel interior and exterior wall systems”. In: *Thin-Walled Structures* 73, pp. 145–157. DOI: <https://doi.org/10.1016/j.tws.2013.07.017>.
- Cheng, S., L.-y. Li, and B. Kim (2015). “Buckling analysis of cold-formed steel channel-section beams at elevated temperatures”. In: *Journal of Constructional Steel Research* 104, pp. 74–80. DOI: <http://dx.doi.org/10.1016/j.jcsr.2014.10.004>.
- Collier, P. C. (2002). “Height extrapolation of fire resistant non-loadbearing steel framed walls”. In: *Fire and Materials* 26.3, pp. 111–120. ISSN: 03080501. DOI: [10.1002/fam.787](https://doi.org/10.1002/fam.787).
- Desmond, T. P., G. Winter, and T. Pekoz (1981). “Edge Stiffeners for Thin-Walled Members”. In: *Journal of the Structural Division* 107.2, pp. 329–353.
- Dias, Y., P. Keerthan, and M. Mahendran (2018a). “Fire performance of steel and plasterboard sheathed non-load bearing LSF walls”. In: *Fire Safety Journal*. ISSN: 03797112. DOI: [10.1016/j.firesaf.2018.11.005](https://doi.org/10.1016/j.firesaf.2018.11.005).

- Dias, Y., P. Keerthan, and M. Mahendran (Aug. 2018b). “Predicting the fire performance of LSF walls made of web stiffened channel sections”. In: *Engineering Structures* 168, pp. 320–332. ISSN: 18737323. DOI: [10.1016/j.engstruct.2018.04.072](https://doi.org/10.1016/j.engstruct.2018.04.072).
- Dias, Y., M. Mahendran, and K. Poologanathan (2019a). “Full-scale fire resistance tests of steel and plasterboard sheathed web-stiffened stud walls”. In: *Thin-Walled Structures* 137, pp. 81–93. ISSN: 0263-8231. DOI: <https://doi.org/10.1016/j.tws.2018.12.027>.
- Dias, Y., M. Mahendran, and K. Poologanathan (2019b). “Full-scale fire resistance tests of steel and plasterboard sheathed web-stiffened stud walls”. In: *Thin-Walled Structures* 137. December 2018, pp. 81–93. ISSN: 02638231. DOI: [10.1016/j.tws.2018.12.027](https://doi.org/10.1016/j.tws.2018.12.027).
- Dodangoda, M. T. (2018). “Improving the fire resistance of cold-formed steel frame wall systems using enhanced plasterboards”. PhD thesis. Queensland University of Technology. DOI: [10.5204/thesis.eprints.122456](https://hdl.handle.net/122456).
- Feng, M. and Y. C. Wang (2005). “An experimental study of loaded full-scale cold-formed thin-walled steel structural panels under fire conditions”. In: *Fire Safety Journal* 40.1, pp. 43–63. DOI: <http://dx.doi.org/10.1016/j.firesaf.2004.08.002>.
- Feng, M., Y. Wang, and J. Davies (2003a). “Structural behaviour of cold-formed thin-walled short steel channel columns at elevated temperatures. Part 2: Design calculations and numerical analysis”. In: *Thin-Walled Structures* 41.6, pp. 571–594. DOI: [http://dx.doi.org/10.1016/S0263-8231\(03\)00003-X](http://dx.doi.org/10.1016/S0263-8231(03)00003-X).
- Feng, M., Y. C. Wang, and J. M. Davies (Dec. 2003b). “Axial strength of cold-formed thin-walled steel channels under non-uniform temperatures in fire”. In: *Fire Safety Journal* 38.8, pp. 679–707. ISSN: 03797112. DOI: [10.1016/S0379-7112\(03\)00070-5](https://doi.org/10.1016/S0379-7112(03)00070-5).
- Feng, M., Y. C. Wang, and J. M. Davies (June 2003c). “Thermal performance of cold-formed thin-walled steel panel systems in fire”. In: *Fire Safety Journal* 38.4, pp. 365–394. ISSN: 03797112. DOI: [10.1016/S0379-7112\(02\)00090-5](https://doi.org/10.1016/S0379-7112(02)00090-5).

- Franssen, J.-M. and T. Gernay (2017). “Modeling structures in fire with SAFIR®: theoretical background and capabilities”. In: *Journal of Structural Fire Engineering* 8.3, pp. 300–323. DOI: [10.1108/JSFE-07-2016-0010](https://doi.org/10.1108/JSFE-07-2016-0010).
- Gerlich, J. T., P. C. Collier, and A. H. Buchanan (1996). “Design of light steel-framed walls for fire resistance”. In: *Fire and Materials* 20.2, pp. 79–96. ISSN: 03080501. DOI: [10.1002/\(SICI\)1099-1018\(199603\)20:2<79::AID-FAM566>3.0.CO;2-N](https://doi.org/10.1002/(SICI)1099-1018(199603)20:2<79::AID-FAM566>3.0.CO;2-N).
- Ghazi Wakili, K., E. Hugi, L. Wullschleger, and T. H. Frank (May 2007). “Gypsum Board in Fire — Modeling and Experimental Validation”. In: *Journal of Fire Sciences* 25.3, pp. 267–282. ISSN: 0734-9041. DOI: [10.1177/0734904107072883](https://doi.org/10.1177/0734904107072883).
- Gunalan, S., Y. Bandula Heva, and M. Mahendran (2015). “Local buckling studies of cold-formed steel compression members at elevated temperatures”. In: *Journal of Constructional Steel Research* 108, pp. 31–45. DOI: <http://dx.doi.org/10.1016/j.jcsr.2015.01.011>.
- Gunalan, S., P. Kolarkar, and M. Mahendran (2013). “Experimental study of load bearing cold-formed steel wall systems under fire conditions”. In: *Thin-Walled Structures* 65, pp. 72–92. DOI: <http://dx.doi.org/10.1016/j.tws.2013.01.005>.
- Gunalan, S. and M. Mahendran (2013a). “Development of improved fire design rules for cold-formed steel wall systems”. In: *Journal of Constructional Steel Research* 88, pp. 339–362. ISSN: 0143974X. DOI: [10.1016/j.jcsr.2013.05.021](https://doi.org/10.1016/j.jcsr.2013.05.021).
- Gunalan, S. and M. Mahendran (2013b). “Finite element modelling of load bearing cold-formed steel wall systems under fire conditions”. In: *Engineering Structures* 56, pp. 1007–1027. ISSN: 01410296. DOI: [10.1016/j.engstruct.2013.06.022](https://doi.org/10.1016/j.engstruct.2013.06.022).
- Gunalan, S. and M. Mahendran (2014). “Review of current fire design rules for cold-formed steel wall systems”. In: *Journal of Fire Sciences* 32.1, pp. 3–34. DOI: [10.1177/0734904113488336](https://doi.org/10.1177/0734904113488336).
- Horvat, A., Y. Sinai, and P. Tofilo (2009). “Semi-Analytical Treatment of Wall Heat Transfer Coupled to a Numerical Simulation Model of Fire”. In: *Numerical Heat Transfer, Part A: Applications* 55.6, pp. 517–533. DOI: [10.1080/10407780902821128](https://doi.org/10.1080/10407780902821128).
- ISO 834 (2014). *ISO 834-11:2014. Fire resistance tests – Elements of building construction – Part 11: Specific requirements for the assessment of fire protection to structural steel elements.*

- Jones, B. (2001). *Performance of Gypsum Plasterboard Assemblies Exposed to Real Building Fires.*
- Kankanamge, N. D. and M. Mahendran (2011). “Mechanical properties of cold-formed steels at elevated temperatures”. In: *Thin-Walled Structures* 49.1, pp. 26–44. DOI: <http://dx.doi.org/10.1016/j.tws.2010.08.004>.
- Keerthan, P. and M. Mahendran (2012a). “Numerical modelling of non-load-bearing light gauge cold-formed steel frame walls under fire conditions”. In: *Journal of Fire Sciences* 30.5, pp. 375–403. DOI: [10.1177/0734904112440688](https://doi.org/10.1177/0734904112440688).
- Keerthan, P. and M. Mahendran (2012b). “Numerical studies of gypsum plasterboard panels under standard fire conditions”. In: *Fire Safety Journal* 53, pp. 105–119. DOI: <http://dx.doi.org/10.1016/j.firesaf.2012.06.007>.
- Keerthan, P. and M. Mahendran (2013). “Thermal Performance of Composite Panels Under Fire Conditions Using Numerical Studies: Plasterboards, Rockwool, Glass Fibre and Cellulose Insulations”. English. In: *Fire Technology* 49.2, pp. 329–356. DOI: <http://dx.doi.org/10.1007/s10694-012-0269-6>.
- Kesawan, S. and M. Mahendran (2015). “Fire tests of load-bearing LSF walls made of hollow flange channel sections”. In: *Journal of Constructional Steel Research* 115, pp. 191–205. ISSN: 0143974X. DOI: [10.1016/j.jcsr.2015.07.020](https://doi.org/10.1016/j.jcsr.2015.07.020).
- Kesawan, S. and M. Mahendran (2016a). “Fire design rules for LSF walls made of hollow flange channel sections”. In: *Thin-Walled Structures* 107, pp. 300–314. ISSN: 02638231. DOI: [10.1016/j.tws.2016.05.022](http://dx.doi.org/10.1016/j.tws.2016.05.022).
- Kesawan, S. and M. Mahendran (2016b). “Predicting the performance of LSF walls made of hollow flange channel sections in fire”. In: *Thin-Walled Structures* 98, Part A, pp. 111–126. DOI: <http://dx.doi.org/10.1016/j.tws.2015.03.014>.
- Kesawan, S. and M. Mahendran (2016c). “Thermal performance of load-bearing walls made of cold-formed hollow flange channel sections in fire”. In: *Fire and Materials* 40.5, pp. 704–730. ISSN: 10991018. DOI: [10.1002/fam.2337](https://doi.org/10.1002/fam.2337).
- Kesawan, S. and M. Mahendran (Jan. 2018). “A Review of Parameters Influencing the Fire Performance of Light Gauge Steel Frame Walls”. In: *Fire Technology* 54.1, pp. 3–35. ISSN: 15728099. DOI: [10.1007/s10694-017-0669-8](https://doi.org/10.1007/s10694-017-0669-8).

- Klippstein, K. H. (1978). "STRENGTH OF COLD-FORMED STEEL STUDS EXPOSED TO FIRE." In: *Proceedings - Annual Public Water Supply Engineers' Conference* 1, pp. 513–555.
- Knobloch, M. and M. Fontana (2006). "Strain-based approach to local buckling of steel sections subjected to fire". In: *Journal of Constructional Steel Research* 62.1–2, pp. 44–67. DOI: <https://doi.org/10.1016/j.jcsr.2005.04.007>.
- Kodur, V. K. R. and M. A. Sultan (2006). "Factors Influencing Fire Resistance of Load-bearing Steel Stud Walls". English. In: *Fire Technology* 42.1, pp. 5–26. DOI: <http://dx.doi.org/10.1007/s10694-005-3730-y>.
- Kodur, V. K., M. A. Sultan, J. C. Latour, P. Leroux, and R. Monette (2013). *Experimental studies on the fire resistance of load-bearing steel stud walls*. Tech. rep. Research Report (National Research Council Canada. Construction); no. RR-343. DOI: <10.4224/21268483>.
- Kolaitis, D. I. and M. A. Founti (2013). "Development of a solid reaction kinetics gypsum dehydration model appropriate for CFD simulation of gypsum plasterboard wall assemblies exposed to fire". In: *Fire Safety Journal* 58, pp. 151–159. DOI: <http://dx.doi.org/10.1016/j.firesaf.2013.01.029>.
- Kolarkar, P. and M. Mahendran (2012). "Experimental studies of non-load bearing steel wall systems under fire conditions". In: *Fire Safety Journal* 53, pp. 85–104. DOI: <http://dx.doi.org/10.1016/j.firesaf.2012.06.009>.
- Kolarkar, P. and M. Mahendran (2014). "Experimental studies of gypsum plasterboards and composite panels under fire conditions". In: *Fire and Materials* 38.1, pp. 13–35. ISSN: 03080501. DOI: <10.1002/fam.2155>.
- Kolarkar, P. N. and M. Mahendran (2008). *Thermal performance of plasterboard lined steel stud walls*.
- Kontogeorgos, D., I. Mandilaras, and M. Founti (2011). "Scrutinizing Gypsum Board Thermal Performance at Dehydration Temperatures". In: *Journal of Fire Sciences* 29.2, pp. 111–130. DOI: <doi:10.1177/0734904110381731>.
- Lázaro, D., E. Puente, J. Peña, and D. Alvear (Mar. 2018). "Gypsum board failure model based on cardboard behaviour". In: *Fire and Materials* 42.2, pp. 221–233. ISSN: 10991018. DOI: <10.1002/fam.2483>.

- Lázaro, D., E. Puente, M. Lázaro, P. G. Lázaro, and J. Peña (2016). “Thermal modelling of gypsum plasterboard assemblies exposed to standard fire tests”. In: *Fire and Materials* 40.4, pp. 568–585. DOI: [10.1002/fam.2311](https://doi.org/10.1002/fam.2311).
- Li, Z. and B. Schafer (2010). “Buckling analysis of cold-formed steel members with general boundary conditions using CUFSM conventional and constrained finite strip methods”. In: *Proceedings of the 20th International Spec. Conference on Cold-Formed Steel Structures, St. Louis, MO*.
- Magnussen, B. F. and B. H. Hjertager (1977). “On mathematical modeling of turbulent combustion with special emphasis on soot formation and combustion”. In: *Symposium (International) on Combustion* 16.1, pp. 719–729. ISSN: 00820784. DOI: [10.1016/S0082-0784\(77\)80366-4](https://doi.org/10.1016/S0082-0784(77)80366-4).
- Malendowski, M. and A. Glema (2017). “Development and Implementation of Coupling Method for CFD-FEM Analyses of Steel Structures in Natural Fire”. In: *Procedia Engineering* 172, pp. 692–700. DOI: <https://doi.org/10.1016/j.proeng.2017.02.082>.
- Manzello, S. L., R. G. Gann, S. R. Kukuck, K. Prasad, and W. W. Jones (2005). “Real fire performance of partition assemblies”. In: *Fire and Materials* 29.6, pp. 351–366. DOI: [10.1002/fam.892](https://doi.org/10.1002/fam.892).
- Manzello, S. L., R. G. Gann, S. R. Kukuck, K. Prasad, and W. W. Jones (2007). “Performance of a non-load-bearing steel stud gypsum board wall assembly: Experiments and modelling”. In: *Fire and Materials* 31.5, pp. 297–310. DOI: [10.1002/fam.939](https://doi.org/10.1002/fam.939).
- McGrattan, K., S. Hostikka, R. McDermott, J. Floyd, C. Weinschenk, and K. Overholt (2013). *Fire Dynamics SimulatorUser’s Guide*. Maryland, USA.
- Mehaffey, J. R., P. Cuerrier, and G. Carisse (1994). “A model for predicting heat transfer through gypsum-board/wood-stud walls exposed to fire”. In: *Fire and Materials* 18.5, pp. 297–305. DOI: [10.1002/fam.810180505](https://doi.org/10.1002/fam.810180505).
- Nassif, A. Y., I. Yoshitake, and A. Allam (May 2014). “Full-scale fire testing and numerical modelling of the transient thermo-mechanical behaviour of steel-stud gypsum board partition walls”. In: *Construction and Building Materials* 59, pp. 51–61. ISSN: 09500618. DOI: [10.1016/j.conbuildmat.2014.02.027](https://doi.org/10.1016/j.conbuildmat.2014.02.027).

- Nguyen, Q. T., T. Ngo, P. Tran, P. Mendis, L. Aye, and S. K. Baduge (June 2018). “Fire resistance of a prefabricated bushfire bunker using aerated concrete panels”. In: *Construction and Building Materials* 174, pp. 410–420. ISSN: 09500618. DOI: [10.1016/j.conbuildmat.2018.04.065](https://doi.org/10.1016/j.conbuildmat.2018.04.065).
- Outinen, J., J. Kesti, and P. Mäkeläinen (1997). “Fire design model for structural steel S355 based upon transient state tensile test results”. In: *Journal of Constructional Steel Research* 42.3, pp. 161–169. DOI: [http://dx.doi.org/10.1016/S0143-974X\(97\)00018-7](http://dx.doi.org/10.1016/S0143-974X(97)00018-7).
- Pyl, L., L. Schueremans, W. Dierckx, and I. Georgieva (2012). “Fire safety analysis of a 3D frame structure based on a full-scale fire test”. In: *Thin-Walled Structures* 61, pp. 204–212. DOI: <http://dx.doi.org/10.1016/j.tws.2012.03.023>.
- Rahmanian, I. (2011). “Thermal And Mechanical Properties Of Gypsum Boards And Their Influences On Fire Resistance Of Gypsum Board Based Systems”. PhD thesis.
- Ranawaka, T. and M. Mahendran (2009a). “Distortional buckling tests of cold-formed steel compression members at elevated temperatures”. In: *Journal of Constructional Steel Research* 65.2, pp. 249–259. DOI: <http://dx.doi.org/10.1016/j.jcsr.2008.09.002>.
- Ranawaka, T. and M. Mahendran (2009b). “Experimental study of the mechanical properties of light gauge cold-formed steels at elevated temperatures”. In: *Fire Safety Journal* 44.2, pp. 219–229. DOI: <http://dx.doi.org/10.1016/j.firesaf.2008.06.006>.
- Rokilan, M. and M. Mahendran (Nov. 2019). “Elevated temperature mechanical properties of cold-rolled steel sheets and cold-formed steel sections”. In: *Journal of Constructional Steel Research*, p. 105851. ISSN: 0143974X. DOI: [10.1016/j.jcsr.2019.105851](https://doi.org/10.1016/j.jcsr.2019.105851).
- Rusthi, M., A. Ariyanayagam, M. Mahendran, and P. Keerthan (June 2017a). “Fire tests of Magnesium Oxide board lined light gauge steel frame wall systems”. In: *Fire Safety Journal* 90, pp. 15–27. ISSN: 03797112. DOI: [10.1016/j.firesaf.2017.03.004](https://doi.org/10.1016/j.firesaf.2017.03.004).
- Rusthi, M., A. D. Ariyanayagam, and M. Mahendran (June 2018). “Fire design of LSF wall systems made of web-stiffened lipped channel studs”. In: *Thin-Walled*

- Structures* 127, pp. 588–603. ISSN: 02638231. DOI: [10.1016/j.tws.2018.02.020](https://doi.org/10.1016/j.tws.2018.02.020).
- Rusthi, M., P. Keerthan, M. Mahendran, and A. Ariyanayagam (Dec. 2017b). “Investigating the fire performance of LSF wall systems using finite element analyses”. In: *Journal of Structural Fire Engineering* 8.4, pp. 354–376. ISSN: 20402325. DOI: [10.1108/JFFE-04-2016-0002](https://doi.org/10.1108/JFFE-04-2016-0002).
- SA (2014). *AS 1530.4 - Methods for fire tests on building materials, components and structures, Part 4: Fire-resistance test of elements of construction*.
- SA (2018). “AS/NZS 4600, Cold-formed steel structures, Sydney, Australia, 2018”. In:
- Sakumoto, Y., T. Hirakawa, H. Masuda, and K. Nakamura (2003). “Fire Resistance of Walls and Floors Using Light-Gauge Steel Shapes”. In: *Journal of Structural Engineering* 129.11, pp. 1522–1530. DOI: [doi:10.1061/\(ASCE\)0733-9445\(2003\)129:11\(1522\)](https://doi.org/10.1061/(ASCE)0733-9445(2003)129:11(1522)).
- Schafer, B. W., Z. Li, and C. D. Moen (2010). “Computational modeling of cold-formed steel”. In: *Thin-Walled Structures* 48.10, pp. 752–762. DOI: [http://dx.doi.org/10.1016/j.tws.2010.04.008](https://doi.org/10.1016/j.tws.2010.04.008).
- Schafer, B. W. (July 2008). “Review: The Direct Strength Method of cold-formed steel member design”. In: *Journal of Constructional Steel Research* 64.7-8, pp. 766–778. ISSN: 0143974X. DOI: [10.1016/j.jcsr.2008.01.022](https://doi.org/10.1016/j.jcsr.2008.01.022).
- Shahbazian, A. and Y. C. Wang (2011). “Application of the Direct Strength Method to local buckling resistance of thin-walled steel members with non-uniform elevated temperatures under axial compression”. In: *Thin-Walled Structures* 49.12, pp. 1573–1583. DOI: [http://dx.doi.org/10.1016/j.tws.2011.08.005](https://doi.org/10.1016/j.tws.2011.08.005).
- Shahbazian, A. and Y. C. Wang (2012). “Direct Strength Method for calculating distortional buckling capacity of cold-formed thin-walled steel columns with uniform and non-uniform elevated temperatures”. In: *Thin-Walled Structures* 53, pp. 188–199. DOI: <https://doi.org/10.1016/j.tws.2012.01.006>.
- Simulia Corporation, D. S. (2017). *Abaqus/CAE User’s Guide*.
- Standard Method of Fire Endurance Tests of Building Construction and Materials* (1989).

- Steau, E., M. Mahendran, and K. Poologanathan (Mar. 2020). “Elevated temperature thermal properties of carbon steels used in cold-formed light gauge steel frame systems”. In: *Journal of Building Engineering* 28, p. 101074. ISSN: 23527102. DOI: [10.1016/j.jobe.2019.101074](https://doi.org/10.1016/j.jobe.2019.101074).
- Sultan, M. A. (1996). “A model for predicting heat transfer through noninsulated unloaded steel-stud gypsum board wall assemblies exposed to fire”. In: *Fire Technology* 32.3, pp. 239–259. ISSN: 0015-2684. DOI: [10.1007/BF01040217](https://doi.org/10.1007/BF01040217).
- Sultan, M. A. and V. R. Kodur (2000). “Light-weight frame wall assemblies: Parameters for consideration in fire resistance performance-based design”. English. In: *Fire Technology* 36.2, p. 75.
- Sultan, M. A. (2015). “Effect of Gypsum Board Orientation on Board Fall-Off in Fire Resistance Test Assemblies”. In: *Advances in Gypsum Technologies and Building Systems, ASTM STP1588*, pp. 10–29. ISSN: 00660558. DOI: [10.1520/stp158820150013](https://doi.org/10.1520/stp158820150013).
- Thanasoulas, I. D., I. K. Vardakoulias, D. I. Kolaitis, C. J. Gantes, and M. A. Founti (2016). “Thermal and Mechanical Computational Study of Load-Bearing Cold-Formed Steel Drywall Systems Exposed to Fire”. In: *Fire Technology* 52.6, pp. 2071–2092. ISSN: 15728099. DOI: [10.1007/s10694-016-0604-4](https://doi.org/10.1007/s10694-016-0604-4).
- Thanasoulas, I. D., I. K. Vardakoulias, D. I. Kolaitis, C. J. Gantes, and M. A. Founti (June 2018). “Coupled thermo-mechanical simulation for the performance-based fire design of CFS drywall systems”. In: *Journal of Constructional Steel Research* 145, pp. 196–209. ISSN: 0143974X. DOI: [10.1016/j.jcsr.2018.02.022](https://doi.org/10.1016/j.jcsr.2018.02.022).
- Tofilo, P., M. A. Delichatsios, and G. W. H. Silcock (2005). “Effect of fuel sootiness on the heat fluxes to the walls in enclosure fires”. In: vol. 8, pp. 987–998. ISBN: 1817-4299. DOI: [10.3801/IAFSS.FSS.8-987](https://doi.org/10.3801/IAFSS.FSS.8-987).
- Young, B. K. and J. H. Gregory (1992). “Tests of Cold-Formed Channels with Local and Distortional Buckling”. In: *Journal of Structural Engineering* 118.7, pp. 1786–1803. DOI: [10.1061/\(ASCE\)0733-9445\(1992\)118:7\(1786\)](https://doi.org/10.1061/(ASCE)0733-9445(1992)118:7(1786)).
- Yu, C. and B. W. Schafer (May 2007). “Simulation of cold-formed steel beams in local and distortional buckling with applications to the direct strength method”. In: *Journal of Constructional Steel Research* 63.5, pp. 581–590. ISSN: 0143974X. DOI: [10.1016/j.jcsr.2006.07.008](https://doi.org/10.1016/j.jcsr.2006.07.008).